DIFFUSE BOUNDARY LAYER EFFECTS ON THE PROPERTIES OF METAL IN METAL MATRIX COMPOSITES MANUFACTURED WITH THE FIELD ASSISTED SINTERING TECHNIQUE

By

RYAN THOMAS HOOKE

A dissertation submitted to the

School of Graduate Studies

Rutgers, The State University of New Jersey

In partial fulfillment of requirements

For the degree of

Doctor of Philosophy

Graduate Program in Materials Science & Engineering

Written under the direction of

Dr. Lisa Klein

And approved by

_____

_____

_____

_____

_____

New Brunswick, New Jersey

JANUARY 2018

ABSTRACT OF THE DISSERTATION

Diffuse Boundary Layer Effects on the Properties of Metal in Metal Matrix Composites Manufactured with the Field Assisted Sintering Technique

By RYAN HOOKE

Dissertation Director:
Dr. Lisa Klein

The focus of this thesis is the effect of diffuse boundary layers on overall material failure in a tungsten heavy alloy (WHA) and D2 tool steel composite. D2 tool steel powder was sintered and joined to macroscopic WHA material using field assisted sintering, where high DC fields are introduced during the consolidation process. Diffuse boundary layers were formed during the field assisted sintering of the metal in metal matrix. To investigate the failure mechanisms, bulk and localized material properties of the metal in metal matrix composites were determined, including impact energy and hardness and findings suggest the diffusion zone is not uniformly thick. The diffusion zone is approximately 40-50 µm thick. Mechanical properties are generally bilaterally affected 30-40 µm deep into the WHA compared to wrought, but can also be affected up to 10 µm into the D2 steel, while the impact toughness of the composite is close to that of wrought D2 tool steel.

Material specimens were processed using equipment located at US Army RDECOM ARDEC. The resulting microstructures were examined using optical and scanning electron microscopy. Mechanical properties and failure properties were measured using equipment located at Rutgers University and US Army RDECOM ARDEC. The mechanical properties were evaluated at room temperature using custom impact testing and nanoindentation. Failure modes were examined with respect to metal boundary separation, crack initiation, and propagation due to strain, at, in, or near the diffusion affected zone and onset of fracture was found to occur at the interface as well as in the bulk WHA.

These methods and data were used in the determination of constitutive model parameters. A validation of model parameters was completed with an explicit finite element model of the composite configurations. Initial assessments of damage were modeled using Johnson-Cook material and damage models. The models were refined and results represent fracture location, deformation, and failure modes.

ACKNOWLEDGEMENTS

I am grateful to the US Army RDECOM ARDEC and my supervisors for allowing me to pursue my interests in science and engineering and for this nation, its freedoms, and all those who have served to allow such pursuits.

I would like to thank my professor and advisor Lisa Klein, who has provided the vision and scientific line to follow to this end as well as the fundamental building blocks to support my endeavors through her teachings.

My thanks go to Darold Martin, Kendall Mills, Shawn Ward, and Rob Garron for help in sample manufacturing, measurements, and instrumentation tutelage as well as David Geissler and Dr. Stephen Recchia for their FEA guidance.

I would also like to thank Shawn Ward and Dr. Adrian Mann for their consultation on nanoindentation and Shaw for running the nanoindentation experiments.

DEDICATION

To my lovely wife, you have been instrumental in many adventures including this one, allowed me to overcome writer's block and focus long enough to turn these efforts to words. Thank you for your patience, devotion, understanding, and your love.

To my father and mother who instilled great values, talked me into going to college, provided a wonderful home, upbringing, and for providing confidence I can do anything I put my mind to.

To my grandad for the great work ethic he gave me.

Table of Contents

List of Tables

List of Illustrations

List of Appendix Illustrations

Chapter 1: Introduction and Literature Review

1.1 Motivation for Work

The ability to predict material failure using finite element analysis (FEA) is very important to engineers to ensure safe, cost-effective designs. In order to accurately model designs one must determine the appropriate materials and damage models needed to accurately represent reality. Now and in the future, the behavior and response of additively manufactured composites and structures under load will need to be modeled and predicted with FEA to reduce cost and increase safety. With the rapid advances in powder metallurgy [1] and additive manufacturing, new methods are possible to make composites from pre-existing structures using diffusion to bond materials together. To accurately understand how the diffusion layer drives the surface energy to separate these materials, mechanical properties at the interface, and the overall failure of a composite made with a diffusion bond, field assisted sintering technique (FAST) was used to create material samples to study this diffusion affected zone (DAZ) in order to obtain material properties, characterize, and model failure. This work will allow similar composites to be engineered, manufactured using FAST, and incorporated into future applications.

1.2 Literature Review

Steel and tungsten alloys are used in combination in a wide range of applications including cutting tools, drills, rocket motors, shielding radiation, plasma-facing components, counterweights, and numerous defense related applications [2] [3] [4] [5]. Tungsten has made x-rays and incandescent light bulbs possible as well as revolutionized

the modern world [2]. Tungsten and tungsten alloys, unlike steel, have limited structural applications [6] and are often brazed, cemented, or coated onto higher strength materials to allow use in structural applications [7].

Tungsten alloys made from refractory metals have many applications, but tungsten heavy alloys made from non-refractory metals like iron and nickel are also important for many defense related applications [3] [8]. These Tungsten heavy alloys (WHAs) can be made with solid-state sintering [9], with FAST [10] and liquid phase sintering, where binders such as iron and nickel become liquid while the tungsten remains solid to form the structure [4]. They usually vary in alloy content and density from 80-97% density by weight tungsten [11]. Often the alloy composition, powder processing, and sintering process will dictate the grain size and final density of the WHAs [12]. These WHAs themselves have been studied to obtain their physical, mechanical, chemical and crystalline properties from the different processing [13] and alloying techniques [6], but little work has been carried out on making composites utilizing WHA diffusion bonded to steel with FAST. Thus, it is important to understand how the FAST method can affect a composite of steel and WHA itself, the matrix material of the WHA, and the interface when powder metallurgy and FAST are used to create the diffusion bond.

Powder metallurgy in combination with additive manufacturing (AM) are at the forefront of creating composites, which common steels can even be considered [1]. For this reason, looking into the future of AM and the ability to make composites, the ability to diffusion bond or sinter steel next to tungsten or tungsten alloy and understand the diffusion effects on fracture and hardness will be critical. Recent work shows the field

assisted sintering technique (FAST) may be a practical method for manufacturing tungsten alloys made from refractory metals and provides some insight into the mechanical properties which can be achieved at room and elevated temperatures [6] [10]. FAST uses pulsed direct electrical current (DC), in an inert atmosphere and uniaxial force which results in concentrated heat and pressure with high heating and cooling rates which promotes diffusion mechanisms; this leads to densification over grain growth which can control grain size and is ideal for nanopowders [14]. The pulsing high amperage DC flows through the powder, creating joule heating which in turn results in volumetric heating of the sample and promoting material transfer paths between the particles (**Figure 1.2.1**) [15] [14].

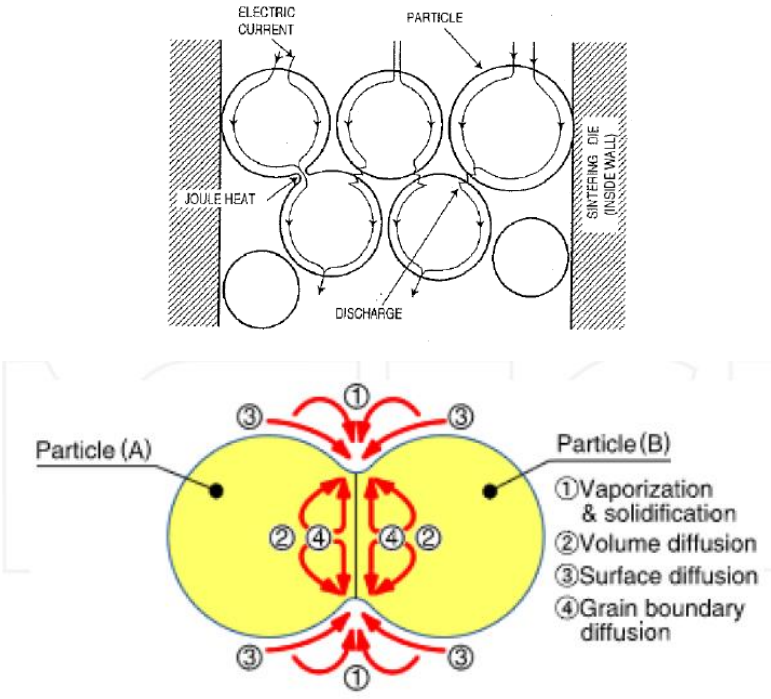

Figure 1.2.1 Current and Mass Flow During FAST [15]

FAST, also known as spark plasma sintering (SPS), pulsed electric current sintering (PECS) and plasma-assisted sintering (PAS), has been around for eight decades

and has shown advantages over conventional sintering methods with shorter sintering times, improved material properties and lower sintering temperatures; this has resulted in exponential growth in research in the field based on the quantity of scholarly papers published each year [16]. Other methods such as microwave heating also induce volumetric heating which produces smaller grain sizes for sintered tungsten powder. A. Mondal et al. reported grain sizes of 2.6 µm @ 95% Theoretical Density (TD) compared to 2.9 µm @ 90% TD and higher mechanical properties over conventional sintering methods [13]. These grain sizes are smaller than those reported for FAST which range from 5.82 µm – 39.46 µm, but FAST seems to produce higher relative densities up to 95.93% [17]. This may be attributed to the Joule heating plus high pressure, versus just the joule heating. Already FAST has been used to manufacture carbon fiber reinforced carbon composites using Ti3SiC2 tape when carbon fiber / carbon can be difficult to manufacture, [18] and it has proven to increase the limit strength of WHA [19].

The focus of the current work is mainly to show how diffusion defines the interface, the chemistry at the interface, and ultimately the mechanical properties across the bond of a composite manufactured with the FAST process. Specifically, the surface energy required to create a new surface between the matrix and particulate is what is of highest interest. It has been shown that finite element analysis modeling can be used to predict structural response, failure modes, and damage evolution given the material is characterized and a model exists [20] [21]. Therefore a series of FEA models were correlated to impact testing and model parameters fit to provide the best means of replicating the test results with the FEA. This method of using testing and FEA to aid in material model parameter generation has proven effective in accurate simulations [22].

Using empirical testing and FEA analysis to simulate the testing in combination with well-defined material models one can determine the mechanical properties and the diffusion layer thickness of a composite structure. This method will allow one to understand the significance of the diffusion bond and how the impact toughness of the bond can be used to predict the failure mechanism of the composite. This will be very useful when WHA or tungsten is diffusion-bonded to higher ductility and lower density materials in future applications.

The work of interest here is specifically based around the macroscopic and microstructure scale, as well as utilizing metal in metal matrix composites (MIMCs) formed utilizing field assisted sintering to understand the effect of the diffusion boundary layer on material properties. MIMCs will be defined as a bulk incompressible metal within another metal which is formed into a composite using the field assisted sintering technique (FAST). The process to form these MIMCs is also known as spark-plasma-sintering joining which is attractive for a range of materials from silicon carbide and graphite [23], stainless steel [24] to W/Fe via a titanium interlayer [25]. Specifically the effort will look at Tungsten Heavy Alloys (WHA) embedded in a D2 steel matrix manufactured using FAST. This work is to determine if this unique method of producing a MIMC can be used to control the microstructure at the material interface of the different metals utilizing diffusion control theory and determine how to model them.

Thus, the effect of the diffusion boundary layer on overall material failure will be well-characterized in this work. The localized material properties of the MIMC will be determined through theory and testing to include impact energy and hardness. Some bulk properties will be derived from test data and unique test fixtures designed because

an ASTM sample could not be fabricated. Failure and damage modes of the MIMC interfaces will be researched, imaged, and quantified as ductile or brittle in nature and the location of the failure with respect to the interface will be analyzed.

Material specimens were created using equipment located at the U.S. Army RDECOM's Armaments Research Development and Engineering Center, Picatinny Arsenal, NJ. Modeling, material microscopy, and mechanical and failure properties were obtained using equipment located at Rutgers the State University of New Jersey (New Brunswick, NJ), and U.S. Army RDECOM ARDEC. The data gathered was used to correlate energy-dispersive X-ray spectroscopy (EDS) to nanoindentation measurements and nanoindentation measurement to fracture toughness values gathered with the new impact fixture. These results were further used in the determination of constitutive finite element model parameters. A validation of damage model parameters was carried out using an explicit finite element model of the experiments conducted. Damage was modeled using Johnson-Cook damage models with modified material models. It is believed this type of material characterization methodology can be used to study and predict different MIMC matrix failure modes in the future.

Chapter 2: FAST Processing

2.1 FAST Sample Preparation

To understand the surface energy required to generate a new surface between WHA and steel, a single surface between WHA and steel needed to be manufactured. Since WHA is more difficult to machine than steel and WHA can be easily purchased in cube, sphere, or rod form, a cube would be the best starting geometry to generate a single surface interface. Therefore if a WHA cube could only have steel diffusion bonded to one surface, the steel could be held and the WHA cleaved off with an impactor. The amount of energy needed to break the WHA cube off of the steel would be directly proportional to the surface energy required to create a new surface assuming inelastic contact. Exact ASTM International standards would be difficult to manufacture given the resourcing, therefore using drop impact test equipment and standards as a guide [26] [27] [28] [29], a composite geometry of approximately 3mm x 3mm x 9mm (**Figure 2.1.1**) was identified as possible to produce and test. The important aspects of the sample were to have the diffusion layer perpendicular to the surfaces on which it would be held and impacted so no angular influences would be generated during the impact testing.

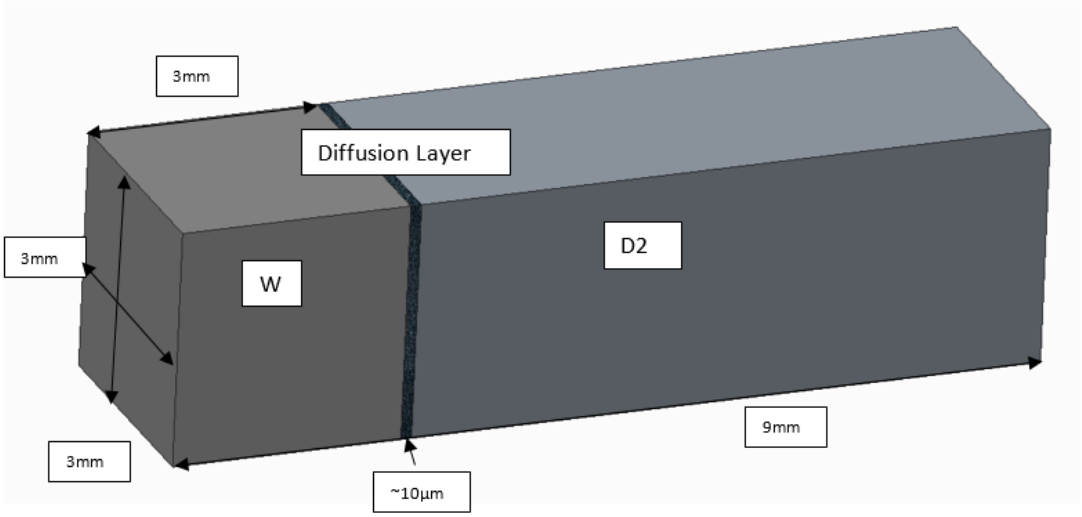

Figure 2.1.1 3mm x 3mm x 9mm WHA and D2 Composite Specimen

Class 4 [30], WHA cubes were sourced and a rapid prototyping specimen layout grid was 3D printed (**Figure 2.1.2**) to set the distance between the WHA cubes to allow the samples to later be machined out of the bulk specimen.

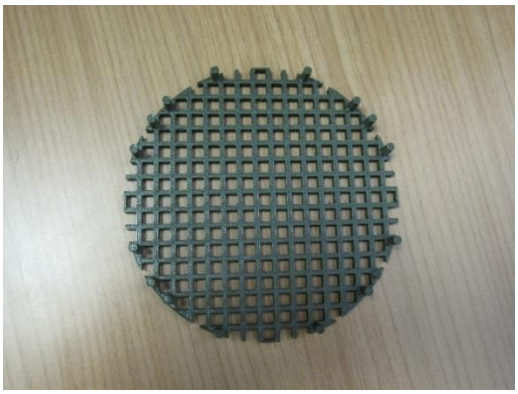

Figure 2.1.2 Specimen Layout Grid

Graphite dies were lined with graphite foil to protect the dies. A pre-weighed amount of D2 Nanopowder was then placed into the die, vibratory compacted and cold pressed to approximately 100 kg/cm^2 (1422 psi) (**Figure 2.1.3**). This layer was to protect the die and create a solid bed for WHA placement, but would also serve as a sacrificial

layer for the carbon uptake; G. Lee et al. have found the graphite to produce a carbide rich external shell on specimens from carbon diffusion during the FAST process [17] [31].

Figure 2.1.3 Cold Pressed D2 Powder Bed

The specimen layout grid was then used to arrange the tungsten cubes on the cold pressed powder bed, gently removed, and approximately 781 grams of D2 nanopowder was backfilled overtop of the cubes carefully trying not to disturb the pattern. The dies were then placed into the FAST (**Figure 2.1.4**).

Figure 2.1.4 Setup Placed into the FAST.

The WHA and D2 powder was then subjected to the FAST process (**Figure 2.1.5**) which utilized approximately 38.25 minutes of heating, reaching a maximum temperature of 1000°C in the sample, soaked at 1000°C under 565 kN, producing 50 MPa in the

sample, and cooled for approximately 30.5 minutes under 16 kN to generate the composite (**Figure 2.1.6**).

D2 Tool Steel sample with WHA cubes 15 minutes @ 1000°C @ 565 kN 781g D2 207 g WHA		
		Time (min)
1	Weighed out pre-layer and vibrated pre-layer	
2	Pre-Pressed pre-layer 100 kg/cm^2	~1:00
3	Positioned WHA with specimen layout gig	
4	Pre-press to 100 kN @ 0°C	2:00
5	Y-constant Heat 55% to 450°C	15:00
6	Pyro Ramp to to 800°C and full load (565 kN) @ 200°C/ minute in	3:30
7	Pyro Ramp to to 1000°C at Full load (565 kN) @ 200°C/ minute in	2:00
8	Soak at 1000°C and full load (565 kN)	15:00
9	Release Hold @ 1000°C and release to 16 kN	0:45
10	Cool to 0.0°C with 16 kN load	30:30
Took aboout 5:30 minutes to stabilize in soak Tmax = 1032°C Tc1max: 331°C Used N2 for chamber gas		

Figure 2.1.5 FAST Inputs for Specimen Manufacture

Figure 2.1.6 D2 and WHA Composite Manufactured with FAST

In order to obtain the required geometry, slivers were electro-discharge machined to create parallel surfaces to hold and the carbon-enriched layer was milled away to expose the WHA and create a perpendicular surface; an attempt to saw-cut the required 3mm x 3mm x 9mm samples out was made to no avail (**Figure 2.1.7**).

Figure 2.1.7 First Attempt at Sample Creation

The next attempt was to mill the front and back of the sample (350 rpms) to generate parallel faces to clamp, then a tungsten carbide slot cutter (100 rpm) was used to create perpendicular cuts to those surfaces to create thin slivers which contained the specimens. These slivers were then clamped vertically and the slot cutter used again to make perpendicular cuts to the face ensuring the diffusion layer will be in plane with the direction of impact and as close to perpendicular as possible (**Figure 2.1.8**). Milling speeds were kept low and coolant used to reduce the thermal loads so no thermal fatigue would be imparted in the sample during manufacturing.

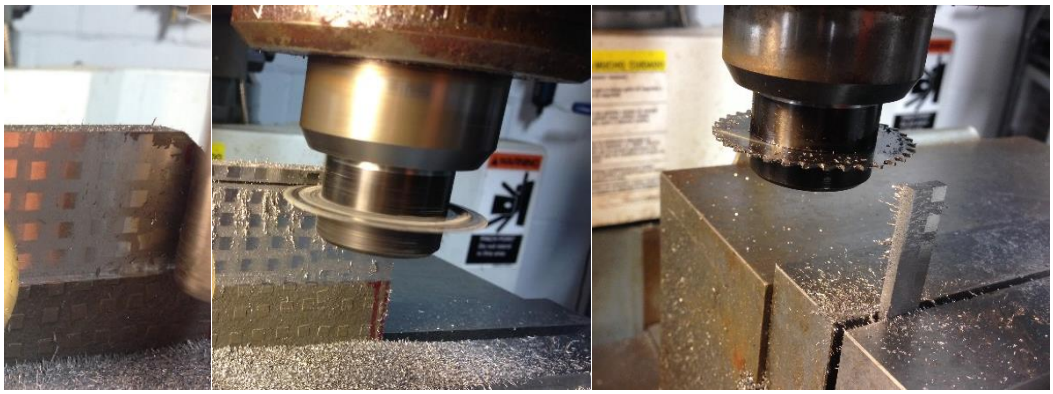

Figure 2.1.8 Machining the Sample Geometries.

The low speeds and feeds of the machining operation left a desirable surface finish of approximately 63 Ra, but were then lapped on 220 grit 3M sandpaper resulting in a < 15 Ra surface finish [32]. Tensile strength measurements in small specimen testing can be drastically affected by sample preparation and surface finish [33], thus five samples were further lapped with 3M 600 grit sandpaper and 800 grit paper (**Figure 2.1.9**). Then another ten samples were lapped with 220-3000 grit abrasive paper to determine how the impact toughness is affected by the surface roughness.

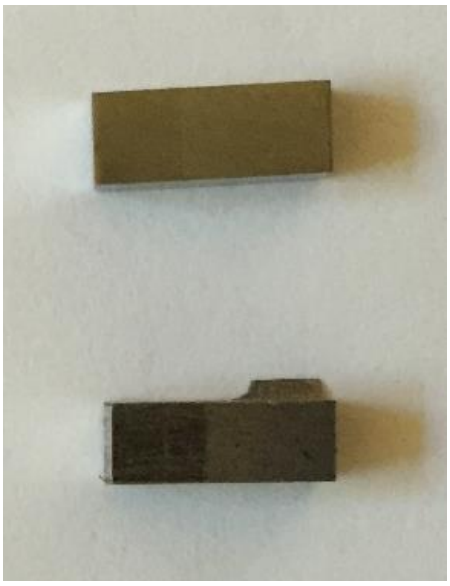

Figure 2.1.9 Specimen Samples, Lapped with 220-800 Grit Abrasive Paper (Top), as Machined (Bottom).

2.2 Microstructure Using Optical Microscopy

2.2.1 Polished Samples

The sample imaged in this chapter was mounted in the same manner as all samples for the effort. It was mounted with ClaroCit Powder ®, an acrylic with an 85 Shore D hardness [34], and polished using 320 grit silicon carbide foil, 9µm DiaPro on MD-Largo, and 3µm DiaPro on MD-Dac. The polished sample was first imaged with a microscope and looked like the left sample in **Figure 2.2.1** then etched resulting in the right image in **Figure 2.2.1**.

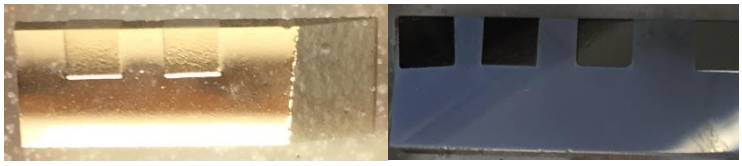

Figure 2.2.1 WHA in D2 Polished Sample (Left) Etched Sample (Right)

2.2.2 Interfaces in Polished Samples

The interface of the D2 to the WHA cube is shown in **Figure 2.2.2** at 100x to give an idea of the interface.

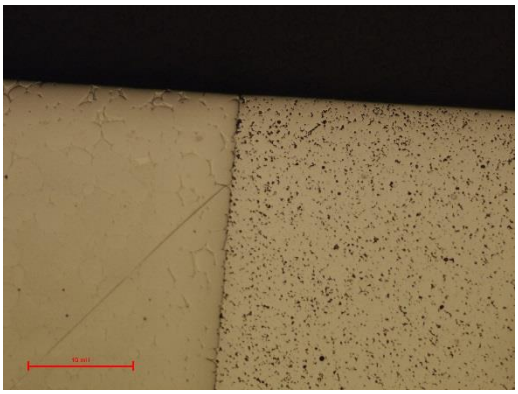

Figure 2.2.2 As Polished D2 Between WHA Interface 100x

At 500x, the height difference between the D2 and the WHA becomes noticeable as there are different focal planes needed to see each surface clearly as indicated in **Figure 2.2.3**. This interface is the one which gets machined away to create the impact samples, but it is interesting to see how the powder kept its spherical shape and though unconsolidated, diffusion between the WHA and the D2 appears to have occurred based on the images in **Figure 2.2.4**.

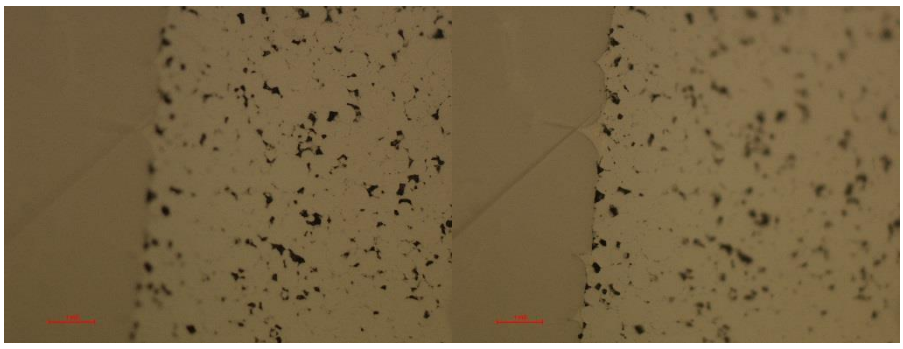

Figure 2.2.3 As Polished D2 Between WHA Interface 500x

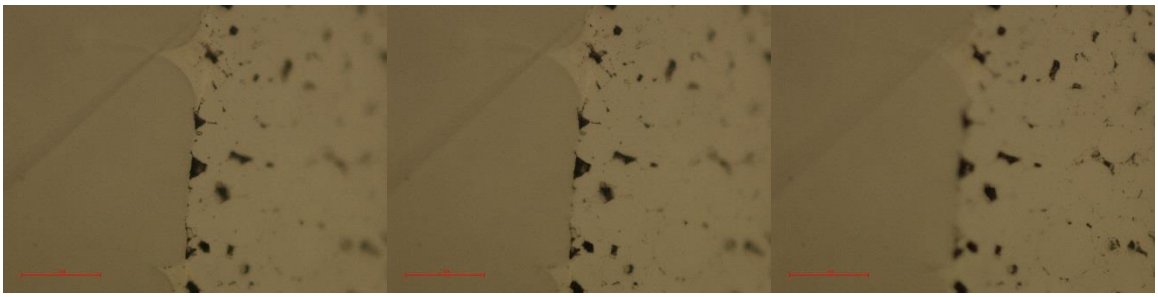

Figure 2.2.4 As Polished D2 between WHA Interface WHA Focus (Left) Interface Focus (Middle) D2 Focus (Right) 1000x

To confirm the bonding, another area was examined along the same interface and the images in **Figure 2.2.5** again suggest there is diffusion and adhesion occurring.

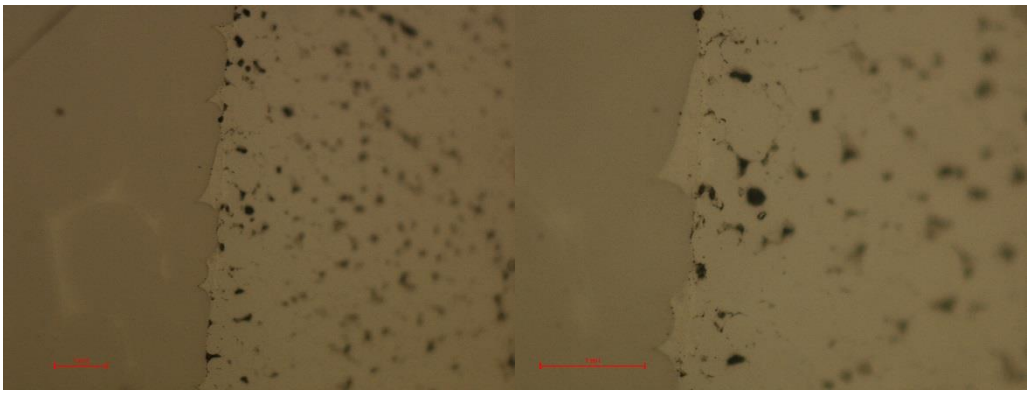

Figure 2.2.5 As Polished D2 Between WHA Interface 500x (Left) 1000x (Right)

Even at 50x the quality of adhesion and consolidation between the WHA and the D2 on the surface of interest is extremely promising as seen in **Figure 2.2.6**.

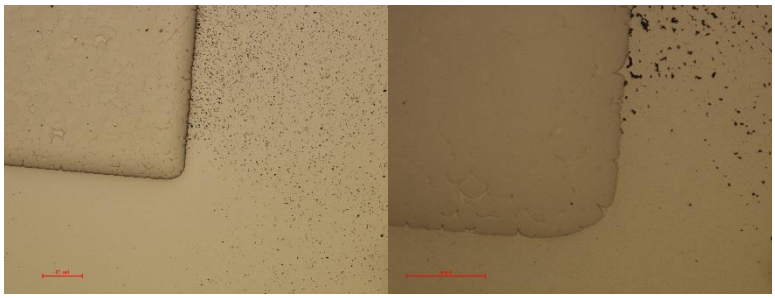

Figure 2.2.6 Bottom Right Corner of WHA 50x (Left), 200x (Right)

At 1000x (**Figure 2.2.7**) there is some porosity at the interface but there is also a distinct “halo” surrounding the WHA. This halo will be investigated with a SEM using EDS in later chapters and appendices while characterizing the interface.

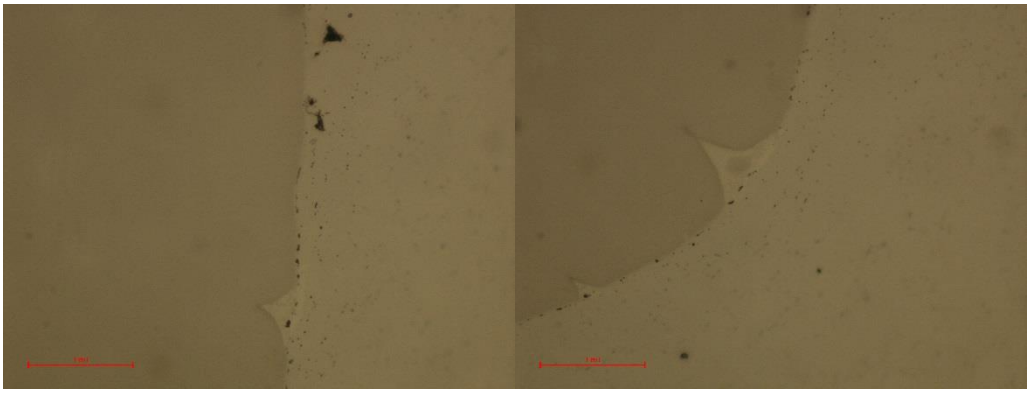

Figure 2.2.7 Bottom Right Corner 1000x

The interface of most interest is the one shown in **Figure 2.2.8** between the WHA and D2 which holds the diffusion layer created perpendicular to the FAST load which is also why there is good consolidation of the D2 and the reason the FAST was used to create the specimens in the first place.

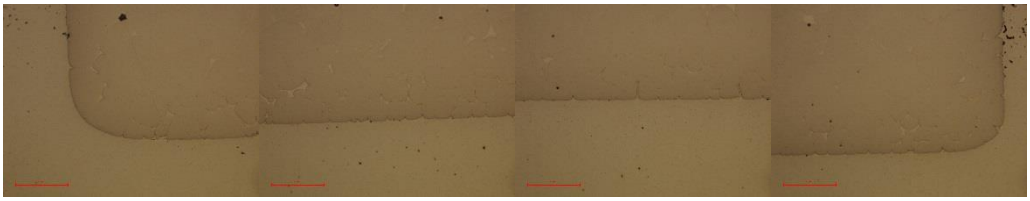

Figure 2.2.8 Bottom Edge of WHA 200x

AT 500x and 1000x (**Figure 2.2.9)** there is some porosity on the interface at the corner of the cube. This porosity could reduce the impact toughness as these are stress concentrations and locations where cracks can nucleate and grow [35].

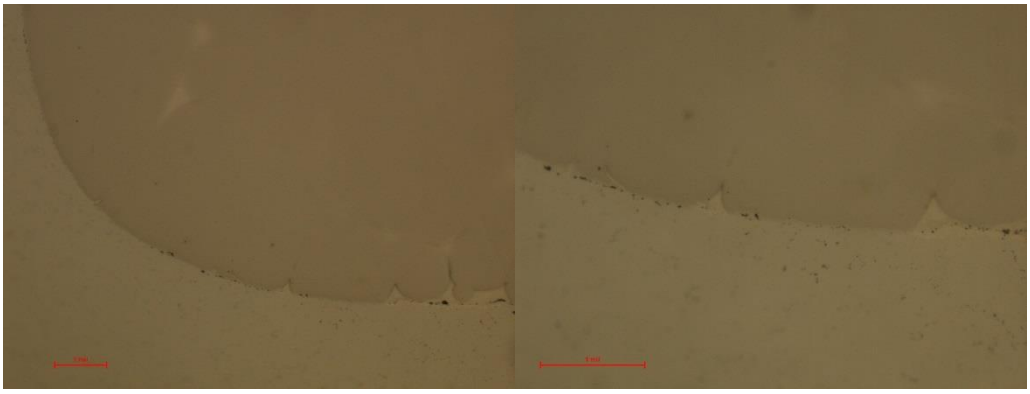

Figure 2.2.9 Bottom Left Corner of WHA 500x (Left) 1000x (Right)

2.2.3 Tungsten Heavy Alloy (WHA) in Polished Sample

The WHA has very low porosity compared to the D2 and nothing abnormal is present for this type of WHA as shown in **Figure 2.2.10**.

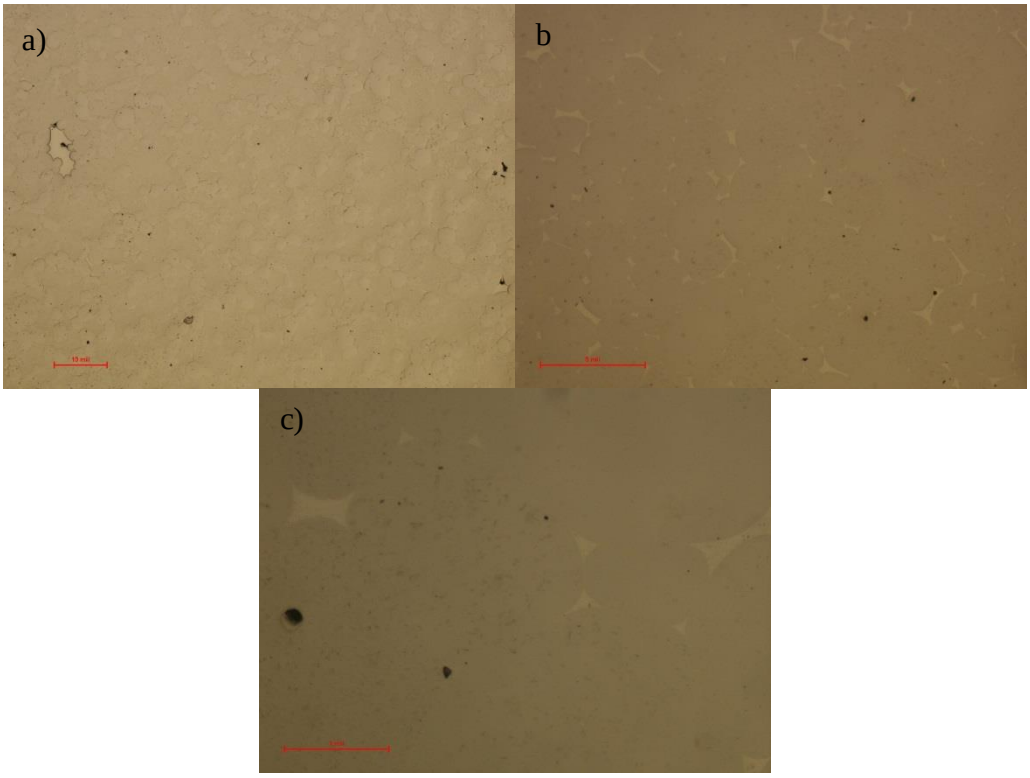

Figure 2.2.10 Polished WHA a) 100x b) 500x c) 1000x

2.2.4 Tool Steel (D2) in Polished Sample

Looking at the sample in the polished state at 100x, the D2 tool steel section between the WHA cubes show a lot of porosity as seen in **Figure 2.2.11**. The D2 has high porosity in these areas where pressure and joule heating could not work in tandem to consolidate the powder given the pressures used but could be consolidated with the FAST if desired.

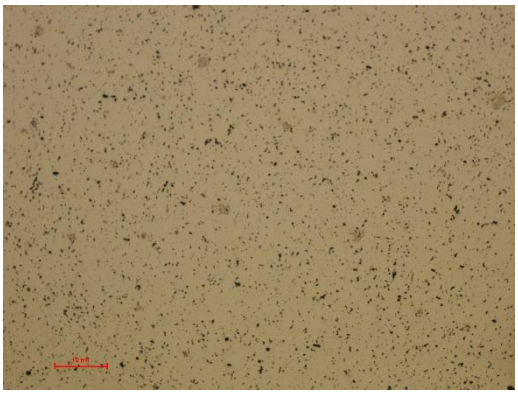

Figure 2.2.11 D2 Porosity in Between WHA Cubes 100x

Close to the top of the WHA cube where slightly better consolidation was achieved, there are some small islands of unknown material which are shown in the higher magnification images in **Figure 2.2.12** and **Figure 2.2.13**.

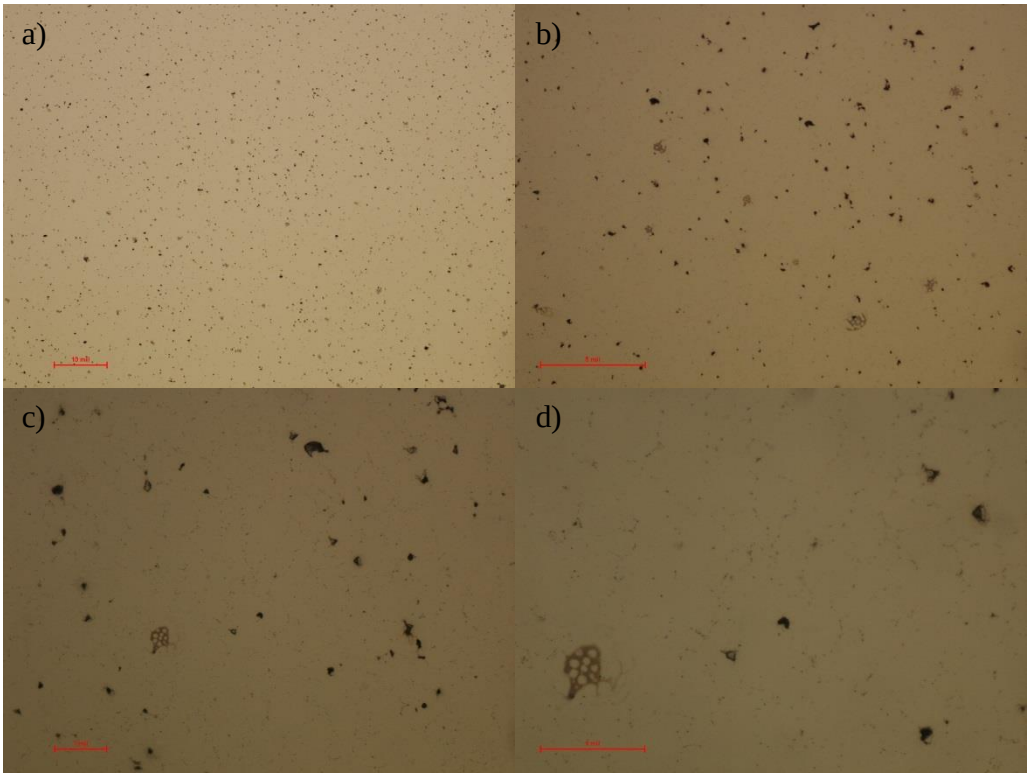

Figure 2.2.12 Polished D2 a) 100x b) 200x c) 500x d) 1000x

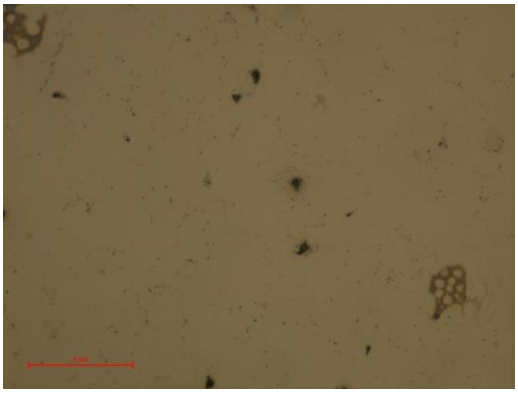

Figure 2.2.13 Polished D2 1000x

2.2.5 Microscopy of Etched Sample

The same polished sample used for the other optical images was then chemically etched with 3% Nital solution using a swab carrying the acid. The face of the sample was

gently and continually rubbed back and forth for approximately five-ten seconds, rinsed with water, and then rinsed with methanol and air dried under a hand dryer.

The etched sample in **Figure 2.2.14** highlights the unconsolidated D2 in between WHA cubes in the areas where the majority of the sintering energy was in the form of joule heating rather than pressure given the loads used.

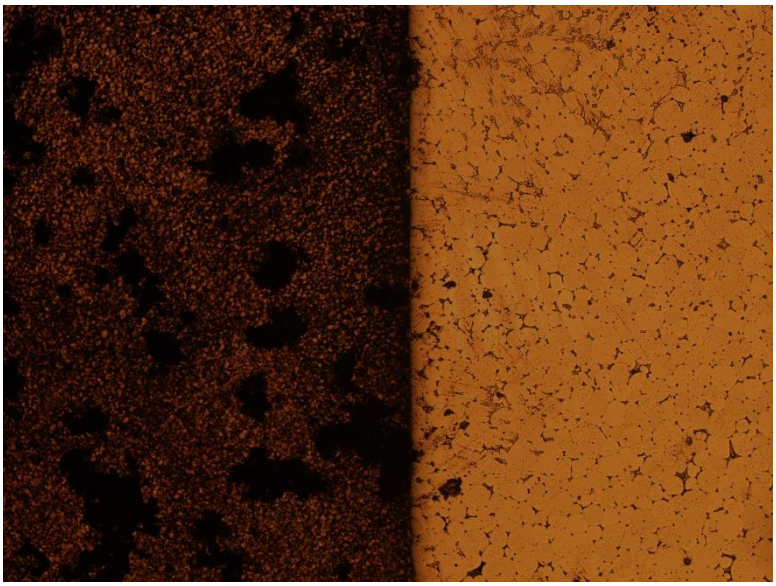

Figure 2.2.14 Etched Sample of Unconsolidated D2 Next to WHA 50x

The interface of interest and to be interrogated with the impact test is shown in **Figure 2.2.15**, where the consolidation of the D2 powder resulted in a good bond and high density. The halo which could be seen in the polished sample is much more pronounced now and seems to be adjacent to locations containing the iron and nickel binder matrix of the WHA.

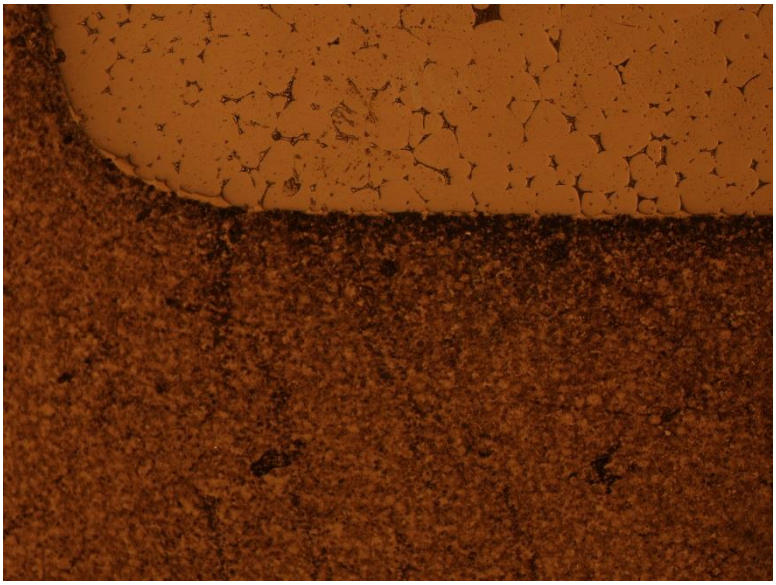

Figure 2.2.15 Bottom of Etched D2 to WHA Interface 100x

At 1000x the optical image in **Figure 2.2.16** shows the halo is also adjacent to the tungsten and the nickel and iron binder for the WHA. The D2 appears to mostly be a martensitic structure directly adjacent to the WHA with some ferritic structures.

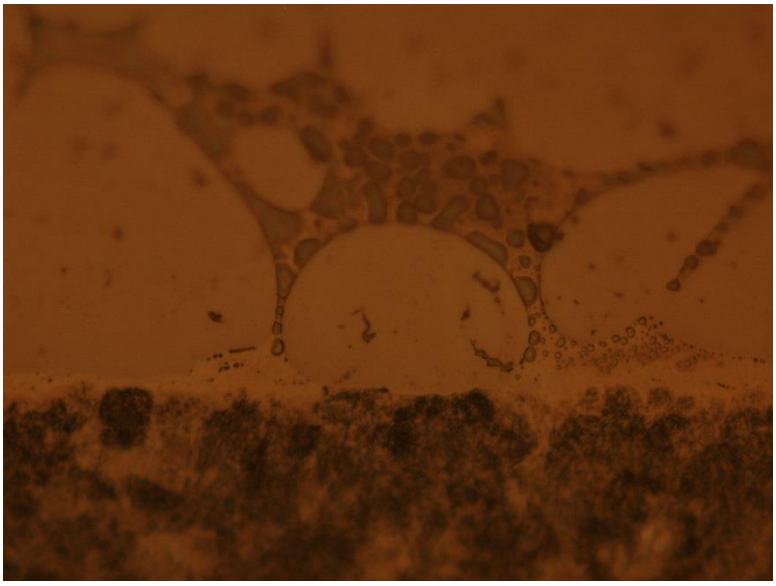

Figure 2.2.16 Etched D2 to WHA Interface 1000x

Upon further examination of the D2, the body-centered tetragonal (BCT) martensite seems to be the predominate phase with ferrite or austenite islands mixed in as shown in **Figure 2.2.17** [36]. The white islands are most likely body-centered cubic (bcc) α-iron ferrite given the sample is magnetic and was made around 1000°C and air cooling most likely prevented the formation of face-centered cubic (fcc) γ-iron austenite which is stable from 912°C -1394°C [36].

Figure 2.2.17 Etched D2 Showing Martensite and Ferrite 1000x

A better look at the interface (**Figure 2.2.18**) also reveals martensite with a few ferrite islands intermixed confirming the grain structure of the D2.

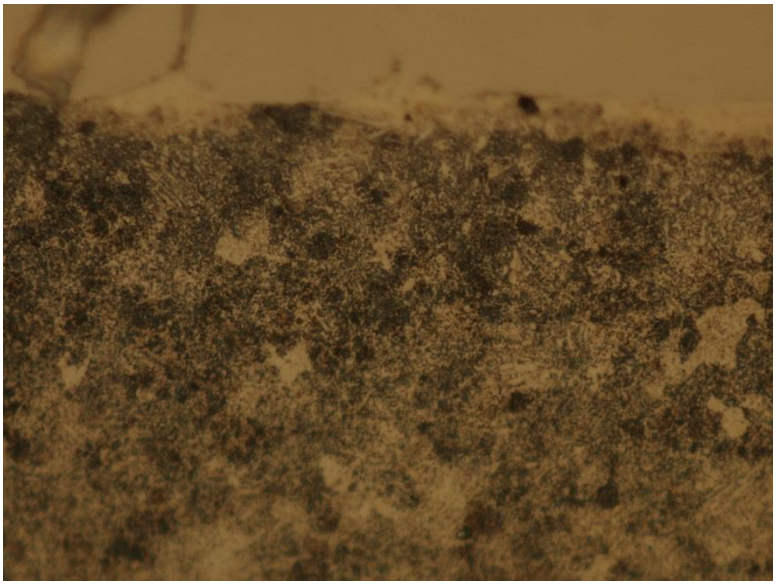

Figure 2.2.18 Etched D2 Interface with WHA Showing Martensite and Ferrite 1000x

The etched WHA cubes also show good consolidation as presented in (**Figure 2.2.19**).

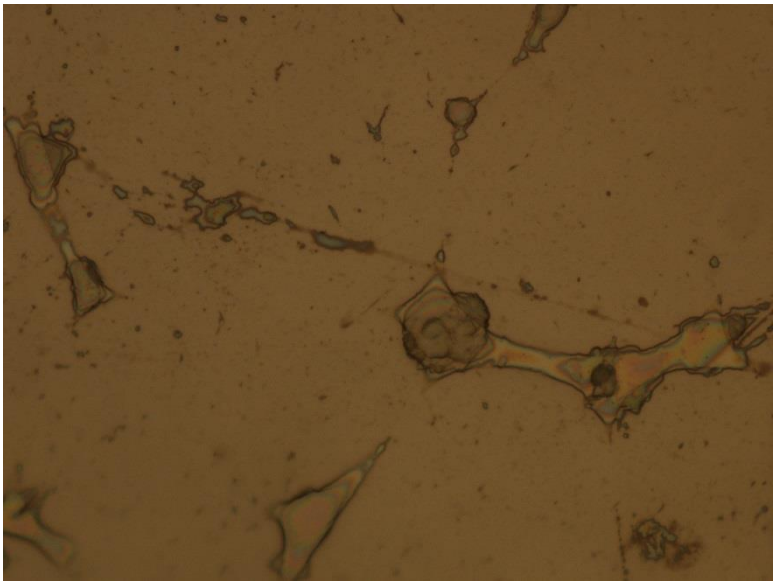

Figure 2.2.19 Etched WHA 1000x

For completeness, a better look at the D2 between the WHA cubes is also shown in **Figure 2.2.20**, which also shows the martensitic structure with some ferritic islands as well as powder which has partially necked.

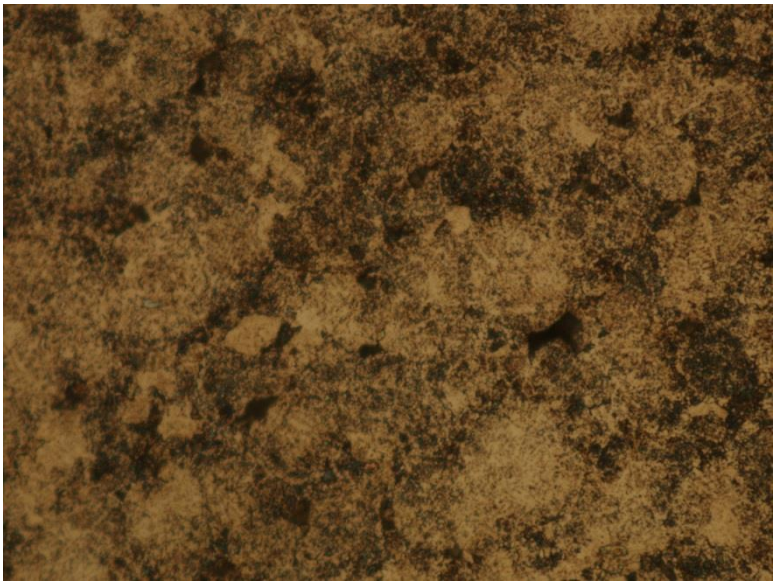

Figure 2.2.20 Etched D2 Between WHA Cubes Showing Martensite and Ferrite 1000x

Chapter 3: Microstructure and Chemical Analysis in Scanning Electron Microscope (SEM)

3.1 SEM and Energy Dispersive X-Ray Spectroscopy (EDS) of Etched Sample

Initial imaging characterization has been done with a JEOL JSM-6510LV Scanning Electron Microscope (SEM) at 30 kV which has been integrated with an EDS-IXRF at US Army ARDEC Picatinny Arsenal, NJ. The combination of an SEM and energy-dispersive X-ray spectroscopy (EDS) with x-ray fluorescence (XRF) provides a good method of examining multiple aspects of the material at once. At eighteen power, (**Figure 3.1.1**) the WHA cube's porosity can be seen but shows no migration of tungsten into the D2 steel matrix on the etched sample.

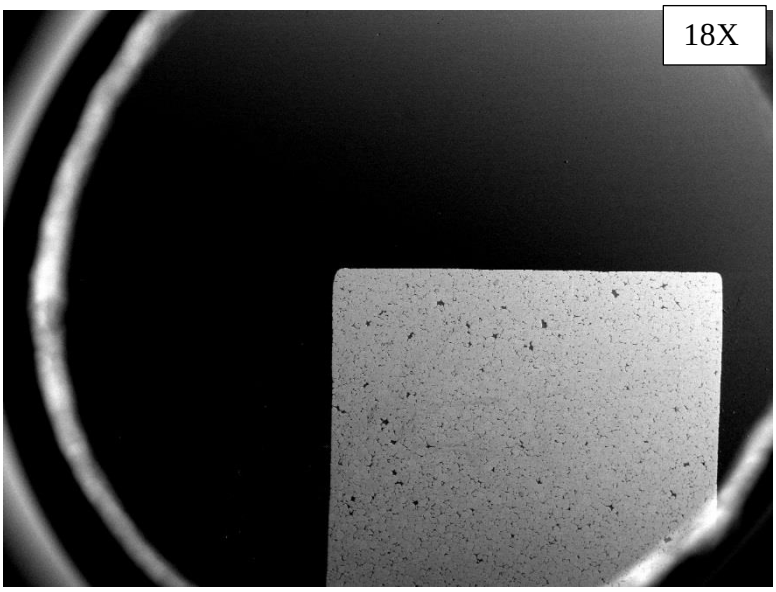

Figure 3.1.1 SEM Image at 30kV, 18x Magnification of FAST WHA in D2

Upon higher magnification at 220X and 550X (**Figure 3.1.2 and Figure 3.1.3**) one can start to see some voids in the tungsten, scratches on tungsten grains along with the iron and nickel matrix material of the WHA, as well as the slight halo surrounding the WHA and potentially some porosity at the interface.

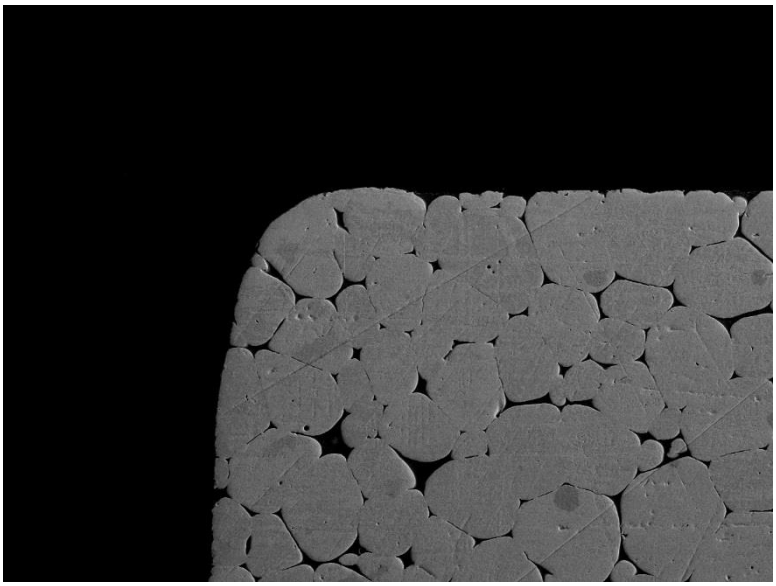

Figure 3.1.2 SEM Image at 30kV, 220x Magnification of FAST WHA in D2

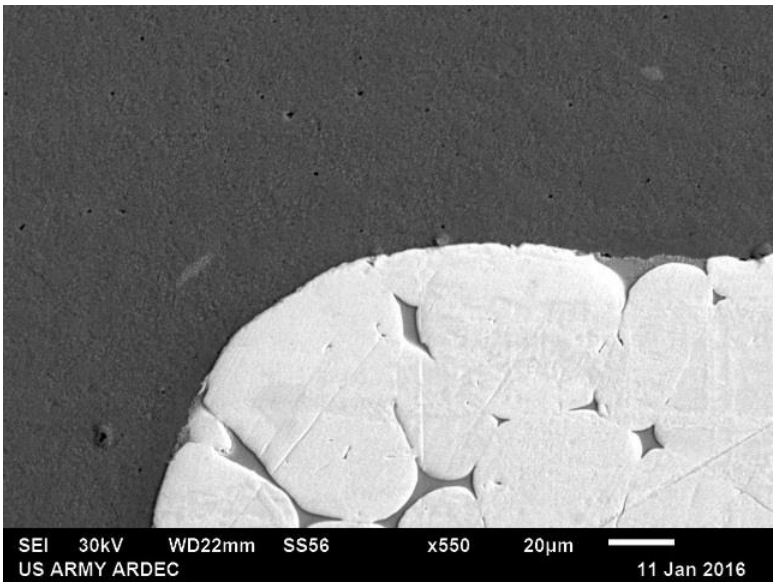

Figure 3.1.3 SEM Image at 30kV, 550x Magnification of FAST WHA in D2

Using the EDS-IXRF and picking a point far away from the WHA, one should get a chemical return which matches that of the D2 tool steel chemistry (**Figure 3.1.4 and Figure 3.1.5**)

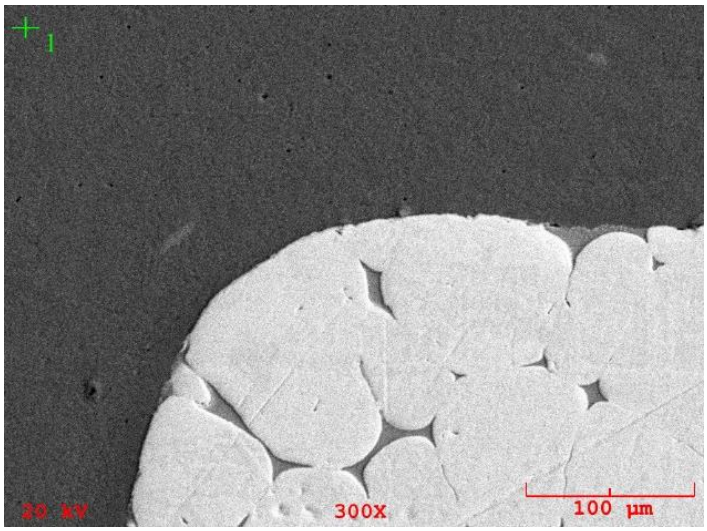

Figure 3.1.4 SEM Image at 20kV, 300x Magnification, EDS Taken at Point 1

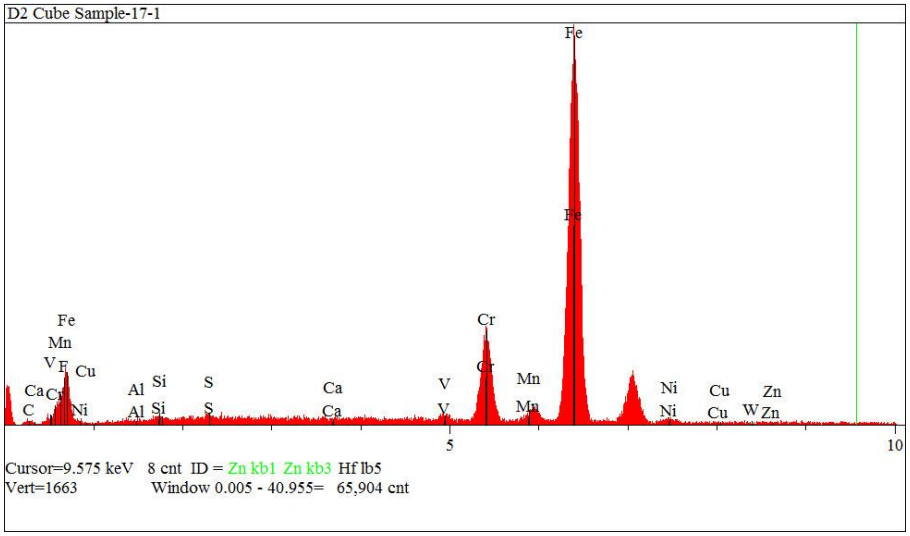

Figure 3.1.5 EDS Output Traces for Point 1 in Figure 14

As can be seen from the EDS in **Figure 3.1.5**, the D2 matrix material far from the tungsten heavy alloy does not have any sizeable tungsten peaks and the D2 alloy itself should not contain tungsten according to the standard (**Table 3.1-1**) [37]. Additionally

the arc spark results taken on the sample confirms the D2 chemistry is a little outside the requirements for Chromium (low), having trace nickel content but the carbon is almost twice the allowable limit (**Table 3.1-1**). This is not a surprise since the arc spark measurements were taken almost on the surface of the sample which was in direct contact with the graphite paper (the surface was prepared). To determine the diffusion rate of the carbon using the distance and arc spark measurements, the Van-Ostrand Dewey solution can be utilized [38].

$$\frac{Cc - Cs}{Co - Cs} = \text{erf}(\frac{x}{2\sqrt{Dt}})$$

Cs = surface concentration of element (carbon),

Co – initial element carbon level in Fe,

D = diffusion coefficient for element (carbon)

Cc = element (carbon) concentration as a function of distance X and time t from the surface at X = 0.

Assuming the carbon concentration just under the surface (from grinding) at 0.1 cm from the arc spark is Cc = 2.9685% and initial carbon level was Co = 1.50% (the average of the min and max from the D2 ASTM standard) and the surface concentration was 100% given the surface was exposed to graphite dies and graphite foil over approximate 1260 seconds the diffusion coefficient would be D = 6.707 x 10^{-7} cm^2/s. Given the diffusion rates for carbon are 1.7 x 10^{-6} cm^2/s into BCC at 800°C and 6.7 x 10^{-7} cm^2/s into the FCC at 1100°C such as this sample, this is a reasonable carbon diffusion rate [39]. Further, literature has shown the diffusion coefficient for carbon in H13 tool

steel to be 1.97×10^{-8} cm^2/s [40] as well as a good approximation of carbon diffusivity in austenite to be D = 0.12 exp (-16104.7/T), T in Kelvin for temperature, D in units of cm^2/s which would be 3.84535×10^{-7} cm^2/s at 1000°C [41].

Using the average carbon percentage of the P2 Marker, which will be discussed later, as the concentration at 5.571 mm from the surface resulted in a carbon concentration of Cc = 6.002% at time t = 1260 and the initial carbon level used was the average of the min and max from the D2 ASTM standard as before, Co = 1.50% and the surface concentration was 100% given the surface was exposed to graphite dies and graphite foil the diffusion coefficient would have to be D = 3.0847 x 10^{-5} cm^2/s which is fast.

ASTM A 681 - 08

TABLE 1 Chemical Requirements, % [A]

UNS Designation[B]	Type	Carbon		Manganese[C]		Phosporus	Sulfur,[D] max	Silicon		Chromium		Vanadium		Tungsten		Molybdenum	
		Min	Max	Min	Max	Max	Max	Min	Max	Min	Max	Min	Max	Min	Max	Min	Max
T30402	D2	1.40	1.60	0.10	0.60	0.030	0.030	0.10	0.60	11.00	13.00	0.50	1.10	...	...	0.70	1.200
T41907	S7	0.45	0.55	0.20	0.90	0.030	0.030	0.20	1	3	3.50	...	0.35	...	...	1.30	1.800

[A] Chemistry limits include product analysis tolerances. Unless otherwise specified, nickel plus copper equal 0.75 % max for all types.
[B] New designation established in accordance with Practice E 527 and SAEJ1086.
[C] Manganese limit is 1.0 % max for H13 resulfurized.
[D] Where specified, sulfur may be 0.06 to 0.15 % to improve machinability.

Arc Spark Results

	Fe	C	Mn	Si	P	S	Ni	Cr	
Percentage	83.47894	2.9685	0.31055	0.49328	0.02530	0.00833	0.09135	10.75337	
SD %	0.12	3.04	0.14	0.11	3.74	0.33	0.13	0.10	
	Cu	Mo	V	Ti	Al	Nb	W	As	
Percentage	0.01567	1.08412	0.76945	0.00209	0.00830	0.00508	-0.00247	0.0023	
SD %	2.27	.51	.57	.67	20.72	0.37	39.73	4.40	
	Sn	Co	Pb	B	Zr	Bi	Mg	Zn	Fe4
Percentage	0.00157	0.02100	0.00217	0.0031	0.00425	0.00179	0.01014	-0.05540	25.1215
SD %	8.01	.81	8.33	14.45	6.61	11.83	5.76	0.47	1.32

Table 3.3-1 ASTM D2 Tool Steel Chemical Requirements [31] (Top) Arc Spark Results (Bottom)

EDS was then used to identify the chemistry within the matrix material of the WHA to understand if any of the D2 elements diffused into the matrix material (**Figure 3.1.6 and Figure 3.1.7**).

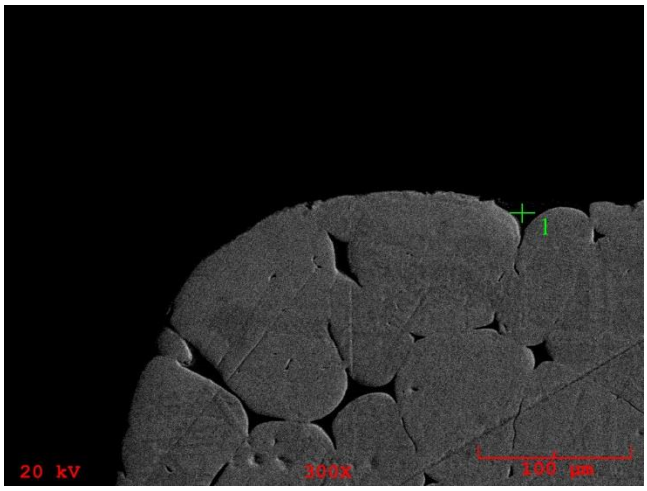

Figure 3.1.6 SEM at 20 kV, 300x Magnification, EDS Taken at Point 1

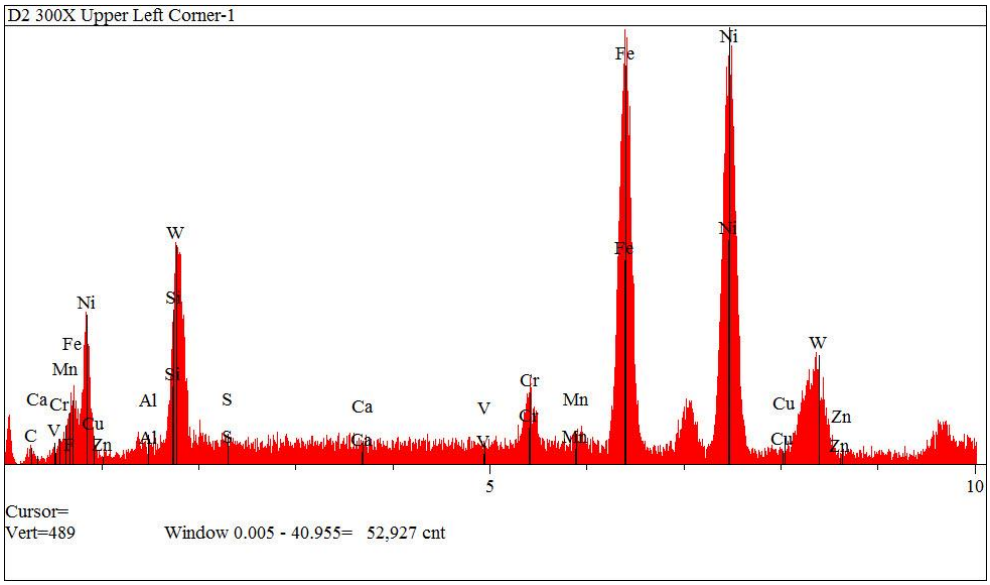

Figure 3.1.7 EDS of Point 1 In Figure 16 Showing Matrix Material Signal.

The matrix material of the WHA on the other hand does have noticeable tungsten peaks along with substantial Fe and Ni which are the major alloying elements of WHA but also elements from the D2 trace which suggests diffusion of elements from the D2

into the WHA matrix is occurring, but could be contamination from sample preparation at this point and other areas around the cube and other samples were to be investigated. Upon further examination of the same location it can be seen that there is a slight void (point 1 in **Figure 3.1.8**), and a visible diffusion boundary layer around the WHA cube is noticeable where the WHA matrix is adjacent to the D2.

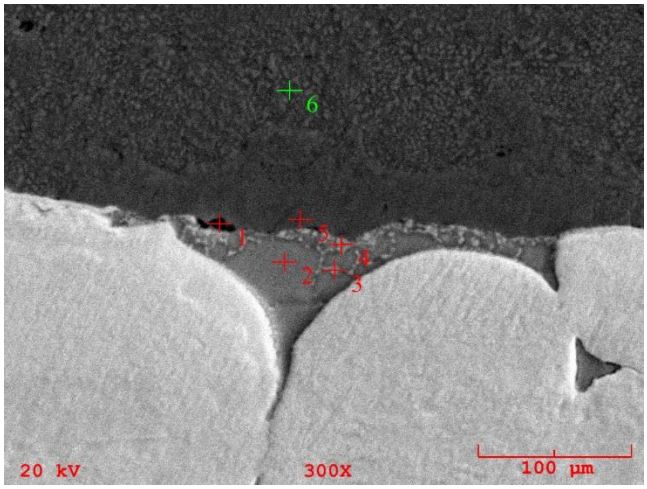

Figure 3.1.8 EDS of the Void and Other Artifacts of the Image.

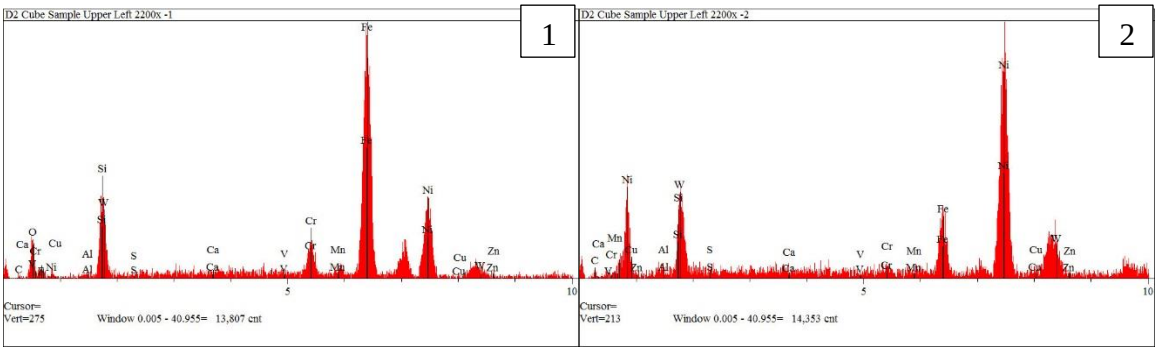

Figure 3.1.9 EDS Results for Points 1 (Left) and 2 (Right) in Image 3.1.8

EDS of the void (point 1) compared to what was thought to be a large nickel island (point 2) (**Figure 3.1.9**) potentially shows an oxide may exist in this area. The difference in concentrations between locations three and four suggests there is a higher concentration of iron near the WHA, but again more locations and samples will need to

be investigated as well as further investigation of elemental concentrations in the D2 and the WHA to determine the concentration gradient. Thus, the arc spark results of the D2 sample in **Table 3.3-2** will further be used to help determine concentration gradients and diffusion rates in following chapters. Points three through six are shown in **Figure 3.1.10** and **Figure 3.1.11** and the original D2 point from **Figure 3.1.4** is again shown for reference in **Figure 3.1.12**.

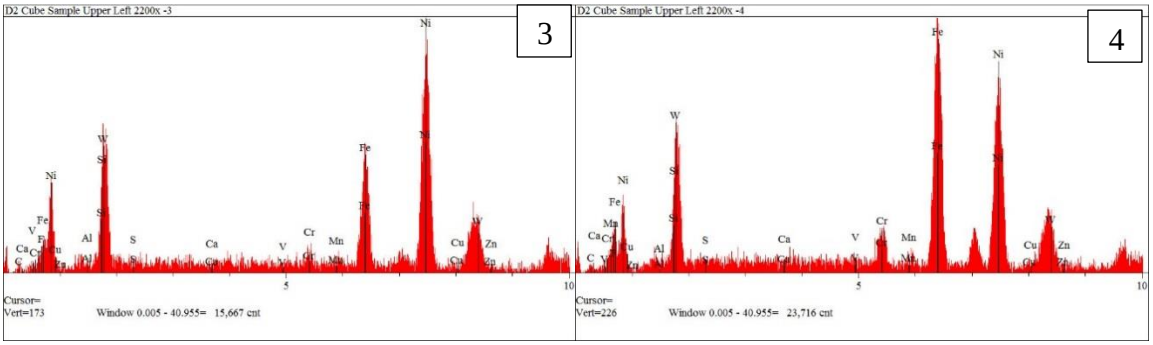

Figure 3.1.10 EDS Results for Points 3 (Left) and 4 (Right) in Image 3.1.8

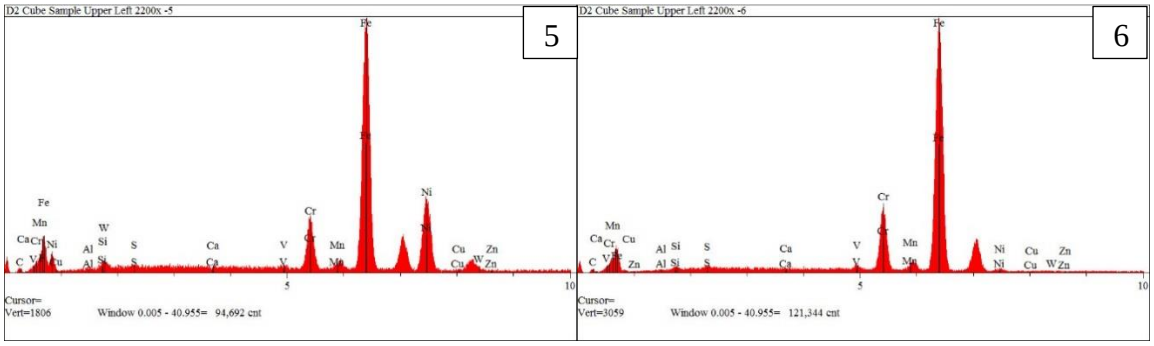

Figure 3.1.11 EDS Results for Points 5 (Left) and 6 (Right) in Image 3.1.8

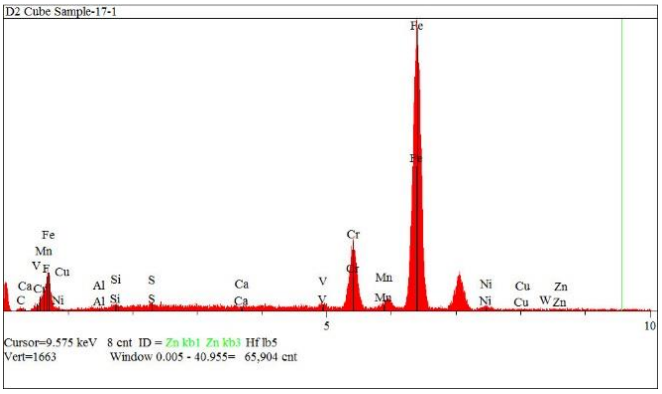

Figure 3.1.12 D2 Only EDS Signal From Figure 3.1.4

It was then decided to try to map the concentrations over what is presumed to be the diffusion affected zone (**Figure 3.1.13**) and to determine where the diffusion affected zone ends by comparing the EDS traces to the original D2 point in **Figure 3.1.4** which was far away from the WHA. EDS of points 1-3 (**Figure 3.1.14**) suggests there are still trace amounts of nickel which have diffused out of the WHA matrix in point 3, but point

2 closely resembles D2 traces so the diffusion affected zone is most likely smaller than the distance between point 2 and the WHA.

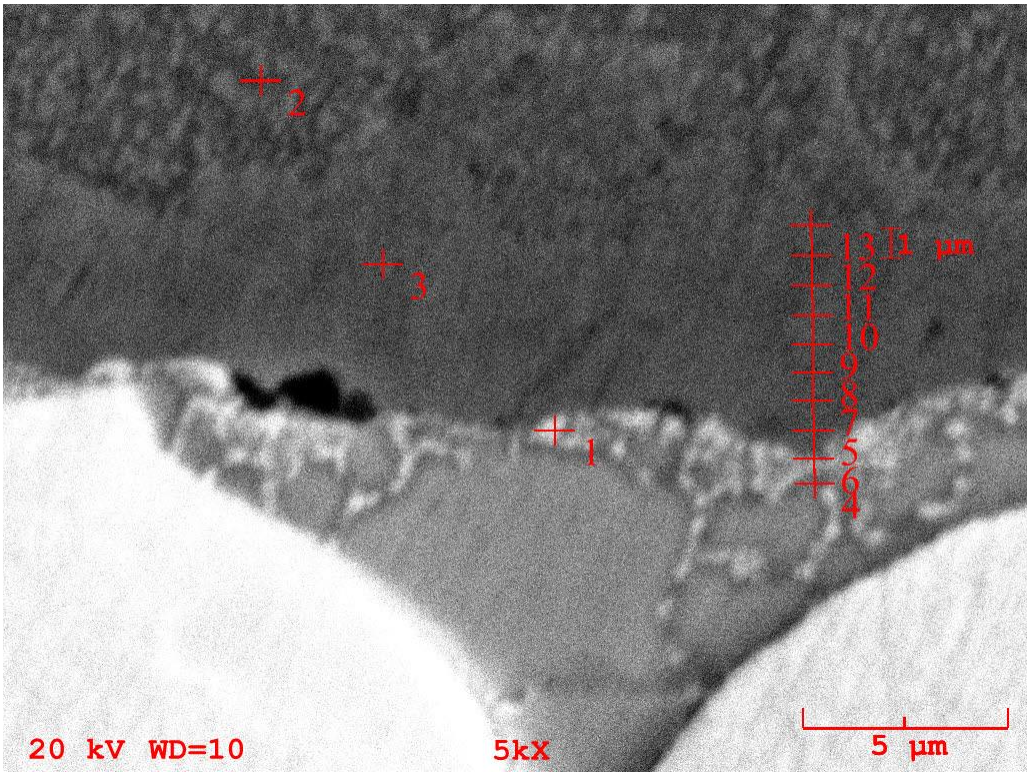

Figure 3.1.13 EDS Points Across the Diffusion Affected Zone

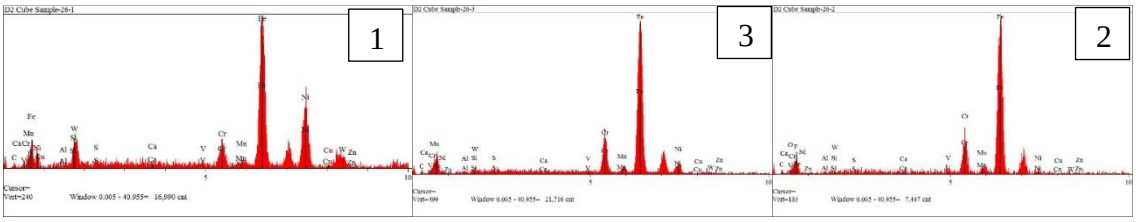

Figure 3.1.14 EDS Point 1 (Left) Point 3 (Middle) Point 2 (Right)

To understand the exact distance the diffusion affected zone occupies, it was decided to take EDS about every one µm to determine when the traces would hit steady state and match the return of the D2 trace. **Figures 3.1.13-3.1.16** show the steady decline of tungsten and nickel from point four to point thirteen, but point thirteen's response

suggests the end of the diffusion affected zone has not been reached as point thirteen has slightly more nickel than the D2 trace which should be zero based off **Table 3.1.1**. At this time it looks like the diffusion affected zone (DAZ) is visually different and there is a diffusion layer approximately 10 µm wide at this location. More locations adjacent to varying areas of WHA matrix will have to be estimated to get a representative volume element (RVE) estimate which both powder metallurgist [1] and finite element analyst use to accurately model powders and microstructures [21].

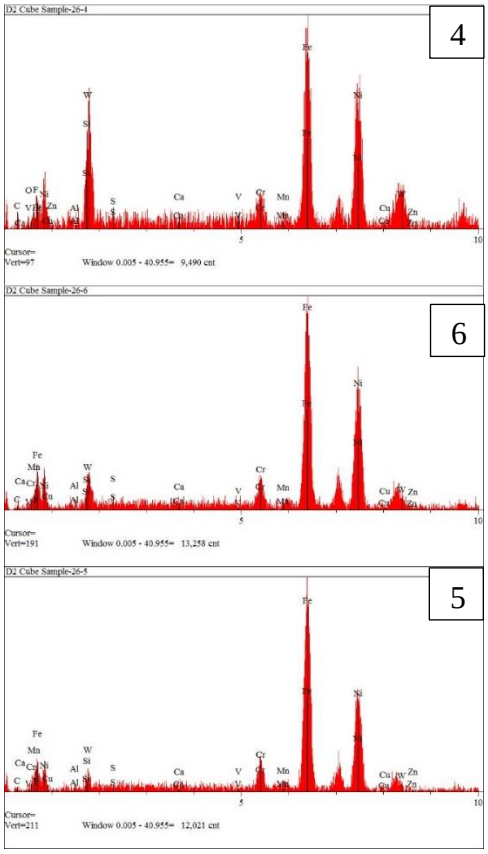

Figure 3.1.15 EDS Point 1 (Top) Point 3 (Middle) Point 2 (Bottom)

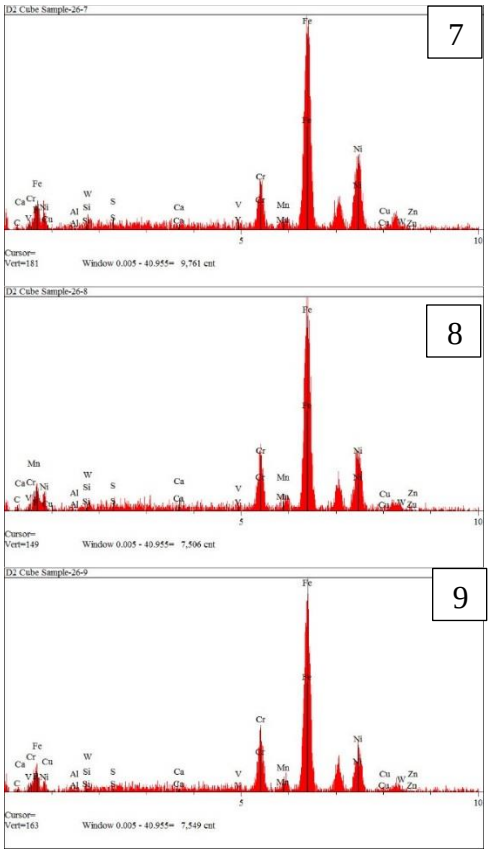

Figure 3.1.16 EDS Point 7 (Top) Point 8 (Middle) Point 9 (Bottom)

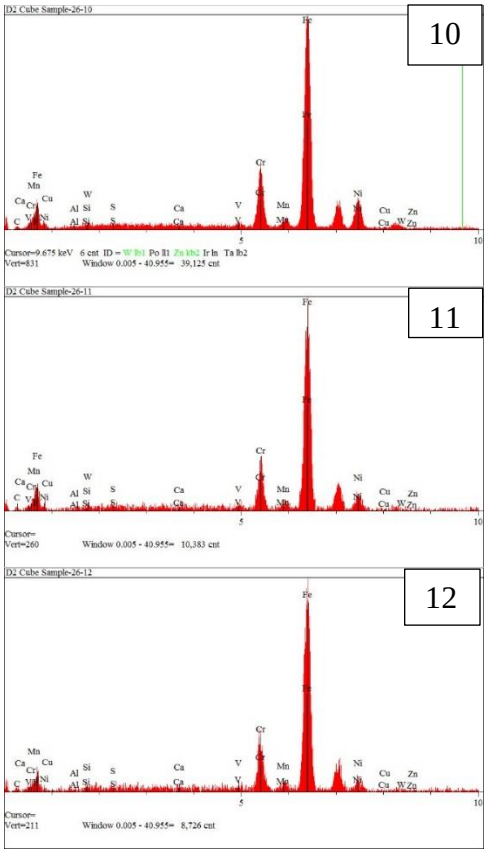

Figure 3.1.17 EDS Point 10 (Top) Point 11 (Middle) Point 12 (Bottom)

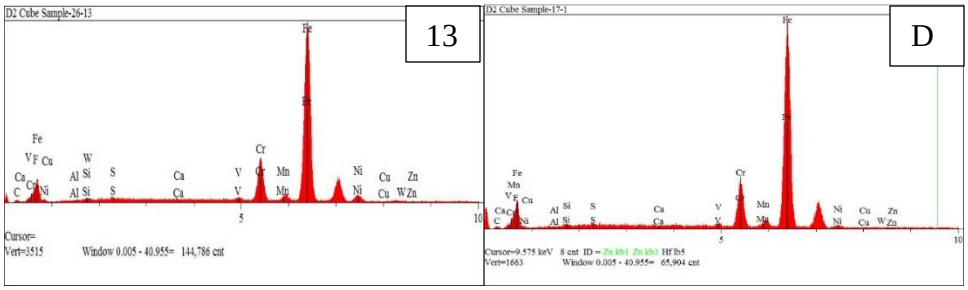

Figure 3.1.18 EDS Point 13 (Left) D2 Trace (Right)

From the empirical measurements used to find the diffusion layer thickness, a finite element analysis can now be developed to match reality. Still, electron backscatter diffraction (EBSD) could be utilized to determine the grain sizes generated and if they match those in the literature, as well as if the crystal structure remains a face centered cubic (FCC) throughout the WHA [4] or HCP, but is not the focus of this work.

Additionally, microscopy will need to be carried out on the fracture surfaces after impact testing to determine location of fracture and the mode of fracture. A theoretical diffusion layer analysis will also be completed to understand if the empirical results match the theory.

3.2 **SEM of Additional Etched Sample**

Additional SEM imaging of a another etched specimen (**Figure 3.2.1**) was also carried out on the same JEOL JSM-6510LV Scanning Electron Microscope (SEM) integrated with an EDS-IXRF at US Army ARDEC Picatinny Arsenal, NJ, but at 20 kV. The sample was mounted with ClaroCit Powder ®, an acrylic with an 85 Shore D hardness [34], and polished using 320 grit silicon carbide foil, 9µm DiaPro on MD-Largo, and 3µm DiaPro on MD-Dac to achieve the desired finish. It was then chemically etched with 3% Nital solution using a swab while gently rubbing back and forth on the face of the sample for approximately five-ten seconds, rinsed with water, then rinsed with methanol then air dried under a hand dryer to achieve the sample in Figure 3.2.11.

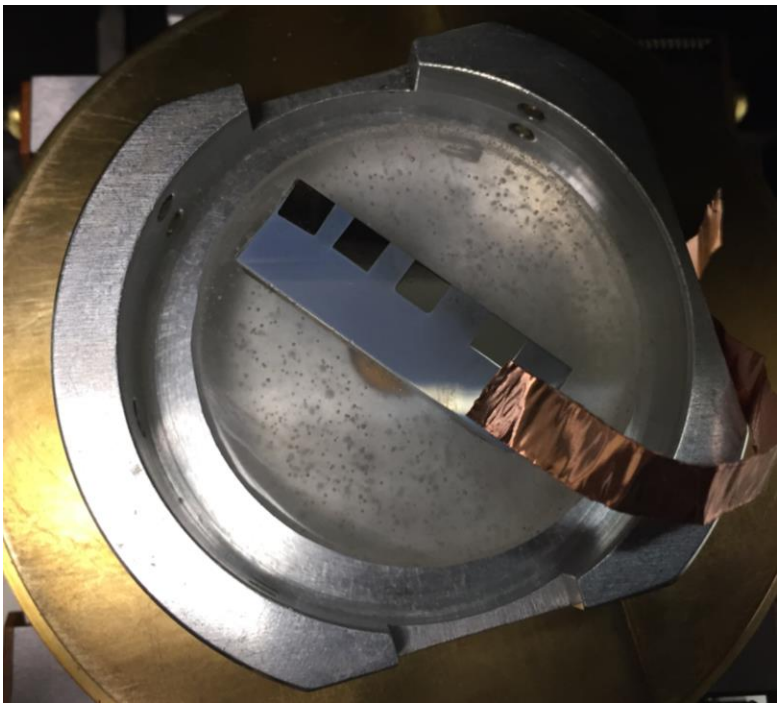

Figure 3.2.1 D2 Acid Etched Specimen

At twenty-five power, porosity is visible meaning the D2 powder did not consolidate between the WHA cubes parallel to the FAST force vector (**Figure 3.2.2**) as evidenced by the large void, but at 100 power (**Figure 3.2.3**) you can see the D2 powder did consolidate perpendicular to the force vector compared to the D2 powder between the WHA cubes. This is to be expected since bridging in the powder would occur and reduce the pressure between the cubes as the FAST produces uniaxial pressure and not hydrostatic pressure.

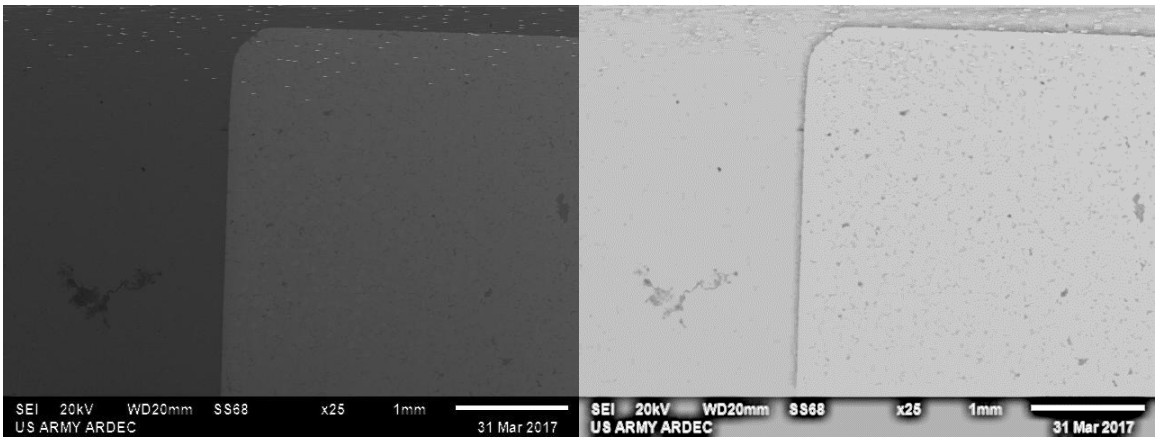

Figure 3.2.2 D2 Etched at x25 SEM Image (Left) SEM Image Modified with Word Photocopy Artistic Effects (Right)

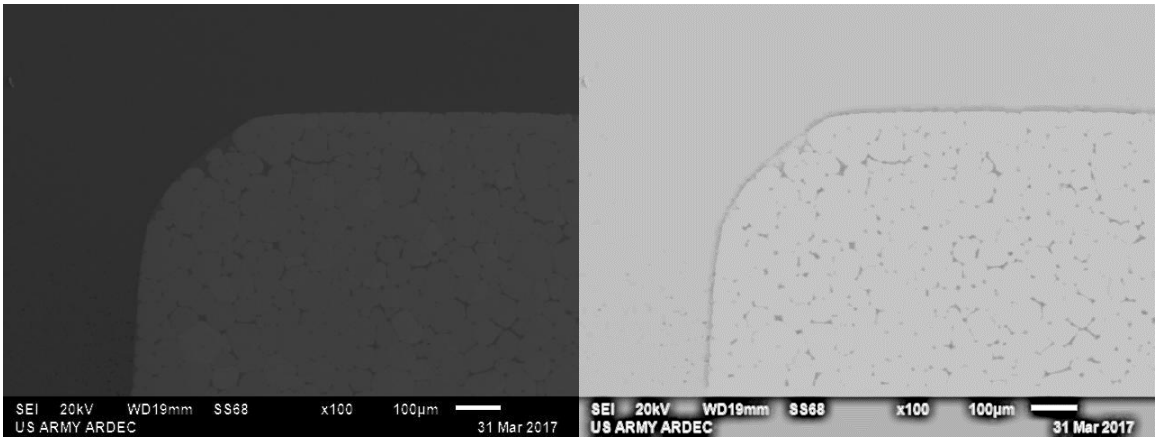

Figure 3.2.3 D2 Etched x100 SEM Image (Left) SEM Image Modified with Word Photocopy Artistic Effects (Right)

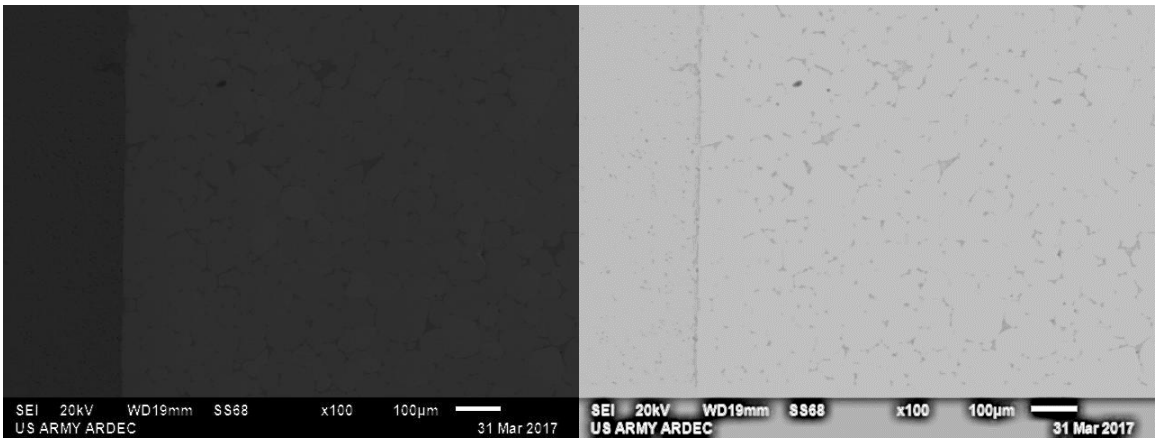

Figure 3.2.4 D2 Etched x100 SEM Image (Left) SEM Image Modified with Word Photocopy Artistic Effects (Right)

At 300 power (**Figure 3.2.5**) the porosity seems to decrease at some angle of repose relative to the WHA face and axis of force confirming bridging most likely occurred and reduced the force on the particles in between the cubes.

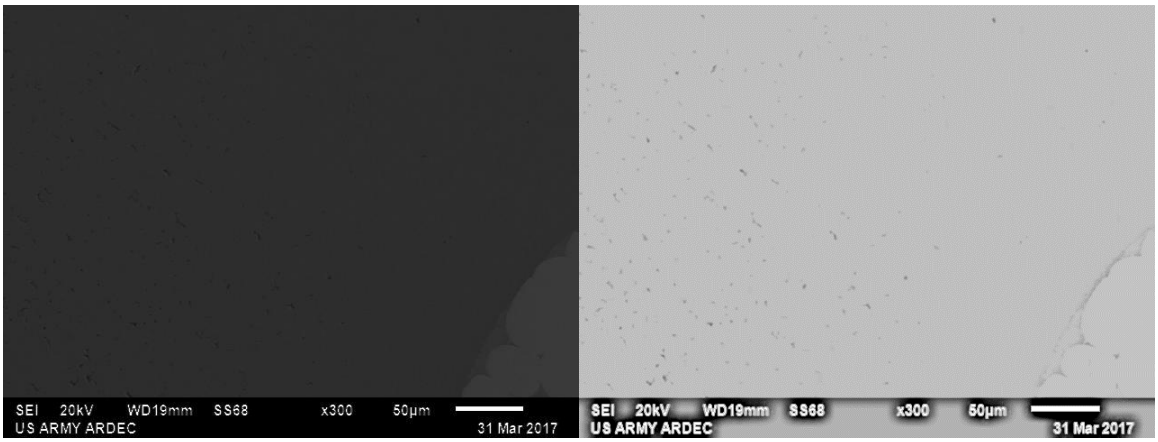

Figure 3.2.5 D2 Etched x300 SEM Image (Left) SEM Image Modified with Word Photocopy Artistic Effects (Right)

In between two WHA cubes it is clearly evident at 1000 power (**Figure 3.2.6**) and 2000 power (**Figure 3.2.7**) the powder did not consolidate given pores remain and spherical shapes indicating necking has barely started to occur in this region.

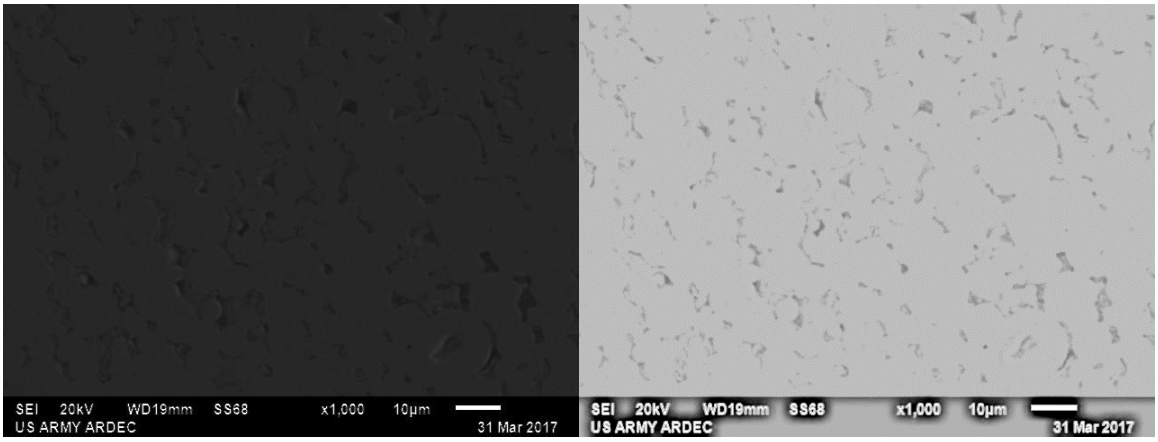

Figure 3.2.6 D2 Etched x1000 Between Two Cubes SEM Image (Left) SEM Image Modified with Word Photocopy Artistic Effects (Right)

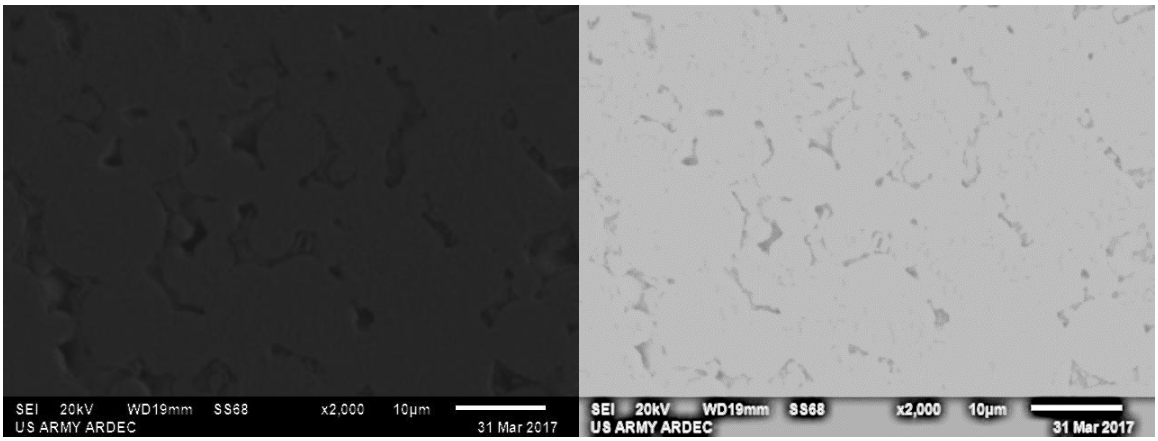

Figure 3.2.7 D2 Etched x2000 Between Two Cubes SEM Image (Left) SEM Image Modified with Word Photocopy Artistic Effects (Right)

The WHA at 1000 power (**Figure 3.2.8**) seems to be unchanged in structure and is typical of a WHA of this chemistry.

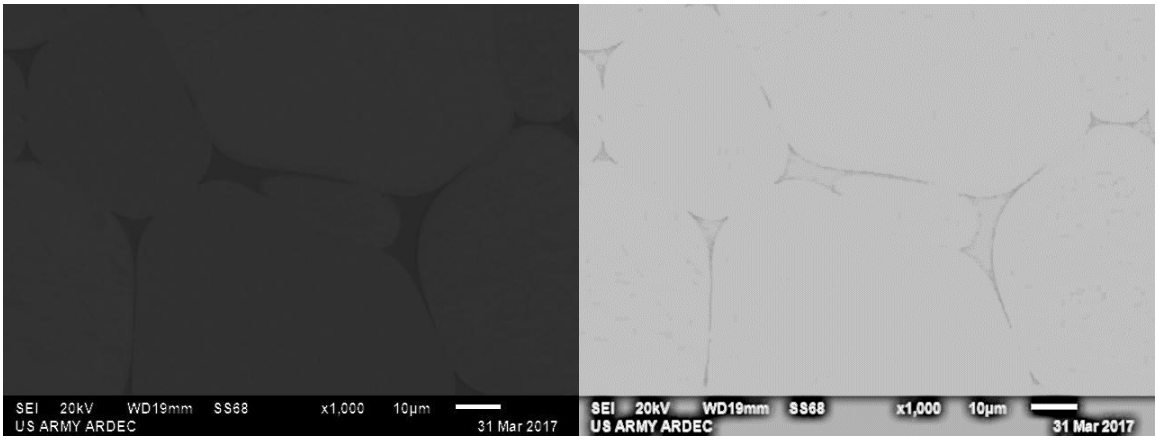

Figure 3.2.8 D2 Etched x1000 SEM Image of WHA (Left) SEM Image of WHA Modified with Word Photocopy Artistic Effects (Right)

At 1500 power (**Figure 3.2.9**), the interfaces seems to be free of major voids indicating some adhesion is taking place between the D2 and the WHA. There is a slight halo around the WHA again indicating there may be some diffusion given the heat and pressure provided by the FAST process, and the concentration gradient between the elements in WHA and the D2 alloy.

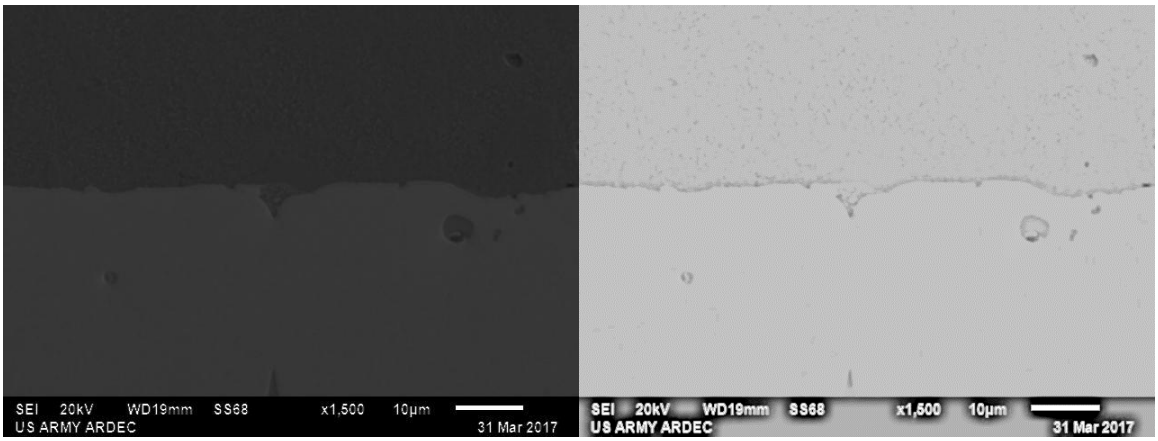

Figure 3.2.9 D2 Etched x1500 SEM Image of Interface Perpendicular to Load (Left) SEM Image of Interface Perpendicular to Load Modified with Word Photocopy Artistic Effects (Right)

Examination of the D2 at 2000 power (**Figure 3.2.10**) directly above the interface shows uniform consolidation with minimal defects or porosity. In the Figure below one of these defects is presented to show the size of porosity which is on the same order of magnitude as the porosity along the interface perpendicular to the uniaxial force vector of the FAST.

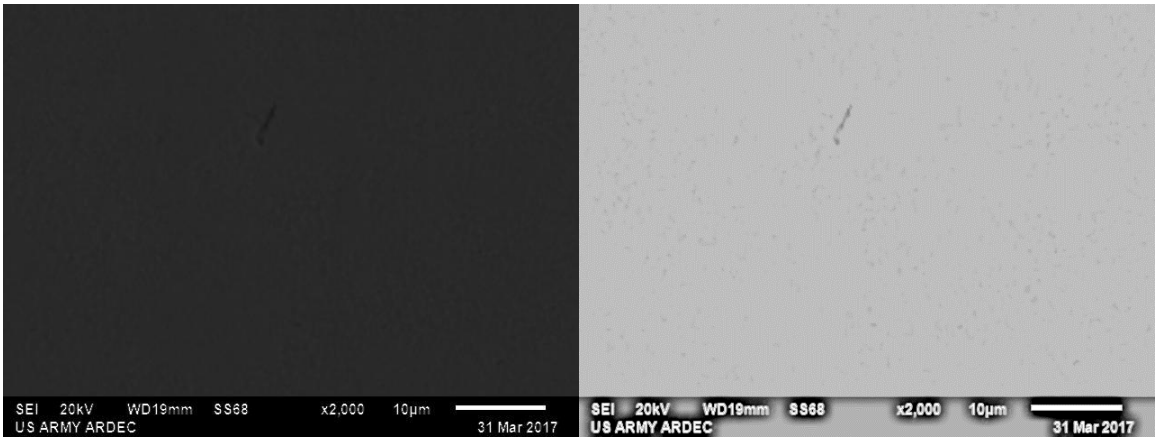

Figure 3.2.10 D2 Etched x2000 SEM Image of D2 Above Interface (Left) SEM Image of D2 Above Interface Modified with Word Photocopy Artistic Effects (Right)

Upon further examination of different acid etched samples with multiple WHA cubes embedded in them, the powder in between the WHA cubes was again not

consolidated, but the powder on the interface perpendicular to the axis of force is consolidated rather nicely and appears to be providing some level of adhesion between the WHA cube and the D2 alloy based on a contrasting visual layer between the D2 alloy and the WHA.

To further examine this adhesive interaction, non-etched samples were evaluated in the same SEM microscope. Even at 30 power (**Figure 3.2.11 and 3.2.12**) it is clear with the additional samples powder is consolidated on the axis of compression from the FAST, but not on the side walls parallel to the axis of compression between the WHA cubes. This can be expected as WHA cubes act as large powder particles, because they have already been sintered and do not allow significant compaction of the powder between the WHA cubes via pressure, thus the majority of the diffusion energy for powder consolidation between the cubes is only being provided in the form of joule heating given the pressures used.

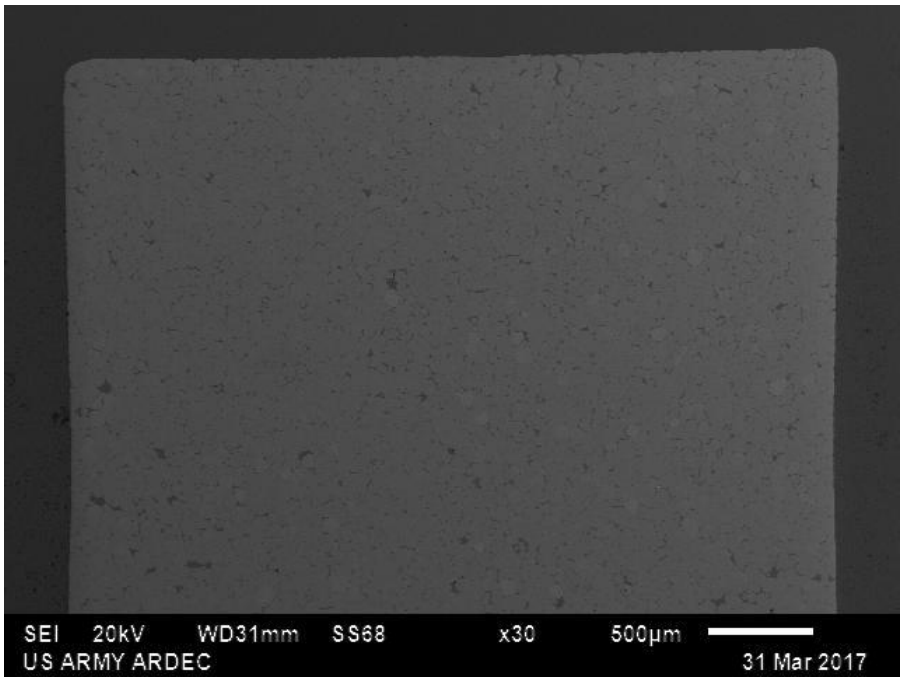

Figure 3.2.11 SEM Image of D2 P2 WHA x30

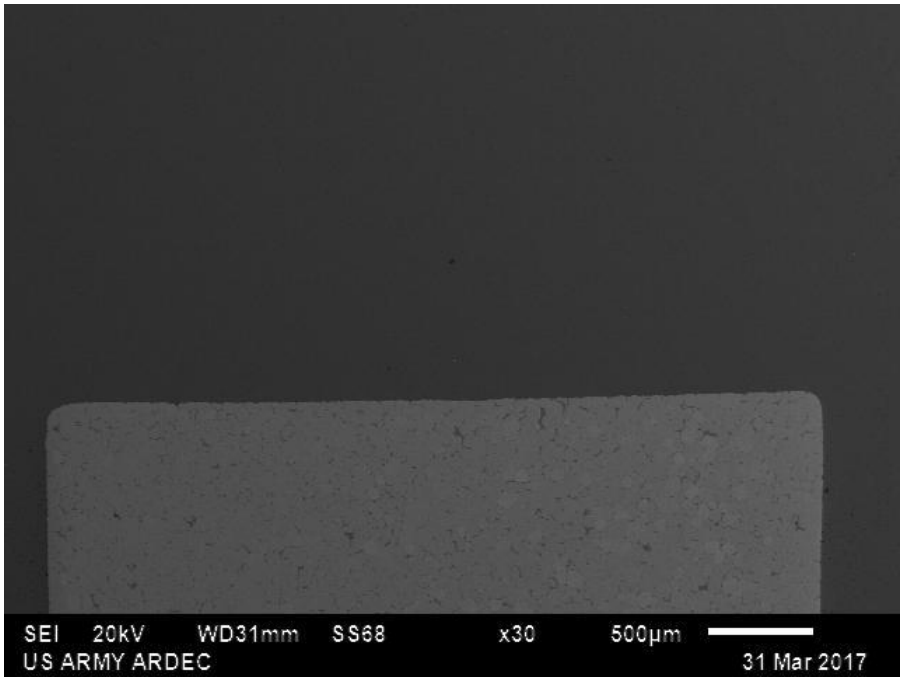

Figure 3.2.12 SEM Image D2 P2 WHA Interface Perpendicular to Load x30

3.3 SEM with EDS of Nanoindentation Sample

An additional specimen was machined from the bulk sample which was close to the carbon dies, again mounted with ClaroCit Powder ®, an acrylic with an 85 Shore D hardness [34], and polished using 320 grit silicon carbide foil, 9µm DiaPro on MD-Largo, and 3µm DiaPro on MD-Dac to achieve a mirror finish as seen in **Figure 3.3.1** below.

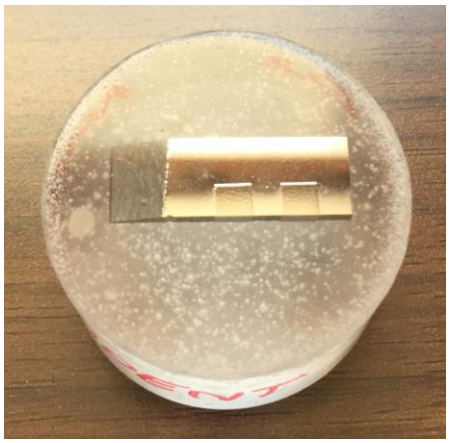

Figure 3.3.1 Polished D2 P1 and P2 Nanoindent Sample

This specimen was also used to probe the interface between the D2 and WHA using nanoindentation across the boundary and the nanoindentation results for this specimen (2 of 2), which will be covered in chapter four of this work, was useful to compare this sample to the images from the etched SEM work. The layout in **Figure 3.3.2** shows sample two of two and where nanoindentation measurements were carried out and **Figure 3.3.3** shows the SEM setup.

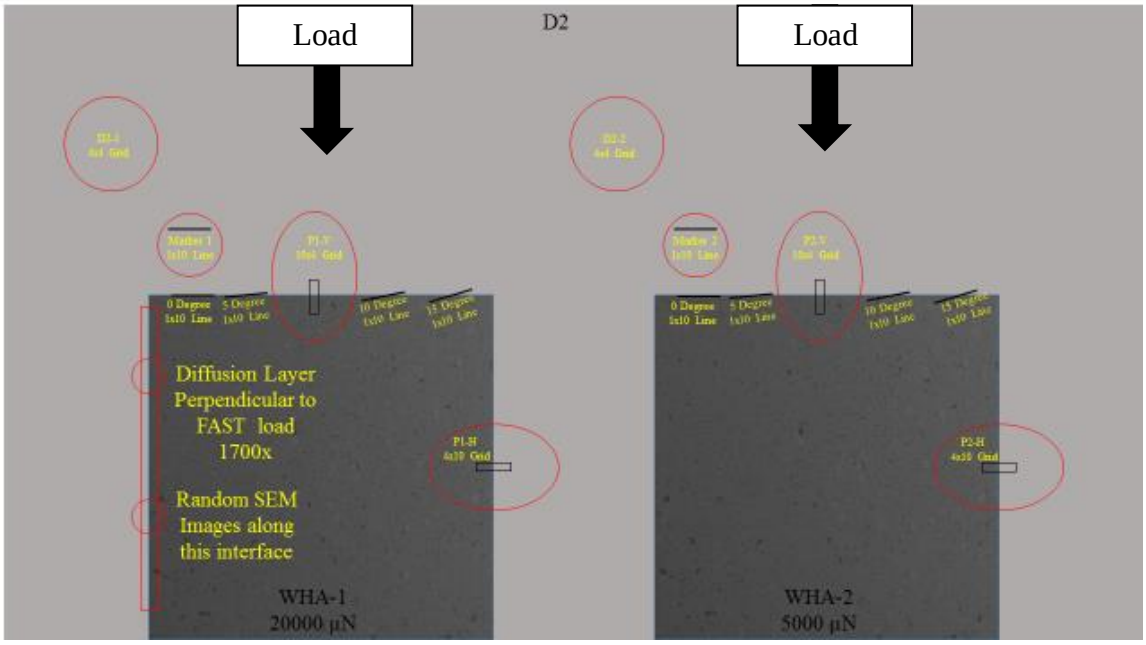

Figure 3.3.2 Nanoindentation Measurement and SEM Imaging Layout: P1 Taken Around WHA-1 (Left) P2 Taken Around WHA-2 (Right)

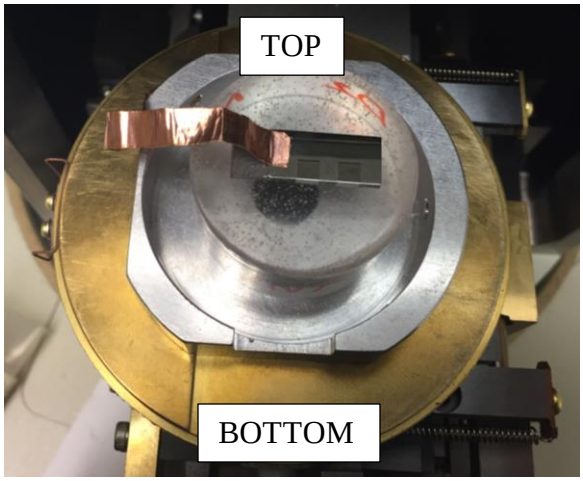

Figure 3.3.3 Polished D2 P1 and P2 Nanoindent Sample in SEM

SEM images in **Figures 3.3.4 – 3.3.7** were taken on the left side of the WHA-1 P1 cube and **Figure 3.3.8** was taken on the right side of WHA-1 just below P1-H. At x1000 (**Figure 3.3.5**) power the porosity in the D2 starts to become evident with voids around 5 µm near the top of the sample and greater than 10 µm towards the bottom. The large

double pore in **Figure 3.3.5** was enlarged (**Figure 3.3.6**) to show some nodules which may be evidence of carbides forming on the surfaces of the pores.

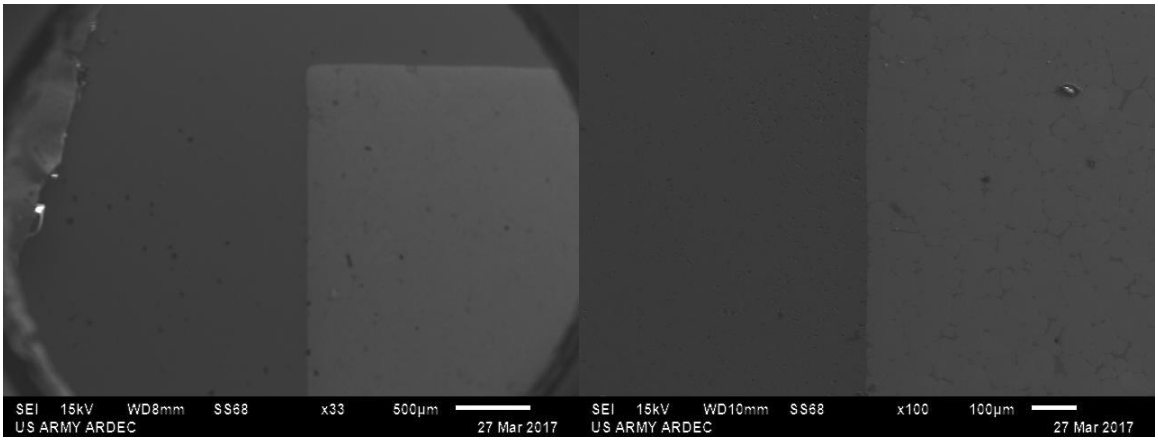

Figure 3.3.4 SEM of Nanoindented Sample P1 x33 (Left) x100 (Right)

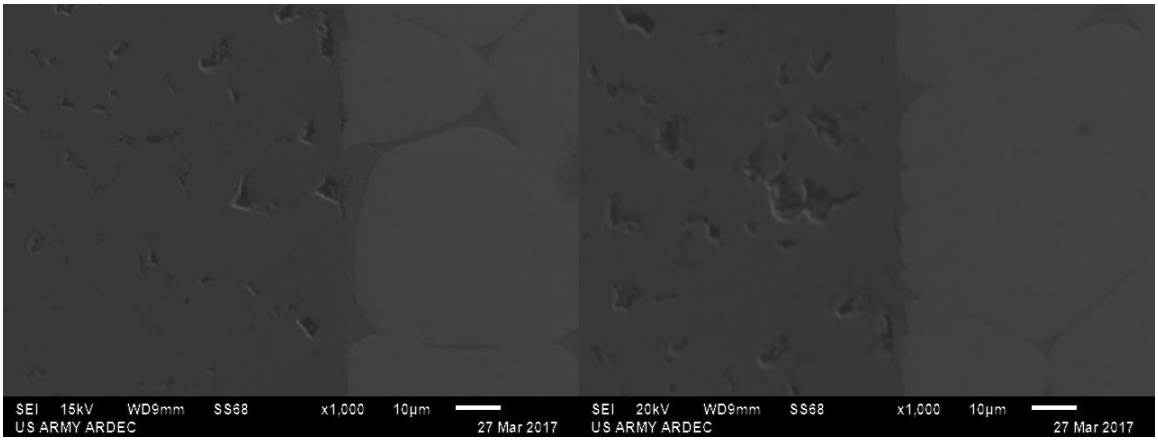

Figure 3.3.5 SEM of Nanoindented Sample P1 x1000

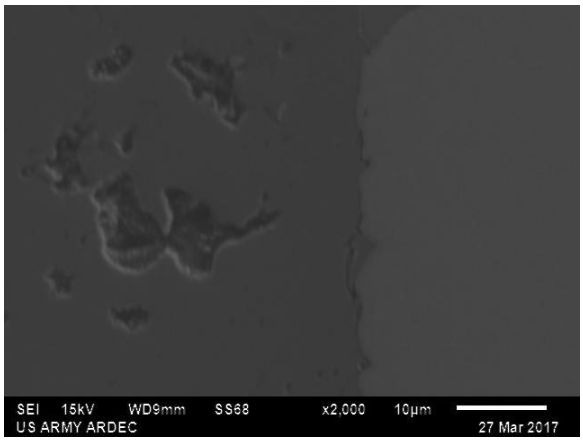

Figure 3.3.6 SEM of Nanoindented Sample P1 with Nodules in Pore x2000

Focus was turned back to the interface, where bonding was not coherent along the entire interface as voids are present adjacent to the tungsten grains as well as the nickel and iron binder matrix material of the WHA cube. There does not appear to be any correlation as to why or where these voids occur, much like the random distribution of voids in the D2 alloy itself, but may be Kirkendall porosity if regions are deficient of one species of atom causing shrinkage and creating tension while other regions have excess of one species of atoms creating compressive stresses [39]. In **Figure 3.3.7** voids are visible adjacent to the tungsten as well as a void of comparable length adjacent to the iron and nickel binder in the WHA. Perhaps these voids in the section of the composite are a function of the starting powder size and bridging which can occur creating cavities and angles which diffusion cannot overcome through joule heating and pressure. Additionally, pores and gradients in the nickel and iron binder matrix seem to be occurring much like those seen in **Figure 3.1.8** with white islands similar to point 1 in **Figure 3.1.11** occurring on this edge of the WHA cube. This could indicate the formation of the pores and gradients are independent to the orientation to the axis of force and driven by diffusion.

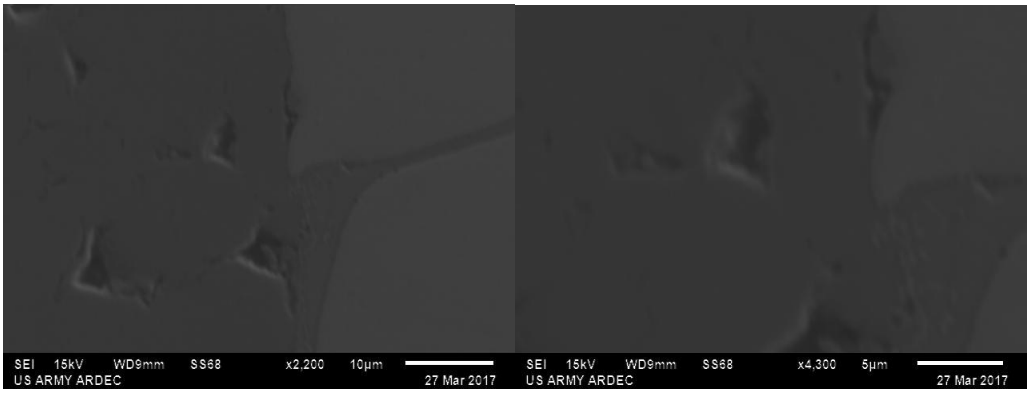

Figure 3.3.7 SEM of NanoIndented Sample P1 x2200 (Left) x4300 (Right)

Logic would suggest the other side of the WHA1 cube farther from the carbon die's surface would exhibit the same porosity and **Figure 3.3.8** confirms the hypothesis that the carbon foil inside the carbon die is not causing the porosity as carbon foil has only created a WC-containing layer about 100µm in a Ni-W alloy [31]. This does not mean the carbon could not diffuse upwards from the carbon foil which lined the bottom carbon die. Carbon at a diffusion rate of 1.7×10^{-6} cm^2/s into BCC at 800°C and 6.7×10^{-7} cm^2/s into the FCC at 1100°C [39] would suggest it would take 124 hours compared to the 1260 seconds available to diffuse.

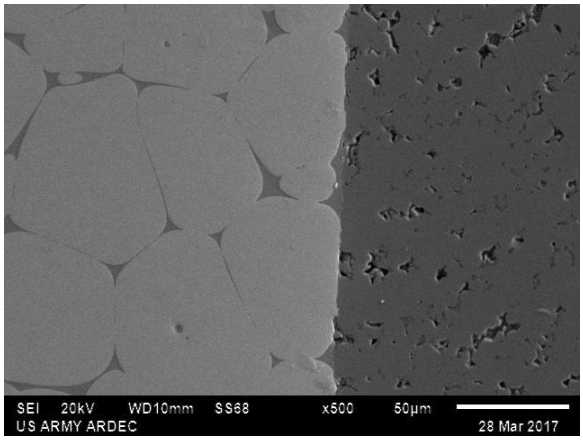

Figure 3.3.8 SEM Image of P1 Interface between P1 and P2 x500

An extreme example of the unconsolidated powder is shown in **Figure 3.3.9** where the powder is still in its starting spherical condition, though its shape is reminiscent of an Osage orange now. Though counts were low, EDS measurements were carried out in an attempt to help understand what elements and phases might exist, and the results are shown in the **Table 3.3-2**, graphically in **Figure 3.3.10** and by spectrum in **Figure 3.3.11**. Points 1 through 4 suggest there is a high concentration of chromium in the area compared to the ASTM standard [37] and point 5 on the visible band in the binder suggest there is a high carbon concentration on the interface while points 6 and 11 suggest there is still an appreciable amount of tungsten, potentially forming a tungsten carbide or oxide on the interface. Nanoindentation results will help confirm if WC alloy or a WO alloy has been formed using the hardness nanoindentation measurements covered in later chapters.

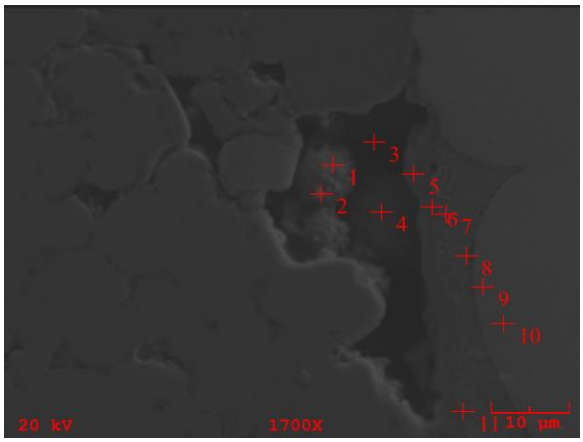

Figure 3.3.9 SEM and EDS of Nanoindented Sample P1 x1700

Spectrum	C	Si	P	S	V	Cr	Mn	Fe	Ni	Cu	Mo	W
1700x-1	7.87	0.68	0.222	0.695	4.207	59.456	3.568	17.375	0	3.951	0	1.976
1700x-2	6.001	1.03	0.414	0.408	1.183	22.975	0.296	63.02	0	1.94	1.821	0.912
1700x-3	3.322	0.819	1.395	0	5.316	57.52	9.06	9.66	0	6.231	3.839	2.84

1700x-4	4.109	0.77	0.437	0	1.568	29.754	1.155	51.183	7.382	2.033	1.609	0
1700x-5	16.353	1.124	0.037	0	0.328	7.532	0.894	37.941	28.335	4.169	0.913	2.373
1700x-6	4.718	0.177	0.209	0.097	0.273	4.129	0.102	11.768	8.116	1.959	0	68.451
1700x-7	5.168	0	0.265	0.227	0.516	3.078	0.287	11.738	19.18	1.967	0	57.574
1700x-8	4.362	0	0.277	0	0.39	1.778	0.567	10.222	38.757	1.836	0.158	41.654
1700x-9	2.936	0.459	0	0	0.197	0.411	0.115	0.337	0	2.052	0	93.492
1700x-10	3.718	0.18	0.024	0.046	0.221	0.357	0.322	0.778	0	1.757	0	92.596
1700x-11	4.937	0	0.462	0	0.462	2.763	0.483	12.249	35.594	1.569	0.205	41.275
Mean	5.772	0.476	0.34	0.134	1.333	17.25	1.532	20.57	12.488	2.679	0.777	36.649
Std. Dev.	3.763	0.428	0.386	0.227	1.766	22.534	2.683	20.744	15.313	1.471	1.221	37.413
Min	2.936	0	0	0	0.197	0.357	0.102	0.337	0	1.569	0	0
Max	16.353	1.124	1.395	0.695	5.316	59.456	9.06	63.02	38.757	6.231	3.839	93.492

Table 3.3-2 Table of Elements Present on Vertical Interface ref. Fig 3.3.9 SEM 1700x

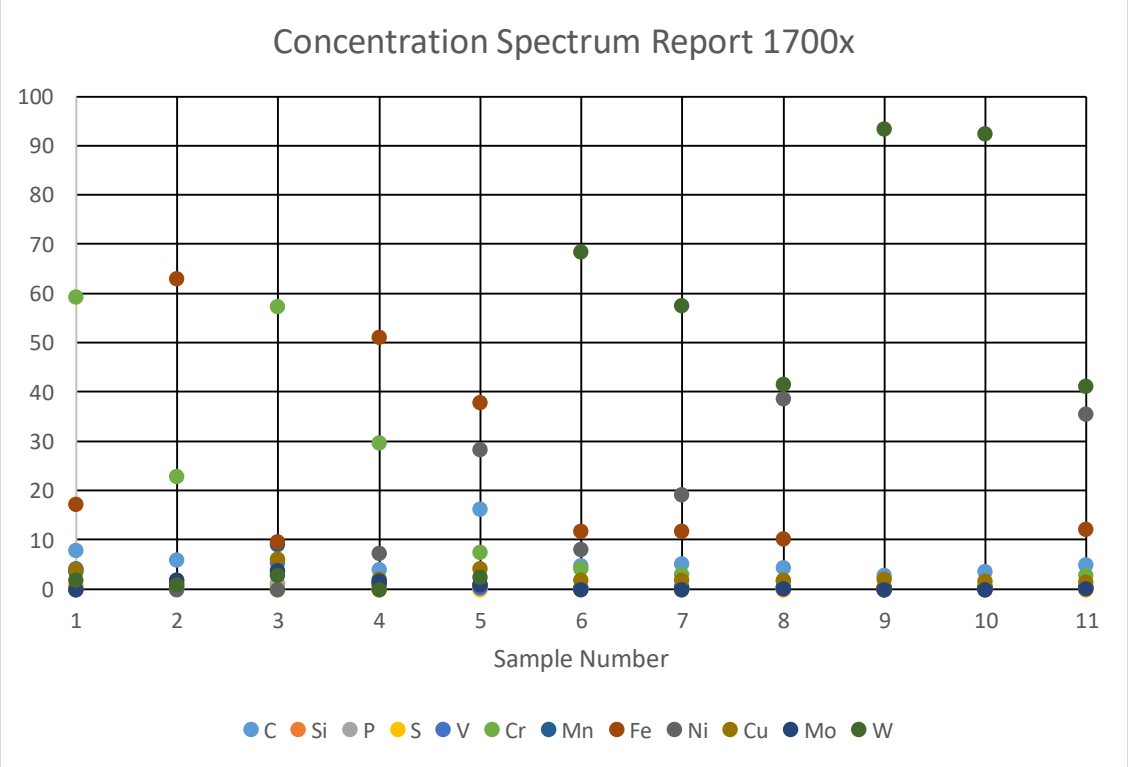

Figure 3.3.10 Concentration Spectrum of Elements Present on Vertical Interface ref. Fig. 3.3.9 EDS

3.4 **EDS Mapping**

The JEOL JSM-6510LV Scanning Electron Microscope (SEM) was again utilized at 20 kV with the integrated EDS-IXRF at US Army ARDEC Picatinny Arsenal, NJ, to produce some EDS maps of the sample around the P1-V nanoindented area. The following elements were selected to be mapped: carbon, nitrogen, oxygen, silicon, phosphorus, chromium, magnesium, iron, cobalt, nickel, copper, molybdenum, and tungsten. Vanadium was accidently left out, but since the surface was ablated as will be shown in the APPENDIX the analysis was not carried out again.

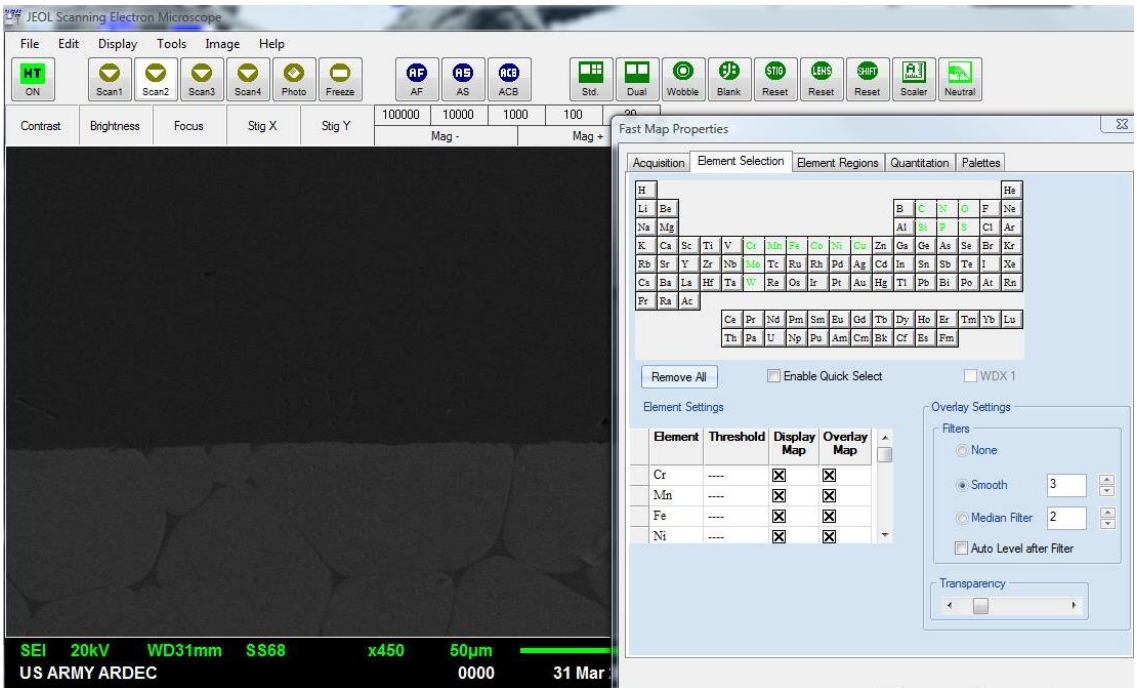

Figure 3.4.1 EDS-IXRF Mapping Centered on P1-V Nanoindents at x450

The SEM image and elemental maps for the P1-V image are in **APPENDIX D** while just the plots are enlarged in **Figure 3.4.2** to give an idea of the trend.

C

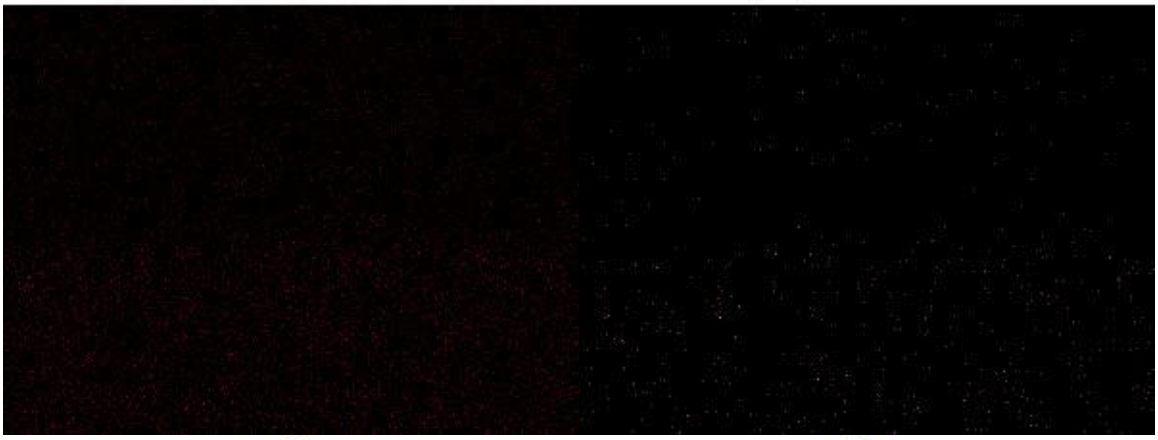

Co

Cr

Cu

Fe

Mn

Mo

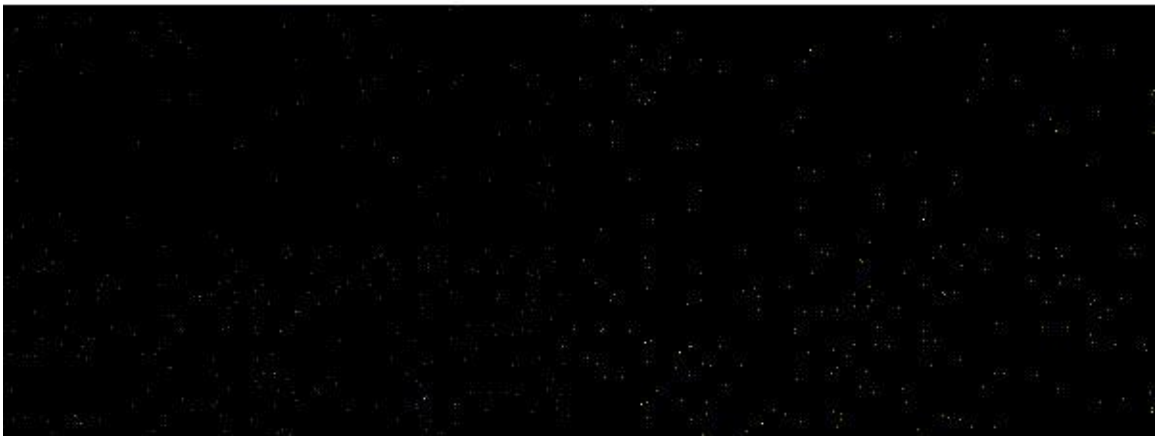

N

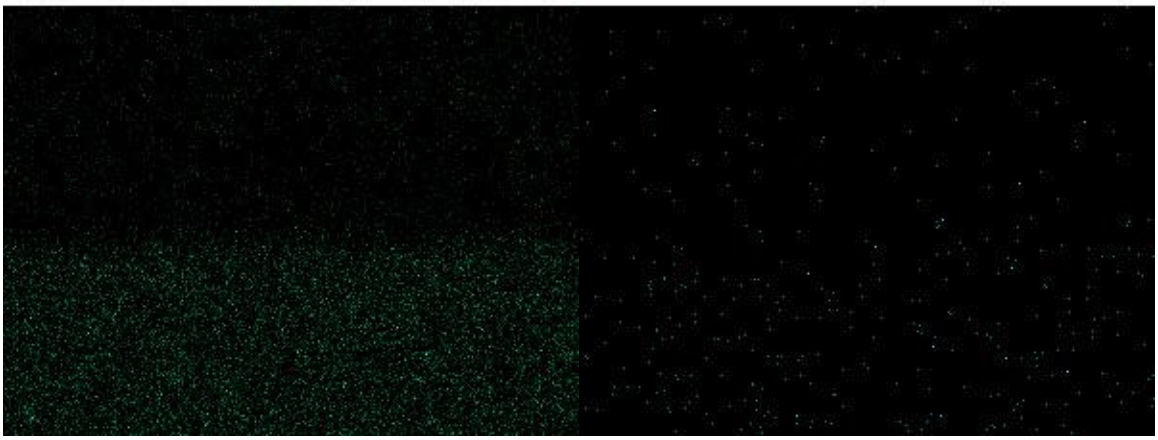

Ni

O

P

S

Figure 3.4.2 D2 P1 Individual Element EDS-IXRF Maps

Given the halo surround the WHA, and the results of the nanoindentation which will be covered in chapter 4, it was decided to see if there were large carbon concentrations on the interface. The post processing features in the EDS-IXRF were utilized to produce the images in **Figure 3.4.3** and **Figure 3.4.4**. **Figure 3.4.3** does not produce anything which suggests there is a carbon gradient on the WHA, but in **Figure 3.4.4** when viewed three-dimensionally there is a gradient of increasing carbon as the interface is approached from the WHA side which points to the potential to have WC alloys here.

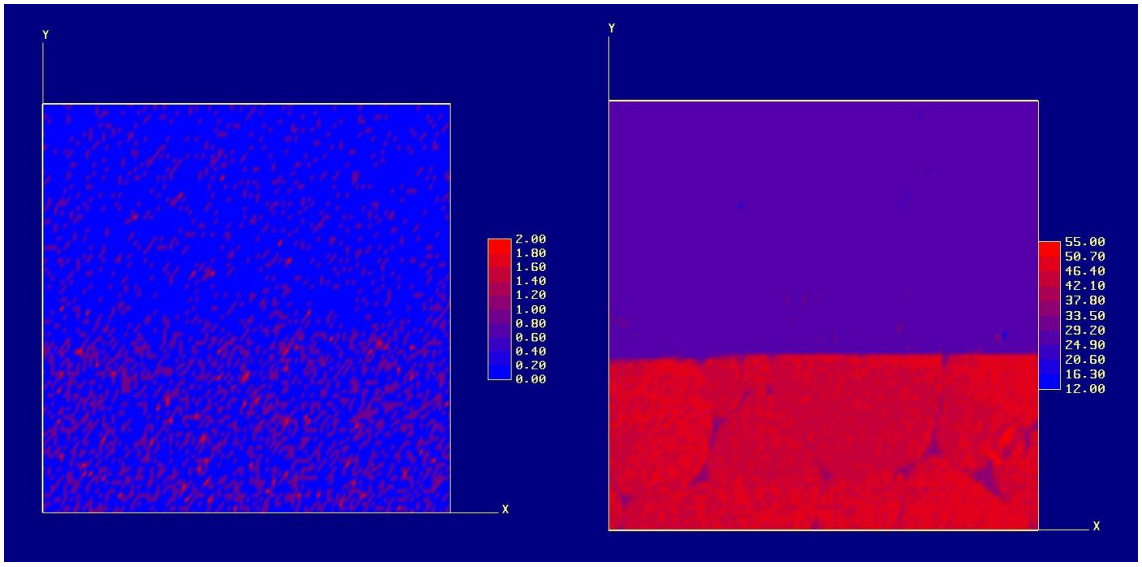

Figure 3.4.3 Carbon Map of D2 P1 SEM Grid (Left) and Flat (Right)

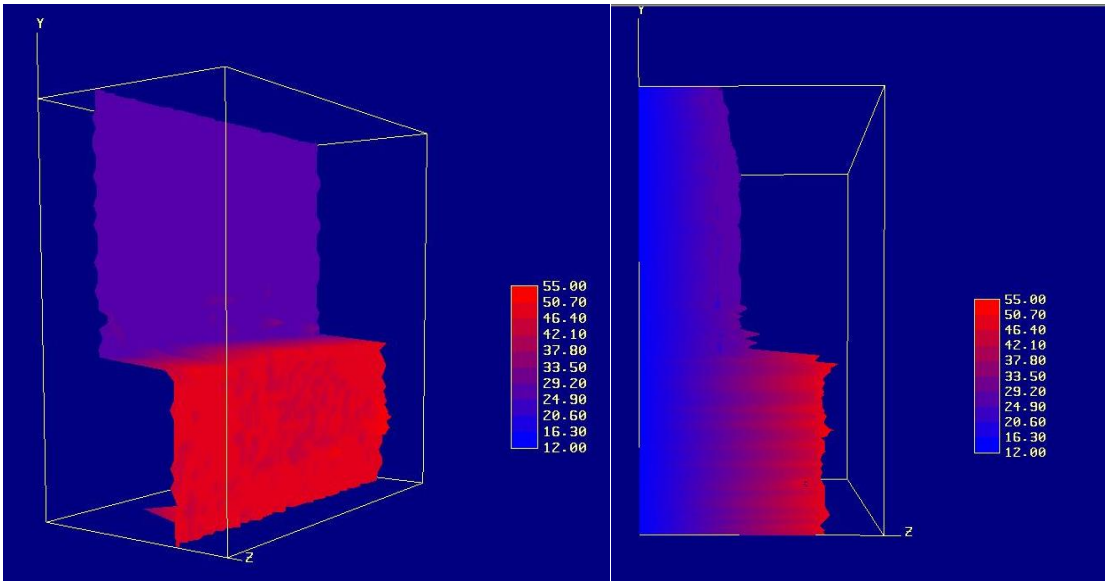

Figure 3.4.4 Carbon Map of D2 P1 SEM Solid, Tilted (Left) Left Side (Right)

Chapter 4: SEM of Nanoindentations on Samples P1 and P2

Specimen one of two which was hand polished and will be discussed in chapter 5 was not imaged do to its high surface roughness and variability. Thus, any variability may be from surface roughness or porosity. As shown in chapter three, specimen two of two used for the nanoindentation measurements was imaged with the JEOL JSM-6510LV Scanning Electron Microscope (SEM) integrated with an EDS-IXRF at US Army ARDEC Picatinny Arsenal, NJ to ensure this specimen was no different the previously specimens examined. This chapter will specifically cover the SEM imaging of the nanoindentation measurements taken on this 2nd sample along a WHA cube to D2 interface designated P1, and then a second WHA cube to D2 interface designated as P2 to interrogate the diffusion layers perpendicular and parallel to the FAST's load axis. Since a cube is symmetric it was decided not to interrogate all interfaces on the first cube, thus P2 measurements were carried out across a second set of interfaces on another WHA cube in the same sample. The layout of indentation measurements and interfaces on specimen two of two are again referenced in **Figure 3.3.1** and **Figure 3.3.2**.

An overview of the nanoindented sample can be seen below in **Figure 3.4.1** with the x18 SEM images spliced together to resemble the specimen. The foil tape next to P-1 was used to help reduce charge buildup on the sample and accidently contacted the P-2 10 degree area and the consequences will be discussed later in this chapter.

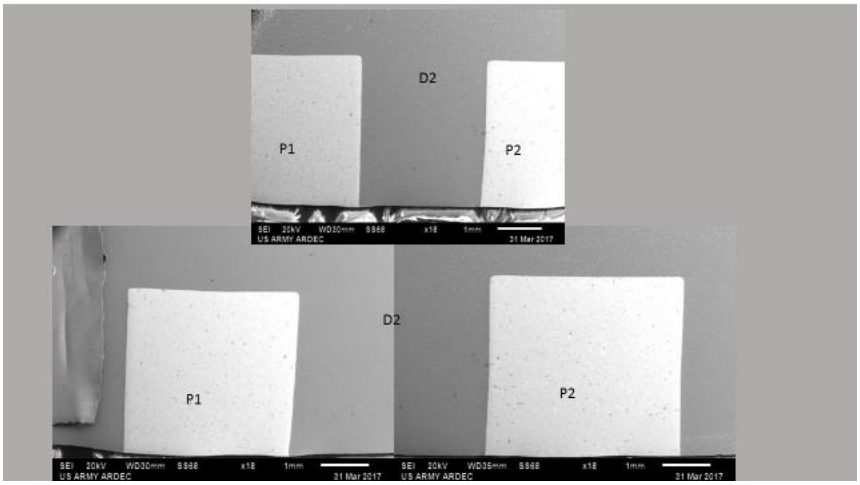

Figure 3.4.1 SEM Image of Overall Nanoindented Sample

4.1 SEM of P1 Along a WHA Cube to the D2 Interface

The SEM images showing the nanoindents on area P1 are shown below in **Figure 4.1.1** and are at approximately the same magnification to give an idea of the different nanoindentation areas and scale of the indents which are spaced 10 µm apart in the vertical and horizontal plane. Unfortunately the P1-Marker indent in the D2 could not be located in the time allotted even though P1 measurements used a 20000 µN indent load creating more pronounced indents than the P2; 0, 5, 10, 15 degree measurements which used a 5000 µN. It was decided not to continue looking for the P1-Marker because the location of the indents were in the highly consolidated area of the D2 and the nanoindentation results had little variability so time was better utilized on the interface of interest.

The first set of nanoindentation measurements on this sample were taken perpendicular to the WHA-D2 boundary using a 10x4 matrix centered on the boundary

perpendicular to the FAST's load, and a 4x10 matrix centered on the boundary parallel to the FAST's load.

Post processing of the first indents resulted in a need for a second occasion of indentation measurements taken at angles relative to the interface to obtain higher resolution measurements. There will be more discussion on these indents in section 4.1.2. These indents were taken at 0, 5, 10, and 15 degree increments relative to the perceived interface which is perpendicular to the FAST's load. The interface across which all vertical and angled indents were taken is the only interface which remains after the sample is machined into the impact specimens and theoretically has the lowest porosity and highest bond strength and diffusion rates.

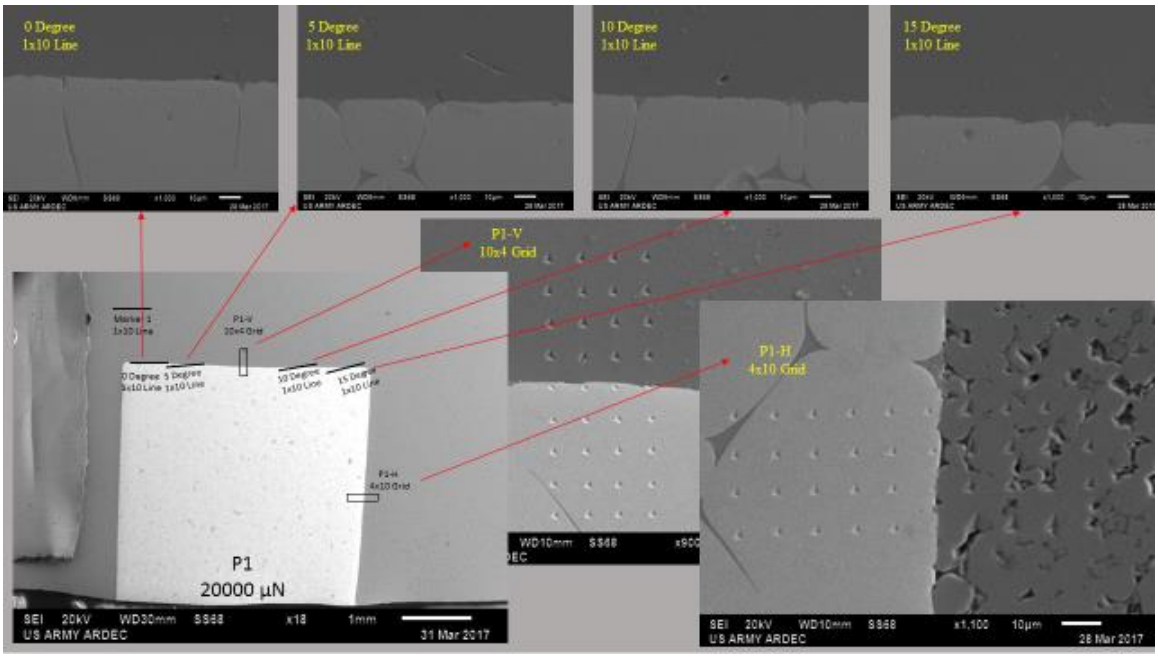

Figure 4.1.1 P1 Overall SEM Images of Nanoindents

In **Figure 4.1.2**, the SEM images are again shown at approximately the same magnification to give an idea of the different nanoindentation areas and scale for the

indents in area P2 since P2-V and P2-H used a 20000 µN load for the indent and whereas the P2-Marker, 0, 5, 10 and 15 degree indents were made with a 5000 µN indent load. The 15-degree indent could not be found, and even at x1000 the indents were difficult to see except at very high absorption times making rastering difficult. The P2 10-degree indent shows the unfortunate consequence of accidently contacting the area with foil in an attempt to reduce charge buildup and gather better image quality which resulted in residue covering a few of the indents.

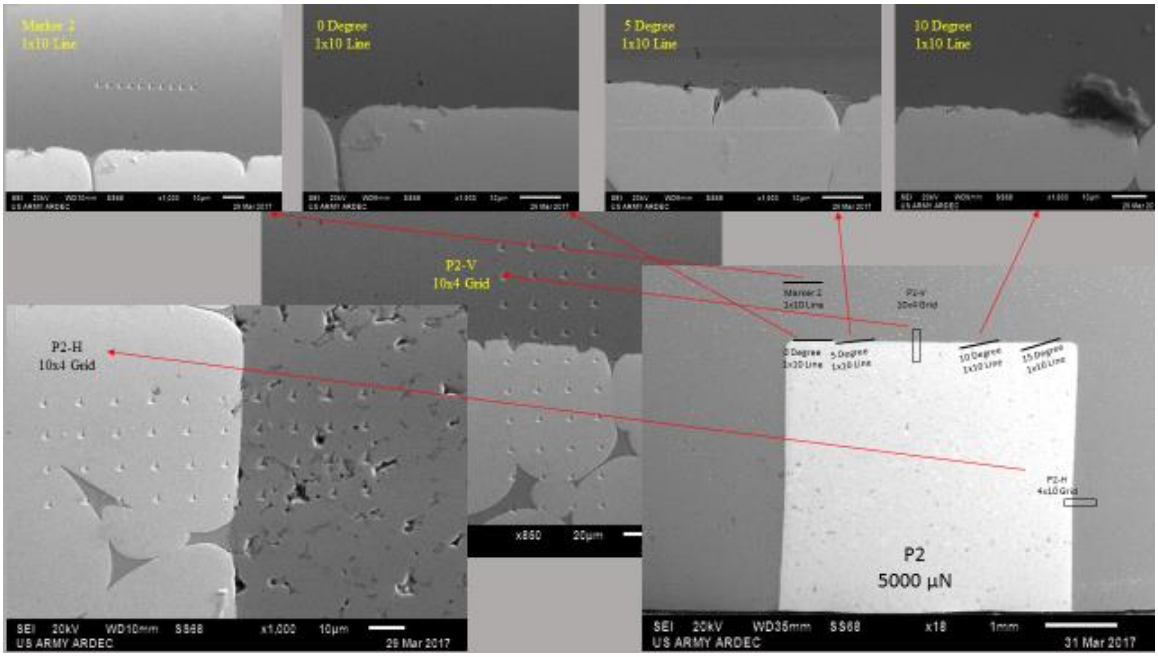

Figure 4.1.2 P2 Overall SEM Images of Nanoindents

4.1.1 SEM of P1 Matrices (Perpendicular and Parallel to Load Axis), 20000 µN Load

The first set of nanoindentation measurements were taken perpendicular to the FAST load for P1; P1-V are shown below in **Figure 4.1.3** and are labeled to correspond to the raw data. With a 20000 µN there are measurable differences in the size of the

indents in the D2 compared to those in the WHA even at 900x. The sixth row up on the interface (points 21-25) also seem to be slightly smaller in area, suggesting the indents are shallower than the rest of the indents in the WHA corresponding to high hardness in this area and will be confirmed with the nanoindentation analysis in chapter 5. None of the indents coalesced with a void though point 26 looks to be adjacent to a void, but did not present an outlier response in the nanoindentation analysis. Indent number 24 was perfectly centered on the interface.

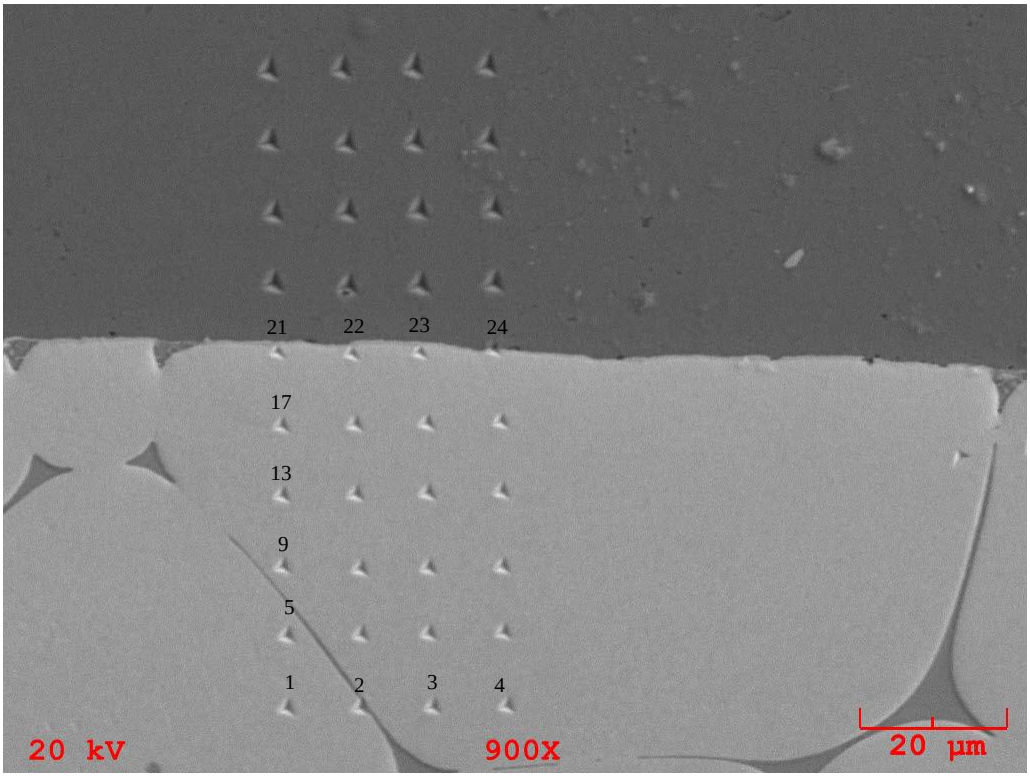

Figure 4.1.3 P1-V 10x4 Grid Indents

The second set of nanoindentation measurements parallel to the FAST's load for P1; P1-H are shown below in **Figure 4.1.4** and again are labeled to correspond to the raw data. Again the 20000 µN produced indents with measurable differences in size in the D2 compared to those in the WHA at this magnification and on this interface. The sixth

column of indents (indents 6,16,26,36) on the interface seem to be slightly smaller in area, again suggesting the indents are shallower than the rest of other indents in the WHA corresponding to higher hardness in this area compared to others. Unlike P1-V indents, the majority of the P1-H indents in the D2 are into porous metal and the hardness and modulus results from the nanoindentation of this area should be approached with caution and will be further explored in chapter 5 of this work.

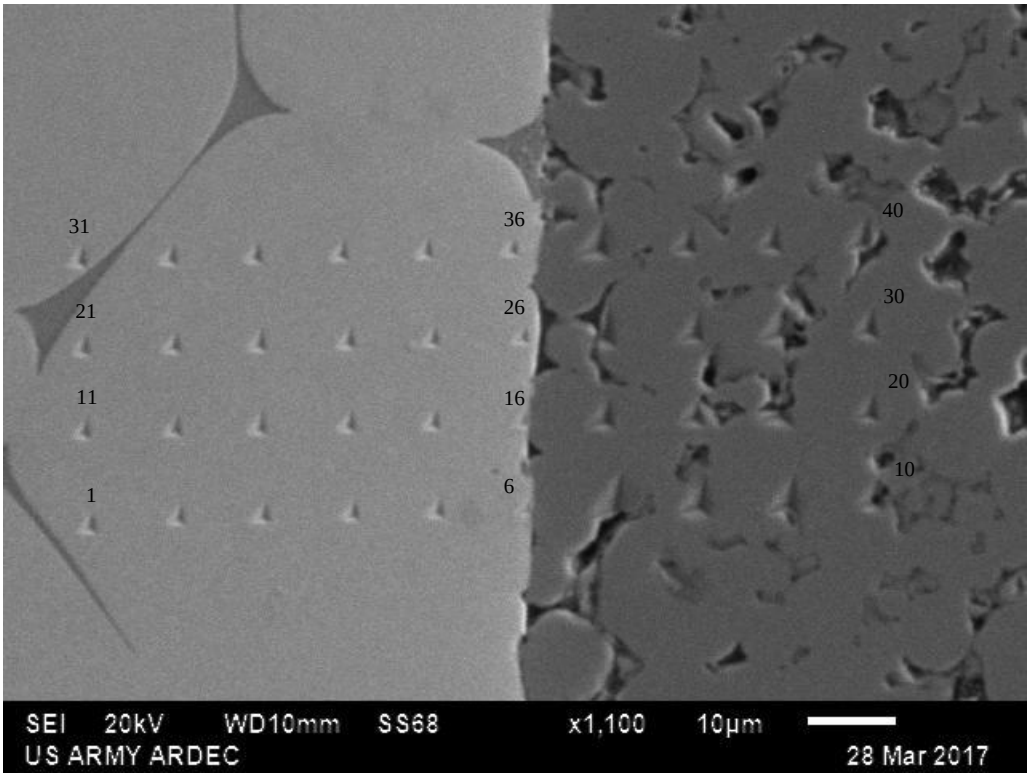

Figure 4.1.4 P1-H 4x10 Grid Indents

4.1.2 SEM of P1- 0, 5, 10, 15 Degree Indents 20000 µN load

Working on a nano-scale is difficult and the ability to orient and locate with respect to a line which appears straight at low magnification is not always straight at high magnification. Since the ability to accurately locate an indent a set distance from an

interface or place an indent on an interface when the reference line is facetted suggests multiple indents in a line close together would be the solution. That is before the distance between indents to prevent edge effects for the 20000 μN loads is factored in, which prevents multiple measurements close together in a single line from being made perpendicular to the WHA. Thus, it was decided to place a line of indents at a low angle relative to the perceived interface at the appropriate distance not to create edge effects while still allowing one to interpolate across the interface using simple geometry. This technique has also been employed to observe welding interfaces by expanding narrow transition zones [42].

Even using this approach, the 0-degree indents in **Figure 4.1.5** show the difficulty of placing nanoindents on a meandering interface. These indents missed the boundary layer by only about 5-6μm. Though an accident, this resulted in the 3rd indent landing approximately 1.4μm away from the binder matrix of the WHA and 5.7μm away from the interface. Any change in the hardness and modulus at this location could indicate a diffusion layer may also exist within the WHA around the WHA's binder matrix itself.

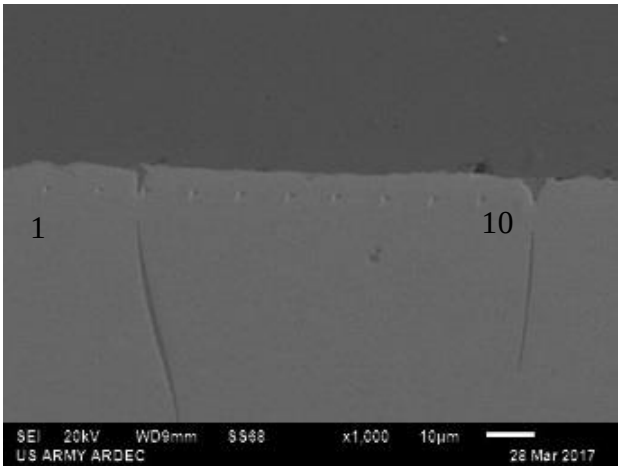

Figure 4.1.5 P1 0 Degree Indents

Judging from the 5 degree line shown in **Figure 4.1.5**, where the goal was to have the 5th indent on the interface, the accuracy of the placement was again off by approximately 5µm. Though not ideal, the vertical and horizontal grids perpendicular to the interface were to gather hardness and modulus values at incremental distances from the interface, while the intent of taking indents at specified angles relative to the interface was to increase the probability of an indent coalescing on the interface as well as getting multiple indents close to the boundary.

Indent number 1 in **Figure 4.1.6** is approximately 10 µm away from the interface and indent 2 is close to a WHA binder matrix interface, while point 10 is on the WHA-D2 interface while no indents were on a void. Additionally, point 6 and 10 are smaller in size which would correspond to the higher hardness in the area.

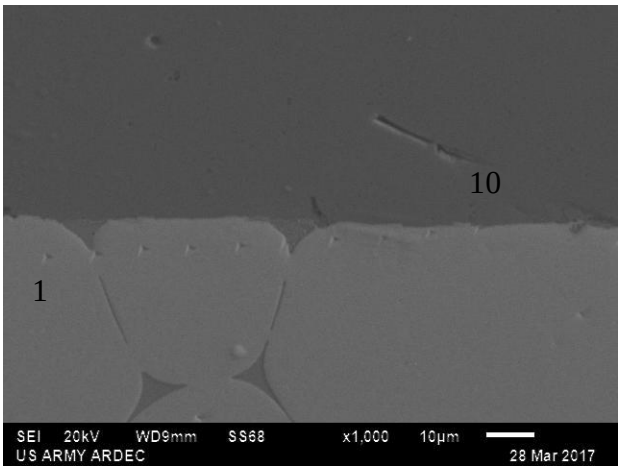

Figure 4.1.6 P1 5 Degree Indents

In **Figure 4.1.7** the 8th indent is on a tungsten to D2 interface and indent number 9 is close to a D2 binder matrix interface as well as a portion of the 15 degree indents in view. Again no indents are on voids which should provide solid nanoindentation results.

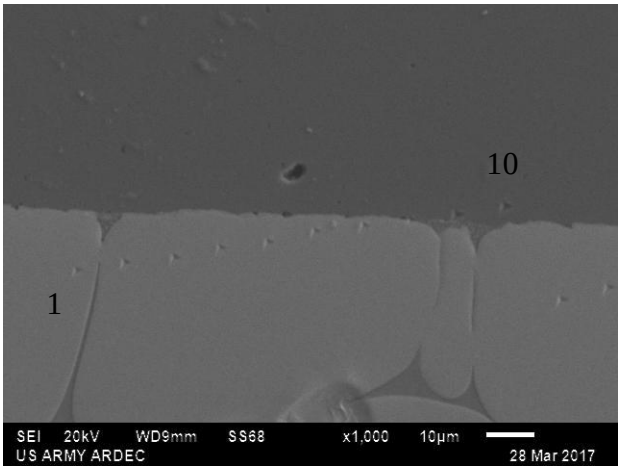

Figure 4.1.7 P1 10 Degree Indents

The 15 degree nanoindents (**Figure 4.1.8**) have the 6th and 7th point on the interface thanks to an irregularly shaped tungsten island; though point 8 also appears to lie on the interface it coalesces with a void potentially providing erroneous results. If this work was carried out again, all the WHA cubes should be polished prior to making the composite.

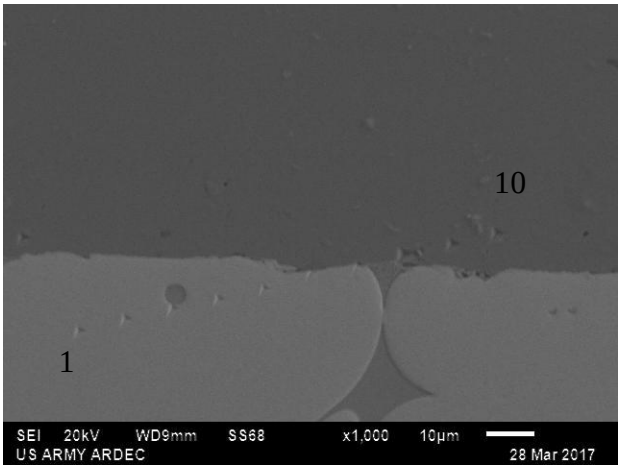

Figure 4.1.8 P1 15 Degree Indents

4.2 SEM of P2 Along an Additional WHA Cube to D2 Interface

In **Figure 4.2.1**, the SEM images are again shown at approximately the same magnification to give an idea of the different nanoindentation areas and scale for the P2 indents since P2-V and P2-H used a 20000 µN load for the indent and whereas the P2-Marker, 0, 5, 10 and 15 degree indents were made with a 5000 µN indent load. The 15-degree indent could not be found, and even at x1000 the other indents were difficult to see except at very high absorption times making rastering difficult.

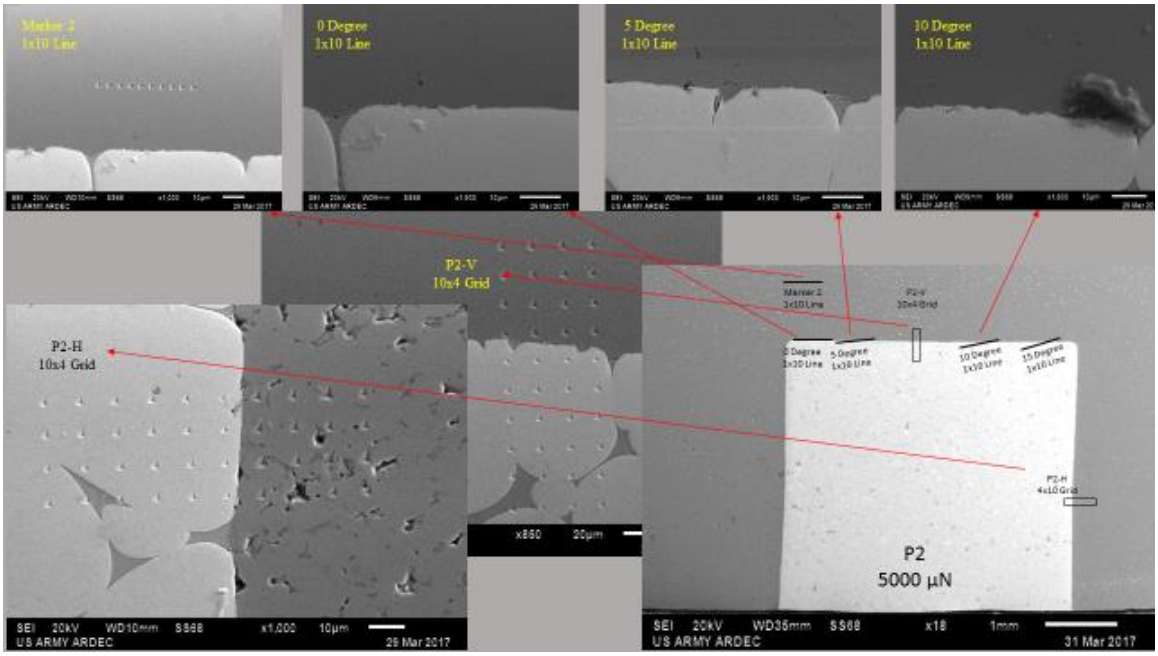

Figure 4.2.1 P2 Overall SEM Images of Nanoindents

4.2.1 SEM of P2 Matrices (perpendicular and parallel to load axis), 20000 µN Load

The same numbering scheme was used for P2-V and P2-H as in P1 and is shown in **Figure 4.2.2** and **Figure 4.2.3** again for reference to match the raw data as well as to

show which indents maybe overlap with a void or an interface. None of the indents from P2-V were on the interfaces or voids though, and like the P1 images the indents in the D2 are much larger than the indents in the WHA. Visually there does not seem to be a noticeable difference in any of the indents in the WHA but the nanoindentation analysis in chapter 5 will show any measureable differences.

The P2-H indents 6, 16, 26, and 36 do seem to be less pronounced than the other indents in the tungsten suggesting this area of the material is again harder, but will also be quantified with the nanoindentation analysis in chapter 5. The D2 indents are again overlapping voids with indent number 8 directly at the vertex of what appears to be three distinct particles which have not necked and will be a perfect example of hardness and modulus properties of a void compared to the other indents representing partially necked and sintered powder

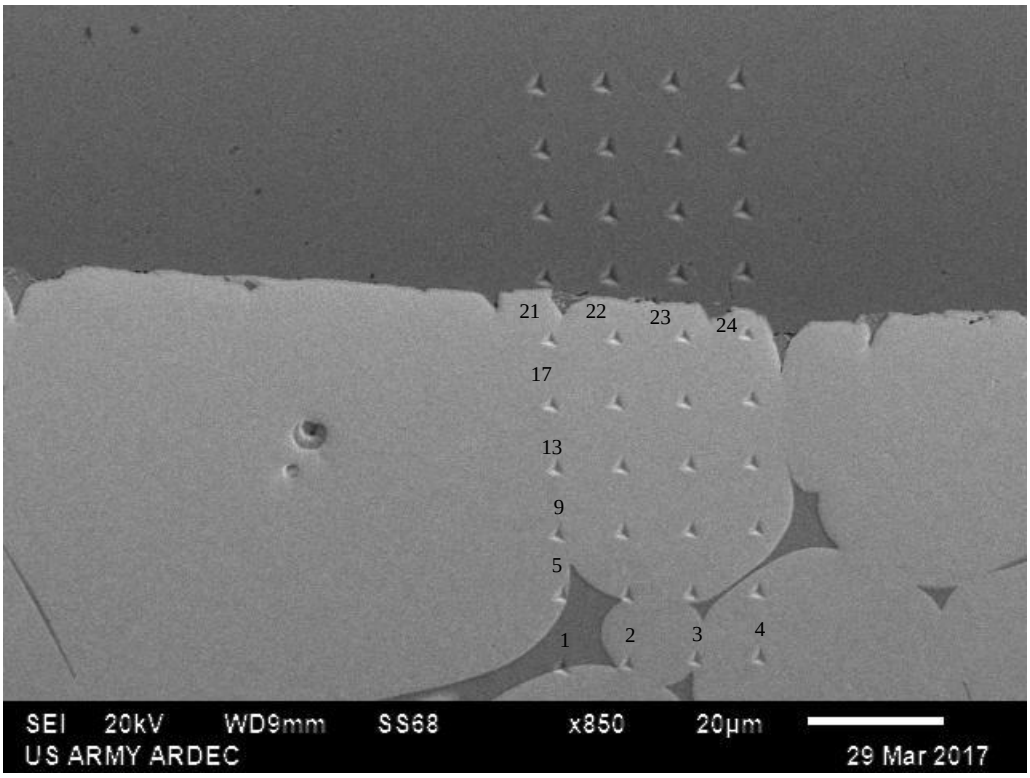

Figure 4.2.2 P2-V 10x4 Grid Indents

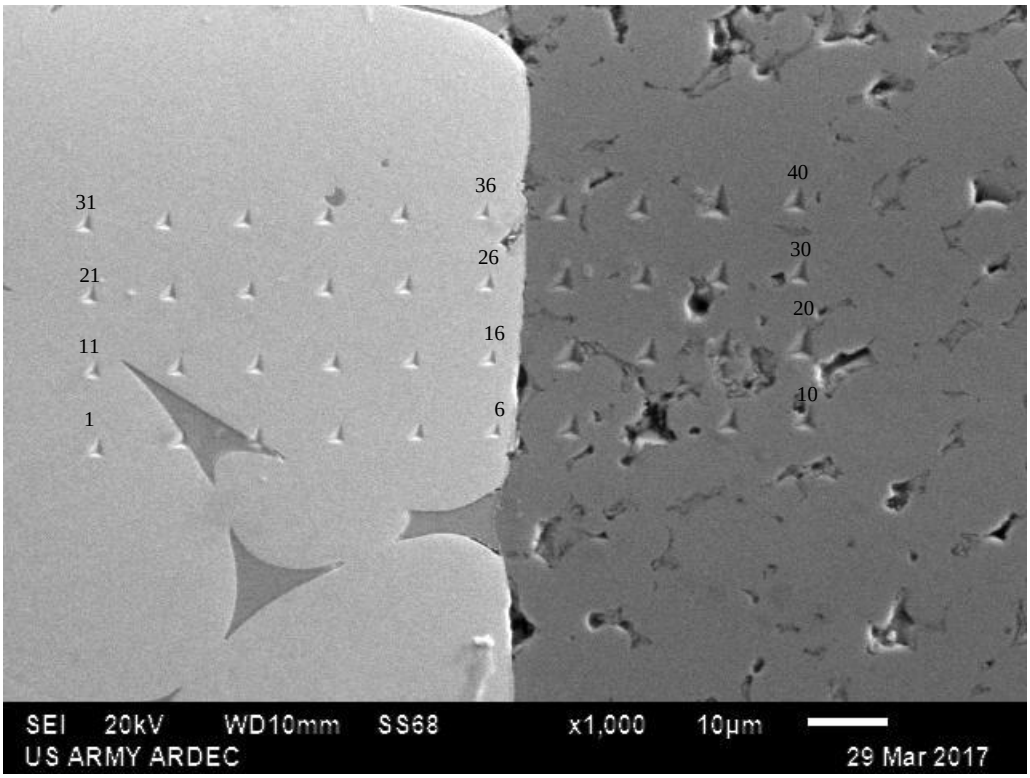

Figure 4.2.3 P2-H 4x10 Grid Indents

4.2.2 SEM of P2- Marker 2, 0, 5, 10, Degree Indents 5000 µN load

The Marker-2 results (**Figure 4.2.4**) do not show anything abnormal and will be a good average value for the D2 modulus and hardness though it is within 50 µm of interface compared to the D2 indents in sample one of two which were taken far away from the WHA cube.

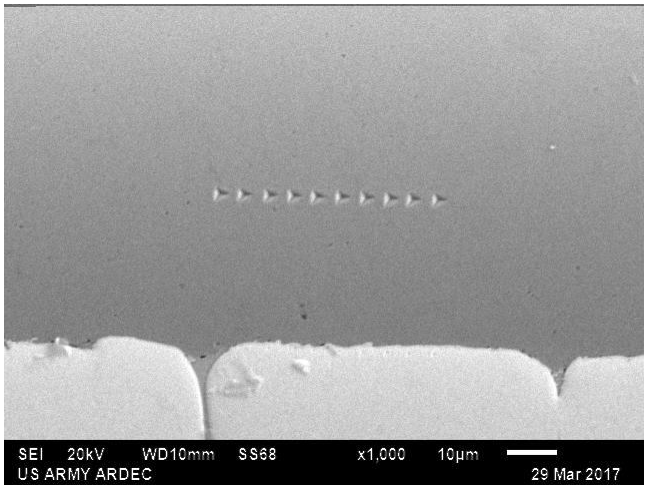

Figure 4.2.4 D2 Marker Number Two

The 0, 5, and 10-degree indents were very hard to see even with known locations. Even with a new nanoindentation probe, at 5000 µN load it is difficult to see the 0-degree indents at x1900 as shown **Figures 4.2.5**. The 0-degree set of indents are of most interest since they closely follow the boundary layer with indent 5 touching the "halo" along with indent 2, though indent 2 is in close proximity to a void which may affect the measurement.

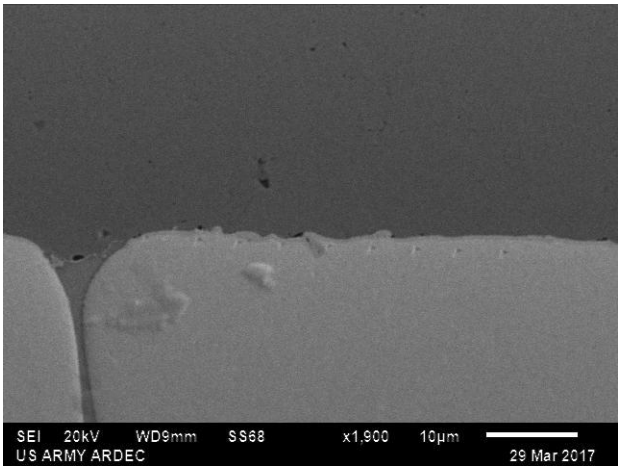

Figure 4.2.5 P2 0 Degree Indents

The 5-degree indent series (**Figure 4.2.6**) also has some indents close to inclusions and could provide insight as to how defects in the WHA can affect nanoindentation measurements.

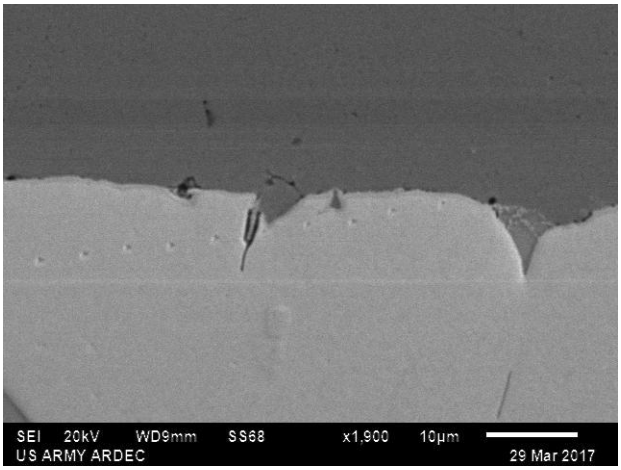

Figure 4.2.6 P2 5 Degree Indents

It was decided to use x1600 for the 10-degree indents (**Figure 4.2.7**) to fully showcase the residue of the foil tape. After EDS measurements were taken, the specimen was cleaned with simple green and a methanol rise, but the residue remained (**Figure 4.2.8**).

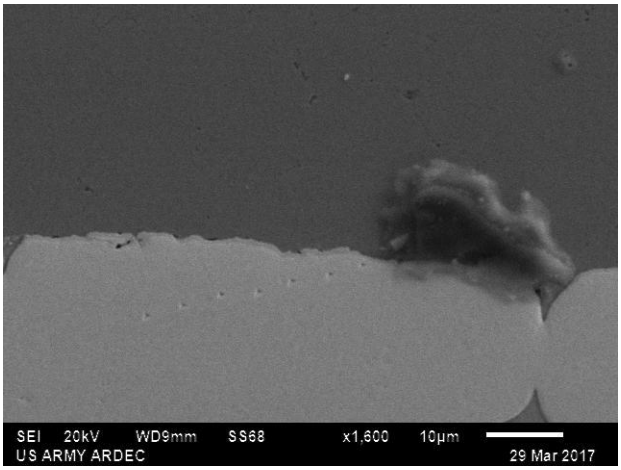

Figure 4.2.7 P2 10 Degree Indents

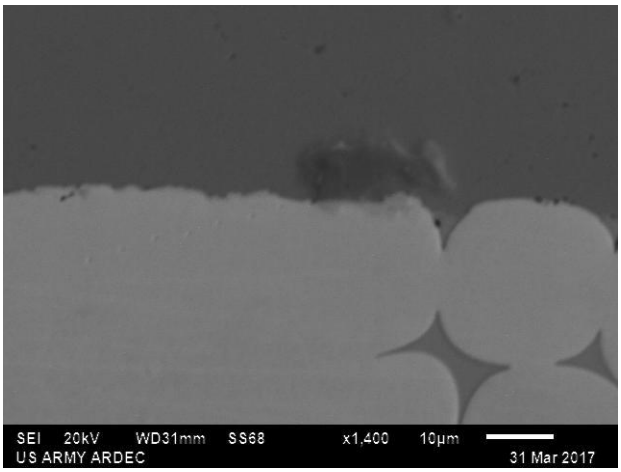

Figure 4.2.8 P2 10 Degree Indents Post Clean

Though less residue remained on the sample after cleaning, there was really nothing more which could be done to correlate the results of nanoindentation points 8-10 to anomalies or the perceived interface.

Chapter 5: Nanoindentation and Microhardness Measurements

In order to compare the latest finite element modeling methods, measurements were taken across the diffusion layer to gather material properties for the D2, the WHA, and the interface. Given the small diffusion layer, nanoindentation was utilized to obtain hardness and elastic modulus properties across the interface and in the samples [43]. These will be directly used in future FEA modeling efforts, but were not the focus of this effort. The nanoindentation did help to characterize the diffusion layer and characterized how the material properties change around the boundary of the WHA. This additional data will only help in characterizing and understanding how the diffusion-affected zone should be modeled, how it affects the material properties, and will be used to help validate theoretical and empirical findings later in this thesis.

5.1 Hand Polished Sample

The first nanoindentation measurements were carried on sample one of two, a hand polished sample shown in **Figure 5.1.1,** with the assistance of Shawn Ward, using a TriboIndenter and TriboScan software at Rutgers the State University of New Jersey, New Brunswick Campus. Initially the surface finish looked acceptable to the eye. After the results were analyzed it was decided the surface topology needed refinement in order to obtain high resolution measurements at the diffusion boundary. Initially six different tungsten to D2 interfaces were interrogated with the indenter using a 5 x 5 grid with 8 μms between indents centered on the boundary layer, ramping to a 20mN load over 20

seconds with a 10 second dwell and a 20 second unload. This particular sample shows a random WHA cube which has floated during the sample manufacturing process.

Figure 5.1.1 Hand Polished NanoIndent Sample

The sample was divided up into multiple areas to interrogate and were located around the perimeters of two of the cubes in the sample as show in **Figure 5.1.2**. The first cube, WHA-1, had three locations W1-146, W1-147, and W1-148 interrogated while the second cube, WHA-2, had locations W2-149, W2-150, and W2-151 interrogated.

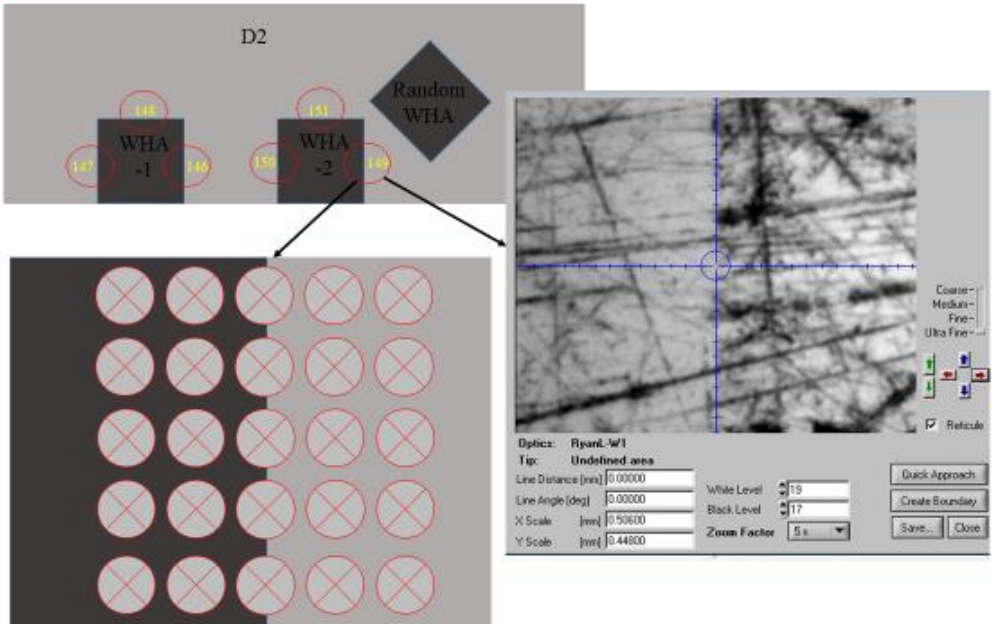

Figure 5.1.2 Layout of First Nanoindentation Measurements

5.1.1 W-1 Nanoindentation in Area with Striations

Striations are easily seen in the image taken for position 146 in **Figure 5.1.2** showing the sample needed to be further polished to prevent surface topology from affecting measurements. The image of position 146 clearly shows the striations are shallower on the tungsten (the left side of the cross hairs) compared to those on the D2 (the right side of the cross hairs), which is ironic as the striations themselves highlight the change in hardness across the tungsten and the difference between the D2 and the WHA in relative hardness though they can obstruct nanoindentation measurements. Large changes in surface topology can affect measurements because the indentor is small enough to make contact at an angle with the sample in one of the valleys introducing abnormal moments and stresses in the indentor and sample. The striations, though potentially bad if the indenter were to interact with them, were very useful in finding the interface between the WHA cube and the D2 alloy and visually depicting the change in hardness.

The modulus of elasticity computed for the W1-146 5x5 grid is graphically represented in **Figure 5.1.3** and the hardness is represented in **Figure 5.1.4**. Even with the striations there is a noticeable discontinuity where the interface should be. In chapter 4 it was shown the accuracy of the indent location was within approximately 5 μms and given the change in depth of striations one can be confident the discontinuity in **Figure 5.1.3** is the interface between the WHA and the D2. Additionally the variation in indent depth and corresponding modulus and hardness in the x-axis, specifically -72.614003 mm and -72.606003 mm in **Figures 5.1.3 and 5.1.4** can be explained by the low densification in the D2 powder adjacent to the WHA as seen in the SEM images of Chapter 4.

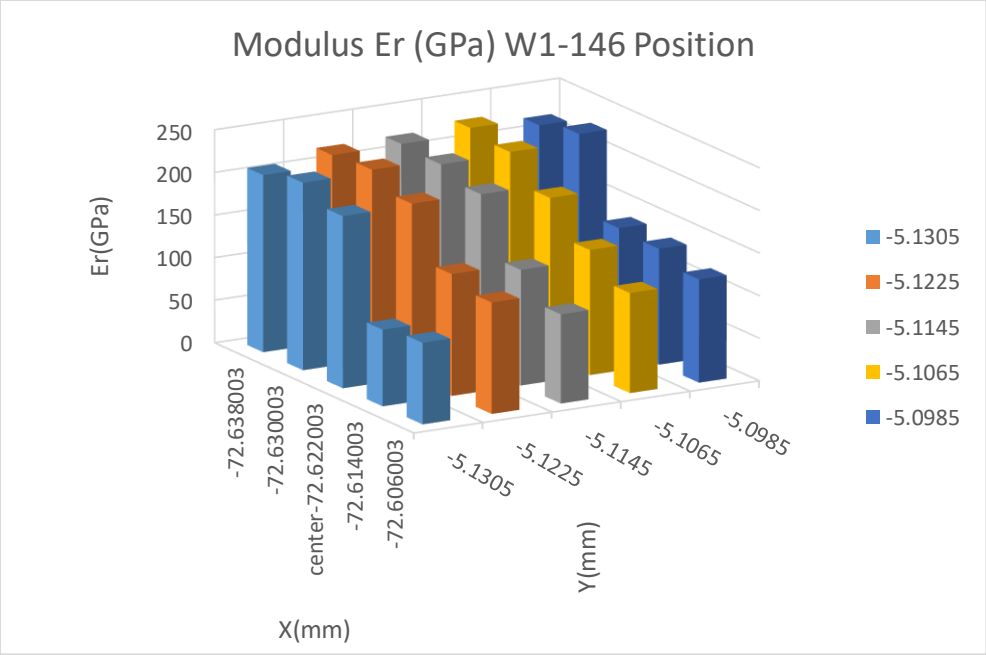

Figure 5.1.3 Nanoindentation Results Right Side W1-146 Er (GPa)

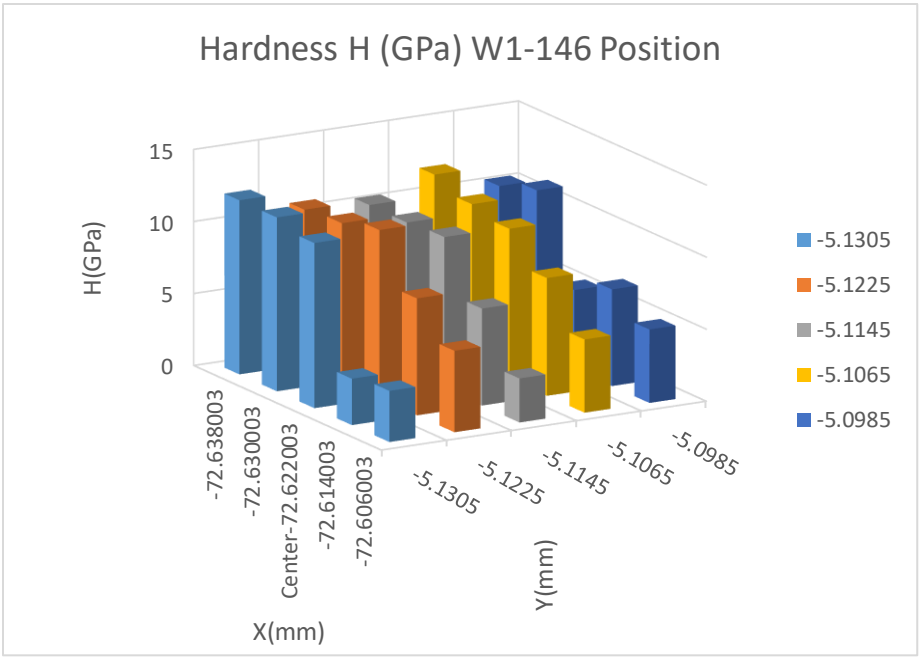

Figure 5.1.4 Nanoindentation Results Right Side W1-146 H (GPa)

The hardness and modulus nanoindentation results for the top interface are shown in **Figures 5.1.5 - 5.1.6** and show some variation without a delineation line which is attributed to the rough surfaces of both the D2 and the WHA.

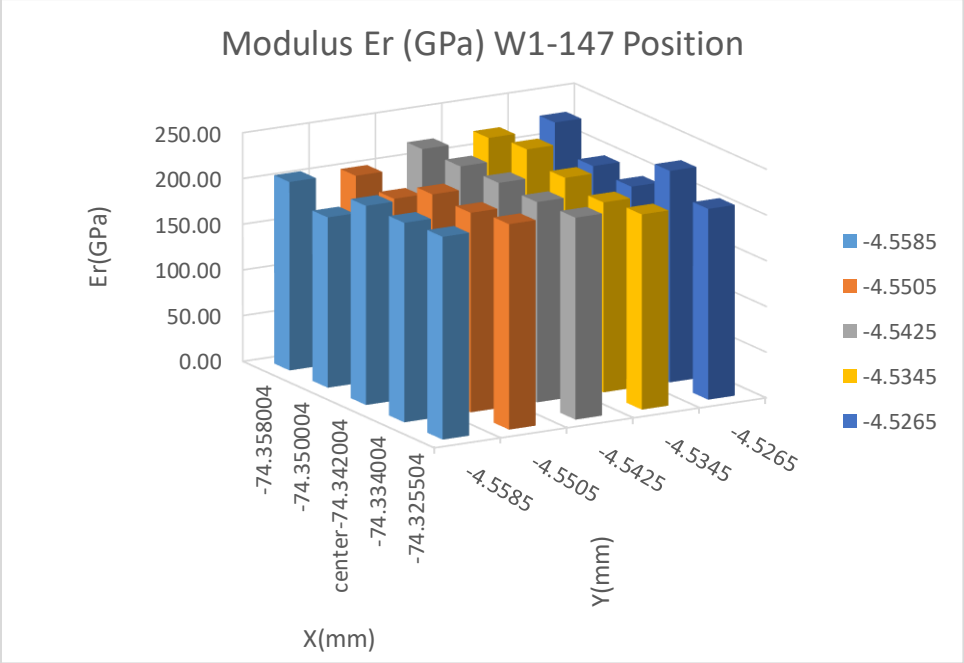

Figure 5.1.5 Nanoindentation Results Top W1-147 Er (GPa)

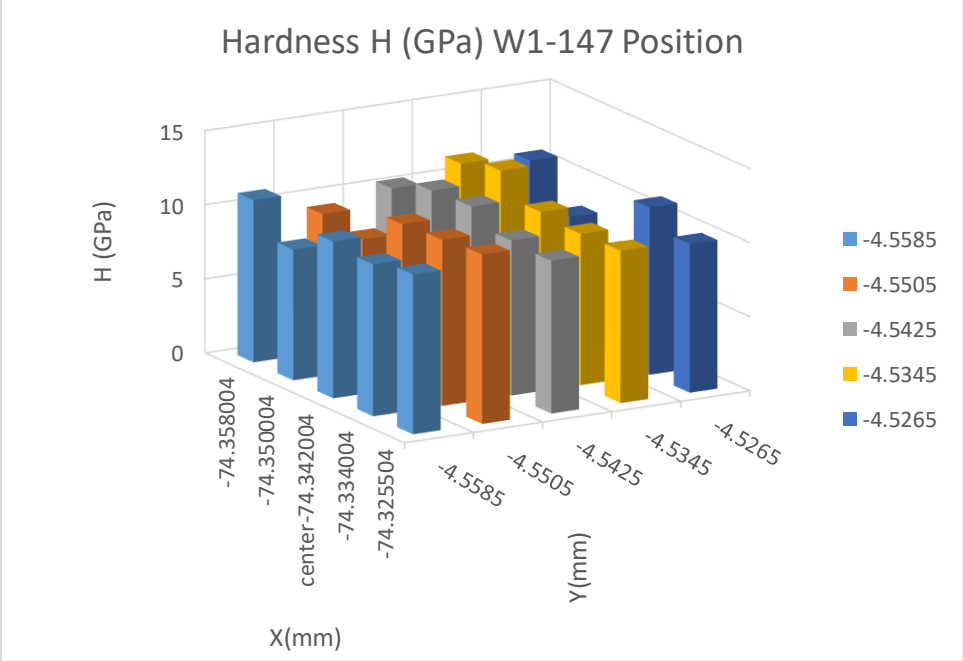

Figure 5.1.6 Nanoindentation Results Top W1-147 H (GPa)

Likewise the hardness and modulus nanoindentation results for the left interface are shown in **Figures 5.1.7 - 5.1.8** and show greater variation than the top interface potentially due to the low densification in this area. Again there is no clear delineation line which can be attributed to the rough surfaces of both the D2 and the WHA.

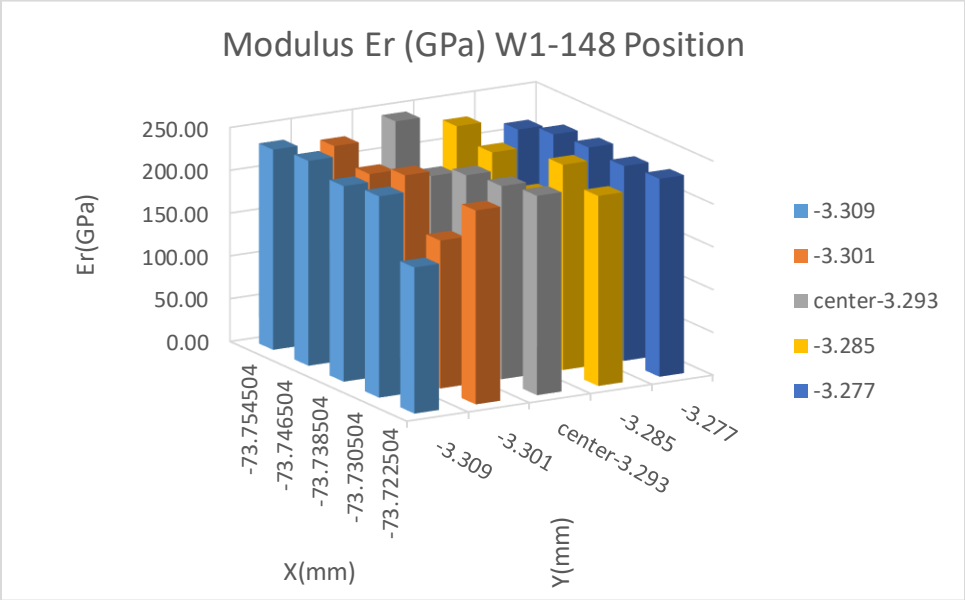

Figure 5.1.7 Nanoindentation Results Left Side W1-148 Er (GPa)

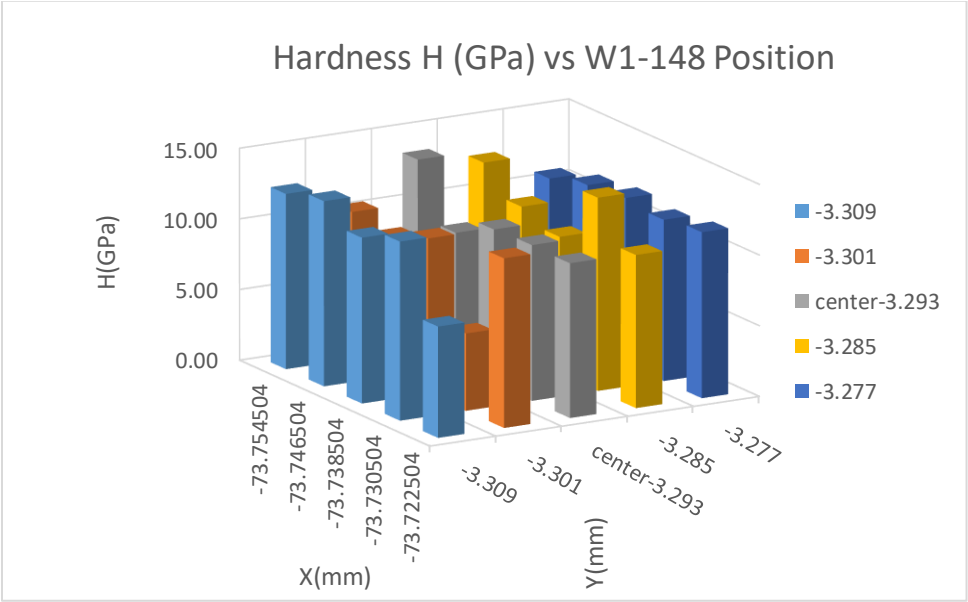

Figure 5.1.8 Nanoindentation Results Left Side W1-148 H (GPa)

All the results are graphed together for W-1 indents in **Figure 5.1.9** and **Figure 5.1.10,** which suggest indents for positions 147 and 148 are most likely only on the WHA. The wide variation is most likely from the striations, since indents falling on the WHA's nickel and iron binder matrix should produce a hardness of 3.10 ± 0.2 GPa and 4.33 ± 0.3 GPa if on the tungsten grain [44] rather than the 7.67 GPa ± 0.2 GPa observed. The modulus observed is also quite high, with greater than 180 GPa compared to literature's ~1050 MPa [44] suggesting hardness and modulus of the WHA may have increased with this process.

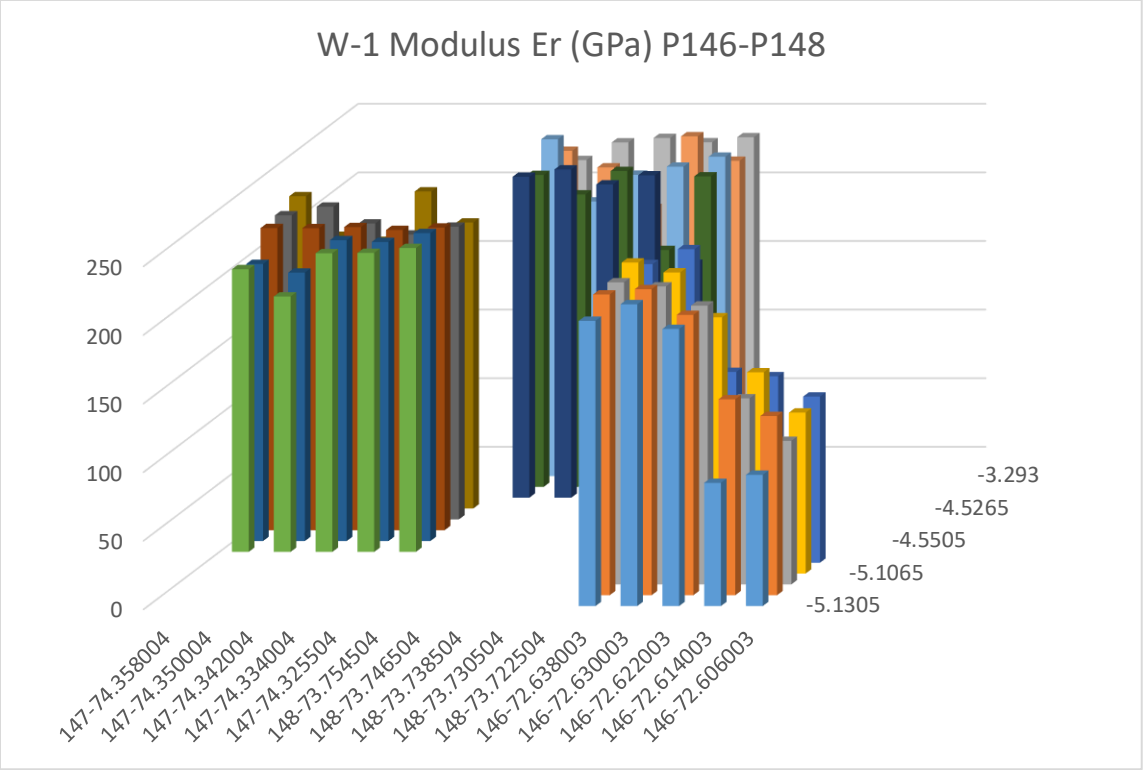

Figure 5.1.9 Nanoindent Results W-1 Er (GPa) P146-P148

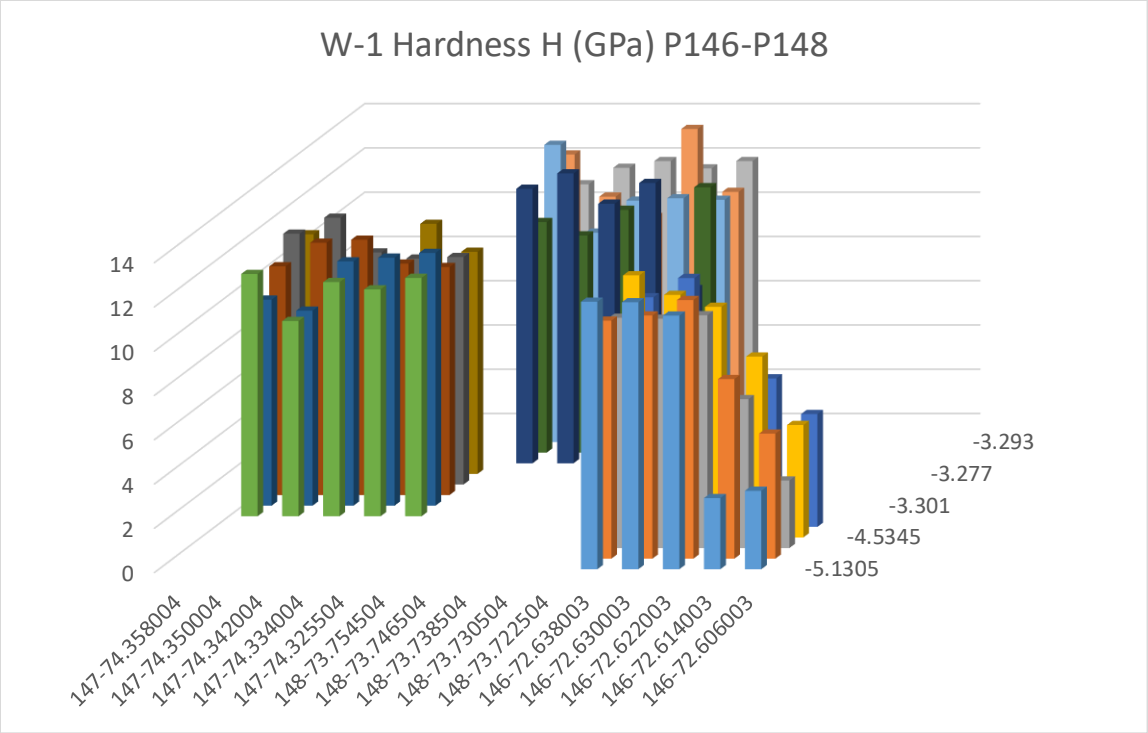

Figure 5.1.10 Nanoindent Results W-1 H (GPa) P146-P148

Graphing all the indents on one chart provides a good characterization of the homogeneity of the different interfaces relative to the FAST's load axis. This can help with RVE development in the future but also identifying variance along an interface.

5.1.2 W-2 Nanoindentation in the Boundary Area

The indents and corresponding modulus and hardness for W-2 are shown in **Figure 5.1.11** and **Figure 5.1.12**. These results along with the images in **Figure 5.1.13** suggest P149 and P150 spanned the boundary layer. The image in **Figure 5.1.13** also depicts a slightly better surface for P149 and P151 than P146 which may explain the lower variation in the results; though the accuracy of the results cannot be fully verified

since SEM of the indents were not carried out since a smoother sample was prepared (two of two) and a better nanoindentation method was developed for the sample.

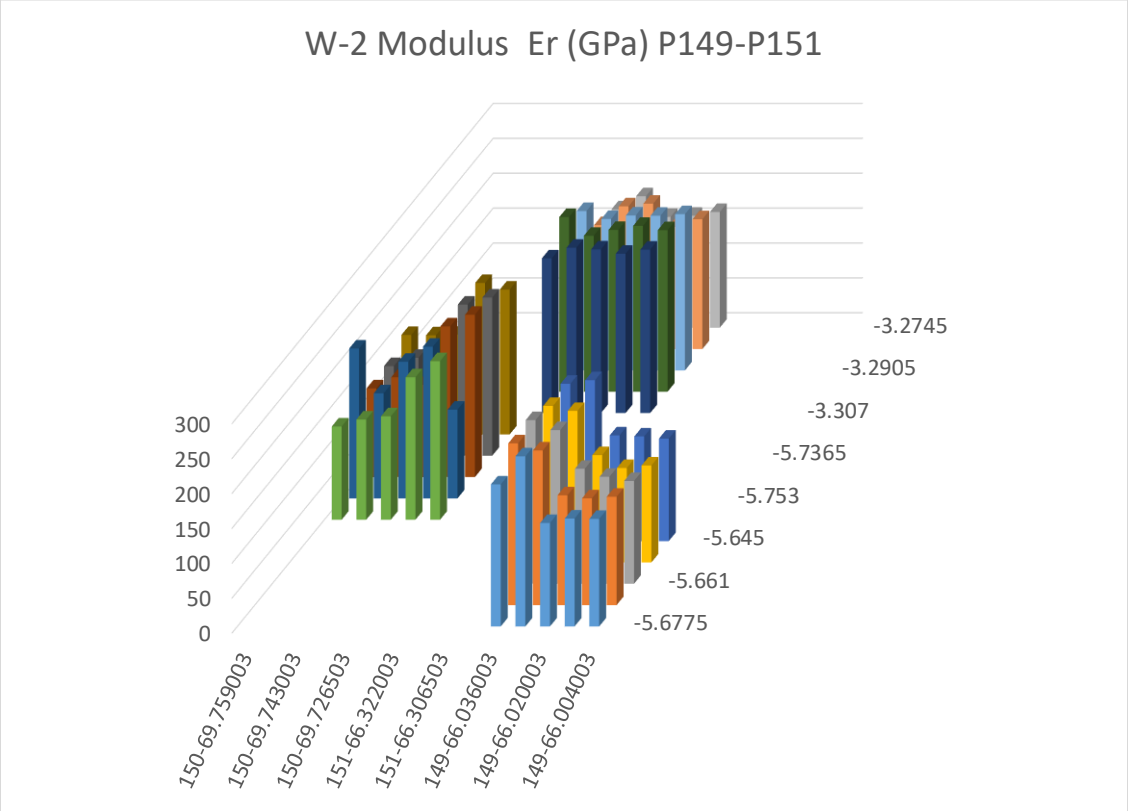

Figure 5.1.11 Nanoindent Results W-2 Er (GPa) P149-P151

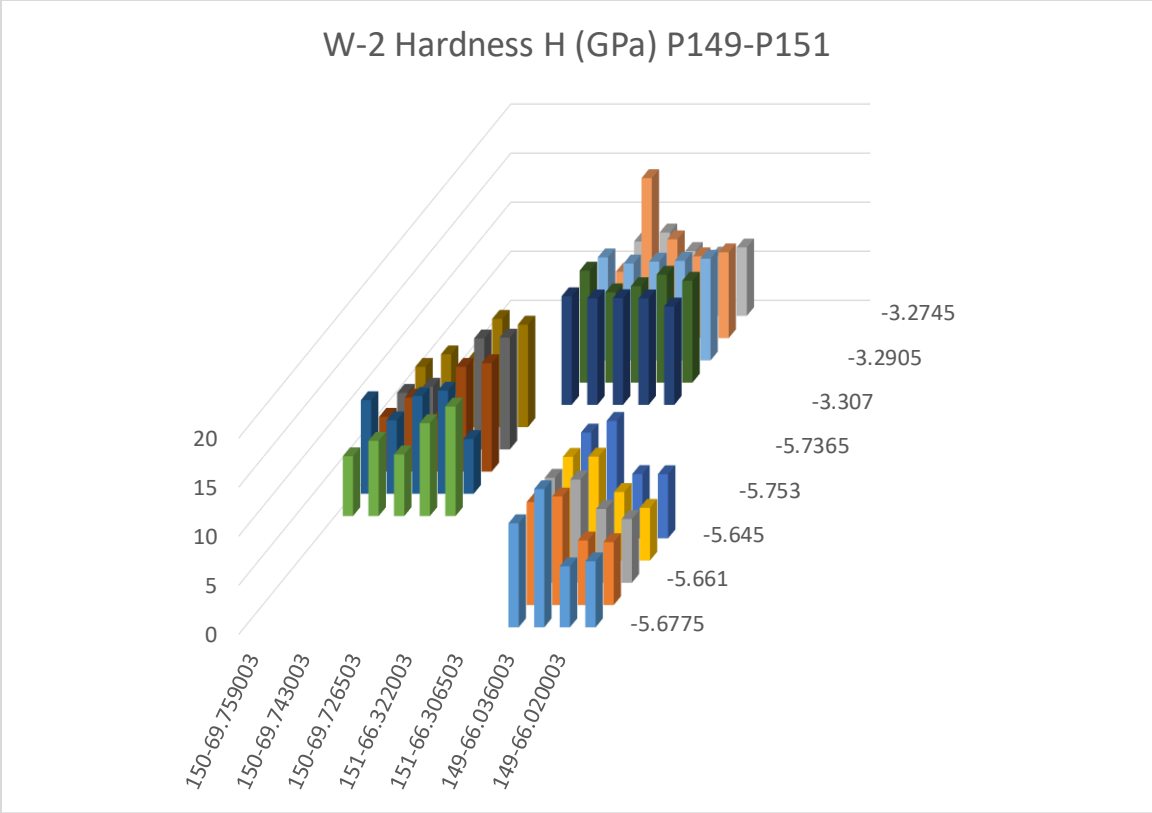

Figure 5.1.12 Nanoindent Results W-2 H (GPa) P149-P151

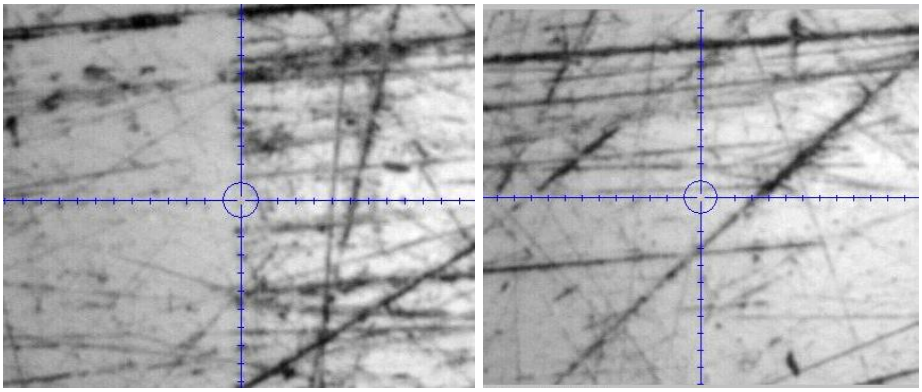

Figure 5.1.13 W2- p149 (Left) p151 (Right)

5.2 Machine Polished Sample

Chapters 1, 2 and 4 covered how sample two of two was prepared. Sample two of two depicted in **Figure 3.3.1** and **Figure 3.3.2** was used for the remainder of the nanoindentation measurements which will be discussed in this section.

5.2.1 Vertical and Horizontal Nanoindents Taken Across Boundary Layers Perpendicular and Parallel to Load Axis

The first nanoindents carried out were the vertical and horizontal indents; P1-V, P1-H, P2-V and P2-H using a 4x10 and 10x4 grid respectively with 10 μms spacing between indents with the grids centered on the boundary layer. The indent was ramped to a 20mN load over 20 seconds with a 10 second dwell and a 20 second unload. As can be seen in **Figure 5.2.1,** the surface finish of the D2 and WHA is much better compared to the first sample and porosity and tungsten grains and binder are now distinguishable. This is invaluable for the placement of the nanoindentations measurements along the interface. Additionally, the surface is good enough the nanoindents can actually be seen with TriboIndenter's camera which aids in nanoindentation placement. The images in **Figure 5.2.1** are taken of the D2-2 and W-2 4x4 indent grid whose values were used to gather nanoindent measurements far from the WHA-D2 interfaces to determine if bulk hardness and modulus properties were increased compared to properties obtained from conventional methods. Though the exact compositions and processes used are distinct, W, Ni, Fe, and Co alloys prepared by SPS have produced tungsten grains with comparable hardness properties ranging from ~10.5 GPa – 13 GPa [10].

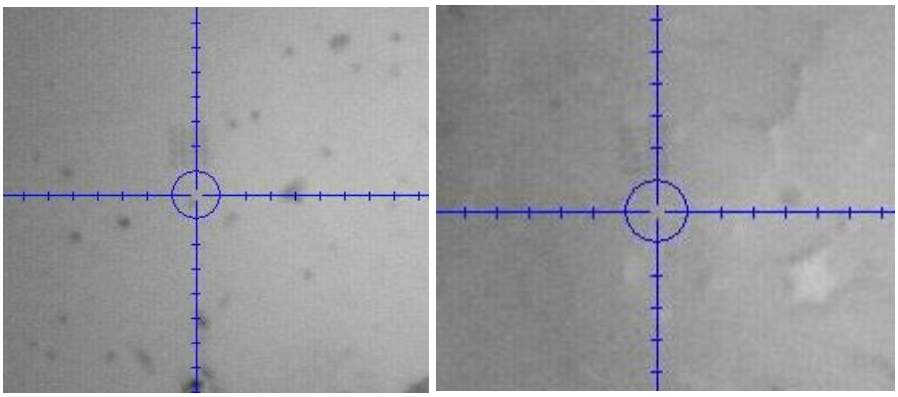

Figure 5.2.1 D2-2 (Left) W-2 (Right)

In this sample the D2 hardness is on par with ASTM A681 Standard Specification for Tool Steels Alloys with minimum hardness of 59 HRC or 674 HV corresponding to 6.61 GPa [37] [45] as well as what has been found in literature. The sample was produced at 1000℃ and was not tempered compared to those samples in literature which utilized austenitizing temperatures of 1025°C; these produced 63 HRC or 772 HV or 6.2 GPa with one temper at 205°C/2hrs or 47 HRC or 471 HV or 4.6 GPa with 1 temper at 538℃ which corresponds to 4.6 GPa [46] [45] [47] [48]. Thus, the D2 hardness values shown in **Table 5-1** are within the bounds of standards and literature given it was prepared with FAST and not standard methods. The hardness for the D2 seems to be rather uniform given the two different points are very close to the same hardness which would contradict the SEM images, but it should be noted these measurements were taken in the area where the D2 powder had both pressure and joule heating aiding the consolidated. Even then the modulus seems to be very low compared to published results and should be closer to 200-250 GPa [48].

	Average (GPa)	Std. Deviation (Gpa)
D2-1 Modulus	100.213	3.743
D2-2 Modulus	120.681	3.193
D2-1 Hardness	4.125	0.313
D2-2 Hardness	4.242	0.154
W-1 Modulus	181.539	4.654
W-2 Modulus	181.736	7.896
W-1 Hardness	8.542	0.173
W-2 Hardness	6.796	0.312
All D2 Modulus	110.4475	10.9465
All D2 Hardness	4.1834	0.2497
All W Modulus	181.6372	6.3764
All W Hardness	7.6693	0.9210

Table 5-1 Average and Std. Deviation of Modulus and Hardness Values for "Bulk" D2 and WHA

The individual results are also graphed in **Figures 5.2.2** and **Figure 5.2.3** as well as in the **APPENDIX A** to show there are no major outliers as SEM imaging was not taken for these areas to determine if voids coalesced with the indents.

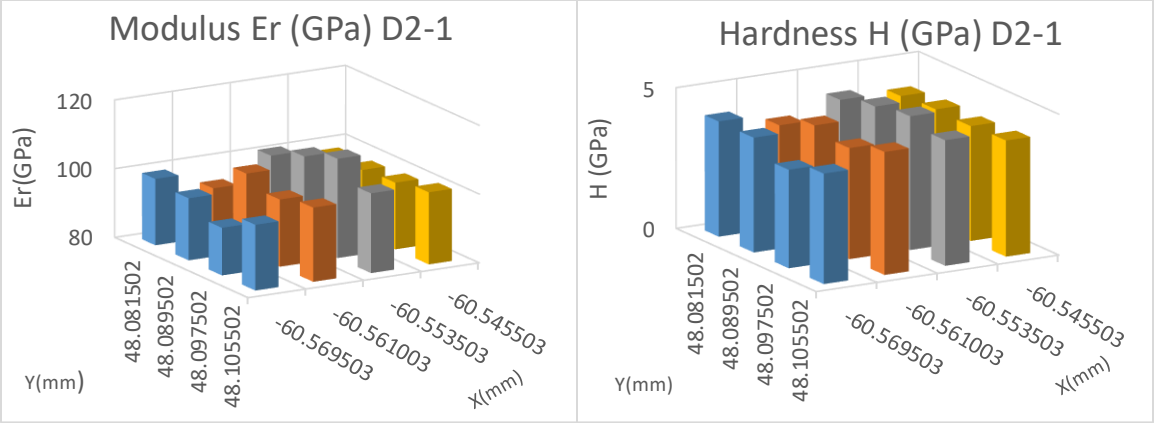

Figure 5.2.2 Nanoindent Results for Bulk Material, D2-1 Location

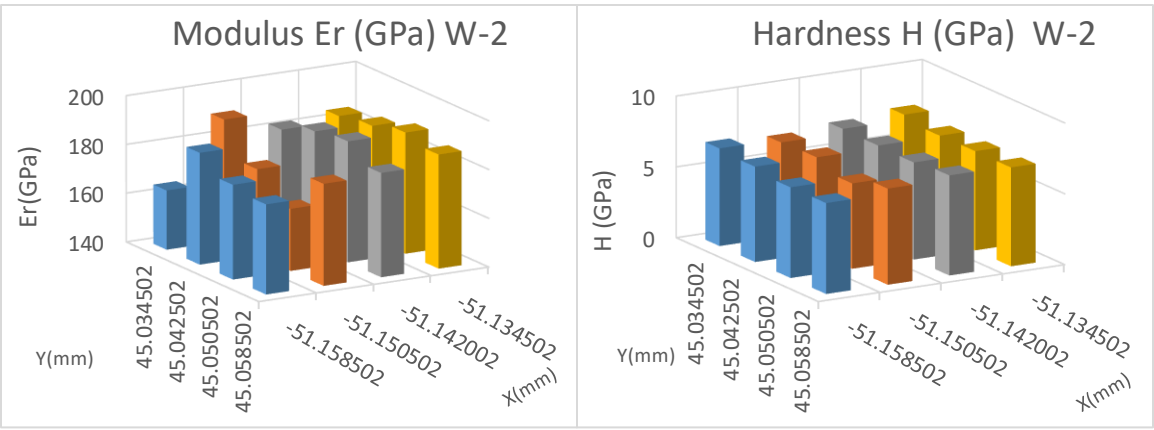

Figure 5.2.3 Nanoindent Results for Bulk Material, W-2 Location

The TriboIndenter images taken of the P1-V, P1-H, P2-V, P2-H indents can be seen in **Figure 5.2.4** and clearly show nice clean transitions between the WHA and the D2. Care was taken not to place the indents on large voids as best as possible and the shadow on the interface may be the change in height between the two surfaces as the optical imagery revealed in chapter 2.

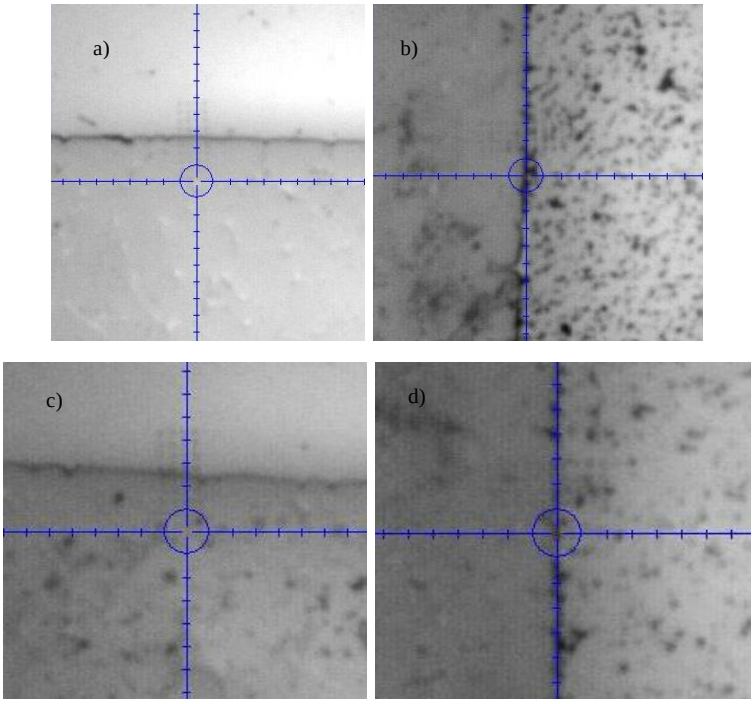

Figure 5.2.4 P1-V (a), P1-H (b), P2-V (c), P2-H (d)

The modulus results for P1-V nanoindents are shown in bar chart format **Figure 5.2.5** for topographical visualization along with a few data labels and numbers for clarity which correspond to the SEM and EDS points (Chapter 4's work). Indent number 24 was directly on the interface (y = 47.690502 mm). The modulus actually increases as the interface is approached and then sharply drops off to the average values obtained and provided in **Table 5-1** which is better visualized with the use of the 2D line chart in **Figure 5.2.6** which averages the four columns of data in **Figure 5.2.5**. The average modulus of the WHA can be approximated by a 5^{th} order polynomial and the D2's average modulus can be approximated by a 4^{th} order polynomial.

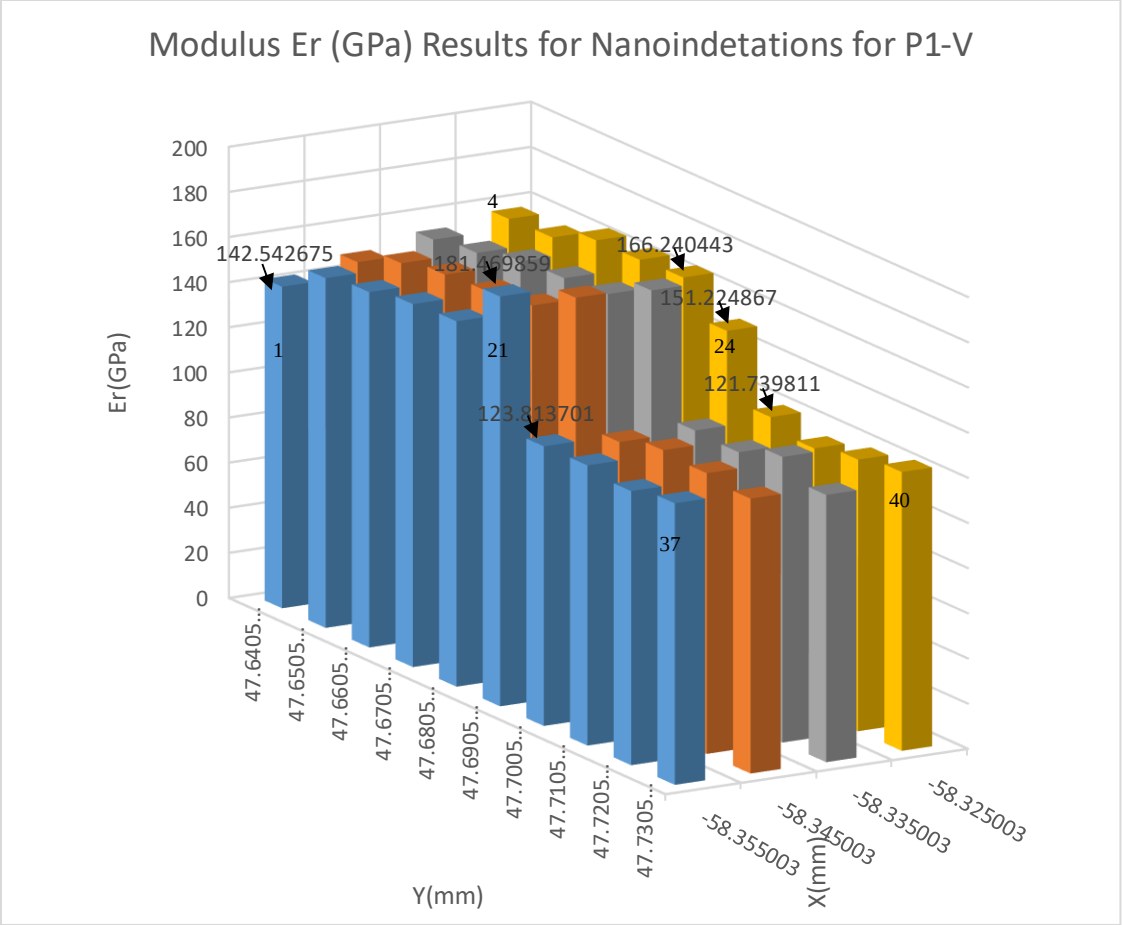

Figure 5.2.5 Modulus Results of Nanoindentations Taken Vertically Across Interfaces for P1-V, Rotated

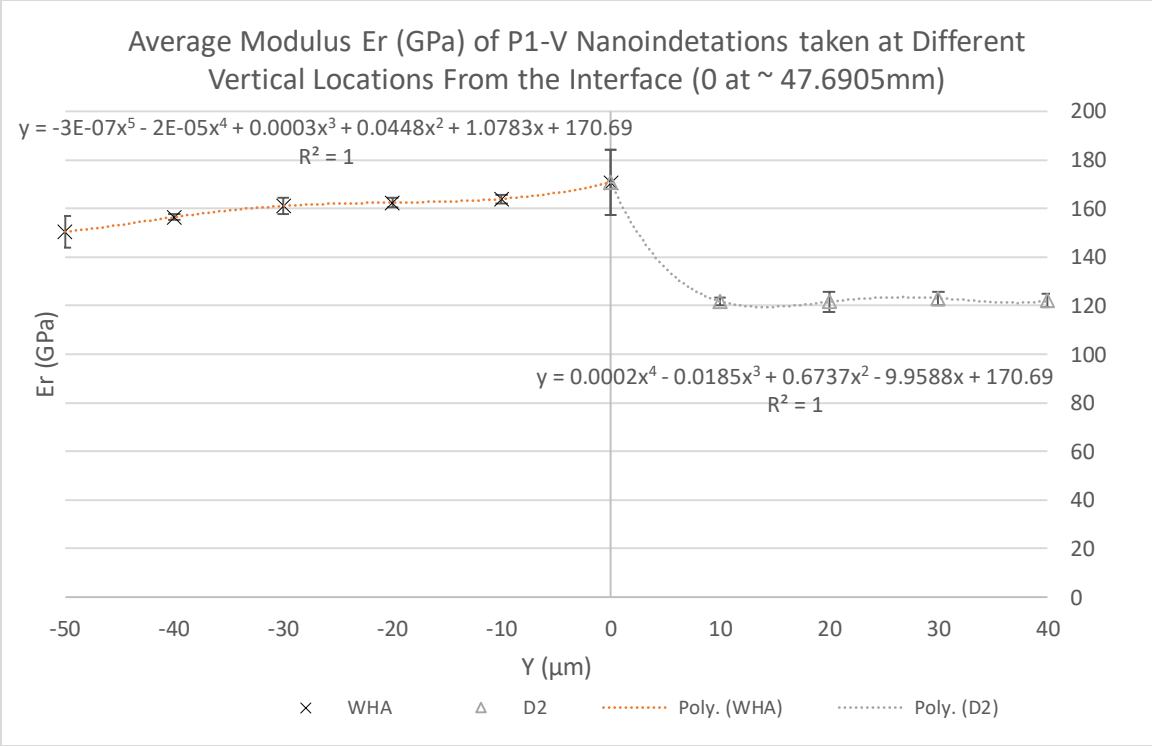

Figure 5.2.6 Average Modulus Results of P1-V Nanoindentations Taken at Different Distances from Interface

The corresponding hardness results for P1-V are show in **Figure 5.2.7** and are even more interesting as the hardness increases almost exponentially on the WHA side as the interface is approached (**Figure 5.2.8)**, but then sharply drops off to the average D2 hardness. These measurements suggest either a WO or WC alloy has formed since $W_{25}O_{75}$ has produced hardness values of 7.7 GPa, while $W_{87}O_{13}$ has produced hardness values of 25 GPa, [49]; single crystal WC has produced hardness values of 8-18 GPa depending on the influences of hexagonal crystallographic orientation with respect to the indenter [50]

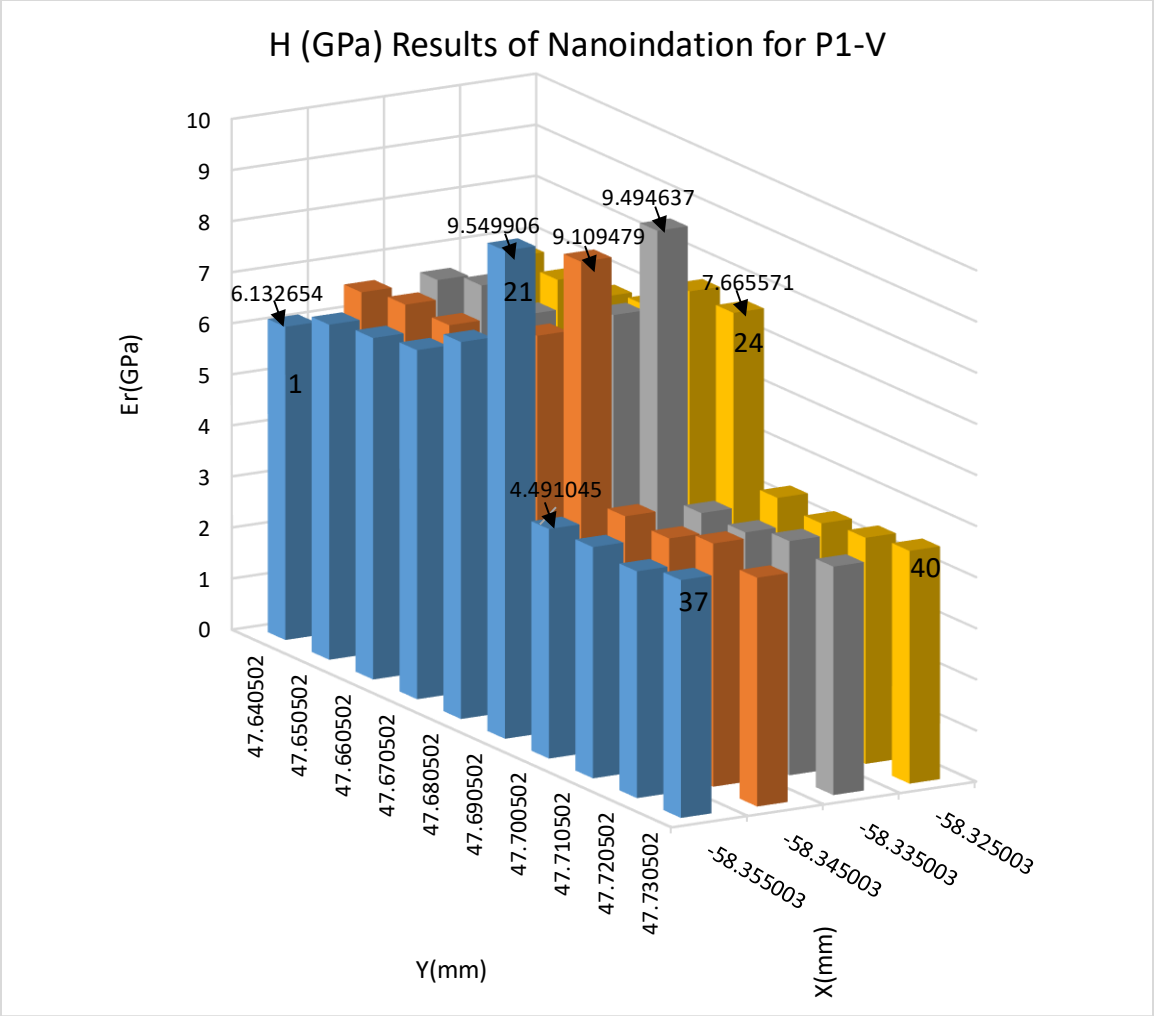

Figure 5.2.7 Hardness Results of Nanoindentations Taken Vertically Across Interfaces at P1-V, Rotated

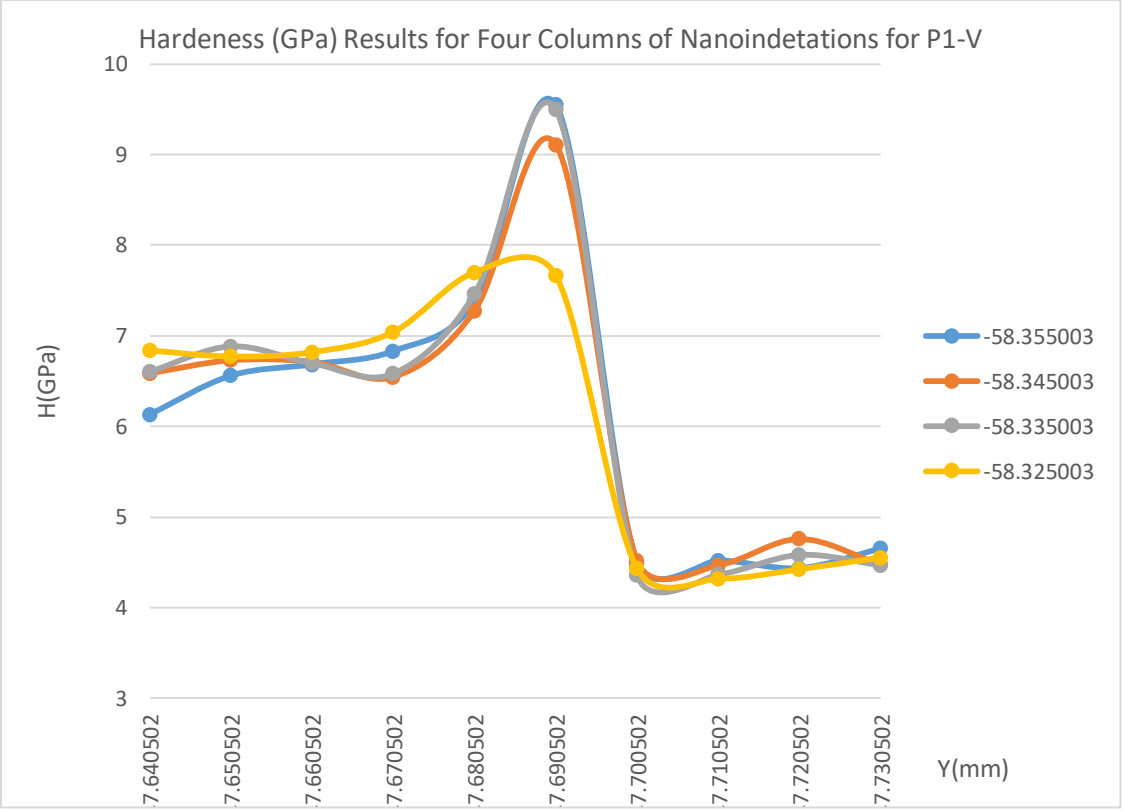

Figure 5.2.8 Hardness Results of Four Columns of Nanoindentations Taken Vertically Across Interfaces at P1-V

The hardness and modulus do appear to follow a simple diffusion couple as shown in **Figure 5.2.7** and **Figure 5.2.8** [39] with point 21 about one µm from the interface on the WHA side and point 24 directly on the interface. Both figures also show the extent of the diffusion affected zone and the effects of diffusion on the material properties and the resulting boundary layer. The average hardness results for the four columns of indentations in **Figure 5.2.7 and 5.2.8** are shown in **Figure 5.2.9**. It shows the WHA hardness can be approximated by a 5^{th} order polynomial and the D2 can be

approximated by a 4th order polynomial.

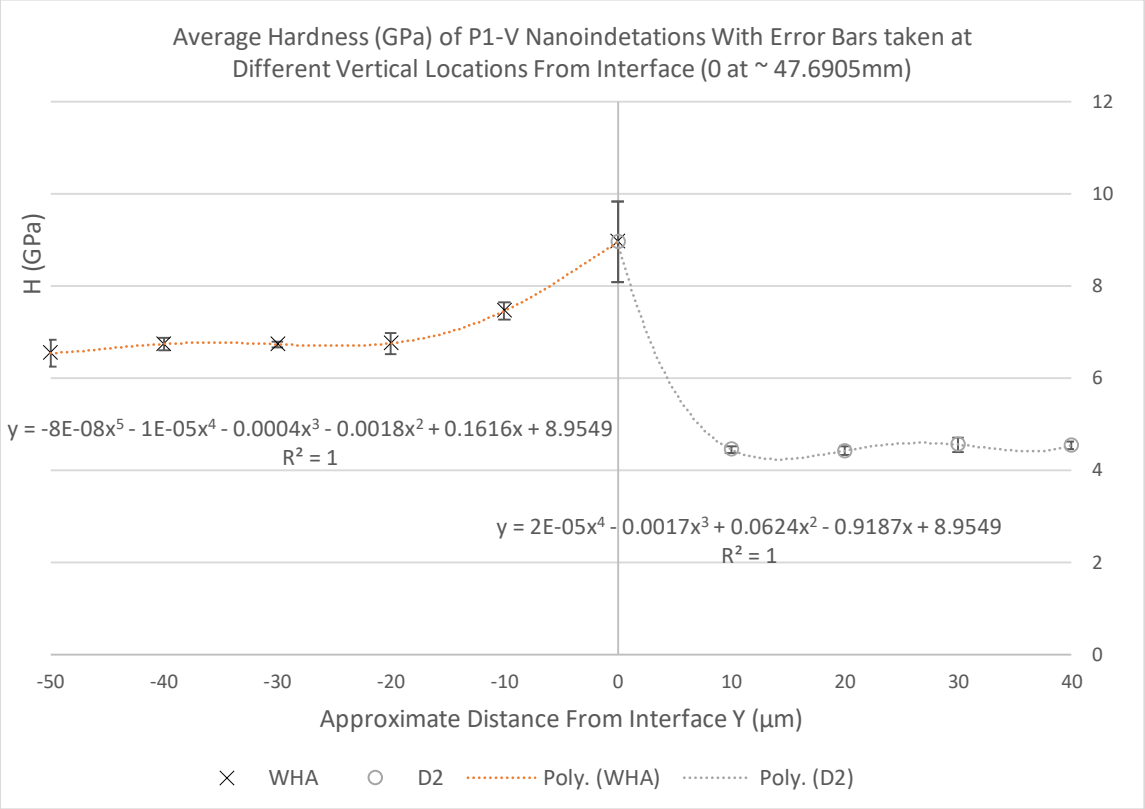

Figure 5.2.9 Hardness Results of Nanoindentations Taken Vertically Across Interfaces at P1-V, Rotated

The indents in the WHA within 10 µm of the boundary layer are on average 9.38 GPa (excluding point 24 since it is on the boundary layer) compared to the average hardness of 8.54 GPa for the W-1 indents. The average modulus for these same indent is 177.2 GPa compared to the D2-1 average of 100.2 GPa. Even though the indents in the WHA 30-40 µm from the interface (point 24) are lower than the average of the W-1 results, it is clear the hardness and modulus values start to increase 30-40 µm from the interface. Therefore the mechanical properties are affected at least 30-40 µm into the WHA resulting in diffusion layer at least 30-40 µm. The same trend does not occur for the D2 hardness and modulus so it is believed the major effect of the diffusion on the mechanical properties for this composite is mostly bilateral into the WHA. Therefore the

following four equations should only be used to approximate the modulus and hardness based within 30-40 µm from interface.

$WHA_{modulus}$ $f(y) = -3E\text{-}07x^5 - 2E\text{-}05x^4 + 0.0003x^3 + 0.0448x^2 + 1.0783x + 170.69$

$D2_{modulus}$ $f(y) = 0.0002x^4 - 0.0185x^3 + 0.6737x^2 - 9.9588x + 170.69$

$WHA_{hardness}$ $f(y) = -8E\text{-}08x^5 - 1E\text{-}05x^4 - 0.0004x^3 - 0.0018x^2 + 0.1616x + 8.9549$

$D2_{hardness}$ $f(y) = 2E\text{-}05x^4 - 0.0017x^3 + 0.0624x^2 - 0.9187x + 8.9549$

The EDS analysis in APPENDIX A will help to determine if traces of carbides or oxides of W appear in the WHA which would explain the higher hardness as the interface is approached in these areas. Given the high carbon content in the D2 and resulting gradient of the D2 alloy to that of the WHA, one would expect carbon to migrate across the boundary layer and produce tungsten carbides which are now being investigated as nanoindenter tips for in-situ additive manufacturing characterization [51].

It is useful to compare the individual columns of the P1-V nanoindentations, specifically the first column of P1-V where point 21 was approximately one µm from the interface (**Figure 5.2.10**) and the last column (**Figure 5.2.11**) where point 24 was directly on the interface. This comparison shows the WHA's hardens is close to 10 GPa based within one µm of the interface based on the first column of data whereas the WHA's hardness would never break 8 GPa based on the last column. This shows the drastic change in material properties within 10 µm from the interface which can occur and the importance of obtaining higher fidelity measurements closer to the interface to determine

what is happening in this region.

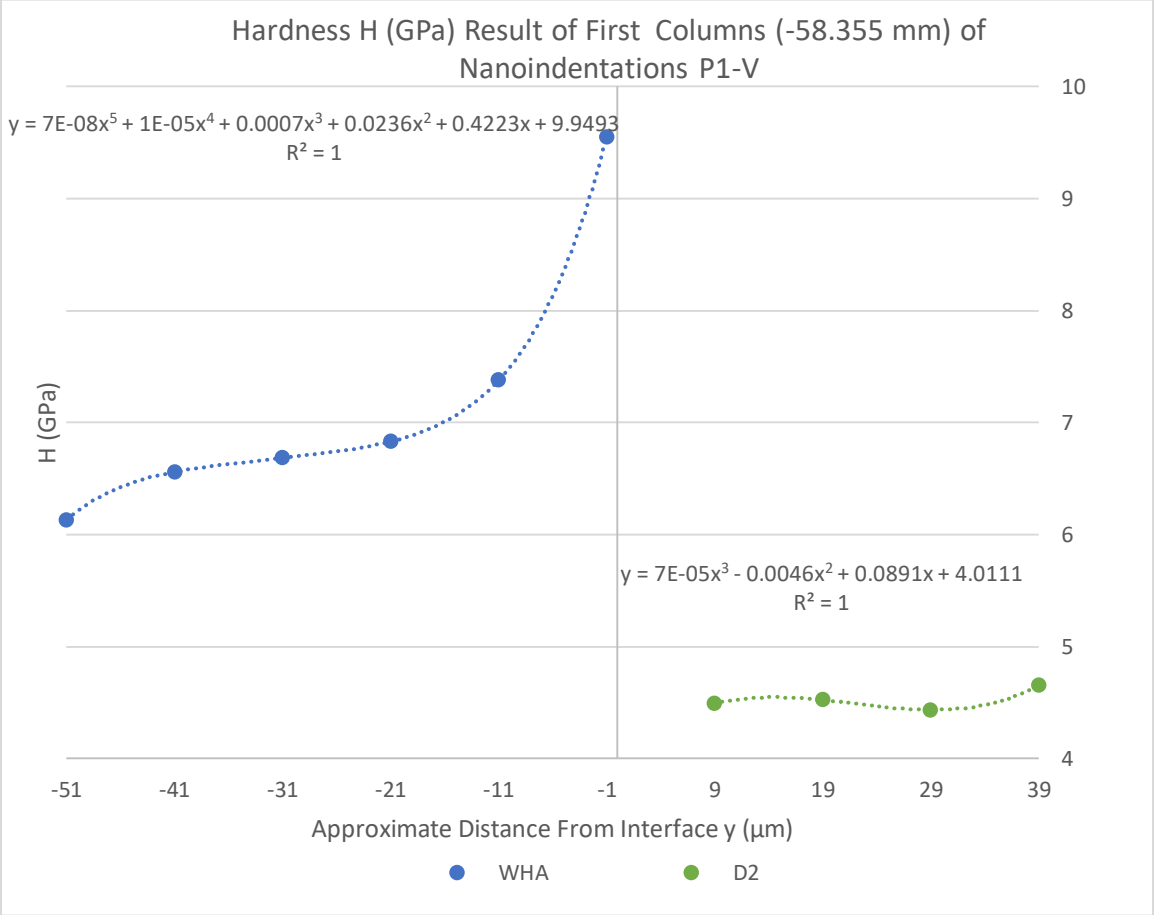

Figure 5.2.10 Hardness Results for the First Column of Indents in the Bar Chart in Figure 5.2.6 (-58.355003 mm) for P1-V with Point 21 One µm from the Interface on the WHA Side

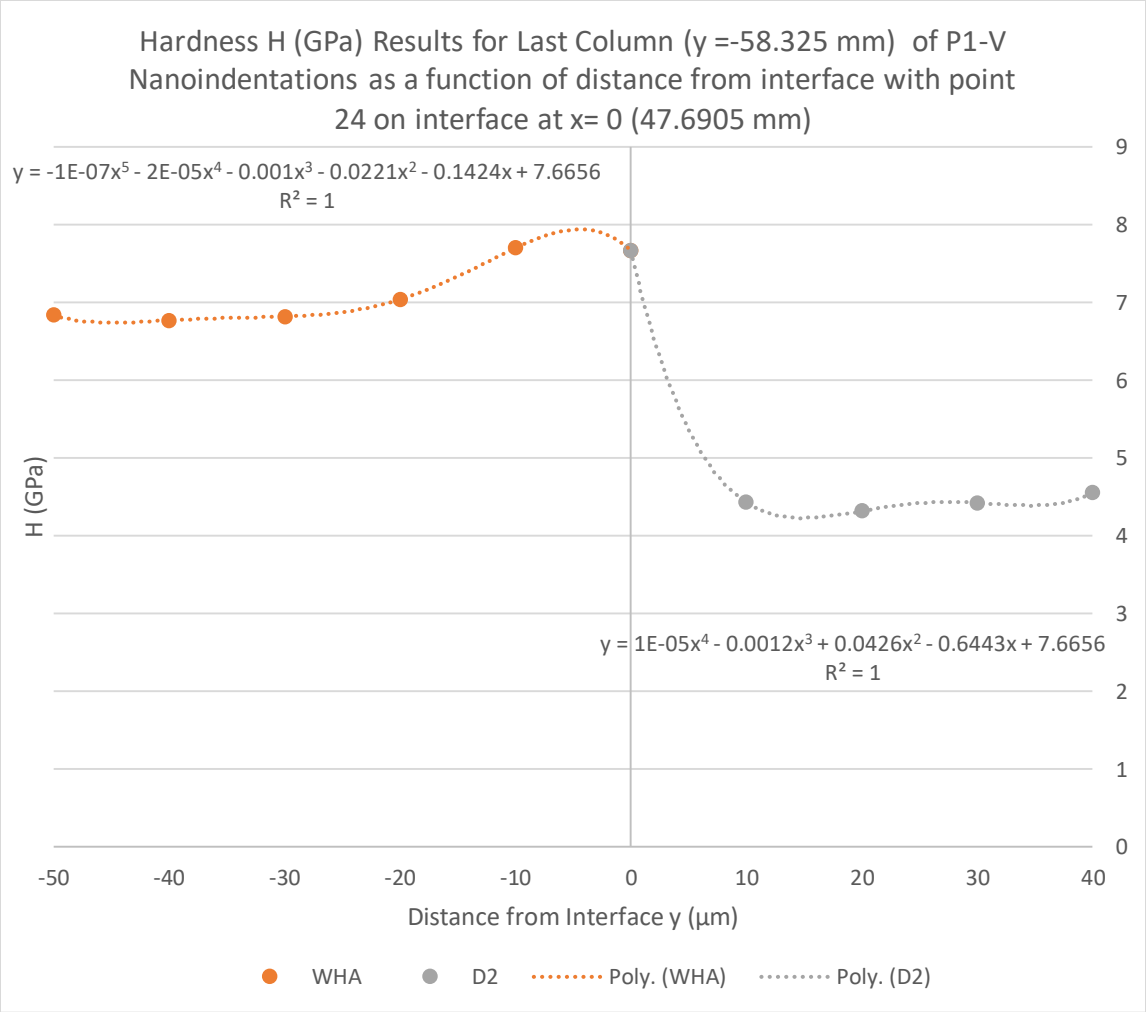

Figure 5.2.11 Hardness Results for the Last Column of Indents in the Bar Chart in Figure 5.2.6 (-58.325003 mm) for P1-V with Point 24 on the Interface

The individual indents for the P1-H are mapped out in APPENDIX B. As can be seen in the hardness results, the 1.7 GPa measurement corresponds perfectly to the 7th indent of P1-H which coalesced with a large void. The large variability in the measurements located in the D2 or to the right of -55.896 mm can be directly attributed to the lack of densification as shown in the SEM images in Chapter 4. This variability can also be seen in the average modulus and hardness values (**Figure 5.2.12)** as a

function of distance from the interface which is assumed to be close to the nanoindentations at -55.9065mm in the bar charts in APPENDIX B.

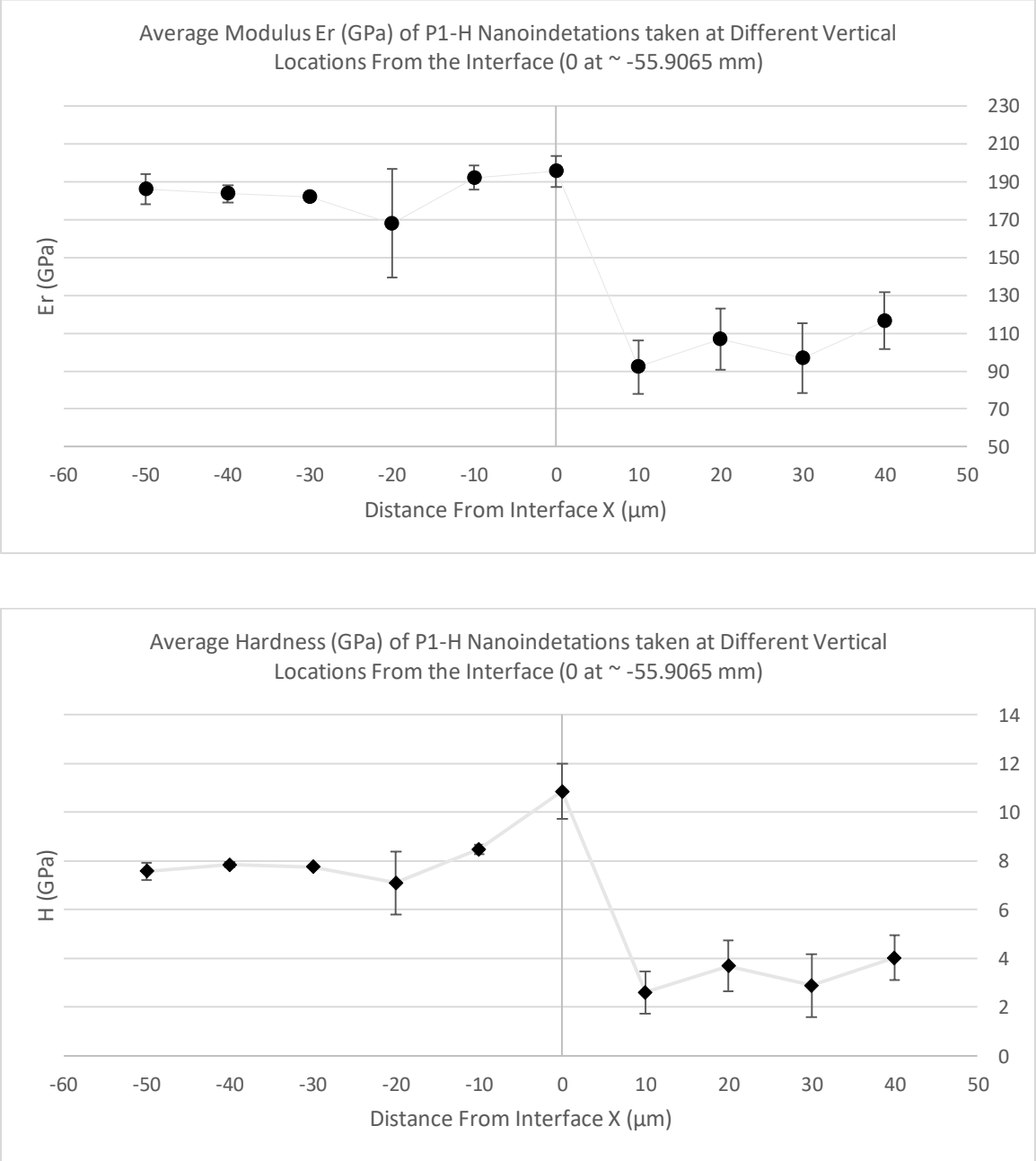

Figure 5.2.12 Average Modulus (Top) and Average Hardness (Bottom) Results of Nanoindentations Taken Horizontally Across the Interface for P1-H

P2-V and P2-H nanoindent measurements for the modulus and hardness are shown in **Figure 5.2.13.** Any variability can be attributed to elemental makeup since no voids were present in the SEM micrographs in chapter 4. Thus in the future, large variability in modulus and hardness nanoindentation results may be an indication of porosity and material properties just as microhardness has been used as an indication of porosity and material properties in the development of low alloy steel by direct metal laser sintering [52]. Additionally the 3rd column of the P2-V nanoindents (x-50.881502 mm) which was across the D2 to WHA interface which was perpendicular to the FAST's load axis is shown in **Figure 5.2.14**. The 3rd indent of P2-V in **Figure 5.2.13** is highlighted along with its associated hardness as it landed on the interface of a W-W island. A hardness of 7.4 GPa can be similar to those points along the boundary layer as seen in **Figure 5.2.14** so nanoindentation must be followed up with SEM imagery to rationalize results. This increase in modulus and hardness on this W-W grain boundary may be driven by carbon diffusion and the nickel in the binder matrix producing N_xW_xC as seen in a Ni-W alloy where carbon uptake from FAST was observed [31].

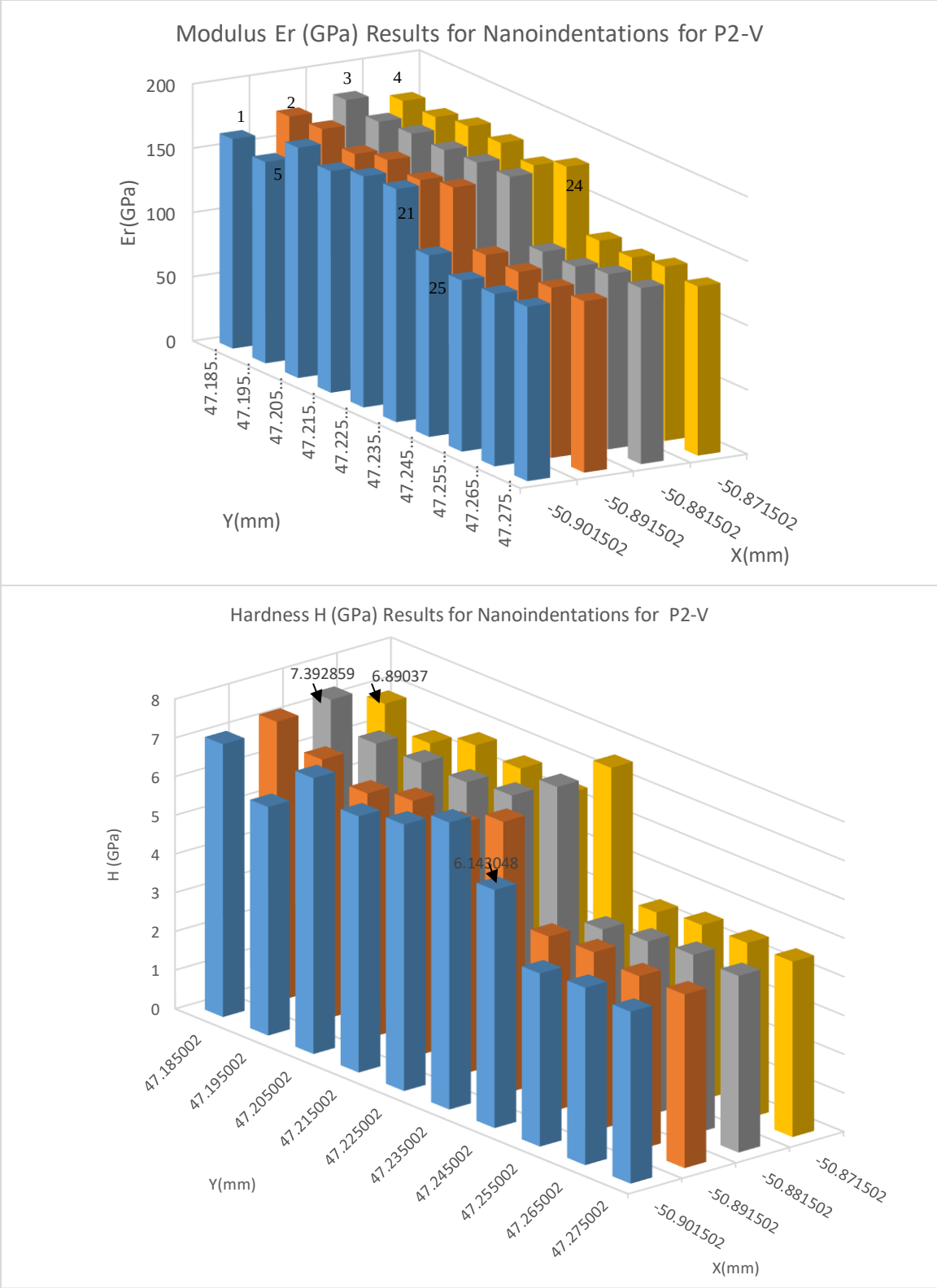

Figure 5.2.13 Modulus (Top) and Hardness (Bottom) Results of Nanoindentations Taken Vertically Across Interfaces at P2-V, Rotated

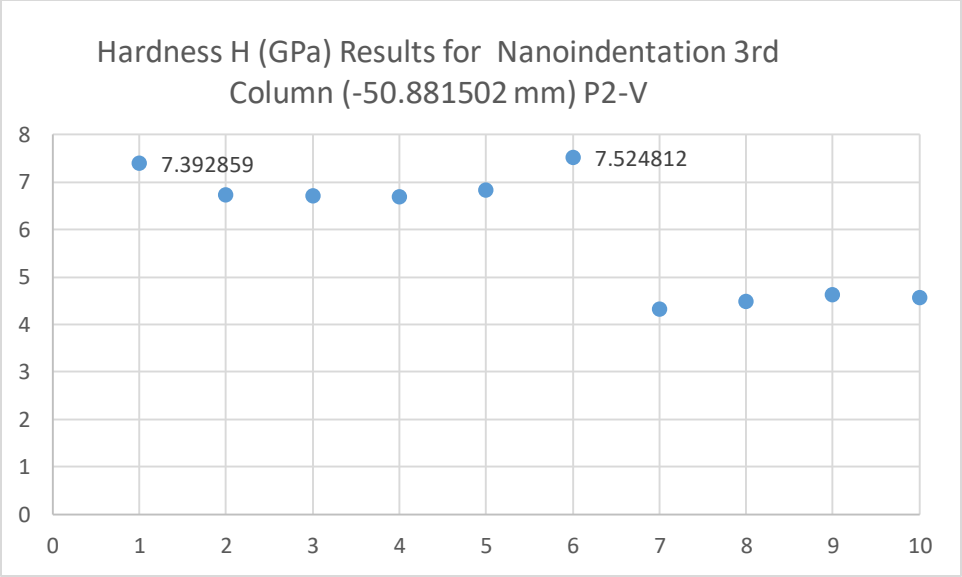

Figure 5.2.14 Hardness Results for 3rd Column (-50.881502mm) of P2-V Nanoindentations

Again P2-H indents are in **APPENDIX B** for completeness rather than to draw conclusions from due to the low densification of the D2 and porosity along the interface. It is interesting to see the 8th indent have only a 0.9 GPa hardness as this indent was directly on the vertex of 3 powder particles which did not consolidate, providing some idea of the hardness in the earliest stages of D2 densification.

The force displacement curves for all nanoindents taken for the P1 sample are shown in **Figure 5.2.15** and nothing abnormal stands out indicating the data and measurements are accurate. There are four distinct groupings in **Figure 5.2.15** however, with the two on the left corresponding to indentations in WHA at P1-V and P1-H, the two in the middle which correspond to indentations in D2 at P1-V and P1-H, and the 7 outliers to the right of middle corresponding to indentations in D2 at the P1-H locations coalescing with voids in the unconsolidated D2 powder.

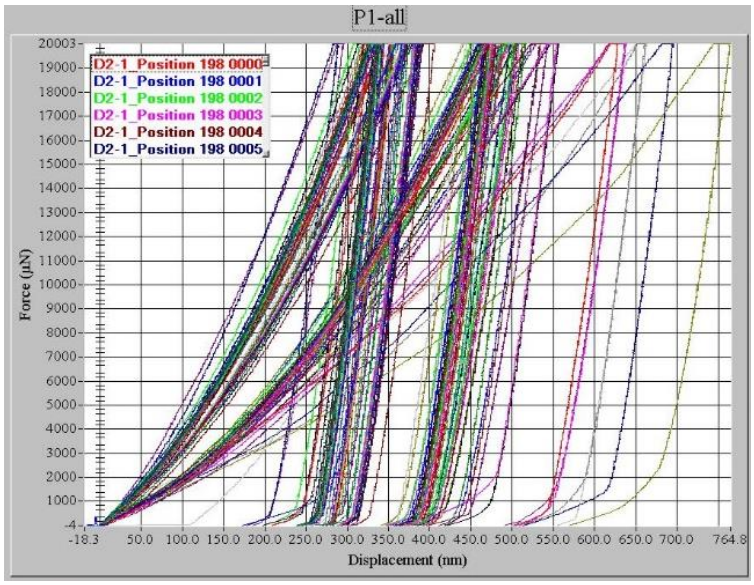

Figure 5.2.15 Force Displacement History for all the Nanoindentations Completed on the P1 Sample Area

The force displacements curves for the P2 indents have lower variation for the P2-H as shown in **Figure 5.2.15** and can be attributed to less indents coalescing with voids. There is only curve which is an outlier, and was the 8th indent on P2-H and is graphed separately in **Figure 5.2.16.**

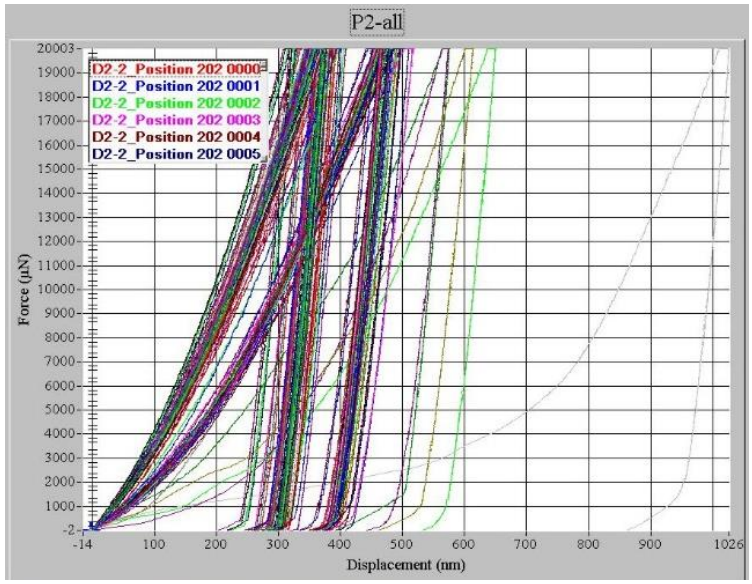

Figure 5.2.16 Force Displacement History for all the Nanoindentations Completed on the P2 Sample Area

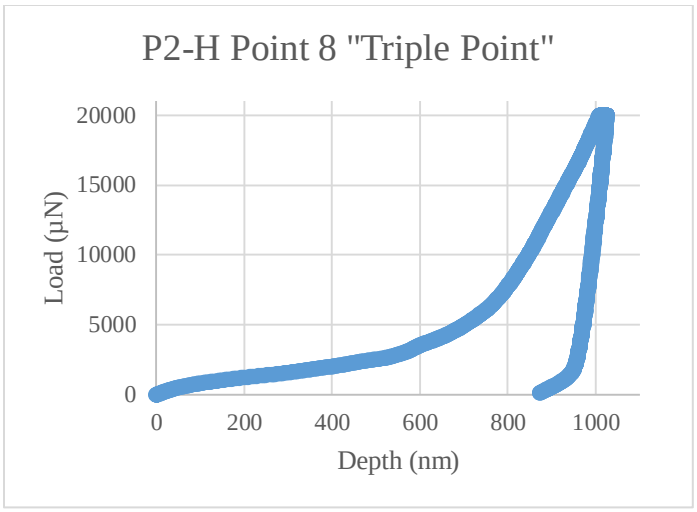

Figure 5.2.17 The Force Displacement of Point 8 in the P2-H Sample Area, Which was on the Vertex of Three Unconsolidated Particles.

The nanoindentation curves for W1 (**Figure 5.2.18**) are straight forward with no anomalies in the force displacement curves indicating good data and similar to those in literature for $W_{87}O_{13}$ [49].

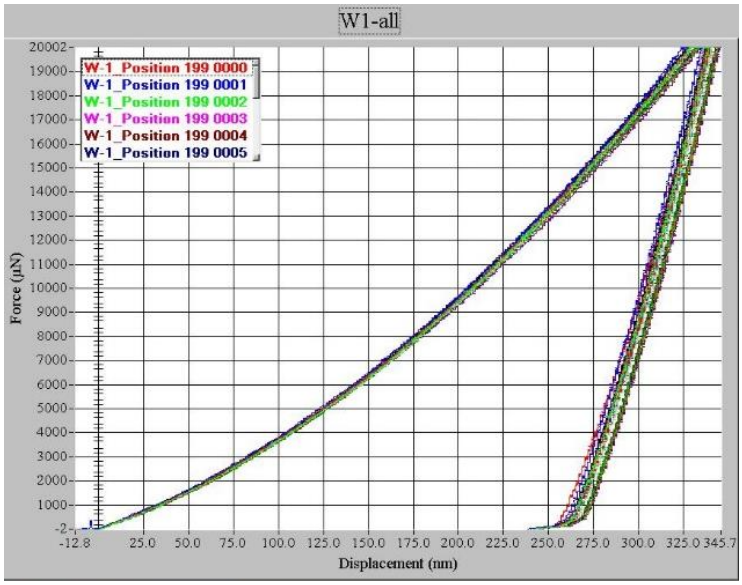

Figure 5.2.18 Force Displacement History for the Nanoindentations Completed on the W1 Sample Area

Combining the nanoindentation curves for W1 and D2-1 (**Figure 5.2.19**), it becomes apparent the variation in indentation depth in the WHA is much lower than the depth variation in the D2 alloy given the same 20mN load. Still the D2 alloy does not exhibit much variability, and inconsistencies in D2 depths could be attributed to a nanoindent landing on a martensitic versus a ferritic grain as seen in chapter 2.

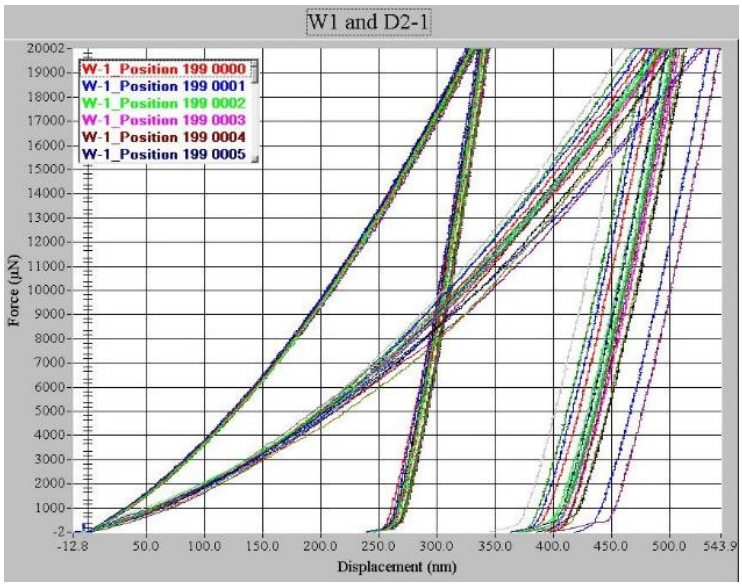

Figure 5.2.19 Comparison of the Force Displacement Histrory for the Nanoindentations Completed on the WHA W1 Sample Area to Those on the D2-1 Sample Area

5.2.2 Angled Indents Relative to Boundary Layer Perpendicular to Load Axis

As shown in chapter 4, working on the nanoscale relative to reference features such as the face of a large WHA cube makes it difficult to orient and locate features with respect to a line which appears straight at low magnification, but is meandering at higher magnification. Given this, how quickly mechanical properties change within 10 µm of the interface and the necessity to space nanoindentations appropriately apart to prevent

edge effects, it was decided to indent at an angle along a straight line relative to the perceived interface to interpolate across the boundary layer.

Hardness and modulus results will be plotted as a function of distance from the interface with a sign convention of negative used for the WHA side of the interface and positive for the D2 side of the interface and will be used throughout this section. Additionally the nanoindentations were carried out from left to right, and correspond to the SEM images in chapter 4 and EDS measurements in APPENDIX C and APPENDIX D.

The individual modulus and hardness results for the 0 degree nanoindentations are shown in **Figure 5.2.20** along with the force displacement curves of the nanoindentations. All indentations for the P1-0 degree indentations were on the WHA. The second indentation is a potential outlier with a hardness of 11.68 GPA since all the indentations are within one µm of each other and at least 4.7 µm from the interface. Additional this indentation was not on a W-W boundary. Previously a nanoindentation on a W-W interface has been harder than an adjacent point in the tungsten grain, but the 3rd indentation of P1-0 was on a W-W interface and did not provide the same response.

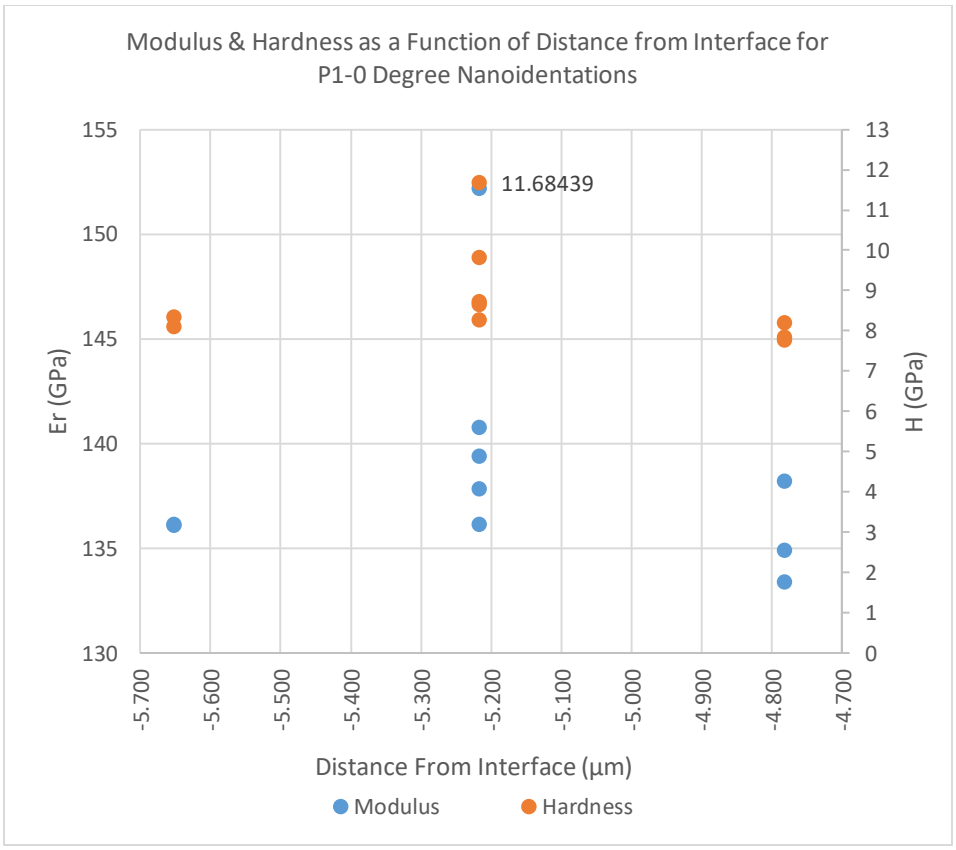
Modulus & Hardness as a Function of Distance from Interface for P1-0 Degree Nanoidentations
11.68439
Er (GPa)
H (GPa)
Distance From Interface (µm)
Modulus
Hardness

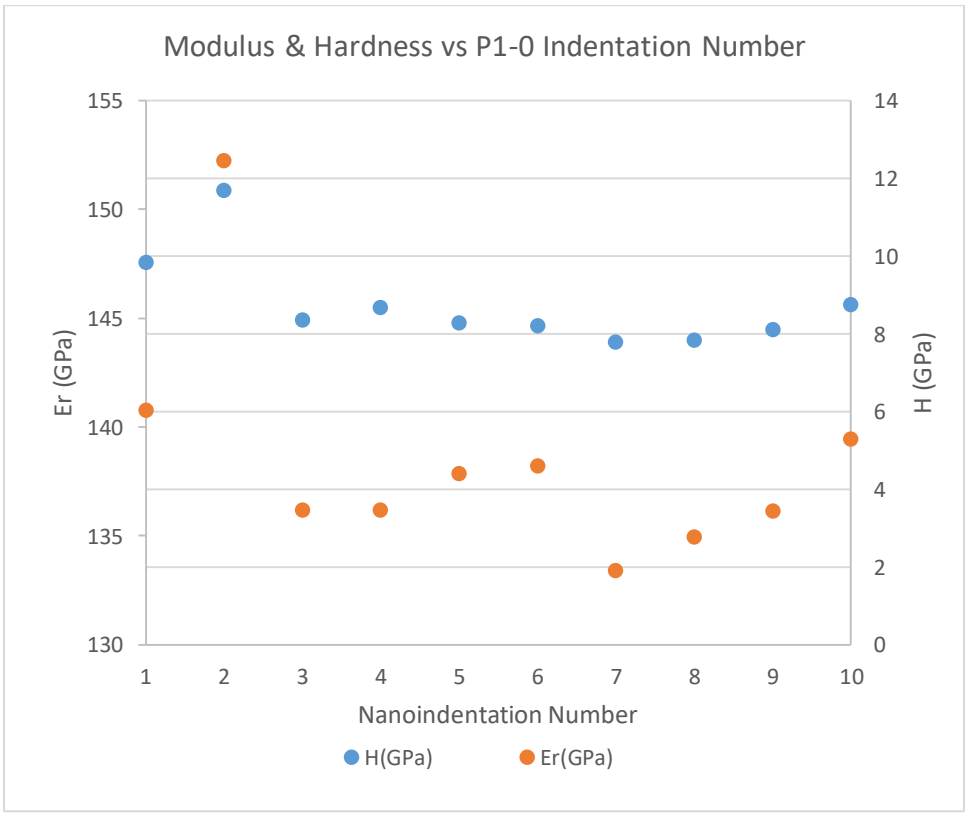
Modulus & Hardness vs P1-0 Indentation Number
Er (GPa)
H (GPa)
Nanoindentation Number
H(GPa)
Er(GPa)

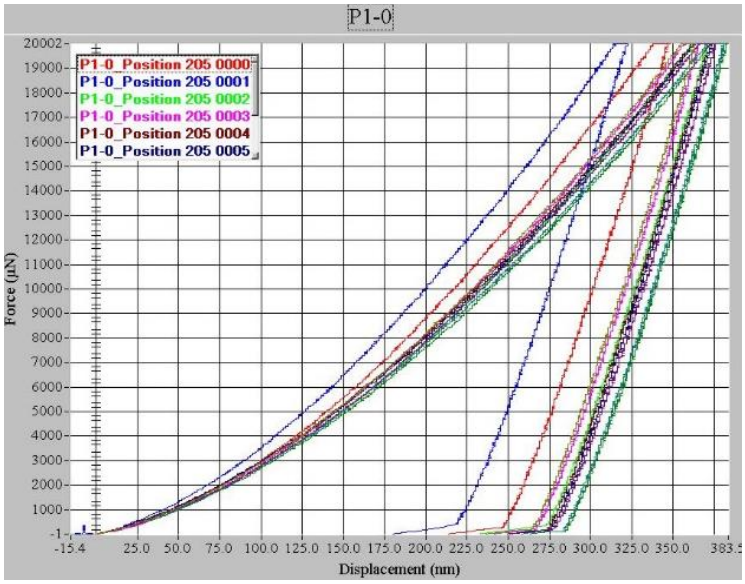

Figure 5.2.20 P1-0 Degree Nanoindentation Results as a Function of Distance to Interface (Top), P1-0 Degree Nanoindentation Results as a Function of Nanoindentation Number (Middle) and P1-0 Force Displacement History for Nanoidentations (Bottom)

The 5-degree indents in **Figure 5.2.21** are a bit more interesting since the hardness does increase for the WHA as the interface is approached and point 6 (12.3 GPa) landed on a nickel and iron binder to W interface and point 10 (14.8 GPa) was on the boundary layer of interest, each showing an increase in hardness. The force displacement curves are nice and smooth and indents did not coalesce with voids, thus they are believed to be accurate and the high hardness of point 6 and 10 may be explained by oxygen or carbon diffusion creating carbides or oxides [31] [39].

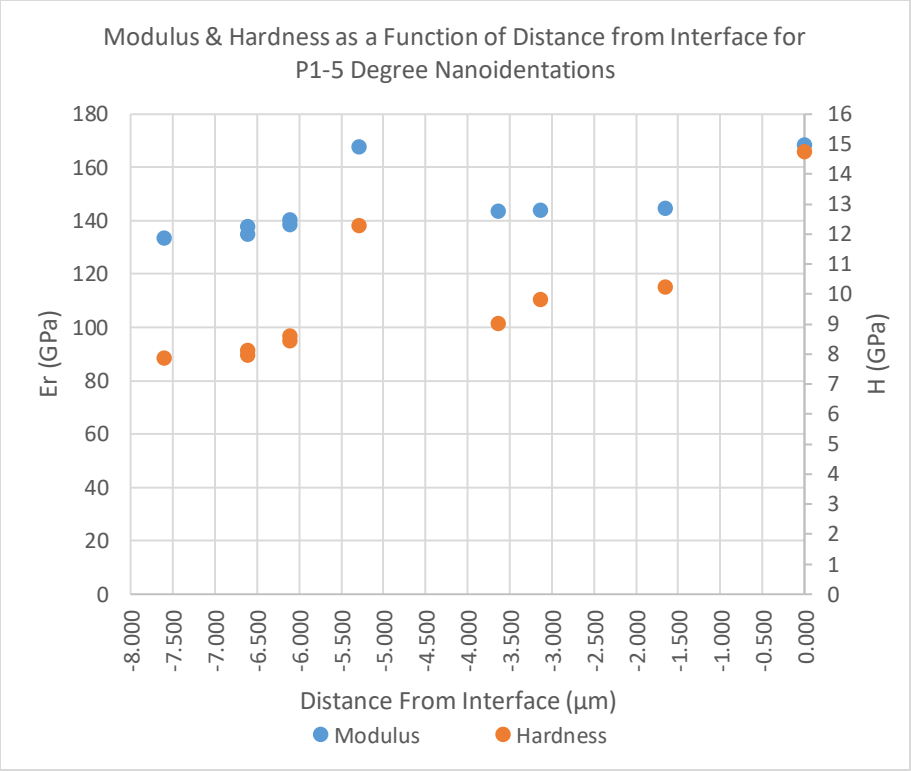
Modulus & Hardness as a Function of Distance from Interface for P1-5 Degree Nanoidentations
Er (GPa)
H (GPa)
Distance From Interface (µm)
Modulus
Hardness

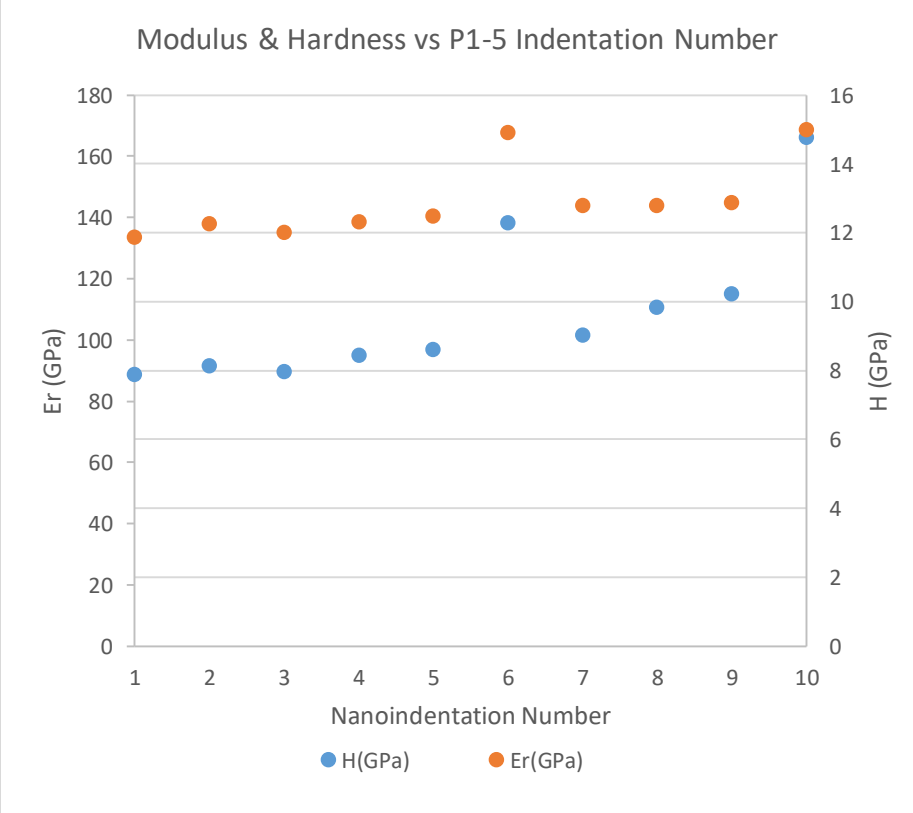
Modulus & Hardness vs P1-5 Indentation Number
Er (GPa)
H (GPa)
Nanoindentation Number
H(GPa)
Er(GPa)

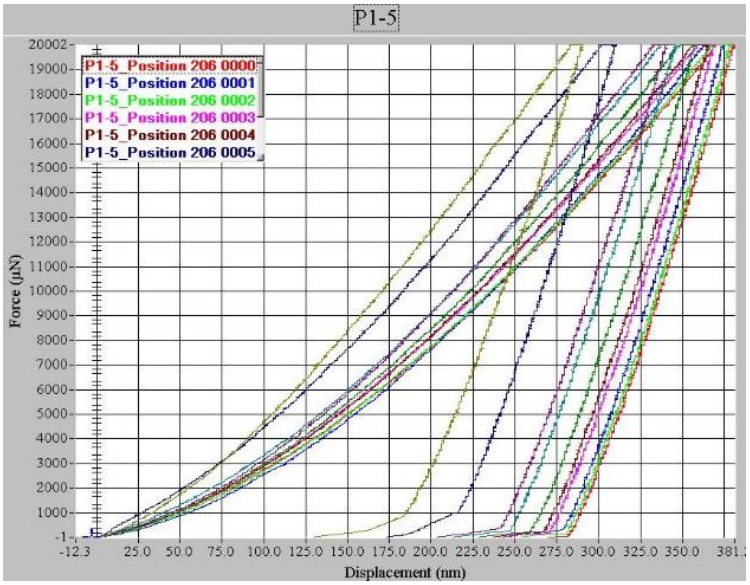

Figure 5.2.21 P1-5 Degree Nanoindentation Results as a Function of Distance to Interface (Top), P1-5 Degree Nanoindentation Results as a Function of Nanoindentation Number (Middle) and P1-5 Force Displacement History for Nanoidentations (Bottom)

The force displacement curves for the 10-degree indents are again normal as shown (**Figure 5.2.22**) with point 8 showing a higher hardness (9.5 GPa) than the others and co-located on the interface of the D2 to WHA while the modulus for the series again shows a simple diffusion couple. Interestingly, points 9 and 10 which are on the D2 did not drop down to the D2 bulk average of 4.2 GPa suggesting they may be within confines of the boundary layer. Assuming a straight interface and using simple trigonometry, knowing point 8 is on the boundary, knowing the indents are 10 µm apart and on a 10 degree line, point 10 can be found to be 3.47 µm from the interface. The SEM images show the interface is not perfect, but using the image to measure the distance, the point is approximately 3 µm from the interface. Both measurement and calculation are an approximation but given the EDS data in chapter 3 can result in a diffusion affected zone of at least 10 µm it is safe to assume these measurements correspond to material within

the diffusion boundary layer. Therefore the diffusion zone is not bilaterally 30-40 µm in the WHA only, but also at least 3.5 µm into the D2.

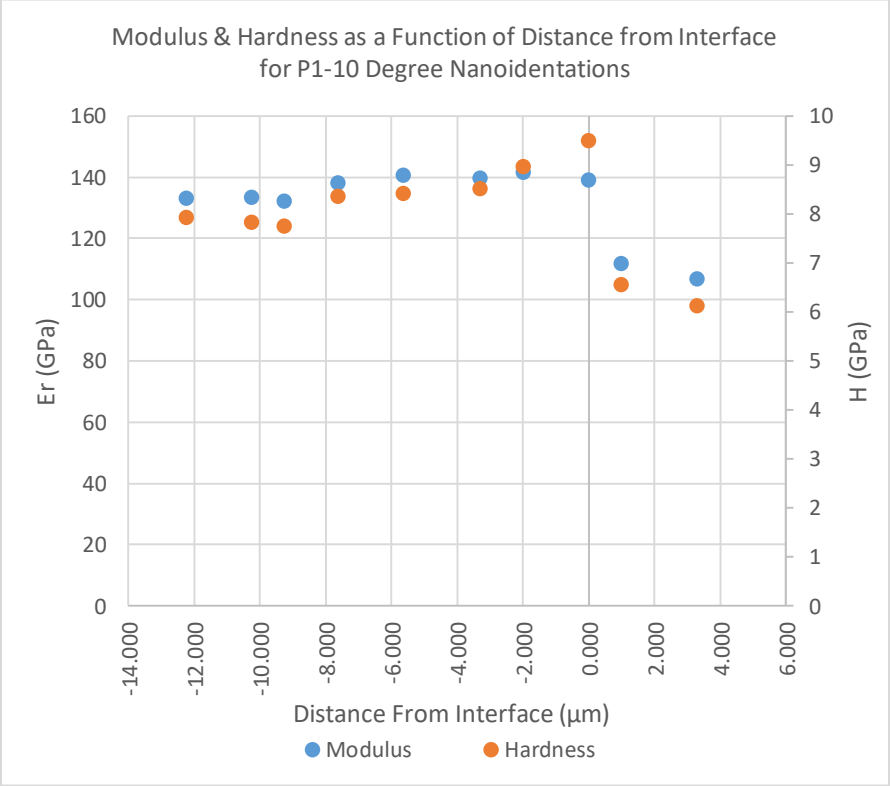

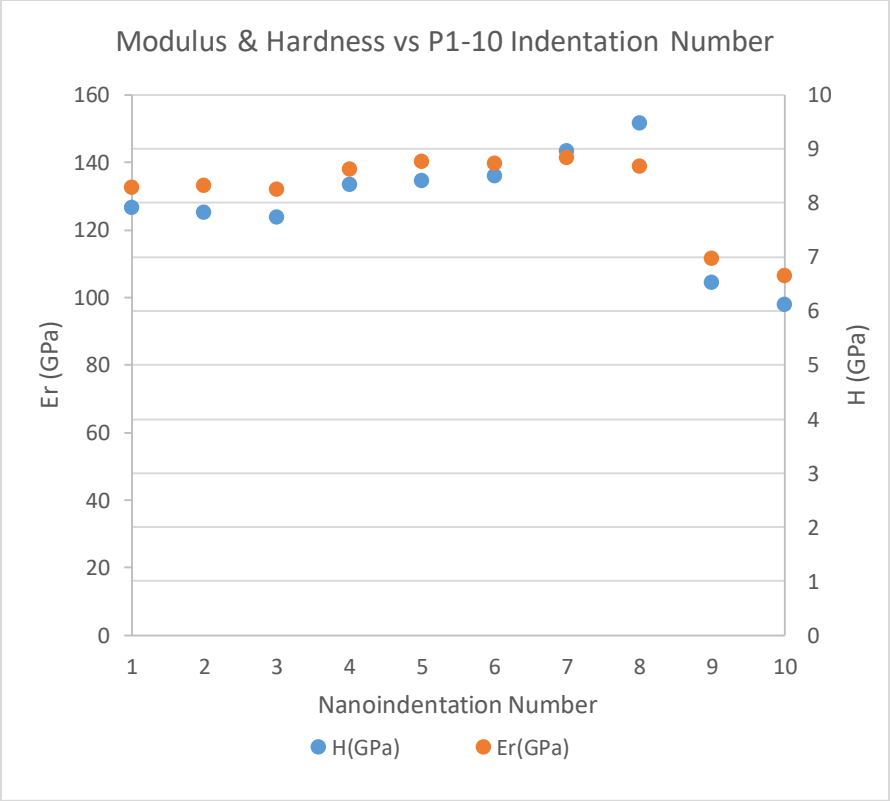

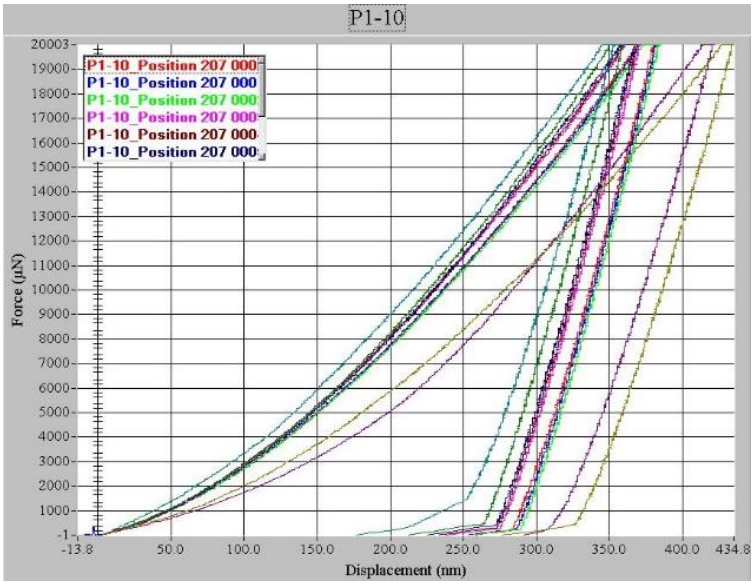

Figure 5.2.22 P1-10 Degree Nanoindentation Results as a Function of Distance to Interface (Top), P1-10 Degree Nanoindentation Results as a Function of Nanoindentation Number (Middle) and P1-10 Force Displacement History for Nanoidentations (Bottom)

The 15-degree indents follow the same trend as the 5-degree and 10-degree indents where point 7 occurred on the diffusion layer with a hardness of 11.4 GPa and is higher than the adjacent indents. Additionally the hardness falls off once over the interface to the bulk hardness found for D2 (4.2 GPa) (**Figure 5.2.23**) when measurements are expected to be near 6 GPa similar to points 9 and 10 in the D2 alloy for the 10-degree indents. Looking at the SEM of the 15-degree indents suggests point 8 is close to a void and could lower the hardness results. Point 9 is approximately 5-5.18 µm from the interface based on trigonometry and measurement; this suggests the diffusion boundary can be up to 10 µm as shown in the EDS work in chapter 3, but is not uniformly thick around the entire interface. Therefore the diffusion zone can be approximately 40-50 µm thick with the major change in material properties bilaterally 30-40 µm in the WHA but can affect the D2 properties at least 10 µm into the D2. Thus, variable diffusion concentrations could result in a non-linear mechanical property gradient around the cube which would make future work on an accurate FEA representative volume element difficult. The force displacement curves are again normal suggesting the data is accurate and diffusion has varied the mechanical properties.

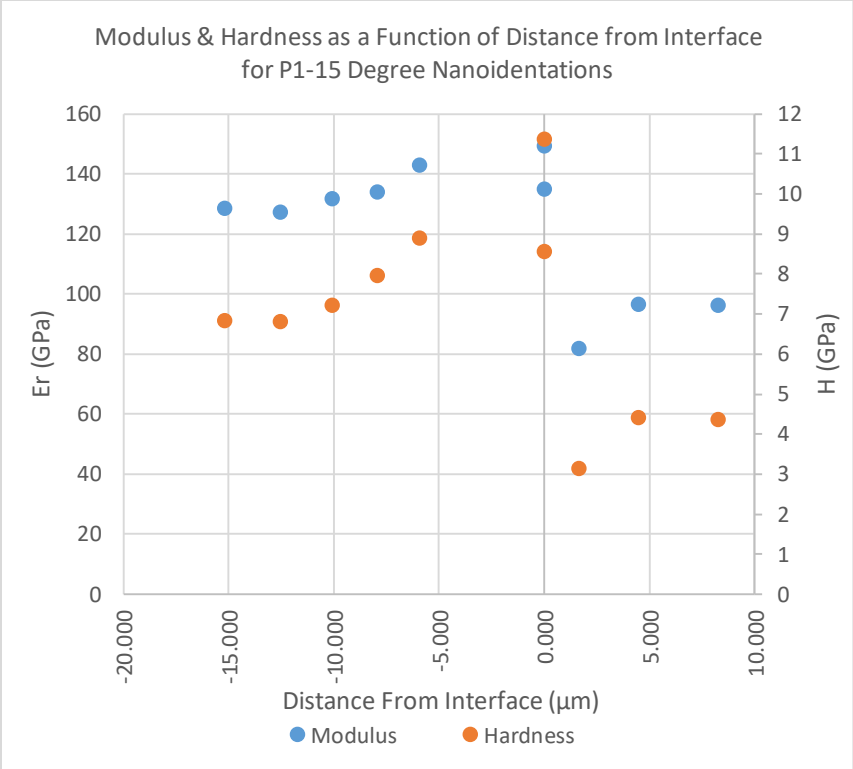
Modulus & Hardness as a Function of Distance from Interface for P1-15 Degree Nanoidentations
Er (GPa)
H (GPa)
160
140
120
100
80
60
40
20
0
12
11
10
9
8
7
6
5
4
3
2
1
0
-20.000
-15.000
-10.000
-5.000
0.000
5.000
10.000
Distance From Interface (µm)
Modulus
Hardness

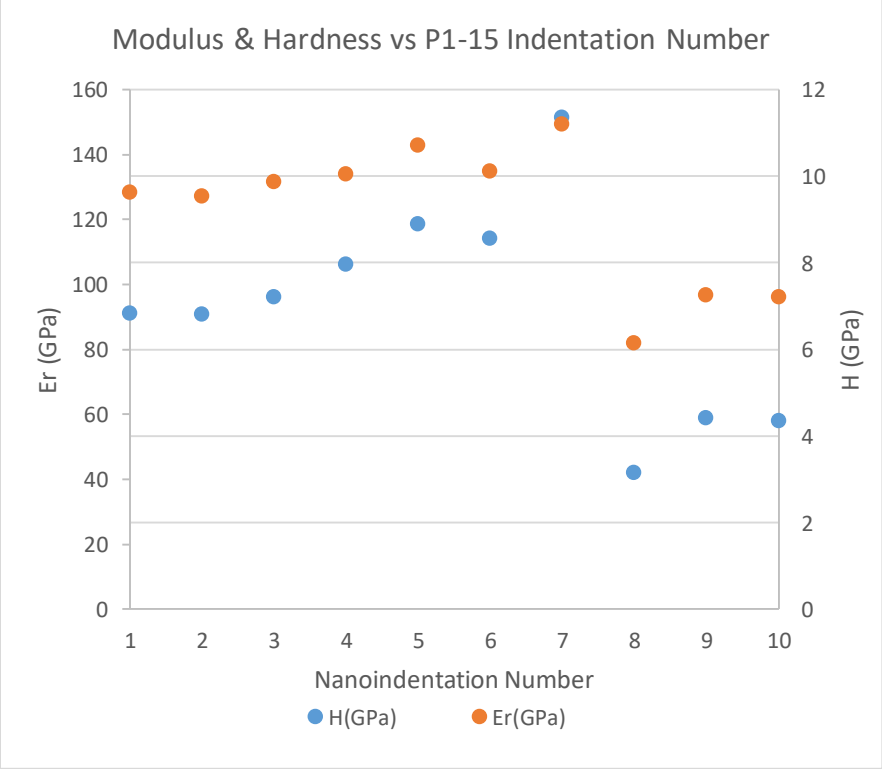
Modulus & Hardness vs P1-15 Indentation Number
Er (GPa)
H (GPa)
160
140
120
100
80
60
40
20
0
12
10
8
6
4
2
0
1
2
3
4
5
6
7
8
9
10
Nanoindentation Number
H(GPa)
Er(GPa)

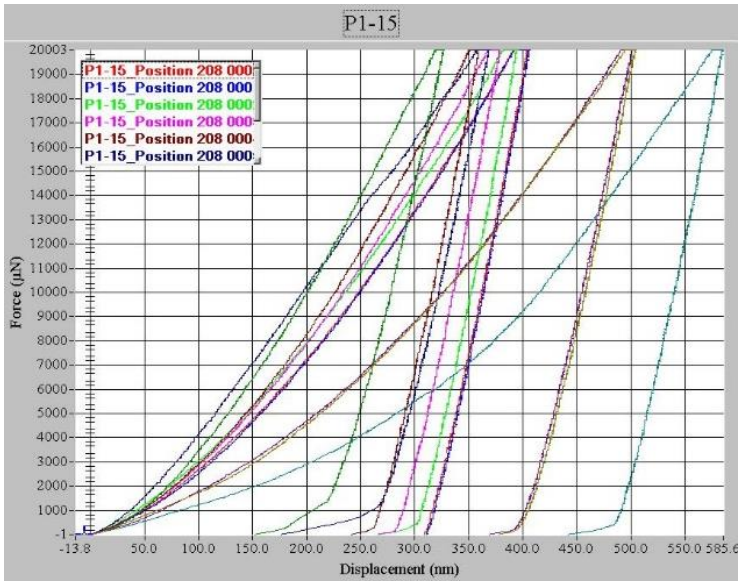

Figure 5.2.23 P1-15 Degree Nanoindentation Results as a Function of Distance to Interface (Top), P1-15 Degree Nanoindentation Results as a Function of Nanoindentation Number (Middle) and P1-15 Force Displacement History for Nanoidentations (Bottom)

Looking at the P2- 0 degree indents (**Figure 5.2.24**), each measurement can be explained via the SEM image given the force displacement curves are normal. Point 1 is actually in the D2, point 2, though on the boundary, is next to a void which can drop the hardness, and point 5 seems to partially interact with a discrete layer on the outer most surface of the tungsten. Points 4 and 6 are approximately the same distance from said layer suggesting this layer is indeed harder than the tungsten itself and is most likely a layer of carbide, oxide or combination of the two given the hardness. Again if this method of composite analysis were carried out for other material combinations, the starting geometries should be polished to have discrete edges instead of meandering boundaries to aid on analysis.

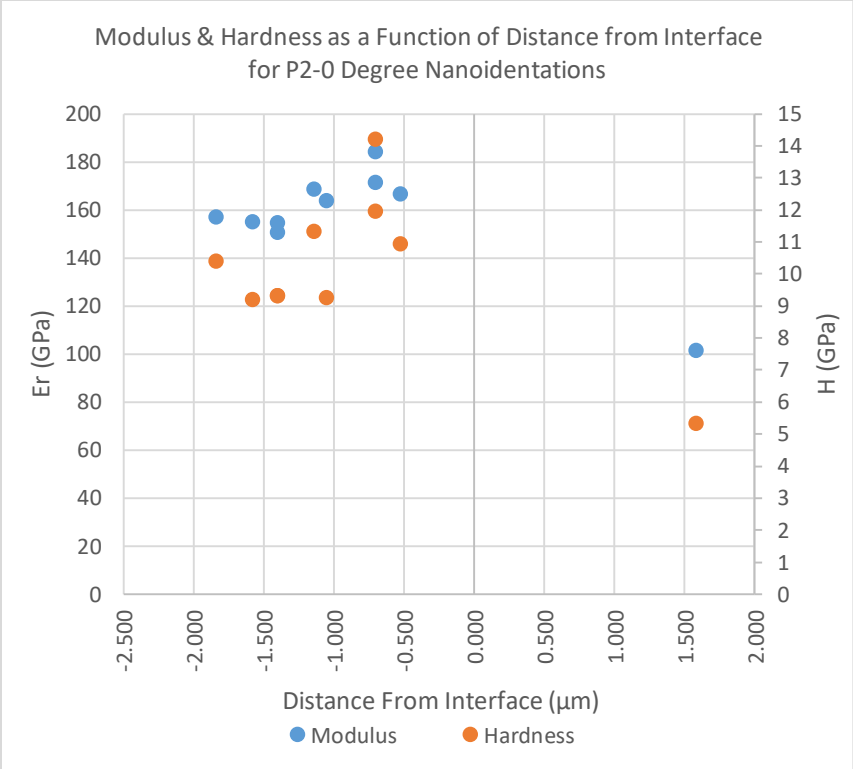
Modulus & Hardness as a Function of Distance from Interface for P2-0 Degree Nanoidentations
Er (GPa)
H (GPa)
Distance From Interface (µm)
Modulus
Hardness

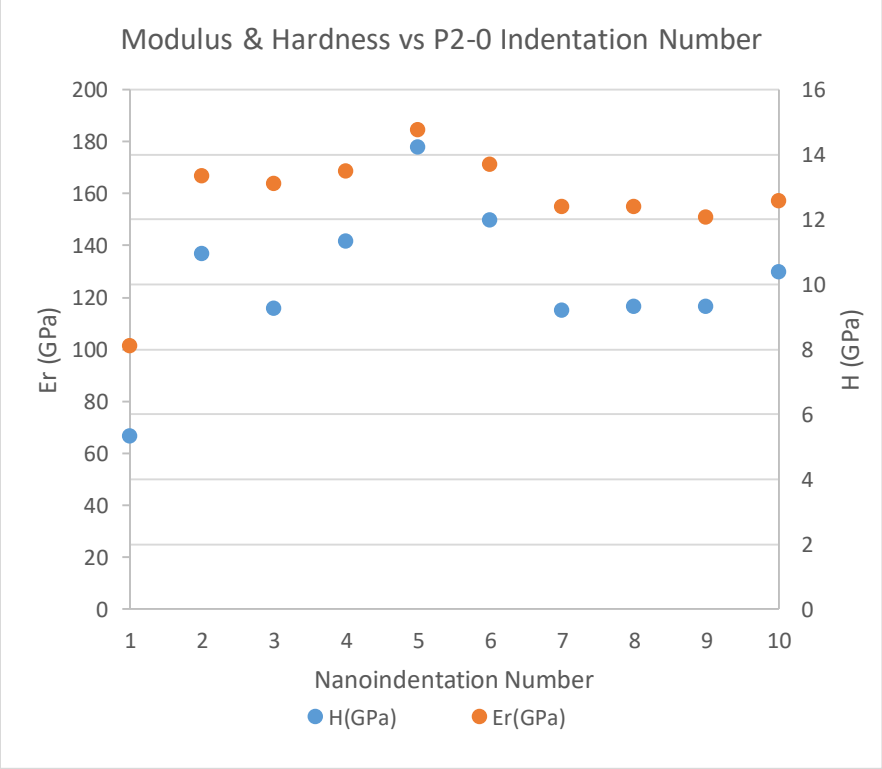
Modulus & Hardness vs P2-0 Indentation Number
Er (GPa)
H (GPa)
Nanoindentation Number
H(GPa)
Er(GPa)

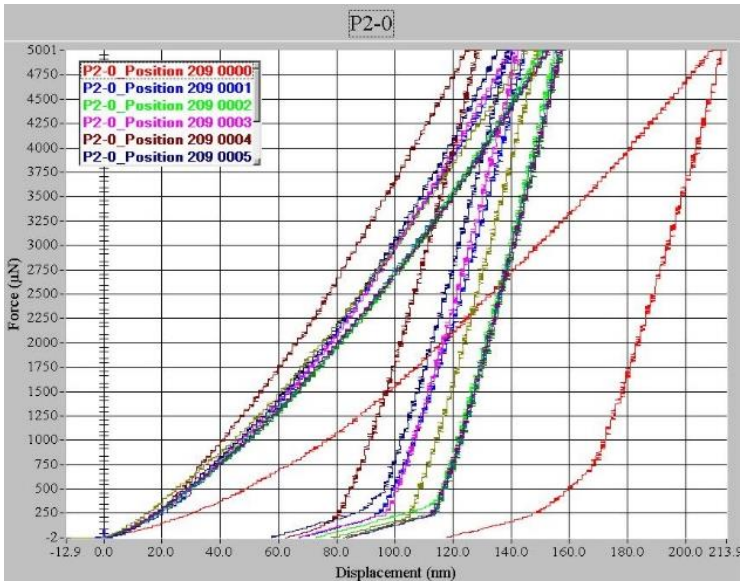

Figure 5.2.24 P2-0 Degree Nanoindentation Results as a Function of Distance to Interface (Top), P2-0 Degree Nanoindentation Results as a Function of Nanoindentation Number (Middle) and P2-0 Force Displacement History for Nanoidentations (Bottom)

The first nanoindent measurement which should be ignored is in the P2-5 degree series (**Figure 5.2.25**) and corresponding point 210 00007 (boxed) from the TriboIndenter and green line (circled) as a portion of the curve is horizontal right in the middle of the curve. There may have been a foreign body or something soft on the sample, and when the indenter punched through the foreign matter the indenter continued to load. Looking at the SEM image of the indent there is nothing abnormal, so a foreign body is the most logical explanation. This point corresponds to point 8 of the modulus and hardness graphs in Figure 5.2.25 as the TriboIndenter first indent is recorded as 0 and has been removed.

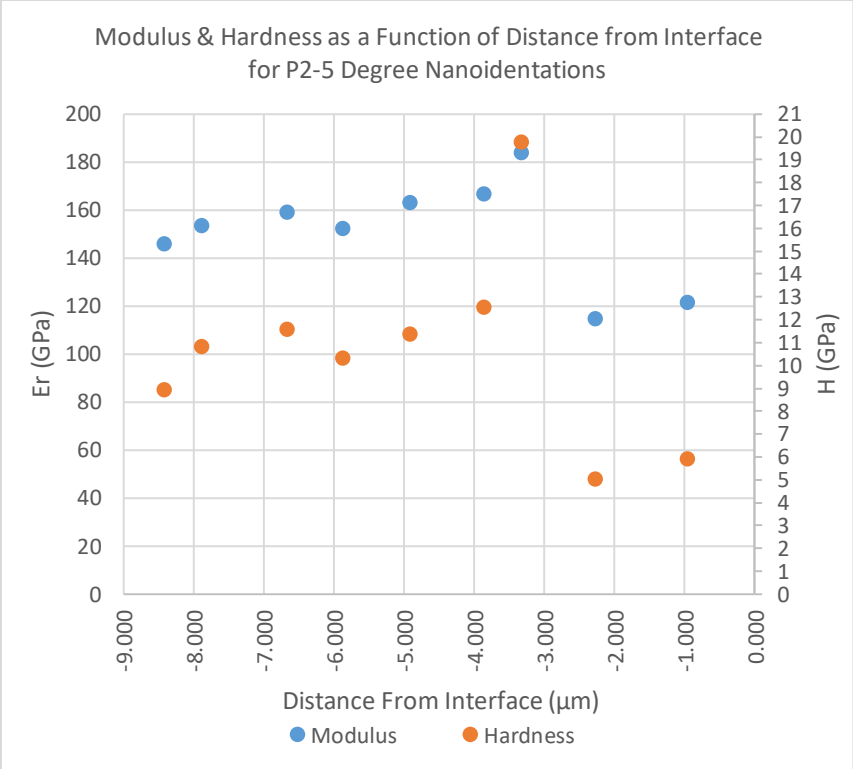
Modulus & Hardness as a Function of Distance from Interface for P2-5 Degree Nanoidentations
Er (GPa)
H (GPa)
Distance From Interface (µm)
Modulus
Hardness

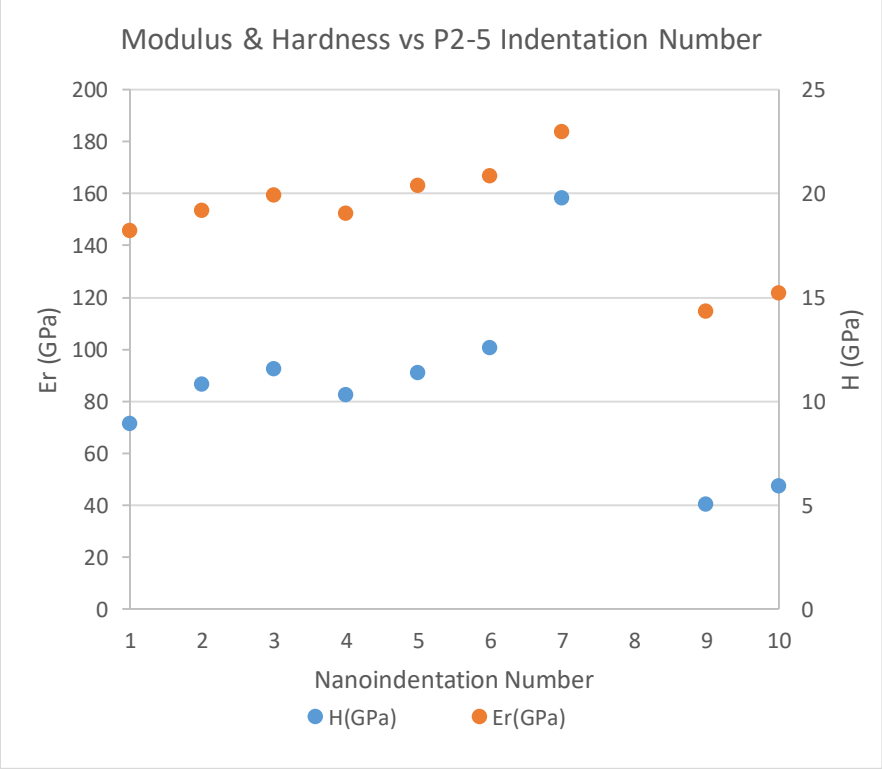
Modulus & Hardness vs P2-5 Indentation Number
Er (GPa)
H (GPa)
Nanoindentation Number
H(GPa)
Er(GPa)

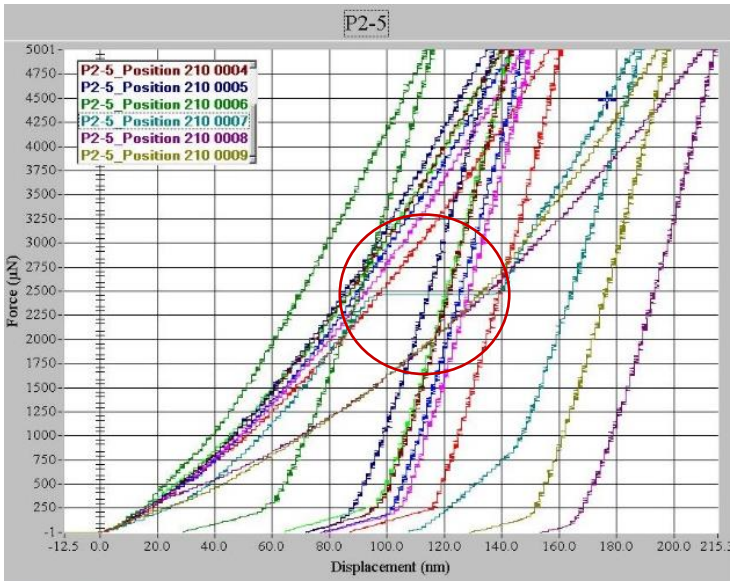

Figure 5.2.25 P2-5 Degree Nanoindentation Results as a Function of Distance to Interface (Top), P2-5 Degree Nanoindentation Results as a Function of Nanoindentation Number (Middle) and P2-5 Force Displacement History for Nanoidentations (Bottom)

Though the first seven indents for P2-10 (**Figure 5.2.26**) seemed to be on a nice homogenous tungsten island, the nanoindentation results in (**Figure 5.2.26**) suggest there is indeed a gradient in material properties within the tungsten grain in addition to the gradient in the discreet outer layer of tungsten as shown in the D2- 0 degree results. Since crystallography was not carried out in this work, and orientation of the tungsten crystal strongly influences the hardness [50], the hardness increase at point 6 may be attributed to crystal orientation. This is likely because the location of point 7 is closer to the D2 material and has a lower hardness than point 6. As mentioned in chapter 4, points 8-10 were not visible to gather distances to the interface.

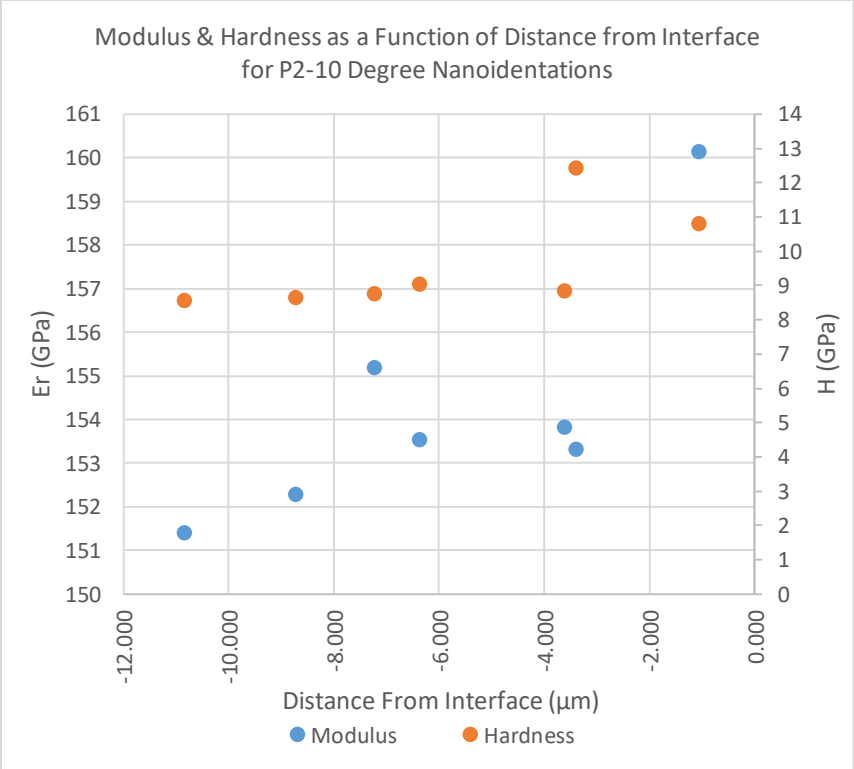
Modulus & Hardness as a Function of Distance from Interface for P2-10 Degree Nanoidentations
Er (GPa)
H (GPa)
161
160
159
158
157
156
155
154
153
152
151
150
14
13
12
11
10
9
8
7
6
5
4
3
2
1
0
-12.000
-10.000
-8.000
-6.000
-4.000
-2.000
0.000
Distance From Interface (µm)
Modulus
Hardness

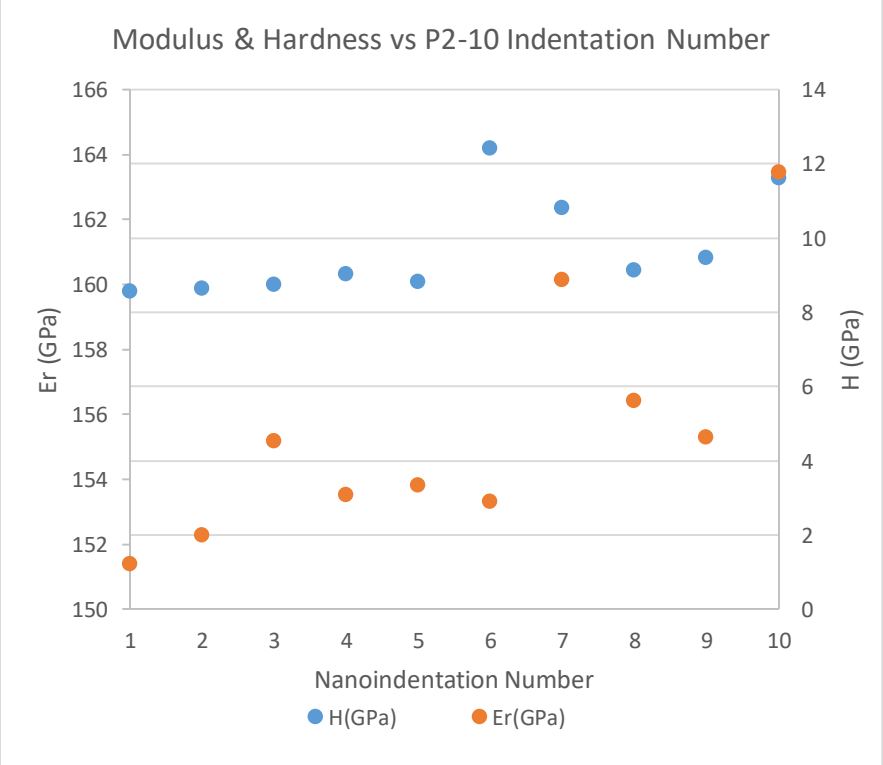
Modulus & Hardness vs P2-10 Indentation Number
Er (GPa)
H (GPa)
166
164
162
160
158
156
154
152
150
14
12
10
8
6
4
2
0
1
2
3
4
5
6
7
8
9
10
Nanoindentation Number
H(GPa)
Er(GPa)

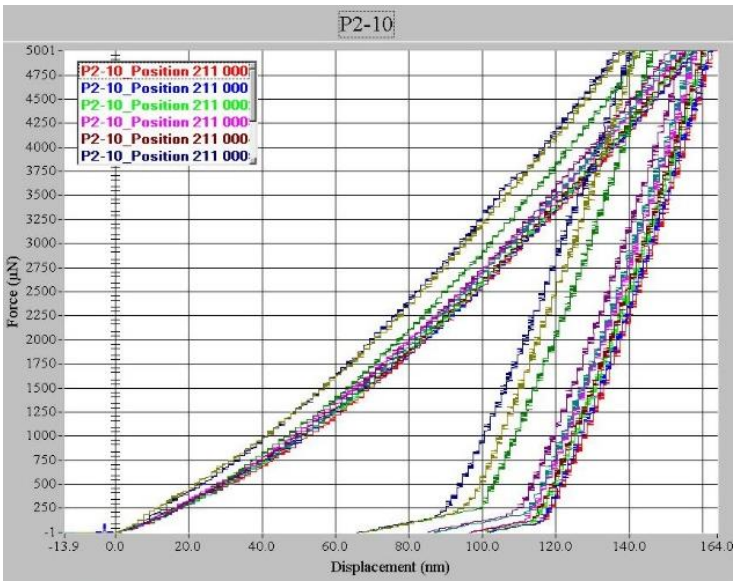

Figure 5.2.26 P2-10 Degree Nanoindentation Results as a Function of Distance to Interface (Top), P2-10 Degree Nanoindentation Results as a Function of Nanoindentation Number (Middle) and P2-10 Force Displacement History for Nanoidentations (Bottom)

There is no associated SEM or EDS for the P2-15 degree indents so measuring the distance of the nanoindentations to the interface is not possible, but the hardness and modulus results as a function of indentation number are shown in (**Figure 5.2.27**) for completeness. Given the force displacement curves are normal one can assume point 7 is on the interface and point 8 within the diffusion layer though these results will not be the sole evidence to draw conclusions from for this work.

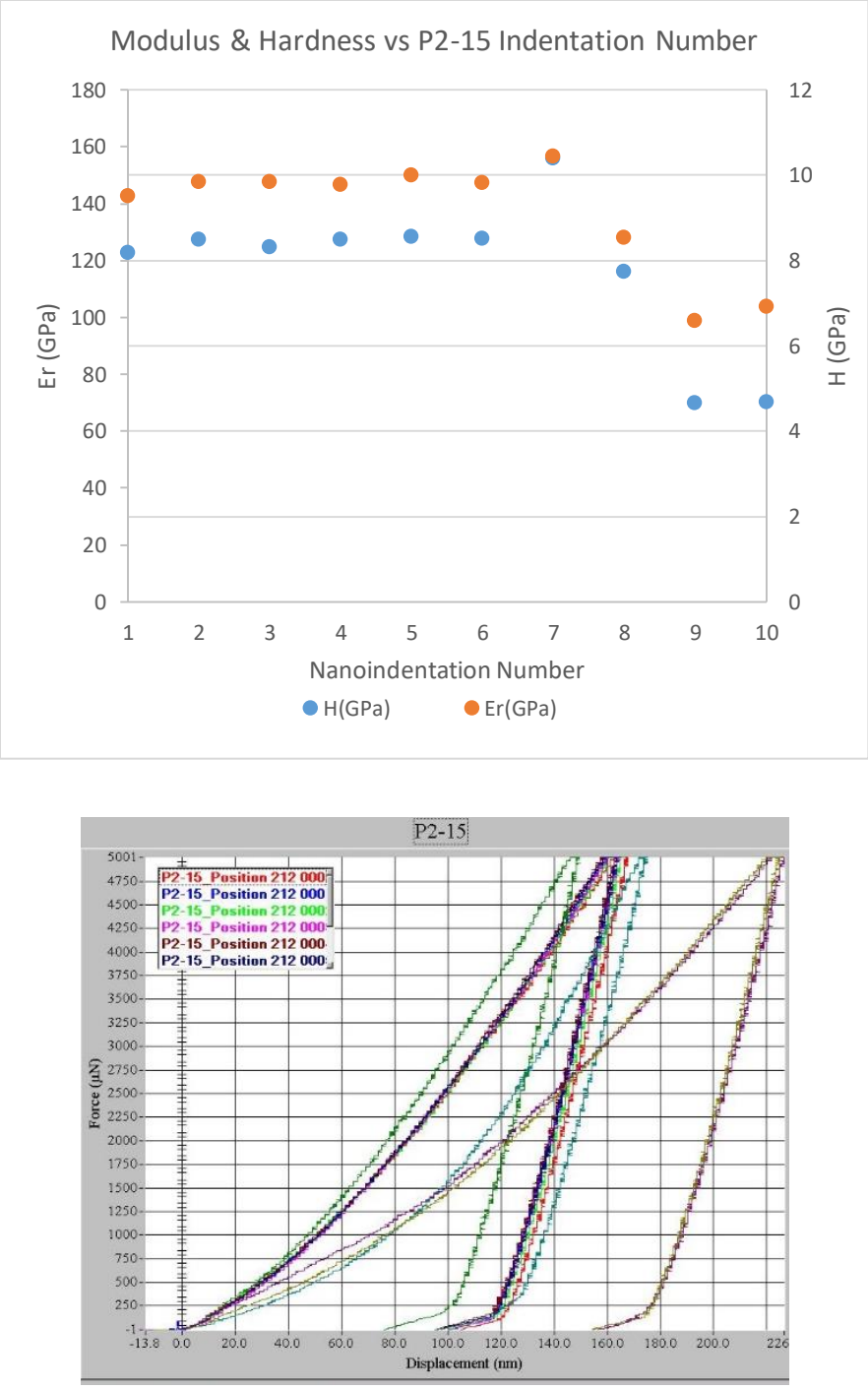

Figure 5.2.27 P2-15 Degree Nanoindentation Results as a Function of Nanoindentation Number (Top) and P2-15 Force Displacement History for Nanoidentations (Bottom)

The force displacement curves for the P2- Marker indents (**Figure 5.2.28)** are also normal and though there seems to be a large variability in the data, the standard deviation

for the modulus is 0.73 GPa and standard deviation for the hardness is 0.09 GPa suggesting any deviation may be attributed to indents interacting with martensitic or ferritic grains since the SEM imagery showed good consolidation.

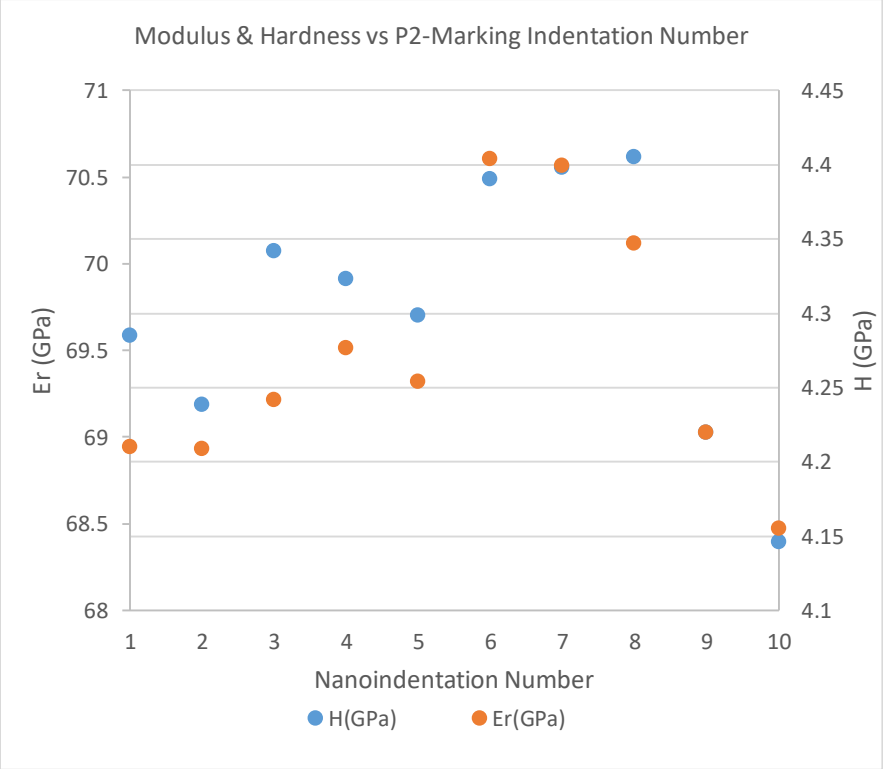

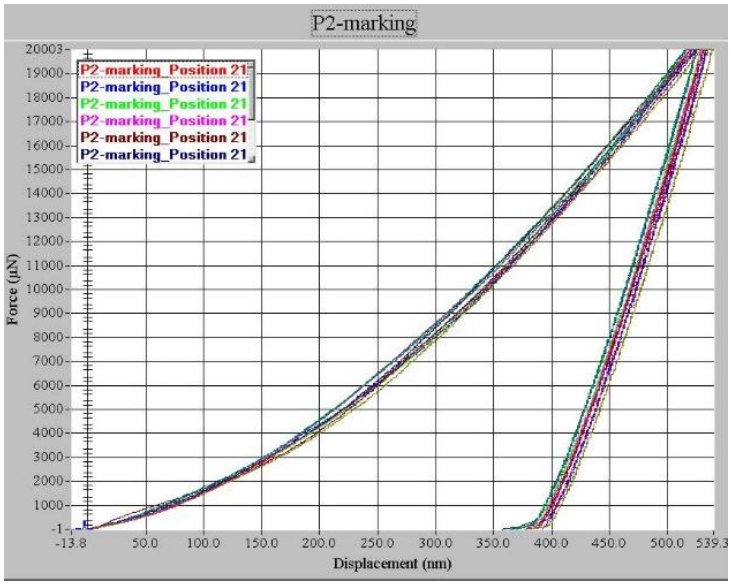

Figure 5.2.28 P2-Marking Nanoindentation Results as a Function of Nanoindentation Number (Top) and P2-15 Force Displacement History for Nanoidentations (Bottom)

5.3 Microhardness

To help understand how the nanoindentation related to the bulk hardness, microhardness measurements were taken using a Struers Durascan on just a WHA cube far from the interface which resulted in an average of 357 HV 0,3 with a standard deviation of 12.1 HV 0,3. Microhardness measurements were also taken across the vertical interface between the D2 and the WHA (**Figure 5.3.1**) which also indicated a slight increase in hardness before dropping off when in the D2 material. The average for the WHA section was 370 HV 0,3 with a standard deviation of 7.5 HV 0,3 which shows the bulk hardness is indeed increasing as the interface is approached. The average value for the D2 was 301 HV 0,3 with a standard deviation of 3 HV 0,3 compared to the 4.2 GPa and though only a few points were measured it looks like the microhardness measurements are off from the nanoindentation measurements by about approximately 1 GPa for the D2 where the WHA nanoindentation measurements are close to 7.7 GPa compared to the 3.4-3.6 GPa from the microhardness testing.

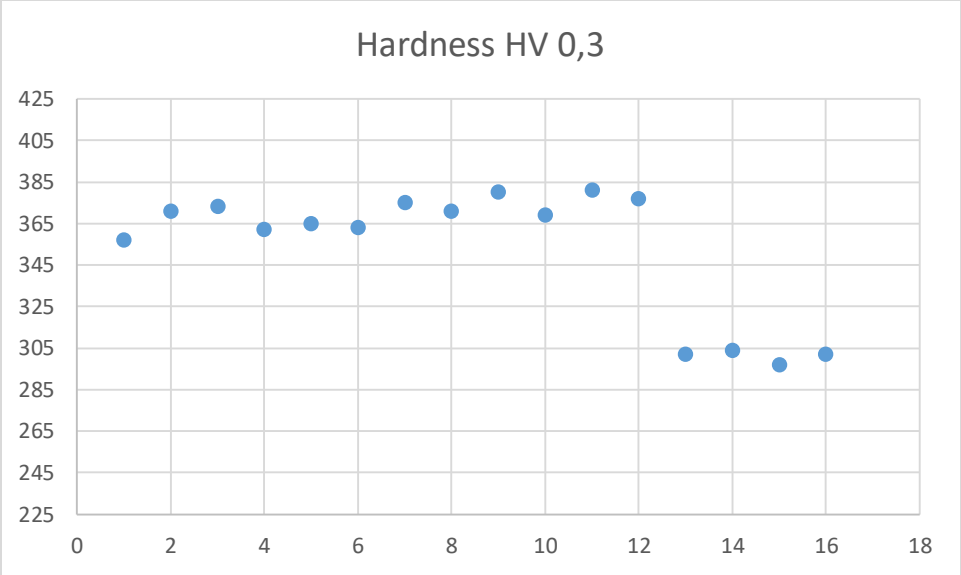

Figure 5.3.1 P2- Marking-2 Nanoindents Results, TriboIndenter image and Force Displacement Curves

Chapter 6: Impact Testing

6.1 Impact Test Fixture

Impact testing was carried out with an Instron Dynatup Impulse Impact Testing System with the Instron Dynatup Model 8200 Drop Weight Impact Testing Instrument. A custom tup insert was utilized which was machined from a grade 8 bolt because of its "as received" hardness (3.119 GPa (32 HRC)) and hardenability. The height of the instrument is 1714 mm (67.5 in.) including the support table. The initial mass to be used needed to be within in the standard drop weight mass and within 80% of the machine's capacity: 3.0 kg to 13.6 kg (6.614 lbs. to 30 lbs.) [53] [54] [27]. The maximum drop height for the machine is 1.0 m (39.37 in.) resulting in a maximum velocity of 4.43 m/s (14.53 ft/s) with an impact energy range from 1.356 J to 132.8 J (1 to 97.9 ft lb) [53] [54].

The velocity at impact is:

$$V = \sqrt{(2gh)}$$ V= theoretical velocity m/sec (ft/sec)

g = 9.80665 m/s^2 or 32.1740 ft/s^2

$$V = \sqrt{(2 * 9.80665 \frac{m}{s^2} * 1.0m} = 4.4272 \text{ m/s} = 15.5298 \text{ ft/s}$$

Conservation of Energy:

Potential Energy of the system = Kinetic Energy of the system

Since exact ASTM samples would be difficult to produce and resource, a sample was designed with a new interface with the Instron machine in mind, attempting to make

repeatable testing possible without energy loses to the system (**Figure 6.1.1**). The specimen holder and new tup had to integrate with the Instron machine available and the new test setup is shown in **Figure 6.1.2** with the fixture integrated with the Instron machine and holding a specimen in **Figure 6.1.3**. Because of its "as received" hardness, a grade 8 bolt was procured and machined with a relief cut on the back side to prevent interference during the impact event after the sample has failed and to reduce energy absorption through prolonged contact. The clearance and area of the sample which is impacted are show in **Figure 6.1.4**. Likewise the holder also has relief cuts on the top and bottom to prevent interference and a positive stop to insure clamp contact and tup contact with the samples are consistent from one sample test event to the next. A CAD model and drawings were produced, a 3D model prototyped, test fitted, and once satisfied with the design using FEA, the parts were machined from bar stock.

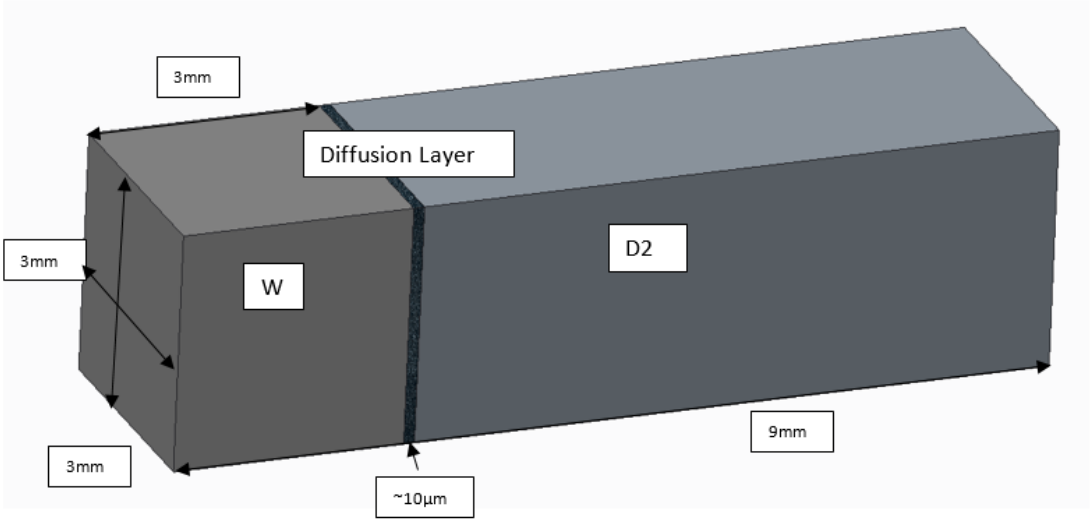

Figure 6.1.1 3mm x 3mm x 9mm WHA and D2 Composite Specimen

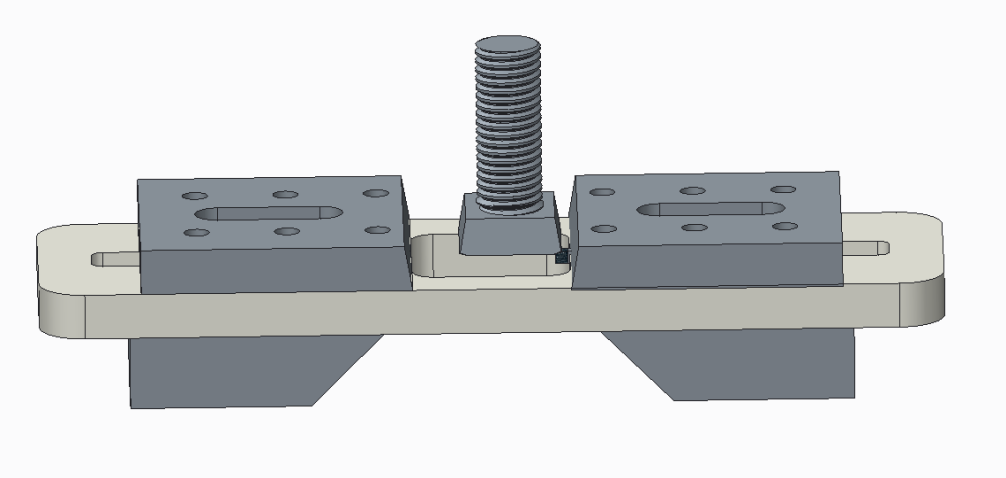

Figure 6.1.2 Drop Impact Tester interface and new tup design.

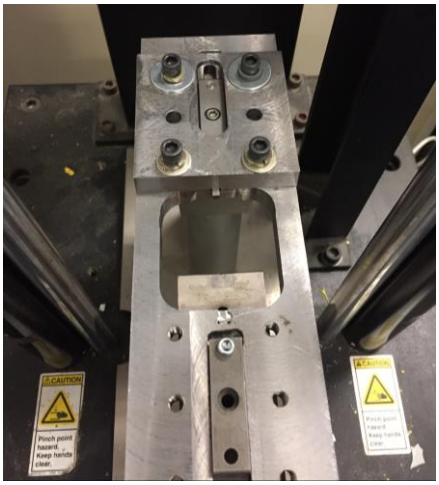

Figure 6.1.3 The Impact Test Fixture with Specimen

Figure 6.1.4 The Impact Test Fixture with Specimen

Hardness of the base of the fixture was 1.765 GPa (89 HRB) and the top plate 1.638 GPa (86 HRB) which is rather low with the thought that having softer material in the fixture would induce less stress in the small specimen during clamping compared to a much harder fixture and the measurement would be accurate as long as deformation did not occur with repeated use. The key item which needed to be as hard as possible would be the striker itself which was made from a grade 8 bolt to prevent elastic and plastic deformation which would absorb energy and lower the results. The new striker was hardness-tested in the "as received", but machined condition with an average hardness of 3.119 GPa (32 HRC).

6.2 **Impact Results for Qualifying Specimens (1-4)**

A trial run was completed to get an idea of impact strength, the fracture area, setup, and test method. The ASTM E23 IZOD Standard Test Methods for Notched Bar Impact Testing of Metallic materials was used since the energy did not exceed 80% of the machine's capacity, the velocity set to be within the 3.048 m/s to 6.096 m/s (10 - 20 ft/sec) requirement, the striker width was greater than the specimen being tested but there was no radius on the striker and it was at 90 degrees relative to the specimen rather than 75 +/- 3 degrees [27]. It was chosen to ignore the radius and angle requirements of this ASTM since it was thought the 75 degree angle would cause abnormal loading for this setup and it was unknown just how much radius would be needed not to cause plastic deformation in the WHA. Additionally one of the purposes of the ASTM is usually to standardize testing and since no standard exists for the perceived potential energy requirement, specimen size and other requirements a starting point with well-defined

boundary conditions was chosen i.e. 90 degrees and no radii. The tup filter was set to 4 kHz to damp out high frequency ringing. Additionally the initial FEA used to prove out the concept did not show a radius and angle would be beneficial during the impact event to prevent abnormal loading or binding. Therefore velocity checks for the machine were completed and each sample was measured and the top marked with a Sharpie® for post analysis orientation purposes as shown in **Figure 6.2.1**.

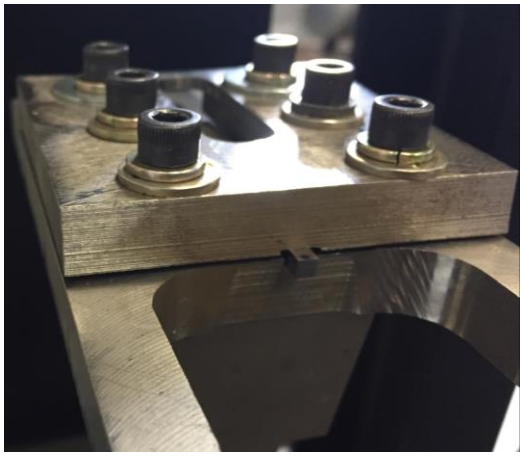

Figure 6.2.1 First Impact Test - Test Setup

The first four specimens were lapped using 220-800 grit abrasive powder and shown again in **Figure 6.2.1** for reference.

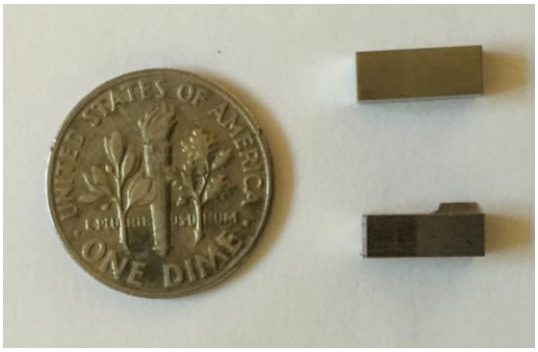

Figure 6.2.2 Specimen Samples, Lapped with 220-800 Grit Abrasive Paper (Top), as Machined (Bottom).

Four impact tests were carried to get an idea if the 3.119 GPa (32 HRC) striker would suffice. For these trials a drop weight of 5.044 kg (11.12 lbs) was used and velocity checks came in at 2.451 m/s (8.04 ft/s) corresponding to a kinetic energy of 15.151 J. Actual velocities recorded during impact test were measured at 2.426 m/s (7.96 ft/s).

1^{st} drop height and mass: 12.5"= 0.3175m , 11.12 lbs = 5.04395 kg

$PE_1 = m_1gh_1 = 5.04395\ kg * 9.80665\ m/s^2 * \sim 0.3175\ m = KE_1 = 15.7049\ J = 11.58\ ft\text{-}lbs$

$KE_{actual} = ½\ m_{actual} * V_{actual}^2 = 0.5 * 5.04395\ kg * 2.426\ m/s^2 = 14.843\ J$

The resulting curves for the first four tests (**Figure 6.2.3)** show nothing abnormal for tests 1, 2, and 4 in terms of the curves and show relatively good energy absorption indicating a good bond. The third specimen was not quite thick enough to clamp appropriately but an attempt to use a shim to clamp the specimen resulted in the specimen being pulled out of the holder rather than breaking. This in turn produced a large deflection of the specimen as evidenced by the prolonged loading (red curve) and the large energy to failure value produced, though the sample deformed but did not break. The energy to failure for the specimens were 0.8813 J (0.65 ft-lbs), 1.0711 J (0.79 ft-lbs), 5.464 J (4.03 ft-lbs) (no-test), and 0.3118 J (0.23 ft-lbs) respectively. Literature shows for D2 austenitizing at 1025℃ and tempering once at 538℃ produces a charpy impact energy of 1.4914 J (1.1 ft-lbs) and tempering of martensite has a large influence on toughness suggesting these are reasonable results since no tempering process was performed [46].

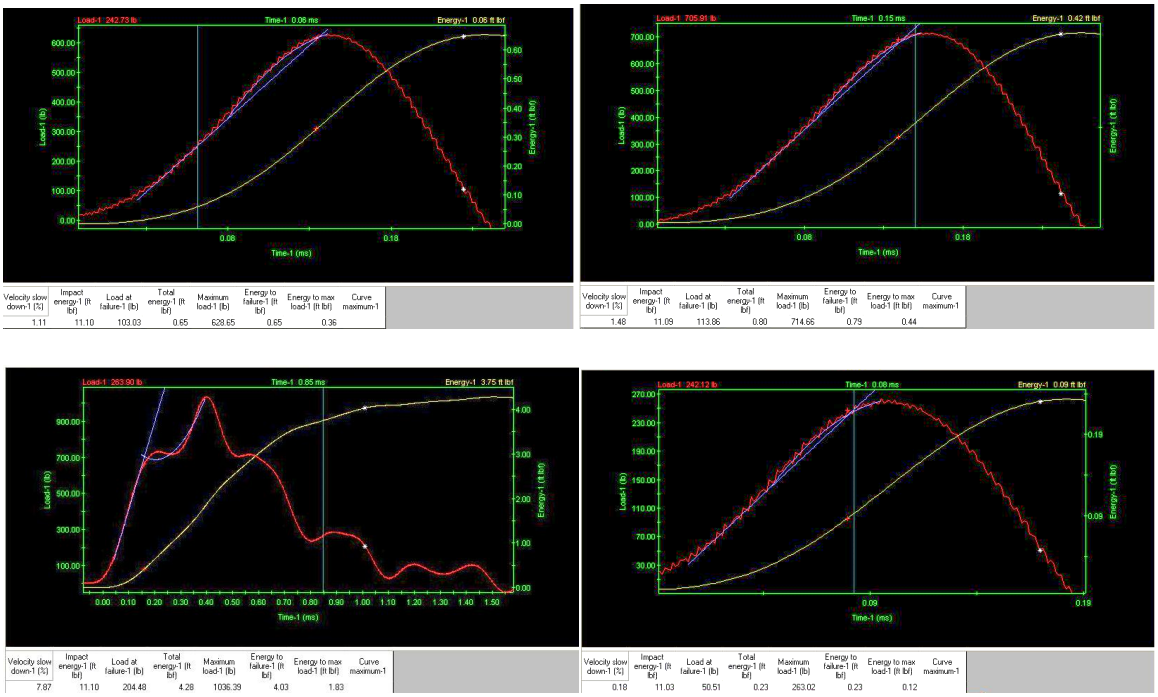

Figure 6.2.3 Impact Test Results for Specimens 1-4

The posttest pictures of the fourth impact test in **Figure 6.2.4** show a nice clean break on the interface and is where almost all specimens fractured.

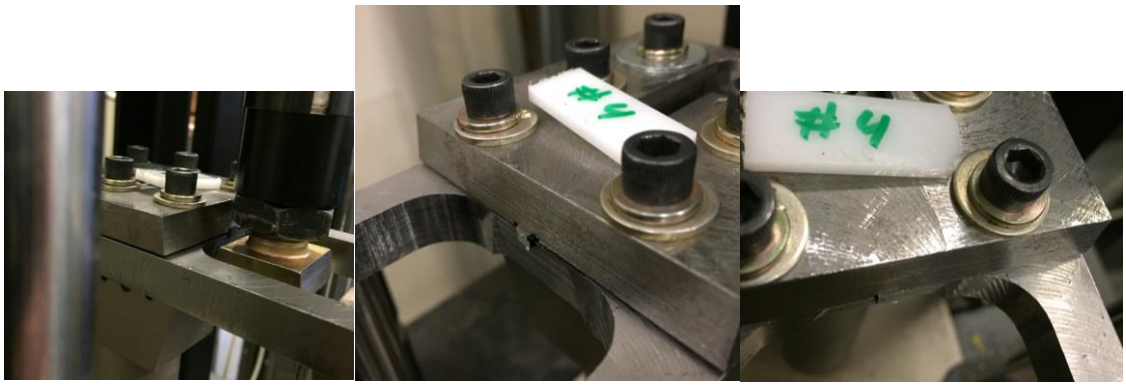

Figure 6.2.4 Posttest Pictures of Specimen 4 Impact Testing

The 3.119 GPa (32 HRC) striker was examined and revealed after 4 impacts slight rounding on the edge which is indicative of deformation and energy being absorbed by the striker itself and not the specimen which would result in energy-to-failure values

lower than actual values. Thus, the testing was halted. It should be noted that only specimen 2's energy to fail value will be used as specimen dimensions were incorrectly input for specimen 1 and 4 though load at failure values will still be utilized for specimens 1 and 4.

The striker was then heated past the austenitizing temperature (> 1000°C), and quenched, then sand blasted to remove the scale, leaving slightly broken edges on the striker compared to the as-machined edges which were sharp and unbroken previously. It was decided the sharp edged could deform absorbing energy, so the slightly broken edges would provide more realistic results. The heat treatment resulted in a hardness of 6.404 - 6.835 GPa for the striker which is a more durable and desirable condition for preventing energy absorption.

6.3 **Impact Results with Improved Surface Finish (5-17)**

To reduce variability, it was also decided to reduce the surface roughness further than the previous lapping efforts. Specimens were hand polished at 150-200 RPM using FEPA 320, 500, and 1200 grit paper consecutively, which resulted in different dimensional specimens whose width and height would be tracked so it could be input during impact testing. This is needed so the stress would be accurately calculated since it is used for the integral of the stress-strain (displacement) curve to calculate the toughness of the interface or the energy absorbed prior to the specimen failing.

2^{nd} drop height and mass: 23.25"= 0.59055m; 11.938 lbs = 5.415 kg

$PE_2 = m_2gh_2$ = 5.415 kg * 9.80665 m/s^2 * 0.59055 m = KE_2 = 31.36 J = 23.13 ft-lbs

$$KE_2 = \frac{1}{2} m_2 v^2 = 0.5 * 5.415 \text{ kg} * 3.389376 \text{ m/s}^2 = 31.103 \text{ J}$$

The height and width of each specimen was then measured using a digital micrometer with an ISO 9001 certification and 0.00005" resolution instead of a caliper which was used for specimens 1-4. With the new striker, better surface finish on the samples and more accurate dimensions, testing resumed. Unsure of the required impact energy needed for all specimens, the height was approximately doubled for the next series of tests. Velocity checks were carried out, test velocities were 3.389 m/s (11.12 ft/s), a slightly different drop weight of 5.415 kg (11.938 lbs) was used, along with an approximately 0.59055 m (23.25 inch) drop height, resulting in an impact energy of 31.103 J. A slightly different calibration factor of 13884.7 N (3121.4 lbf) was used for the tup corresponding to a 4448.22 N (1000.0 lbf) applied load vs the 13873.1 N (3118.8 lbf) calibration factor for a 1334.47 N (300.0 lbf) applied loaded which was used previously. This was because the maximum loads observed during testing of specimens 1-4 were between 2224.11 N (500 lbf) and 4448.22 N (1000 lbf).

6.3.1 **Additively Manufactured Specimens (ABS) Pre- and Post-Test as a Calibration Method.**

It was decided to start and end the testing using an additively manufactured acrylonitrile butadiene styrene (ABS) polymer specimens made in one lot to make sure data acquisition was possible given the limited samples and to determine if the setup drifted over time due to instrumentational or vibrational modes. It should be noted between the pretest and posttest it was decided to change the duration of the data

collection from 10 ms to 30 ms (reduced sampling) as results seemed to drift for the D2 with the thought increased recording time would capture any data (energy absorption) truncated from the shorter sampling duration. Both the pretest curves and posttest curves are shown in **Figure 6.3.1** which resulted in a 84.87 N to 84.69 N load at failure indicating the material fails at almost the same load, but with 0.5288 J and 0.7457 J energy to failure. This difference can be attributed to the orientation of the build layers relative to the striker since the ABS specimens were additively manufactured and are known to have orthotropic properties [55] [56]. The posttest curve also shows there may be some dwell in the force indicating a weight or bolt may have loosened slightly during testing since the striker was checked for loosening after each specimen.

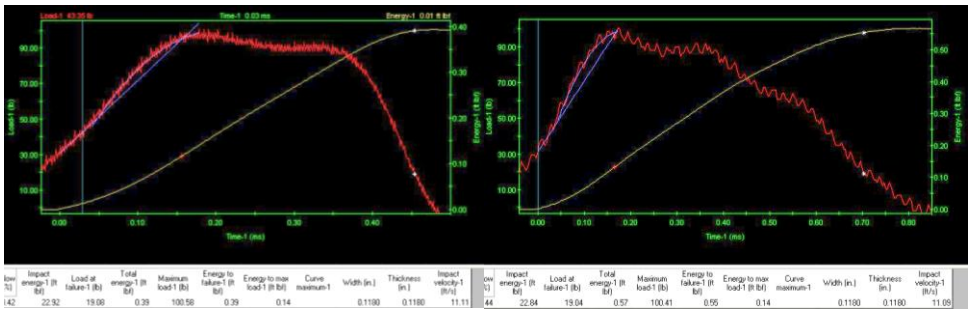

Figure 6.3.1 ABS Pretest 10ms 819.2 kHz Sampling (Left) ABS Posttest 30ms 273.07 kHz Sampling (Right)

6.3.2 D2 Impact Testing Results Specimens 5-17

After the data acquisition checks, the D2 specimen number five was placed in the fixture with the new hardened striker and the impact test carried out which resulted in 0.31184 J (0.23 ft-lbs) of energy to fail at a 184.6 N (41.5 lbf) load at failure creating a brittle failure as shown in **Figure 6.3.2**.

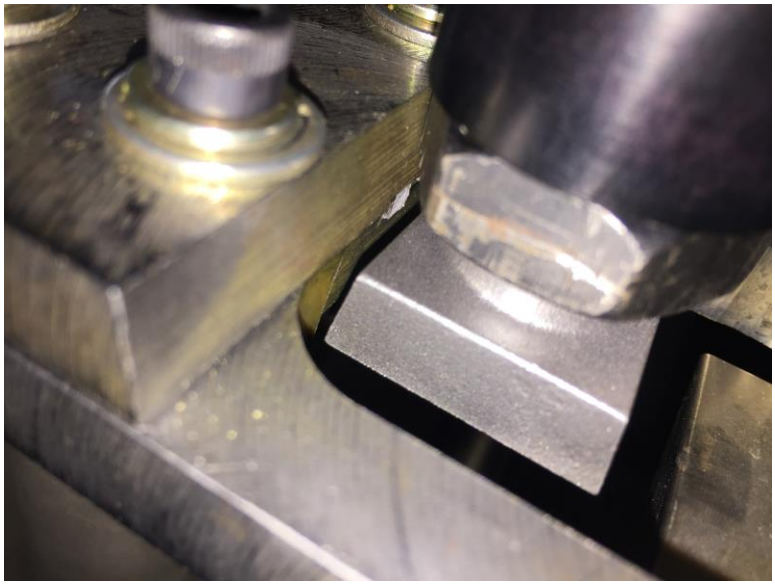

Figure 6.3.2 D2 Impact Testing Sample 5 Hardened Striker

The load curves for specimen 5 and 6 are shown in **Figure 6.3.3**, both normal responses, though specimen 6 required the highest load to fail of all the samples with 769.23 N (172.93 lbf) at failure and a resulting 1.749 J (1.29 ft-lbs) to fail. All specimens had a portion of the fracture on the interface. Some of the fractures were clean along the interface like specimen 5 in **Figure 6.3.2** and some with lips of WHA like specimen 4 in **Figure 6.2.4** where the fracture started in the WHA, but with no real correlation with energy-to-fail.

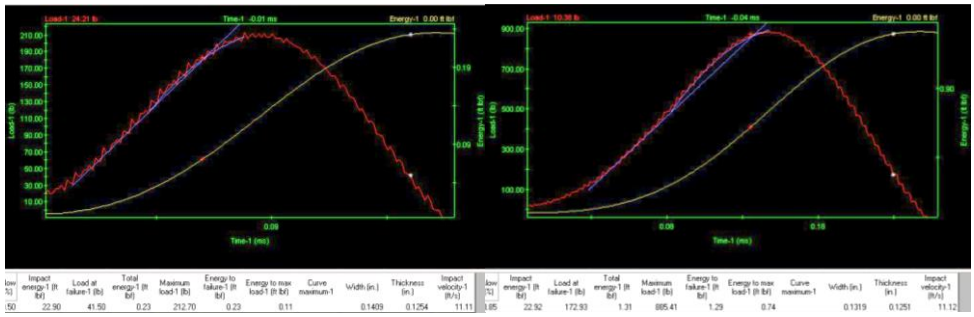

Figure 6.3.3 D2 Sample 5 (Left) D2 Sample 6 (Right)

After specimen 8's 0.759 J (0.56 ft-lb) energy to fail, values seemed to start dropping off with specimen 9 to 0.149 J (0.11 ft-lbs) though the load curve seemed normal. Specimen 10 failed at 0.1898 J (0.14 ft-lbs) and specimen 11 at 0.176 J (0.13 ft-lbs), then sample 12 resulted in a not test resulting in the curves in **Figure 6.3.4**.

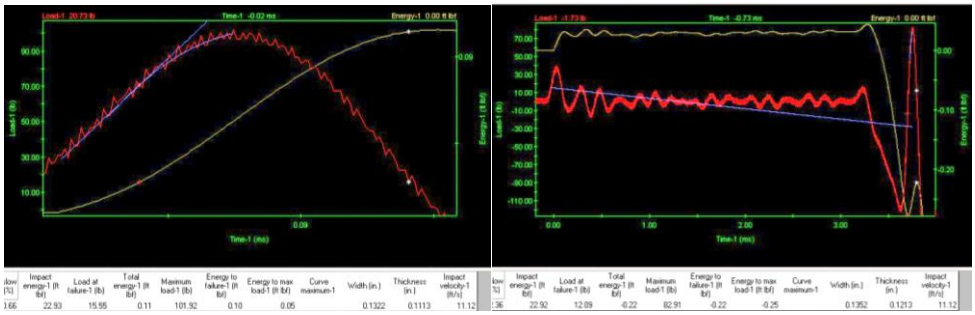

Figure 6.3.4 D2 Sample 9 (left) D2 Sample 12 – No Test (Right)

At this point testing was paused, the fixture checked to make sure nothing was loose, the tup and striker were tight and all weights tight as well as no deformation was occurring on the fixture. There was slight evidence of the sharp edge on the base of the fixture beginning to deform, but perceived to be insignificant. Velocity was checked again with nothing abnormal so the sampling rate was changed to 30ms sample time to make sure the entire fracture event and all absorption energy was being captured since the start of the recording is triggered by a flag and was adjusted to start recording early, just slightly before impact. This was because if the flag adjustment is off, and recording of the event is started and stopped before the event is over it would result in lower energies to failure as only a portion of the energy to break would be recorded and integrated. Thus with the increased recording time, the data is smoothed as shown in **Figure 6.3.5** since the 30ms sample time results in a 273.07 kHz sampling rate vs the 819.2 kHz sampling

rate for a 10ms sample time. This 30 ms sample time was used for the remainder of the testing.

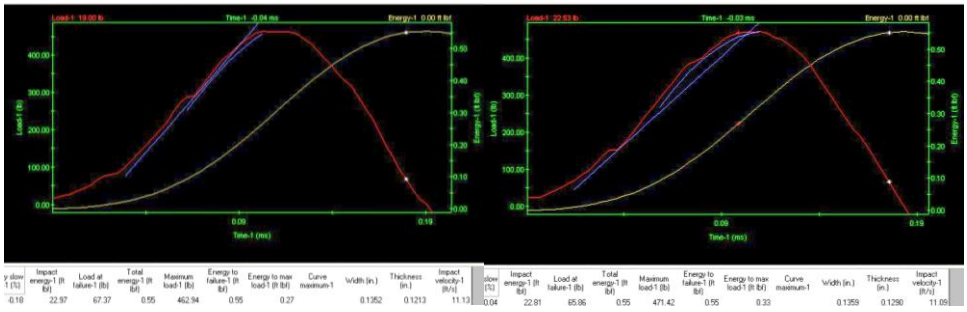

Figure 6.3.5 D2 Sample 13 30ms (Left) D2 Sample 16 30ms (Right)

Though some tests and corresponding data values are questionable, there were 8 good samples of the population which were used in the average and standard deviation calculations shown in **Table 6-1**. These results could be in error with the slight deformation occurring in the fixture which may explain some of the drift. If only sample 2, and samples 5-8 are used for calculations, the average energy needed for failure is 0.8406 J (0.62 ft-lbs) with an average load-to-failure of 390.554 N (87.8 lbf). This sample size is still a significant enough sampling [27] to prove adhesion has occurred and there is a quantifiable diffusion boundary between the WHA and the D2 which requires energy to break. Future works should look at the interface prior to impact testing and use an automated video analysis tool to calculate the porosity on the interface to determine if there is a correlation.

Specimen	Width (mm)	Height (mm)	Area (mm^2)	Energy to Failure (ft-lbs)	Energy to Failure (Joules)	Load at Failure - Newton	Stress MPa	Notes
1	3.197	3.486	11.144	0.65	0.881	459.501	41.234	Specimen Dimensions not updated from ABS*
2	3.170	3.810	12.077	0.79	1.071	506.474	41.936	caliper used
3	3.205	3.373	10.812	4.28	5.803	909.572	84.123	No Test Smeared the Sample - Poped Out of the holder**
4	3.494	2.987	10.436	0.23	0.312	224.680	21.529	136 input for width instead of .136 from caliper*
5	3.578	3.185	11.395	0.23	0.312	184.601	16.200	tight tup and striker
6	3.349	3.176	10.637	1.29	1.749	769.231	72.314	tight tup and striker
7	3.346	2.747	9.193	0.22	0.298	130.778	14.226	tight tup and striker
8	3.301	3.254	10.740	0.56	0.759	361.551	33.665	tight tup and striker
9	3.357	2.826	9.485	0.11	0.149	68.947	7.269	tight tup and striker
10	3.056	3.001	9.170	0.14	0.190	107.647	11.739	tight tup and striker
11	3.364	3.245	10.916	0.13	0.176	107.647	9.861	tight tup and striker
12	3.434	3.081	10.580	-	-	-	-	no test**
13	3.372	2.950	9.948	0.55	0.746	299.677	30.125	30ms data cycle - put sample 12 measurements in instead of 13**
14	3.108	2.421	7.523	-	-	-	-	no read**
15	3.604	3.355	12.094	0.27	0.366	177.395	14.669	specimen had D2 supporting WHA **
16	3.452	3.277	11.310	0.55	0.746	292.960	25.902	Speciment had a chamfer ground on it. **
17	3.679	3.080	11.331	0.18	0.244	146.391	12.920	Is the specimen with a sliver of D2 on one side (SEM Image)**
Average	3.357	3.133	10.517	0.43	0.588	292.106	26.997	* not used in average or std. deviation caluclation for Energy to Failure
Std. Dev.	0.175	0.313	1.162	0.42	0.572	227.651	20.410	** not used in energy to failure, load at failure, or stress average and std deviation

Table 6-1 D2 Charpy Impact Test Results

Chapter 7: Fracture Surfaces of the Impacted Samples

7.1 Optical Images of Fracture Surfaces

7.1.1 Optical Images of Fracture Surfaces of Specimen 1

Fracture of the majority of the specimens occurred in roughly two manners: a "smooth to the eye" surface with a very small lip removed from the top of the WHA and a small lip protruding from the bottom of the D2 surfaces exhibiting shear, and the inverse for the WHA cube which was broken off. The other manner was a partially smooth surface with a large tungsten lip protruding from the top of the D2 surface with a small lip protruding from the bottom of the D2 surface indicating shear and the mirror image on the WHA. In both manners, the WHA did exhibit some deformation from the impactor. In **Figure 7.1.1** the optical microscope is focused on the D2 section on the right side of the screen showing the first manner of fracture where the D2 is taller than the WHA cube on the left side and is out of focus.

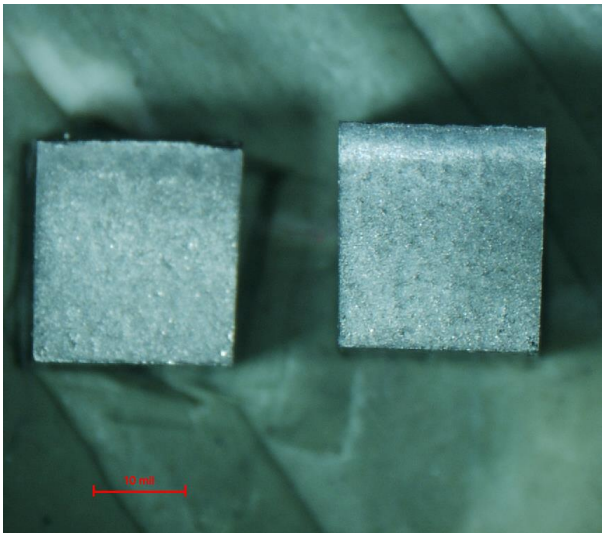

Figure 7.1.1 D2 Sample 1 Impact Test 5x WHA (Left), D2 Side (Right)

At 20x (**Figure 7.1.2)** with both independently focused upon, the “pits” on the WHA surface start to become visible where protrusions mirror the pits on the matting D2 surface, while in **Figure 7.1.3** at 50x the two surfaces look very similar to one another.

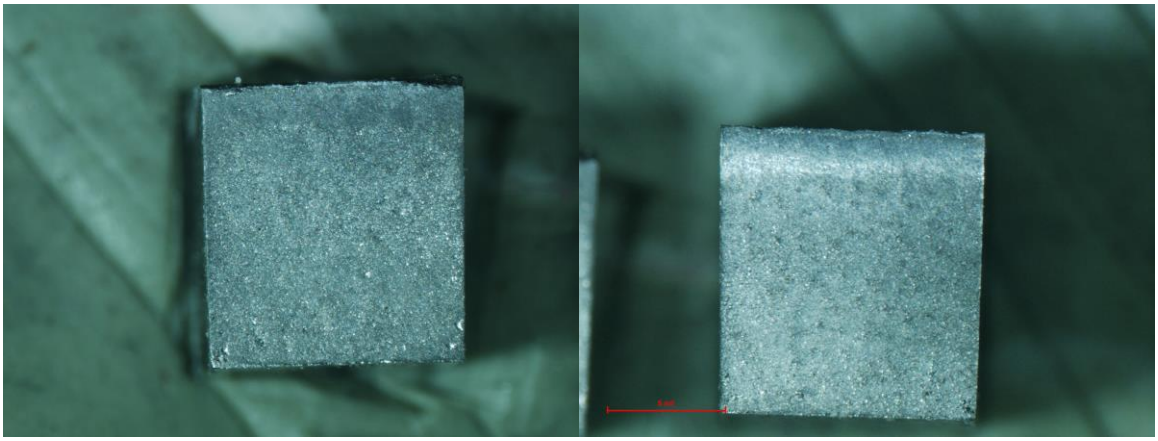

Figure 7.1.2 D2 Sample 1 Impact Test 20x WHA Side (Left) D2 Side (Right)

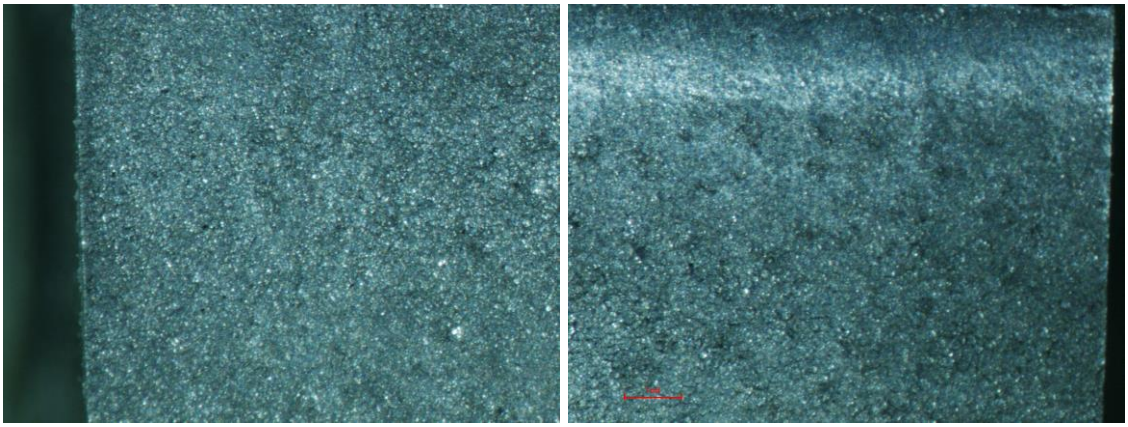

Figure 7.1.3 D2 Sample 2 Impact Test 50x W Side (Left) D2 Side (Right)

7.1.2 Optical Images of Fracture Surfaces of Sample 4

Just like specimen 1, specimen 4 also had a lip protruding from the top side of the D2 though substantially larger than specimens 1’s, and specimen 4 also had a small lip

protruding from the bottom of the D2 side exhibiting shear, except for one small corner which had material protruding perpendicular from the face as shown in **Figure 7.1.4**.

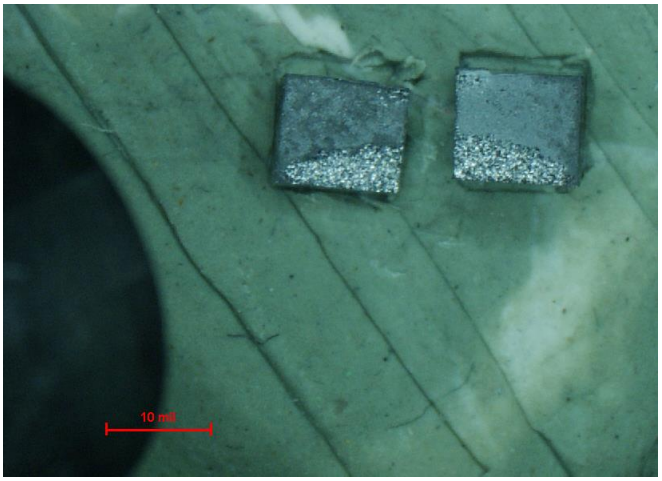

Figure 7.1.4 D2 Sample 4 Impact Test 5x WHA (Left) D2 (Right)

At 20x **Figure 7.1.5** shows the portions of the WHA cube which had material torn out. The orientation of the tare out suggests the cubes faces might not have been perfectly parallel which is possible given the hand polishing needed to reduce the surface finish.

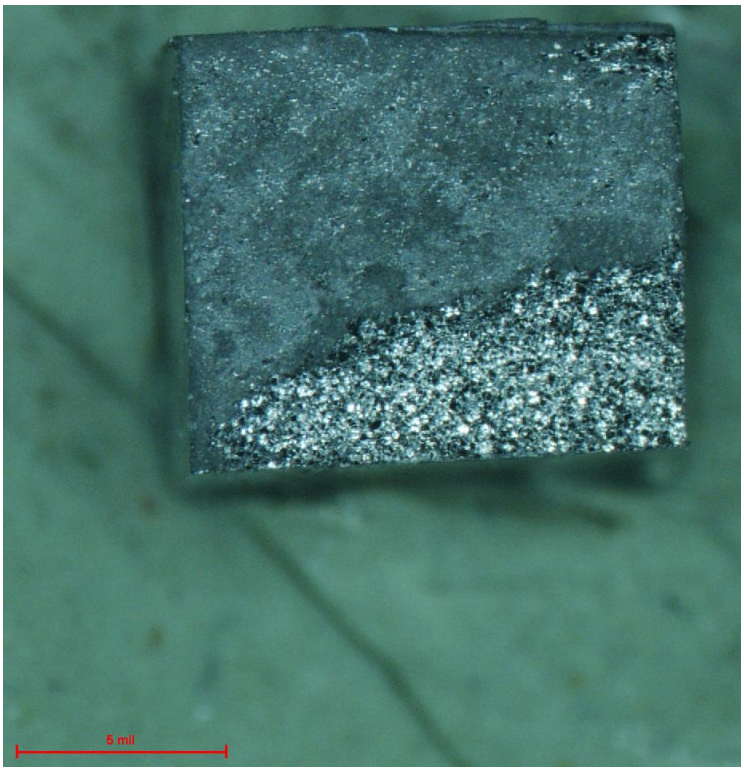

Figure 7.1.5 D2 Sample 4 Impact Test 20x W Side

The small lip which was torn out from the bottom corner of the WHA side is out of focus in **Figure 7.1.6** but a portion is in focus, showing a cupped behavior indicating ductile failure.

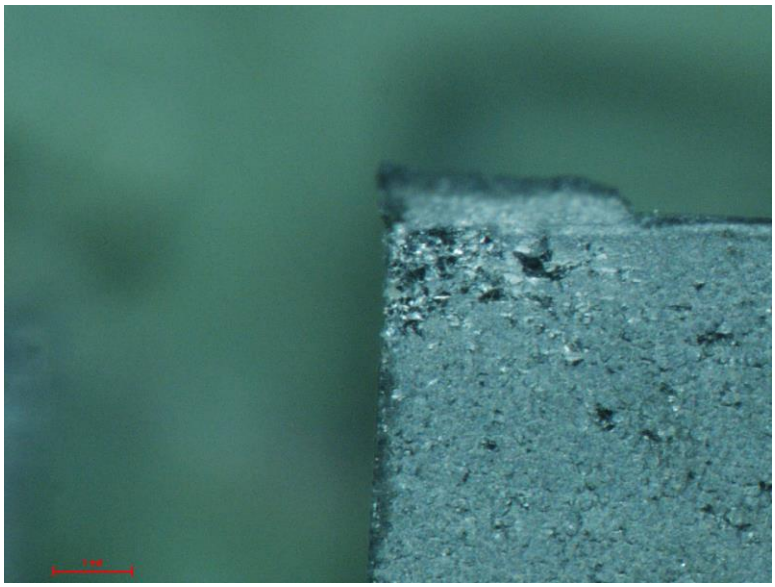

Figure 7.1.6 D2 Sample 4 Impact Test 50x D2 Side Bottom Corner

In **Figure 7.1.7** looking at the D2 side with the WHA protruding out of the image, two focal planes were again needed to look at the surface due to the height difference, but the WHA looks like a ductile failure. The bottom of the D2 surface is shown in **Figure 7.1.8** and looks scaly where the WHA in **Figure 7.1.9** seems to highlight grains with white halos.

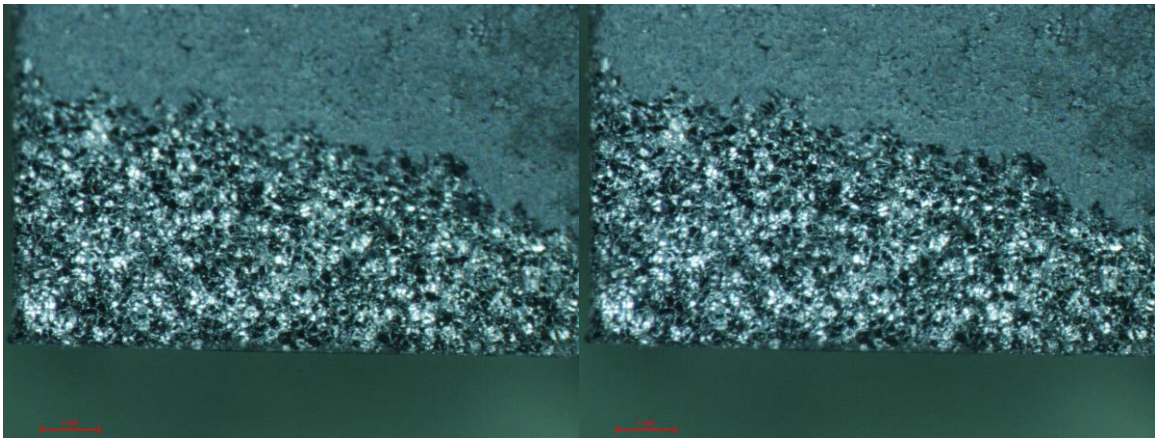

Figure 7.1.7 D2 Sample 4 Impact Test 50x D2 Side Top Corner Focus on Fracture (Left) D2 Side Top Corner Focus on Smooth Surface (Right)

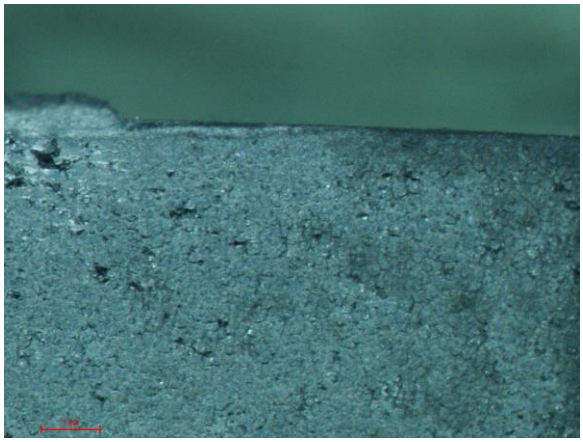

Figure 7.1.8 D2 Sample 4 Impact Test 50x D2

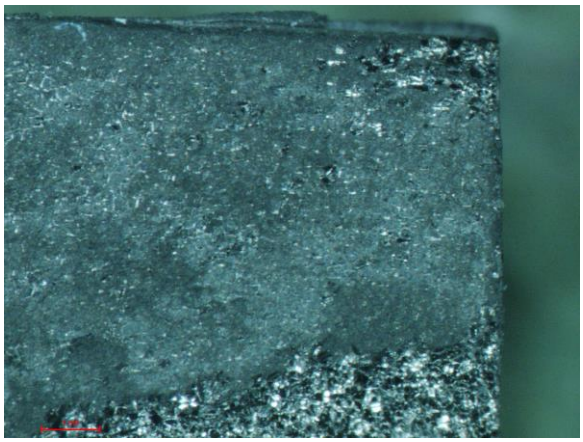

Figure 7.1.9 D2 Sample 4 Impact Test 50x W Side Bottom Corner

The top of the WHA, which is where the fracture should start, is shown in **Figure 7.1.10** and indicates the fracture did occur in the WHA which means the interface has a higher tensile strength then that of the WHA's tensile strength. The magnification limits of the optical microscope were reached without full clarity on what occurred on the surfaces so it was abandoned for the SEM.

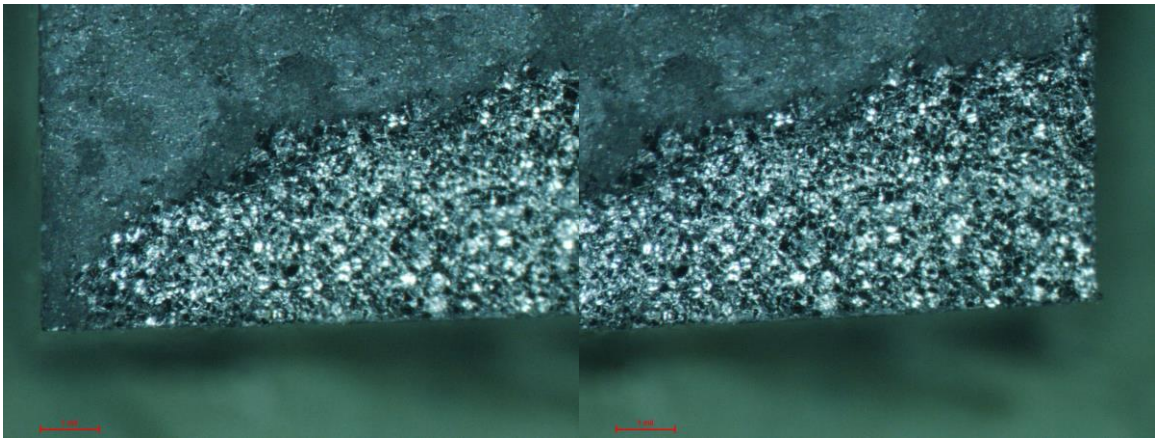

Figure 7.1.10 D2 Sample 4 Impact Test 50x W Side Top Right Corner (Left) Top left Corner (Right)

7.2 SEM Images of Fracture Surface of Specimen 2

Specimens 2 and 4 from the fracture testing were placed in the SEM directly on the carriage as shown in **Figure 7.2.1** below along with specimen 17 prior to it being tested.

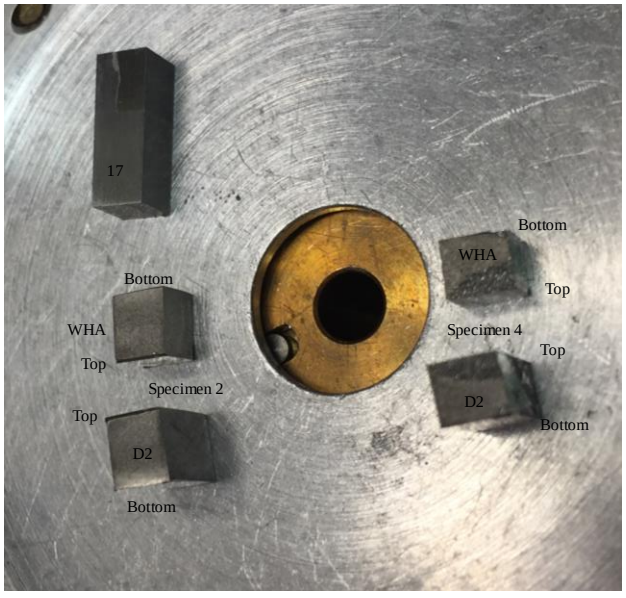

Figure 7.2.1 Specimen Layout for SEM

7.2.1 SEM of Specimen 2 D2 Side

The D2 side of specimen 2 (**Figure 7.2.2**) has a lip protruding from the top suggesting it elongated failing in tension ductility prior to failing along the interface. This suggests the bond was stronger in tension than the D2 at this location but also that there may be a thin layer of D2 on top of the WHA which is what yielded. The thickness of the lip varies along the cross section again suggesting the two faces of the cube may not have been perfectly parallel, most likely do to the manufacturing and polishing method. In the future a trial should be carried out to determine how parallel the faces must be in order not to affect the results with such a small sample.

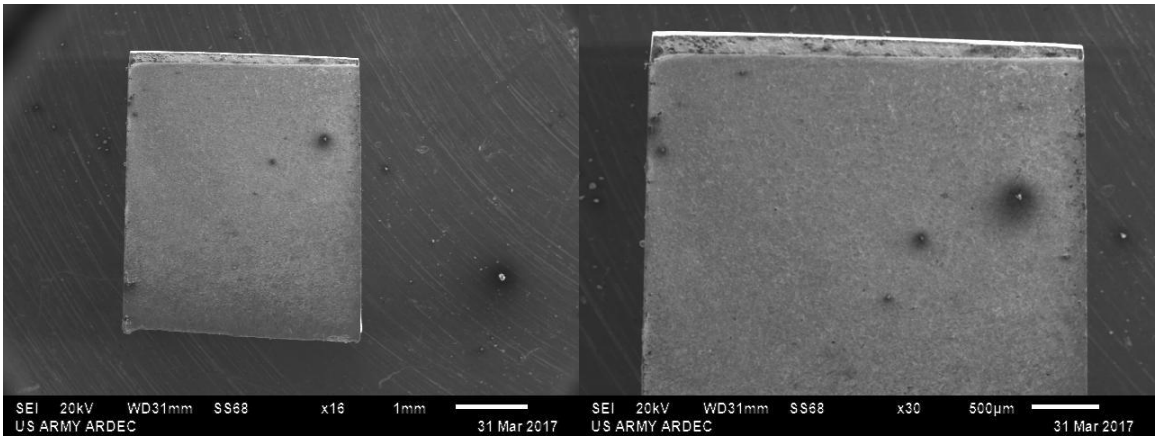

Figure 7.2.2 Impact Specimen 2 D2 Side x16 (Left) x30 (Right)

Focus was turned to the upper left corner of the lip (**Figure 7.2.3**) which shows elongation and necking from the outside of the cube in, as well suggesting there was a reduction in cross section area prior to failure. These artifacts constitute a ductile failure and the load vs. time curve in **Figure 6.2.3** helps confirm this.

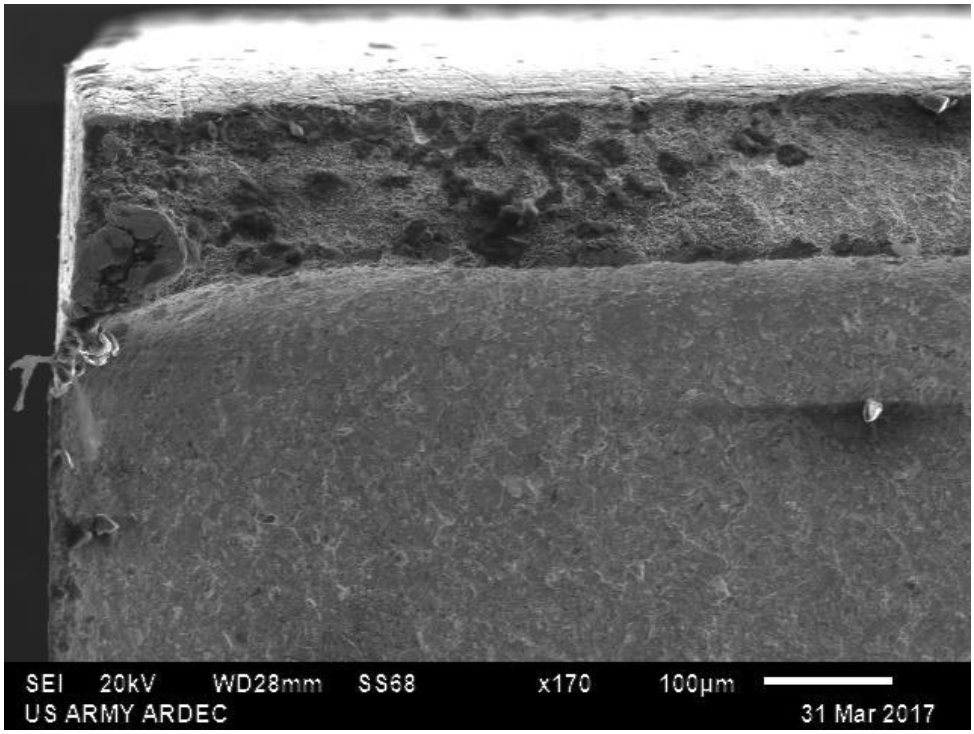

Figure 7.2.3 Impact Specimen 2 D2 Side Upper Left x170

Striations are visible from the lapping process in **Figure 7.2.4** as well as a portion of the D2 on the left side of the lip which appears planar (circled) in nature suggesting this area was adhered to the WHA but it is believed this is a thin layer of D2 which had not been removed and this is an area of unconsolidated powder. This interesting mishap shows the D2 was in tension at this location which aligns with simple cantilever beam mechanics and the bond strength of the joint was sufficient enough to allow ductility. Unfortunately the tup impact location could not be located closer to the joint to apply more of a shear load due to concern of damaging equipment. In **Figure 7.2.5** there is evidence of shear banding near the top surface (circled) showing the shear plane.

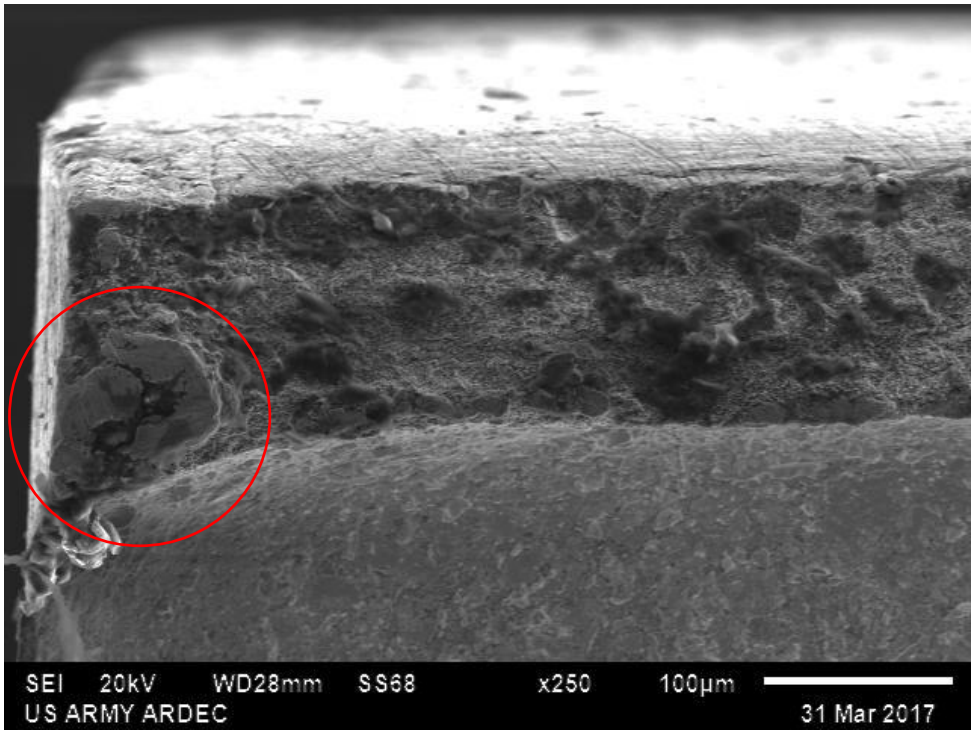

Figure 7.2.4 Impact Specimen 2 D2 Side Upper Left x250

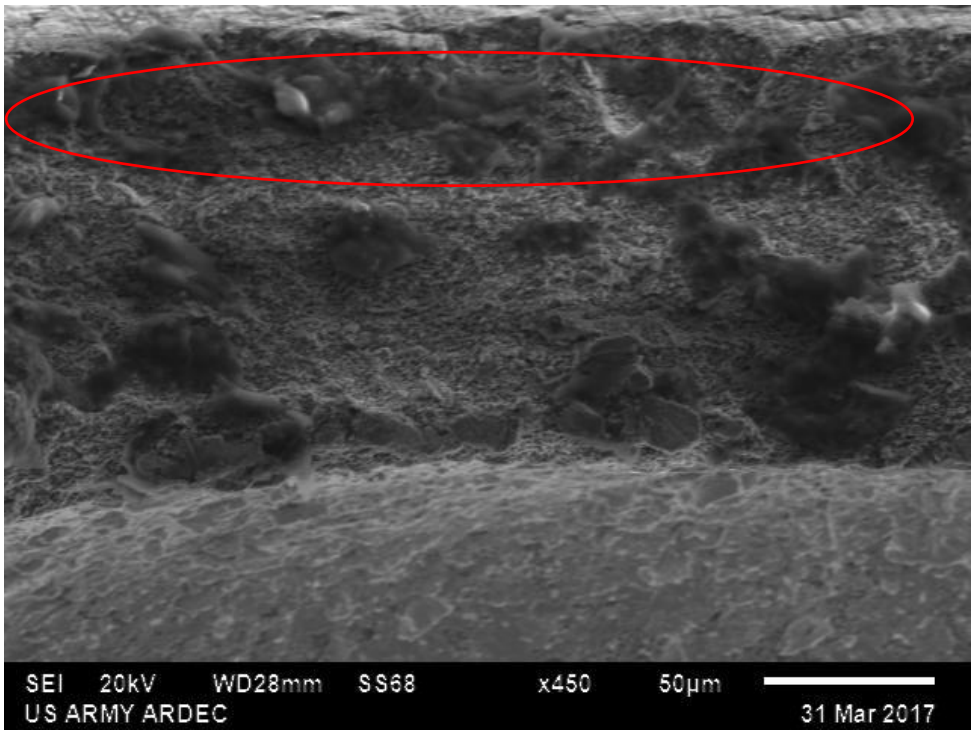

Figure 7.2.5 Impact Specimen 2 D2 Side Upper Left x450

Just beneath the lip previously presented, the grain of the D2 looks to be visible without etching with martensite and ferrite present as shown in **Figure 7.2.6** and **Figure 7.2.7**.

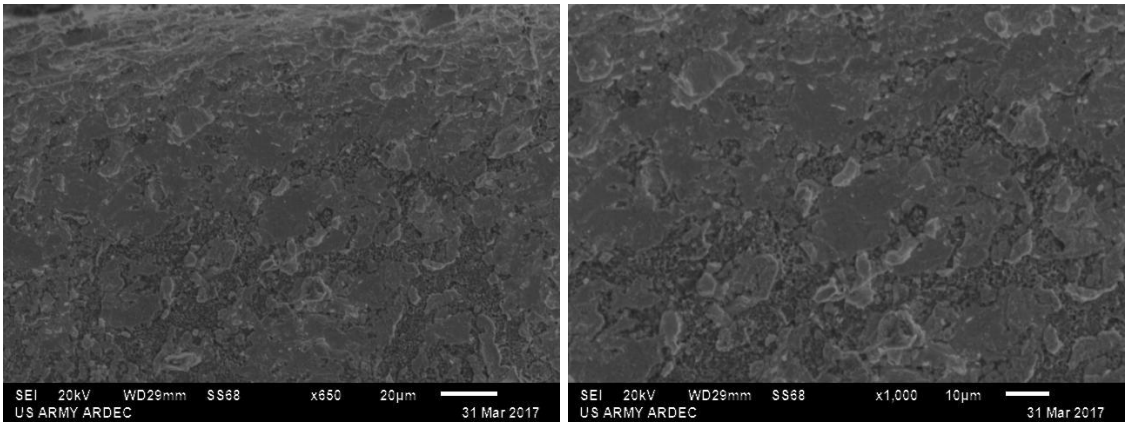

Figure 7.2.6 Impact Specimen 2 D2 Side Upper Left Below Lip x1000

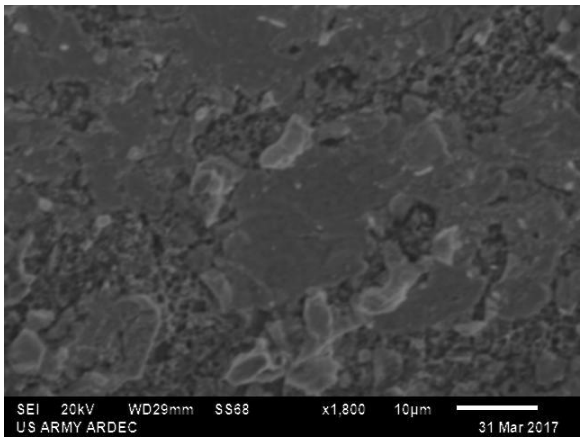

Figure 7.2.7 Impact Specimen 2 D2 Side Upper Left Below Lip x1800

Looking at the shear lip (**Figure 7.2.8** and **Figure 7.2.9)** and the edge of the transition of the lip to the de-bonded area, it appears ductile in nature confirming the load vs time curve is reasonable.

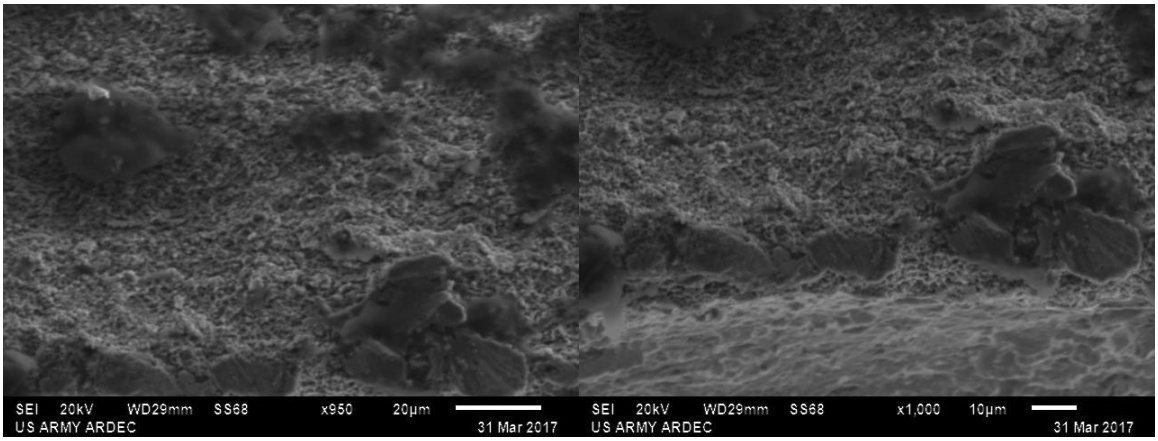

Figure 7.2.8 Impact Specimen 2, D2 Side Upper Lip x950 (Left) x1000 (Right)

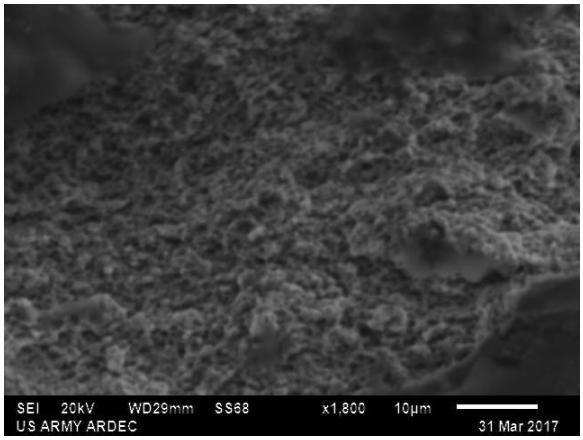

Figure 7.2.9 Impact Specimen 2, D2 Side Upper Lip x1800

7.2.2 SEM of Specimen 2 WHA Side

Looking at the matting part to the D2 fracture surface previously shown, the WHA side in **Figure 7.2.10** looks relatively smooth except the torn out lip.

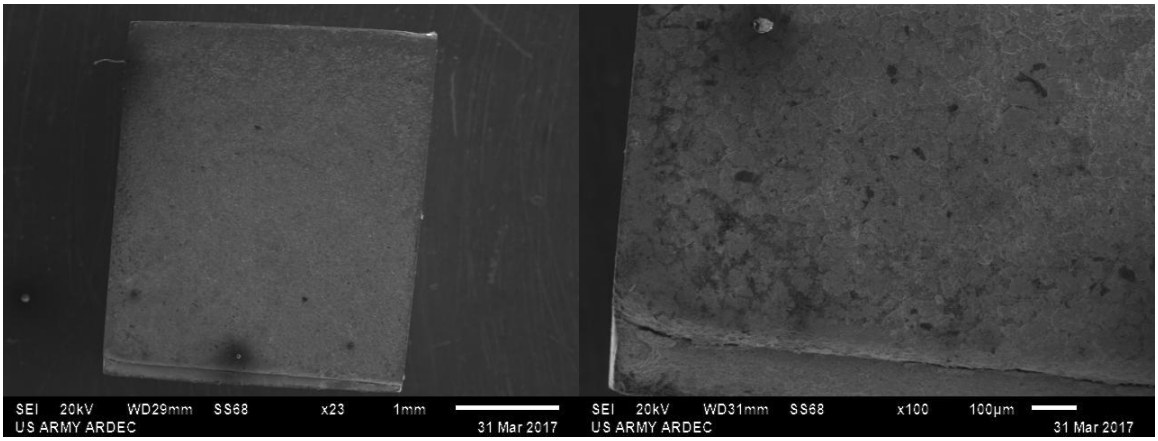

Figure 7.2.10 Impact Specimen 2 WHA Side x23 (Left) x100 (Right)

At higher magnification, **Figure 7.2.11** and **Figure 7.2.12** shows the fracture of the lip area on the WHA and does not represent fractured tungsten as expected confirming there is in fact a thin layer of D2 on top of the WHA.

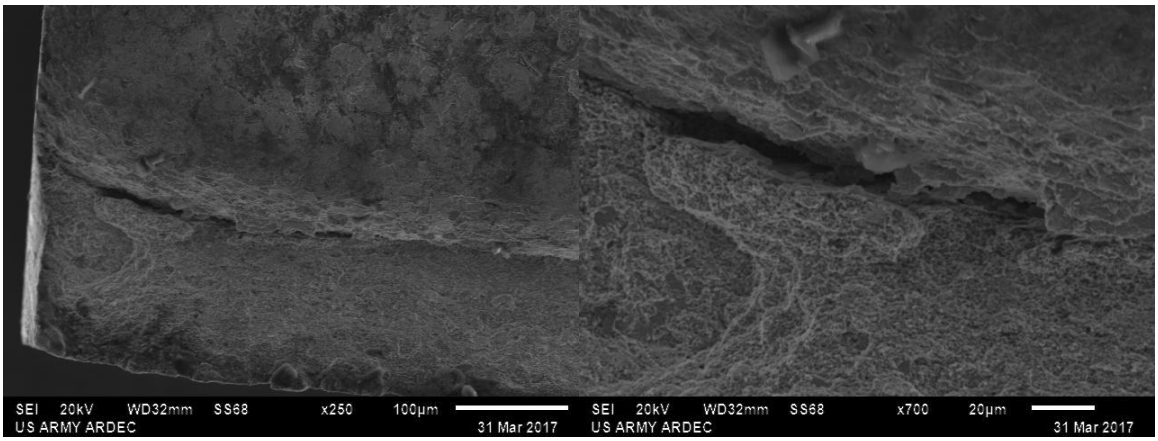

Figure 7.2.11 Impact Specimen 2 WHA Side Upper Lip x250 (Left) x700 (Right)

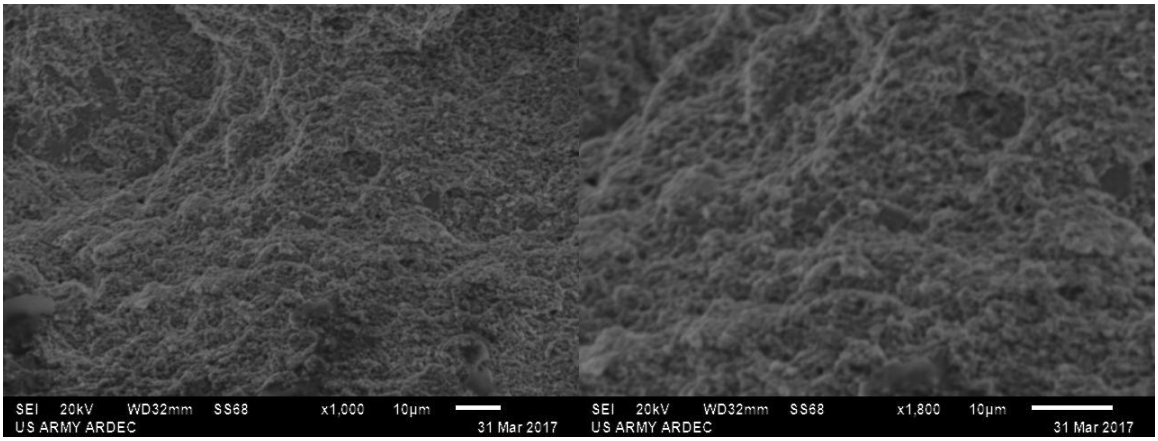

Figure 7.2.12 Impact Specimen 2 WHA Side Upper Lip x1000 (Left) x1800 (Right)

Below the lip on the WHA side (**Figure 7.2.13**), the fracture looks planar and relatively smooth with some pitting which may be explained by higher diffusion rates in the nickel and iron binder matrix making a better bond and if the binder created an island of tungsten grains the bond between the D2 and binder may be stronger than the bond between the tungsten and the WHA binder.

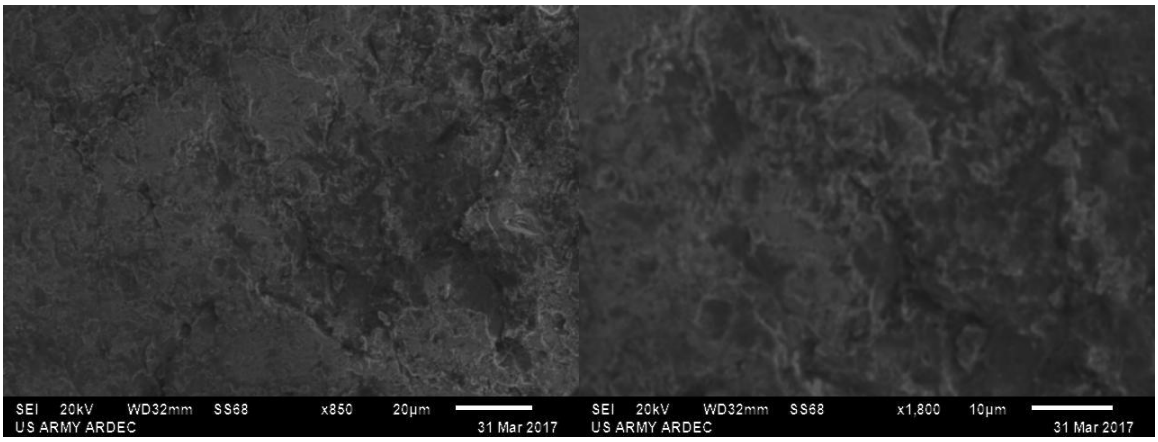

Figure 7.2.13 Impact Specimen 2 WHA Side Below Lip x850 (Left) x1800 (Right)

7.3 SEM Images of Fracture Surface of Specimen 4

7.3.1 SEM of Specimen 4 D2 Side

Specimen 4 is an excellent example of the second type of fracture which occurred were a large portion of tungsten remained on the D2, suggesting the bond between the D2 and WHA was stronger than the tensile strength/bond within the tungsten itself. The overview of the specimen is shown in **Figure 7.3.1** along with a higher magnification image of the smooth surface of the D2 side.

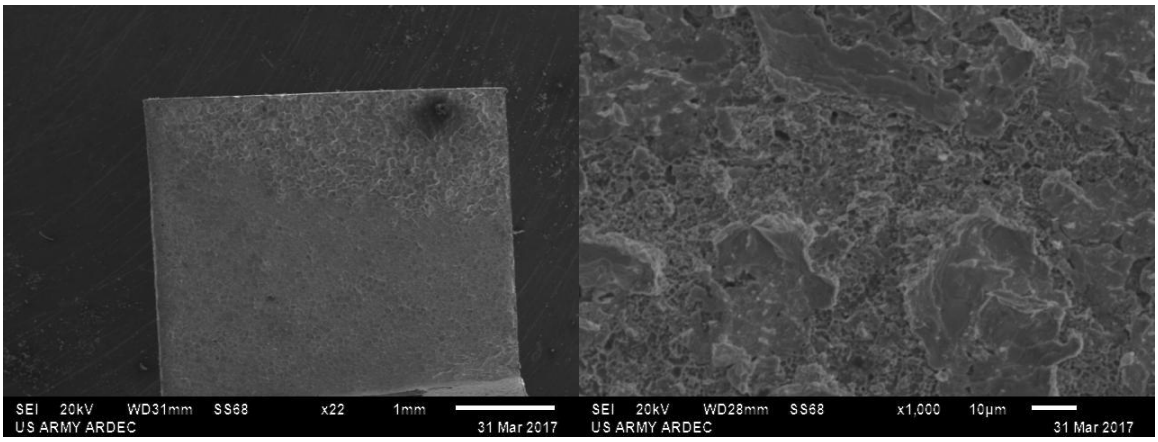

Figure 7.3.1 Impact Specimen 4 D2 Side x22 (Left) Middle of Specimen x1000 (Right)

As the protruding WHA lip of the D2 is further examined in **Figure 7.3.2**, it appears faceted but not feathered suggesting a brittle failure occurred in the material. At x750 (**Figure 7.3.3**) portions of the nickel and iron binder seem to be dis-bonded from the tungsten grains and in **Figure 7.3.4** these brittle features are highly visible along with some tungsten grains which appear feather-like showing more brittle failure. One such feathered tungsten grain is the central focus of the image in **Figure 7.3.5**.

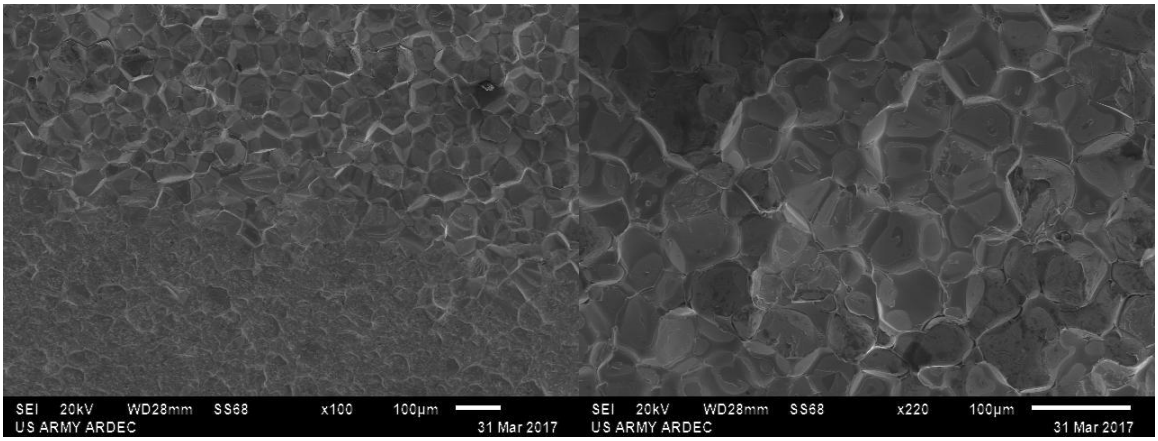

Figure 7.3.2 Impact Specimen 4 D2 Side Upper Right Lip x100 (Left) x220 (Right)

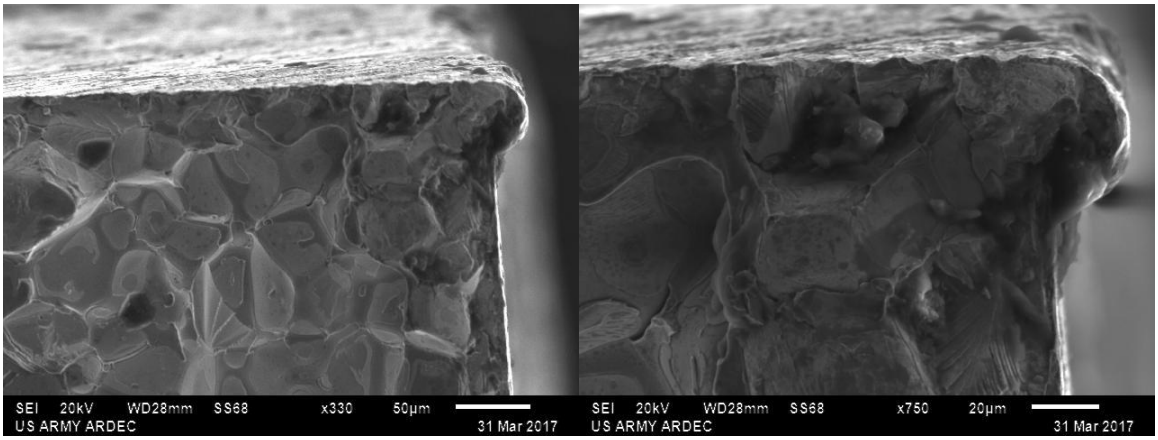

Figure 7.3.3 Impact Specimen 4 D2 Side Upper Right Lip x330 (Left) x750 (Right)

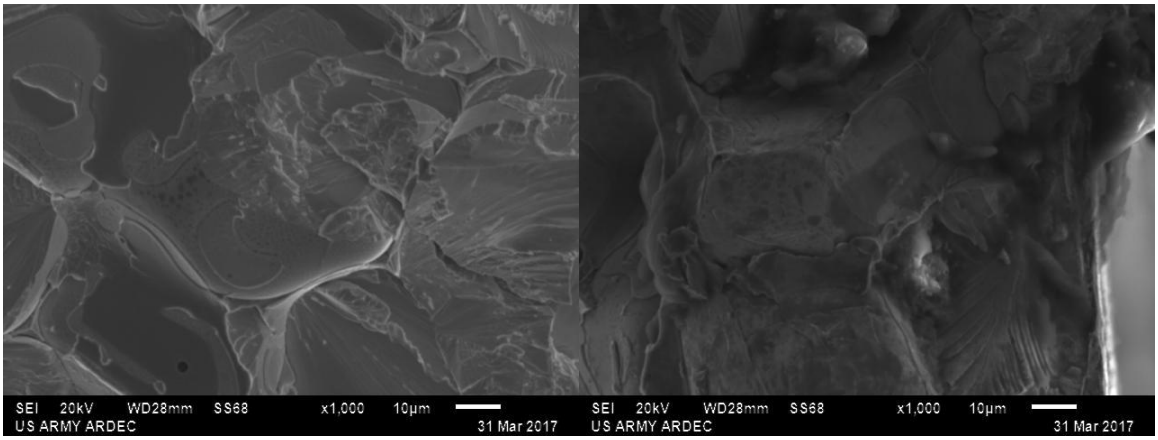

Figure 7.3.4 Impact Specimen 4 D2 Side Upper Right Lip x1000

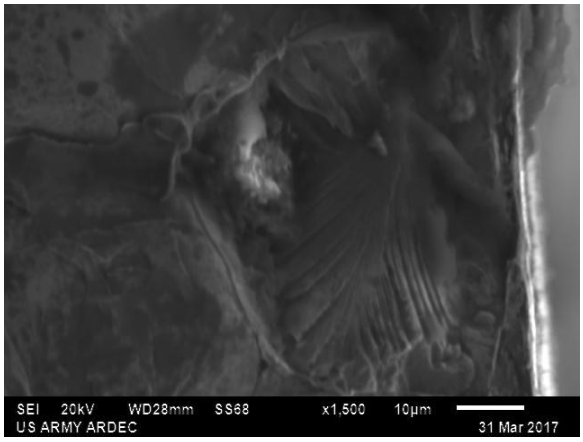

Figure 7.3.5 Impact Specimen 4 D2 Side Upper Right Lip x1500

The lower lip is different in nature (**Figure 7.3.6** and **Figure 7.3.7**), very ductile and similar to the lip on specimen 2 which suggests a thin portion of D2 remained bonded to the WHA and was not polished away. This thin layer of D2 is plausible as the location of the interface on the samples became less apparent as they were polished and further analysis on the broken portions of specimen 4 reveals a thin layer of D2 is still present. One purposeful example of such a thin layer of D2 remaining like a bridge across the interface is specimen 17 and will be presented later.

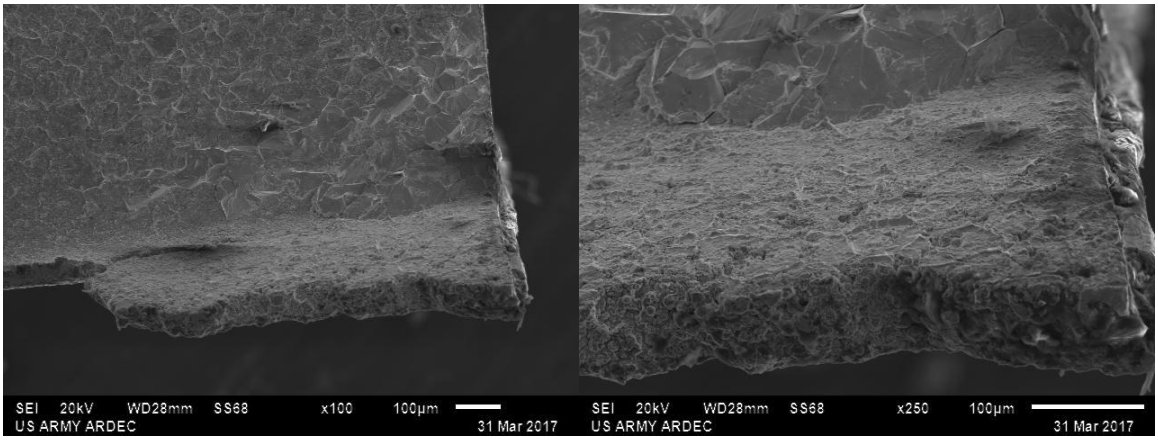

Figure 7.3.6 Impact Specimen 4 D2 Side Bottom Right Lip x100 (Left) x250 (Right)

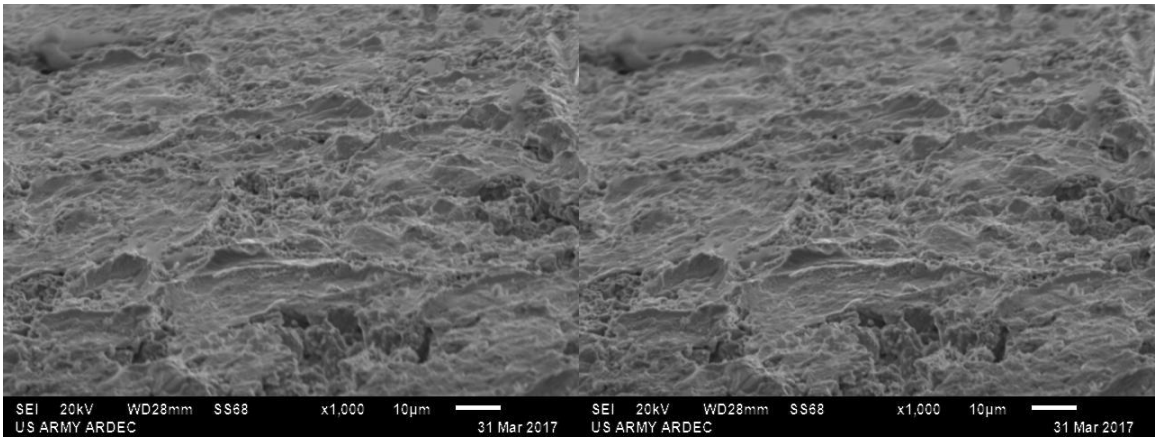

Figure 7.3.7 Impact Specimen 4 D2 Side Bottom Right Lip x1000

7.3.2 SEM of Specimen 4 WHA Side

Again the mating fracture surface of specimen 4 is the WHA side which is shown in **Figure 7.3.8**. This particular WHA cube had one edge fractured off and is actually the edge at the top of the specimen. This portion of the specimen would be in tension from the impact loading and suggests the tensile strength of the bond is higher than that of the WHA at this location. In **Figure 7.3.9**, the surface which is presumed to be the interface is shown along with the transition from the fractured edge to the interface. It is believed the majority of the fracture was in the WHA matrix binder rather than through tungsten grain as **Figure 7.3.10** shows cracks in this binder at the transition location rather than fractured grains.

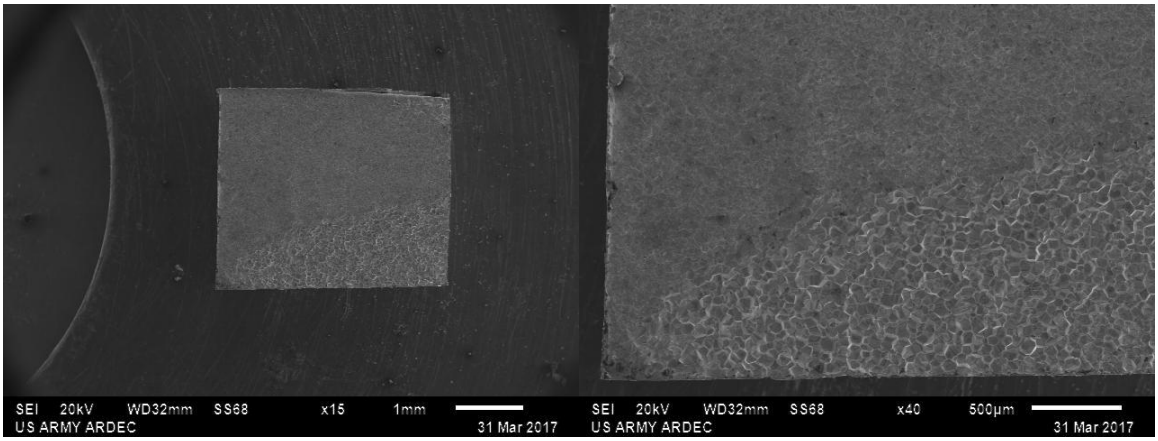

Figure 7.3.8 Impact Specimen 4 WHA x15 (Left) x40 (Right)

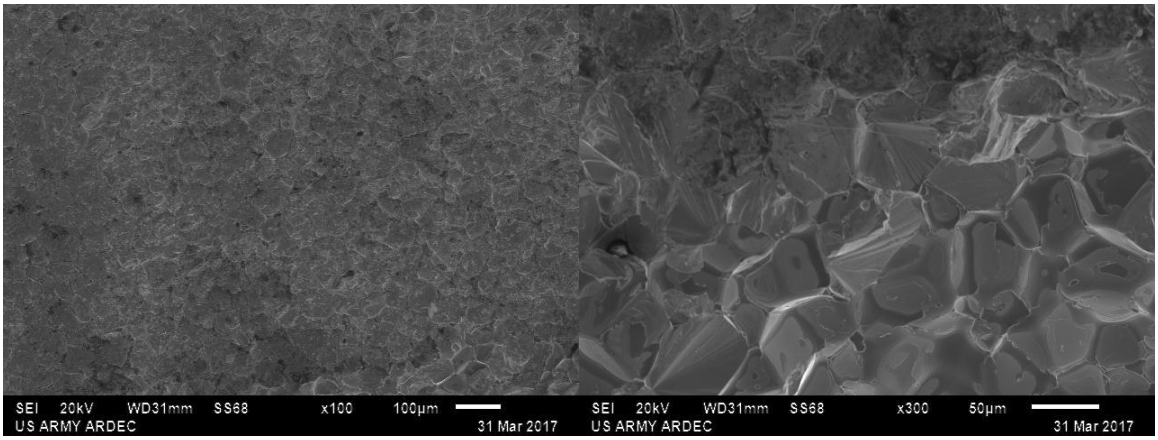

Figure 7.3.9 Impact Specimen 4 WHA Edge Interface x100 (Left) x300 (Right)

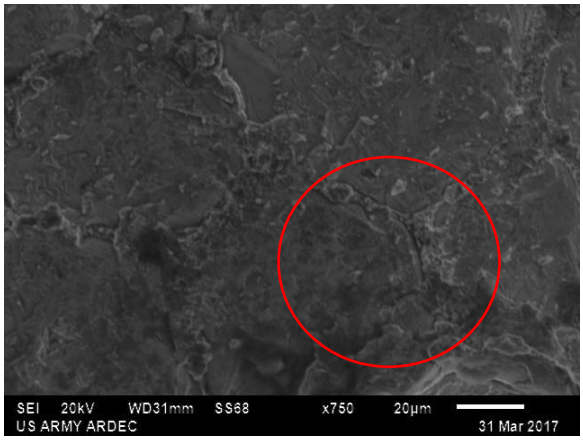

Figure 7.3.10 Impact Specimen 4 WHA Edge Interface x750

The image of the fractured edge (**Figure 7.3.11)** confirms the majority of the fracture occurred on the grain boundary of the nickel and iron matrix to tungsten as evidenced by the faceted images which appeared ductile in the optical microscope at lower power. These facets are more pronounced in **Figure 7.3.12** and only upon higher magnification (**Figure 7.3.13)** and searching can a tungsten grain exhibiting brittle failure be found which has fractured in two as evidence by the feathering texture of the surface [57].

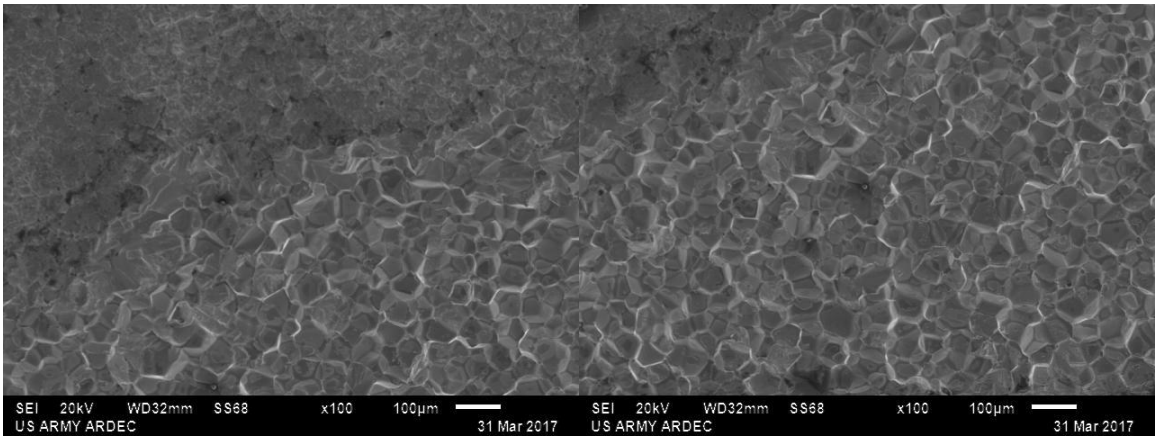

Figure 7.3.11 Impact Specimen 4 WHA Edge x100 (Left) x100 (Right)

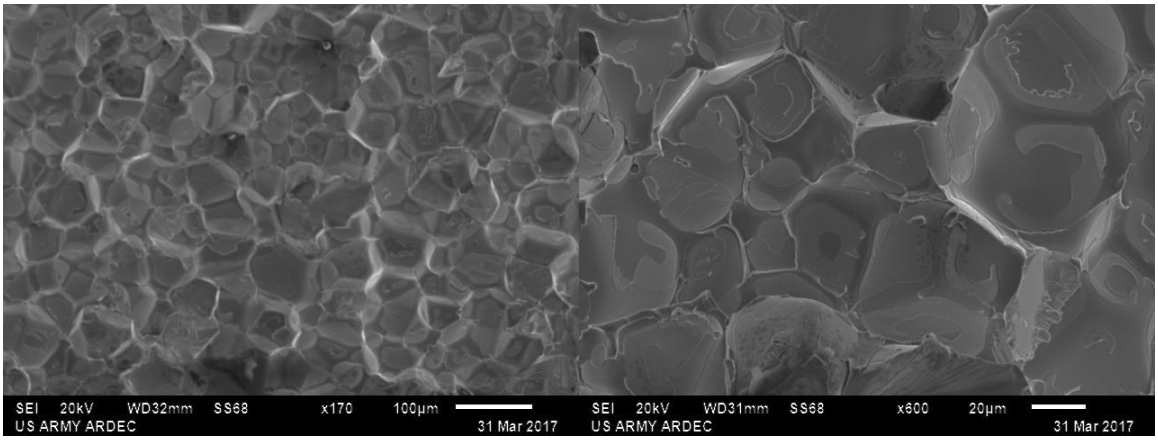

Figure 7.3.12 Impact Specimen 4 WHA Edge x170 (Left) x600 (Right)

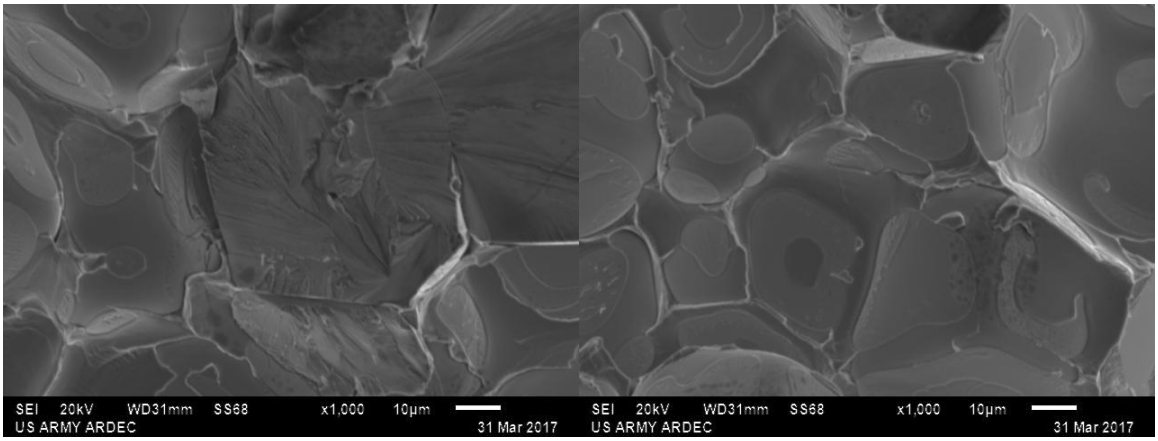

Figure 7.3.13 Impact Specimen 4 WHA Edge x1000

7.4 **SEM Images of Flaking Interface**

In specimen 17, (**Figure 7.4.1**) the interface between the WHA and the D2 is presented at an angle relative to the polished surface similar to how the angled nanoindentation relative to the interface was carried in order to get higher fidelity along the interface. Similar layers occurred on specimen 2 and 4 and were not noticed with the original polishing method. Even at 15X the tungsten grains are visible as the D2 has been flaked off during polishing with 1200 grit paper. This particular interface is the interface which has shown to have high porosity in the D2 as well as at the interface of the D2 and WHA. This high porosity most likely led to poor diffusion of the D2 to the WHA on this plane and resulted in insufficient adhesion to prevent the polishing from delaminated the interface as shown in **Figure 7.4.2** and **Figure 7.4.3**. In **Figure 7.4.4** the striations from the 1200 grit paper are visible on the D2, but not on the WHA. This is evidence the adhesion between the D2 and WHA was low enough that the polishing could de-bond the D2 from the WHA in this area. Additionally, the D2 itself is only a

few grains thick in the thinner areas and was not strong enough to prevent fracture from induced tensile stresses during polishing.

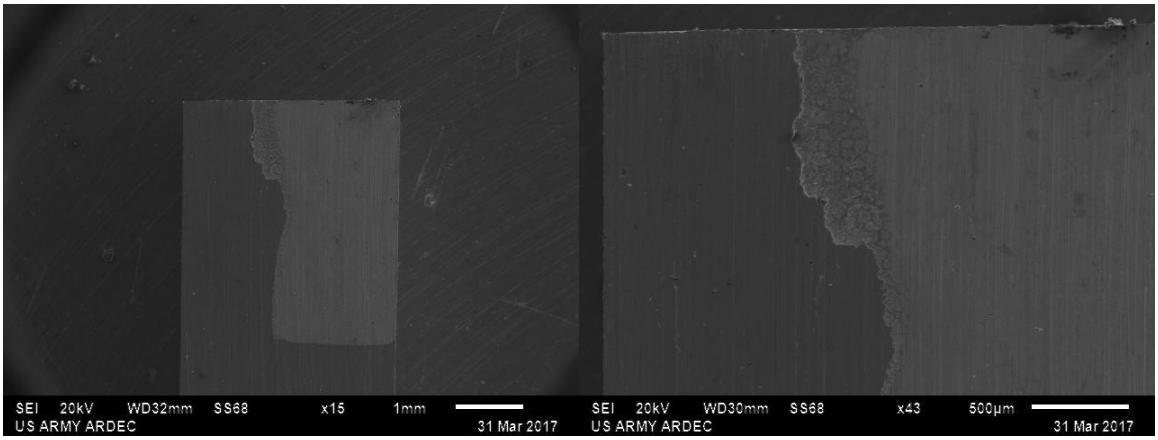

Figure 7.4.1 Impact Specimen 17 Flake Interface, Polished 1200 Grit, x15 (Left) x43 (Right)

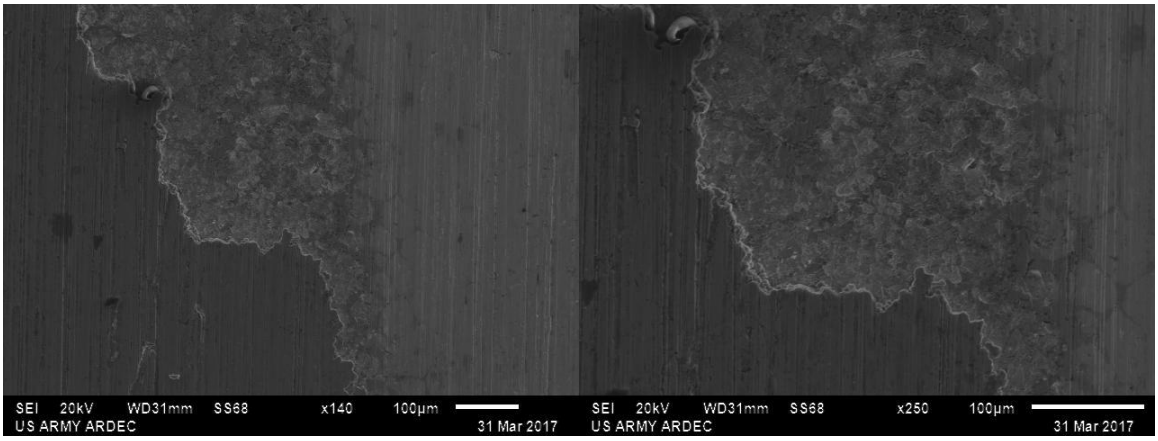

Figure 7.4.2 Impact Specimen 17 Flake Interface, Polished 1200 Grit, x140 (Left) x250 (Right)

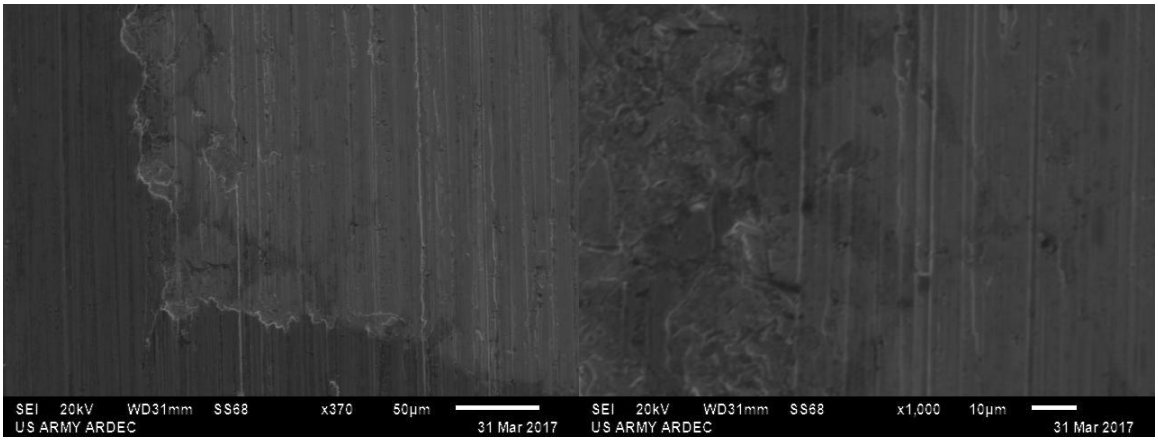

Figure 7.4.3 Impact Specimen 17 Flake Interface, Polished 1200 Grit, x370 (Left) x1000 (Right)

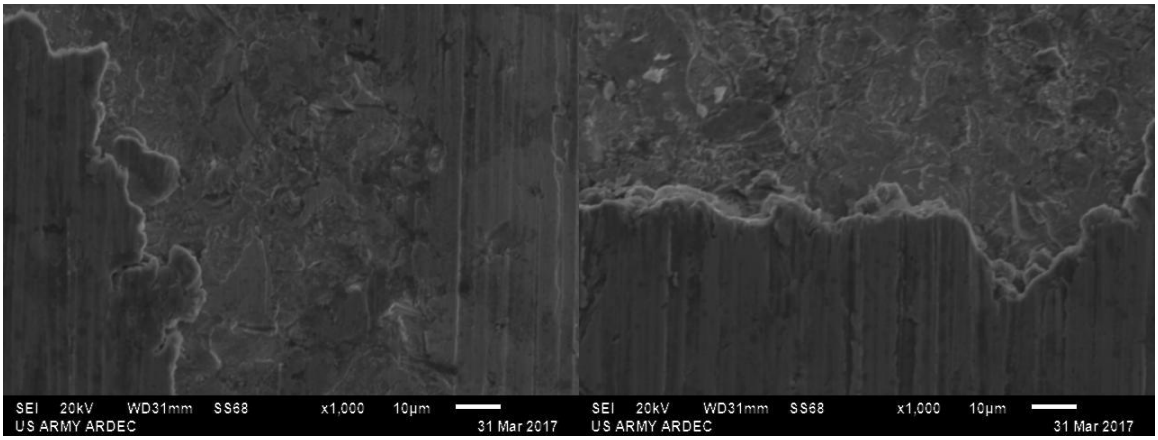

Figure 7.4.4 Impact Specimen 17 Flake Interface, Polished 1200 Grit, x1000

Chapter 8: Determining an Appropriate Finite Element Analysis Model to Accurately Model the Material Response

Prior to impact testing, finite element analysis (FEA) was utilized to help estimate the appropriate drop weight and height to start at for the impact testing. Ghaith et al. showed a 3D FEA was superior to a 2D FEA during a parametric study simulating an ASTM E-23 impact test with Abaqus 6.1 explicit, achieving only a 7% error from that experiment when integrating the force-displacement curve to capture the impact energy in the specimen [58]. Abaqus explicit finite element analysis software was also utilized for this work and all modeling was done in 3D for this effort. Johnson-Cook (J-C) material and failure models for a Class 1 WHA were used. The tup, and specimen holders were initially approximated by a Johnson-Cook material model for 1006 steel and the D2 model utilized an AISI 1070 or S7 J-C as a D2 J-C model was not available. Wang et al. have validated the use of Abaqus explicit and Johnson-Cook plasticity and damage models using an impact experiment [22]. Cateine et al. also showed a 3D FEA is more accurate than a 2D FEA and were able to use FEA to get good correlation of predicted subsize Charpy-V to dynamic test results [59]. Therefore it is believed a 3D FEA with appropriate material models can predict the impact energy required to create a new surface between the WHA and the D2 matrix and replicate the experiment accurately.

8.1 Initial FEA Model Development Prior to Impact Testing: Using Two Parts, Two Material Assignments, and Contact Force to Represent the Specimen

Initially the specimen was modeled assuming individual components of the composite with a single interface governed by friction and contact forces which could promote failure in a weaker node; this will be compared to the experimental results in this section (**Figure 8.1.1**). Brick elements were used for the mesh, ensuring at least four elements through every cross section was achieved. Additionally a fine mesh on the sample was used (**Figure 8.1.2**), but mesh refinement will need to be evaluated in any future modeling work on these new composites with FEA since it was not the primary focus of this work.

Figure 8.1.1 Depiction of How the Specimen was Initially Modeled.

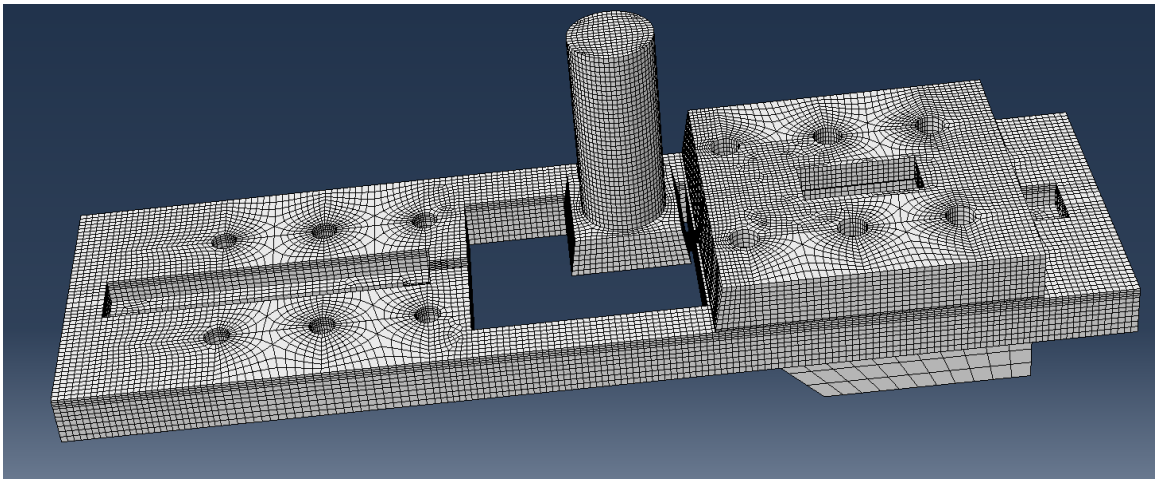

Figure 8.1.2 Mesh Resolution of Parts

The tup, specimen holders and base were modeled with frictionless contact between all the parts and the specimens. The tup was constrained to only move perpendicular to the specimen (**Figure 8.1.3**).

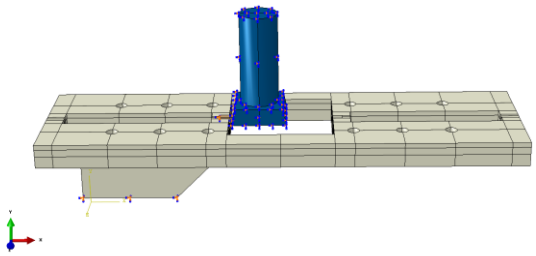

Figure 8.1.3 Boundary Conditions

The first cut FEA with individual components governed by friction and contact forces used an artificially high impact velocity for the tup, a generic 4340 material model for all the steel and a J-C model for the WHA to get the model running and used 177,005 elements, but some interesting results were obtained showing gross deformation of some elements within the sample (**Figure 8.1.4**).

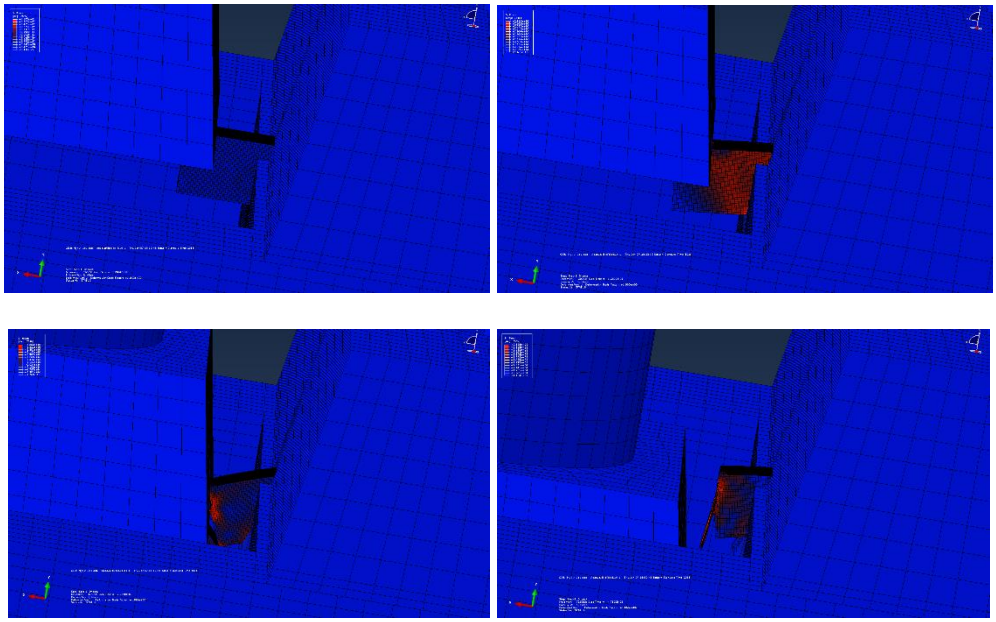

Figure 8.1.4 First FEA with Artificially High Impact Velocity and Tup Weight.

The second FEA again used the same specimen and material configuration, used 4.4 m/s impact velocity and the 3.0 kg tup weight, used 177,005 elements, and showed drastically different results (no excessive element distortion) than the higher strain rate case. This analysis provided what seemed to be reasonable results in terms of fracture locations and responses which could be induced within the bounds of the drop weight impact tester given the 29 Joules of kinetic energy (**Figure 8.1.5-8.1.7**).

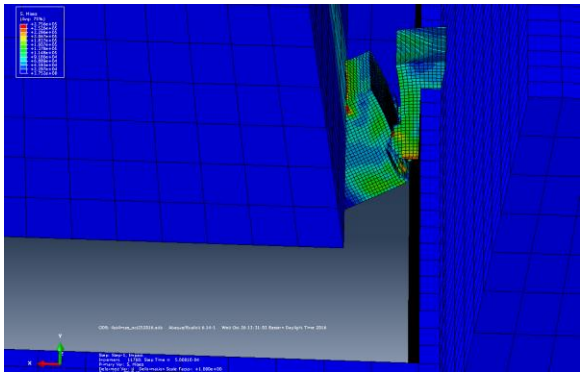

Figure 8.1.5 FEA with 4.4272 m/s Impact Velocity and Tup Artificially Set to 3.0 kg Onset of Damage

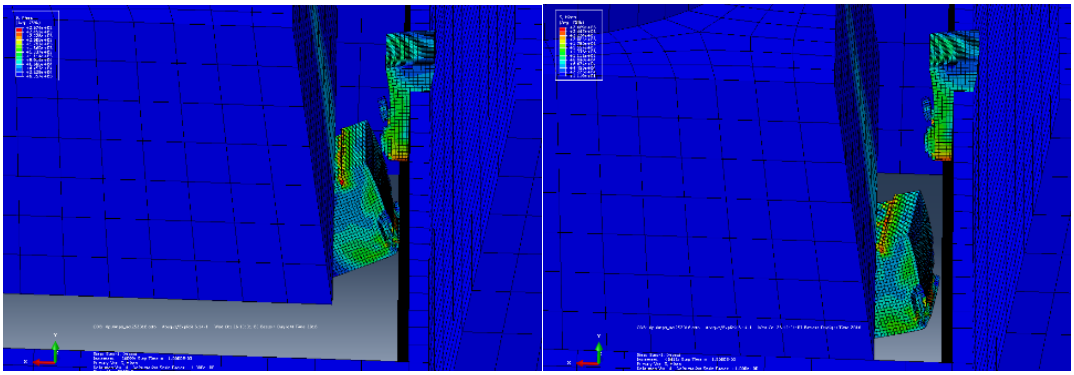

Figure 8.1.6 FEA with 4.4272 m/s Impact Velocity and Tup Artificially Set to 3.0 kg.

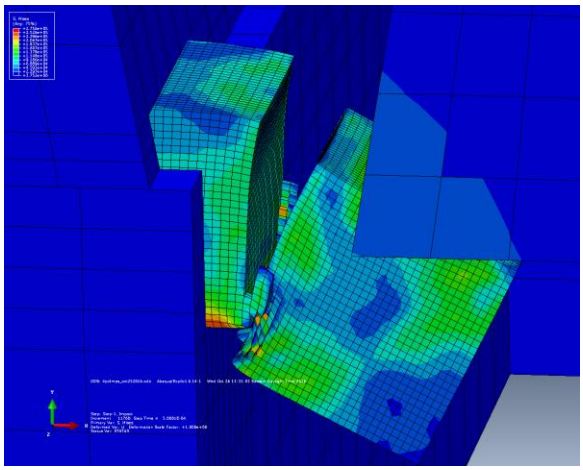

Figure 8.1.7 4.4272 m/s with Tie Constraints Between Two Parts.

Though these results looked good prior to impact testing, it is clear from the post-test results the fracture did not occur in this manner during either impact test using the 14.8 Joule or 31.1 Joule energy levels..

8.2 FEA Model Refinement after Impact Testing: Using One Part and Two Material Assignments to Represent the Specimen

After impact testing the original FEA model was updated to one part to represent the specimen instead of two, with appropriate velocities, new substitutional materials for the fixture and drop weights and used 161993 elements. The new material substitutions

are in **Figure 8.2.1** where the white is steel 1006, red is a 1006 steel, blue is a modified 4340 steel with density increased to approximately 405.8 g/cc to account for the 5.415 kg (11.938 lbs) impact load and was given an initial velocity of 3.389 m/s (133.44 in/sec) replicating the 31.1 joule energy level during testing. In **Figure 8.2.2** the specimen materials are shown which represent one part instance with two different sections and two different material assignments compared to two parts, two materials and contact force to govern fracture. The tan is a tool steel, S-7 Johnson Cook and the gray is a Johnson Cook WHA material. The Von Mises stress contours are shown **Figure 8.2.3** and exactly match the expected profile needed to produce the fractures from the impact testing.

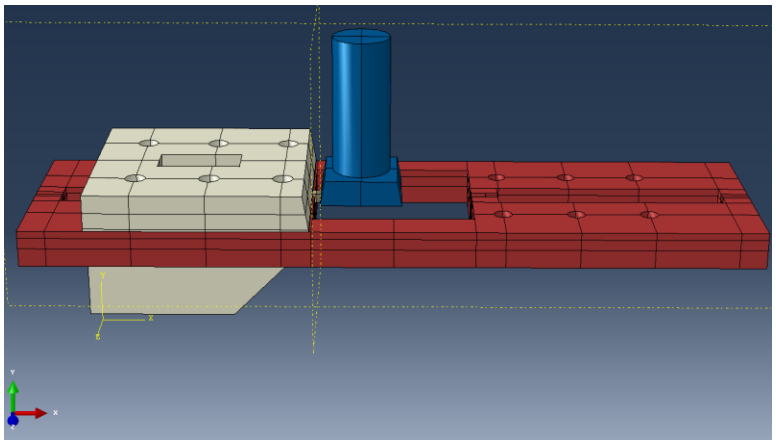

Figure 8.2.1 Fixture Material Assignment.

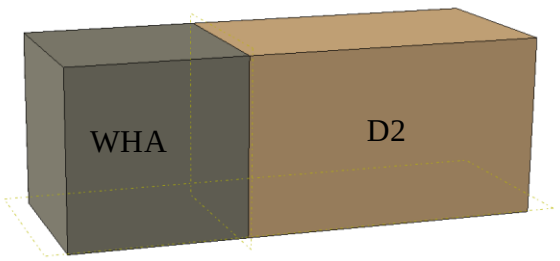

Figure 8.2.2 Specimen Material Assignment, JC WHA (left), JC S-7 (Right).

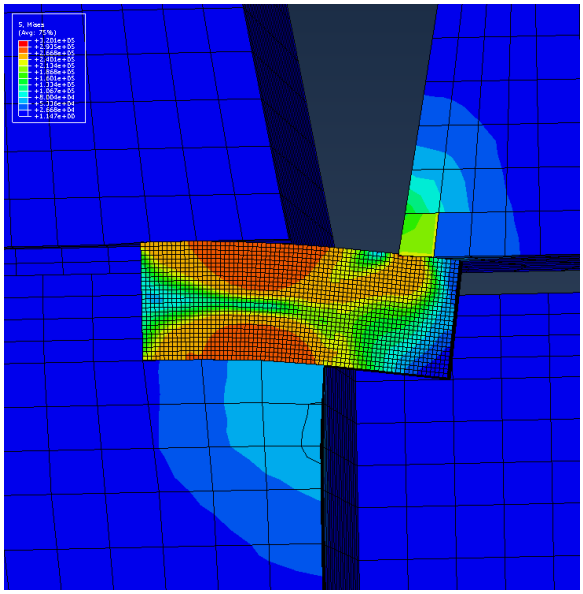

Figure 8.2.3 Von Mises Stresses with Base as 1006 Steel.

Given the deformation in the base in **Figure 8.2.3** it was decide to run the exact same model but switch the base material to a 4340 steel (red in **Figure 8.2.1**) since initially there was no deformation in the base during testing. The Von Mises stresses and specimen deformation and facture match the second type of failure seen during testing and is believed to be a good approximation to reality **(Figure 8.2.4** and **Figure 8.2.5)**.

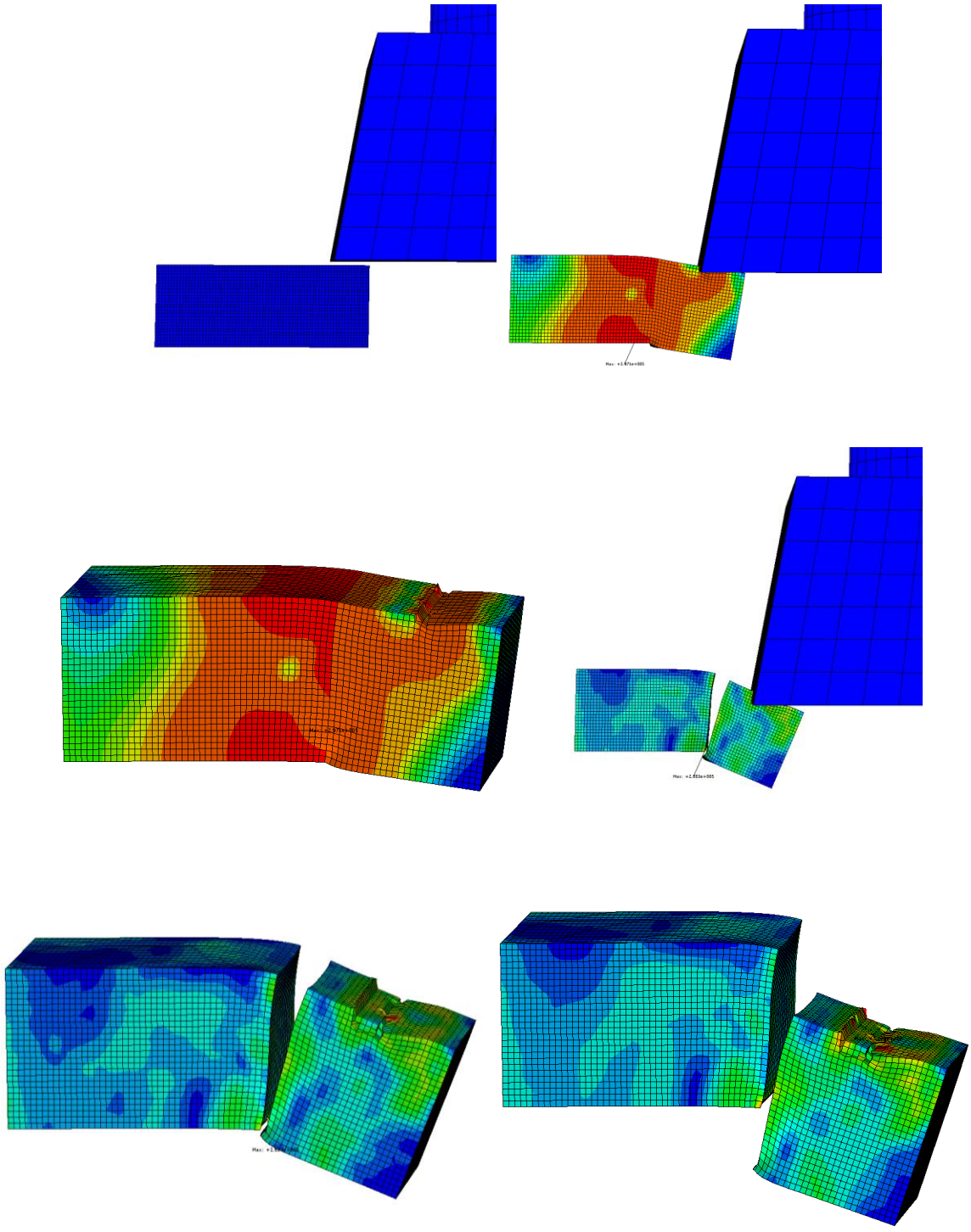

Figure 8.2.4 Von Mises Stresses with Base as 4340 Steel.

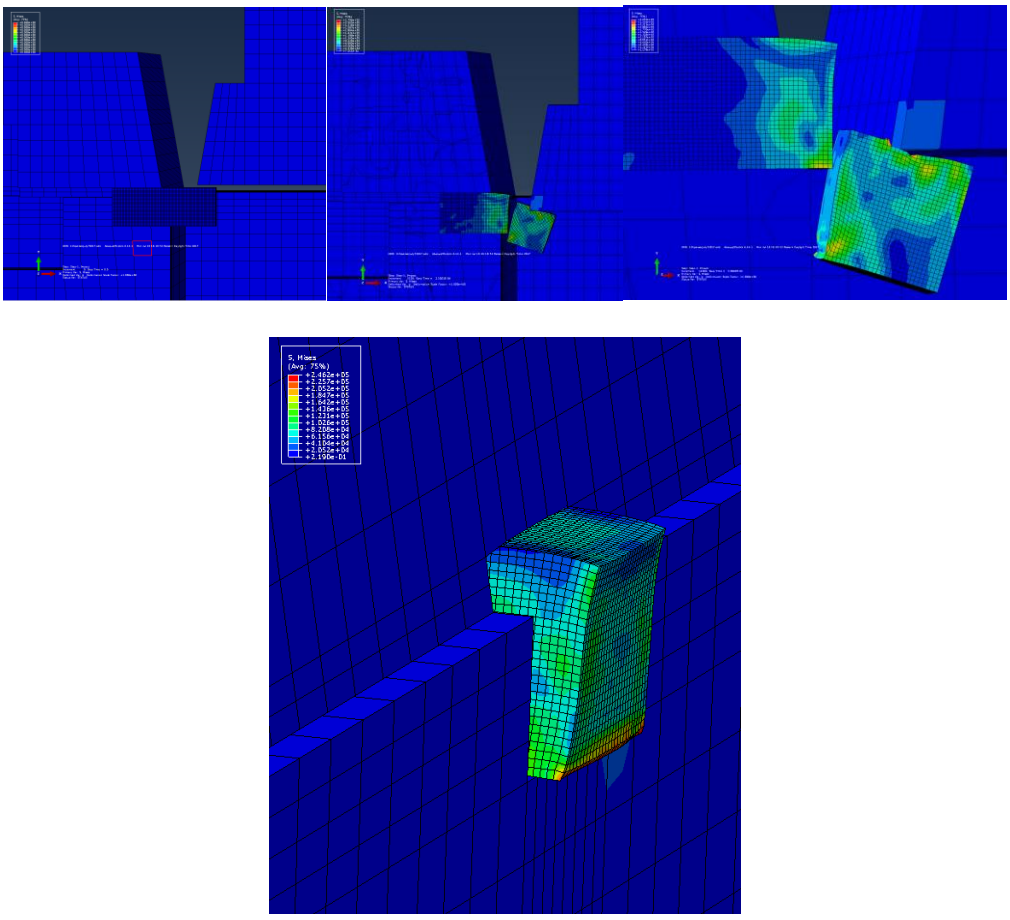

Figure 8.2.5 Von Mises Stresses with Base as 4340 Steel.

8.3 Continued FEA Model Refinement after Impact Testing: Using Two Parts, Two Material Assignments, and Cohesive Contact to Represent the Specimen

Though the material response using one instance with different material sections to represent the specimen provided reasonable results, it was decided to see if the actual diffusion layer could be modeled with cohesive contact. Thus, the specimen and element types used in the FEA model for 8.2 were altered to allow cohesive contact to govern damage behavior. The specimen was again modeled as one piece, but with a gradient

interface governed by a 40 µm cohesive zone governed by damage evolution to represent the diffusion layer observed (**Figure 8.3.1**).

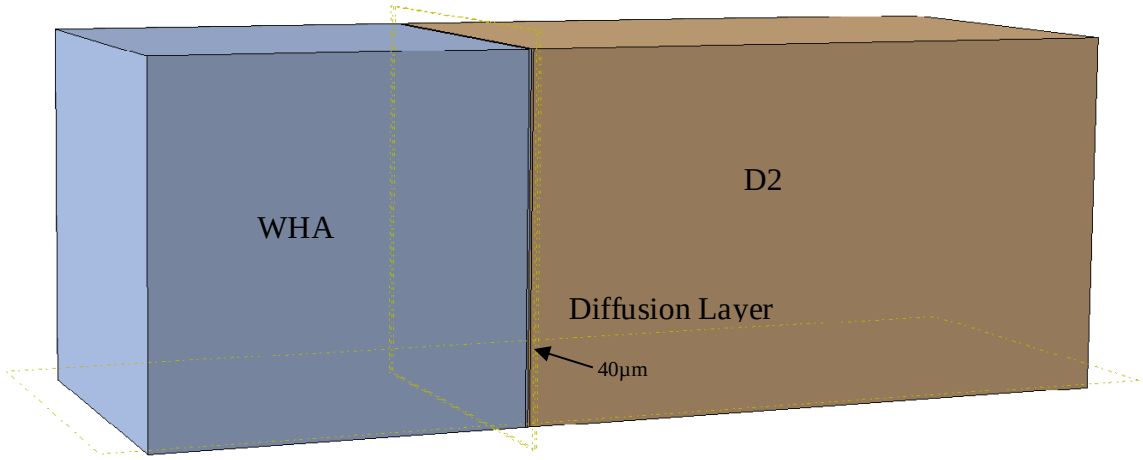

Figure 8.3.1 Mises Stresses with Base as 4340 Steel

The Von Mises results are shown in **Figure 8.3.2.** and are promising even though they do not match up perfectly. They suggest a similar location of high stress as seen in the results of section 8.2 and where fracture was observed. With refinement it is believed this modeling method could provide higher fidelity results by directly inputting the modulus values for the diffusion layer from nanoindentation measurements or use better damage parameters for these specific material sets, but since the modeling scheme in section 8.2 provides reasonable results additional effort was not warranted at this time.

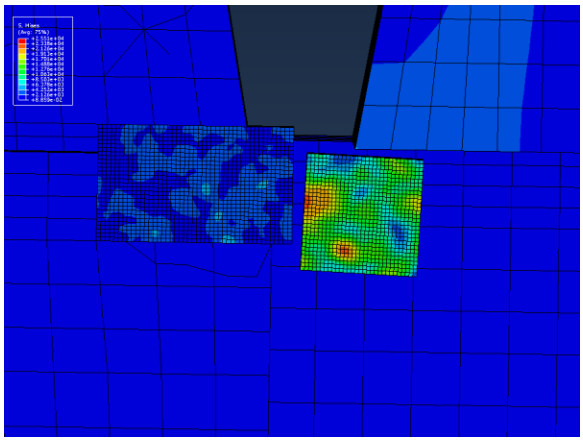

Figure 8.3.2 Von Mises Stresses for Interface Modeled with Cohesive Contact

Chapter 9: Conclusions

9.1 Correlation of EDS and Nanoindentation

Nanoindentation of consolidated D2 powder shows an average modulus of 110 GPa and hardness of 4.2 GPa, where the D2 was partially sintered and the nanoindenter interacted with a pore, the hardness was 1.7 GPa, and where the nanoindenter interacted with a triple point of powder which had not necked, hardness was 0.9 GPa. Therefore large variations in nanoindentation results in the D2 can be due to low densification and high porosity rather than correlated to chemical makeup, requiring SEM imagery (or other means of determining densification) to be used in conjunction with EDS analysis. Densification dictates hardness/modulus as well as the chemistry of the alloy, thus controlled porosity or chemistry via diffusion control can be used to determine or control failure.

As the interface is approached from the D2 side the EDS shows a slight increase in concentration of most of the elements, and the concentration increases correlate well with the increase in hardness and modulus. Carbon (3.955%-5.026%), Sulphur (0.068%), Oxygen (0.968%) and Phosphorous (0.97%) all have higher concentrations at or near the interface, which is best evidenced by the P1-10 Degree EDS results. The effect of the diffusion affected zone on chemistry stretches about 30 μm in both directions from the interface whereas the effect of the diffusion boundary layer on hardness and modulus is generally about 30-40 μm bilaterally into the WHA with potential changes in the D2 within 10 μm of the interface. There were no noticeable variations in the D2's hardness

and modulus which could be attributed to changes in chemical concentrations near the interface.

Additionally the arc spark results taken on the sample confirms the D2 chemistry was low on the Chromium (10.75%) content compared to the standard (11%-13%), had trace nickel (0.0914%) content and a carbon (2.969%) content almost twice the allowable limit (1.4%-1.6%). This is not a surprise since the arc spark was taken close to the surface of the sample which was in direct contact with the graphite foil.

The surface carbon content from the arc spark showed 3% while the EDS at the P2 Marker showed 6% which is confusing. Further, the carbon, oxygen and nitrogen concentrations from the EDS analysis suggest the closer to the FAST dies the sample is, the higher the carbon concentrations, which tracks with the diffusivity of carbon and the high carbon concentration gradient at the surface. Therefore the arc spark results may be inaccurate.

For carbon to diffuse from the bottom of the carbon die to the P2 Marker location with a diffusion rate of 1.7×10^{-6} cm^2/s into BCC at 800°C and 6.7×10^{-7} cm^2/s into the FCC at 1100°C [39] such as this sample would suggest it would take 124 hours compared to the 1260 seconds it had. To diffuse a distance of 5.571mm in 1260 seconds, it would require a diffusion rate of $D = 3.0847 \times 10^{-5}$ cm^2/s which is high. This high diffusion rate for carbon could be explained and attributed to the localized joule heating combined with the electric current to produce localized high temperature pathways on the exterior of the particles.

Again molybdenum, silicon, and nitrogen do not seem to migrate across the interface from the D2 into the WHA, while sulfur and phosphorous seem to congregate at the interface. The atomic size of molybdenum and silicon may explain why they do not diffuse across the interface, but nitrogen should given its atomic size is between carbon and oxygen both of which diffuse across the interface. Therefore it can be assumed the nonmetals nitrogen, sulfur, and phosphorus are finding lower energy states in their respective areas of concentration. Higher concentrations of oxygen are present in the WHA than in the D2 and versus for carbon suggesting there is an inverse relationship between the two elements. All elements in the D2 alloy have diffused into the WHA though, and nickel and tungsten have diffused into the D2 proving advection has occurred. Iron displays the inverse of the tungsten's diffusion behavior and chromium also shows the same inverse behavior compared to the tungsten's flux.

In future work, all the WHA cubes should be polished prior to making the composite so a very distinct interface is created and 1-D diffusion theory can be applied.

9.2 Correlation of Nanoindentation and Impact Toughness

Onset of failure seems to be caused from the tensile stress in the WHA and not the joint/interface on some samples while others exhibited failure at the bond line. The later could be because the test setup placed the specimens' interfaces in shear more so than in tension through bending. In the future, a purely shear or tension load should be applied, perhaps through a bolt load compact specimen or a "Tophat" shear punch.

The average energy needed for failure during impact testing was 0.841 J (0.62 ft-lbs) with an average load-to-failure of 390.6 N (87.8 lbf) whereas literature has showed

for D2 austenitizing at 1025℃ and tempering once at 538℃ produces a charpy impact energy of 1.491 J (1.1 ft-lbs) and that tempering of martensite has a large influence on toughness [46]. Comparing literature to the impact energies in testing suggest the composite impact energies are close to wrought D2 impact energies. Nanoindentation and microhardness measurements on the D2 also fall within wrought hardness measurements for D2. The average microhardness value for the D2 was 2.952 GPa (301 HV 0,3) with a standard deviation of 0.0294 GPa (3 HV 0,3) compared to the 4.2 GPa for the nanoindentation, where literature shows 3.5 GPa for "as received" or 6.6 GPa for heat treated and air cooled [48]. Though the D2 nanonindentation results seem to match literature, it does not explain the approximately 1 GPa difference between the microhardness measurements and the nanoindentation measurements for the D2. WHA nanoindentation measurements are close to 7.7 GPa compared to the microhardness results of 3.4-3.6 GPa. These differences are beyond the difference in how the contact area is defined for the two methods, and could be attributed to the nanonindenation measurements being highly localized on individual grains while the microhardness measurements would be an average of multiple grains, orientations, and defects.

Given the hardness appears to increase exponentially from the WHA side as the interface is approached and the D2 does not exhibit the same trends there is a sharp discontinuity in elastic modulus which would localize the stress at the joint, and hence be the location of fracture. Additionally, polishing and machining produces two different heights of material between the WHA and the D2 which would introduce a physical stress concentration at the interface. Both of these would lead to fracture on the interface which was witnessed during impact testing.

In the future a trial should be carried out to determine how parallel the faces must be in order not to affect the results with such a small sample.

9.3 Correlation between FEA and Testing

Though mesh refinement was not utilized, the FEA correlates well with the fracture location, stress profile derived from the fracture location, deformation exhibited, and damage seen at the interface and on the WHA cube. Thus, the ability to use an RVE with cohesion contact in the future to predict ductile failure is plausible. Since a critical crack analysis was not completed, nor was XFEM utilized, brittle failure mechanism analysis will have to be carried out in the future, utilizing any ductile to brittle transition data which may be obtained through the same test methodology used in this research.

9.4 Conclusion

Samples were successfully created using an additive manufacturing process which utilized FAST to diffusion bond bulk liquid phase sintered WHA to D2, which had never been attempted to be manufactured before. This alone can allow new tooling to be produced with this technique and suggests WC can be a natural byproduct of the process.

Specimens were successfully extracted from this new composite and a methodology and fixture was developed to characterize and test a diffusion bond for impact toughness, hardness, and modulus properties across the interface. This methodology can be used to characterize and evaluate similar composites and structures, and can be used as a starting place to create a standard for additively manufactured composites which have been created through diffusion bonding.

Empirical results were correlated to nanoindentation and EDS analysis, showing the diffusion affected zone is 40-50 μm thick and does affect the mechanical properties of the interface and the mode of failure. The failures resulting from the impact testing were replicated with finite element models, proving that with proper material and damage models these types of analysis can aid in the use of these composites in structural applications.

Overall, this research has laid the ground work on how to manufacture and characterize a new additively manufactured metal in metal matrix composite, identifies the importance of the diffusion zone on the overall impact toughness of the composite, and shows the importance of the different characterization methods in identifying material flaws versus changes in material properties. Thus, the work feeds the ability to engineer a diffusion bond to exhibit tailored mechanical properties in the future for application-specific structures.

Chapter 10: Suggestions for Future Work

10.1 Additional Samples, FAST Parameters, and Matrix Materials

Given the relative roughness of the WHA, it would be beneficial to start with WHA specimens which have been ground, polished and lapped, squared and then processed with the FAST parameters used to generate the samples for this work and repeat the work carried out. Polishing and lapping of the WHA would lead to a definitive interface instead of a meandering interface which would allow better understanding of material properties at the interface. This would help to explain the changes in hardness and modulus some of which seem to stem from defects on the surface as well as providing higher fidelity diffusion coefficients. Additional macroscopic single crystal tungsten could also be joined to D2 and other steels to understand the diffusion rates on and along the grain boundaries versus across grains. These findings could help determine if crystal orientation can influence failure modes via elemental gradients or elemental depletion zones which could act as stress concentration and crack initiation locations. Additionally it would be interesting to see how different starting powder chemistries and particle sizes could alter the diffusion rates calculated and the failure modes witnessed, as well as how different grades of steel or elemental additions could increase the mechanical properties across the boundary layer.

10.2 Additional Hardness Testing

Due to the large diffusion boundary, it would be interesting to get more data points on a higher fidelity boundary, as well as a continuous line of modulus and

hardness data via a touch and drag technique instead of at discrete locations. Additionally the nanoindentation measurements were only carried out on a few cross sections of samples and additional nanoindentation should be carried out across these cross sections and in more planes to determine where effects become negligible. These measurements and processes should then be repeated with microhardness indentation to understand the resolution needed to characterize the material and the interface to help define the representative volume element which can be used to model the interface.

10.3 **Additional Mechanical Testing**

If possible full scale Charpy specimens should be created and tested to compare to these findings to help determine size sensitivity factors and to help validate the test method used. Additionally notched homogeneous specimens should be created and tested with the custom impact testing which will also help validate the test method. It would be advantageous to use both methods to validate the testing as full scale Charpy specimens would not be possible for some applications. Additional samples and specimens should also be tested at hot and cold with a fixture which has higher yield strength and hardness, as well as the ability to vary the grip site relative to the boundary layer. This would help determine if there is a ductile to brittle transition temperature and if deformation in the fixture used has absorbed energy. With more samples one could also dial in the starting potential energy to get higher resolution results. Gathering tensile properties of the metal matrix composites would also be of great value and help with modeling the composites. Thus, new samples with different spacing between the macroscopic tungsten should be

manufactured with the FAST and tensile specimens taken and tested to provide the stress-strain data to help build a higher fidelity Johnson-Cook model.

10.4 **Higher Fidelity FEA Simulation**

Given that the two parts, cohesive contact model resulted in similar stress locations to those as the one part with two materials model, it is believed this method could provide higher fidelity results. This may be achieved because the actual boundary layer thickness in the metal matrix composite would be modeled and the method could provide higher fidelity results using the additional information one could obtain from data gathered in section 11.1, 11.2, and 11.3 to help define better damage parameters. Therefore it is believed the two parts, cohesive contact modeling method should be pursued since the actual boundary layer thickness is modeled discretely, and modulus and hardness values from the nanoindentation method could be assigned directly to the boundary layer sections, as well as any other material properties gathered.

Chapter 11: References

[1] B. Roebuck and L. Winkless, "Powder Metallurgy at the National Physical Laboratory," *Metal Powder Report,* pp. 126-129, Vol 71 No 2, March/April 2016.

[2] Kennametal, "Tungsten Heavy Alloys Kennametal Densalloy™ Engineering Guide," Kennametal, Pittsburg, PA, 2014.

[3] X. Zhou, S. Li, J. Liu, Y. Wang and X. Wang, "Self-sharpening Behavior During Ballistic Impact of the Tungsten Heavy Alloy Rod Penetrators Processed by Hot-Hydrostatic Extrusion and Hot Torsion," *Materials Science and Engineering A,* vol. 527, pp. 4881-4886, 2010.

[4] A. Upadhyaya, "Processing Strategy for Consolidating Tungsten Heavy Alloys for Ordnance Applications," *Materials Chemistry and Physics,* pp. 101-110, 2001.

[5] X.-Y. Tan, L.-M. Luo, Z.-L. Lu, G.-N. Luo, X. Zan, J.-G. Cheng and Y.-C. Wu, "Development of Tungsten as Plasma-Facing Materials by Doping Tantalum Carbide Nanoparticles," *Powder Technology,* vol. 269, pp. 437-442, 2015.

[6] P. N. Browning, S. Alagic, L. Matson and J. Singh, "Room and Ultrahigh Temperature Structure-mechanical Property Relationships of Tungsten Alloys Formed by Field Assisted Sintering Technique (FAST)," *Material Science & Engineering A 674,* pp. 701-712, 2016.

[7] M. J. Kupczyk, A. Michalski, P. Siwak and M. Rosinski, "Evaluation of Cutting Edges Made of Nanocrystalline Cemented Carbides Sintered by the Pulse Plasma Method," *Journal of ASTM International,* vol. 8, no. 2, pp. 1-9, 2011.

[8] K. D. Dhote, K. P. Murthy, K. M. Rajan and M. M. Sucheendran, "Dynamics of Multi Layered Fragment Separation by Explosion," *International Journal of Impact Engineering,* pp. 194-202, 75 (2015).

[9] S. H. Hong and H. J. Ryu, "Combination of Mechanical Alloying and Two-stage Sintering of a 93W-5.6Ni-1.4Fe Tungsten Heavy Alloy," *Materials Science and Engineering A,* vol. 344, pp. 253-260, 2003.

[10] N. Ermakov, M. Yurlova and E. Grigoryev, "Properties of Tungsten Heavy Alloys, Prepared by Spark-Plasma Sintering," *Materials Science and Engineering: 2016 IOP Conference Series,* Vols. 130 / doi:10.1088/1757-899X/130/1/012050, no. Conference 1, p. 7 (012050), 2016.

[11] R. Gero, L. Borukhin and I. Pikus, "Some Structural Effects of Plastic Deformation on Tungsten Heavy Metal Alloys," *Materials Science and Engineering A,* vol. 302, pp. 162-167, 2001.

[12] H. J. Ryu, S. H. Hong and W. H. Baek, "Mechanical Alloying Process of 93W-5.6Ni-1.4Fe Tungsten Heavy Alloy," *Journal ofMaterials Processing Technology,* vol. 63, pp. 292-297, 1997.

[13] A. Mondal, A. Upadhyaya and D. Agrawal, "Effect of Heating Mode on Sintering of Tungsten," *Int. Journal of Refractory Metals and Hard Materials,* vol. 28, pp. 597-600, 2010.

[14] R. Castro and K. van Benthem, Sintering: Mechanisms of Convention Nanodensification and Field Assisted Processes, Verlag Berlin Heidelberg: Springer, 2013.

[15] M. Suárez, A. Fernández, J. Menéndez, R. Torrecillas, H. Kessel, J. Hennicke, R. Kirchner and T. Kessel, "Sintering Applications," in *Challenges and Opportunities for Spark Plasma Sintering: A Key Technology for a New Generation of Materials*, B. Ertuğ, Ed., Open Access DOI: 10.5772/53706, InTech ISBN 978-953-51-0974-7, 2013, pp. 319-342.

[16] Z. A. Munir, U. Anselmi-Tamburini and M. Ohyanag, "The Effect of Electric Field and Pressure on the Synthesis and Consolidation of Materials: A Review of the Spark Plasma Sintering Method," *Journal of Materials Science,* vol. 41, pp. 763-777, 2006.

[17] G. Lee, J. McKittrick, E. Ivanov and E. Olevsky, "Densification Mechanism and Mechanical Properties of Tungsten Powder Consolidated by Spark Plasma Sintering," *Int. Journal of Refractory Metals and Hard Materials,* vol. 61, pp. 22-29, 2016.

[18] X. Zhou, H. Yang, F. Chen, Y.-H. Han, J. Lee, S. Du and Q. Huang, "Joining of Carbon Fiber Reinforced Carbon Composites with Ti3SiC2 Tape Film by Electric Field Assisted Sintering Technique," *Carbon,* vol. 102, pp. 106-115, February 2016.

[19] V. Chuvildeev, D. Panov, M. Boldin, A. Nokhrin, Y. Blagoveshchensky, N. Sakharov, S. Shotin and D. Kotkov, "Structure and Properties of Advanced Materials Obtained by Spark Plasma Sintering," *Acta Astronautica 109,* vol. 109, pp. 172-176, 109 (2015).

[20] L. Li and L. Sun, "Failure Mechanisms of Weld Bonded Lap Joints Between Composite/Metal Adherends," in *Proceedings of the ASME 2014 International Mechanical Engineering Congress and Exposition IMECE2014*, Montreal, Quebec, Canada, 2014.

[21] J. Clayton, "Modeling Dynamic Plasticity and Spall Fracture in High Density Polycrystalline Alloys," *International Journal of Solids and Structures,* vol. 42, pp. 4613-4640, 2005.

[22] X. Wang and J. Shi, "Validation of Johnson-Cook Plasticity and Damage Model Using Impact Experiment," *International Journal of Impact Engineering,* vol. 60, pp. 67-75, 2013.

[23] T. Okuni, Y. Miyamoto, H. Ab and M. Naito, "Joining of Silicon Carbide and Graphite by Spark Plasma Sintering," *Ceramics International,* vol. 40, no. http://dx.doi.org/10.1016/j.ceramint.2013.07.017, pp. 1359-1363, 2014.

[24] J. Yang, J. Trapp, Q. Guo and B. Kieback, "Joining of 316L Stainless Steel by Using Spark Plasma Sintering Method," *Materials and Design,* vol. 52, no. http://dx.doi.org/10.1016/j.matdes.2013.04.091, pp. 179-189, 2013.

[25] H.-Y. Chen, L.-M. Luo, J. Zhang, X. Zan, X.-Y. Zhu, G.-N. Luo and Y.-C. Wu, "Investigation on W/Fe Diffusion Bonding Using Ti foil and Ti Powder Interlayer by SPS," *Journal of Nuclear Materials,* vol. 467, no. https://doi.org/10.1016/j.jnucmat.2015.10.045, pp. 566-571, 2015.

[26] E. Lucon, "Certified Miniaturized Charpy Specimens for the Indirect Verification of Small-Size Impact Machines," *Materials Performance and Characterization , Vol. 2, No. 1,* pp. 183-193, 2013.

[27] ASTM International, "ASTM E23-16b Standard Test Methods for Notched Bar Impact Testing of Metallic Materials," *ASTM International,* pp. 1-26, 2016.

[28] E. Lucon, C. McCowan, R. Santoyo and J. Splett, "Certification Report for SRM 2216, 2218, 2219: KLST (Miniaturized) Charpy V-Notch Impact Specimens," *NIST Special Publication 260-180,* Vols. Special Publication 260-180, pp. 1-57, 2013.

[29] E. Lucon and M. Scibetta, "Use of KLST-Type Miniature Charpy Specimens for Measuring Dynamic Fracture Toughness under Impact Loading Rates," *Journal of ASTM International,* vol. 4, no. 10, pp. 1-8, 2006.

[30] ASTM International, "Standard Specifications for Tungsten Base, High-Density Metal B777 - 07," *ASTM International,* vol. 07, pp. 1-3, 2007.

[31] B. B. Bokhonov, A. V. Ukhina, D. V. Dudina, A. G. Anisimov, V. I. Malic and I. S. Batraev, "Carbon Uptake During Spark Plasma Sintering: Investigation Through the Analysis of the Carbide “footprint” in a Ni–W Alloy," *The Royal Society of Chemistry Advances,* vol. 5, no. 98, DOI: 10.1039/c5ra15439a, p. 80228–80237, 2015.

[32] B. Mell, "Sandpaper Roughness Measurement using 3D Profilometry," Nanovea, Irvine CA, 2010.

[33] S. Suzuki, S. Sato, M. Suzuki, H. Kinoshita, S. Sato, S. Jitsukawa and H. Tanigawa, "Influence of Surface Roughness on Tensile Strength of Reduced-Activation Ferritic/Martensitic Steels Using Small Specimens," *ASTM International,* vol. 6, pp. 9-18, 2015.

[34] Struers ApS, "Cold Mounting English pdf," Struers A/S, DK-2750 Ballerup, Denmark, 2014.

[35] J. E. Shigley, C. R. Mischke and R. G. Budynas, Mechanical Engineering Design Seventh Edition, New York, NY: McGraw-Hill, 2004.

[36] W. D. Callister, Jr., Materials Science and Engineering An Introduction Fifth Edition, New York, NY: John Wiley & Sons, Inc., 2000.

[37] ASTM International, "ASTM A 681 - 08 Standard Specfications for Tool Steels Alloy," *ASTM International*, pp. 1-14, 2008.

[38] J. I. Goldstein and A. E. Moren, "Diffusion Modeling of the Carburization Process," *Metallurgical Transactions A - American Society for Metals and The Metallurgical Society of Aime,* vol. 9A, pp. 1515-1525, November 1978.

[39] M. E. Glicksman, Diffusion in Solids Field Theroy, Solid-State Principles, and Applications, New York: Jon Wiley & Sons, Inc., 2000.

[40] M. Ramezani, T. Pasang, Z. Chen, T. Neitzert and D. Au, "Evaluation of Carbon Diffusion in Heat Treatment of H13 Tool Steel Under Different Atmospheric Conditions," *Journal of Materials Research and Technology,* vol. 4, no. 2 http://dx.doi.org/10.1016/j.jmrt.2014.10.014, pp. 114-125, 2015.

[41] J. D. Verhoeven, Metallurgy of Steel for Bladesmiths & Others who Heat Treat and Forge Steel, Ames, IA: Iowa State University, 2005, p. 68.

[42] B. T. Alexandrov, J. C. Lippold, J. W. Sowards, A. T. Hope and D. R. Saltzmann, "Fusion Boundary Microstructure Evolution Associated with Embrittlement of Ni–base Alloy Overlays Applied to Carbon Steel," *Weld World,* Vols. 57 :DOI 10.1007/s40194-012-0007-1, no. 1, pp. 39-53, 2013.

[43] A. Fischer-Cripps, "Nanoindentation Testing," in *Nanoindentation*, Springer New York Dordrecht Heidelberg London, Springer, 2002, pp. 21-37.

[44] J. Das, G. A. Rao and S. Pabi, "Microstructure and Mechanical Properties of Tungsten Heavy Alloys," *Materials Science and Engineering A,* vol. 527, no. 29-30, pp. 7841-7847, 2010.

[45] ASTM International, "ASTM E140-12be1 Standard Hardness Conversion Tables for Metals Relationship Among Brinell Hardness, Vickers Hardness, Rockwell Hardness, Superficial Hardness, Knoop Hardness,Scleroscope Hardness, and Leeb Hardness," ASTM International https://doi.org/10.1520/E0140, West Conshohocken, PA, 2012.

[46] A. Attaullah, "Heat Treatment and Toughness Behavior of Tool Steels (D2 and H13) for Cutting Blades," National Library of Canada, Ottawa ON, 1999.

[47] ASTM International, "ASTM E91 - 17 Standard Test Methods for Vickers Hardness and Knoop Hardness of Metallic Materials," ASTM International DOI:10.1520/E0092-17, West Conshohocken, Pennsylvania, 2017.

[48] U. C. Okafor, "Mechanical Characterization of A2 and D2 Tool Steels by Nanoindentation," University of North Texas, Denton, Texas, 2012.

[49] T. Polcar, N. Parreira and A. Cavaleiro, "Tungsten Oxide with Different Oxygen Contents: Sliding Properties," *Vacuum Surface Engineering, Surface Instrumentation, & Vacuum Technology,* vol. 81, no. doi:10.1016/j.vacuum.2007.04.001, pp. 1426-1429, 2007.

[50] R. Armstrong, "The Hardness and Strength Properties of WC-Co Composites," *Materials,* vol. 4, no. doi:10.3390/ma4071287, pp. 1287-1308, 2011.

[51] J. Kolopus, L. Boatner and J. Swindeman, "Single-Crystal Tungsten Carbide in High-Temperature In-Situ Additive Manufcatuing Characterization," Oak Ridge National Laboratory managed by UT-Battelle, LLC for the US Department of Energy under contract DE-AC05-00OR22725, Oak Ridge, Tennessee, 2017.

[52] E. Jelis, "Development of Low Alloy Steel by Direct Metal Laser Sintering," New Jersey Institue of Technology, Newark, NJ, 2017.

[53] Instron Corporation, Instron Dynatup Impulse Impact Testing System Operating Instructions M14-14066-EN, Instron Corporation, 2003.

[54] Instron Corporation, Instron Dynatup Model 8200 Drop Weight Impact Testing Instrument Operating Insturctions M14-14103-EN, Instron Corporation, 2004.

[55] J. Cantrell, S. Rohnde, D. Damiani, R. Gurnani, L. DiSandro, J. Anton, A. Young, A. Jerez, D. Steinbach, C. Kroese and P. Ifju, "Experimental Characterization of the Mechanical Properties of 3D-Printed ABS and Polycarbonate Parts," *Advancement of Optical Methods in Experimental Mechanics,* vol. 3, no. Springer International Publishing, pp. 89-105, 2017.

[56] A. M. Forster, "Materials Testing Standards for Addaitive Manufacturing of Polymer Materials: State of the Art and Standards Applicability," National Institue of Stndards and Technology U.S. Department of Commerce, Gaithersburg, MD http://dx.doi.org/10.6028/NIST.IR.8059, 2015.

[57] K. Churn and R. German, "Fracture Behavior of W-Ni-Fe Heavy Alloys," *Metallurgical Transactions A,* vol. 15A, pp. 331-338, 1984.

[58] F. Ghaith and K. Fahad, "Three Dimensional Nonlinera Finite Element Modeling of Charpy Impact Test," *International Journal of Mechanical Engineering and Technology,* pp. Vol 4 Issue 4 pp. 377-386, August 2013.

[59] C. Sainte Cateine, C. Poussard, J. Vodinh, R. Schill, N. Hourdequin, P. Galon and P. Forget, "Finite Element Simulations and Empirical Correlation for Charpy-V and

Subsize Charpy Tests on Unirradiated Low-Alloy RPV Ferritic Steel," *Small Specimen Test Techniques: Fourth Volume, ASTM STP 1418,* pp. 107-135, 2002.

[60] P. Dong, Z. Wang, W. Wang, S. Chen and J. Zhou, "Understanding the Spark Plasma Sintering from the View of Materials Joining," *Scripta Materialia,* vol. 123, no. https://doi.org/10.1016/j.scriptamat.2016.06.014, pp. 118-121, 2016.

APPENDIX A: Nanoindentatino Results for Bulk D2 and Bulk WHA

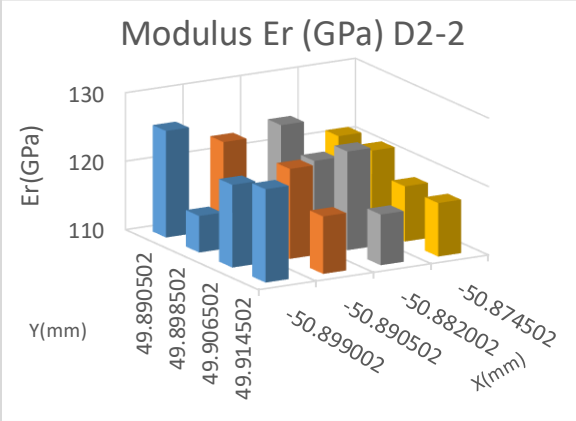

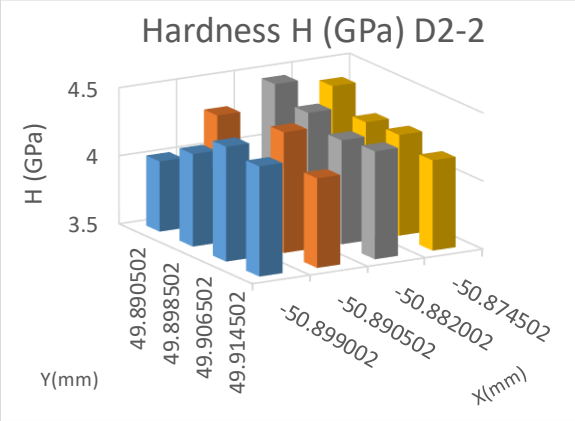

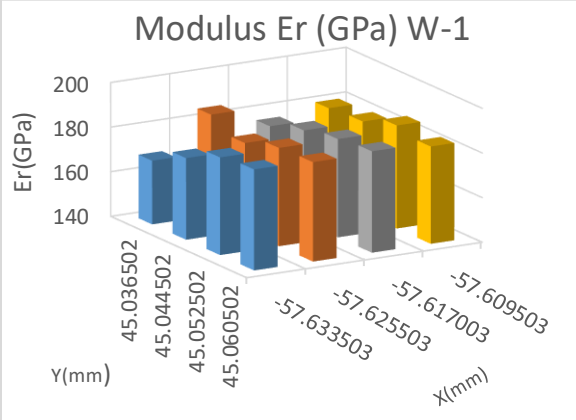

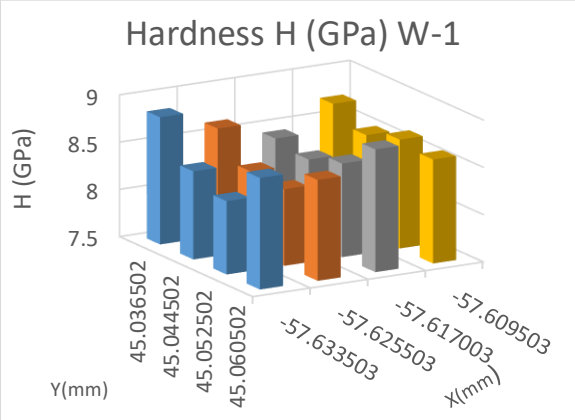

APPENDIX B: Nanoindentation Results at Interfaces Parrallel to FAST Load Axis

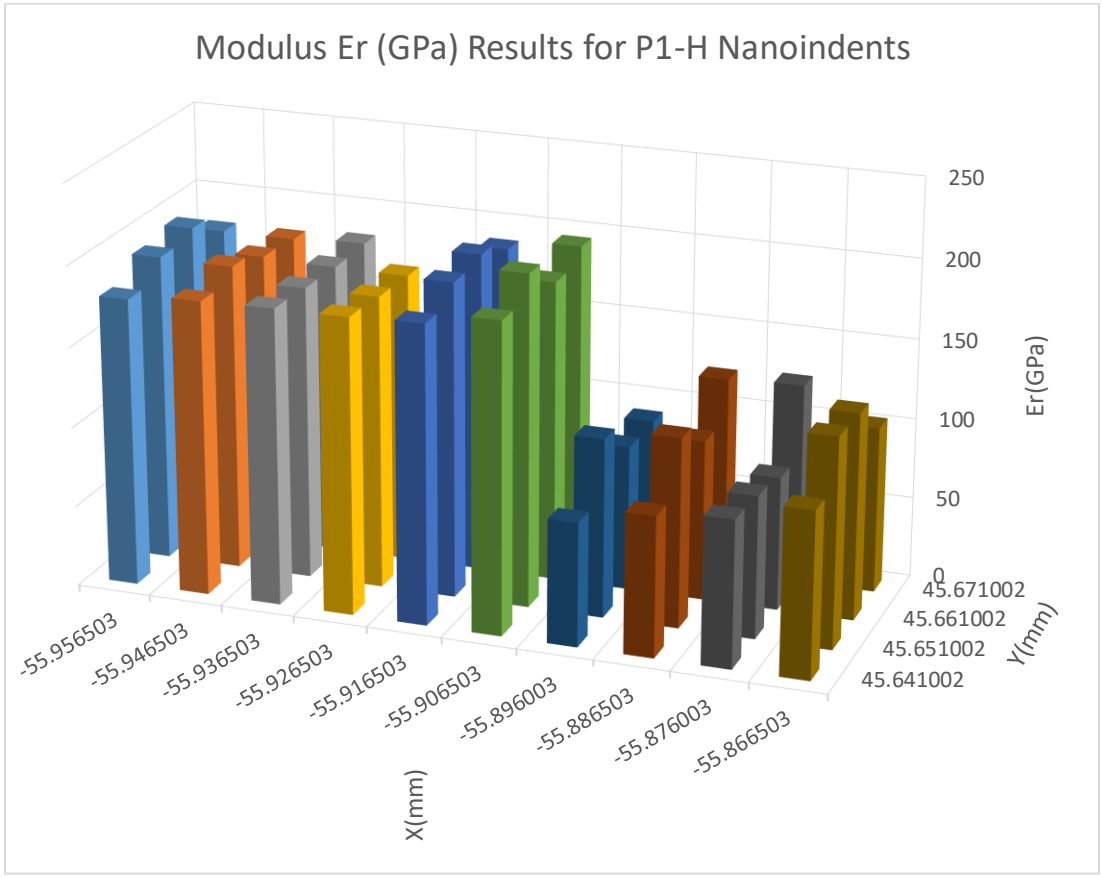

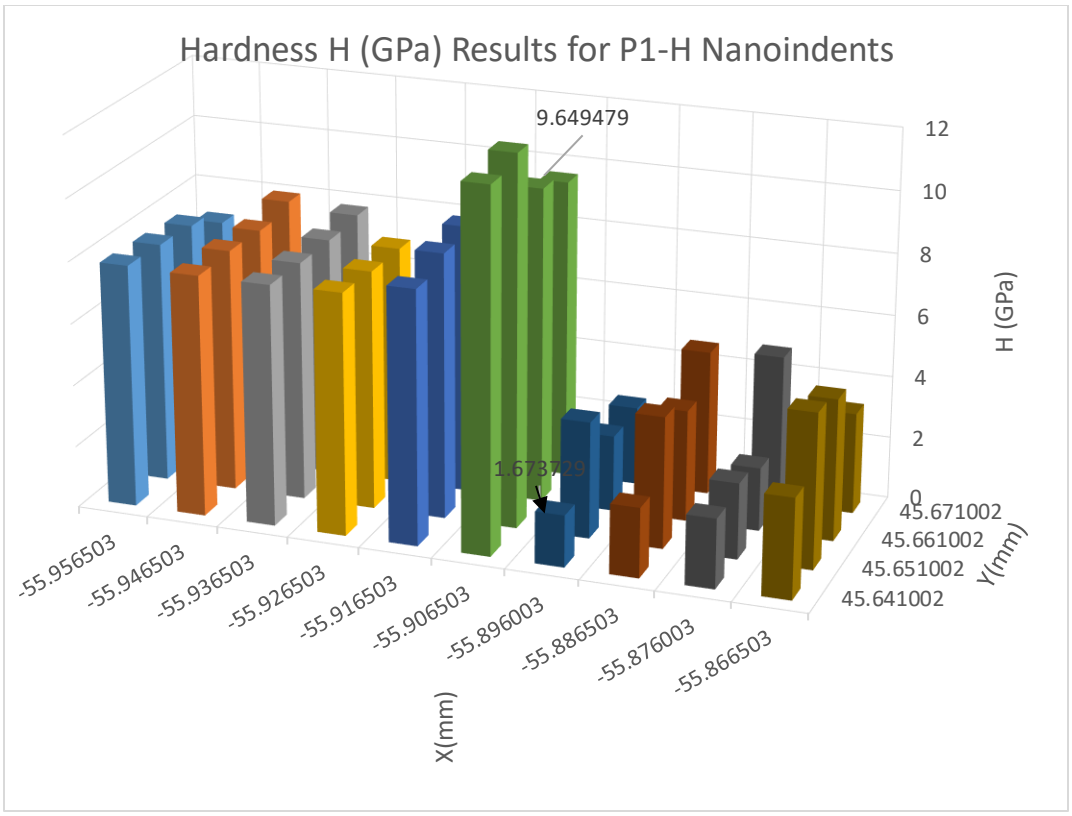
Hardness H (GPa) Results for P1-H Nanoindents
9.649479
1.673729
12
10
8
6
4
2
0
H (GPa)
-55.956503
-55.946503
-55.936503
-55.926503
-55.916503
-55.906503
-55.896003
-55.886503
-55.876003
-55.866503
X(mm)
45.671002
45.661002
45.651002
45.641002
Y(mm)

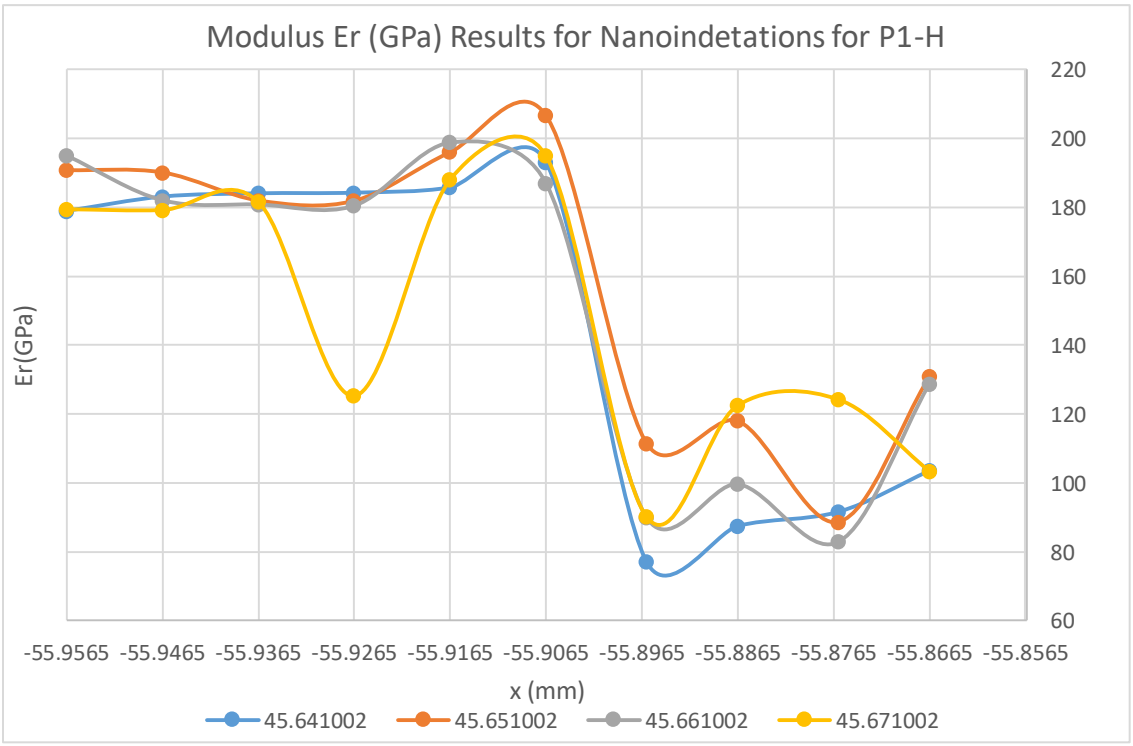
Modulus Er (GPa) Results for Nanoindetations for P1-H
220
200
180
160
140
120
100
80
60
Er(GPa)
-55.9565
-55.9465
-55.9365
-55.9265
-55.9165
-55.9065
-55.8965
-55.8865
-55.8765
-55.8665
-55.8565
x (mm)
45.641002
45.651002
45.661002
45.671002

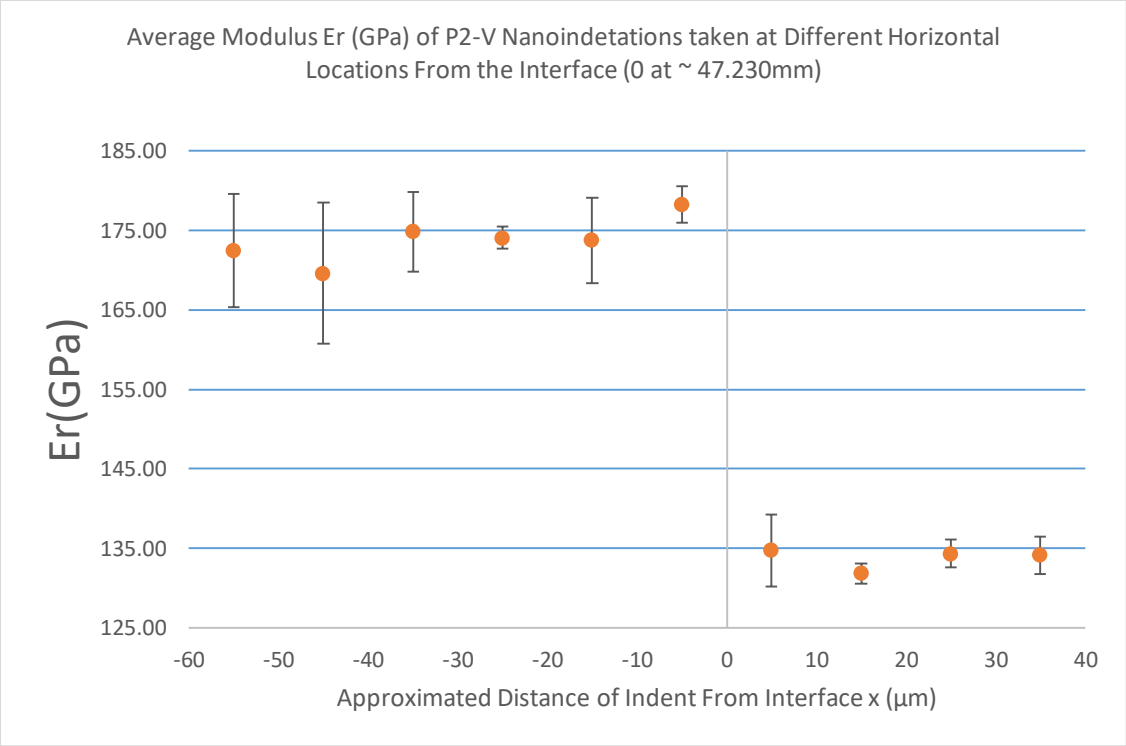
Average Modulus Er (GPa) of P2-V Nanoindetations taken at Different Horizontal Locations From the Interface (0 at ~ 47.230mm)
Er(GPa)
185.00
175.00
165.00
155.00
145.00
135.00
125.00
-60
-50
-40
-30
-20
-10
0
10
20
30
40
Approximated Distance of Indent From Interface x (µm)

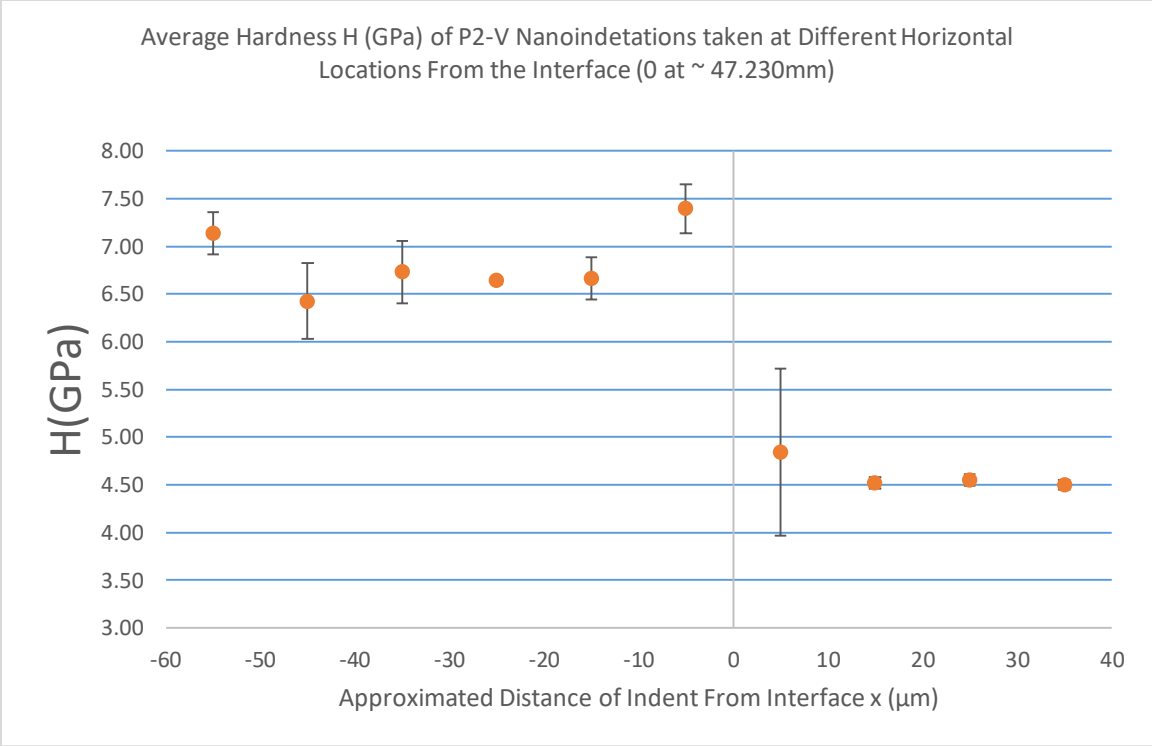
Average Hardness H (GPa) of P2-V Nanoindetations taken at Different Horizontal Locations From the Interface (0 at ~ 47.230mm)
H(GPa)
8.00
7.50
7.00
6.50
6.00
5.50
5.00
4.50
4.00
3.50
3.00
-60
-50
-40
-30
-20
-10
0
10
20
30
40
Approximated Distance of Indent From Interface x (µm)

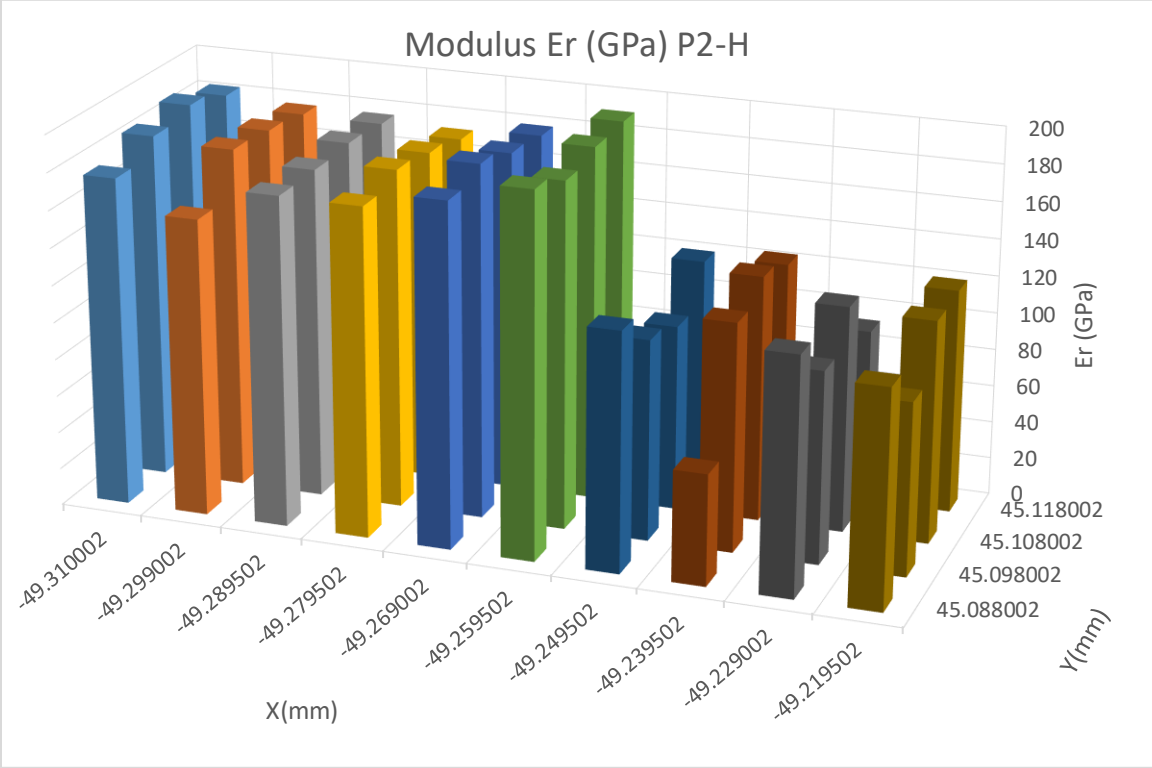
Modulus Er (GPa) P2-H
200
180
160
140
120
100
80
60
40
20
0
Er (GPa)
45.118002
45.108002
45.098002
45.088002
Y(mm)
-49.310002
-49.299002
-49.289502
-49.279502
-49.269002
-49.259502
-49.249502
-49.239502
-49.229002
-49.219502
X(mm)

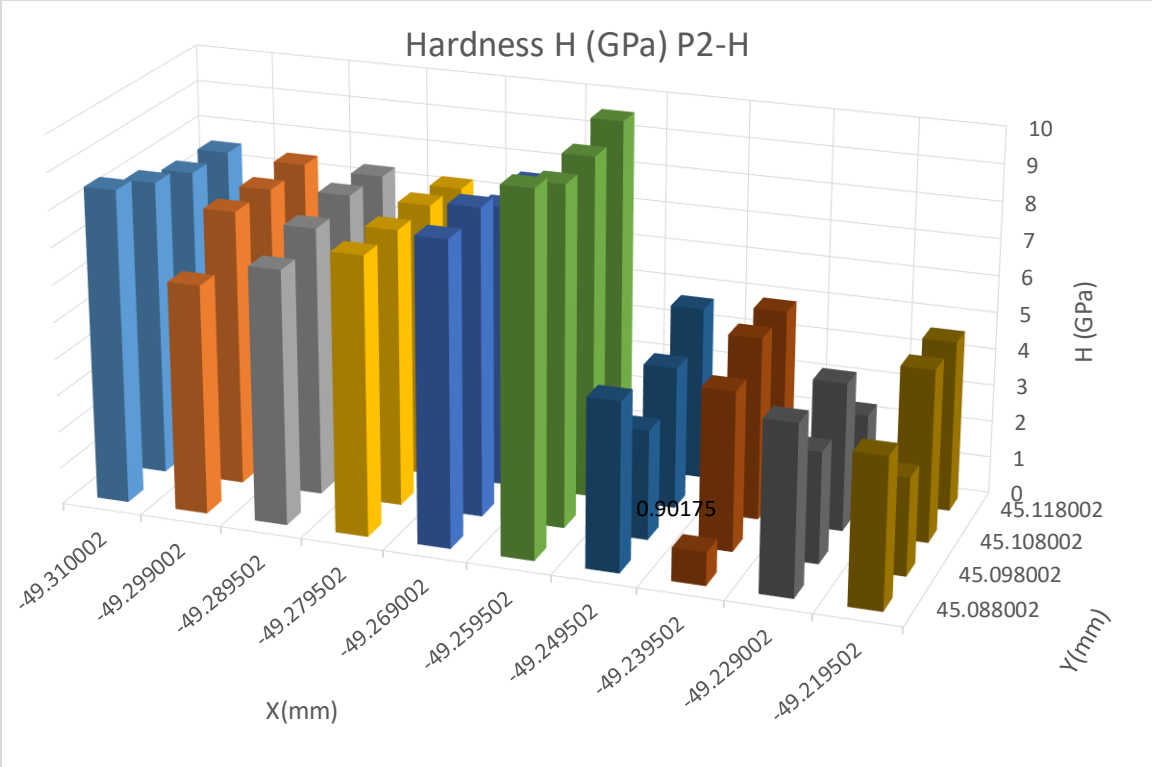
Hardness H (GPa) P2-H
10
9
8
7
6
5
4
3
2
1
0
H (GPa)
0.90175
-49.310002
-49.299002
-49.289502
-49.279502
-49.269002
-49.259502
-49.249502
-49.239502
-49.229002
-49.219502
X(mm)
45.118002
45.108002
45.098002
45.088002
Y(mm)

APPENDIX C: EDS of Nanoindents

While looking at the nanoindentation under the JEOL JSM-6510LV SEM to understand if nanoindents coalesced with voids, it was decided to use the integrated EDS-IXRF to take EDS measurements on the nanoindentation points to see if there could be a correlation between the hardness, modulus, and chemical makeup, but also to have a highly accurate map of the chemistry. Thus, the nanoindented areas were broken up into sections D2-P1 and D2-P2 as before.

D2 - P1

P1-V 10x4 Grid EDS of Nanoindents

In **Appendix Figure C.1**, P1-V is shown with the 10-degree nanoindents in view to provide an idea of relative placement of nanoindentation on the WHA-1 cube.

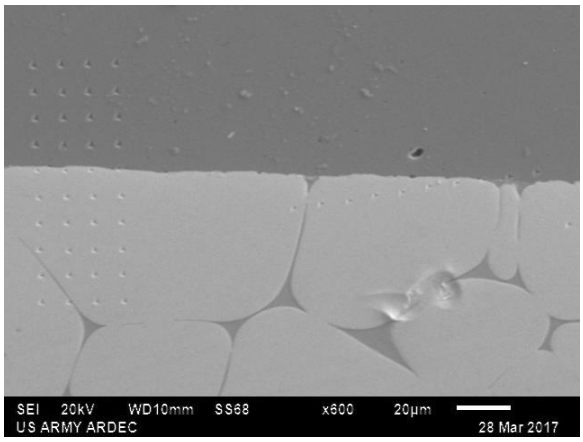

Appendix Figure C. 1 P1-V 10x4 Grid Indents with 10 Degree Nanoindentation Line Visible x600

At x900 power, P1-V (**Appendix Figure C.2**) is nice and crisp for reference and **Appendix Figure C.3** shows the order and points on which the EDS was taken. Point 35

for the EDS lines up with point 24 of the nanoindentation measurements. In the future one should use the same nomenclature across interrogation techniques as well as potential markers on the surface of the WHA similar to the Kirkendall Experiment [39]. Using a pure known marker element with well-defined diffusion rates would allow one to determine how the advection (lattice flow) changes the material properties and if Kirkendall porosity is occurring [39].

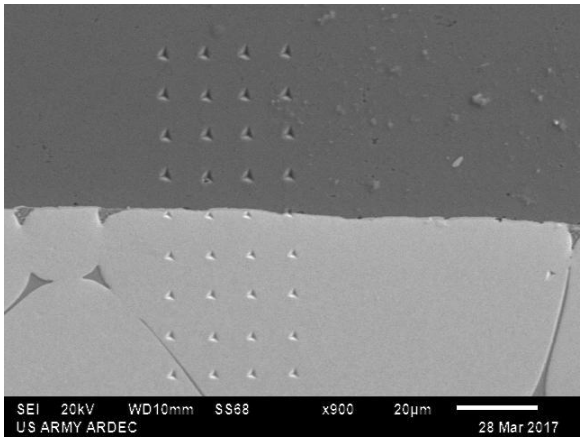

Appendix Figure C. 2 P1-V 10x4 Grid Indents x900

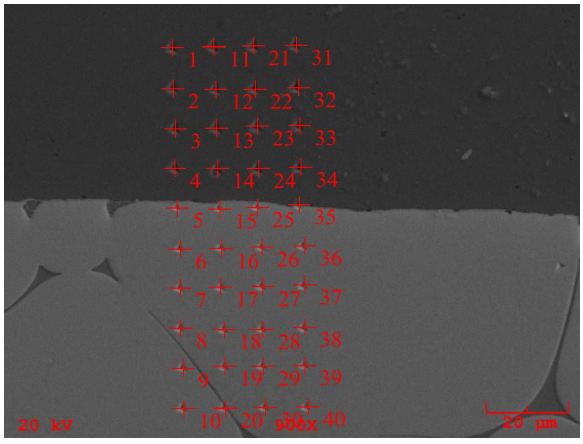

Appendix Figure C. 3 P1-V 10x4 Grid Indents x900

The concentration spectrum report for P1-V is shown in **Appendix Figure C.4** to understand how the elements inter-diffuse. Only the elementals specified in the D2 and

WHA compositions are shown. The concentration of the tungsten, iron, and chromium drown out the lower elemental concentrations on a scale of 1-100 so these elements were removed to reveal the next highest concentration elements and their concentrations. Further it is not clearly evident inter-diffusion is occurring but there is a repeating pattern within the deviations occurring on the WHA side, suggesting counts may have been low or contamination has occurred as evidenced by points 36 and 37 showing low concentrations of tungsten when the indents and EDS points were clearly on a tungsten grain as chapter 4 showed. Thus, these measurements should not be taken at face value but more the trend should be the focus, as diffusivity rates would change along meandering boundary and changing concentrations and ultimately mechanical properties. Hind sight would also use pure tungsten and a well characterized steel alloy with low sulfur, phosphorus and other known detrimental elements to fracture toughness for steel.

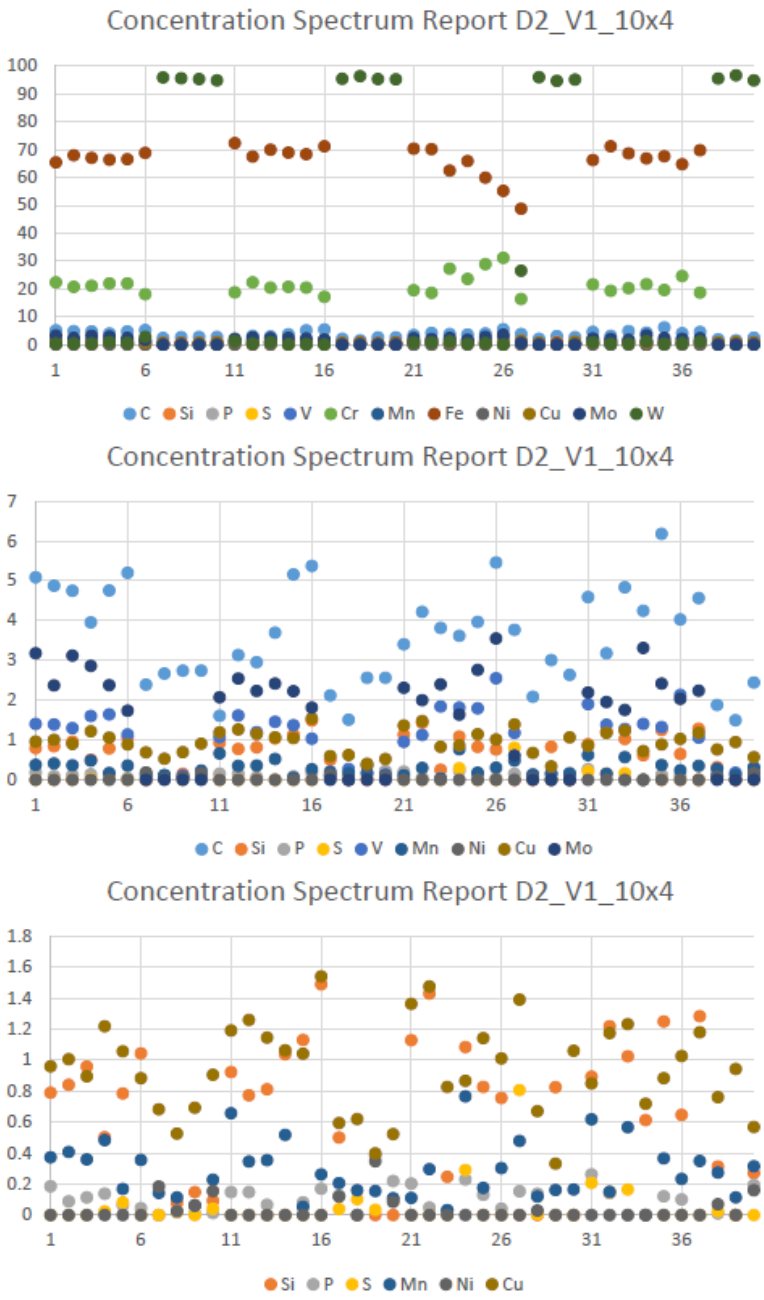

Appendix Figure C. 4 P1-V Concentration Spectrum Reports Pts 1-40

Since there is a lot of information obscured by the different scales when showing all four columns at once, each column for the P1-V 4x10 grid was plotted individually in the same manner as before, removing highly concentrated elements so trends in lower concentration elements can be observed as shown in **Appendix Figure C.5**.

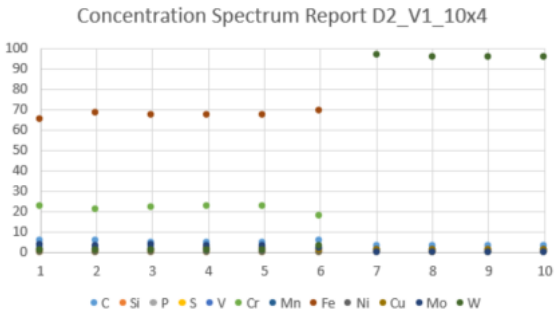
Concentration Spectrum Report D2_V1_10x4
C Si P S V Cr Mn Fe Ni Cu Mo W

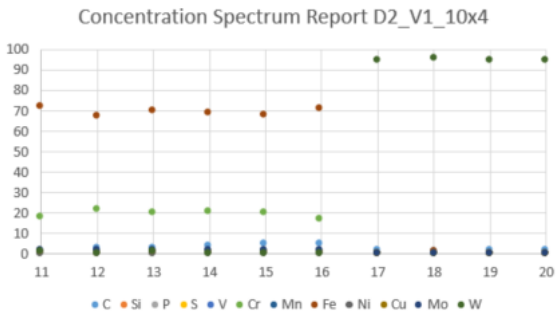
Concentration Spectrum Report D2_V1_10x4
C Si P S V Cr Mn Fe Ni Cu Mo W

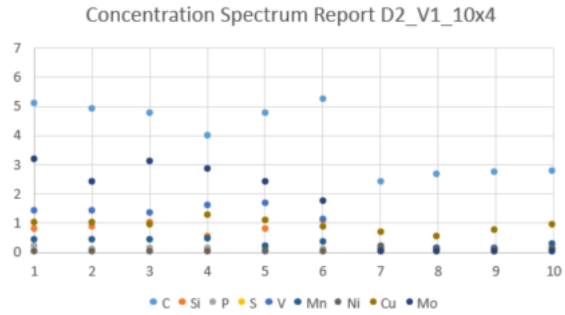
Concentration Spectrum Report D2_V1_10x4
C Si P S V Mn Ni Cu Mo

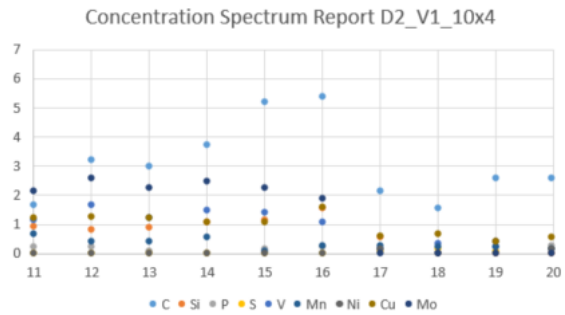
Concentration Spectrum Report D2_V1_10x4
C Si P S V Mn Ni Cu Mo

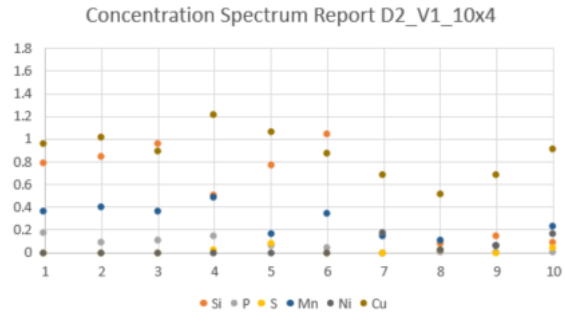
Concentration Spectrum Report D2_V1_10x4
Si P S Mn Ni Cu

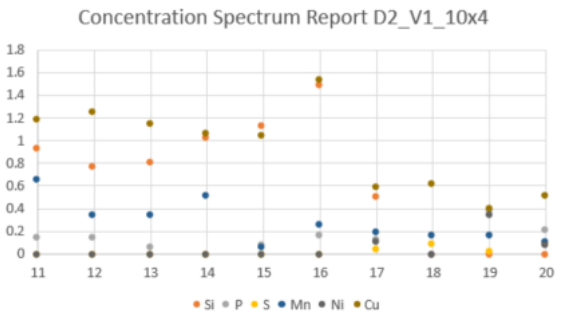
Concentration Spectrum Report D2_V1_10x4
Si P S Mn Ni Cu

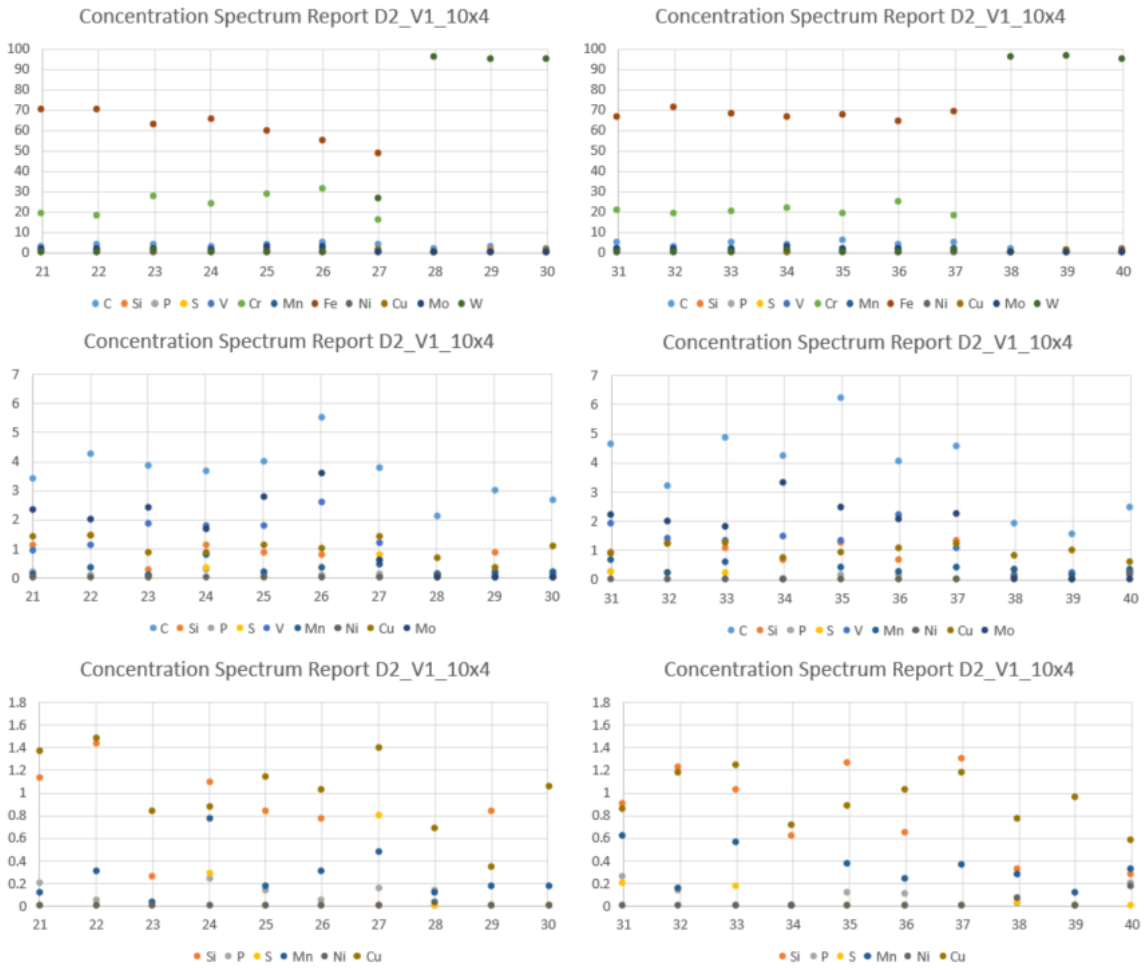

Appendix Figure C. 5 P1-V Concentration Spectrum Reports Broken Out by Column a) pts 1-10 and 11-20 b) pts 21-30 and 31-40

Since the 35th EDS point was in the last column of points, (31-40) and was on the interface, it was decided to plot each element separately (**Appendix Figure C. 6**) to determine for these points to see if there was a noticeable trend in elemental concentrations. Again the tungsten plot shows close to zero tungsten concentration at points 36 and 37 even though they were clearly on a tungsten grain so there may be some error in the EDS measurements though it was calibrated just prior to use. The majority of the elements for the D2 follow the same trend: relatively level in concentration until the interface, at which point the element's concentration climbs for approximately 10 µm and

then drops off and behaves similarly to a binary diffusion couple [39]. The carbon and silicon exhibit different behavior which appears to be random in concentration until the interface and after 10 μm when the carbon's average concentration shifts down in concentration by a factor of two and silicon by a factor of four then resumes a random pattern about a lower average concentration again. The average phosphorus concentration seems to be dimensioning over the 10 points taken as the last point seems to be an outlier. Sulfur remains relatively constant up until 20 μm from the interface when it drops to almost zero. The tungsten and nickel concentrations also drop in concentration as the interface is approached from their respective side and since the iron is in both the D2 and the WHA alloys it seems to increase slightly up to 20 μm past the interface into the WHA alloy.

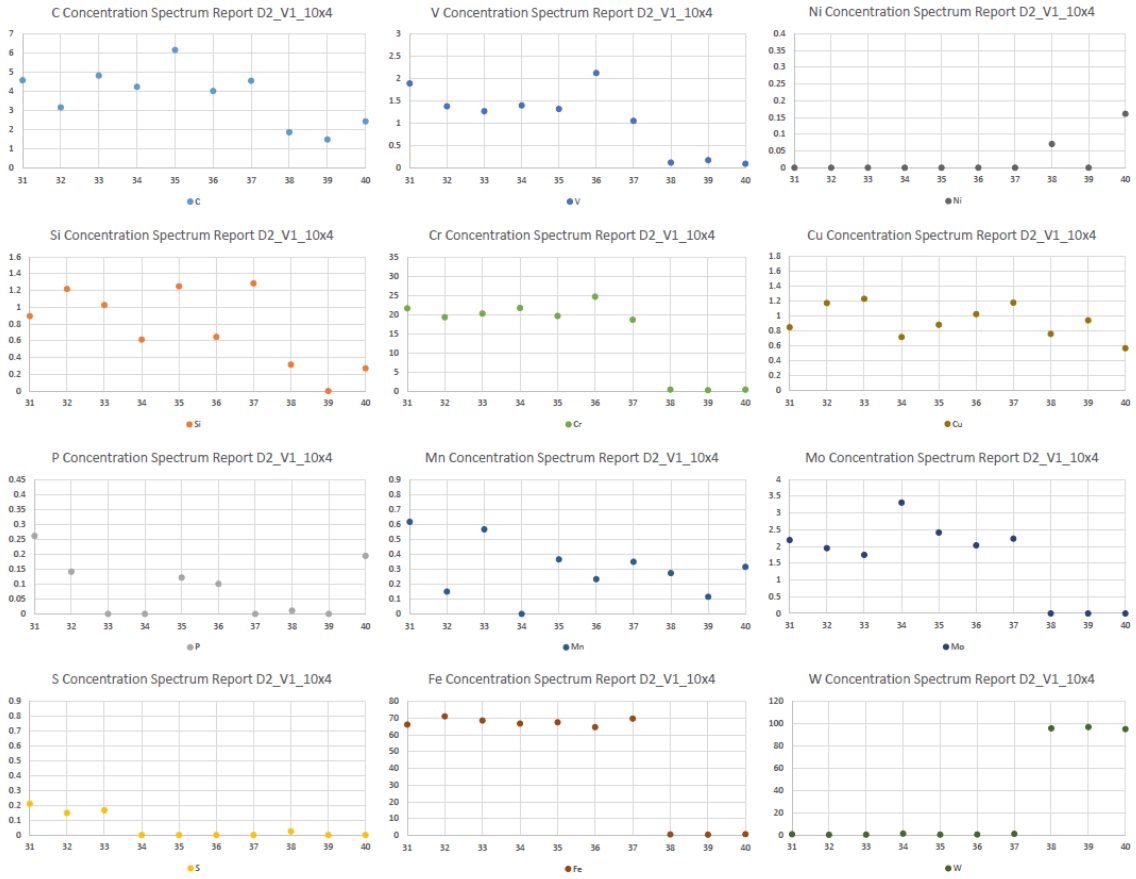

Appendix Figure C. 6 P1-V Concentration Spectrum Reports for Each Element for Points 31-40

The individual concentrations for all P1-V points are shown below in **Appendix Table C-1** and were obtained by using 100 second absorption times for the first 10 points and points 5, 15, and 35. Then 30 second absorption times were used for the remainder of the points achieving counts in excess of 67,000 counts which should provide a relatively good approximation.

Spectrum	C	Si	P	S	V	Cr	Mn	Fe	Ni	Cu	Mo	W
D2_V1_10x4-1	5.084	0.791	0.186	0	1.4	22.299	0.374	65.348	0	0.961	3.178	0.38
D2_V1_10x4-2	4.874	0.842	0.089	0	1.39	20.717	0.407	67.924	0	1.007	2.367	0.384
D2_V1_10x4-3	4.744	0.96	0.114	0	1.295	21.129	0.36	66.998	0	0.896	3.12	0.383
D2_V1_10x4-4	3.952	0.503	0.139	0.024	1.602	21.978	0.484	66.342	0	1.219	2.857	0.9
D2_V1_10x4-5	4.751	0.785	0.064	0.083	1.638	21.934	0.169	66.53	0	1.058	2.375	0.613

D2_V1_10x4-6	5.197	1.045	0.045	0	1.137	18.072	0.357	68.81	0	0.885	1.733	2.719
D2_V1_10x4-7	2.388	0	0.001	0	0.086	0.166	0.143	0.458	0.185	0.684	0	95.889
D2_V1_10x4-8	2.668	0.079	0.017	0.023	0.108	0.244	0.115	0.669	0.026	0.527	0	95.524
D2_V1_10x4-9	2.739	0.149	0.008	0	0.112	0.342	0.061	0.538	0.064	0.694	0	95.293
D2_V1_10x4-10	2.742	0.092	0.014	0.041	0.091	0.205	0.229	0.714	0.156	0.907	0	94.808
D2_V1_10x4-11	1.608	0.924	0.148	0	1.068	18.723	0.658	72.329	0	1.193	2.071	1.278
D2_V1_10x4-12	3.128	0.773	0.149	0	1.614	22.347	0.347	67.473	0	1.26	2.542	0.366
D2_V1_10x4-13	2.951	0.812	0.067	0	1.196	20.477	0.354	69.954	0	1.147	2.229	0.811
D2_V1_10x4-14	3.694	1.039	0	0	1.455	20.756	0.518	68.926	0	1.065	2.416	0.131
D2_V1_10x4-15	5.16	1.131	0.082	0	1.368	20.405	0.053	68.347	0	1.042	2.221	0.191
D2_V1_10x4-16	5.369	1.491	0.17	0	1.033	17.134	0.262	71.19	0	1.542	1.81	0
D2_V1_10x4-17	2.12	0.501	0.127	0.039	0.09	0.354	0.206	0.5	0.119	0.595	0	95.347
D2_V1_10x4-18	1.508	0	0	0.102	0.272	0.257	0.161	0.797	0	0.62	0	96.284
D2_V1_10x4-19	2.564	0	0.385	0.035	0.175	0.188	0.156	0.47	0.348	0.399	0	95.279
D2_V1_10x4-20	2.561	0	0.221	0.101	0.13	0.323	0.109	0.769	0.085	0.523	0	95.177
D2_V1_10x4-21	3.403	1.129	0.203	0	0.952	19.457	0.112	70.309	0	1.365	2.311	0.759
D2_V1_10x4-22	4.215	1.431	0.048	0	1.125	18.586	0.297	70.088	0	1.477	1.995	0.738
D2_V1_10x4-23	3.81	0.248	0.033	0	1.84	27.295	0.031	62.486	0	0.829	2.396	1.033
D2_V1_10x4-24	3.613	1.086	0.23	0.292	1.814	23.528	0.767	65.87	0	0.867	1.632	0.3
D2_V1_10x4-25	3.967	0.829	0.131	0	1.793	28.836	0.176	59.861	0	1.143	2.758	0.505
D2_V1_10x4-26	5.457	0.757	0.042	0	2.546	31.143	0.303	55.194	0	1.012	3.546	0
D2_V1_10x4-27	3.768	0	0.153	0.807	1.179	16.336	0.479	48.768	0	1.391	0.604	26.515
D2_V1_10x4-28	2.082	0	0.139	0.006	0.122	0.298	0.119	0.589	0.03	0.671	0	95.946
D2_V1_10x4-29	3.004	0.827	0	0	0.137	0.297	0.162	0.591	0	0.333	0	94.65
D2_V1_10x4-30	2.633	0	0	0.001	0.141	0.274	0.166	0.664	0	1.062	0	95.059
D2_V1_10x4-31	4.586	0.894	0.262	0.209	1.896	21.58	0.618	66.187	0	0.85	2.192	0.726
D2_V1_10x4-32	3.174	1.219	0.142	0.148	1.385	19.274	0.15	71.134	0	1.175	1.952	0.244
D2_V1_10x4-33	4.831	1.026	0	0.166	1.273	20.225	0.568	68.641	0	1.234	1.751	0.286
D2_V1_10x4-34	4.245	0.614	0	0	1.405	21.694	0	66.828	0	0.72	3.311	1.184
D2_V1_10x4-35	6.174	1.25	0.122	0	1.325	19.603	0.366	67.546	0	0.885	2.417	0.312
D2_V1_10x4-36	4.027	0.647	0.101	0	2.128	24.618	0.233	64.699	0	1.027	2.034	0.486
D2_V1_10x4-37	4.563	1.285	0	0	1.059	18.6	0.35	69.711	0	1.18	2.234	1.018
D2_V1_10x4-38	1.876	0.314	0.011	0.025	0.123	0.384	0.274	0.662	0.071	0.761	0	95.499
D2_V1_10x4-39	1.493	0	0	0	0.179	0.214	0.115	0.481	0	0.944	0	96.574
D2_V1_10x4-40	2.439	0.271	0.195	0	0.1	0.351	0.316	0.784	0.161	0.569	0	94.813

Appendix Table C-1 P1-V 10x4 Grid Chemistry

The individual EDS plots are in Appendix A, but shown here by relative row in **Appendix Figure C. 7- Appendix Figure C. 16** to see the changes in the returns and the different phases of the elements.

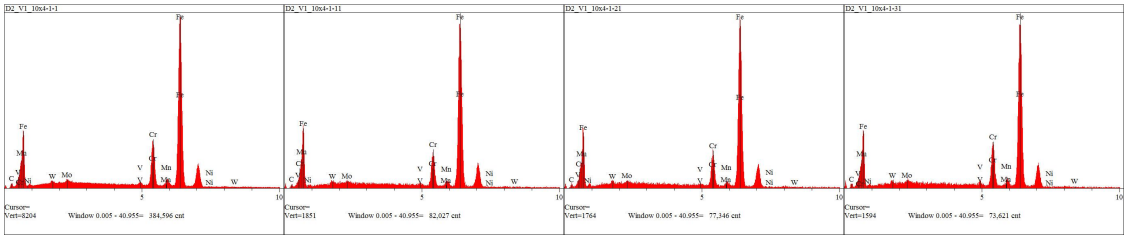

Appendix Figure C. 7 P1-V 10x4 EDS plots; row 1,11,21,31

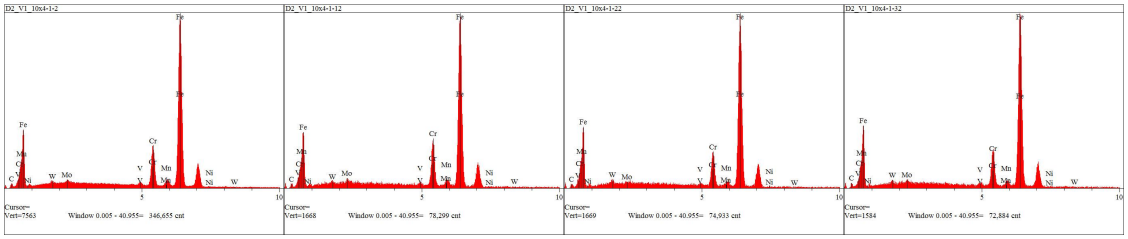

Appendix Figure C. 8 P1-V 10x4 EDS plots; row 2,12,22,32

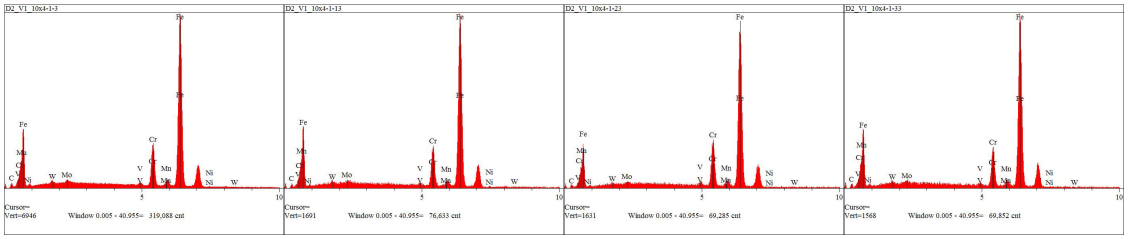

Appendix Figure C. 9 P1-V 10x4 EDS plots; row 3,13,23,33

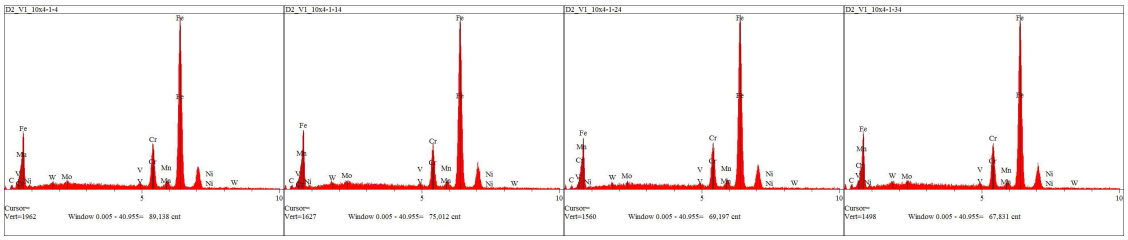

Appendix Figure C. 10 P1-V 10x4 EDS plots; row 4,14,24,34

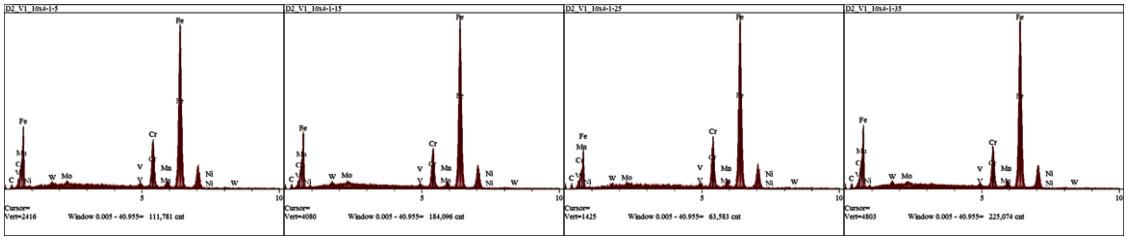

Appendix Figure C. 11 P1-V 10x4 EDS plots; row 5,15,25,35 Adjacent to Interface (pt 35 on interface)

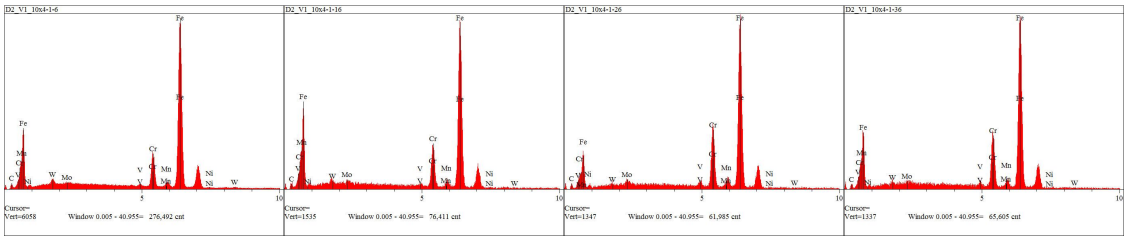

Appendix Figure C. 12 P1-V 10x4 EDS plots; row; 6,16,26,36

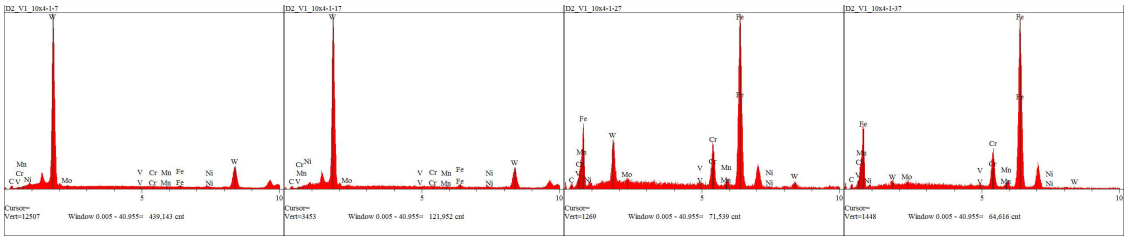

Appendix Figure C. 13 P1-V 10x4 EDS plots; row; 7,17,27,37

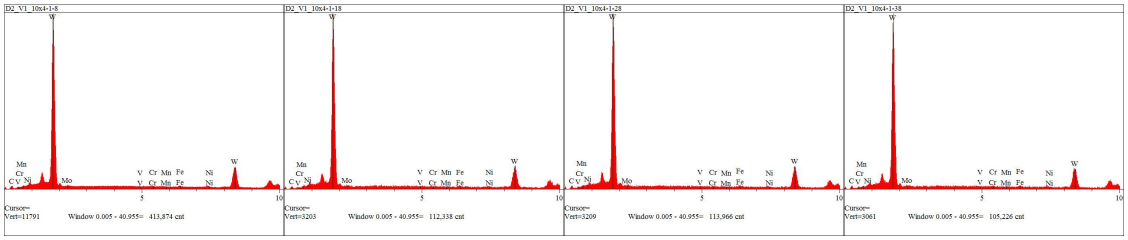

Appendix Figure C. 14 P1-V 10x4 EDS plots; row; 8,18,28,38

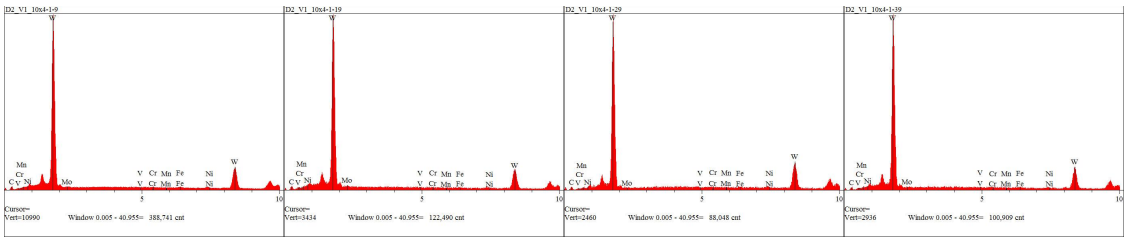

Appendix Figure C. 15 P1-V 10x4 EDS plots; row; 9,19,29,39

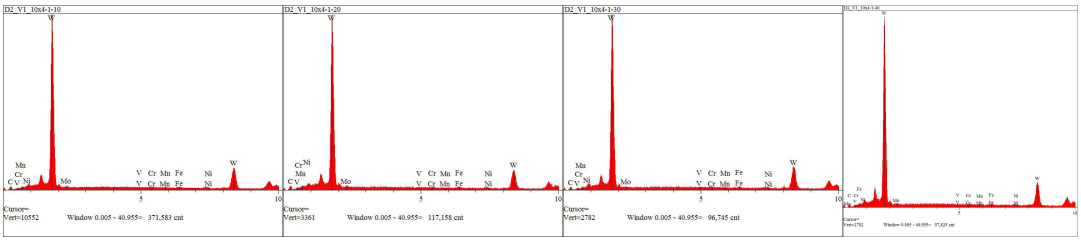

Appendix Figure C. 16 P1-V 10x4 EDS plots; row; 10,20,30,40

P1-H-4x10

Similarly to the P1-V EDS analysis, the P1-H elemental concentrations exhibit similar trends. Though all numerical identifiers are not shown in **Appendix Figure C. 17**, the convention is shown with the first row of EDS points 1-10 and the last row, 31-40.

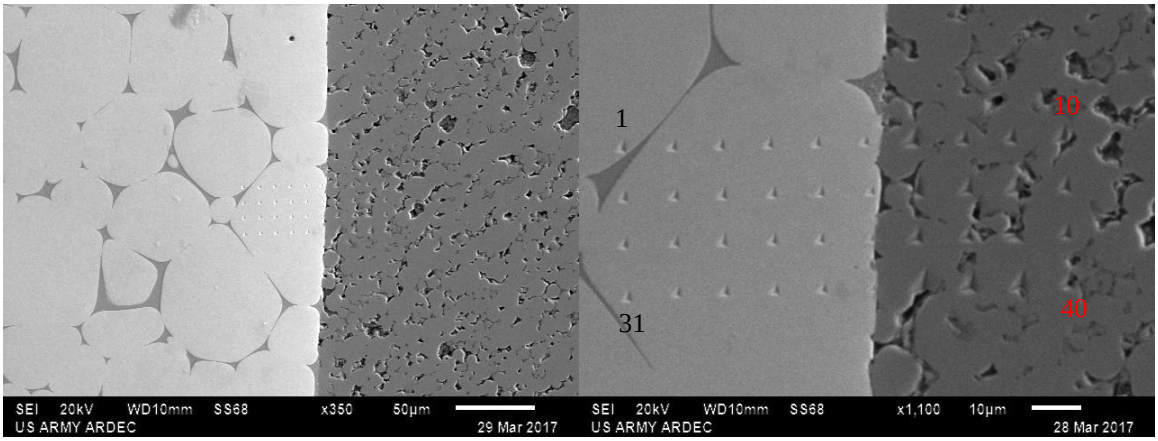

Appendix Figure C. 17 P1-H 4x10 Nanoindentations x350

Again the concentration spectrum reports are shown for the 40 points on one graph to get an idea of the trends with 4 separate rows spanning the interface as shown in **Appendix Figure C. 18-21**. In **Appendix Figure C. 19** tungsten, iron and chromium elements were removed to better visualize trends in the lower concentrated elements

while **Appendix Figure C. 19** also removes carbon and nickel elements to allow trends in the lowest elemental concentrations to be observed. Finally only sulfur, phosphorus and silicon are displayed in **Appendix Figure C.21** with the majority of the concentration occurring in the D2 material.

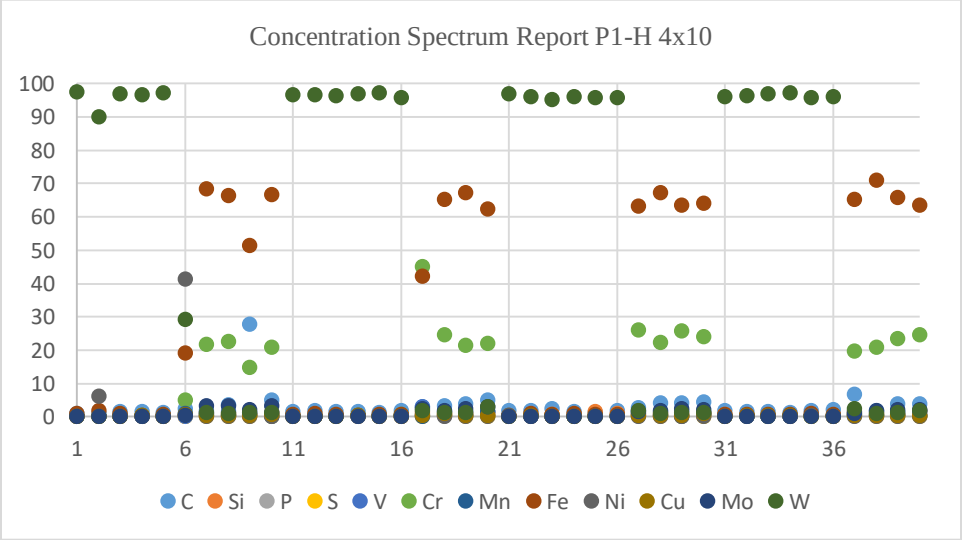

Appendix Figure C. 18 P1-H 4x10 Grid Chemistry WHA and D2 Elements

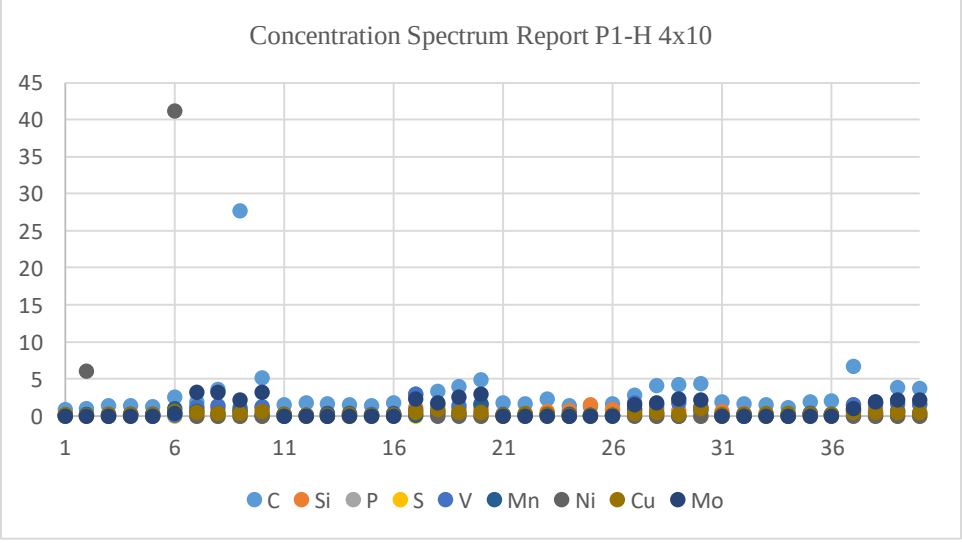

Appendix Figure C. 19 P1-H 10x4 Grid Chemistry WHA and D2 Elements Minus W, Fe, Cr Elements

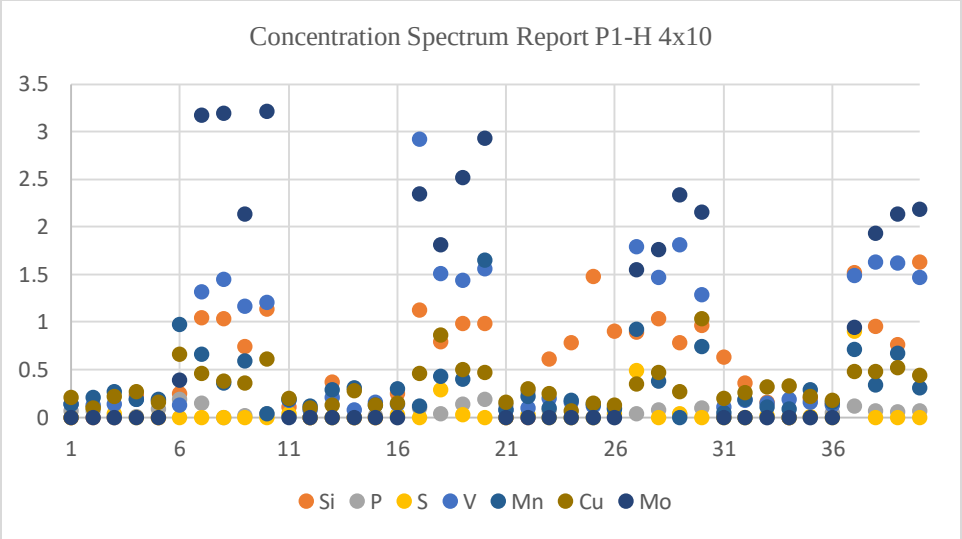

Appendix Figure C. 20 P1-H 10x4 Grid Chemistry WHA and D2 Elements Minus W, FE, Cr, C, Ni Elements

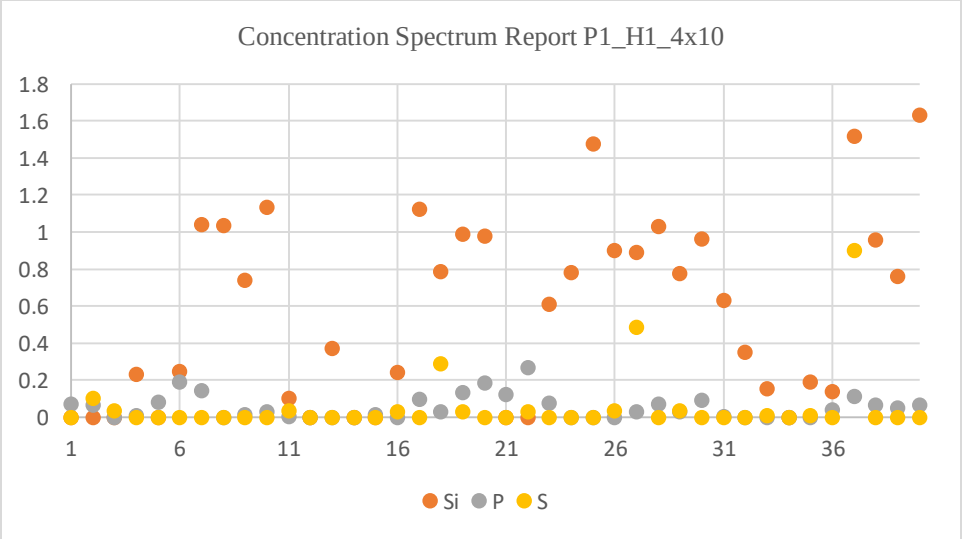

Appendix Figure C. 21 P1-H 10x4 Grid Chemistry WHA and D2, only Si, P, S, Elements

The individual concentration for each point are shown in **Appendix Table C-2** where counts for each point were over 66,000 producing reliable results and since points 26 and 36 were on the interface their absorption time was increased to achieve over 330,000 counts.

Spectrum	C	Si	P	S	V	Cr	Mn	Fe	Ni	Cu	Mo	W

D2_H1_4x10-1	0.847	0	0.07	0	0.134	0.135	0.138	0.905	0.075	0.209	0	97.488
D2_H1_4x10-2	1.032	0	0.066	0.105	0.128	0.223	0.207	1.925	6.079	0.1	0	90.135
D2_H1_4x10-3	1.412	0	0	0.035	0.132	0.157	0.272	0.857	0	0.22	0	96.915
D2_H1_4x10-4	1.408	0.231	0.008	0	0.182	0.274	0.189	0.495	0.224	0.263	0	96.727
D2_H1_4x10-5	1.295	0	0.081	0	0.174	0.283	0.183	0.737	0	0.161	0	97.087
D2_H1_4x10-6	2.536	0.249	0.19	0	0.131	5.086	0.969	19.254	41.195	0.658	0.388	29.343
D2_H1_4x10-7	1.891	1.042	0.142	0	1.32	21.751	0.663	68.424	0	0.462	3.176	1.13
D2_H1_4x10-8	3.57	1.037	0	0	1.443	22.519	0.355	66.444	0	0.379	3.197	1.056
D2_H1_4x10-9	27.746	0.741	0.015	0	1.165	14.765	0.595	51.303	0	0.355	2.131	1.183
D2_H1_4x10-10	5.1	1.136	0.032	0	1.207	20.841	0.033	66.68	0	0.611	3.214	1.146
D2_H1_4x10-11	1.516	0.103	0.005	0.034	0.179	0.29	0.189	0.697	0.022	0.192	0	96.772
D2_H1_4x10-12	1.803	0	0	0	0.073	0.406	0.115	0.881	0.043	0.092	0	96.586
D2_H1_4x10-13	1.656	0.372	0	0	0.205	0.252	0.29	0.799	0	0.122	0	96.304
D2_H1_4x10-14	1.535	0	0	0	0.078	0.274	0.307	0.531	0.125	0.281	0	96.869
D2_H1_4x10-15	1.352	0	0.015	0	0.158	0.291	0.127	0.758	0.032	0.124	0	97.145
D2_H1_4x10-16	1.764	0.245	0	0.029	0.14	0.677	0.3	0.813	0.158	0.146	0	95.727
D2_H1_4x10-17	2.904	1.126	0.098	0	2.92	45.178	0.115	42.189	0.8	0.461	2.344	1.865
D2_H1_4x10-18	3.357	0.787	0.031	0.288	1.513	24.477	0.427	65.283	0	0.867	1.812	1.159
D2_H1_4x10-19	3.983	0.988	0.133	0.028	1.439	21.419	0.394	67.272	0	0.504	2.515	1.325
D2_H1_4x10-20	4.874	0.982	0.188	0	1.562	21.979	1.654	62.254	0	0.473	2.935	3.1
D2_H1_4x10-21	1.818	0	0.125	0	0.071	0.191	0.075	0.467	0.258	0.156	0	96.84
D2_H1_4x10-22	1.698	0	0.27	0.029	0.1	0.366	0.222	0.895	0.073	0.298	0	96.049
D2_H1_4x10-23	2.339	0.61	0.076	0	0.196	0.43	0.092	0.588	0.175	0.243	0	95.249
D2_H1_4x10-24	1.415	0.782	0	0	0.161	0.213	0.181	0.977	0	0.063	0	96.207
D2_H1_4x10-25	1.279	1.477	0	0	0.121	0.261	0.14	0.701	0.085	0.147	0	95.788
D2_H1_4x10-26	1.699	0.902	0	0.038	0.094	0.408	0.09	0.629	0.146	0.129	0	95.864
D2_H1_4x10-27	2.816	0.891	0.032	0.485	1.795	25.962	0.926	63.335	0	0.352	1.544	1.862
D2_H1_4x10-28	4.151	1.029	0.071	0	1.471	22.406	0.379	67.298	0	0.471	1.763	0.96
D2_H1_4x10-29	4.284	0.779	0.029	0.036	1.806	25.752	0	63.545	0	0.272	2.339	1.158
D2_H1_4x10-30	4.337	0.965	0.094	0	1.291	24.06	0.739	64.026	0	1.035	2.154	1.299
D2_H1_4x10-31	1.887	0.631	0.006	0	0.106	0.316	0.042	0.574	0.067	0.197	0	96.174
D2_H1_4x10-32	1.591	0.354	0	0	0.174	0.34	0.187	0.696	0.026	0.259	0	96.373
D2_H1_4x10-33	1.455	0.156	0	0.011	0.149	0.161	0.108	0.719	0.044	0.318	0	96.88
D2_H1_4x10-34	1.162	0	0	0	0.186	0.435	0.085	0.645	0	0.329	0	97.158
D2_H1_4x10-35	1.859	0.192	0	0.009	0.157	0.207	0.29	1.013	0.315	0.216	0	95.744
D2_H1_4x10-36	2.1	0.139	0.041	0	0.122	0.258	0.157	0.776	0.185	0.174	0	96.048
D2_H1_4x10-37	6.695	1.52	0.115	0.903	1.485	19.624	0.711	65.133	0	0.477	0.939	2.398
D2_H1_4x10-38	1.936	0.958	0.067	0	1.625	20.812	0.341	70.973	0	0.479	1.928	0.88
D2_H1_4x10-39	3.875	0.761	0.051	0	1.616	23.323	0.674	65.794	0	0.521	2.133	1.252

D2_H1_4x10-40	3.766	1.634	0.068	0	1.465	24.679	0.312	63.627	0	0.435	2.185	1.828

Appendix Table C-1 P1-H 4x10 Chemistry

The individual EDS plots for P1-H are shown in APPENDIX D. The four points close to the horizontal interface are enlarged here in **Appendix Figure C. 22** to help understand the elemental makeup of the material at or near the interface.

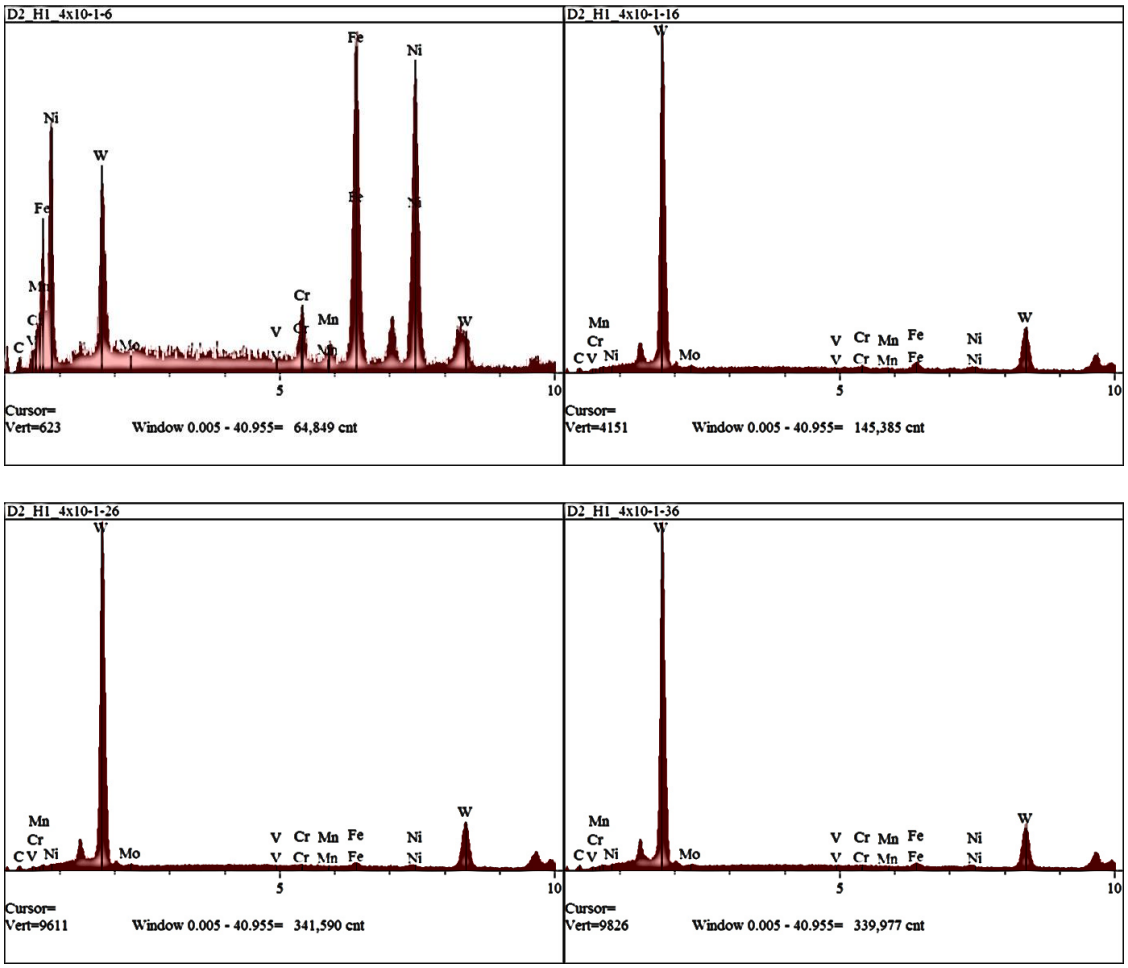

Appendix Figure C. 22 P1-H EDS Plots 6,16,26,36 Close to Interface

P1 0-Degree EDS of Nanoindents

Even though P1 0-degree indents **(Appendix Figure C.23)** did not broach the interface, the EDS analysis is still valuable as the concentration reports shown in **Appendix Figure C. 24 and Appendix Figure C. 25** reveal a relatively stable

concentration profile for each element and shows that 5-6 µm from the interface, diffusion of all D2 elements into the WHA has occurred regardless of the proximity to the nickel and iron matrix in the WHA with the exception of molybdenum.

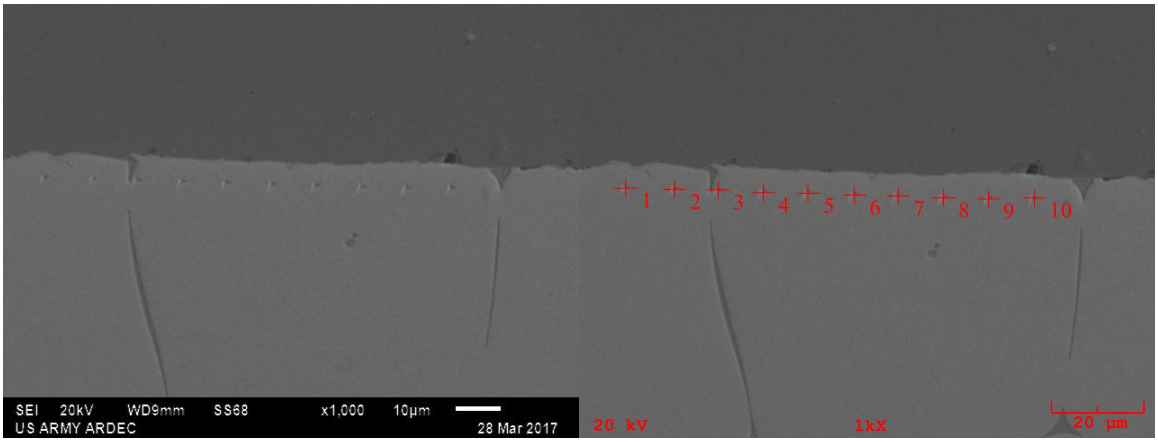

Appendix Figure C. 23 P1 0-Degree Nanoindents and EDS

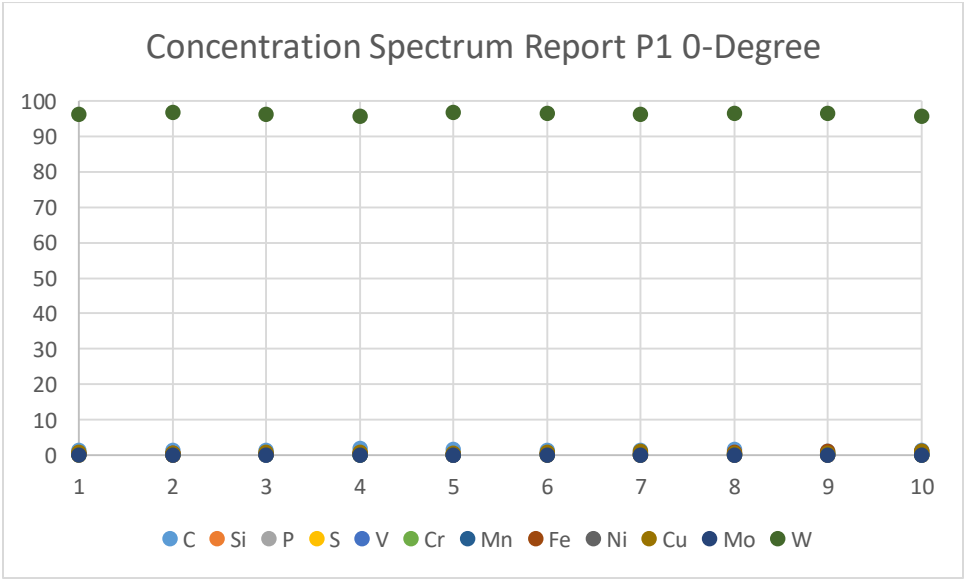

Appendix Figure C. 24 P1 0-Degree Chemistry WHA and D2 Elements

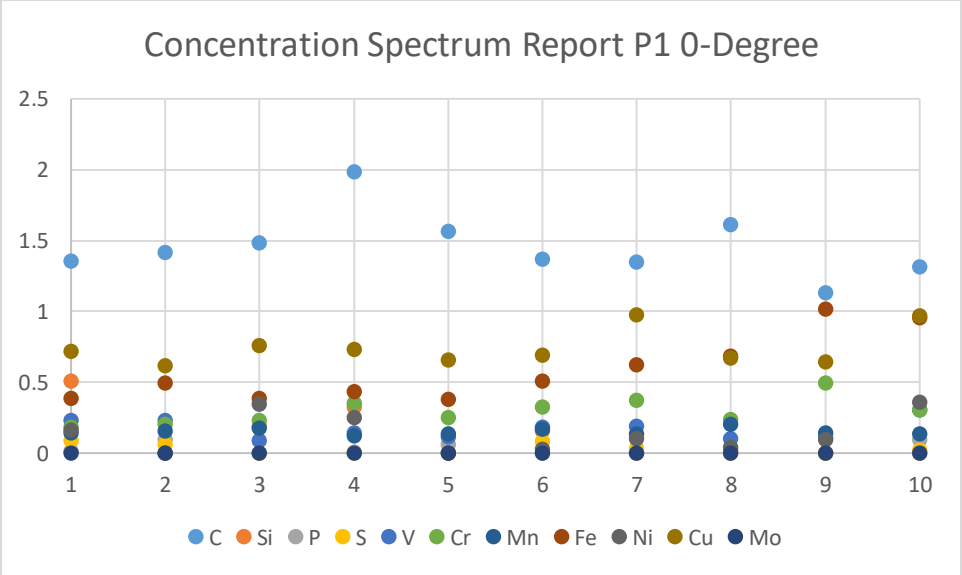

Appendix Figure C. 25 P1 0-Degree Chemistry WHA and D2 Elements Minus W Element

The individual concentrations for P1 0-degree and limited statistical analysis is shown in **Appendix Table C-3** for the ten points. An individual EDS plot is also in **Appendix Figure C. 26** to show the stability along this plane and Figure 6.1.28 shows a readable EDS plot of point 1 which is at a distance of approximately 5-6 µm.

Spectrum	C	Si	P	S	V	Cr	Mn	Fe	Ni	Cu	Mo	W
P1_0_degree-1	1.354	0.506	0.017	0.09	0.229	0.182	0.143	0.383	0.164	0.715	0	96.217
P1_0_degree-2	1.416	0	0.093	0.062	0.228	0.206	0.158	0.498	0	0.616	0	96.723
P1_0_degree-3	1.487	0.19	0	0	0.086	0.229	0.173	0.388	0.346	0.756	0	96.344
P1_0_degree-4	1.984	0.322	0.005	0	0.142	0.35	0.125	0.436	0.25	0.729	0	95.656
P1_0_degree-5	1.563	0	0.059	0	0.114	0.253	0.138	0.378	0	0.655	0	96.841
P1_0_degree-6	1.367	0.157	0	0.084	0.181	0.322	0.171	0.508	0.024	0.692	0	96.492
P1_0_degree-7	1.348	0	0	0.037	0.188	0.374	0.133	0.625	0.104	0.973	0	96.218
P1_0_degree-8	1.612	0	0.03	0.017	0.104	0.238	0.2	0.685	0.04	0.672	0	96.403
P1_0_degree-9	1.133	0	0	0	0.111	0.494	0.141	1.018	0.097	0.642	0	96.364
P1_0_degree-10	1.313	0	0.098	0.022	0.303	0.303	0.138	0.958	0.357	0.967	0	95.542
Mean	1.458	0.118	0.03	0.031	0.169	0.295	0.152	0.588	0.138	0.742	0	96.28
Std. Dev.	0.229	0.177	0.039	0.036	0.07	0.094	0.023	0.235	0.137	0.127	0	0.412

Min	1.133	0	0	0	0.086	0.182	0.125	0.378	0	0.616	0	95.542
Max	1.984	0.506	0.098	0.09	0.303	0.494	0.2	1.018	0.357	0.973	0	96.841

Appendix Table C-2 P1 0-Degree EDS

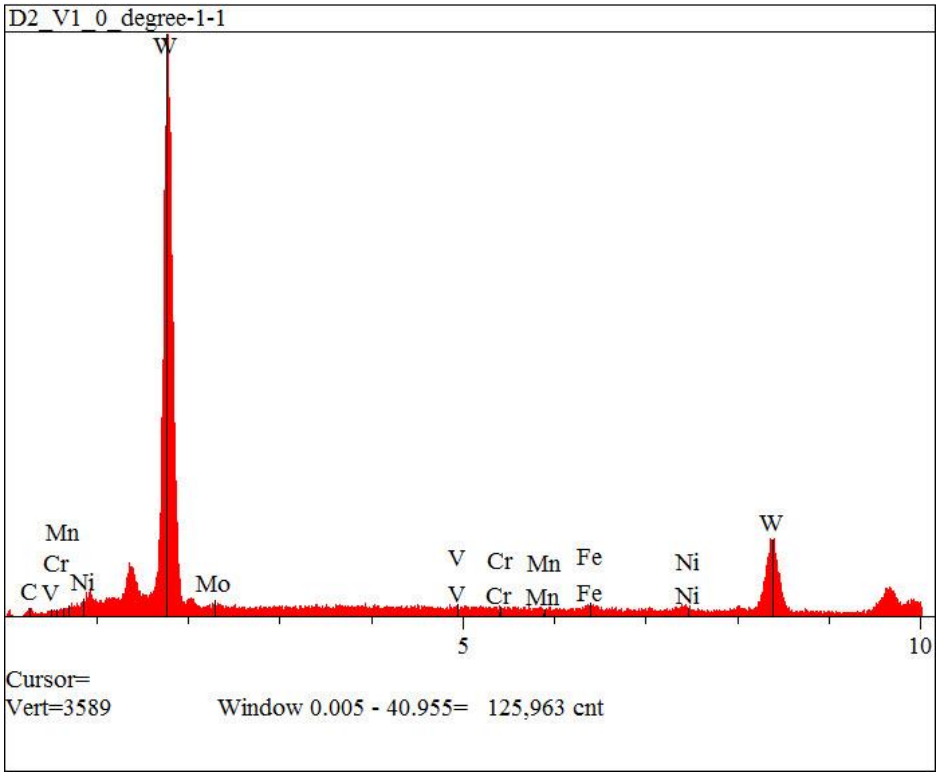

Appendix Figure C. 26 P1 0-Degree EDS Point 1

P1 5-Degree EDS of Nanoindents

The 5-degree EDS analysis was carried out in the same manner using 30 second absorption times with points 1-10 corresponding to **Appendix Figure C.27-C.30**. Only points 6-10 are shown in **Appendix Figure C. 29** and **Appendix Figure C. 30** to highlight the elemental concentration change as the interface is approached while point 10 partially perforates the interface. Even though point 8 is farther from the interface, it has a higher concentration of carbon than point 9 indicating the lattice structure may be affecting the diffusivity of carbon though not statistically evident yet. The individual concentrations are in **Appendix Table C-4**. **Appendix Figure C. 31** shows the EDS

spectrum for the first point as well as the 9th and 10th indicating there is little change from the 1st and 9th with respect to element phase and composition, though the 10th point on the interface shows the change in element phases and concentrations.

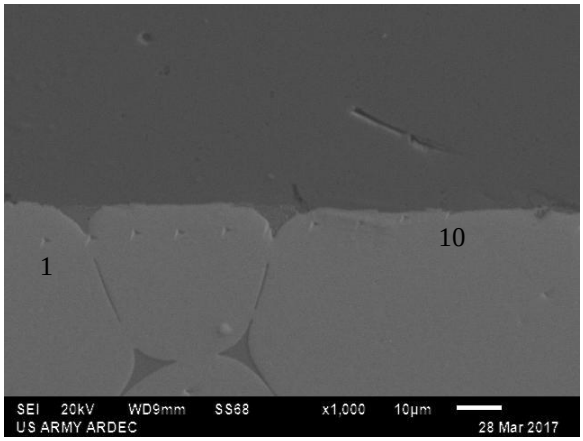

Appendix Figure C. 27 P1 5-Degree Indents

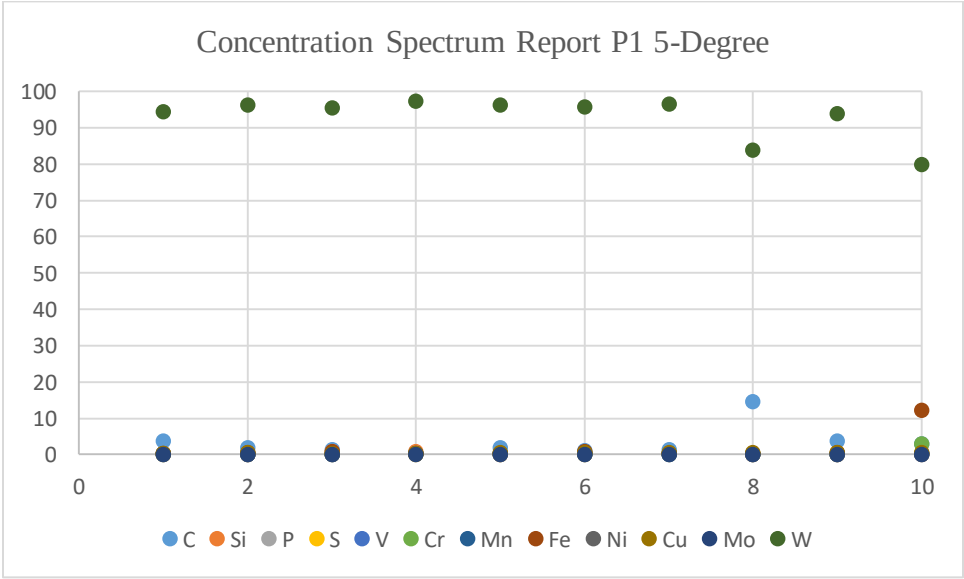

Appendix Figure C. 28 P1 5-Degree Chemistry WHA and D2 Elements

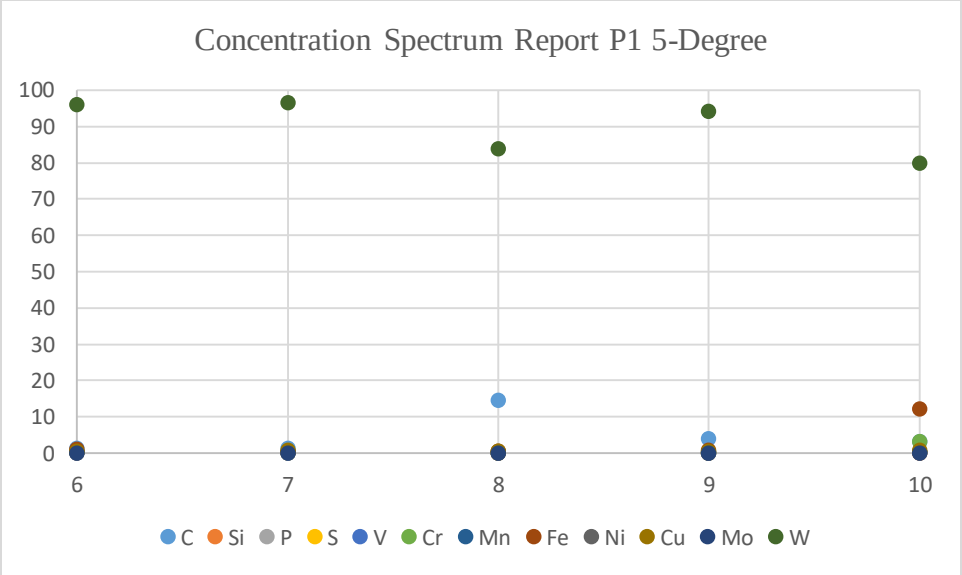

Appendix Figure C. 29 P1 5-Degree Points 6-10 Chemistry WHA and D2 Elements

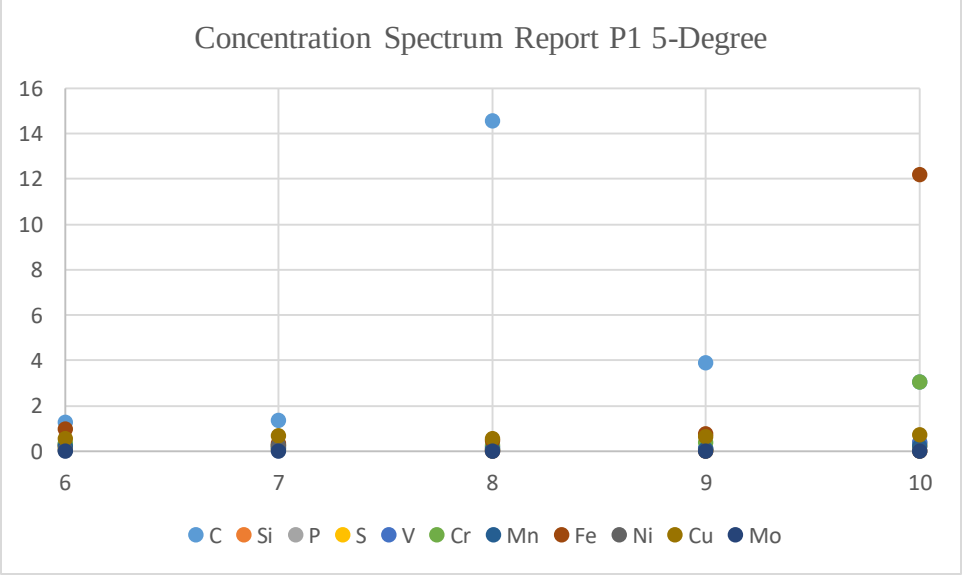

Appendix Figure C. 30 P1 5-Degree Points 6-10 Chemistry WHA and D2 Elements Minus W

Spectrum	C	Si	P	S	V	Cr	Mn	Fe	Ni	Cu	Mo	W
P1_5_degree-1	3.674	0.304	0	0.16	0.326	0.327	0.159	0.254	0	0.228	0	94.569
P1_5_degree-2	1.828	0.112	0.009	0	0.144	0.229	0.105	0.511	0	0.604	0	96.458
P1_5_degree-3	1.538	0.897	0.098	0.177	0.123	0.295	0.211	0.798	0	0.4	0	95.462
P1_5_degree-4	0.283	0.916	0	0	0.254	0.255	0.228	0.445	0	0.283	0	97.336

P1_5_degree-5	1.938	0	0	0	0.175	0.244	0.263	0.442	0	0.594	0	96.344
P1_5_degree-6	1.247	0.255	0.036	0.164	0.297	0.327	0.198	0.963	0.047	0.545	0	95.919
P1_5_degree-7	1.367	0.243	0.024	0.077	0.116	0.253	0.179	0.315	0.24	0.678	0	96.507
P1_5_degree-8	14.542	0	0	0.092	0.167	0.244	0.095	0.456	0	0.523	0	83.88
P1_5_degree-9	3.881	0	0.071	0.03	0.127	0.371	0.059	0.745	0	0.642	0	94.073
P1_5_degree-10	3.048	0	0.369	0.237	0.357	3.056	0.198	12.196	0	0.701	0	79.839
Mean	3.335	0.273	0.061	0.094	0.209	0.56	0.169	1.713	0.029	0.52	0	93.039
Std. Dev.	4.097	0.354	0.114	0.087	0.091	0.878	0.065	3.69	0.076	0.164	0	6.044
Min	0.283	0	0	0	0.116	0.229	0.059	0.254	0	0.228	0	79.839
Max	14.542	0.916	0.369	0.237	0.357	3.056	0.263	12.196	0.24	0.701	0	97.336

Appendix Table C-3 P1 5-Degree EDS 1-10

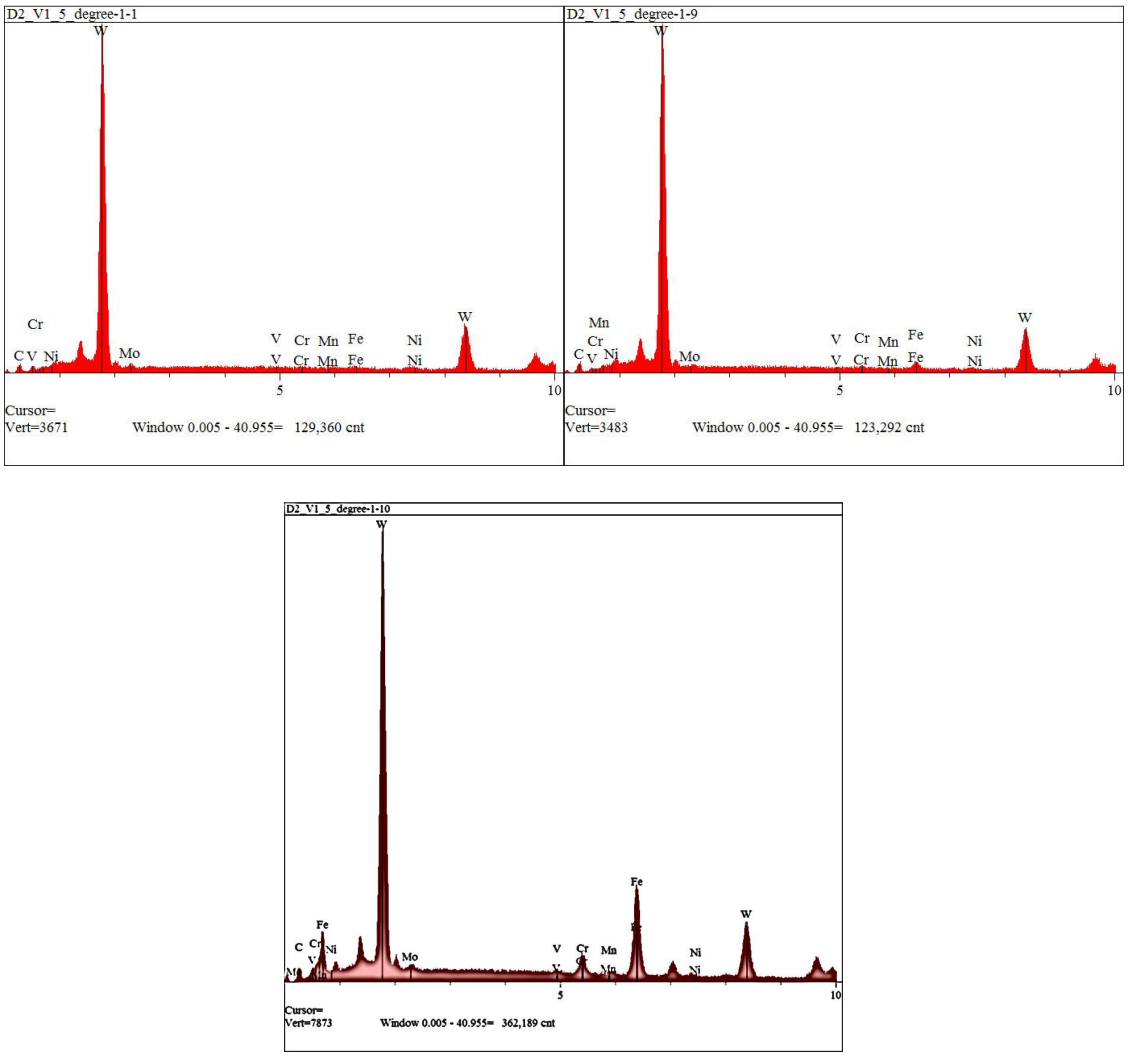

Appendix Figure C. 31 P1 5-Degree EDS Plots 1, 9, 10

P1 10-Degree EDS of Nanoindents

The EDS analysis of the P1 10-degree indents (**Appendix Figure C. 32**) are shown in **Appendix Figure C. 33-34** which are the first to follow intuition. The tabulated concentration values are provided in **Appendix Table C-4**. For this reason all the plots are shown side by side in **Appendix Figure C. 35** and individually in **Appendix Figure C. 36** with point 8 highlighted since it is on the interface. Points 1-4 used a 30 second absorption time while points 5-10 used a 100 second absorption time. The

elemental concentrations from each respective alloy exhibit diffusion couples where higher concentrations on one side of the interface diffuse to the other and vs. including tungsten which has a relative low diffusivity due to its high density. It should also be noted this is the first time oxygen concentration has been traced and the oxygen concentration is zero everywhere but on the interface, indicating an oxide is likely present given the hardness results presented earlier [31] .

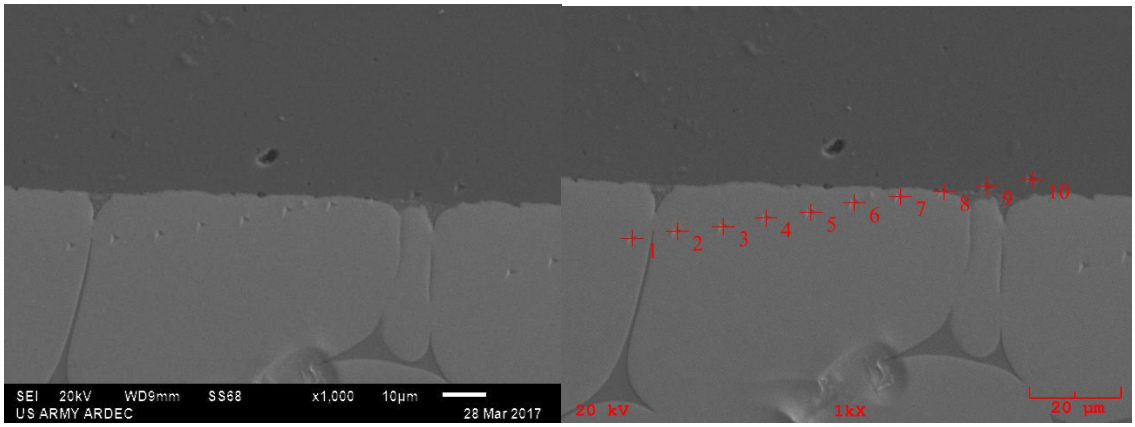

Appendix Figure C. 32 P1 10-Degree EDS

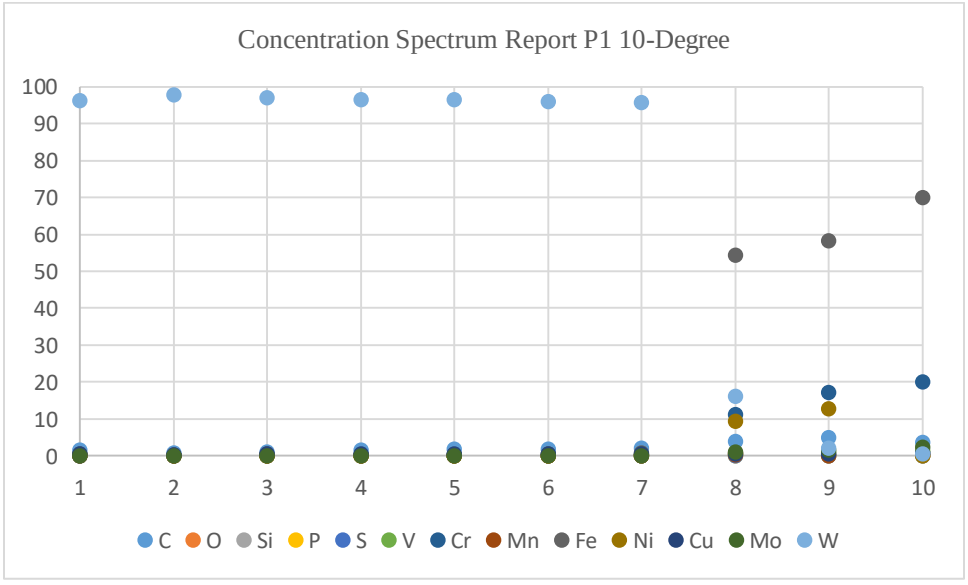

Appendix Figure C. 33 P1 10-Degree Chemistry WHA and D2 Elements

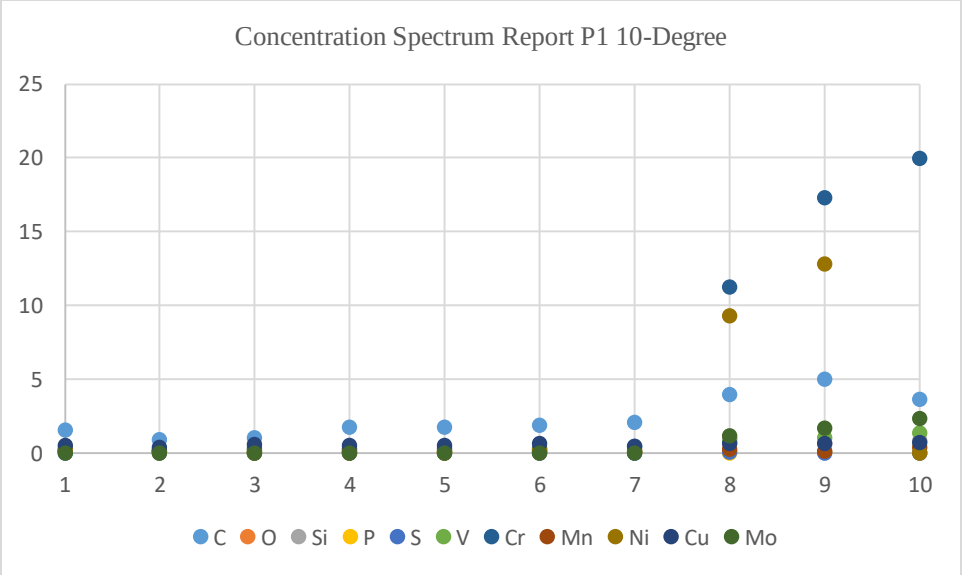

Appendix Figure C. 34 P1 10-Degree Chemistry WHA and D2 Elements Minus W

Spectrum	C	O	Si	P	S	V	Cr	Mn	Fe	Ni	Cu	Mo	W
P_10_degree-1	1.562		0.345	0.082	0	0.135	0.174	0.116	0.56	0.21	0.515	0	96.3
P_10_degree-2	0.884		0.1	0	0	0.114	0.196	0.121	0.273	0.101	0.423	0	97.788
P_10_degree-3	1.04		0	0.076	0	0.166	0.304	0.108	0.627	0.025	0.558	0	97.095
P_10_degree-4	1.728		0.265	0.038	0.023	0.153	0.264	0.066	0.238	0	0.533	0	96.691
P_10_degree-5	1.771		0.212	0.049	0	0.096	0.297	0.128	0.371	0	0.508	0	96.569
P_10_degree-6	1.859		0.203	0.011	0	0.118	0.354	0.076	0.628	0.199	0.629	0	95.923
P_10_degree-7	2.075		0	0.039	0	0.148	0.461	0.063	0.748	0.224	0.48	0	95.761
P_10_degree-8	3.955	0.968	0.879	0.008	0.068	0.717	11.253	0.255	54.421	9.317	0.673	1.156	16.331
P_10_degree-9	5.026		0.66	0.097	0	1.02	17.287	0.144	58.367	12.834	0.643	1.68	2.241
P_10_degree-10	3.638		0.855	0.062	0	1.398	19.99	0.378	70.011	0	0.733	2.327	0.608

Appendix Table C-4 P1 10-Degree EDS

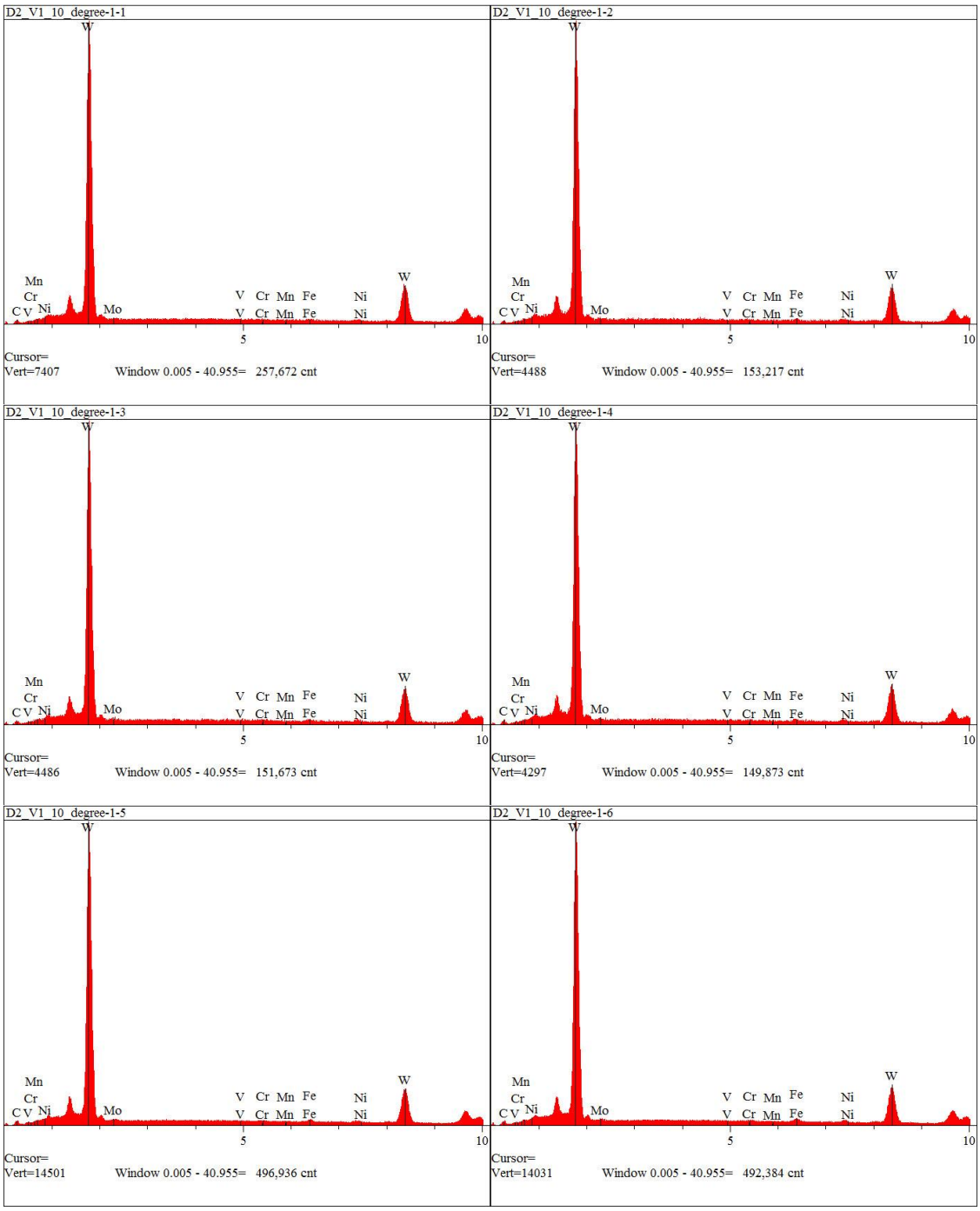
D2_V1_10_degree-1-1
W
Mn
Cr
C V Ni
Mo
V Cr Mn Fe
V Cr Mn Fe
Ni
Ni
W
5
10
Cursor=
Vert=7407
Window 0.005 - 40.955= 257,672 cnt
D2_V1_10_degree-1-2
W
Mn
Cr
C V Ni
Mo
V Cr Mn Fe
V Cr Mn Fe
Ni
Ni
W
5
10
Cursor=
Vert=4488
Window 0.005 - 40.955= 153,217 cnt
D2_V1_10_degree-1-3
W
Mn
Cr
C V Ni
Mo
V Cr Mn Fe
V Cr Mn Fe
Ni
Ni
W
5
10
Cursor=
Vert=4486
Window 0.005 - 40.955= 151,673 cnt
D2_V1_10_degree-1-4
W
Mn
Cr
C V Ni
Mo
V Cr Mn Fe
V Cr Mn Fe
Ni
Ni
W
5
10
Cursor=
Vert=4297
Window 0.005 - 40.955= 149,873 cnt
D2_V1_10_degree-1-5
W
Mn
Cr
C V Ni
Mo
V Cr Mn Fe
V Cr Mn Fe
Ni
Ni
W
5
10
Cursor=
Vert=14501
Window 0.005 - 40.955= 496,936 cnt
D2_V1_10_degree-1-6
W
Mn
Cr
C V Ni
Mo
V Cr Mn Fe
V Cr Mn Fe
Ni
Ni
W
5
10
Cursor=
Vert=14031
Window 0.005 - 40.955= 492,384 cnt

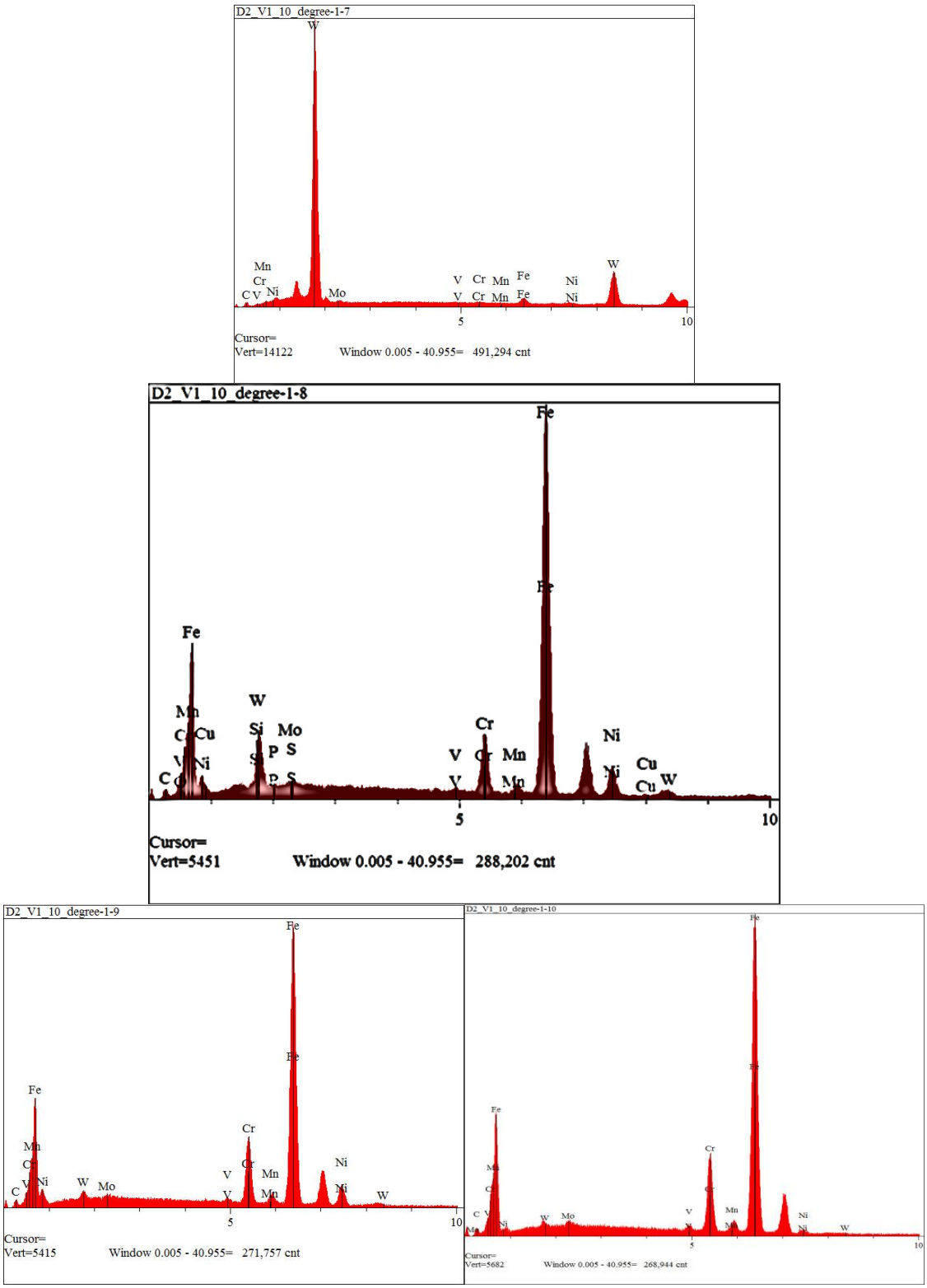

Appendix Figure C. 35 P1 10-Degree EDS Plots #8 is on the Interface

P1 15-Degree EDS of Nanoindents

EDS analysis of P1 15-degree (**Appendix Figure C. 36**) is shown in **Appendix Figure C. 37**, but is not as straight forward as the P1 10-degree analysis. This is because points 6, and 7 are on the interface while the 8th is just adjacent to a void. Still the results follow intuition and diffusion theory [39]with higher concentrations dropping off as alloy transition occurs at the interface. Interestingly, silicon and molybdenum both do not breach the interface, remaining within the D2 alloy while the largest sulfur and phosphorus concentrations are found on the interface at point 6 as shown in **Appendix Table C-5**. All EDS concentration plots for P1 15-degree were derived from 30 second absorption times and shown in **Appendix Figure C. 38** and **Appendix Figure C. 39**.

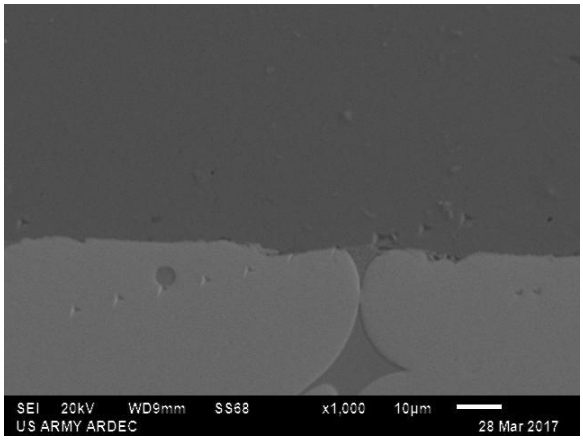

Appendix Figure C. 36 P1 15-Degree EDS

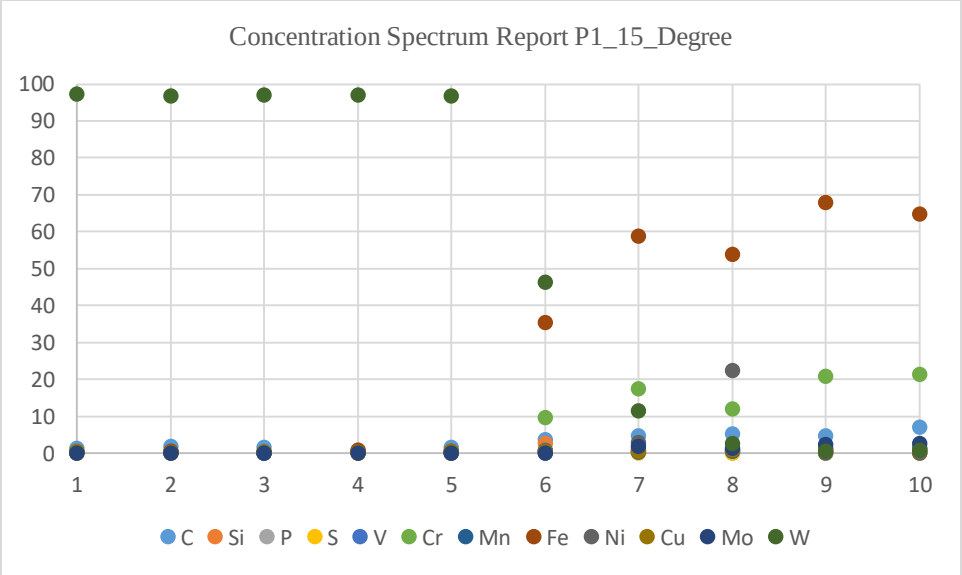

Appendix Figure C. 37 P1 15-Degree Chemistry WHA and D2 Elements

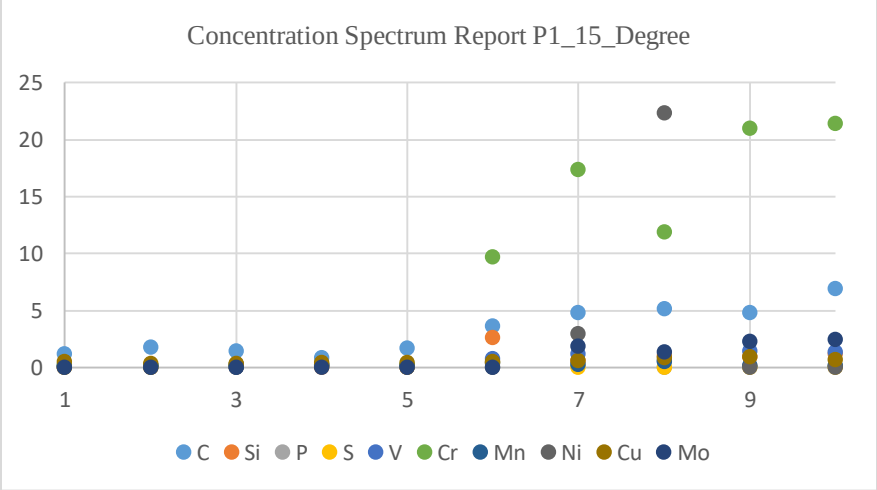

Appendix Figure C. 38 P1 15-Degree Chemistry WHA and D2 Elements Minus W

Spectrum	C	Si	P	S	V	Cr	Mn	Fe	Ni	Cu	Mo	W
P1_15_degree_1	1.198	0	0.024	0	0.197	0.297	0.138	0.283	0	0.54	0	97.323
P1_15_degree_2	1.756	0	0.025	0	0.175	0.157	0.146	0.559	0	0.365	0	96.819
P1_15_degree_3	1.467	0	0.134	0.094	0.096	0.264	0.055	0.341	0.254	0.354	0	96.94
P1_15_degree_4	0.885	0	0.16	0.072	0.213	0.273	0.226	0.744	0.067	0.394	0	96.966
P1_15_degree_5	1.674	0	0.108	0	0.124	0.247	0.171	0.422	0.015	0.446	0	96.793
P1_15_degree_6	3.658	2.653	0.33	0.428	0.769	9.671	0.395	35.337	0	0.504	0	46.253
P1_15_degree_7	4.784	0.643	0.279	0	1.16	17.321	0.266	58.733	2.991	0.629	1.868	11.325
P1_15_degree_8	5.124	0.993	0.048	0	0.607	11.918	0.546	53.741	22.313	0.856	1.374	2.481

P1_15_degree_9	4.793	0.976	0.094	0	1.408	20.932	0.192	67.974	0	0.951	2.28	0.4
P1_15_degree_10	6.914	1.198	0.09	0	1.394	21.374	0.213	64.84	0	0.718	2.484	0.775

Appendix Table C-5 P1 15 Degree EDS

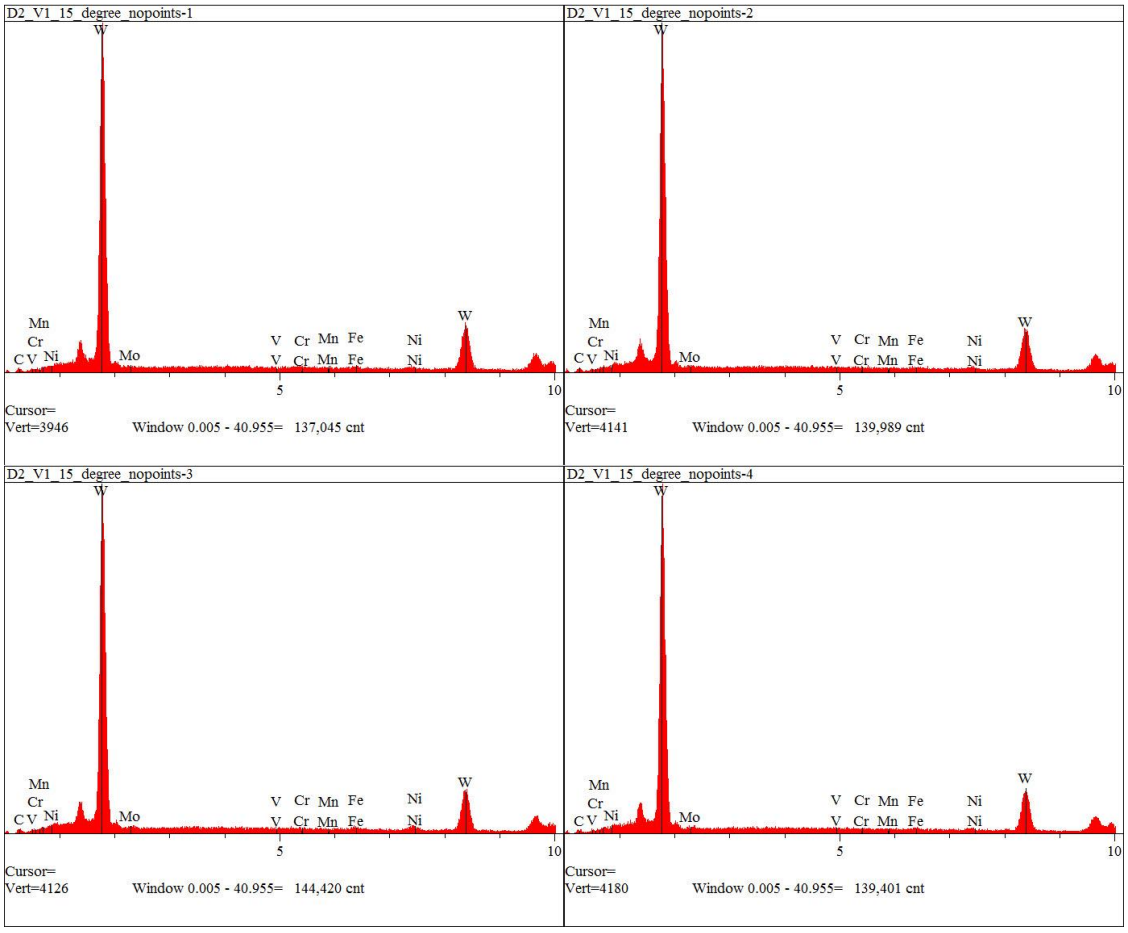

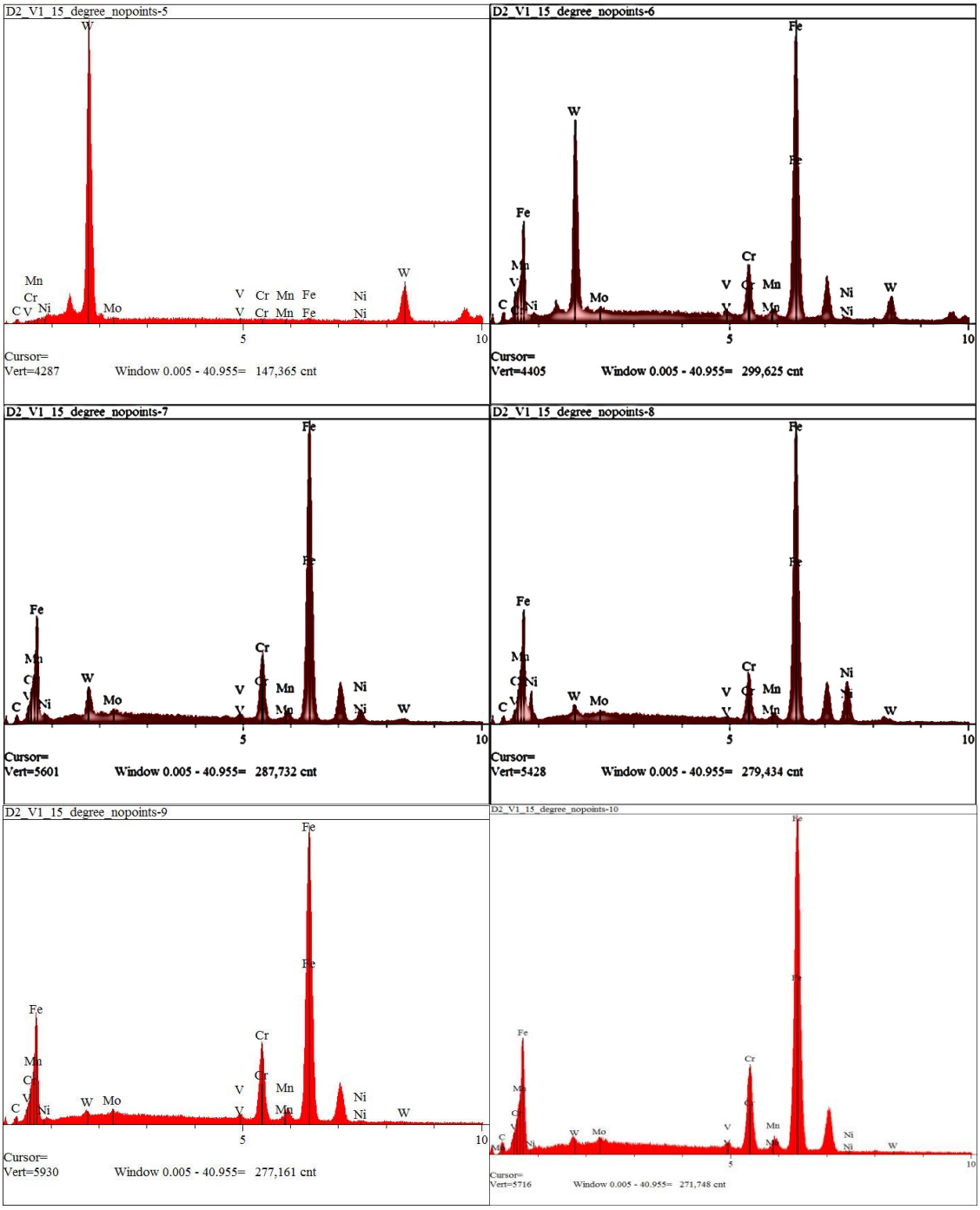

Appendix Figure C. 39 P1 15-Degree Individual EDS Plots

D2- P2

P2 - V 10x4 Grid EDS Taken Horizontally of Nanoindents

Initially P2-V was analyzed horizontally. The SEM image in **Appendix Figure C. 40** at 800 power shows the nanoindenter left clean crisp indents in both the D2 steel on the left and in the WHA alloy on the right creating the 10x4 matrix of data points every 10 µm apart just like all the P1 indents and the remainder of the P2 indents. Though not mentioned in the SEM section, these nanoindents were clean and crisp thanks to a new tip on the nanoindenter. Though none of the indents are on the diffusion interface as hoped, the P2-V indent 40 lies on a tungsten and matrix interface as well as indent 39 on the edge of the tungsten which will provide insight on these boundaries. Nanoindents 2, 3, 6, and 7 which correspond to EDS points 19, 20, 29 and 30 almost perfect surround a tungsten grain within the WHA.

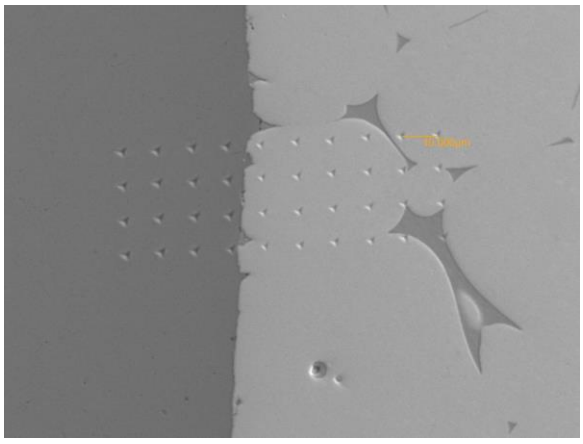

Appendix Figure C. 40 P2-V 10x4 Grid Shown Horizontally Nanoindents Measured x800 measured

In **Appendix Figure C. 41**, at 1300 power it is more clear than the x850 image in chapter 4 that the nanoindents are not orthogonal to this portion of the diffusion layer of interest. At higher magnification the depth of the indents into D2 vs the tungsten starts to become more noticeable which makes perfect sense given D2's lower hardness and

higher modulus of elasticity as confirmed by the nanoindentation and also confirms the results in chapter 4 are logical.

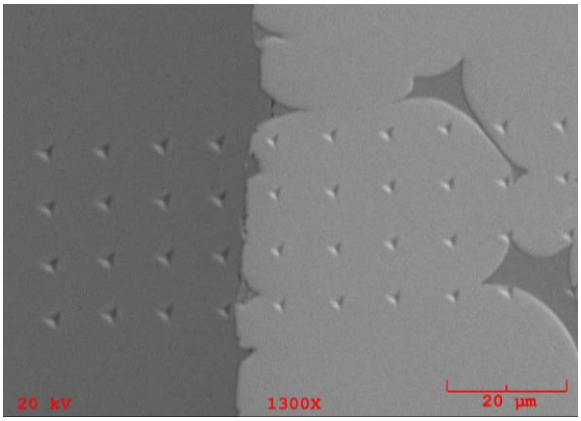

Appendix Figure C. 41 P2-V 10x4 Grid Shown Horizontally x1300

EDS was then taken at the specific nanoindentation points to have corresponding chemistry to correlate to the mechanic properties collected from the nanoindentation trials just as before. The numbering scheme for EDS on nanoindents follow the left to right, top to bottom numbering sequence for all measurements EDS was taken on the first 8 points in the first row as shown in **Appendix Figure C. 42**. **Appendix Figure C. 43** shows the EDS plots for the first 8 points and clearly indicates a transition in elemental concentration and phase between points 4 and 5.

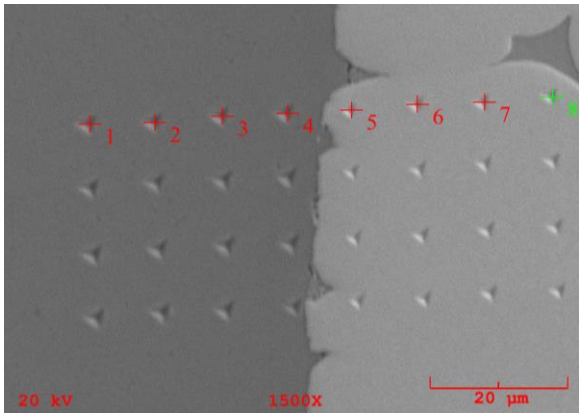

Appendix Figure C. 42 10x4 Grid Shown Horizontally EDS Taken Horizontally 1500x

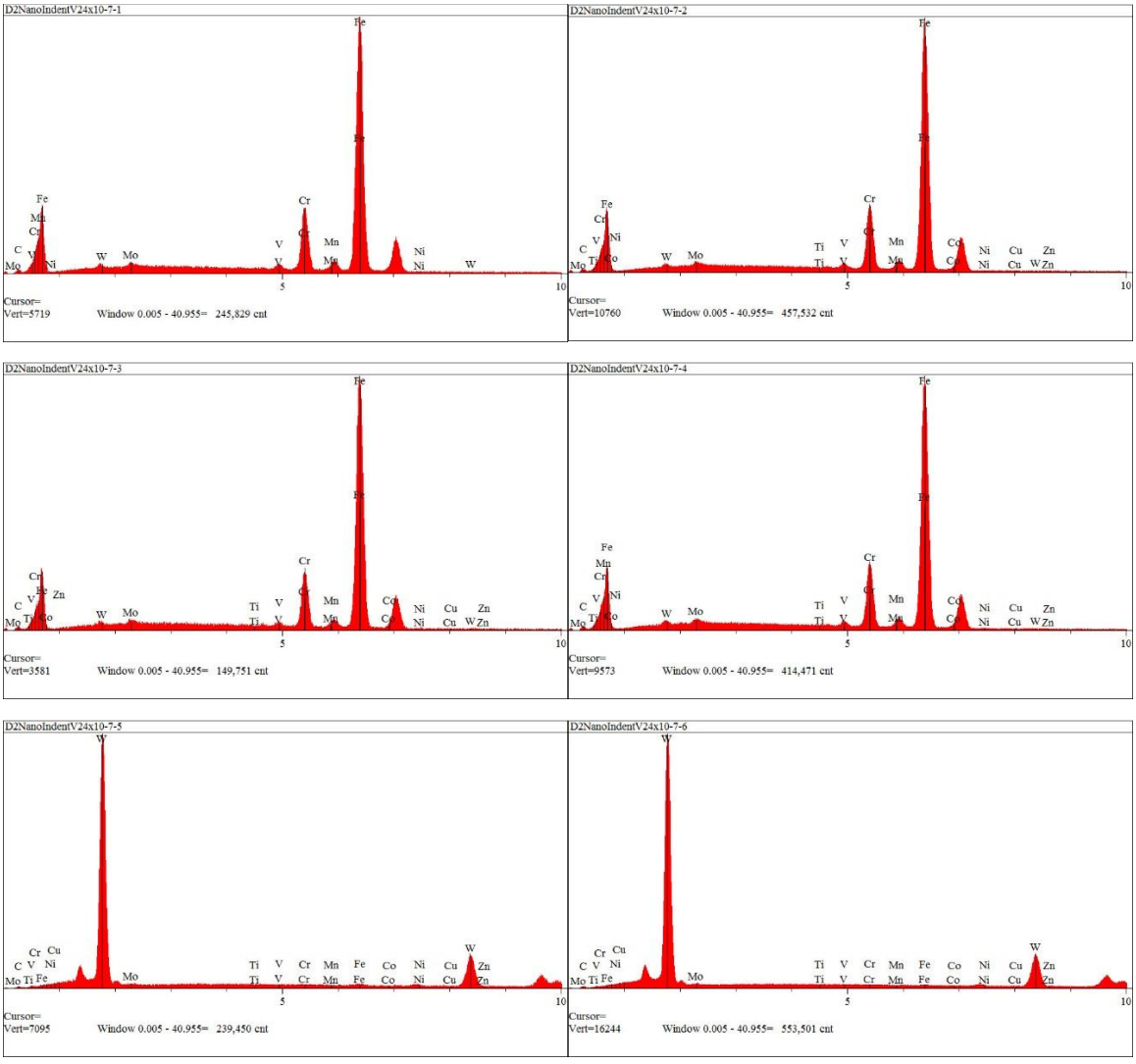

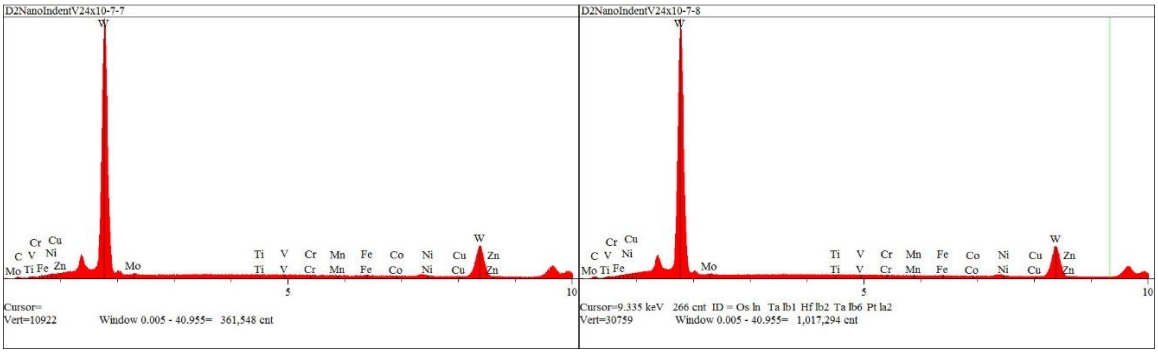

Appendix Figure C. 43 P2-V 10x4 EDS Taken Horizontally, EDS Points 1-8

It was then decided to take all EDS measurements on all 40 points so a side-by-side analysis could compare the P1 results to the P2 results. The numbering scheme for the EDS analysis is shown in **Appendix Figure C. 44** and **Appendix Table C-6** provides the individual results for each reading. The first 10 indents used a 100 second absorption times while the next 30 EDS points were the result of only 30 second absorption times.

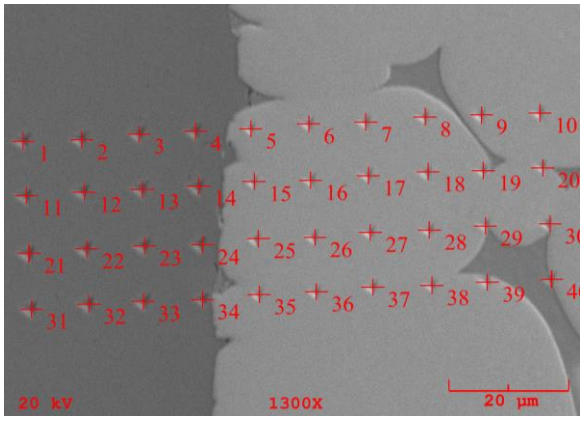

Appendix Figure C. 44 P2-V 10x4 Grid Shown Horizontally with EDS Points

Spectrum	C	Si	P	S	V	Cr	Mn	Fe	Co	Ni	Cu	Zn	Mo	W
P2_V2_4x10-1	4.115				0.953	13.37	0.173	77.268	0.54	0.144	0.11	0.131	1.937	1.229
P2_V2_4x10-2	3.318				0.838	12.12	0.076	79.788	0.616	0.154	0.109	0.114	1.829	0.98
P2_V2_4x10-3	3.226				0.718	10.58	0.071	82.724					1.694	0.989
P2_V2_4x10-4	3.126				0.865	12.26	0.267	80.141					1.994	1.346
P2_V2_4x10-5	1.709							0.085		0.158				98.048
P2_V2_4x10-6	1.551							0.136		0.127				98.186
P2_V2_4x10-7	1.456	0.516	0.064	0	0.056	0.115	0.083	0.152		0.111	0.067		0	97.38

P2_V2_4x10-8	1.278	0.329	0.062	0.003	0.071	0.068	0.052	0.201		0.18	0.099		0	97.658
P2_V2_4x10-9	1.849	0.148	0.029	0.015	0.052	0.093	0.074	0.109		0.108	0.117		0	97.406
P2_V2_4x10-10	1.099	0.236	0.04	0	0.075	0.111	0.061	0.229		0.198	0.081		0	97.87
P2_V2_4x10-11	2.67	0.904	0	0	1.349	19.97	0.08	70.787		0	0.49		2.562	1.193
P2_V2_4x10-12	1.382	1.126	0.108	0	1.337	20.45	0.182	71.599		0	0.223		3.089	0.5
P2_V2_4x10-13	1.648	0.788	0.035	0.105	1.512	21.93	0.301	70.882		0	0.351		1.975	0.471
P2_V2_4x10-14	2.217	1.058	0.063	0	1.627	21.09	0.058	71.123		0	0.248		2.174	0.347
P2_V2_4x10-15	0.27	0.561	0.004	0	0.123	0.277	0.082	0.32		0.176	0.171		0	98.016
P2_V2_4x10-16	0.49	0.187	0.128	0	0.113	0.177	0.061	0.224		0.097	0.092		0	98.431
P2_V2_4x10-17	0.878	0.149	0.117	0.015	0.165	0.172	0.111	0.257		0.133	0.098		0	97.904
P2_V2_4x10-18	0.766	0.231	0.039	0.059	0.082	0.216	0.14	0.125		0.104	0.24		0	97.997
P2_V2_4x10-19	0.641	0.456	0.134	0	0.105	0.076	0.076	0.013		0.11	0.104		0	98.286
P2_V2_4x10-20	0.709	0.069	0.126	0.049	0.111	0.14	0.06	0.167		0.059	0.22		0	98.29
P2_V2_4x10-21	1.798	0.985	0.087	0	1.283	20.26	0.307	71.909		0	0.323		2.82	0.233
P2_V2_4x10-22	1.088	2.125	0.076	0	1.102	19.45	0.281	72.409		0	0.654		2.341	0.472
P2_V2_4x10-23	2.552	0.859	0.083	0	1.321	21	0.087	70.54		0	0.342		2.729	0.49
P2_V2_4x10-24	2.315	0.802	0	0	1.61	22.26	0.424	69.436		0	0.254		2.587	0.31
P2_V2_4x10-25	0.757	0.228	0	0	0.171	0.28	0.116	0.153		0.143	0.117		0	98.035
P2_V2_4x10-26	0.534	0.199	0	0.005	0.103	0.154	0.043	0.18		0.237	0.111		0	98.435
P2_V2_4x10-27	0.574	0.345	0.066	0	0.069	0.102	0.069	0.187		0.204	0.159		0	98.223
P2_V2_4x10-28	0.375	0.184	0	0	0.113	0.103	0.124	0.081		0.149	0.121		0	98.75
P2_V2_4x10-29	0.556	0.412	0.062	0.006	0.096	0.157	0.089	0.117		0.108	0.129		0	98.267
P2_V2_4x10-30	0.647	0.32	0	0	0.109	0.122	0.115	0.086		0.109	0.099		0	98.394
P2_V2_4x10-31	2.021	0.938	0.189	0	1.533	21.03	0.312	70.48		0	0.391		2.443	0.665
P2_V2_4x10-32	2.596	1.068	0.126	0	1.611	22.39	0.377	68.182		0	0.297		2.94	0.415
P2_V2_4x10-33	2.392	1.137	0.11	0	1.224	20.83	0.15	70.529		0	0.337		2.87	0.426
P2_V2_4x10-34	2.678	1.031	0.07	0	1.476	22.78	0.347	68.616		0	0.154		2.626	0.224
P2_V2_4x10-35	0.781	0	0.043	0.063	0.245	0.487	0.15	0.983		0.422	0.132		0	96.694
P2_V2_4x10-36	0.772	0	0.067	0	0.075	0.106	0.103	0.102		0.247	0.114		0	98.413
P2_V2_4x10-37	0.808	0.315	0.014	0	0.155	0.134	0.163	0.049		0.096	0.207		0	98.06
P2_V2_4x10-38	0.797	0	0.057	0.004	0.093	0.199	0.161	0.11		0.207	0.193		0	98.179
P2_V2_4x10-39	0.667	0.248	0.225	0.052	0.226	0.166	0.096	0.239		0.44	0.145		0	97.495
P2_V2_4x10-40	1.342	0.255	0.288	0.092	0.124	0.166	0.239	7.115		47.686	0.406		0	42.288

Appendix Table C-6 Table P2-V 10x4 EDS Concentrations Taken Horizontally

The concentration spectrum for each point are shown in **Appendix Figure C. 45** for all the elements whose chemistry makes up the WHA and D2 alloy. The chromium, iron, and tungsten concentrations again make up the majority of the material. The

concentration spectrum report for points 11-20 of P2-V horizontally are shown in **Appendix Figure C. 46** which behave as expected. Since the WHA was sintered prior to the FAST process it would be expected only diffusion could allow elemental migration.

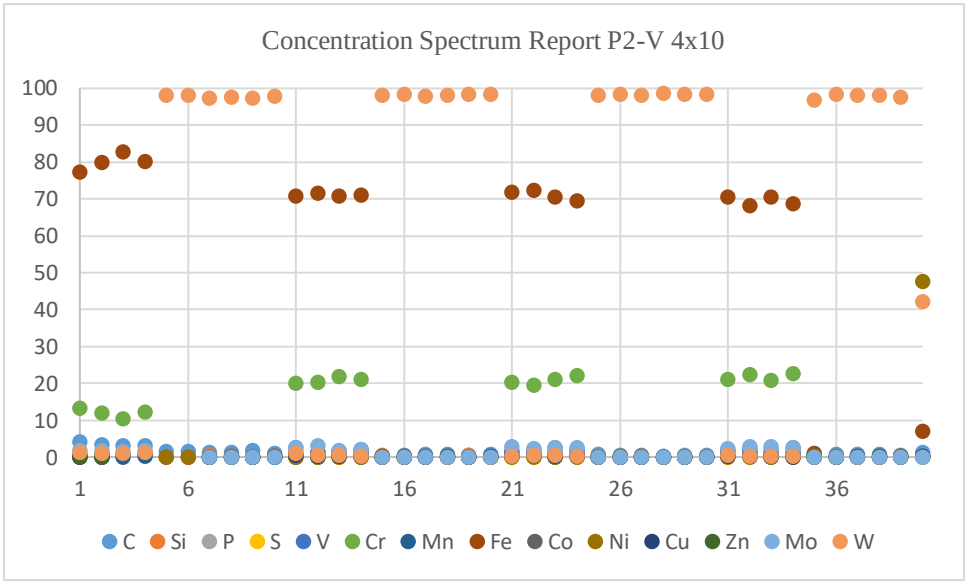

Appendix Figure C. 45 P2-V 10x4 Grid (EDS Taken Horizontally) Chemistry WHA and D2 Elements

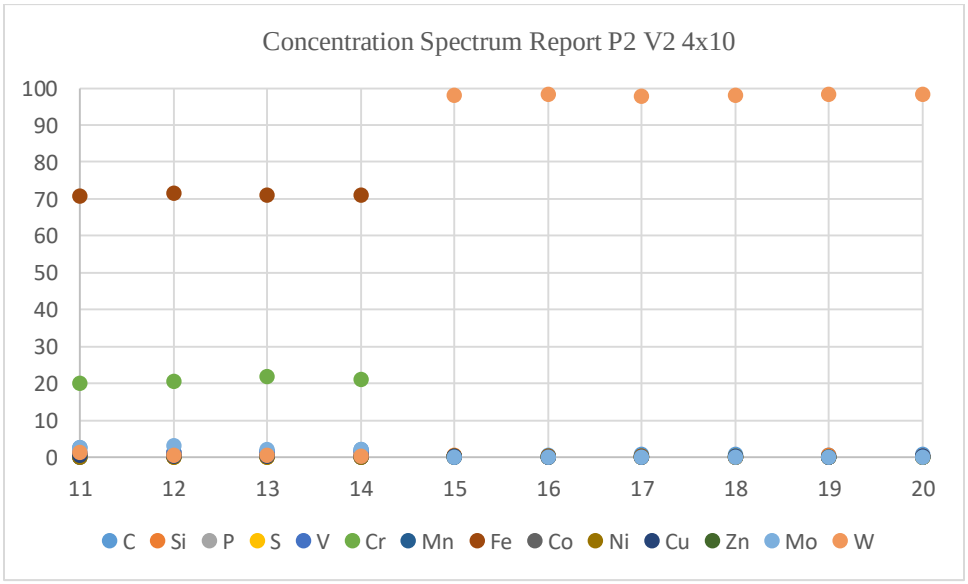

Appendix Figure C. 46 P2-V 10x4 Grid (EDS Taken Horizontally) Points 11-20 Chemistry WHA and D2 Elements

P2-V EDS Taken Vertically of Nanoindents

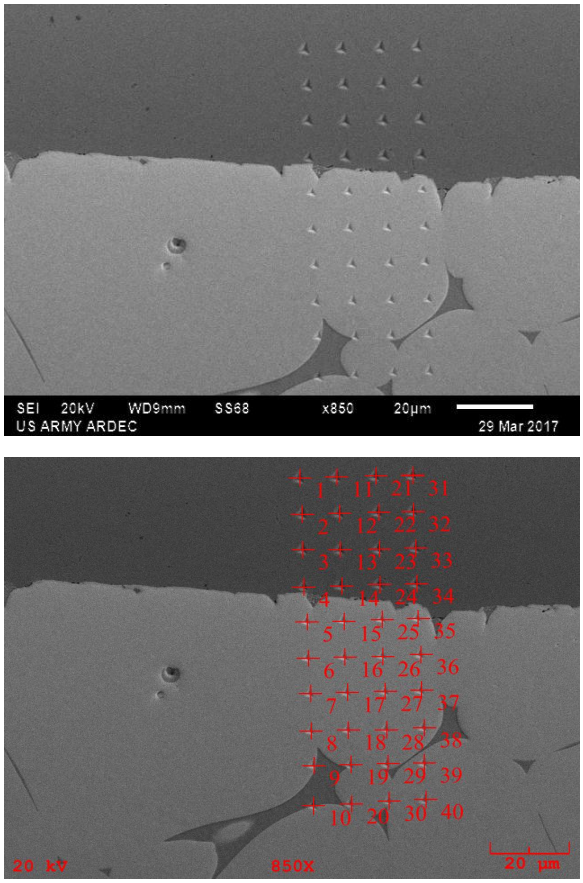

Appendix Figure C. 47 P2-V 10x4 Nanoindents (top) EDS points (bottom)

Given the results from the P1 analysis and those from the horizontal analysis of the P2-V using the 10x4 EDS mapping, it was decided to understand if additional elements may be diffusing across the interface, therefore EDS measurements were taken again on the P2-V 10x4 indents with additional elements which may be forming oxides, carbides, or influence toughness. The individual concentration values are shown in **Appendix Table C-7**. Again molybdenum, silicon, and nitrogen do not seem to migrate across the interface, while sulfur and phosphorous seem to congregate at the interface. **Appendix Figure C. 48** shows the overall concentration report of all the EDS points which were taken while **Appendix Figure C. 49** is from the vertical and **Appendix**

Figure C. 50 is from the horizontal analysis so there is a one-to-one comparison for repeatability as this is the same row of indents. It is interesting that they are not identical and the horizontal analysis resulted in higher chromium concentrations than the vertical but are close to the average of 16.2 percent found during the P2-Marker analysis. Regardless of accuracy the trend is the same for both analysis and variation could be attributed to the fact some material may have been ablated or the focus of the x-ray area between the two measurements could have been different give then spot size.

Spectrum	C	N	O	Si	P	S	V	Cr	Mn	Fe	Co	Ni	Cu	Mo	W
P2_V2_10x4-1	5.327	0.617	0.119	0.475	0	0	0.781	10.814	0.358	78.084	0.471	0.411	0.264	1.597	0.68
P2_V2_10x4-2	5.863	0.231	0.617	0.86	0.059	0	0.824	11.268	0.404	76.775	0.514	0.217	0.351	1.845	0.175
P2_V2_10x4-3	5.288	0.529	0.27	0.932	0.138	0	0.869	10.798	0.112	78.338	0.524	0.152	0.249	1.671	0.129
P2_V2_10x4-4	4.332	0.189	0.33	0.202	0.165	0.237	0.445	6.734	0.275	38.264	0.21	3.516	0.139	0.405	44.557
P2_V2_10x4-5	3.068	0	0.482	0	0.115	0.011	0.154	0.38	0.117	0.794	0.086	0.293	0.152	0	94.348
P2_V2_10x4-6	2.999	0	0.763	0	0.054	0.04	0.067	0.248	0.066	0.632	0.166	0.239	0.183	0	94.544
P2_V2_10x4-7	3.076	0	0.451	0	0.141	0	0.161	0.243	0.135	0.603	0.141	0.3	0.161	0	94.589
P2_V2_10x4-8	3.309	0	0.79	0	0.056	0	0.133	0.321	0.114	0.638	0.289	0.534	0.176	0	93.64
P2_V2_10x4-9	4.312	0	1.099	0	0.111	0.055	0.215	0.367	0.147	2.401	0.226	12.554	0.147	0	78.367
P2_V2_10x4-10	4.365	0	1.243	0	0.151	0.033	0.071	0.223	0.173	3.513	0.247	21.067	0.174	0	68.74
P2_V2_10x4-11	6.29	0.535	1.088	0.94	0.03	0	0.732	10.906	0.272	76.493	0.281	0.127	0.302	1.637	0.366
P2_V2_10x4-12	6.571	1.087	0	0.933	0.093	0	0.671	10.806	0.234	76.483	0.344	0.374	0.225	1.942	0.236
P2_V2_10x4-13	5.927	0.536	0	0.813	0	0	0.682	11.283	0.335	76.808	0.29	0.219	0.423	1.984	0.701
P2_V2_10x4-14	3.783	0.239	1.263	0	0.059	0.365	0.59	5.766	0.148	30.765	0.203	0.137	0.115	0	56.567
P2_V2_10x4-15	3.303	0	0.818	0	0.099	0.024	0.15	0.262	0.164	0.838	0.193	0.467	0.147	0	93.534
P2_V2_10x4-16	3.293	0	0.503	0	0.12	0.055	0.135	0.4	0.21	0.712	0.21	0.165	0.099	0	94.099
P2_V2_10x4-17	3.062	0	0.802	0	0.148	0.082	0.075	0.2	0.077	0.712	0.098	0.144	0.135	0	94.464
P2_V2_10x4-18	3.187	0	0.787	0	0.064	0.003	0.068	0.29	0.094	0.7	0.183	0.208	0.248	0	94.168
P2_V2_10x4-19	3.353	0	0.895	0	0	0	0.103	0.153	0.204	0.732	0.167	0.383	0.072	0	93.937
P2_V2_10x4-20	3.222	0	0.974	0	0.133	0	0.103	0.233	0.222	0.718	0.18	0.565	0.137	0	93.512
P2_V2_10x4-21	6.42	0.971	0.266	0.988	0.046	0.101	0.81	10.724	0.252	76.621	0.512	0.274	0.344	1.378	0.293
P2_V2_10x4-22	6.498	1.09	0	0.81	0.215	0	0.592	9.98	0.081	77.655	0.369	0.332	0.226	1.345	0.807
P2_V2_10x4-23	6.317	0.507	1.269	0.729	0	0.112	0.715	10.63	0.1	76.924	0.501	0.145	0.323	1.11	0.618
P2_V2_10x4-24	3.934	0.433	0	0	0.143	0.37	0.713	7.97	0.069	41.723	0.204	0.233	0.198	0.277	43.735
P2_V2_10x4-25	3.026	0	0.935	0	0.06	0.046	0.127	0.227	0.121	0.906	0.176	0.252	0.138	0	93.989
P2_V2_10x4-26	3.246	0	0.831	0	0.193	0	0.142	0.212	0.183	0.694	0.127	0.23	0.178	0	93.963
P2_V2_10x4-27	3.086	0	0.526	0	0.092	0.01	0.195	0.225	0.107	0.718	0.108	0.211	0.114	0	94.609
P2_V2_10x4-28	3.39	0	0.682	0	0.103	0.079	0.071	0.276	0.238	0.687	0.178	0.402	0.131	0	93.763
P2_V2_10x4-29	3.326	0	0.851	0	0.157	0.015	0.103	0.392	0.106	1.258	0.169	4.331	0.096	0	89.196
P2_V2_10x4-30	3.203	0	0.817	0	0.16	0	0.106	0.204	0.162	0.539	0.092	0.596	0.162	0	93.96

P2_V2_10x4-31	6.76	0.484	0.671	0.827	0.086	0	0.853	11.241	0.203	75.516	0.247	0.22	0.273	2.067	0.553
P2_V2_10x4-32	6.7	0.738	0.585	0.878	0.191	0	0.566	10.413	0	76.984	0.441	0.236	0.238	1.773	0.258
P2_V2_10x4-33	5.544	0.724	1.375	0.783	0.095	0	0.887	11.2	0.237	76.053	0.279	0.166	0.323	1.713	0.622
P2_V2_10x4-34	5.163	0.232	0.724	0.824	0.024	0	0.446	9.223	0.287	80.967	0.309	0.201	0.269	1.169	0.162
P2_V2_10x4-35	4.551	0.21	0	1.215	0.02	0.059	0.413	8.099	0.413	79.877	0.31	1.105	0.249	0.631	2.847
P2_V2_10x4-36	3.455	0	1.02	0	0.076	0	0.124	0.286	0.131	0.935	0.095	0.229	0.106	0	93.542
P2_V2_10x4-37	3.013	0	0.759	0	0.063	0	0.122	0.301	0.086	1.103	0.109	0.244	0.075	0	94.125
P2_V2_10x4-38	3.443	0	0.764	0	0.051	0.085	0.123	0.257	0.13	0.903	0.127	0.278	0.208	0	93.629
P2_V2_10x4-39	3.271	0	0.759	0	0.173	0.187	0.149	0.406	0.132	0.831	0.089	0.346	0.242	0	93.415
P2_V2_10x4-40	4.048	0	1.251	0	0.097	0	0.126	0.307	0.226	1.318	0.157	2.841	0.133	0	89.495

Appendix Table C-7 P2-V 10x4 EDS Concentrations Taken Vertically

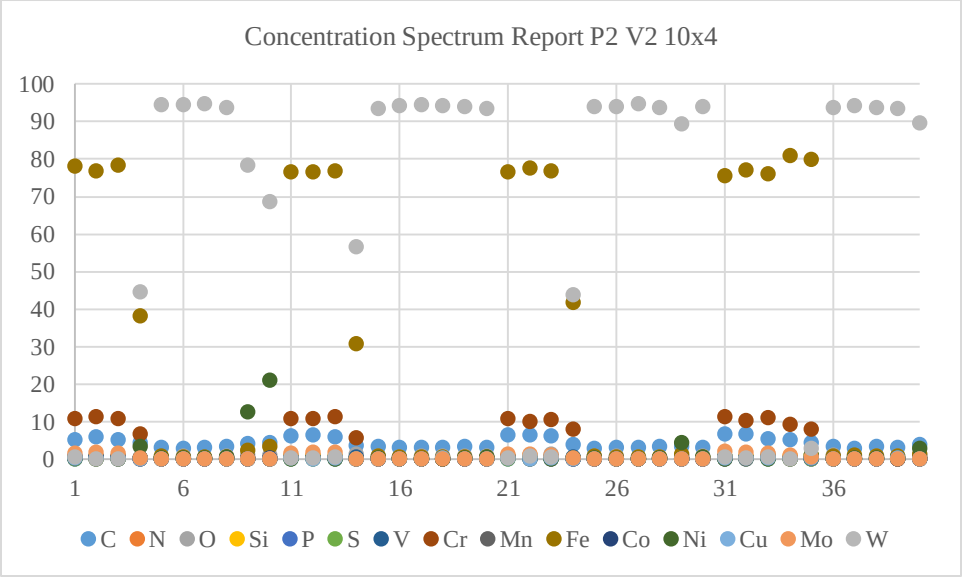

Appendix Figure C. 48 P2-V 10x4 Grid (EDS Taken Vertically) Chemistry WHA and D2 Elements

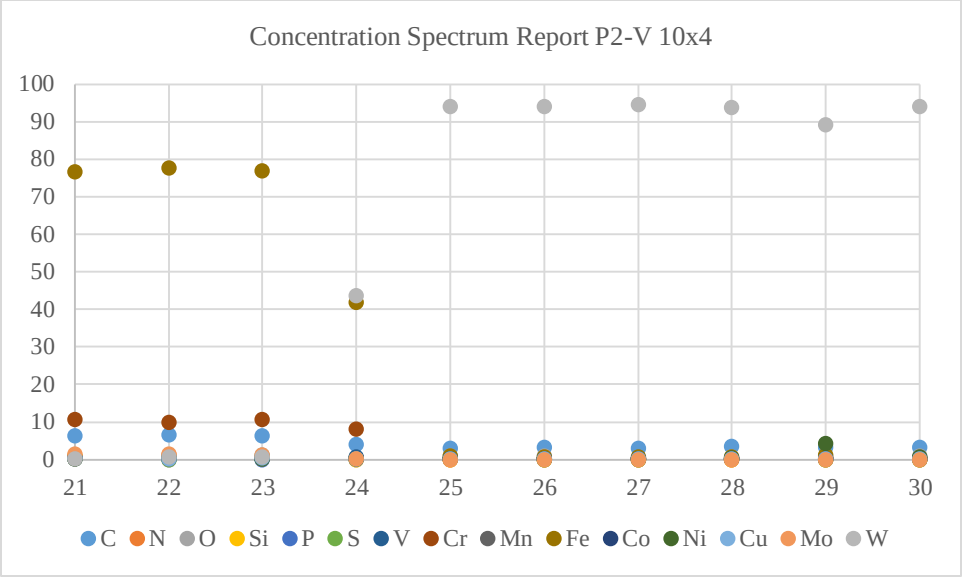

Appendix Figure C. 49 P2-V 10x4 Grid (EDS Taken Vertically) Points 21-30 Chemistry WHA and D2 Elements

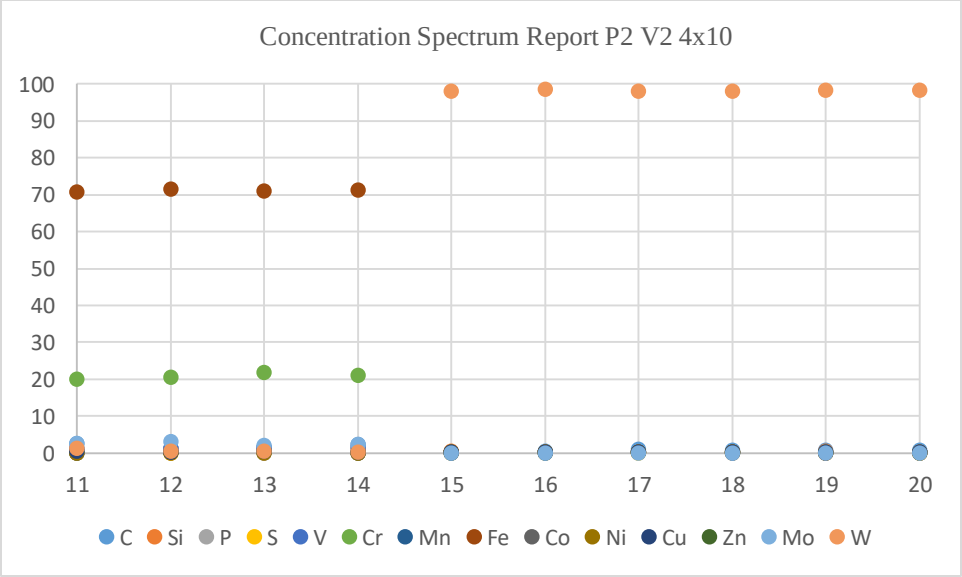

Appendix Figure C. 50 P2-V 4x10 Grid (EDS Taken Horizontally) Points 11-20 Chemistry WHA and D2 Elements

Instead of analyzing the same trends as before it was decided to show how oxygen, nitrogen, and carbon concentrations varied and are shown in **Appendix Figure C. 51, 51 and 53** respectively. Nitrogen does not diffuse across the interface at all while higher concentrations of oxygen seem to be present in the WHA than in the D2 and vice

versa carbon. This could suggest oxygen is scavenged in the WHA to create tungsten oxides while carbon's diffusion could be creating tungsten carbides given the hardness increase as the interface is approached and higher hardness than $W_{25}O_{75}$ values [49]. The individual EDS plots are shown in **Appendix Figure C. 54** to represent the 10x4 grid to understand how the phases and concentrations change across the interface. In both the horizontal and vertical analysis of P2-V, counts were well over 150,000 suggesting an accurate representation of the trend.

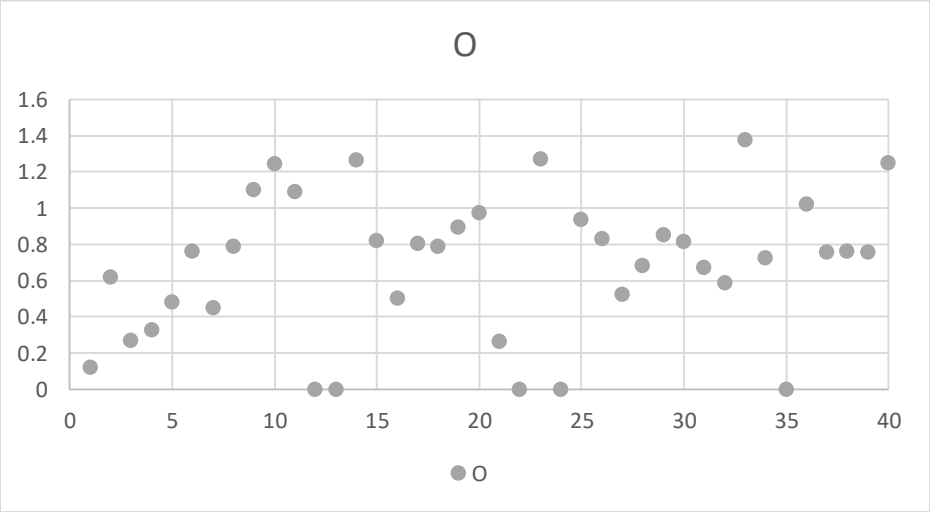

Appendix Figure C. 51 P2-V 10x4 Grid (EDS Taken Vertically) Oxygen Concentration

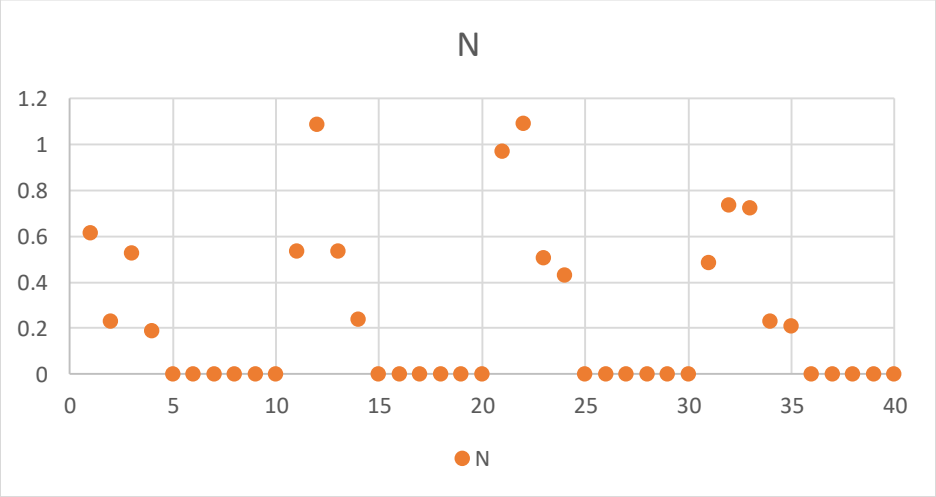

Appendix Figure C. 52 P2-V 10x4 Grid (EDS Taken Vertically) Nitrogen Concentration

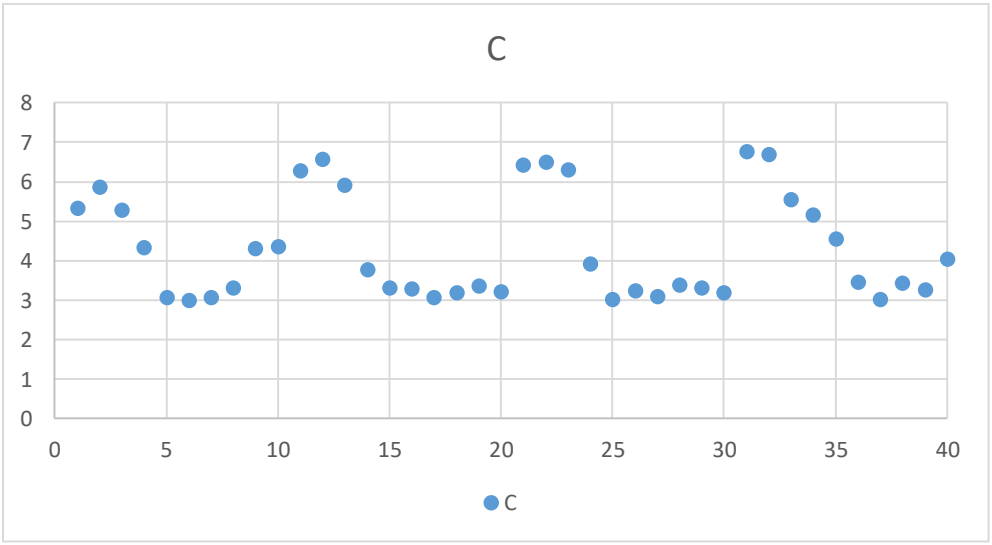

Appendix Figure C. 53 P2-V 10x4 Grid (EDS Taken Vertically) Carbon Concentration

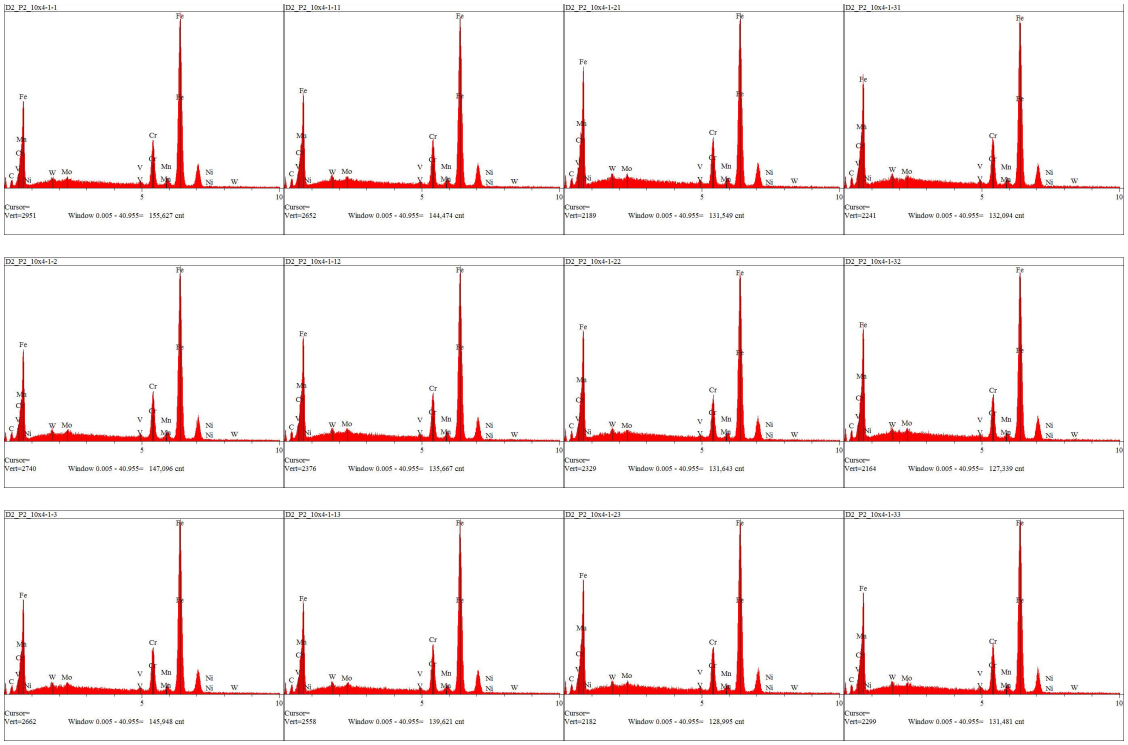


D2_P2_10x4-1-4
Cursor=
Vert=2268 Window 0.005 - 40.955= 170,579 cnt
D2_P2_10x4-1-14
Cursor=
Vert=2989 Window 0.005 - 40.955= 172,879 cnt
D2_P2_10x4-1-24
Cursor=
Vert=1990 Window 0.005 - 40.955= 154,762 cnt
D2_P2_10x4-1-34
Cursor=
Vert=3153 Window 0.005 - 40.955= 151,881 cnt
D2_P2_10x4-1-5
Cursor=
Vert=7510 Window 0.005 - 40.955= 247,502 cnt
D2_P2_10x4-1-15
Cursor=
Vert=7011 Window 0.005 - 40.955= 234,065 cnt
D2_P2_10x4-1-25
Cursor=
Vert=6624 Window 0.005 - 40.955= 217,144 cnt
D2_P2_10x4-1-35
Cursor=
Vert=3065 Window 0.005 - 40.955= 151,071 cnt
D2_P2_10x4-1-6
Cursor=
Vert=6955 Window 0.005 - 40.955= 234,891 cnt
D2_P2_10x4-1-16
Cursor=
Vert=6989 Window 0.005 - 40.955= 234,939 cnt
D2_P2_10x4-1-26
Cursor=
Vert=6274 Window 0.005 - 40.955= 209,794 cnt
D2_P2_10x4-1-36
Cursor=
Vert=7267 Window 0.005 - 40.955= 247,401 cnt
D2_P2_10x4-1-7
Cursor=
Vert=6733 Window 0.005 - 40.955= 222,824 cnt
D2_P2_10x4-1-17
Cursor=
Vert=6535 Window 0.005 - 40.955= 217,238 cnt
D2_P2_10x4-1-27
Cursor=
Vert=6014 Window 0.005 - 40.955= 198,181 cnt
D2_P2_10x4-1-37
Cursor=
Vert=7009 Window 0.005 - 40.955= 236,911 cnt
D2_P2_10x4-1-8
Cursor=
Vert=6248 Window 0.005 - 40.955= 210,758 cnt
D2_P2_10x4-1-18
Cursor=
Vert=6227 Window 0.005 - 40.955= 207,809 cnt
D2_P2_10x4-1-28
Cursor=
Vert=5847 Window 0.005 - 40.955= 193,172 cnt
D2_P2_10x4-1-38
Cursor=
Vert=6987 Window 0.005 - 40.955= 240,073 cnt
D2_P2_10x4-1-9
Cursor=
Vert=4261 Window 0.005 - 40.955= 179,924 cnt
D2_P2_10x4-1-19
Cursor=
Vert=5942 Window 0.005 - 40.955= 199,141 cnt
D2_P2_10x4-1-29
Cursor=
Vert=5020 Window 0.005 - 40.955= 180,626 cnt
D2_P2_10x4-1-39
Cursor=
Vert=6616 Window 0.005 - 40.955= 224,425 cnt

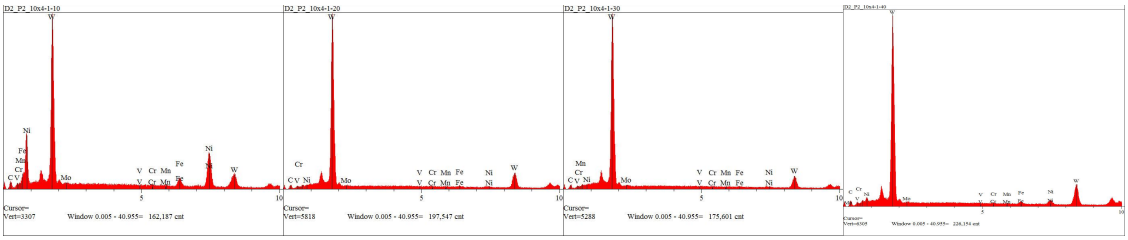

Appendix Figure C. 54 P2-V 10x4 EDS Plots Taken Vertically for each Point

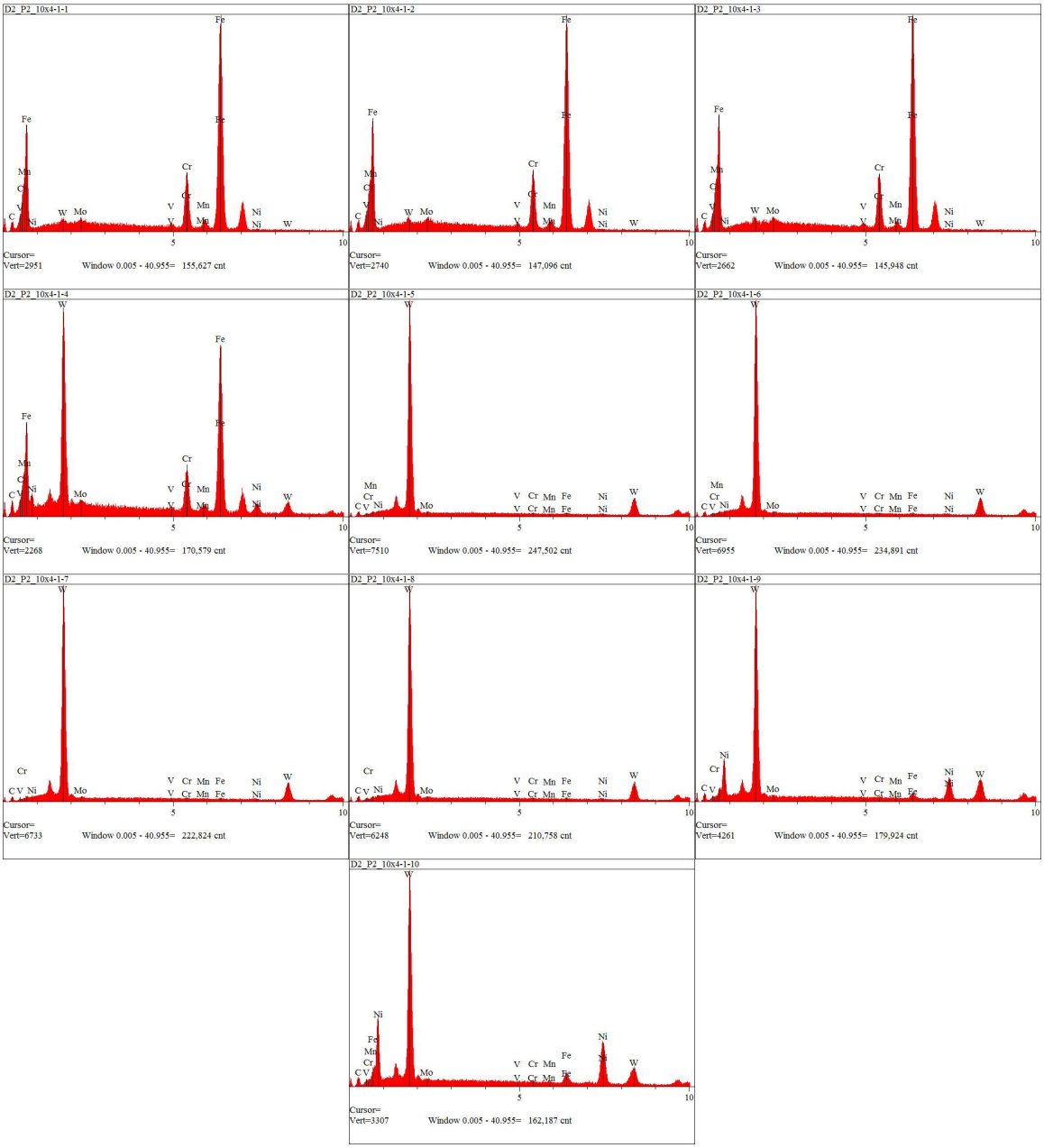

Appendix Figure C. 55 P2-V 10x4 EDS Taken Vertically, Plots 1-10

P2-H2 EDS Taken Horizontally of Nanoindents

P2-H EDS analysis was done horizontally just like the P1-H analysis for a direct comparison to the P1 analysis. **Appendix Figure C. 56** shows the P2-H nanoindents and the EDS map of the indents. The individual concentrations are provided in **Appendix Table C-8** and the concentration spectrum report in **Appendix Figure C. 57**. There is a little more scatter in the data on the D2 side which may be explained from the low densification resulting in an inhomogeneous material and thus chemical diffusion. The carbon, oxygen and nitrogen concentrations are shown in **Appendix Figure C. 58-60** and suggest that the closer to the FAST die the material is, the higher the carbon concentrations are, which tracks with the diffusivity of carbon. The individual EDS plots for P2-H are shown in **Appendix Figure C. 61**, again to understand how the phase and elemental composition changes as the interface is crossed.

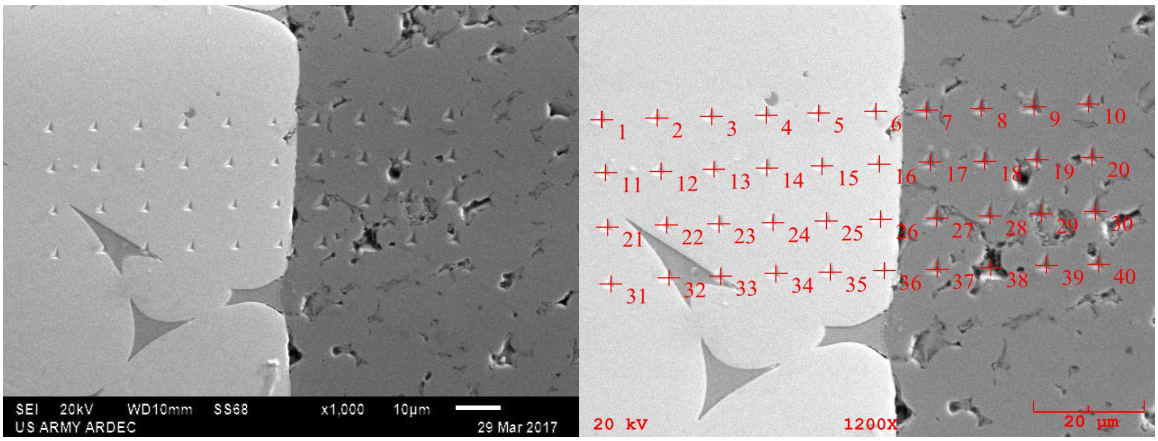

Appendix Figure C. 56 P2-V 10x4 EDS Taken Vertically

Spectrum	C	N	O	Si	P	S	V	Cr	Mn	Fe	Co	Ni	Cu	Mo	W
P2_H2_4x10-1	1.6	0	0.282	0.178	0	0	0.121	0.201	0.09	0.555	0.185	0.298	0.224	0	96.266
P2_H2_4x10-2	1.797	0	0.52	0.415	0.046	0	0.075	0.179	0.231	0.664	0.166	0.166	0.162	0	95.578
P2_H2_4x10-3	1.68	0	0.545	0.145	0	0.037	0.194	0.244	0.224	0.555	0.099	0.226	0.195	0	95.854
P2_H2_4x10-4	1.971	0	0.54	0.444	0	0.025	0.122	0.123	0.152	0.654	0.097	0.355	0.187	0	95.33
P2_H2_4x10-5	2.029	0	0.501	0.186	0	0	0.101	0.229	0.191	1.478	0.072	13.635	0.118	0	81.46

P2_H2_4x10-6	1.864	0	0.396	0.222	0	0	0.121	0.218	0.11	0.706	0.093	0.272	0.175	0	95.821
P2_H2_4x10-7	2.096	0	0.845	0.233	0.109	0.38	0.403	3.267	0.01	18.289	0.101	0.186	0.195	0	73.888
P2_H2_4x10-8	2.795	0.077	0	0.469	0.073	0	0.666	10.304	0.369	82.301	0.602	0.147	0.189	1.376	0.631
P2_H2_4x10-9	3.43	0.193	0.502	0.338	0.025	0	0.922	12.609	0.303	78.258	0.609	0.296	0.234	1.485	0.795
P2_H2_4x10-10	2.772	0.26	0	0.408	0.018	0	0.861	12.085	0.284	79.991	0.534	0.231	0.168	1.799	0.588
P2_H2_4x10-11	2.121	0	0.531	0.191	0	0	0.145	0.206	0.201	0.554	0.109	0.152	0.158	0	95.631
P2_H2_4x10-12	2.213	0	0.298	0.494	0	0	0.115	0.212	0.097	0.589	0.048	0.102	0.144	0	95.689
P2_H2_4x10-13	2.011	0	0.404	0.194	0	0.009	0.133	0.169	0.131	0.61	0.09	0.189	0.141	0	95.918
P2_H2_4x10-14	2.189	0	0.38	0.134	0.025	0	0.115	0.208	0.021	0.65	0.193	0.286	0.134	0	95.664
P2_H2_4x10-15	2.664	0	0.906	0.053	0.006	0.014	0.084	0.256	0.093	0.657	0.115	0.29	0.21	0	94.651
P2_H2_4x10-16	2.303	0	0.486	0.578	0.127	0	0.101	0.232	0.092	0.704	0.226	0.448	0.114	0	94.589
P2_H2_4x10-17	2.329	0	0.52	0.291	0.019	0	0.116	0.4	0.099	1.815	0.123	0.223	0.104	0	93.962
P2_H2_4x10-18	2.602	0	0.026	0.526	0.007	0	0.755	10.622	0.262	82.37	0.579	0.247	0.163	1.378	0.462
P2_H2_4x10-19	4.324	0.319	0.283	0.455	0.051	0	0.936	12.621	0.284	77.653	0.473	0.107	0.11	1.715	0.668
P2_H2_4x10-20	3.262	0.418	0	0.61	0.066	0	0.732	9.314	0.241	83.147	0.42	0.068	0.191	1.049	0.481
P2_H2_4x10-21	2.565	0	0.565	0.542	0.077	0	0.098	0.17	0.043	0.646	0.107	0.239	0.206	0	94.742
P2_H2_4x10-22	2.44	0	0.462	0.16	0	0.054	0.143	0.15	0.059	0.582	0.066	0.147	0.157	0	95.578
P2_H2_4x10-23	2.489	0	0.622	0.456	0	0	0.112	0.164	0.128	0.814	0.152	0.194	0.141	0	94.728
P2_H2_4x10-24	2.341	0	0.43	0.342	0	0	0.14	0.234	0.078	0.603	0.185	0.093	0.137	0	95.417
P2_H2_4x10-25	2.476	0	0.433	0.162	0.002	0	0.125	0.383	0.074	0.567	0.093	0.244	0.102	0	95.338
P2_H2_4x10-26	2.414	0	0.341	0.255	0	0.042	0.092	0.198	0.097	0.739	0.108	0.129	0.154	0	95.432
P2_H2_4x10-27	3.381	0.397	1.787	1.013	0.048	0.108	0.702	8.999	0.206	68.739	0.488	0.796	0.193	0.865	12.279
P2_H2_4x10-28	3.36	0.703	0.513	0.583	0.008	0.013	0.729	10.504	0.198	80.705	0.461	0.188	0.235	1.352	0.448
P2_H2_4x10-29	3.416	0.153	0.299	0.483	0.062	0.115	0.712	10.451	0.288	81.581	0.317	0.125	0.227	1.095	0.675
P2_H2_4x10-30	2.992	0.295	0	0.616	0.041	0	0.372	7.596	0.218	85.281	0.52	0.148	0.275	1.105	0.54
P2_H2_4x10-31	2.696	0	0.41	0	0	0	0.135	0.129	0.168	0.681	0.103	0.324	0.235	0	95.12
P2_H2_4x10-32	2.552	0	0.478	0.346	0.045	0.046	0.132	0.304	0.315	0.758	0.173	0.18	0.256	0	94.414
P2_H2_4x10-33	2.588	0	0.52	0.09	0	0	0.067	0.228	0.095	0.586	0.112	0.181	0.224	0	95.308
P2_H2_4x10-34	2.635	0	0.504	0.672	0	0	0.156	0.157	0.18	0.561	0.167	0.027	0.152	0	94.791
P2_H2_4x10-35	2.595	0	0.307	0.596	0	0	0.124	0.233	0.098	0.649	0.114	0.201	0.147	0	94.936
P2_H2_4x10-36	2.568	0	0.425	0.463	0	0	0.14	0.326	0.177	0.764	0.114	0.06	0.203	0	94.76
P2_H2_4x10-37	4.319	0.17	3.515	3.054	0.006	0	0.928	14.523	0.041	68.42	0.259	0.507	0.129	1.438	2.69
P2_H2_4x10-38	2.937	0.147	0	0.5	0.055	0	0.719	10.085	0.353	82.124	0.42	0.261	0.197	1.452	0.75
P2_H2_4x10-39	2.84	0.082	0	0.567	0.024	0	0.629	10.068	0.21	82.751	0.56	0.141	0.164	1.342	0.621
P2_H2_4x10-40	3.145	0.178	1.505	1.734	0.036	0	0.98	12.939	0.251	76.602	0.414	0.184	0.208	1.267	0.558

Appendix Table C-8 P2-H 4x10 Grid (EDS Taken Horizontally Vertically)

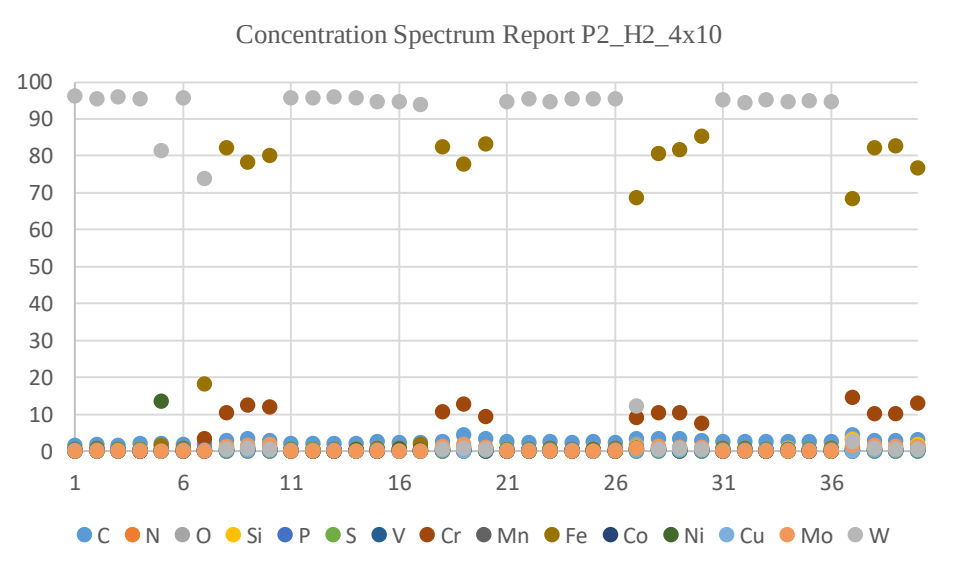

Appendix Figure C. 57 P2-H 4x10 Grid (EDS Taken Horizontally) Chemistry WHA and D2 Elements

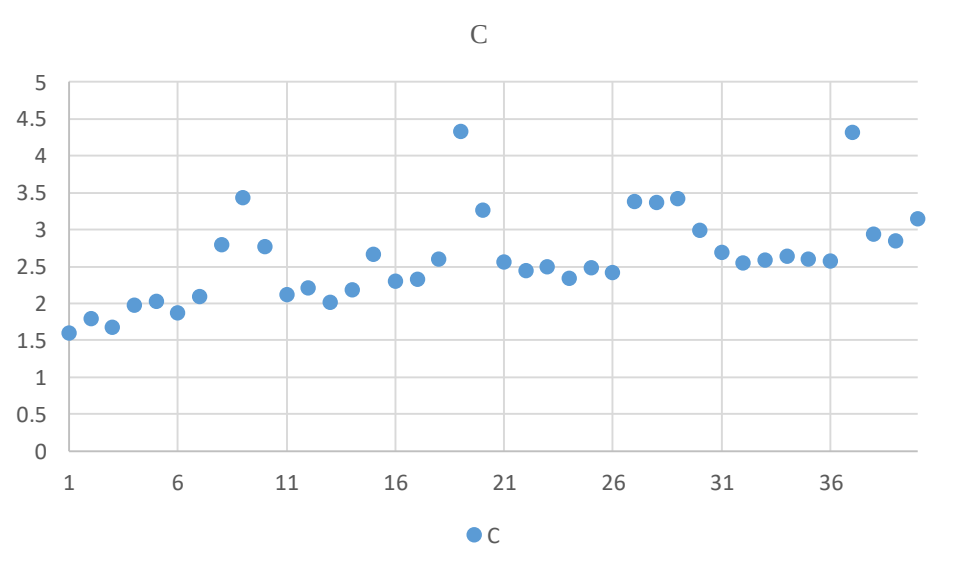

Appendix Figure C. 58 P2-H 4x10 Grid (EDS Taken Horizontally) Carbon Concentration

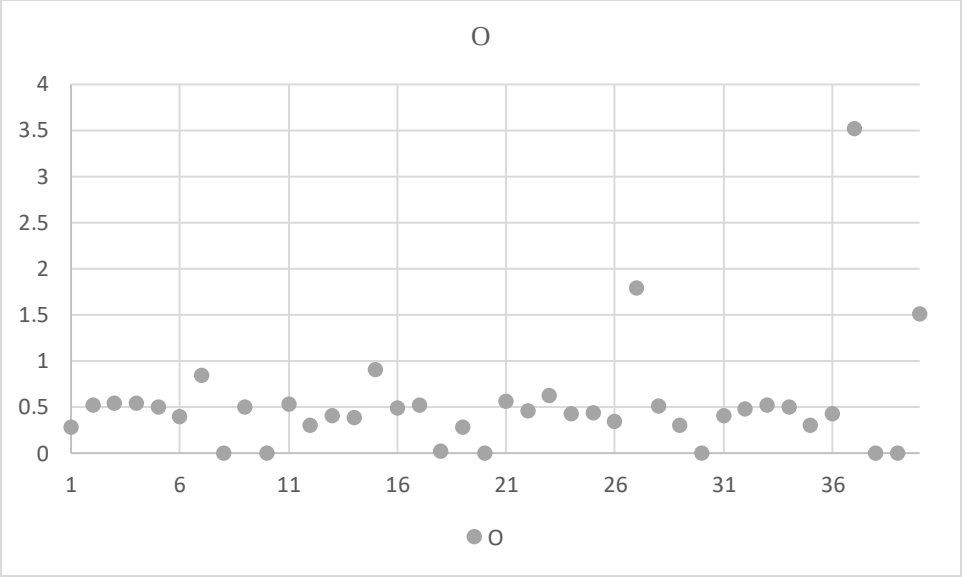

Appendix Figure C. 59 P2-H 4x10 Grid (EDS Taken Horizontally) Oxygen Concentration

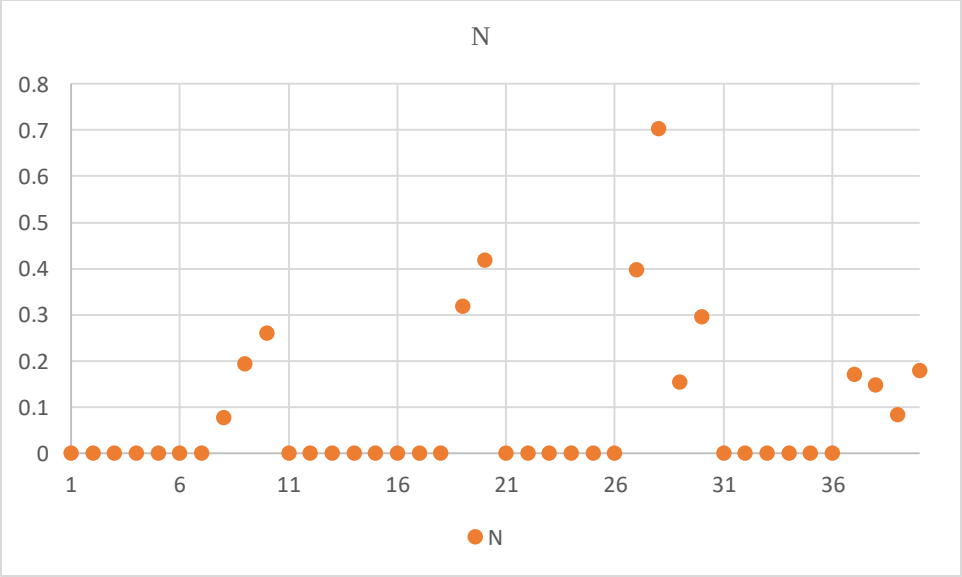

Appendix Figure C. 60 P2-H 4x10 Grid (EDS Taken Horizontally) Nitrogen Concentration

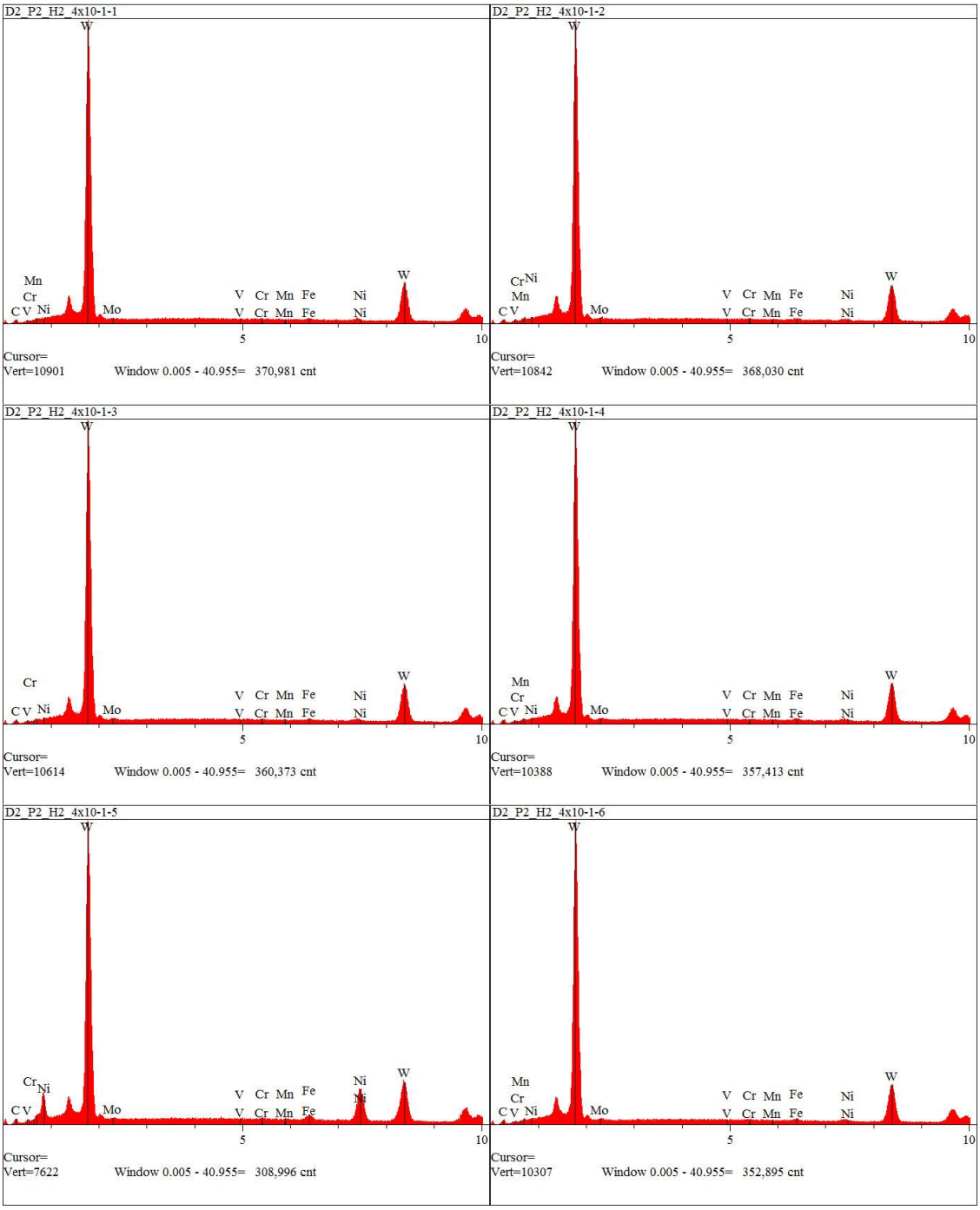
D2_P2_H2_4x10-1-1
W
Mn
Cr
C V Ni
Mo
V Cr Mn Fe
Ni
W
5
10
Cursor=
Vert=10901
Window 0.005 - 40.955= 370,981 cnt
D2_P2_H2_4x10-1-2
W
Cr Ni
Mn
C V
Mo
V Cr Mn Fe
Ni
W
5
10
Cursor=
Vert=10842
Window 0.005 - 40.955= 368,030 cnt
D2_P2_H2_4x10-1-3
W
Cr
C V Ni
Mo
V Cr Mn Fe
Ni
W
5
10
Cursor=
Vert=10614
Window 0.005 - 40.955= 360,373 cnt
D2_P2_H2_4x10-1-4
W
Mn
Cr
C V Ni
Mo
V Cr Mn Fe
Ni
W
5
10
Cursor=
Vert=10388
Window 0.005 - 40.955= 357,413 cnt
D2_P2_H2_4x10-1-5
W
Cr
Ni
C V
Mo
V Cr Mn Fe
Ni
W
5
10
Cursor=
Vert=7622
Window 0.005 - 40.955= 308,996 cnt
D2_P2_H2_4x10-1-6
W
Mn
Cr
C V Ni
Mo
V Cr Mn Fe
Ni
W
5
10
Cursor=
Vert=10307
Window 0.005 - 40.955= 352,895 cnt

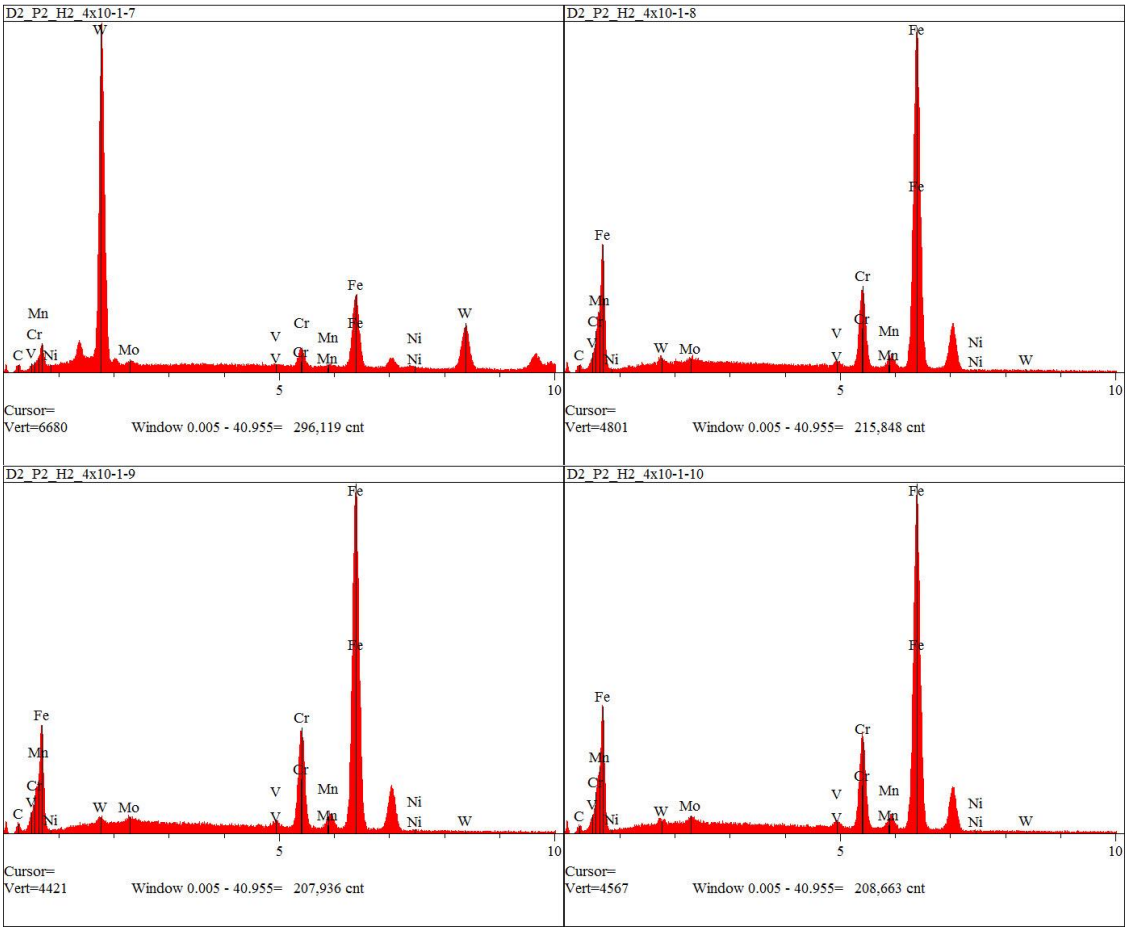

Appendix Figure C. 61 P2-V 4x10 EDS Plots 1-10 Taken Horizontally for each Point

P2-Marker EDS of Nanoindents

The P2-Marker indents and EDS points are shown in **Appendix Figure C. 62** with the individual values in **Appendix Table C-9** as well as the limited statistical analysis. These values were used earlier to compare the P2-V horizontal and P2-V vertical EDS analyses. There is no nickel in D2 and very little sulfur in this particular lot, which is randomly distributed. Thus, when it is concentrated on the interface as shown in the previous analyses, there may be a correlation with the fracture location. **Appendix Figure C. 63** shows the concentration spectrum reports for the ten points and all the elements while **Appendix Figure C. 64** shows the same results without the iron and chromium elements because their concentrations are too high to see small differences

in lower concentrated elements. The variation in elemental concentrations for D2 within a 10 µm span is high and could explain why small changes in location between two different P2-V EDS measurements can drastically be different in terms of the numerical analysis. Nevertheless, **Appendix Figure C. 65** shows a typical EDS plot for the ten points.

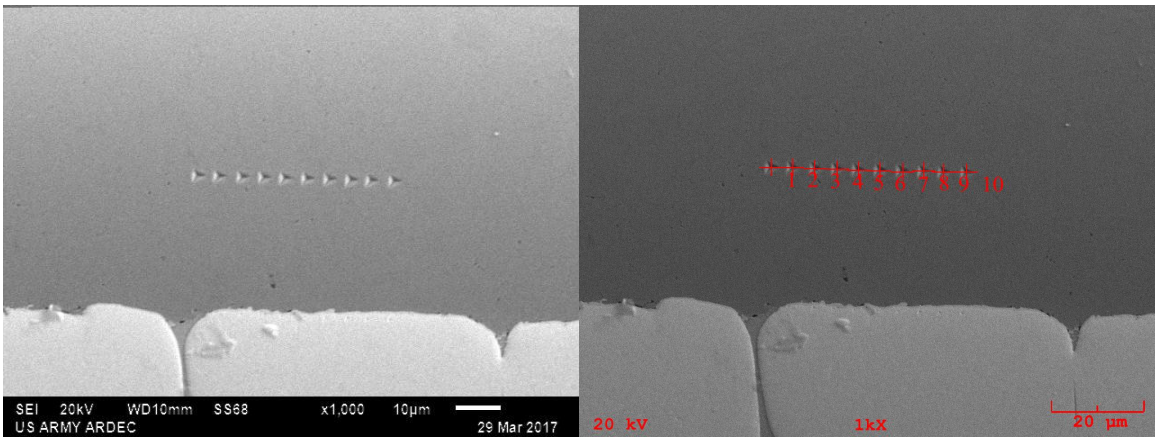

Appendix Figure C. 62 P2-Marker Nanoindents x1000

Spectrum	C	Si	P	S	V	Cr	Mn	Fe	Ni	Cu	Mo	W
D2_P2_Marker-1	8.041	0.931	0.045	0	1.109	16.464	0.338	70.147	0	0.265	2.092	0.567
D2_P2_Marker-2	4.522	1.099	0.038	0	1.232	17.476	0.381	72.331	0	0.396	2.039	0.487
D2_P2_Marker-3	4.751	1.437	0.175	0	0.92	16.969	0.178	72.315	0	0.261	2.872	0.122
D2_P2_Marker-4	5.457	1.116	0.039	0.044	1.106	15.892	0.216	73.213	0	0.38	1.917	0.62
D2_P2_Marker-5	6.744	0.929	0.196	0.305	1.142	15.466	0.467	71.931	0	0.441	1.459	0.919
D2_P2_Marker-6	5.644	0.943	0.151	0	1.213	16.1	0.239	71.667	0	0.389	3.182	0.471
D2_P2_Marker-7	5.902	1.315	0	0.293	1.015	14.428	1.378	70.931	0	0.382	4.357	0
D2_P2_Marker-8	6.67	1.142	0.228	0	1.239	16.197	0.299	72.051	0	0.203	1.971	0
D2_P2_Marker-9	6.371	0.934	0.126	0	1.359	16.529	0.208	71.228	0	0.319	2.37	0.556
D2_P2_Marker-10	5.919	1.217	0	0	1.007	16.056	0.186	72.462	0	0.489	2.45	0.213
Mean	6.002	1.106	0.1	0.064	1.134	16.158	0.389	71.828	0	0.352	2.471	0.395
Std. Dev.	1.027	0.178	0.085	0.125	0.131	0.829	0.36	0.875	0	0.089	0.826	0.301
Min	4.522	0.929	0	0	0.92	14.428	0.178	70.147	0	0.203	1.459	0
Max	8.041	1.437	0.228	0.305	1.359	17.476	1.378	73.213	0	0.489	4.357	0.919

Appendix Table C-9 P2 Marker EDS Results

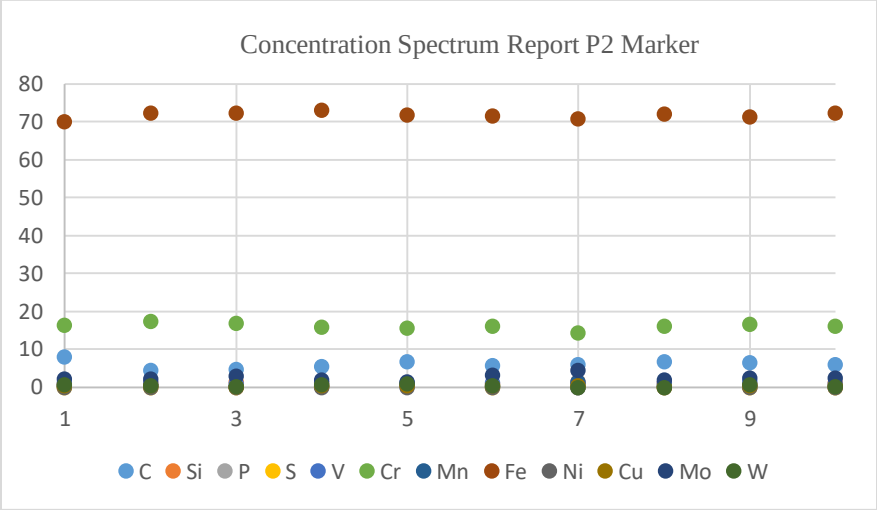

Appendix Figure C. 63 P2 Marker EDS Points 1-10

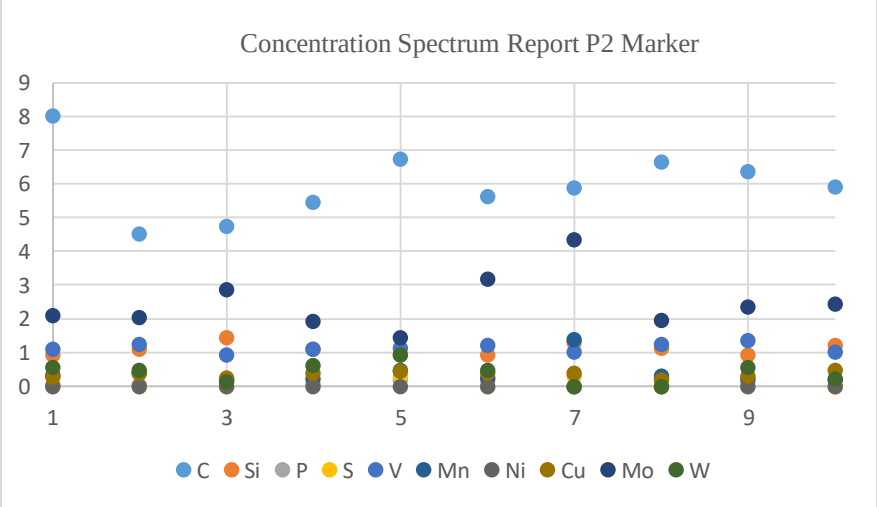

Appendix Figure C. 64 P2 Marker EDS Points 1-10 Minus Fe and Cr

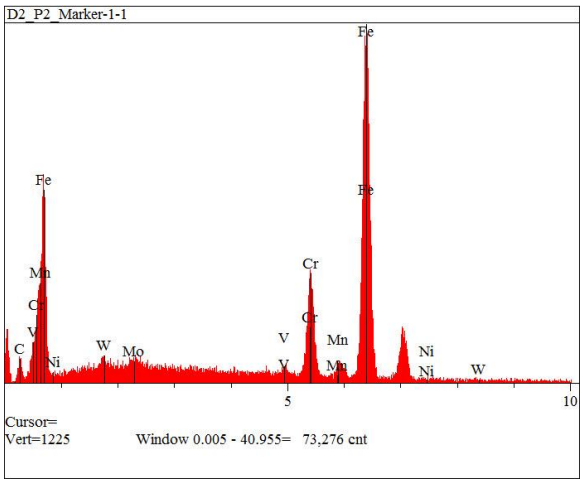

Appendix Figure C. 65 P2 Marker EDS Point 1 Plot

P2 0-Degree EDS of Nanoindents

As seen in chapter 4, the P2 0-degree was very close to falling on the interface as shown in **Appendix Figure C. 66** and the individual EDS results for each point in **Appendix Table C-10** suggests diffusion has occurred for all elements. All elements in the D2 alloy have diffused into the WHA and nickel and tungsten have diffused into the D2.

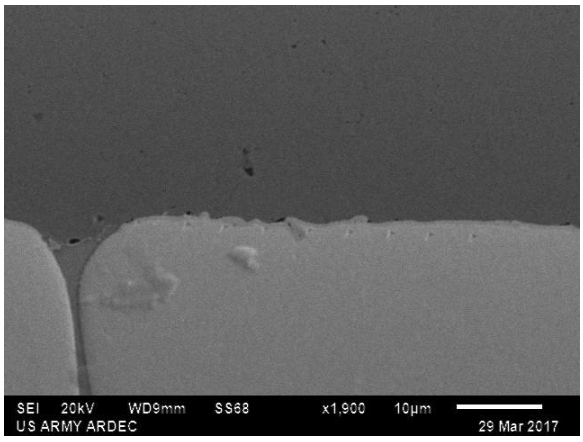

Appendix Figure C. 66 P2 0-Degree Nanoindents x1900

Spectrum	C	Si	P	S	V	Cr	Mn	Fe	Ni	Cu	Mo	W

D2_P2_0degree-1	5.101	0.658	0.149	0.463	0.936	10.91	0.174	47.098	15.541	0.231	0.744	17.994
D2_P2_0degree-2	4.026	0.271	0.229	0.266	0.545	6.342	0	19.831	0.49	0.152	0	67.847
D2_P2_0degree-3	2.967	0	0.065	0.27	0.287	4.855	0.14	17.701	0	0.196	0	73.52
D2_P2_0degree-4	3.143	0.077	0.174	0.232	0.195	3.521	0.248	12.198	0	0.253	0	79.958
D2_P2_0degree-5	3.636	0	0.117	0.269	0.316	4.533	0.39	15.6	0.094	0.209	0	74.838
D2_P2_0degree-6	3.713	0	0.317	0.17	0.455	6.391	0.35	20.81	0	0.205	0.623	66.964
D2_P2_0degree-7	3.498	0	0.007	0.178	0.336	4.52	0.147	18.096	0.268	0.218	0	72.731
D2_P2_0degree-8	3.181	0	0.029	0.219	0.393	3.972	0.14	12.371	0.113	0.213	0	79.371
D2_P2_0degree-9	3.465	0	0.097	0.294	0.19	3.098	0.081	11.047	0	0.139	0	81.589
D2_P2_0degree-10	3.66	0	0.047	0.159	0.41	4.48	0.248	16.835	0	0.204	0	73.956

Appendix Table C-10 P2 0-Degree EDS Results

In **Appendix Figure C. 67**, iron displays the inverse of the tungsten behavior and chromium also shows the same inverse behavior compare to tungsten. It also appears that D2 elements all follow the same trend and carbon concentration seems to be proportional to the distance from the halo surrounding the WHA rather than the distance from the D2. It is difficult to see trends in elements with concentrations less than 1%, but once the higher concentration elements were removed, silicon, phosphorus and sulfur also seem to loosely follow the same trend as the other elements in D2 with sulfur having the strongest correlation. The individual EDS plots are also shown in **Appendix Figure C. 68** with the first plot enlarged as it is on the D2 side of the interface.

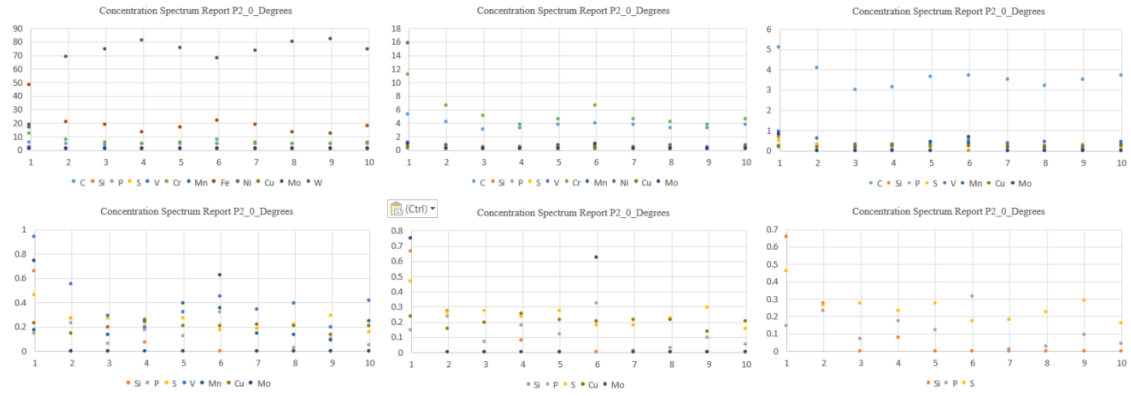

Appendix Figure C. 67 P2 0-Degree Chemistry Points 1-10

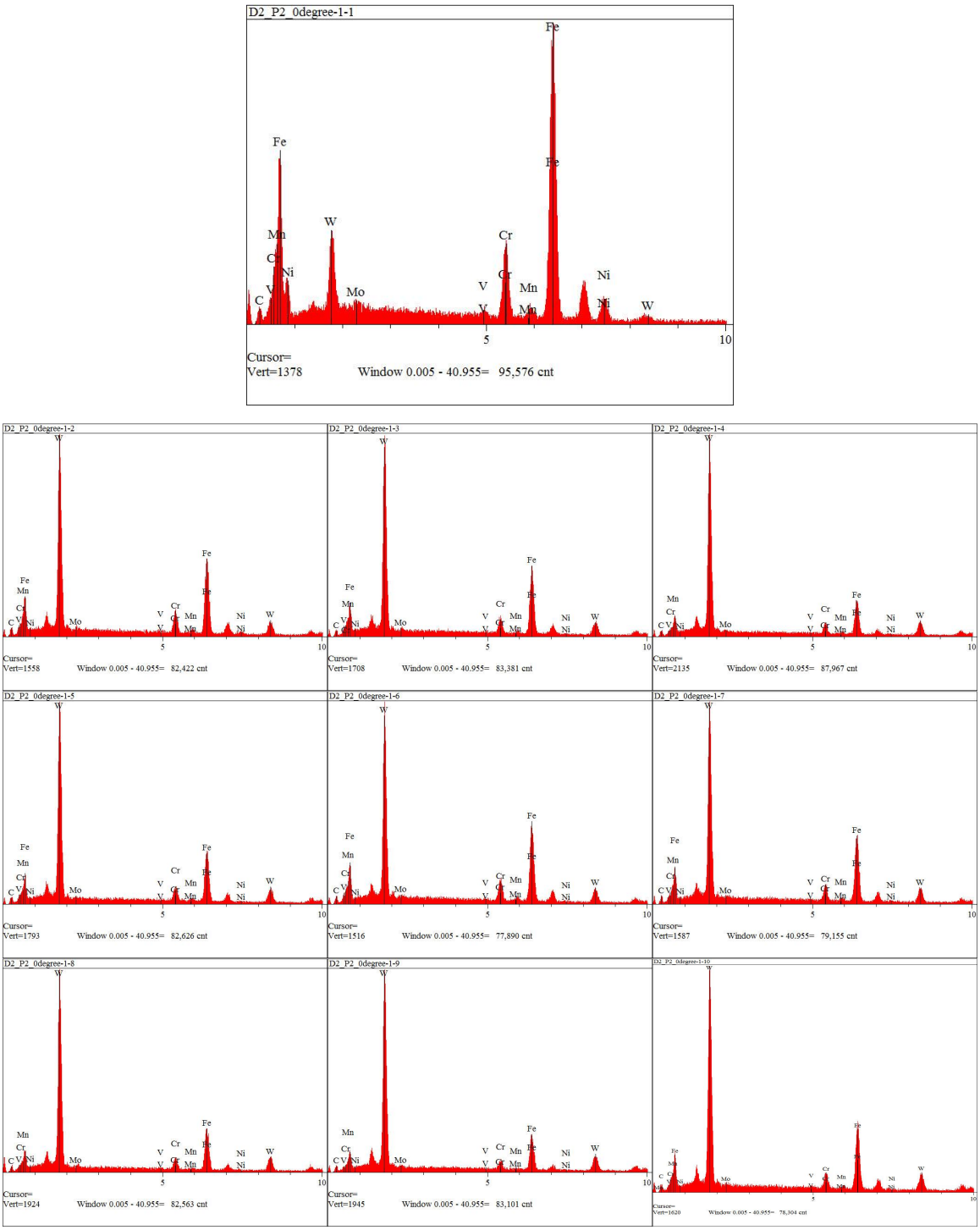

Appendix Figure C. 68 P2 0-Degree Plots 1-10

P2 5-Degree EDS of Nanoindents

The P2 5-degree nanoindents did not seem fruitful given their location was on the WHA side relative to the interface as depicted in **Appendix Figure C. 69**, but as **Appendix Table C-11** and **Appendix Figure C. 70 and 71** show, there are some interesting correlations. Point 6 is unique as it is near an inclusion in the tungsten which appears to be a void, but also on the interface of two joining tungsten grains. Point 6 also 1has the highest oxygen concentration and 2nd highest carbon concentration and also had the highest modulus and hardness of any of the points. This suggests diffusion along tungsten grain boundaries is faster than through tungsten grains. In **Appendix Figure C. 72** the individual EDS plots with phases and concentrations are also shown for reference.

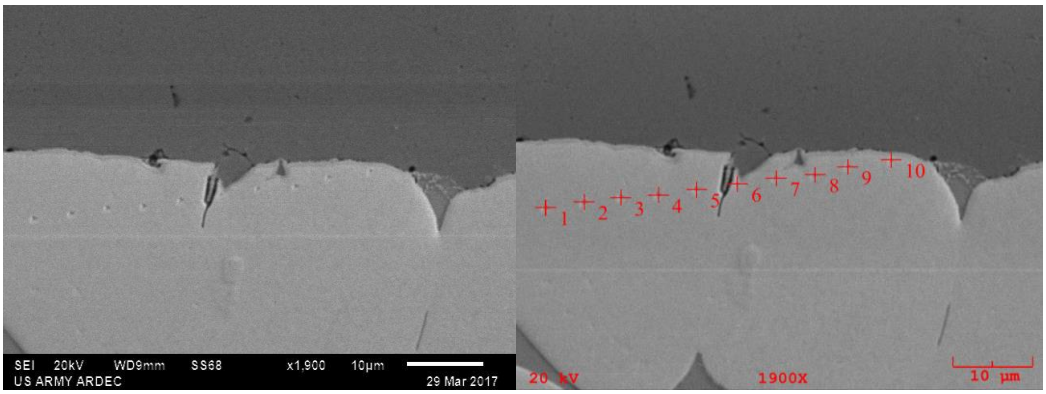

Appendix Figure C. 69 P2 5-Degree Nanoindents x1900

Spectrum	C	N	O	Si	P	S	V	Cr	Mn	Fe	Co	Ni	Cu	Mo	W
D2_P2_5degree-1	2.267	0	0.482	0	0	0	0.175	0.304	0.209	0.725	0.153	0.03	0.153	0	95.502
D2_P2_5degree-2	2.759	0	0.441	0	0.005	0.074	0.098	0.257	0.088	0.867	0.107	0.182	0.17	0	94.952
D2_P2_5degree-3	1.717	0	0.457	0	0.211	0.031	0.346	0.184	0.128	0.867	0.136	0.392	0.132	0	95.398
D2_P2_5degree-4	2.626	0	0.419	0	0.006	0	0.216	0.37	0.093	1.103	0.2	0.201	0.337	0	94.427
D2_P2_5degree-5	2.097	0	0.585	0	0.141	0.124	0.096	0.2	0.189	1.331	0.258	0.203	0.263	0	94.512
D2_P2_5degree-6	3.282	0	7.667	8.291	0.171	0.349	0.583	5.658	0.282	11.496	0.193	9.31	0.199	0	52.519
D2_P2_5degree-7	2.108	0	5.209	4.154	0.038	0.458	0.347	4.543	0.338	45.112	0.176	5.647	0.072	0	31.797
D2_P2_5degree-8	2.655	0	2.518	0.451	0.349	0.411	0.532	3.458	0.425	17.068	0.26	1.042	0.154	0	70.676
D2_P2_5degree-9	3.139	0.586	0	0.711	0.116	0	0.634	9.565	0.636	79.394	0.726	0.548	0.293	0.931	2.72
D2_P2_5degree-10	4.028	0.378	0.161	0.777	0.021	0	0.718	10.11	0.072	80.291	0.199	0.891	0.203	1.04	1.11

Appendix Table C-11 P2 5-Degree EDS Results

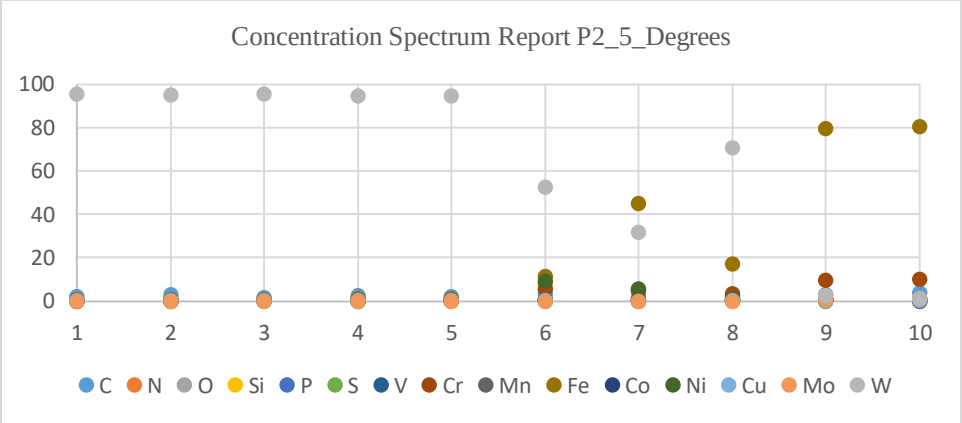

Appendix Figure C. 70 P2 5-Degree EDS Points 1-10

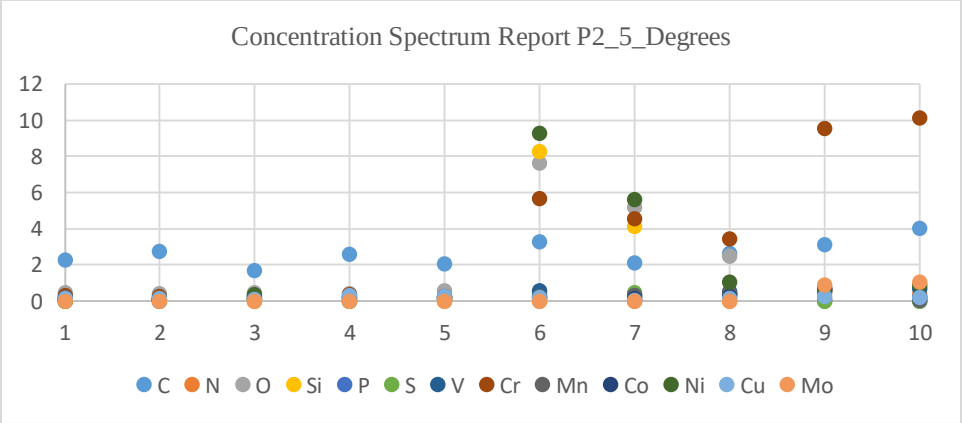

Appendix Figure C. 71 P2 5-Degree EDS Points 1-10

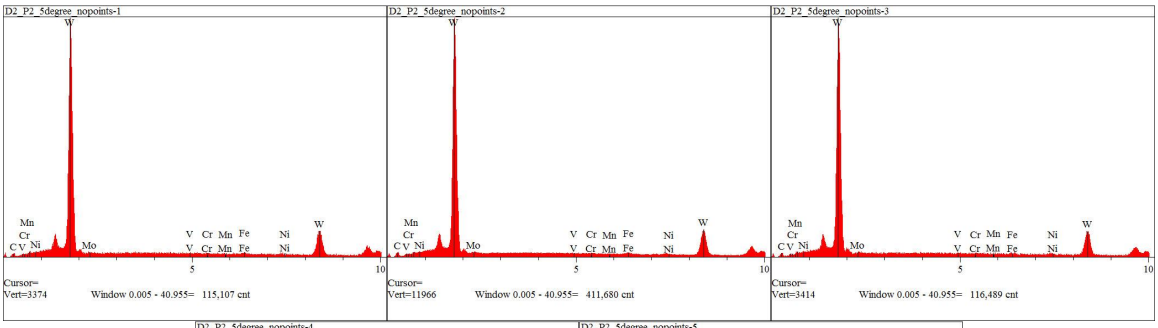
D2_P2_5degree_nopoints-1
Cursor=
Vert=3374
Window 0.005 - 40.955= 115,107 cnt
D2_P2_5degree_nopoints-2
Cursor=
Vert=11966
Window 0.005 - 40.955= 411,680 cnt
D2_P2_5degree_nopoints-3
Cursor=
Vert=3414
Window 0.005 - 40.955= 116,489 cnt

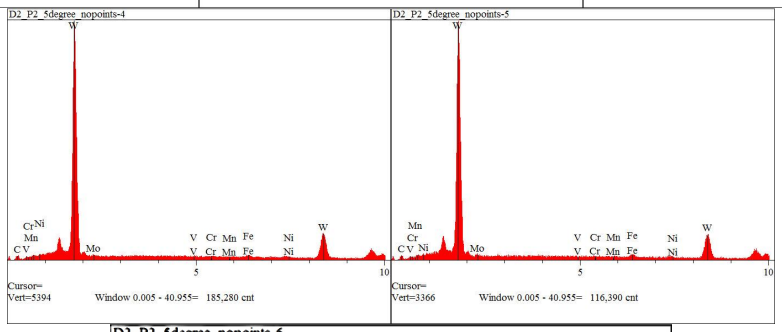
D2_P2_5degree_nopoints-4
Cursor=
Vert=5394
Window 0.005 - 40.955= 185,280 cnt
D2_P2_5degree_nopoints-5
Cursor=
Vert=3366
Window 0.005 - 40.955= 116,390 cnt

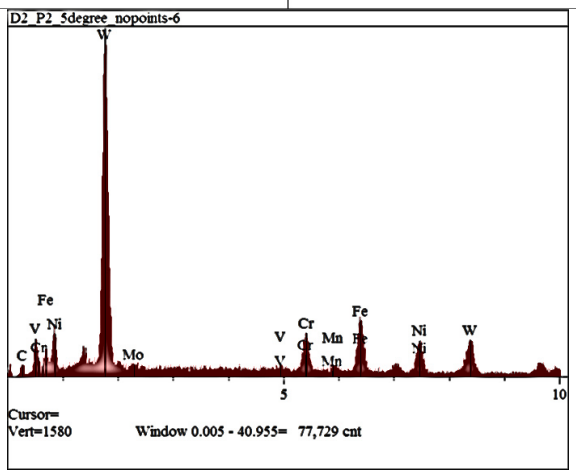
D2_P2_5degree_nopoints-6
Cursor=
Vert=1580
Window 0.005 - 40.955= 77,729 cnt

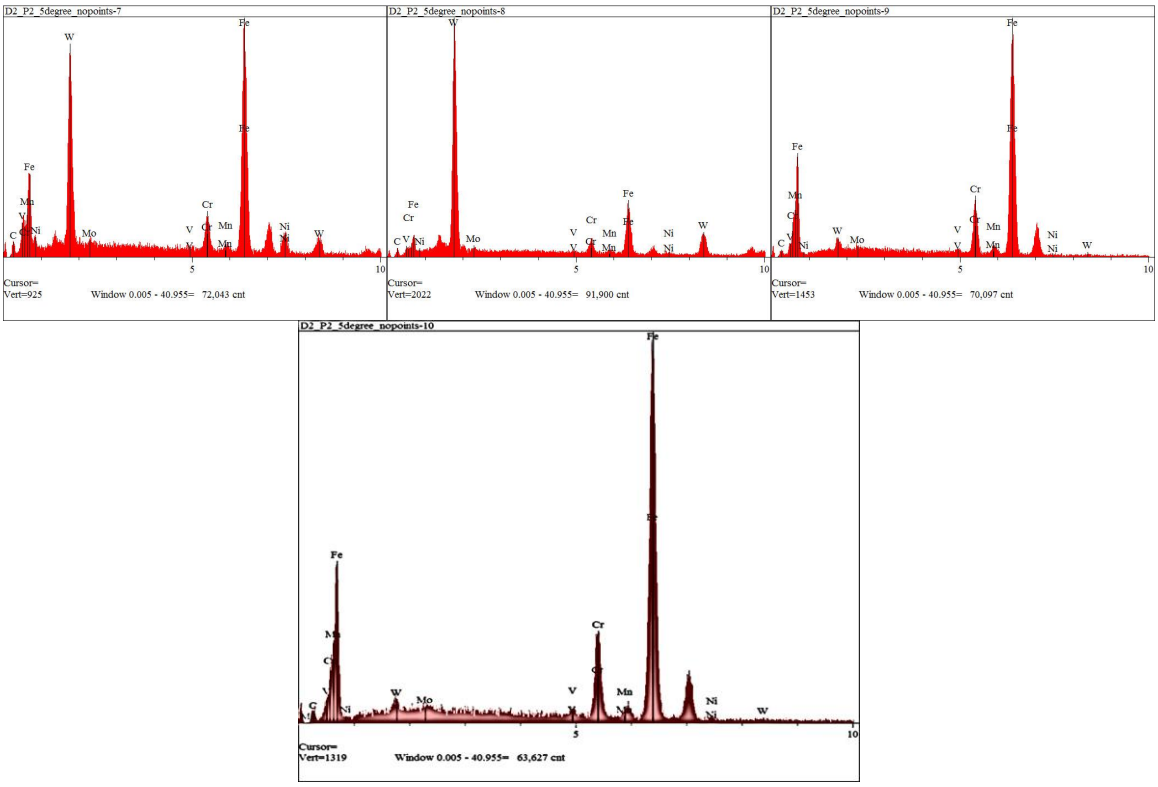

Appendix Figure C. 72 P2 5-Degree Individual EDS Plots Points 1-10

P2 10-degree EDS of Nanoindents

The first seven nanoindents can be seen in **Appendix Figure C. 73** as well as an attempt to gather EDS measurements on the points obscured by the tape residue discussed in chapter 4 since an x-ray can penetrate most materials. Thus, the first 7 points can be used to show the trend here follows those observed in the other analyses as well as the residue is most likely carbon-based as can be seen from the large change in carbon concentration in **Appendix Table C-12 . Appendix Figure C. 74 and 75** show the concentration spectrum reports for P2-10 while **Appendix Figure C. 76** shows the individual EDS plots with phases and concentrations are also shown for reference.

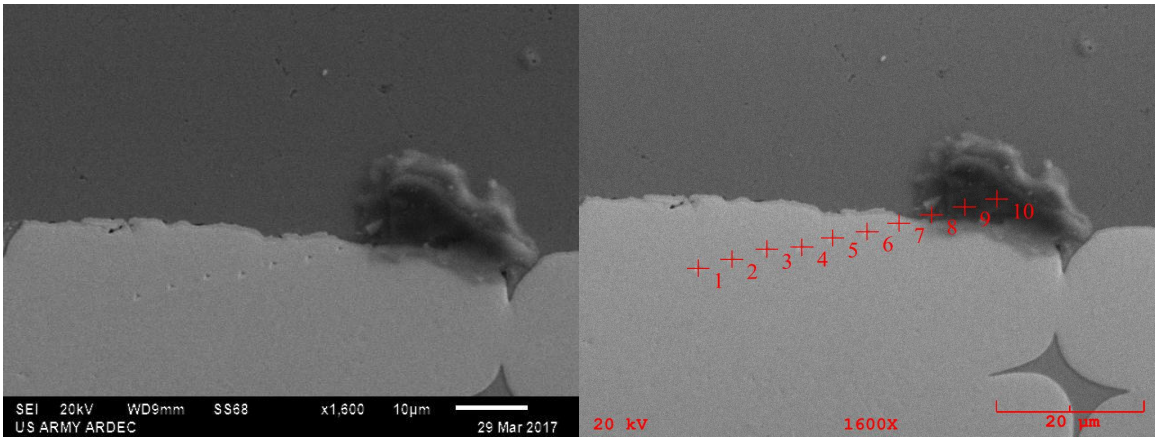

Appendix Figure C. 73 P2 10-Degree Nanoindents x1600

Spectrum	C	N	O	Si	P	S	V	Cr	Mn	Fe	Co	Ni	Cu	Mo	W
P2_10degree-1	3.18	0	0.545	0	0.024	0	0.219	0.292	0.182	0.758	0.293	0.235	0.243	0	94.027
P2_10degree-2	2.859	0	0.917	0	0.09	0.008	0.217	0.206	0.123	0.644	0.089	0.501	0.21	0	94.135
P2_10degree-3	2.326	0	0.68	0	0.107	0.073	0.221	0.417	0.191	0.686	0.168	0.5	0.127	0	94.504
P2_10degree-4	2.068	0	0.922	0	0.239	0.136	0.276	0.367	0.279	0.805	0.082	0.12	0.127	0	94.578
P2_10degree-5	3.031	0	0.849	0	0.153	0.119	0.098	0.813	0.164	3.693	0.146	0.12	0.13	0	90.683
P2_10degree-6	2.335	0	0.999	0.038	0.199	0.223	0.336	1.064	0.294	5.615	0.084	0.334	0.123	0	88.355
P2_10degree-7	2.682	0	1.58	0	0.253	0.16	0.318	2.236	0.12	10.175	0.145	0.112	0.201	0	82.018
P2_10degree-8	8.925	0	3.319	0.46	0.067	0.215	0.451	2.493	0.165	11.643	0.147	0.237	0.173	0	71.706
P2_10degree-9	11.618	0	3.12	0	0.13	0.241	0.207	1.759	0.229	7.042	0.206	0.101	0.139	0	75.207
P2_10degree-10	17.643	0	6.78	0	0.22	0.582	0.265	3.146	0.052	16.028	0.207	0.212	0.209	0	54.656

Appendix Table C-12 P2 10-Degree EDS Results

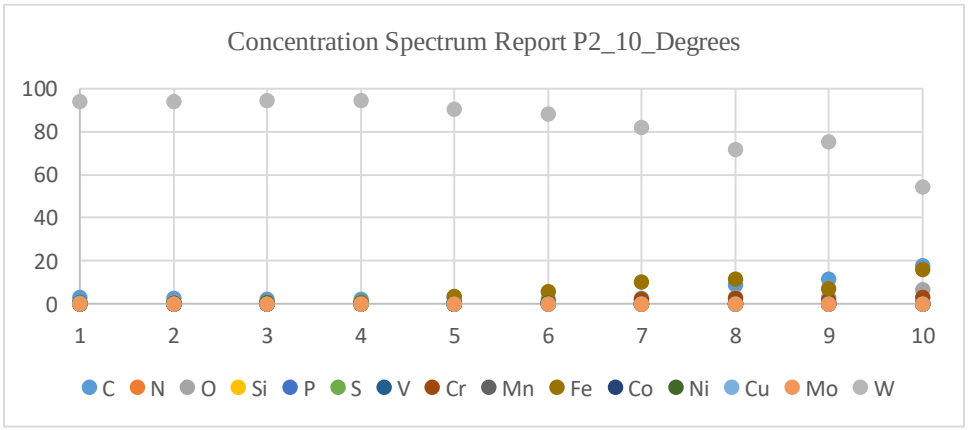

Appendix Figure C. 74 P2 10-Degree EDS Points 1-10

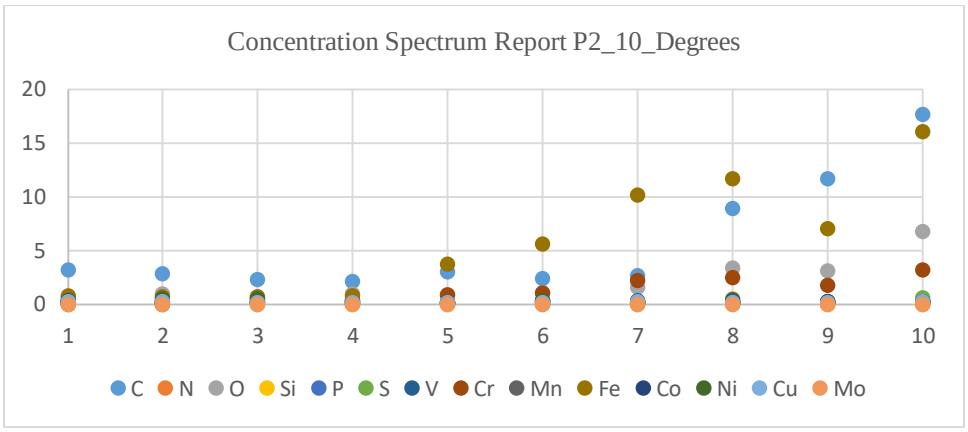

Appendix Figure C. 75 P2 10-Degree EDS Points 1-10

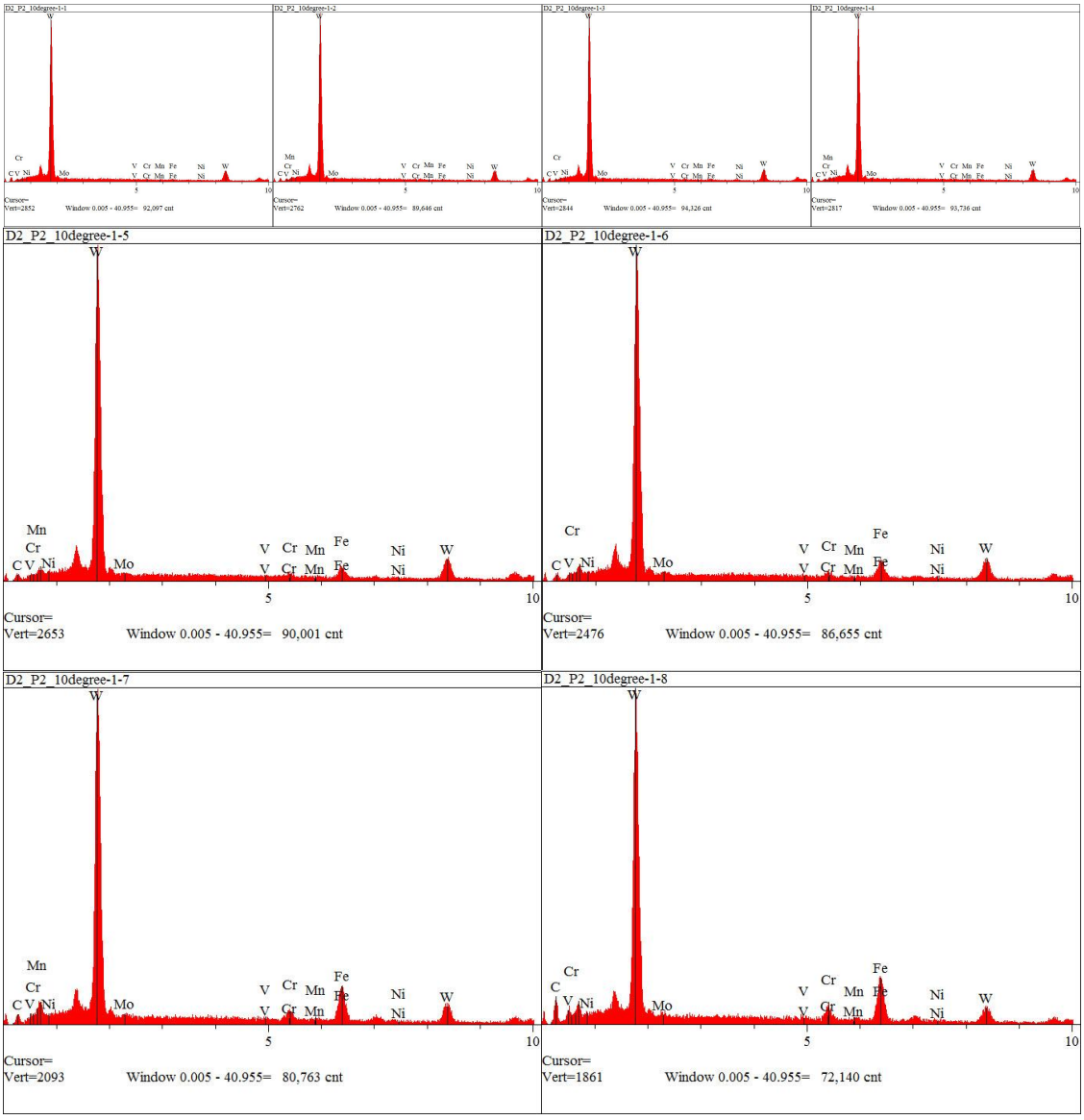

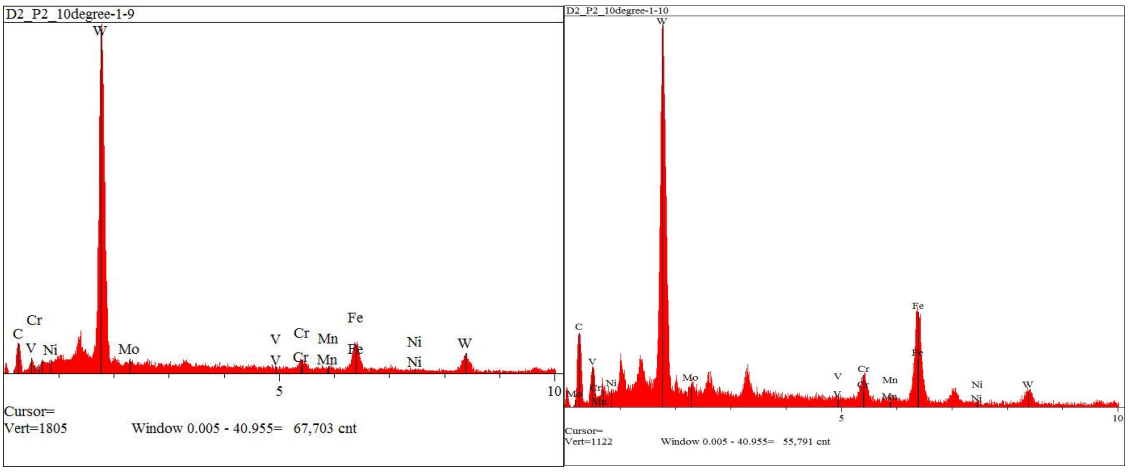

Appendix Figure C. 76 P2 10-Degree Individual EDS Plots Points 1-10

Optical Images of Nanoindents Post EDS

After the nanoindentation, SEM and EDS on the same specimen, it was placed back in the optical microscope to see if the 15 degree indent could be found as rastering was much faster with this instrument though limited to 1000x. The P1-V indents and P2-V indents are visible at 50x as can be seen in **Appendix Figure C. 77**.

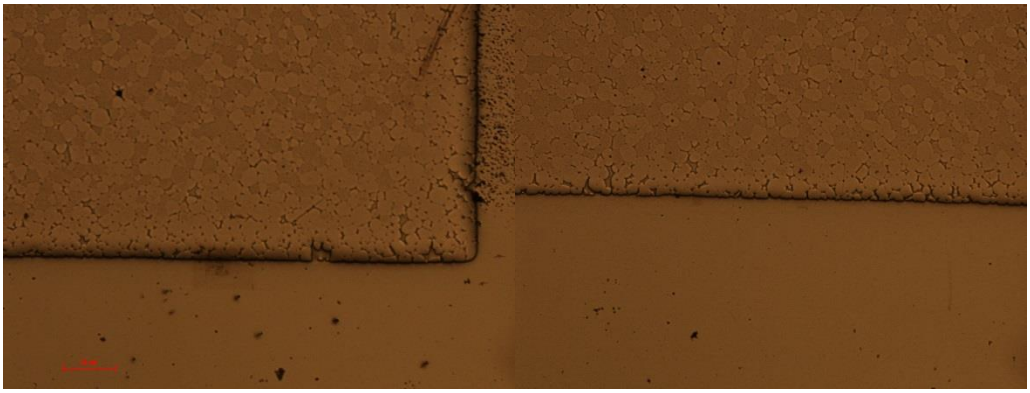

Appendix Figure C. 77 Nanoindents P1-V (left) P2-V (right) 50x

There is evidence of ablation where the EDS measurements were taken on the P1-V. The ablation is clearly visible at 100x as shown in **Appendix Figure C. 78.** Thus,

due to the ablation using the same P1-V area to refine EDS measurements in-between indent points was abandoned.

Appendix Figure C. 78 P1-V ablated 100x

APPENDIX D: Enlarged Individual EDS Plots

D2_V1_10x4 1-40 EDS Plots

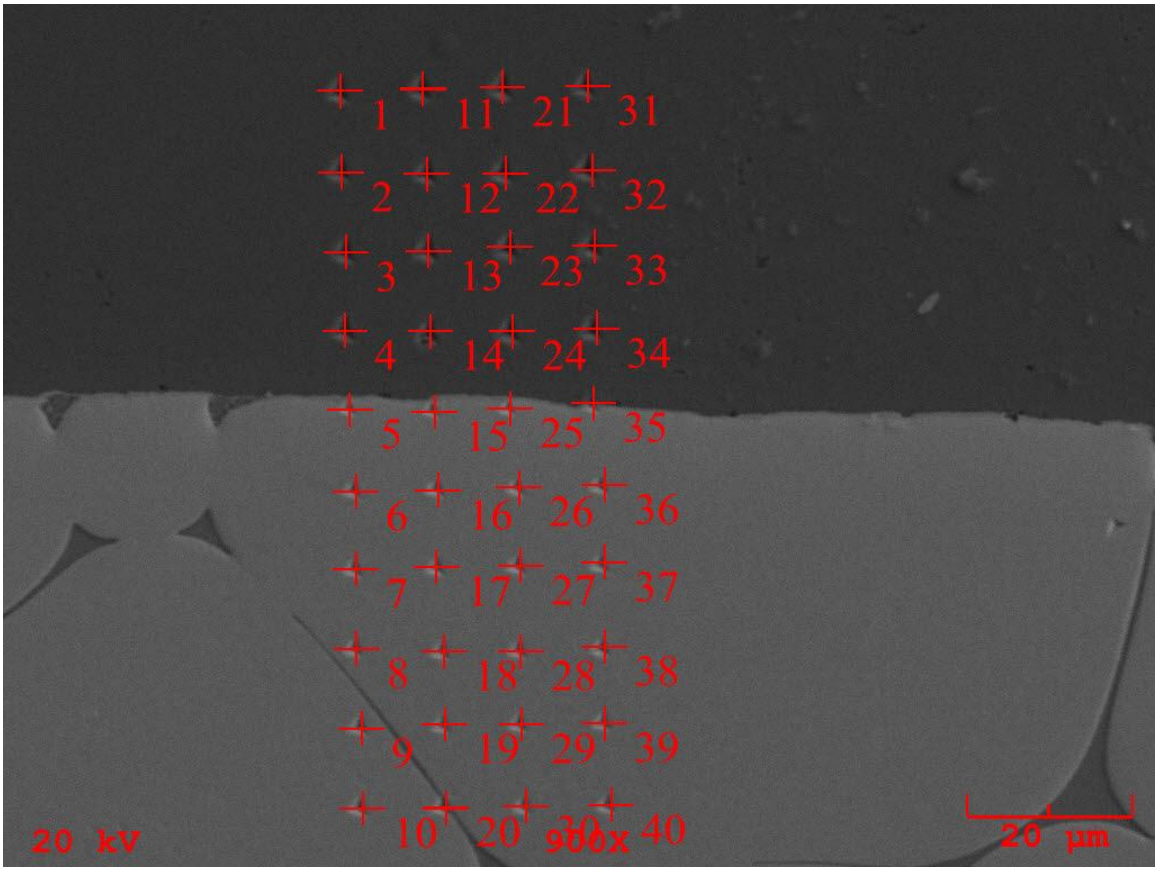

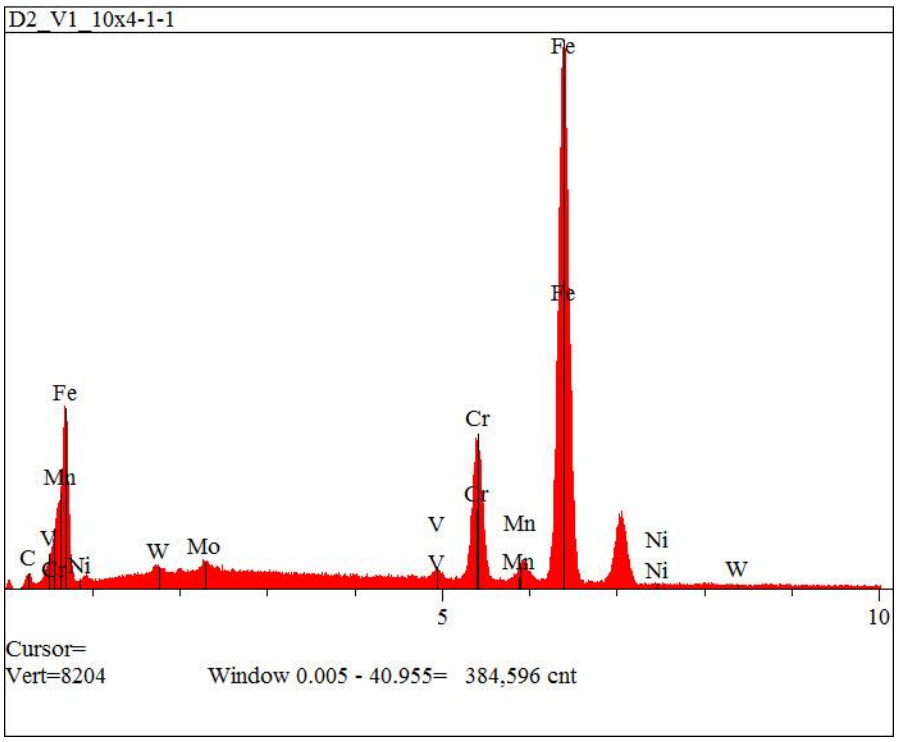
D2_V1_10x4-1-1
Fe
Fe
Fe
Cr
Mn
Cr
V
Mn
Ni
C
Ni
W
Mo
V
Mn
Ni
W
5
10
Cursor=
Vert=8204
Window 0.005 - 40.955= 384,596 cnt

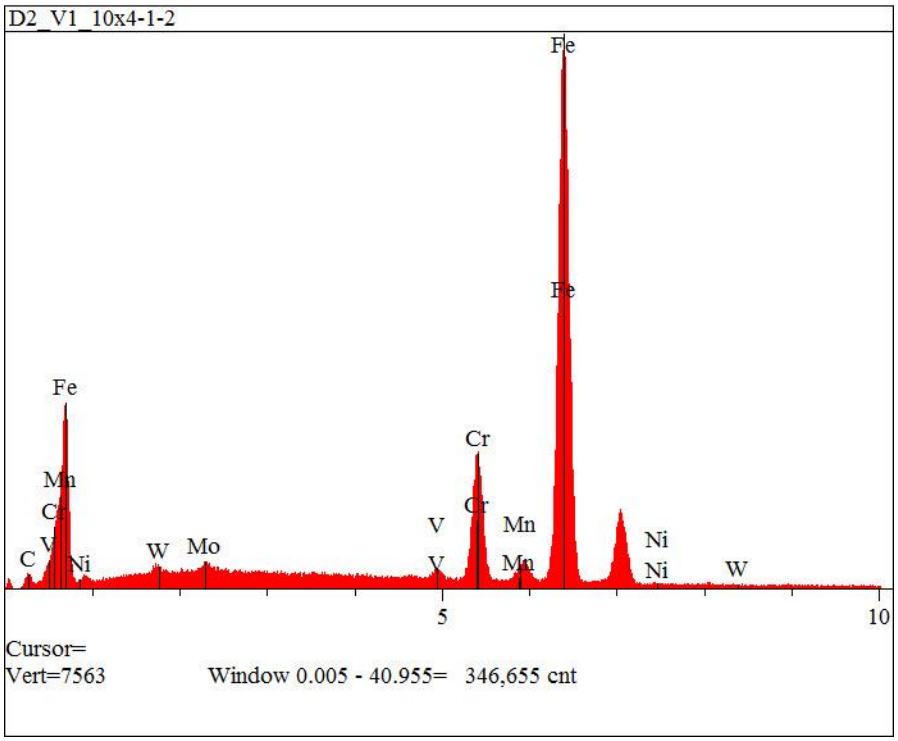
D2_V1_10x4-1-2
Fe
Fe
Fe
Cr
Mn
Cr
V
Mn
Ni
C
Ni
W
Mo
V
Mn
Ni
W
5
10
Cursor=
Vert=7563
Window 0.005 - 40.955= 346,655 cnt

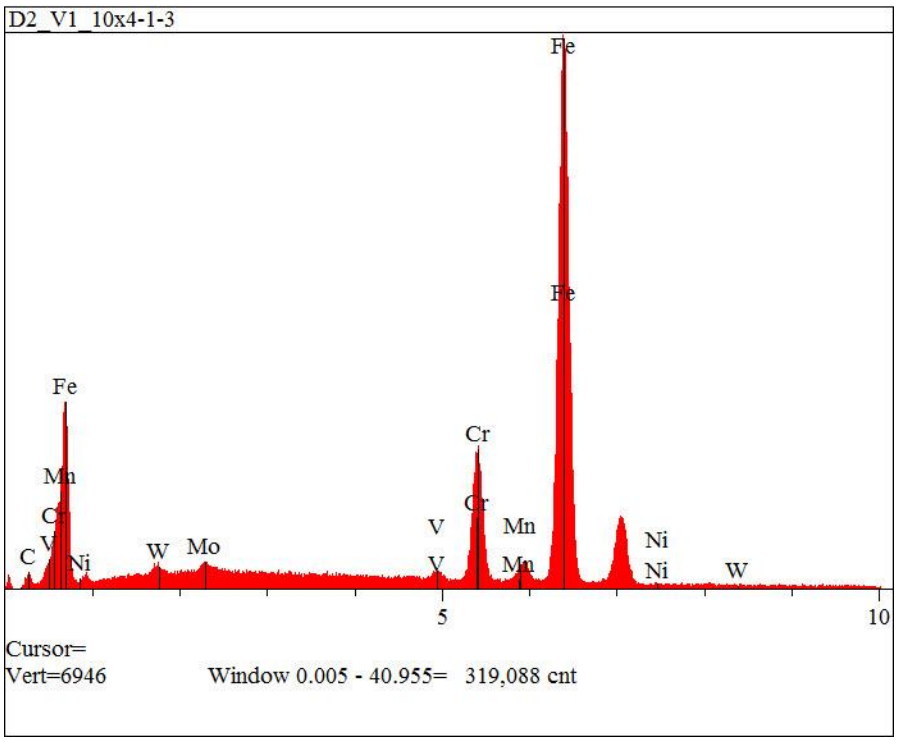
D2_V1_10x4-1-3
Fe
Fe
Fe
Mn
Cr
V
C
Ni
W
Mo
Cr
V
Mn
V
Mn
Ni
Ni
W
5
10
Cursor=
Vert=6946
Window 0.005 - 40.955= 319,088 cnt

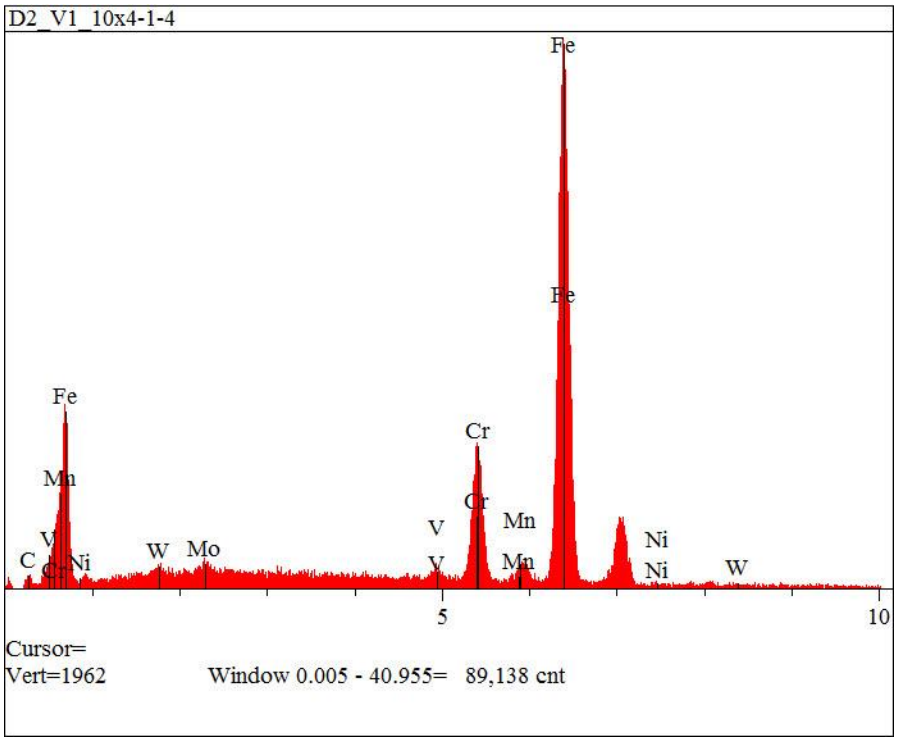
D2_V1_10x4-1-4
Fe
Fe
Fe
Mn
Cr
V
C
Ni
W
Mo
Cr
V
Mn
V
Mn
Ni
Ni
W
5
10
Cursor=
Vert=1962
Window 0.005 - 40.955= 89,138 cnt

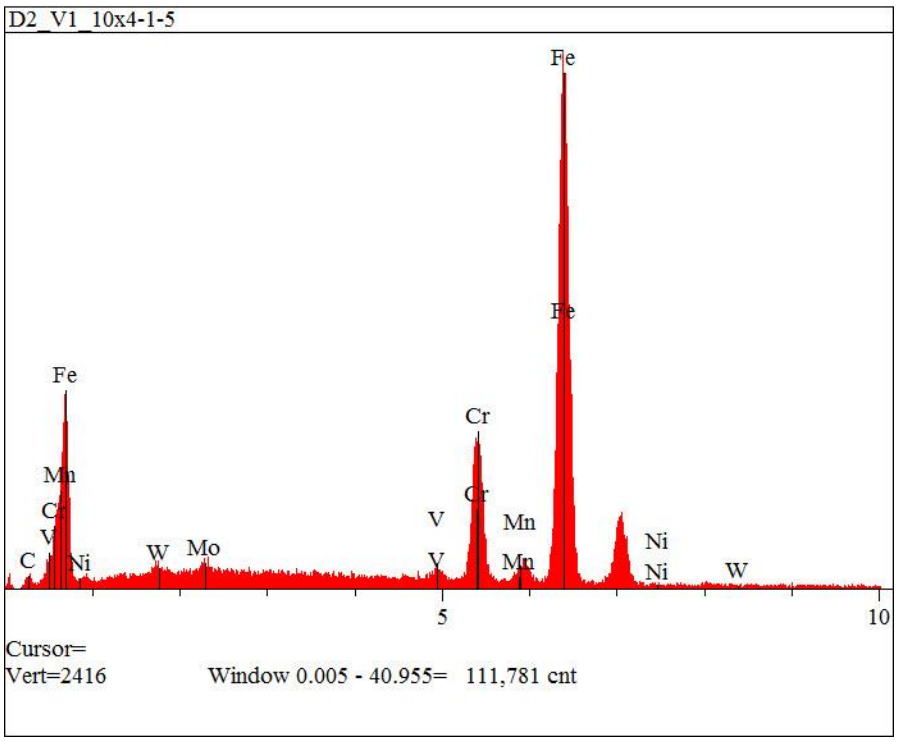
D2_V1_10x4-1-5
Fe
Fe
Fe
Cr
Mn
Cr
V
C
Ni
W
Mo
V
Cr
Mn
Mn
Ni
Ni
W
5
10
Cursor=
Vert=2416
Window 0.005 - 40.955= 111,781 cnt

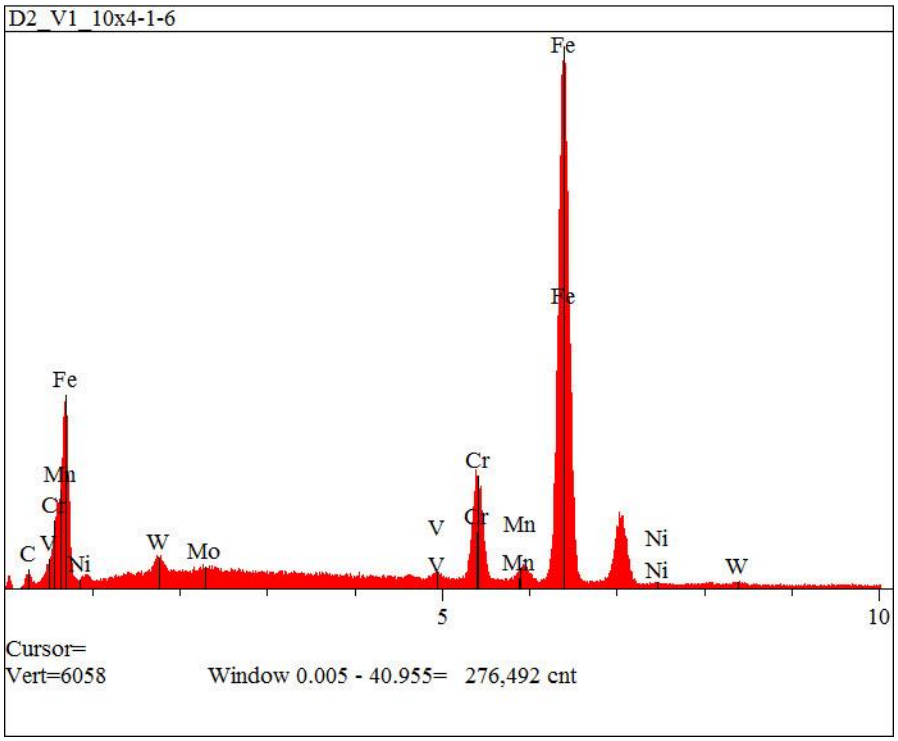
D2_V1_10x4-1-6
Fe
Fe
Fe
Cr
Mn
Cr
V
C
Ni
W
Mo
V
Cr
Mn
Mn
Ni
Ni
W
5
10
Cursor=
Vert=6058
Window 0.005 - 40.955= 276,492 cnt

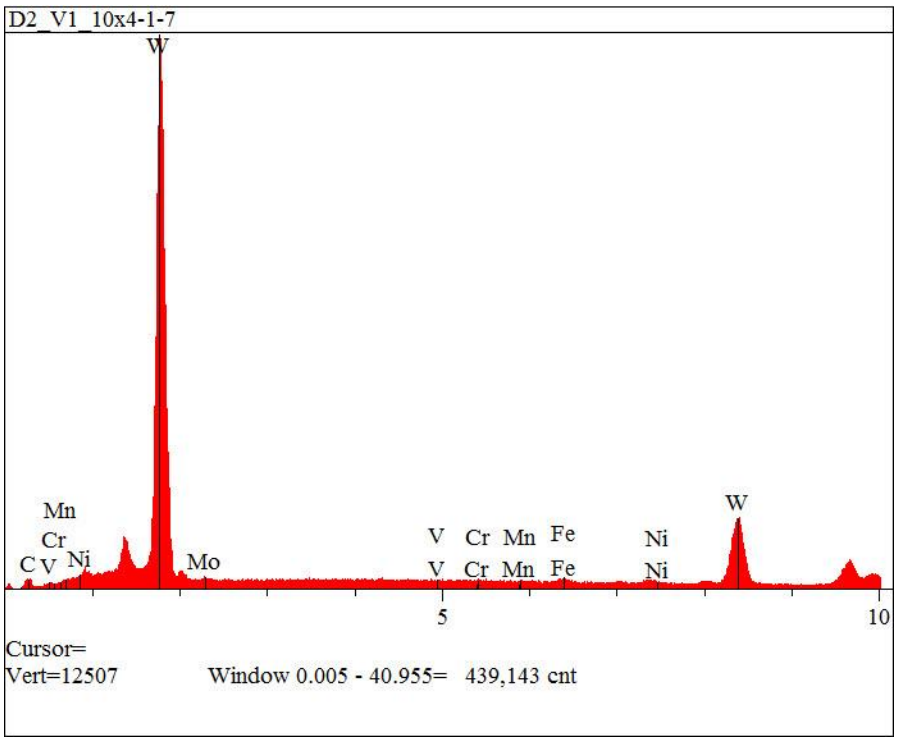
D2_V1_10x4-1-7
W
Mn
Cr
C V Ni
Mo
V Cr Mn Fe
V Cr Mn Fe
Ni
Ni
W
5
10
Cursor=
Vert=12507
Window 0.005 - 40.955= 439,143 cnt

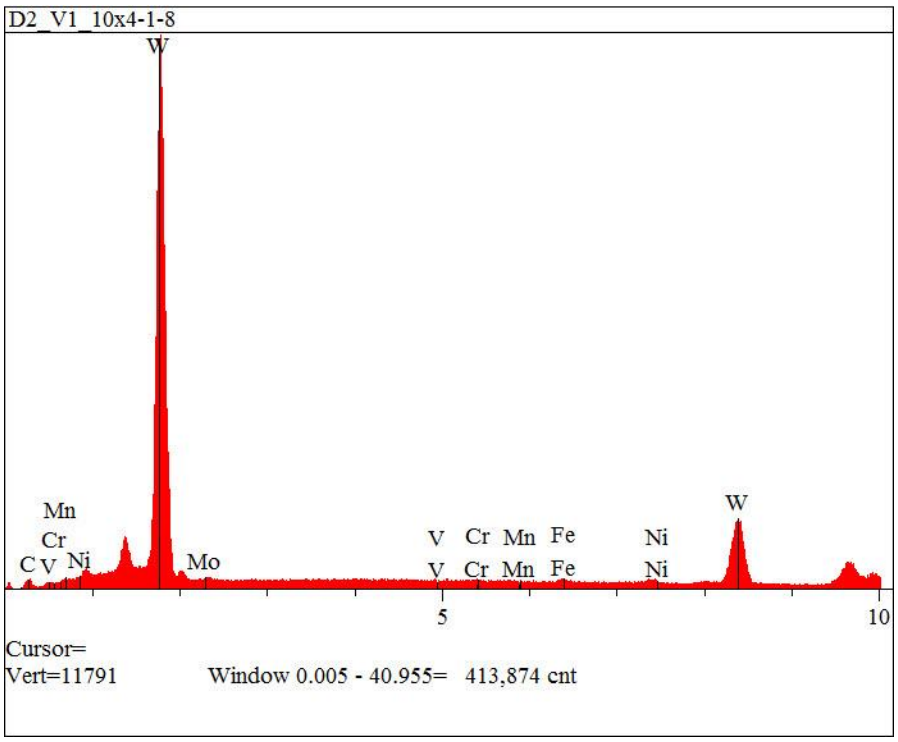
D2_V1_10x4-1-8
W
Mn
Cr
C V Ni
Mo
V Cr Mn Fe Ni
V Cr Mn Fe Ni
W
5
10
Cursor=
Vert=11791
Window 0.005 - 40.955= 413,874 cnt

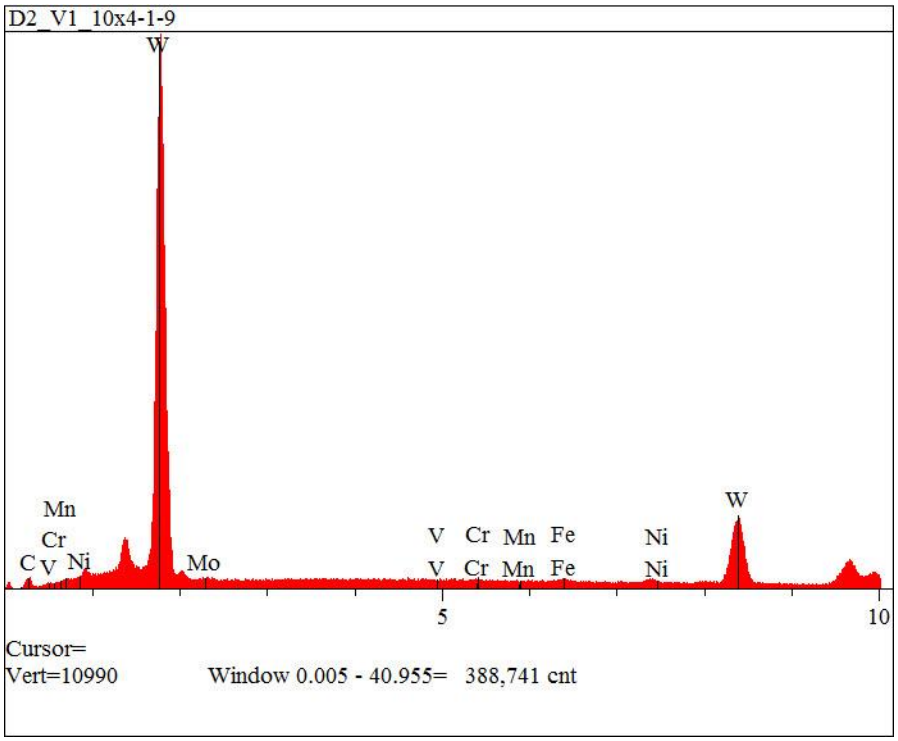
D2_V1_10x4-1-9
W
Mn
Cr
C V Ni
Mo
V Cr Mn Fe Ni
V Cr Mn Fe Ni
W
5
10
Cursor=
Vert=10990
Window 0.005 - 40.955= 388,741 cnt

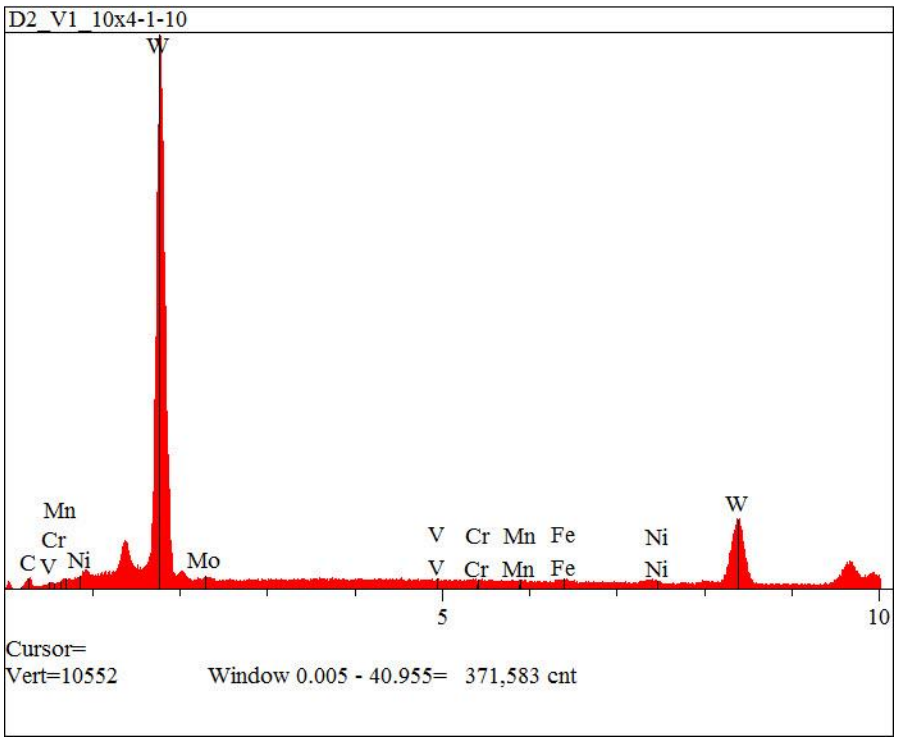
D2_V1_10x4-1-10
W
Mn
Cr
C V Ni
Mo
V Cr Mn Fe
V Cr Mn Fe
Ni
Ni
W
5
10
Cursor=
Vert=10552
Window 0.005 - 40.955= 371,583 cnt

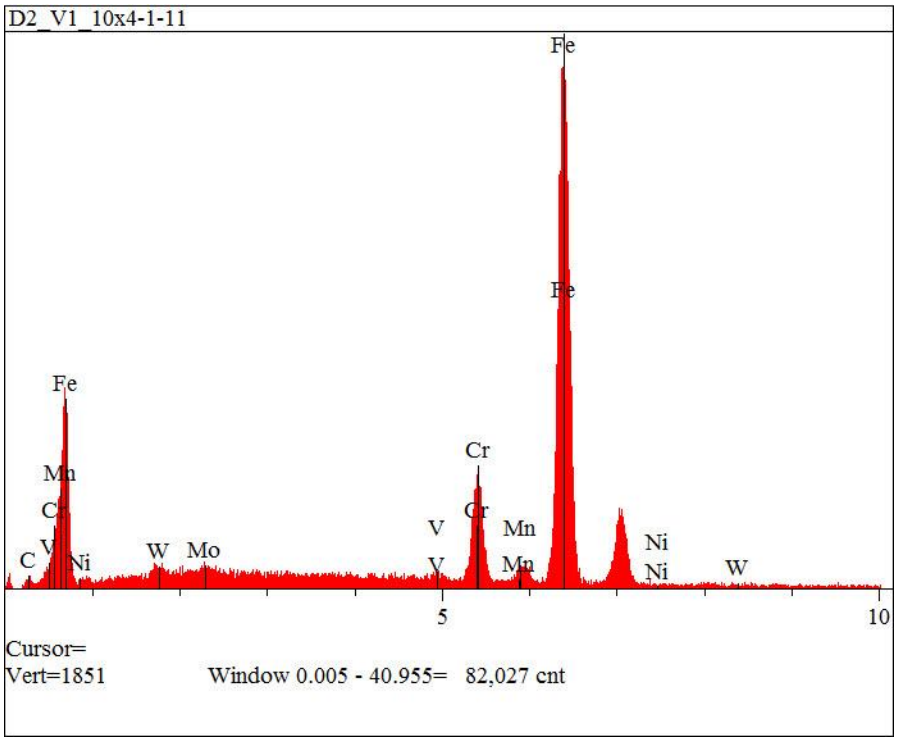
D2_V1_10x4-1-11
Fe
Fe
Fe
Mn
Cr
C V Ni
W Mo
Cr
V
V
Cr
Mn
Mn
Ni
Ni
W
5
10
Cursor=
Vert=1851
Window 0.005 - 40.955= 82,027 cnt

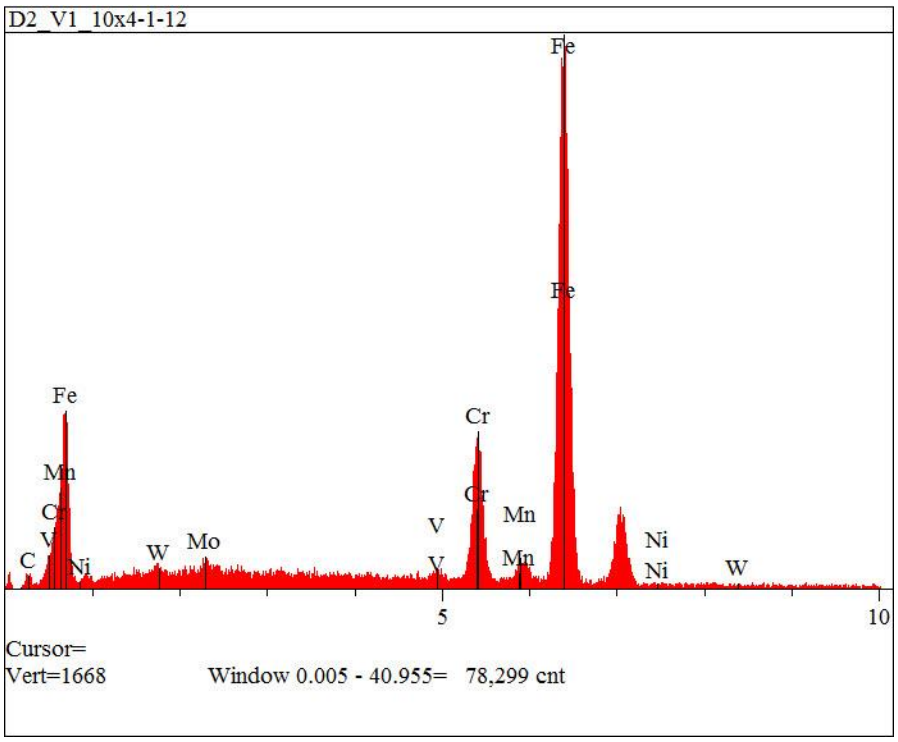
D2_V1_10x4-1-12
Fe
Fe
Fe
Mn
Cr
Cr
Mn
V
Mo
W
C
Ni
V
Mn
Ni
Ni
W
5
10
Cursor=
Vert=1668
Window 0.005 - 40.955= 78,299 cnt

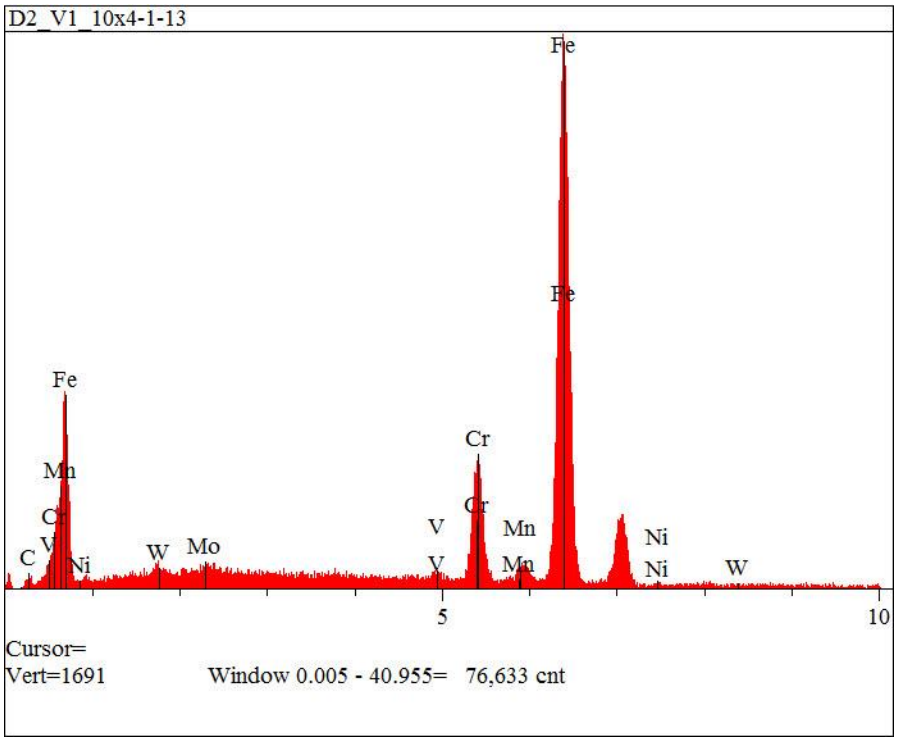
D2_V1_10x4-1-13
Fe
Fe
Fe
Mn
Cr
Cr
Mn
V
Mo
W
C
Ni
V
Mn
Ni
Ni
W
5
10
Cursor=
Vert=1691
Window 0.005 - 40.955= 76,633 cnt

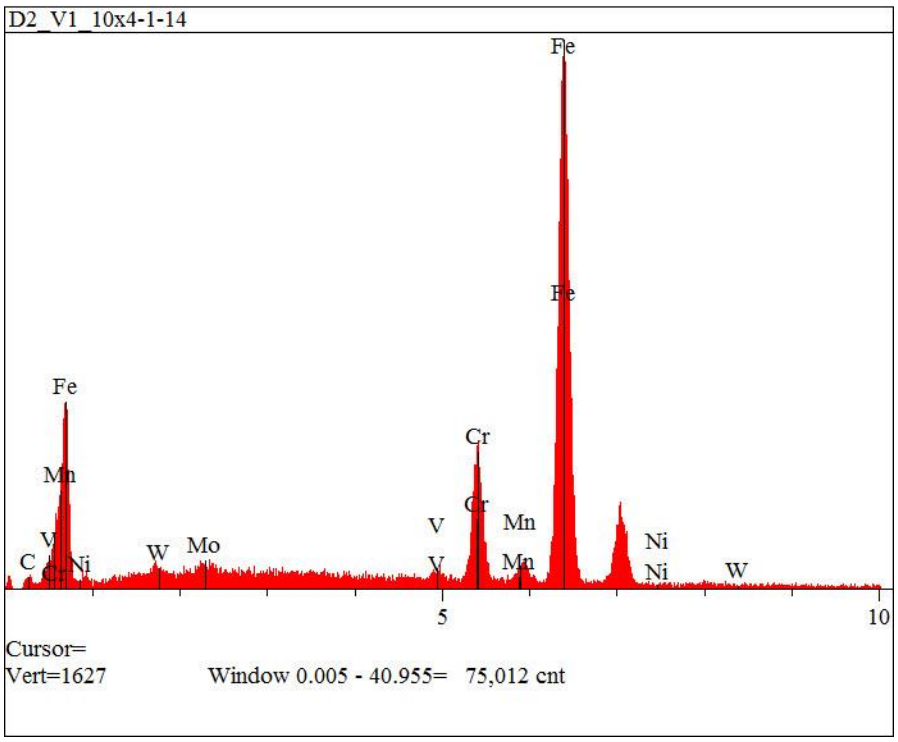
D2_V1_10x4-1-14
Fe
Fe
Fe
Mn
Cr
Cr
V
Mn
Ni
Ni
C
Ni
W
Mo
V
Mn
W
5
10
Cursor=
Vert=1627
Window 0.005 - 40.955= 75,012 cnt

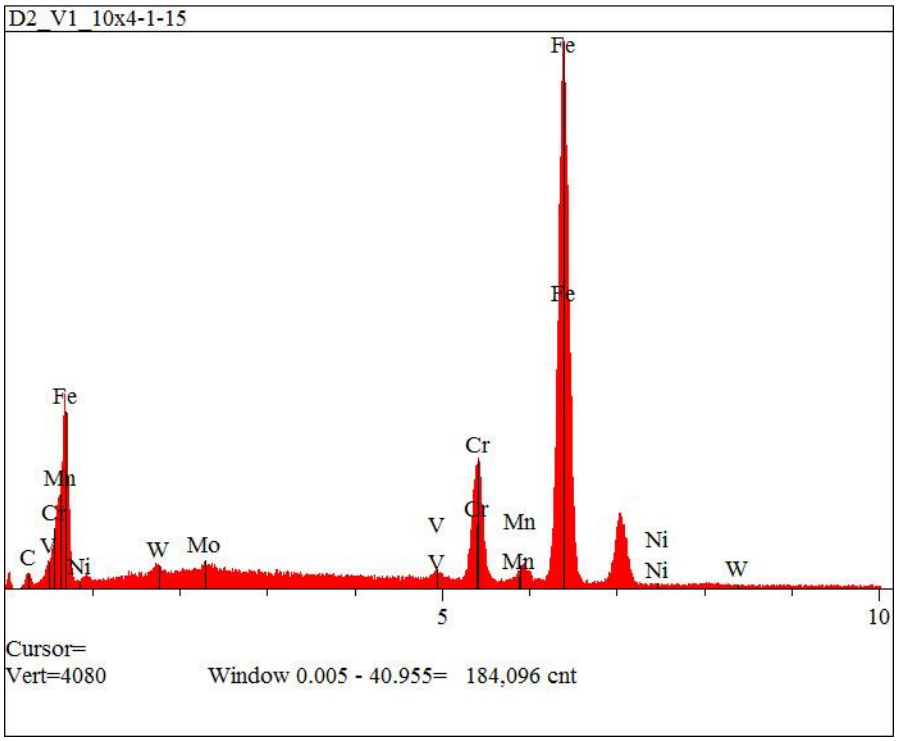
D2_V1_10x4-1-15
Fe
Fe
Fe
Mn
Cr
Cr
V
Mn
Ni
Ni
C
Ni
W
Mo
V
Mn
W
5
10
Cursor=
Vert=4080
Window 0.005 - 40.955= 184,096 cnt

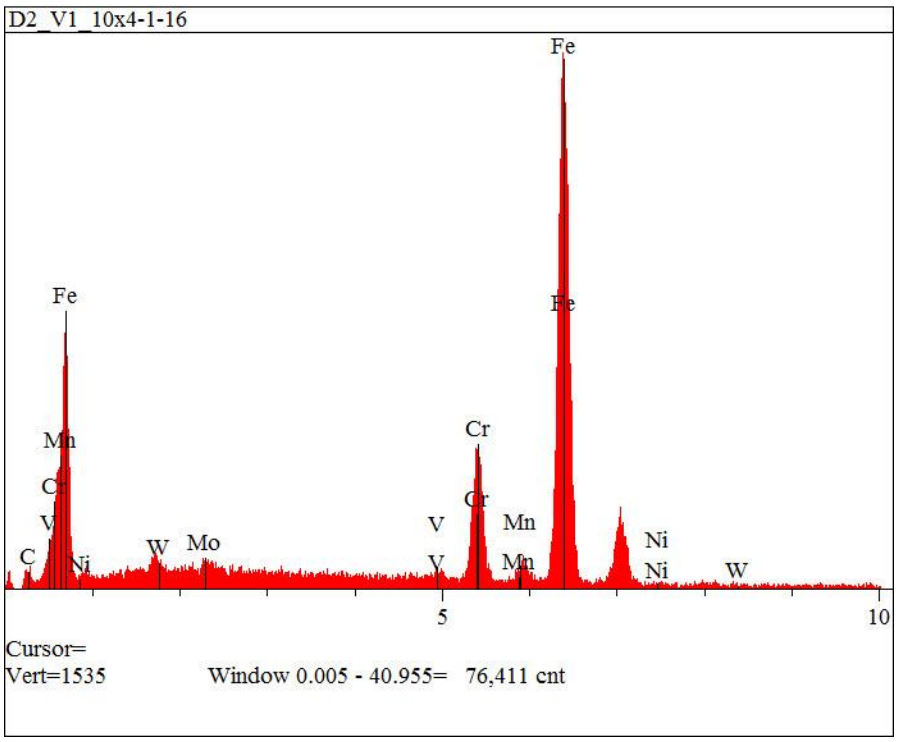
D2_V1_10x4-1-16
Fe
Fe
Mn
Cr
V
C
Ni
W
Mo
V
Cr
Mn
V
Mn
Ni
Ni
W
5
10
Cursor=
Vert=1535
Window 0.005 - 40.955= 76,411 cnt

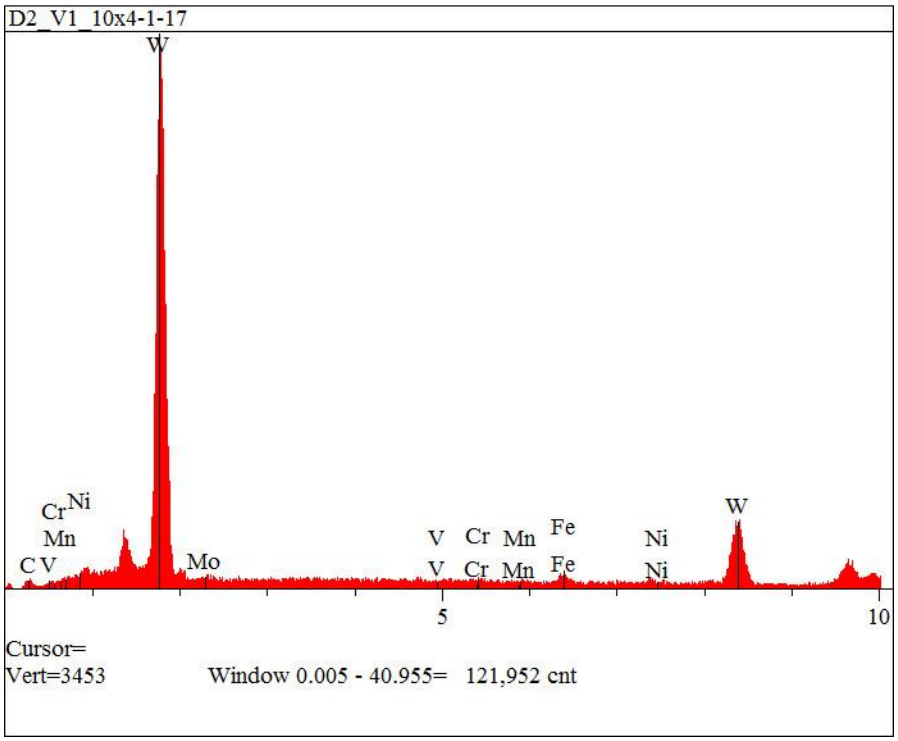
D2_V1_10x4-1-17
W
Cr
Ni
Mn
C
V
Mo
V
Cr
Mn
Fe
V
Cr
Mn
Fe
Ni
Ni
W
5
10
Cursor=
Vert=3453
Window 0.005 - 40.955= 121,952 cnt

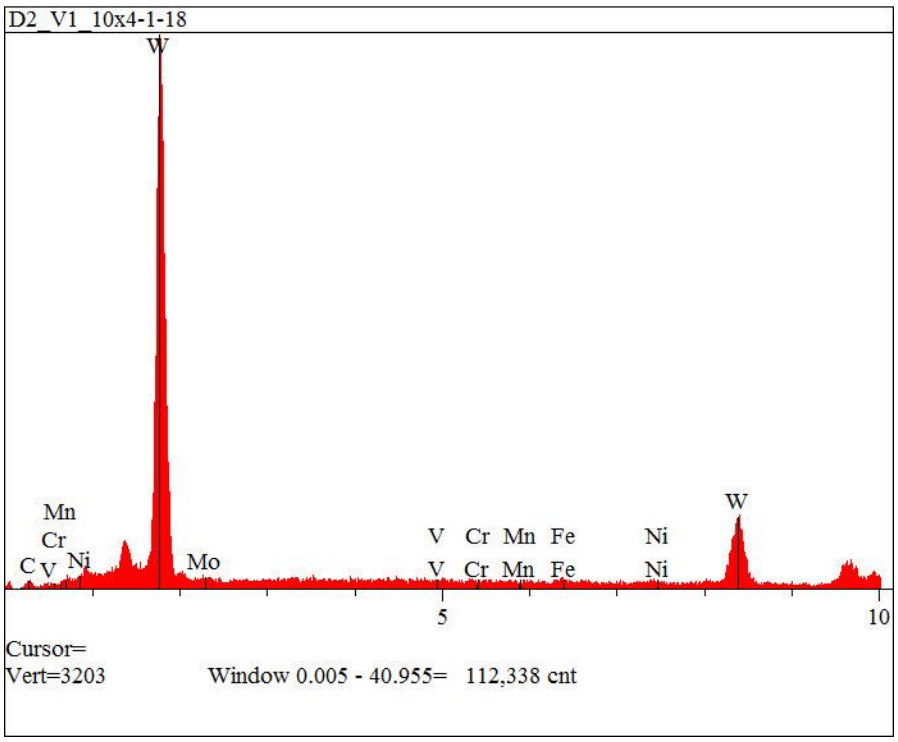
D2_V1_10x4-1-18
W
Mn
Cr
C V Ni
Mo
V Cr Mn Fe
V Cr Mn Fe
Ni
Ni
W
5
10
Cursor=
Vert=3203
Window 0.005 - 40.955= 112,338 cnt

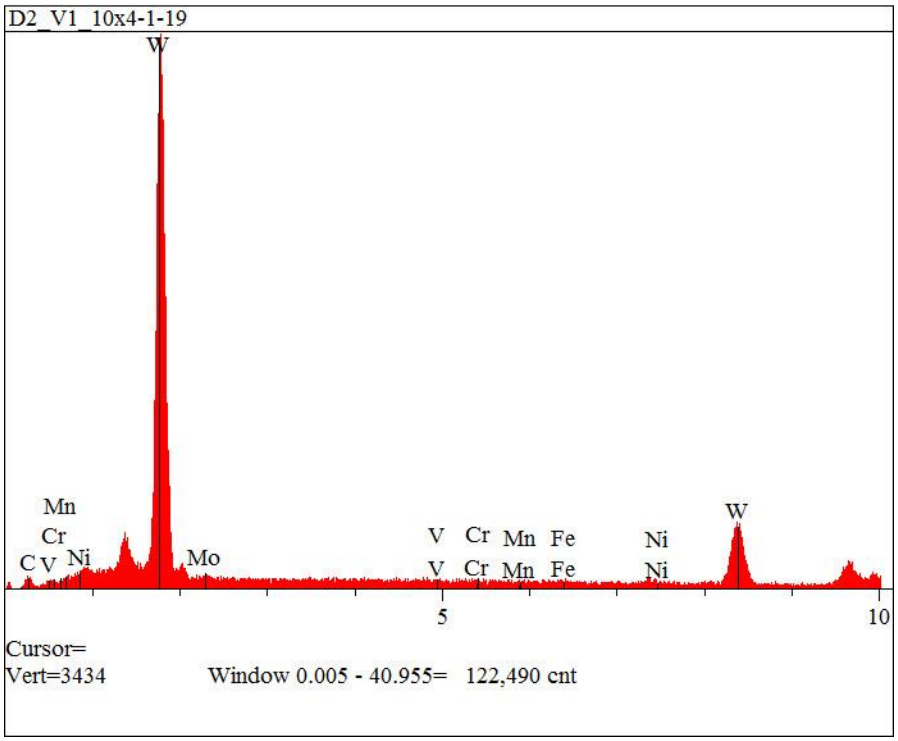
D2_V1_10x4-1-19
W
Mn
Cr
C V Ni
Mo
V Cr Mn Fe
V Cr Mn Fe
Ni
Ni
W
5
10
Cursor=
Vert=3434
Window 0.005 - 40.955= 122,490 cnt

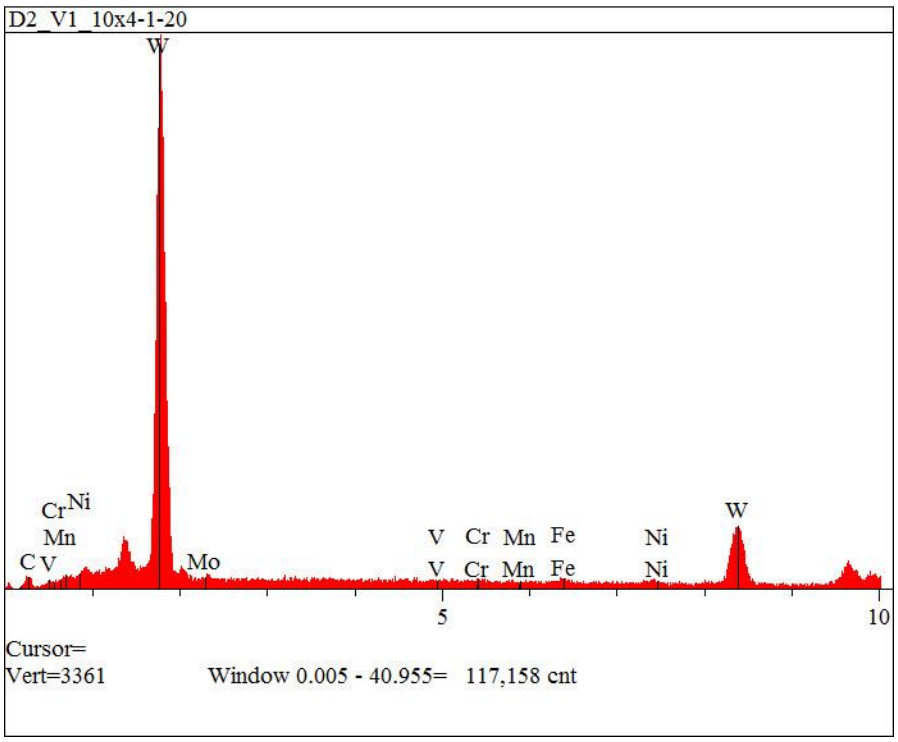
D2_V1_10x4-1-20
W
Cr Ni
Mn
C V
Mo
V Cr Mn Fe
V Cr Mn Fe
Ni
Ni
W
5
10
Cursor=
Vert=3361
Window 0.005 - 40.955= 117,158 cnt

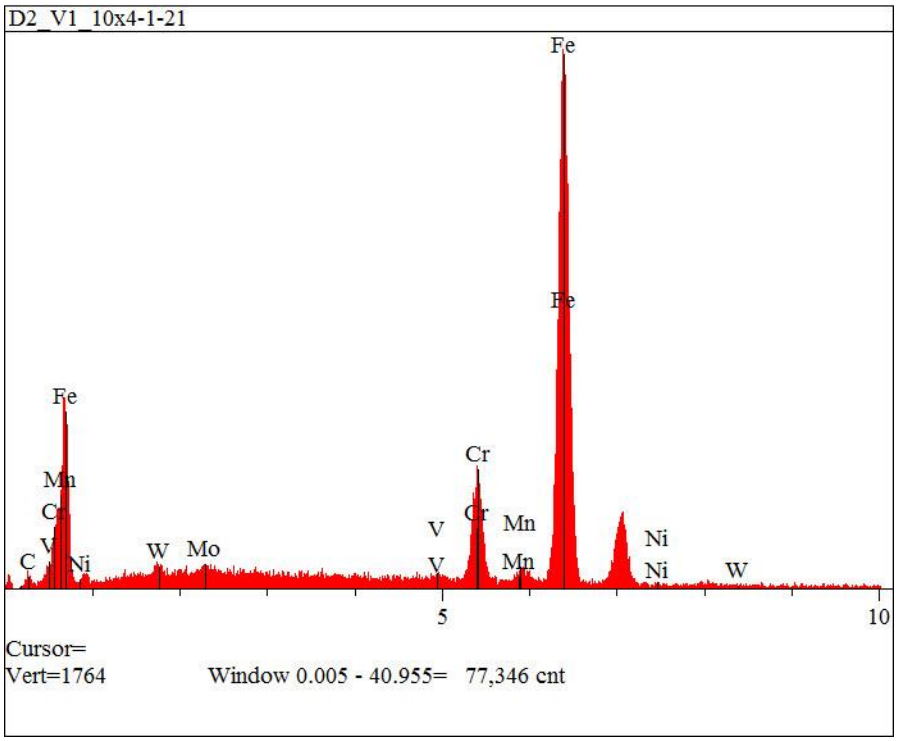
D2_V1_10x4-1-21
Fe
Fe
Fe
Mn
Cr
C
V
Ni
W Mo
Cr
V
Cr Mn
V
Mn
Ni
Ni
W
5
10
Cursor=
Vert=1764
Window 0.005 - 40.955= 77,346 cnt

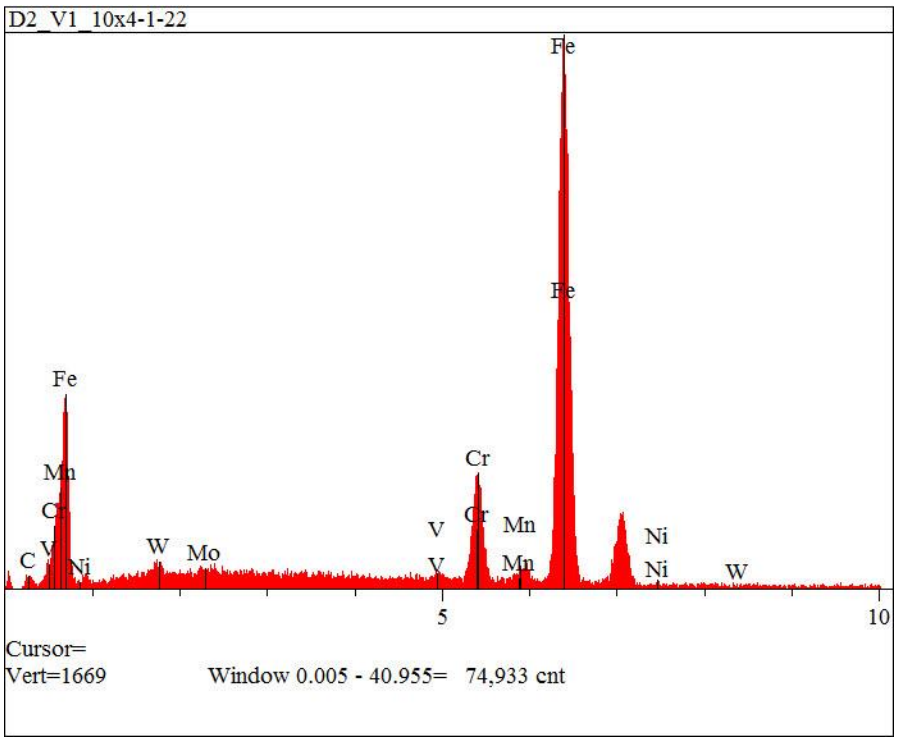
D2_V1_10x4-1-22
Fe
Fe
Fe
Mn
Cr
C
V
Ni
W
Mo
V
Cr
Cr
Mn
V
Mn
Ni
Ni
W
5
10
Cursor=
Vert=1669
Window 0.005 - 40.955= 74,933 cnt

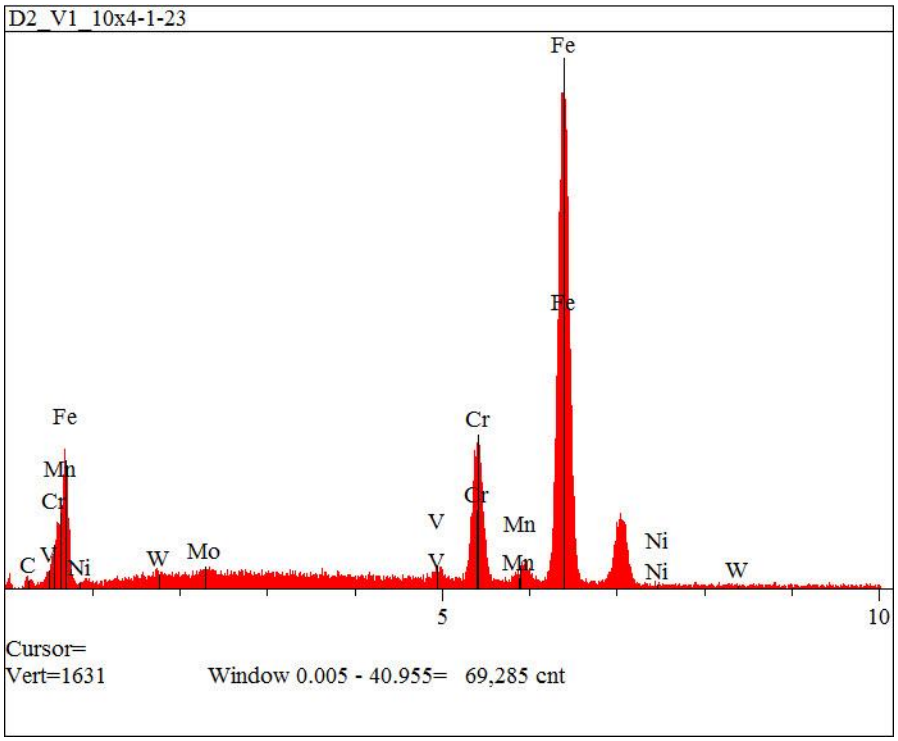
D2_V1_10x4-1-23
Fe
Fe
Fe
Mn
Cr
C
V
Ni
W
Mo
V
Cr
Cr
Mn
V
Mn
Ni
Ni
W
5
10
Cursor=
Vert=1631
Window 0.005 - 40.955= 69,285 cnt

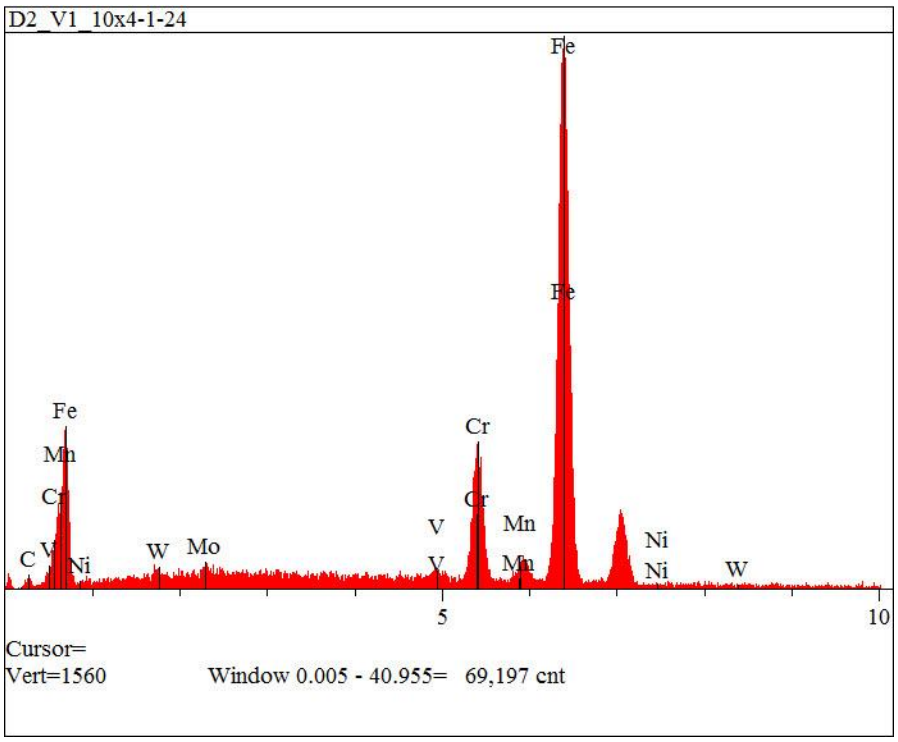
D2_V1_10x4-1-24
Fe
Fe
Fe
Mn
Cr
C
V
Ni
W
Mo
Cr
V
Mn
Ni
Ni
W
5
10
Cursor=
Vert=1560
Window 0.005 - 40.955= 69,197 cnt

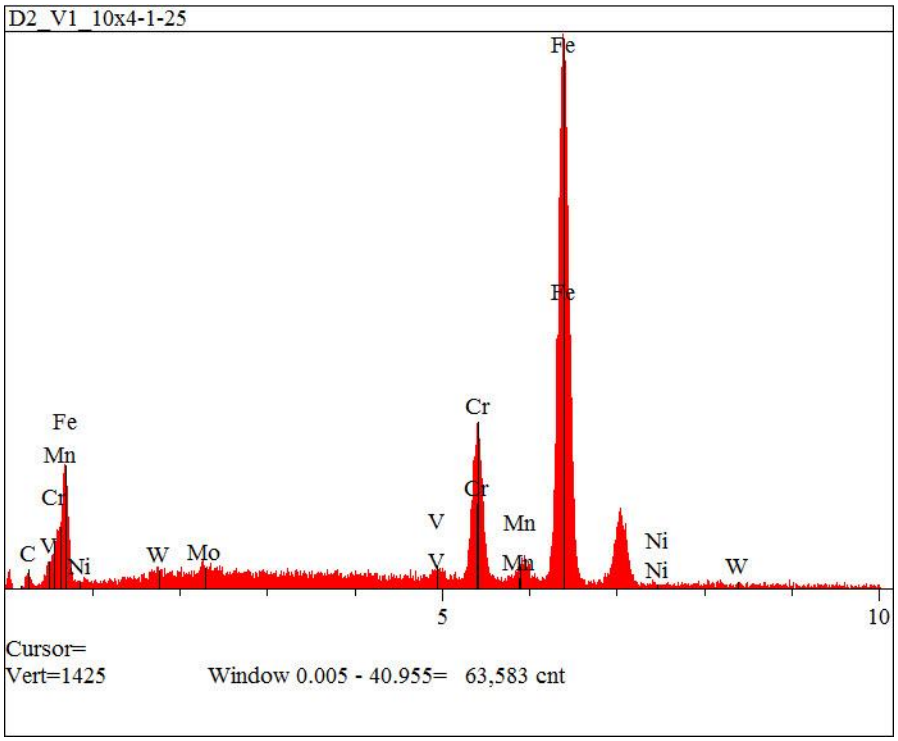
D2_V1_10x4-1-25
Fe
Fe
Fe
Mn
Cr
C
V
Ni
W
Mo
Cr
V
Mn
Ni
Ni
W
5
10
Cursor=
Vert=1425
Window 0.005 - 40.955= 63,583 cnt

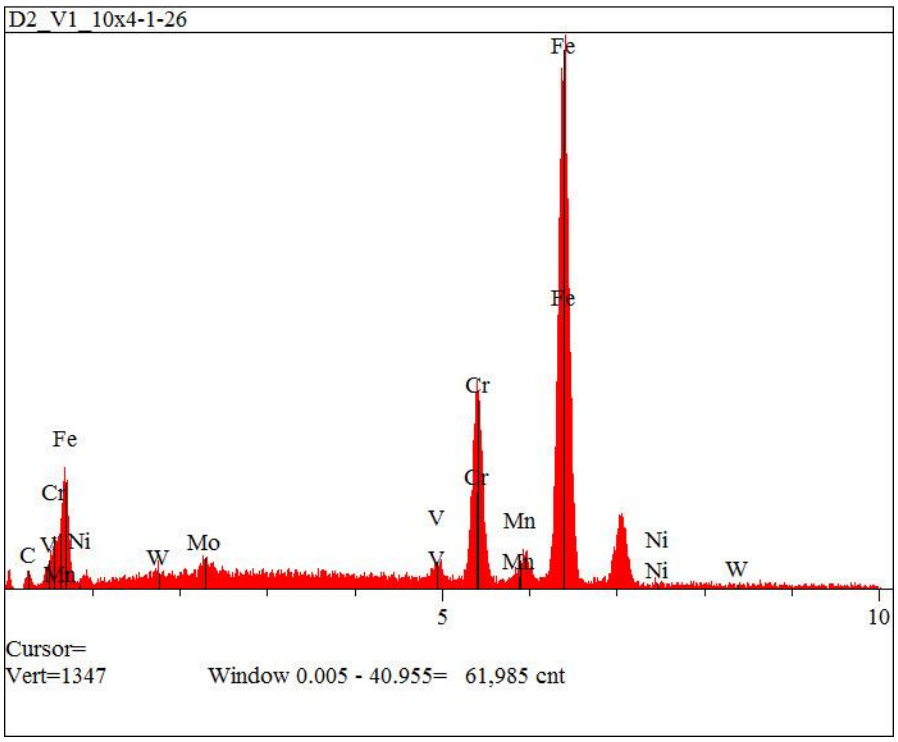
D2_V1_10x4-1-26
Fe
Fe
Cr
Fe
Cr
Cr
V
Mn
Ni
C
V
Ni
W
Mo
V
Mn
Ni
Ni
W
5
10
Cursor=
Vert=1347
Window 0.005 - 40.955= 61,985 cnt

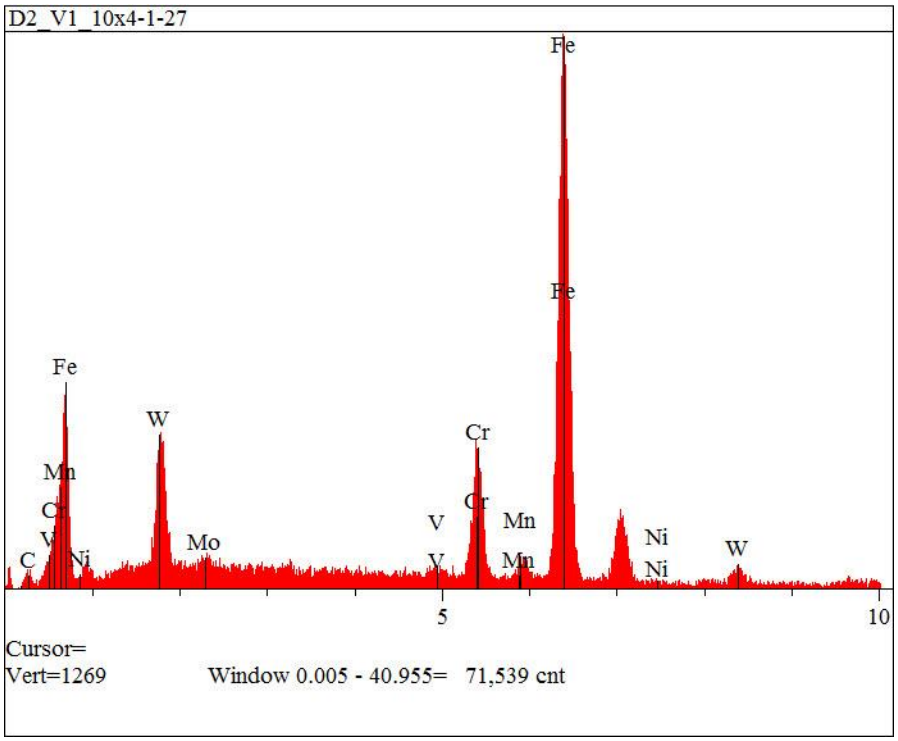
D2_V1_10x4-1-27
Fe
Fe
Fe
W
Cr
Mn
Cr
Cr
V
Mn
Ni
W
C
V
Ni
Mo
V
Mn
Ni
5
10
Cursor=
Vert=1269
Window 0.005 - 40.955= 71,539 cnt

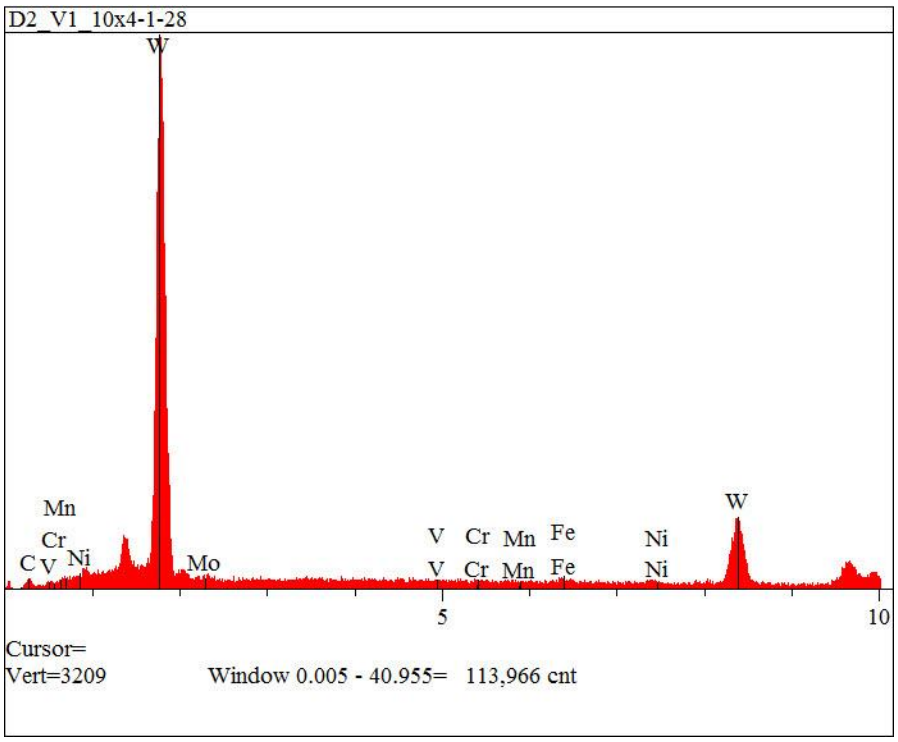
D2_V1_10x4-1-28
W
Mn
Cr
C V Ni
Mo
V Cr Mn Fe
V Cr Mn Fe
Ni
Ni
W
5
10
Cursor=
Vert=3209
Window 0.005 - 40.955= 113,966 cnt

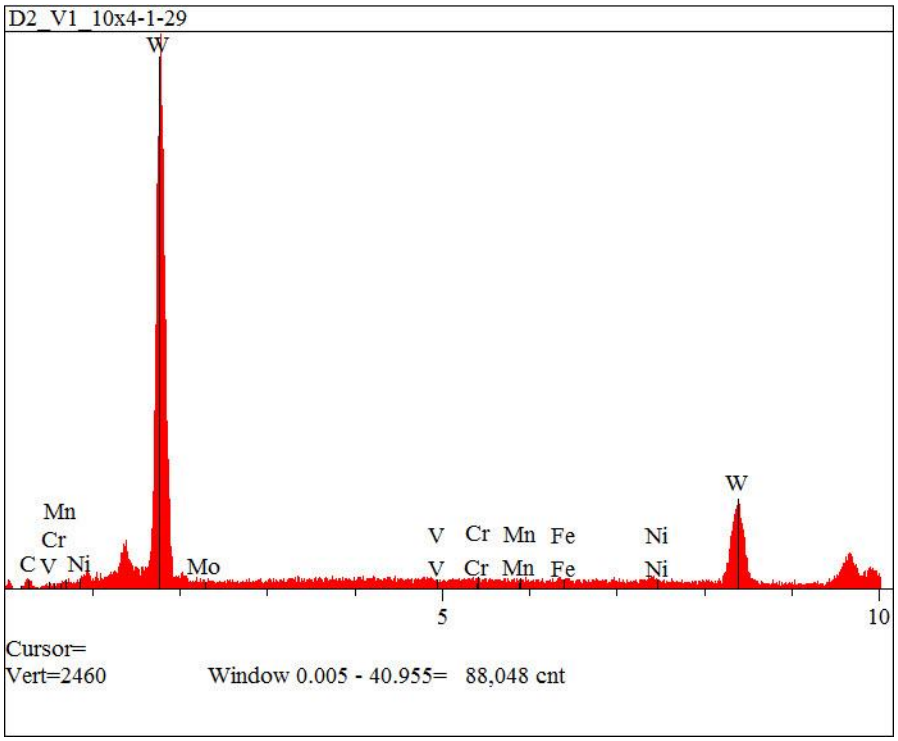
D2_V1_10x4-1-29
W
Mn
Cr
C V Ni
Mo
V Cr Mn Fe
V Cr Mn Fe
Ni
Ni
W
5
10
Cursor=
Vert=2460
Window 0.005 - 40.955= 88,048 cnt

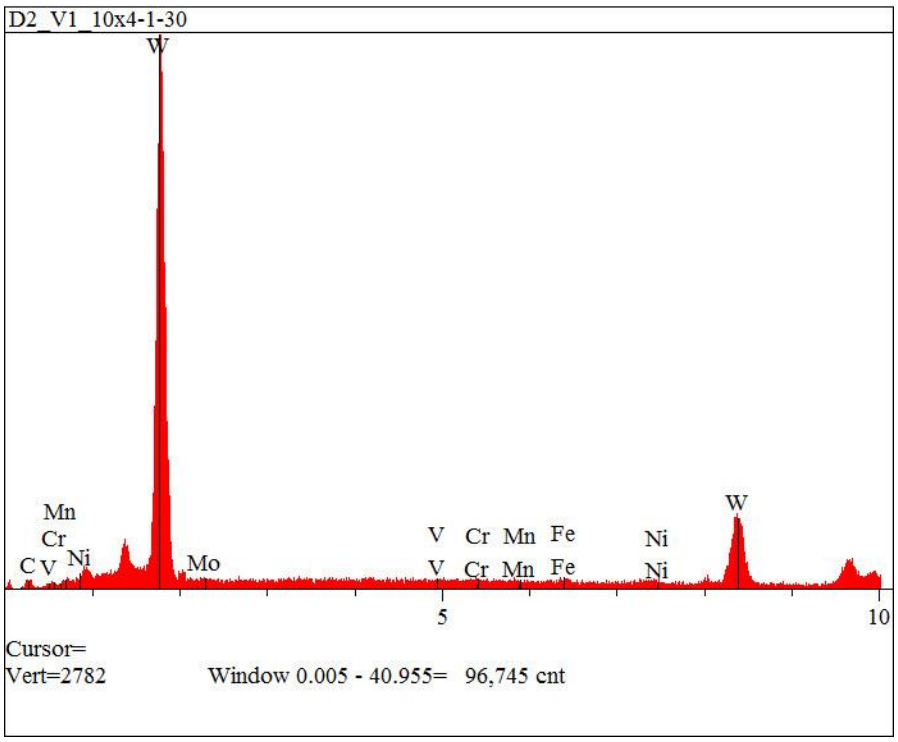
D2_V1_10x4-1-30
W
Mn
Cr
C V Ni
Mo
V Cr Mn Fe
V Cr Mn Fe
Ni
Ni
W
5
10
Cursor=
Vert=2782
Window 0.005 - 40.955= 96,745 cnt

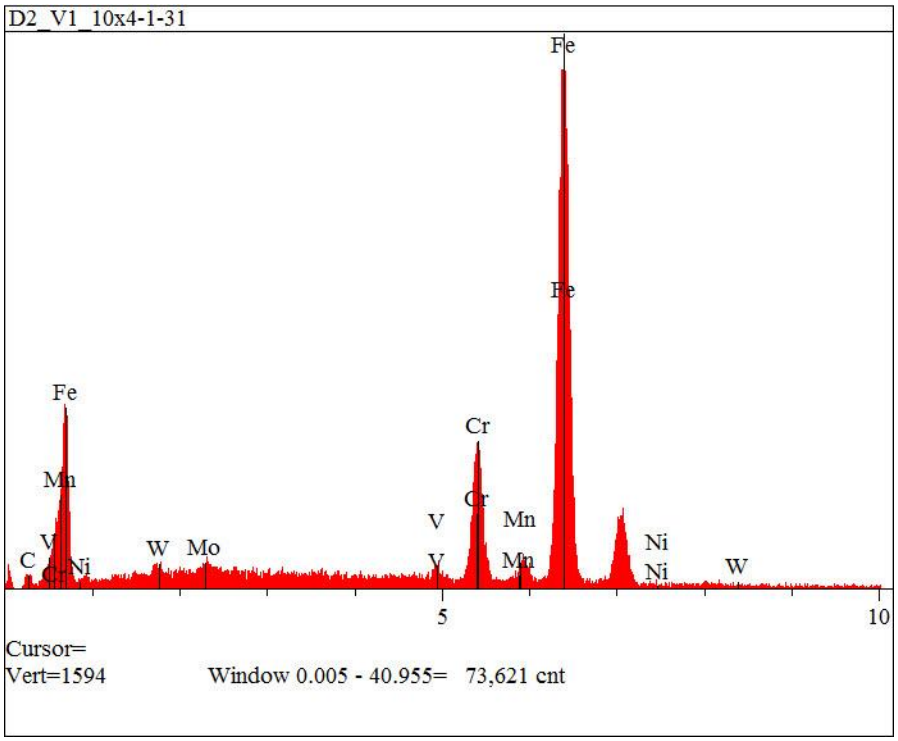
D2_V1_10x4-1-31
Fe
Fe
Fe
Cr
Mn
Cr
V
Mn
V
C
Ni
W Mo
V
Mn
Ni
Ni
W
5
10
Cursor=
Vert=1594
Window 0.005 - 40.955= 73,621 cnt

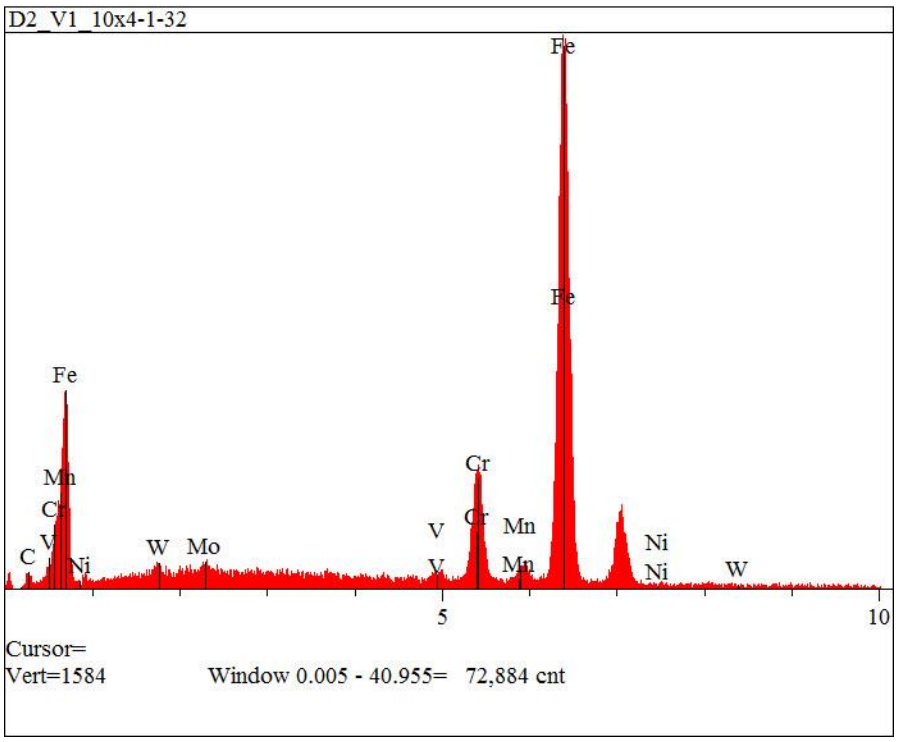
D2_V1_10x4-1-32
Fe
Fe
Fe
Mn
Cr
V
C
Ni
W
Mo
Cr
V
Mn
V
Mn
Ni
Ni
W
5
10
Cursor=
Vert=1584
Window 0.005 - 40.955= 72,884 cnt

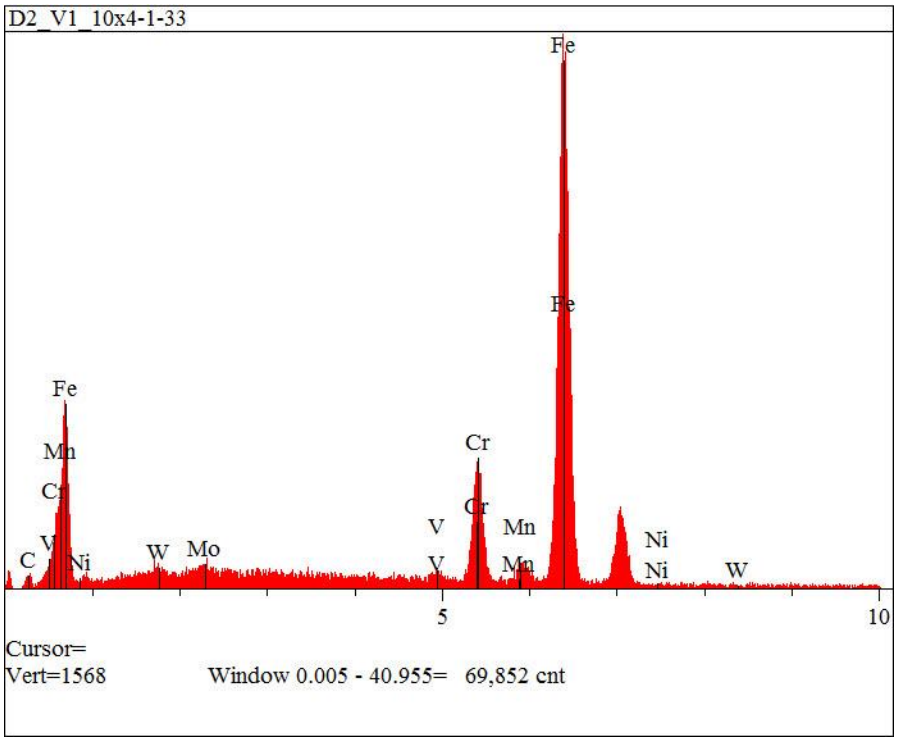
D2_V1_10x4-1-33
Fe
Fe
Fe
Mn
Cr
V
C
Ni
W
Mo
Cr
V
Mn
V
Mn
Ni
Ni
W
5
10
Cursor=
Vert=1568
Window 0.005 - 40.955= 69,852 cnt

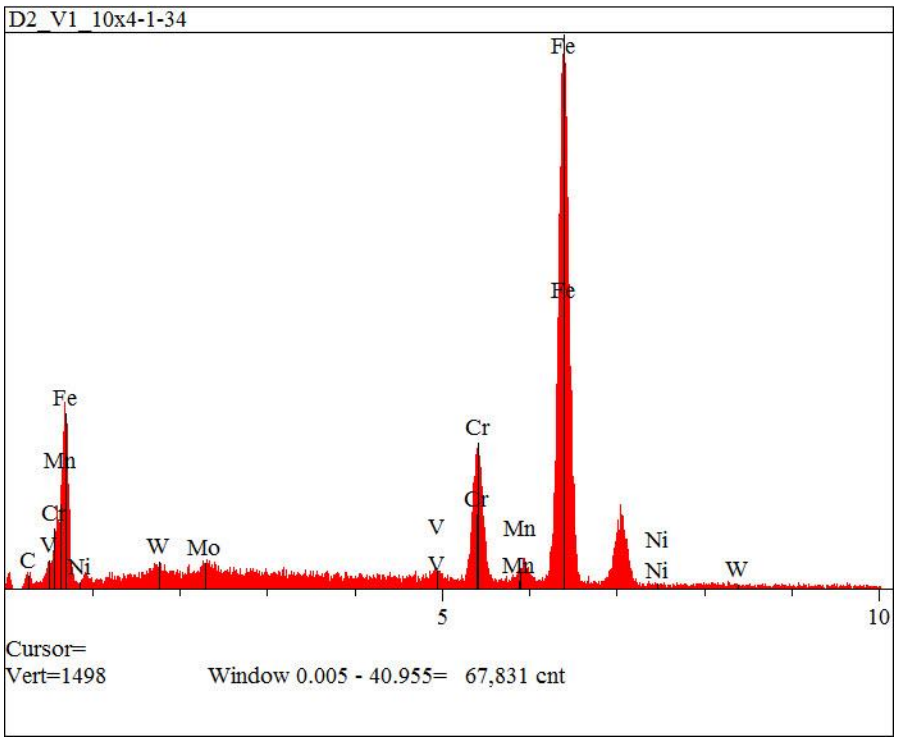
D2_V1_10x4-1-34
Fe
Fe
Fe
Mn
Cr
Cr
V
Mn
Ni
C
V
W
Mo
Ni
V
Mn
Ni
W
5
10
Cursor=
Vert=1498
Window 0.005 - 40.955= 67,831 cnt

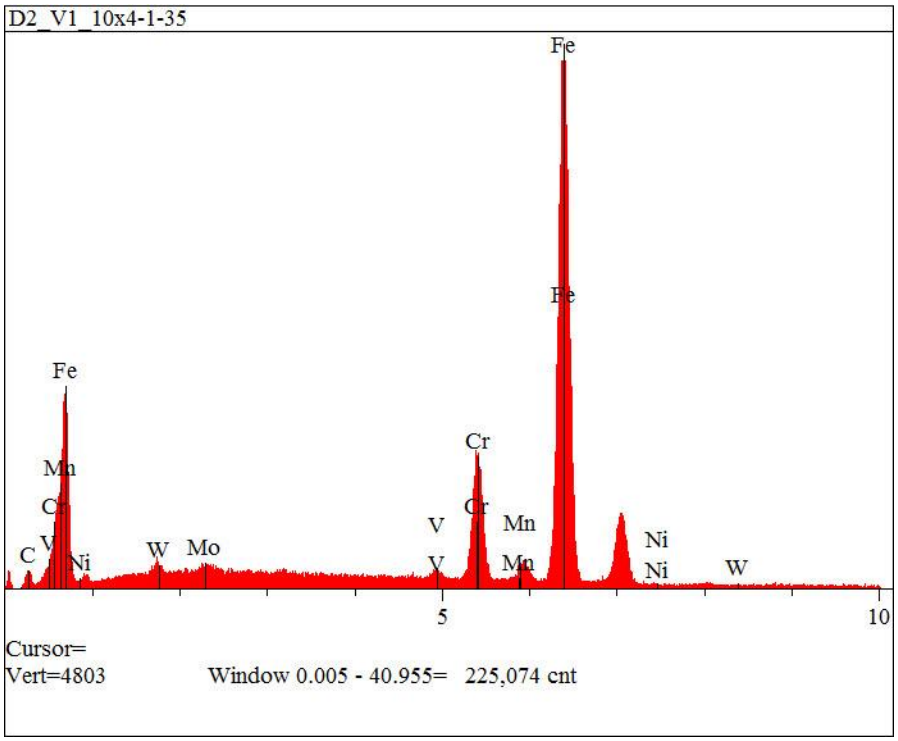
D2_V1_10x4-1-35
Fe
Fe
Fe
Mn
Cr
Cr
V
Mn
Ni
C
V
W
Mo
Ni
V
Mn
Ni
W
5
10
Cursor=
Vert=4803
Window 0.005 - 40.955= 225,074 cnt

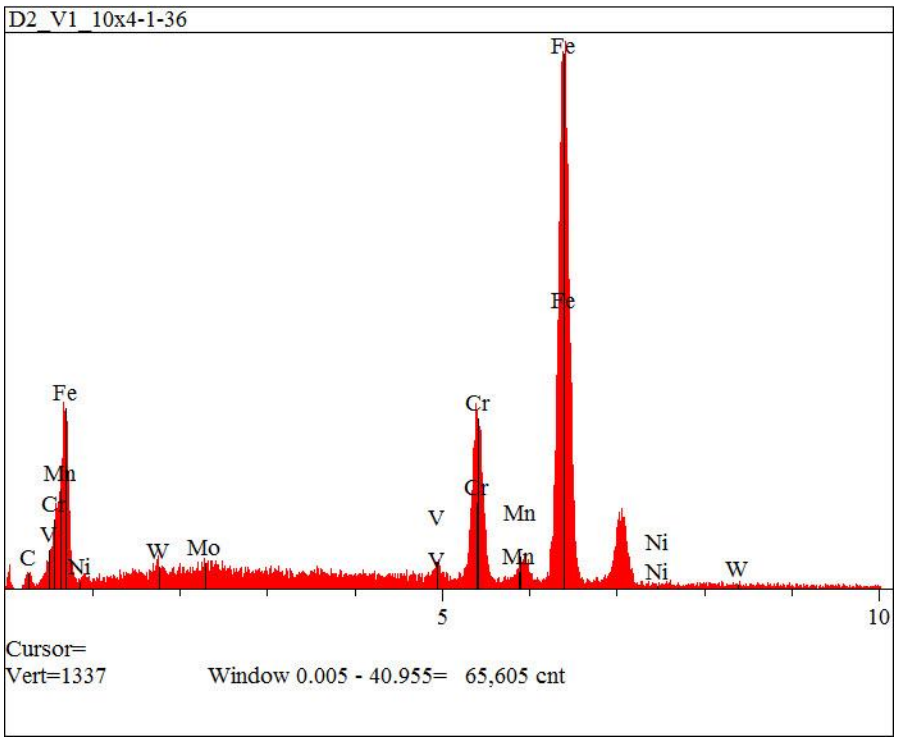
D2_V1_10x4-1-36
Fe
Fe
Fe
Cr
Mn
Cr
V
Mn
C
V
W
Mo
Ni
V
Mn
Ni
Ni
W
5
10
Cursor=
Vert=1337
Window 0.005 - 40.955= 65,605 cnt

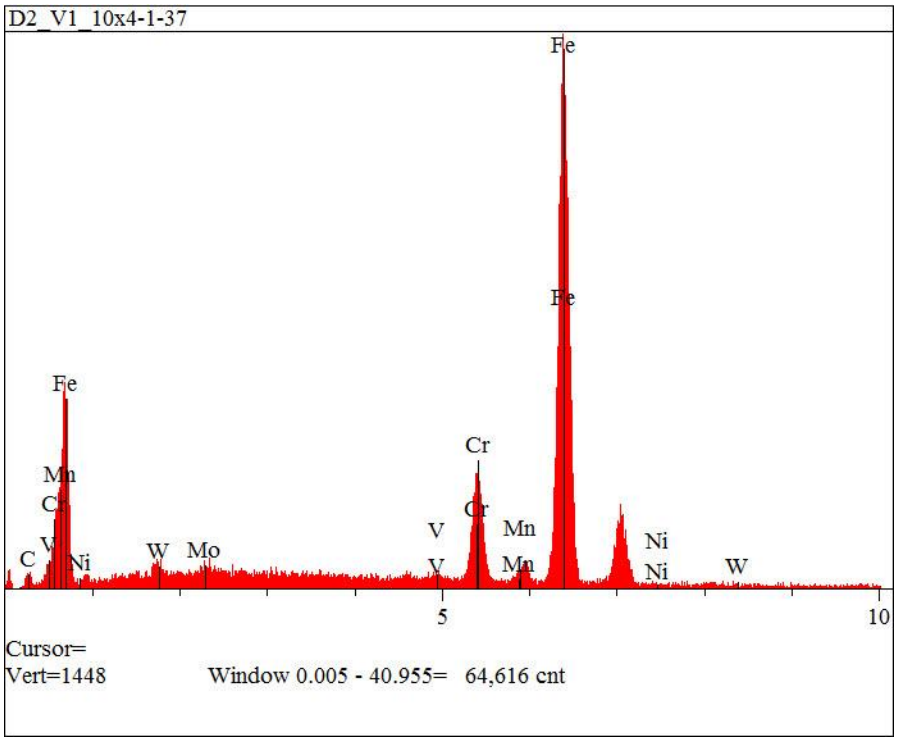
D2_V1_10x4-1-37
Fe
Fe
Fe
Cr
Mn
Cr
V
Mn
C
V
W
Mo
Ni
V
Mn
Ni
Ni
W
5
10
Cursor=
Vert=1448
Window 0.005 - 40.955= 64,616 cnt

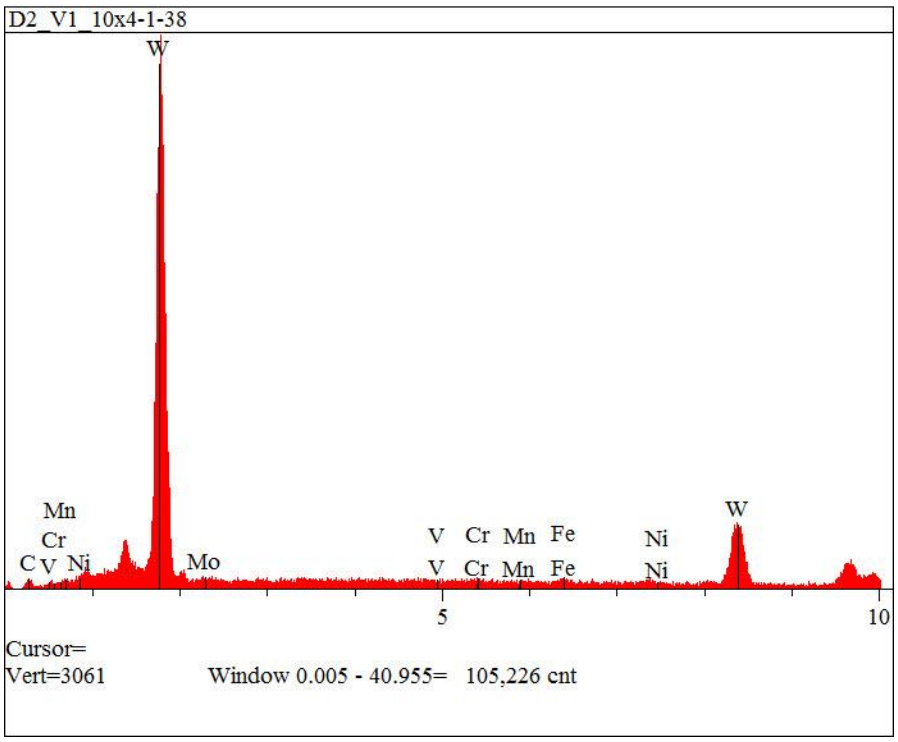
D2_V1_10x4-1-38
W
Mn
Cr
C V Ni
Mo
V Cr Mn Fe
V Cr Mn Fe
Ni
Ni
W
5
10
Cursor=
Vert=3061
Window 0.005 - 40.955= 105,226 cnt

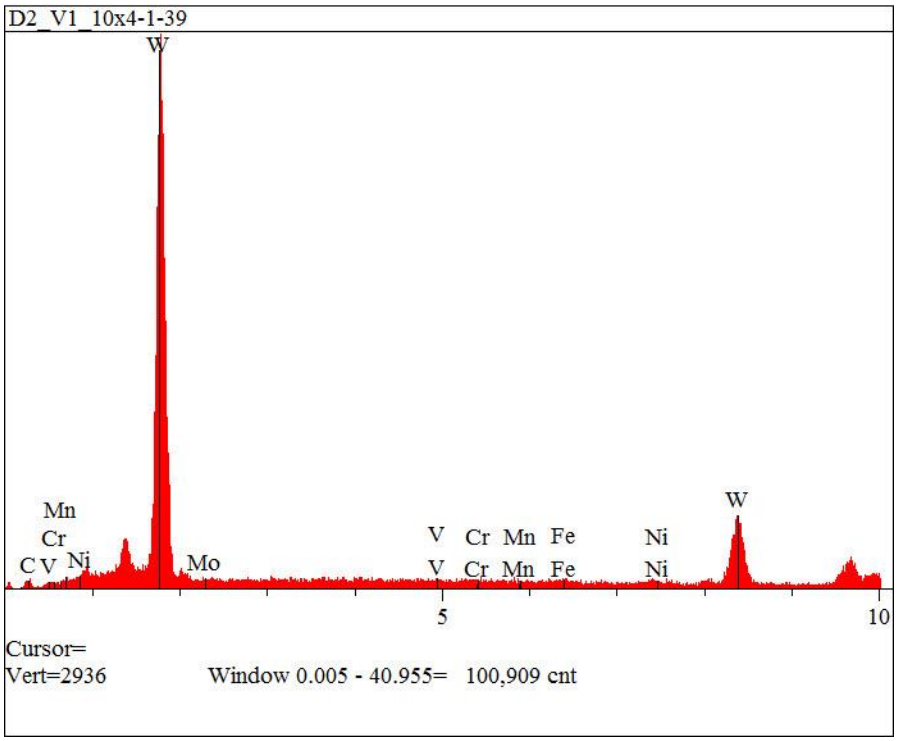
D2_V1_10x4-1-39
W
Mn
Cr
C V Ni
Mo
V Cr Mn Fe
V Cr Mn Fe
Ni
Ni
W
5
10
Cursor=
Vert=2936
Window 0.005 - 40.955= 100,909 cnt

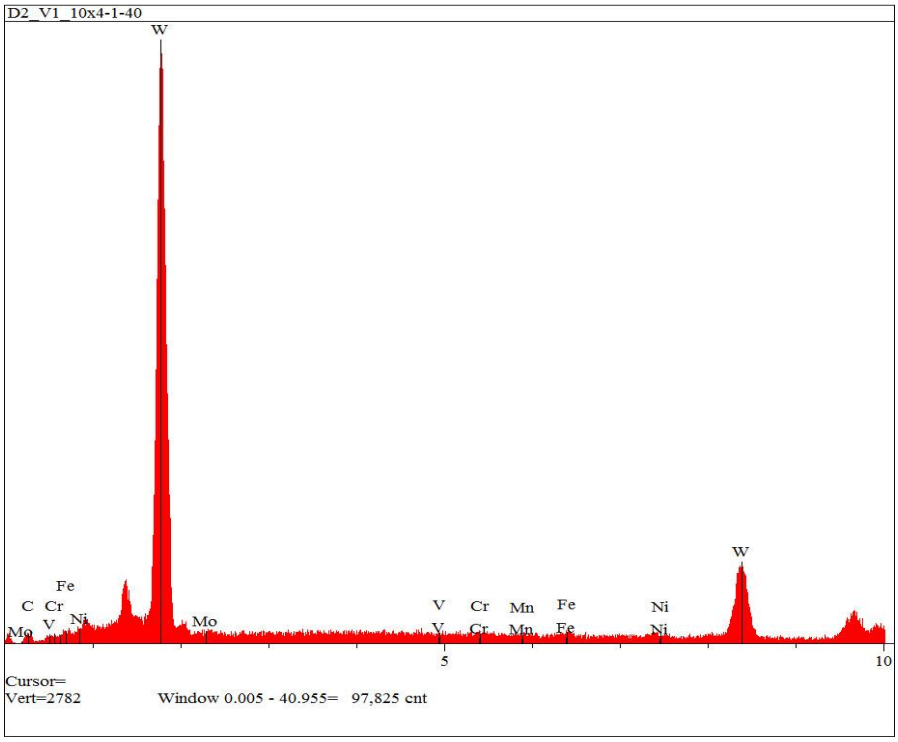
D2_V1_10x4-1-40
W
Fe
C
Cr
V
Ni
Mo
Mo
V
Cr
Mn
Fe
Ni
W
5
10
Cursor=
Vert=2782
Window 0.005 - 40.955= 97,825 cnt

D2_H1_4x10 1-40 EDS Plots

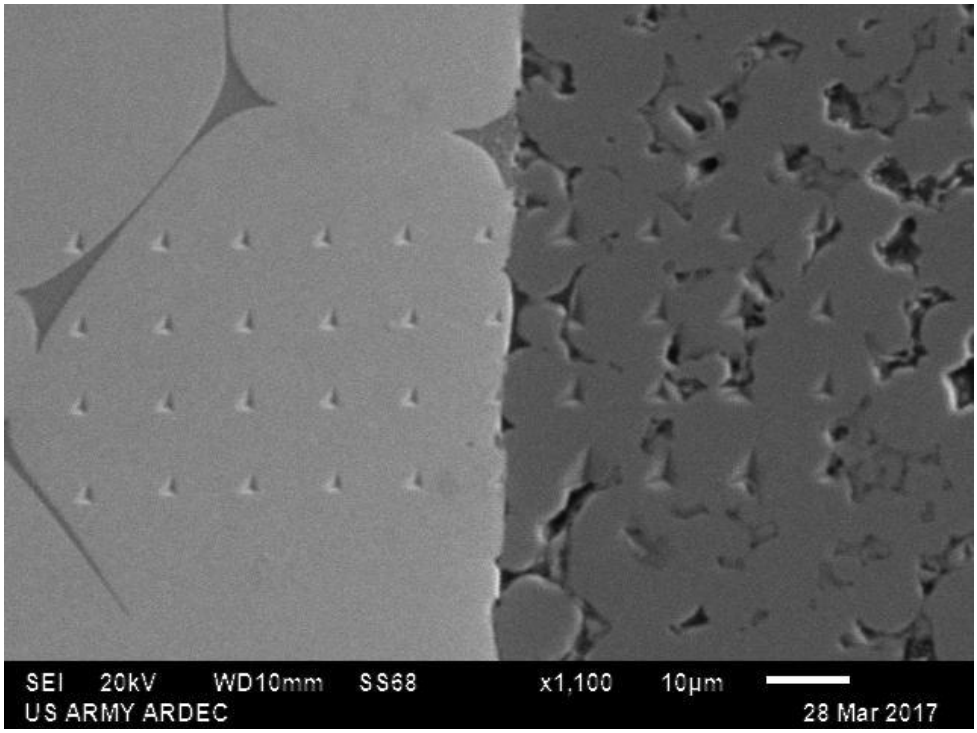

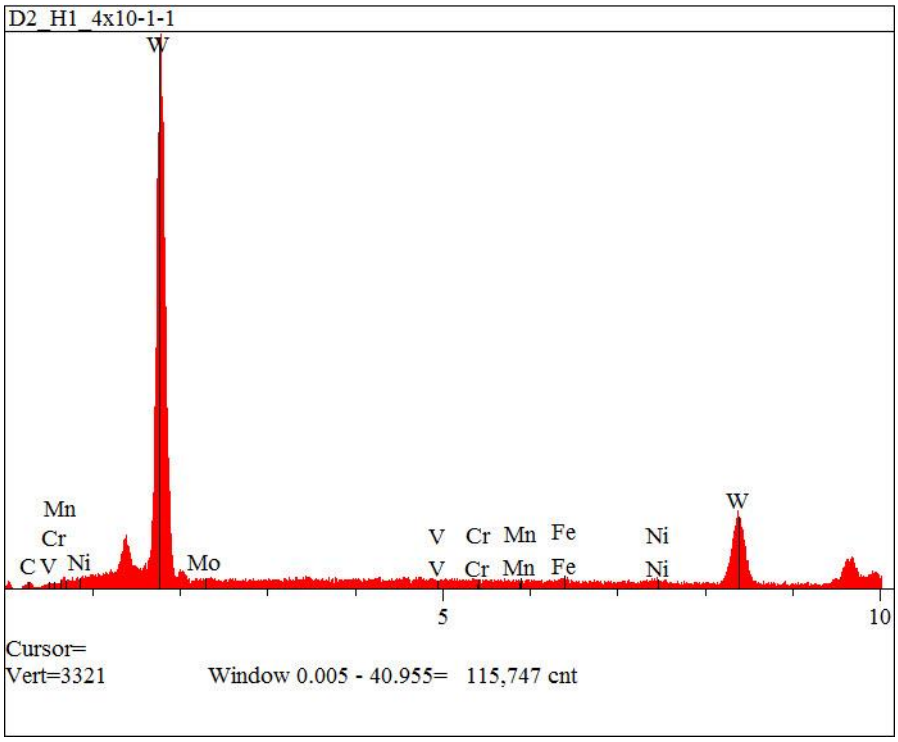
D2_H1_4x10-1-1
W
Mn
Cr
C V Ni
Mo
V Cr Mn Fe
V Cr Mn Fe
Ni
Ni
W
5
10
Cursor=
Vert=3321
Window 0.005 - 40.955= 115,747 cnt

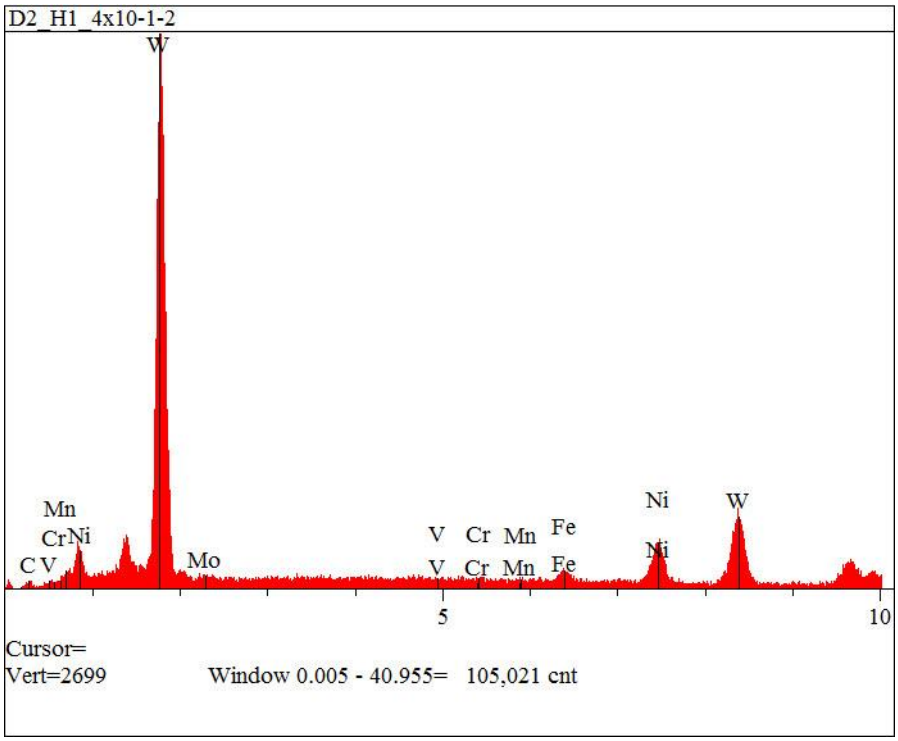
D2_H1_4x10-1-2
W
Mn
CrNi
C V
Mo
V Cr Mn Fe
V Cr Mn Fe
Ni
Ni
W
5
10
Cursor=
Vert=2699
Window 0.005 - 40.955= 105,021 cnt

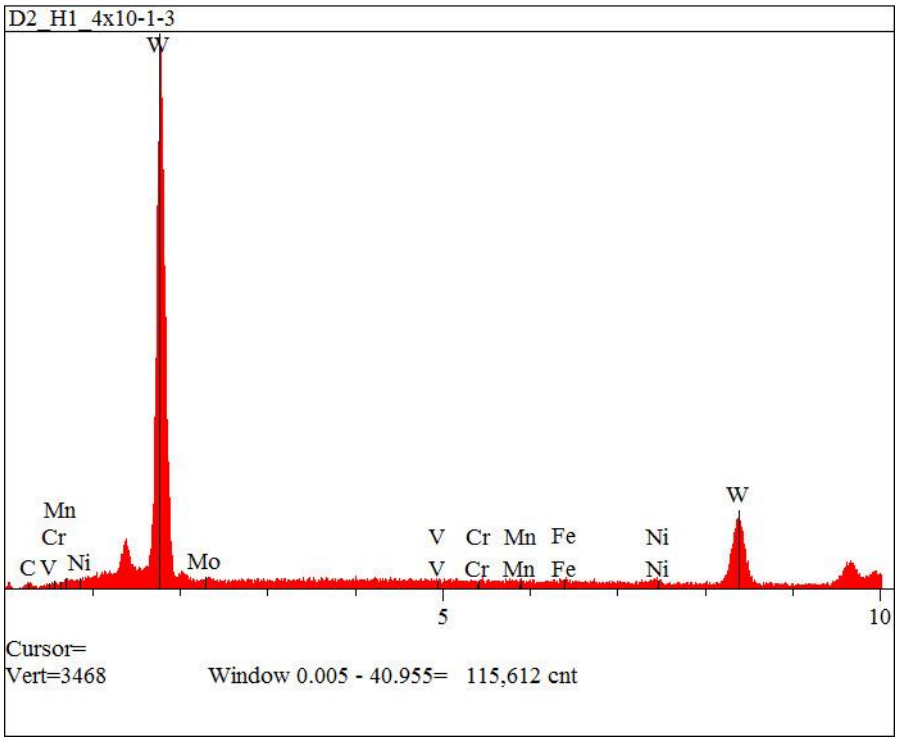
D2_H1_4x10-1-3
W
Mn
Cr
C V Ni
Mo
V Cr Mn Fe Ni
V Cr Mn Fe Ni
W
5
10
Cursor=
Vert=3468
Window 0.005 - 40.955= 115,612 cnt

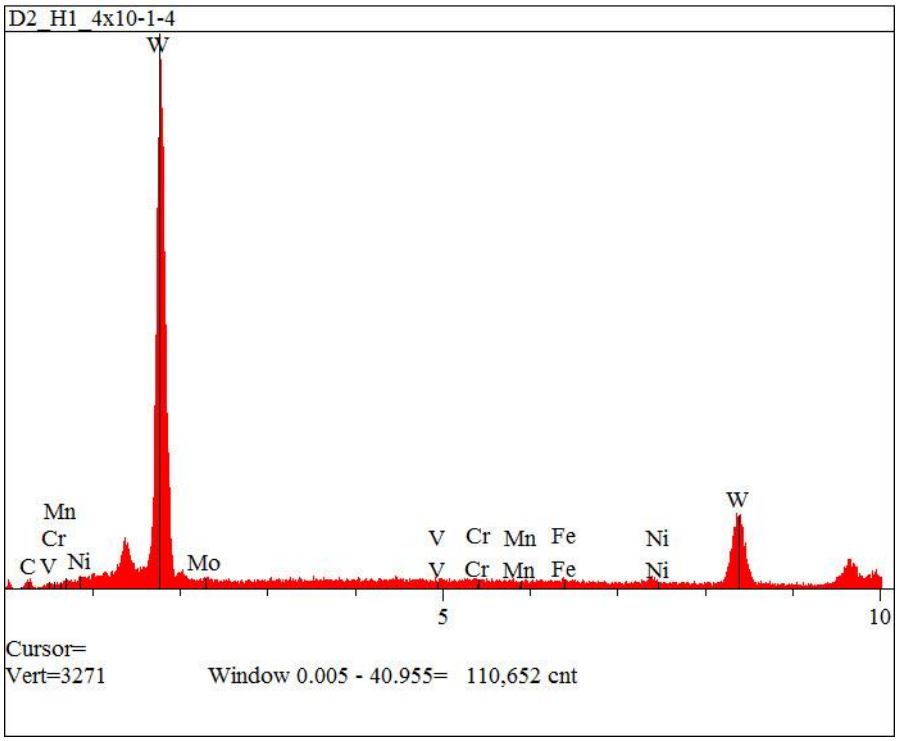
D2_H1_4x10-1-4
W
Mn
Cr
C V Ni
Mo
V Cr Mn Fe Ni
V Cr Mn Fe Ni
W
5
10
Cursor=
Vert=3271
Window 0.005 - 40.955= 110,652 cnt

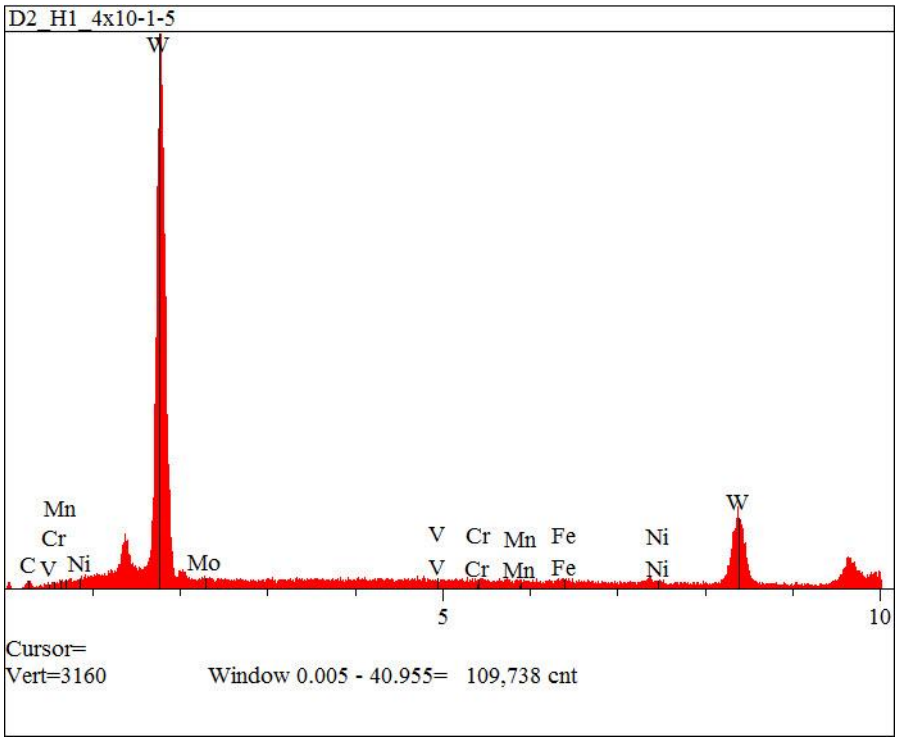
D2_H1_4x10-1-5
W
Mn
Cr
C V Ni
Mo
V Cr Mn Fe
V Cr Mn Fe
Ni
Ni
W
5
10
Cursor=
Vert=3160
Window 0.005 - 40.955= 109,738 cnt

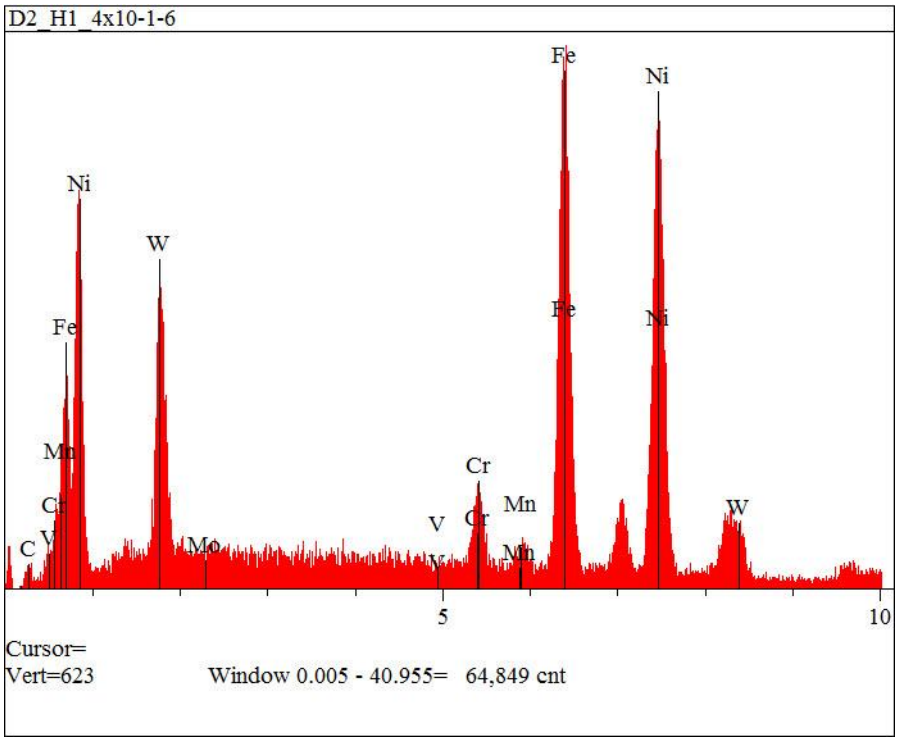
D2_H1_4x10-1-6
Fe
Ni
Ni
W
Fe
Fe
Ni
Mn
Cr
Cr
V
C
Mo
V
Cr
Mn
W
5
10
Cursor=
Vert=623
Window 0.005 - 40.955= 64,849 cnt

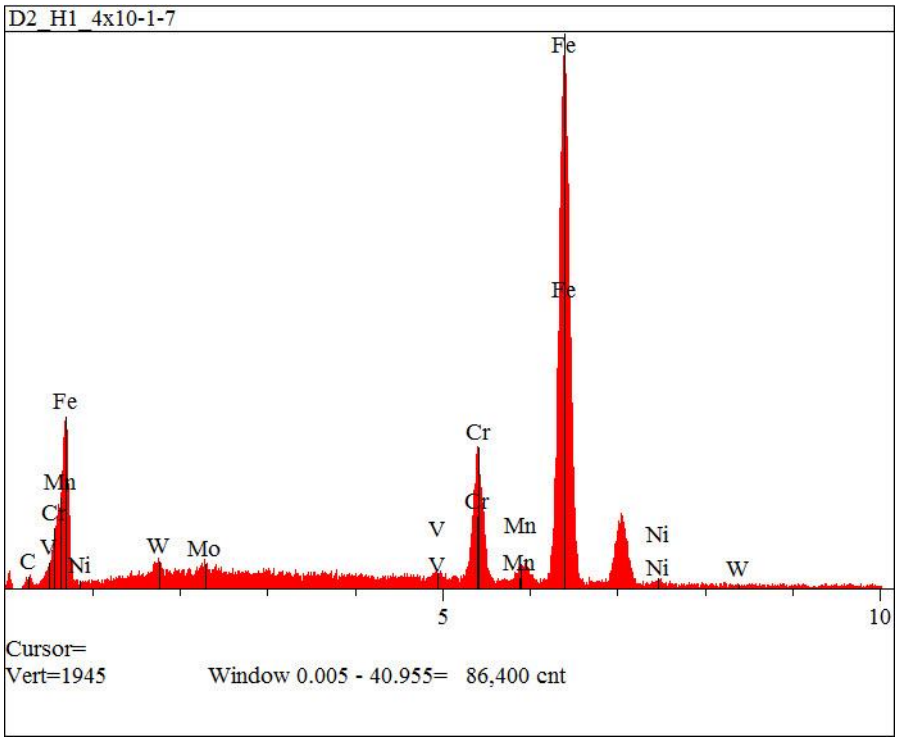
D2_H1_4x10-1-7
Fe
Fe
Fe
Cr
Cr
Mn
Mn
V
V
Mn
Ni
Ni
W
Mo
C
Ni
W
5
10
Cursor=
Vert=1945
Window 0.005 - 40.955= 86,400 cnt

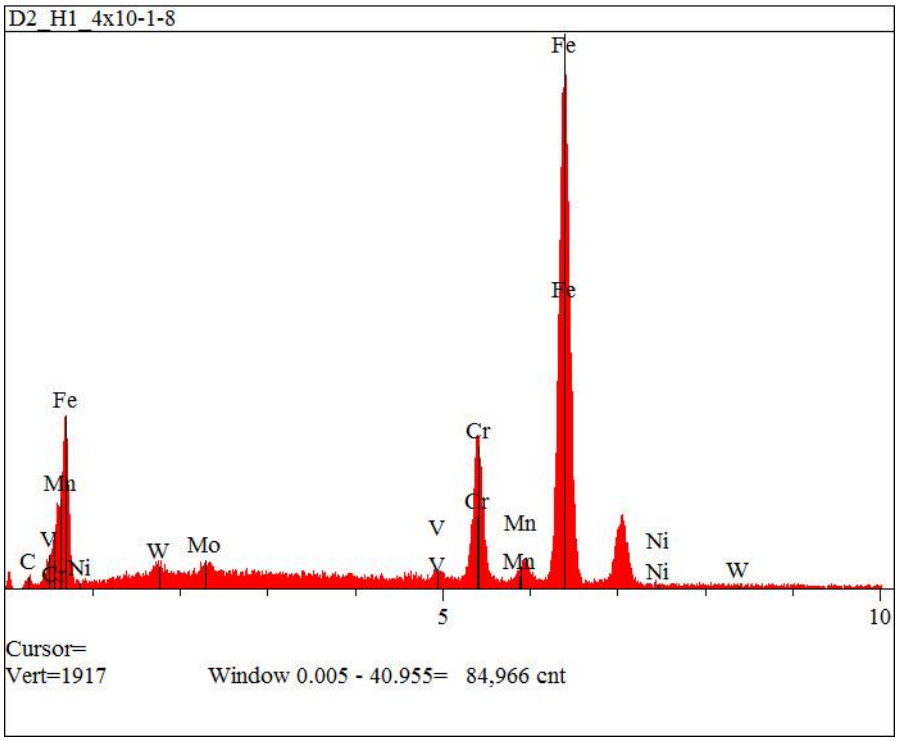
D2_H1_4x10-1-8
Fe
Fe
Fe
Cr
Cr
Mn
Mn
V
V
Mn
Ni
Ni
W
Mo
C
Ni
W
5
10
Cursor=
Vert=1917
Window 0.005 - 40.955= 84,966 cnt

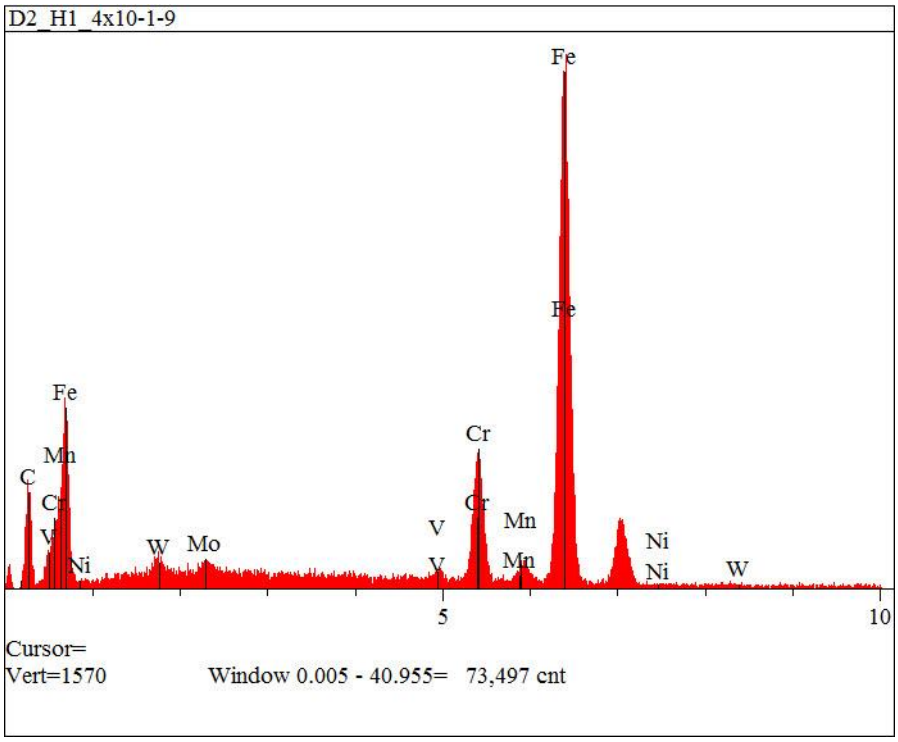
D2_H1_4x10-1-9
Fe
Fe
Fe
Mn
C
Cr
V
Ni
W
Mo
Cr
V
Cr
Mn
V
Mn
Ni
Ni
W
5
10
Cursor=
Vert=1570
Window 0.005 - 40.955= 73,497 cnt

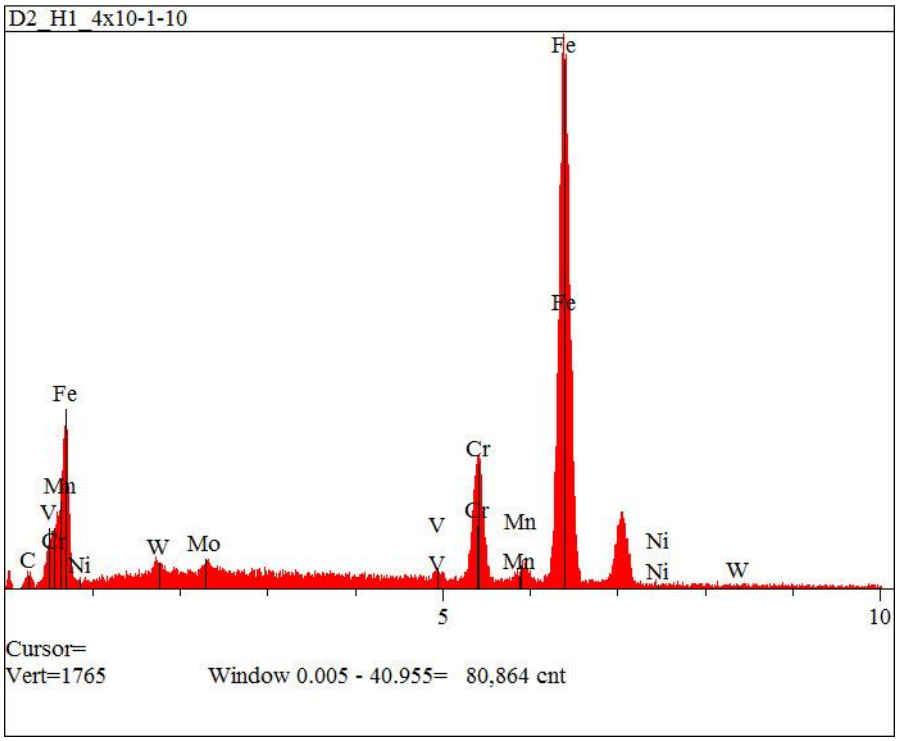
D2_H1_4x10-1-10
Fe
Fe
Fe
Mn
V
Cr
C
Ni
W
Mo
Cr
V
Cr
Mn
V
Mn
Ni
Ni
W
5
10
Cursor=
Vert=1765
Window 0.005 - 40.955= 80,864 cnt

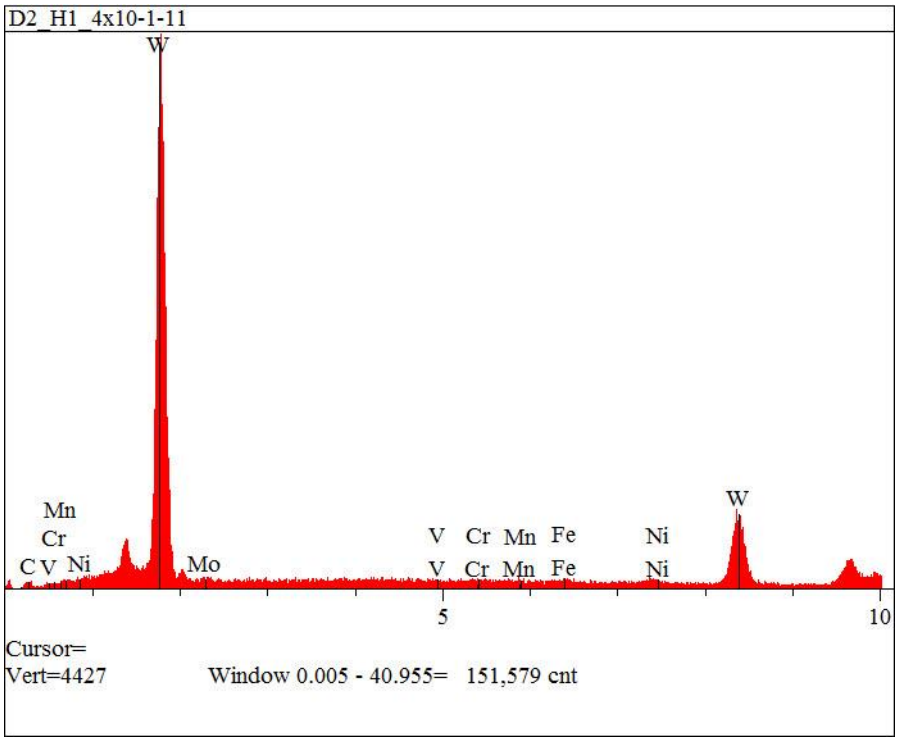
D2_H1_4x10-1-11
W
Mn
Cr
C V Ni
Mo
V Cr Mn Fe Ni
V Cr Mn Fe Ni
W
5
10
Cursor=
Vert=4427
Window 0.005 - 40.955= 151,579 cnt

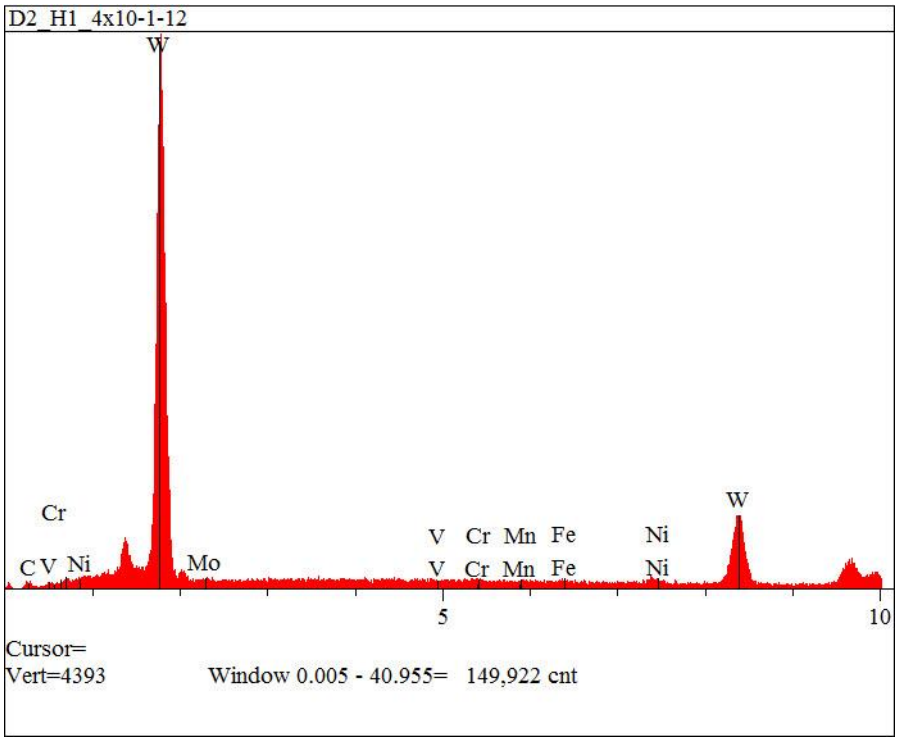
D2_H1_4x10-1-12
W
Cr
C V Ni
Mo
V Cr Mn Fe Ni
V Cr Mn Fe Ni
W
5
10
Cursor=
Vert=4393
Window 0.005 - 40.955= 149,922 cnt

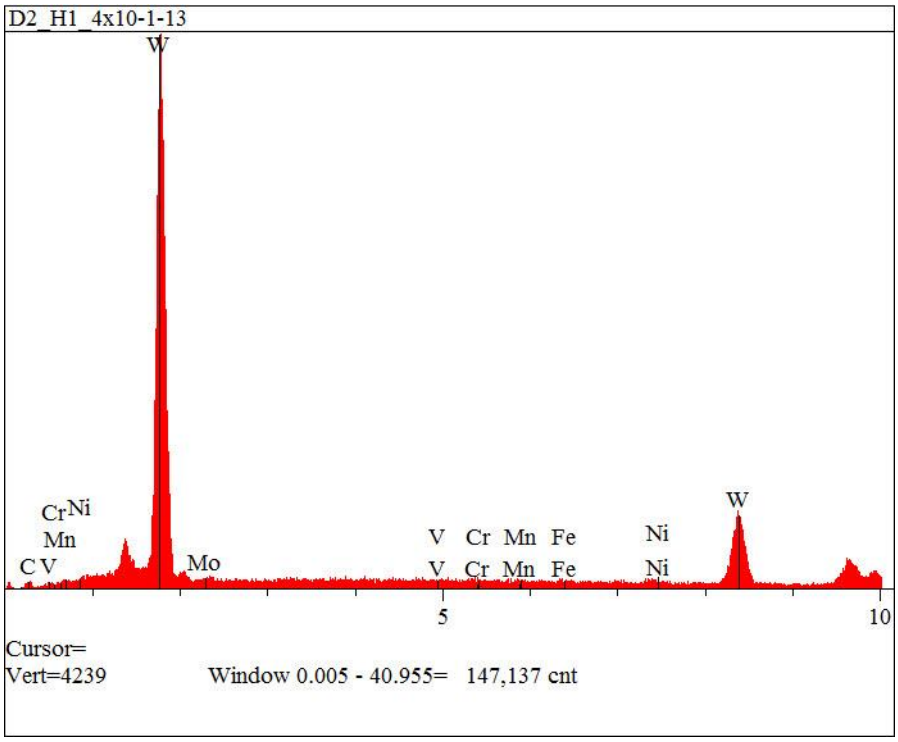
D2_H1_4x10-1-13
W
Cr Ni
Mn
C V
Mo
V Cr Mn Fe
V Cr Mn Fe
Ni
Ni
W
5
10
Cursor=
Vert=4239
Window 0.005 - 40.955= 147,137 cnt

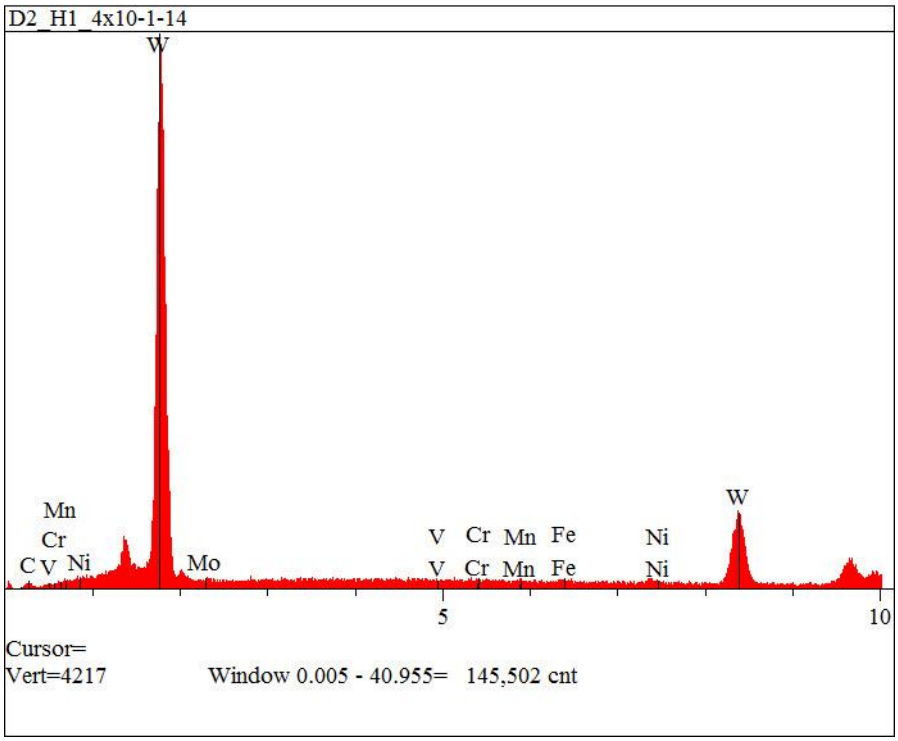
D2_H1_4x10-1-14
W
Mn
Cr
C V Ni
Mo
V Cr Mn Fe
V Cr Mn Fe
Ni
Ni
W
5
10
Cursor=
Vert=4217
Window 0.005 - 40.955= 145,502 cnt

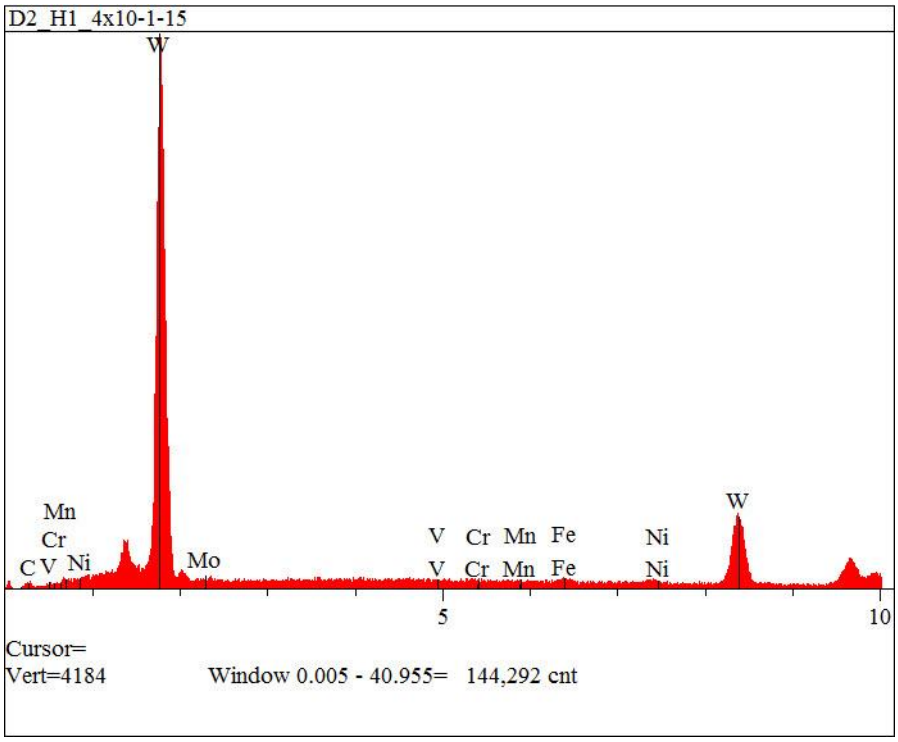
D2_H1_4x10-1-15
W
Mn
Cr
C V Ni
Mo
V Cr Mn Fe
V Cr Mn Fe
Ni
Ni
W
5
10
Cursor=
Vert=4184
Window 0.005 - 40.955= 144,292 cnt

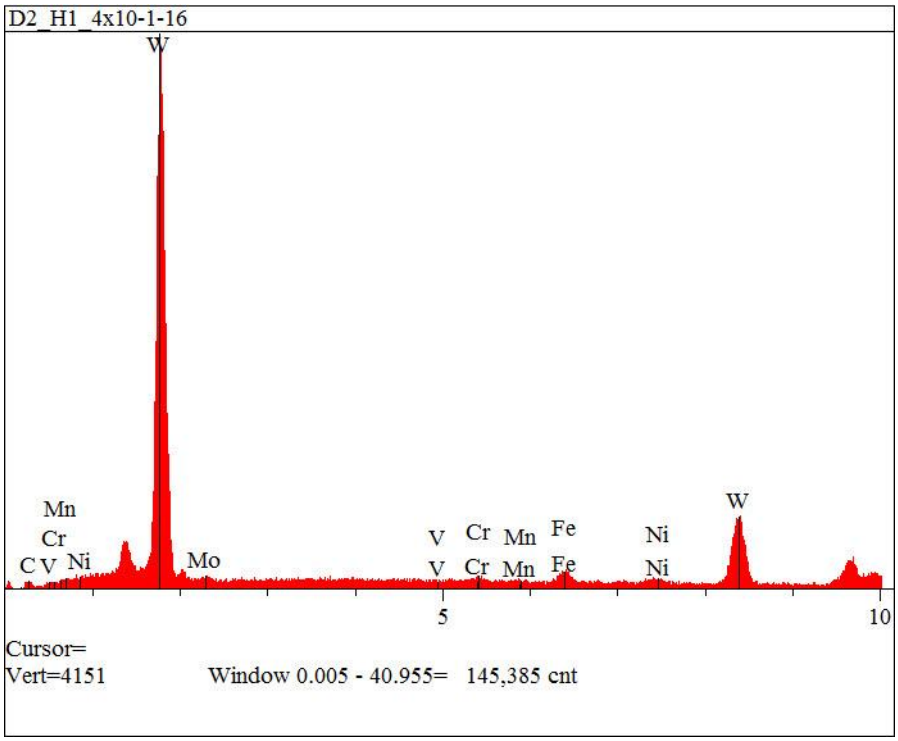
D2_H1_4x10-1-16
W
Mn
Cr
C V Ni
Mo
V Cr Mn Fe
V Cr Mn Fe
Ni
Ni
W
5
10
Cursor=
Vert=4151
Window 0.005 - 40.955= 145,385 cnt

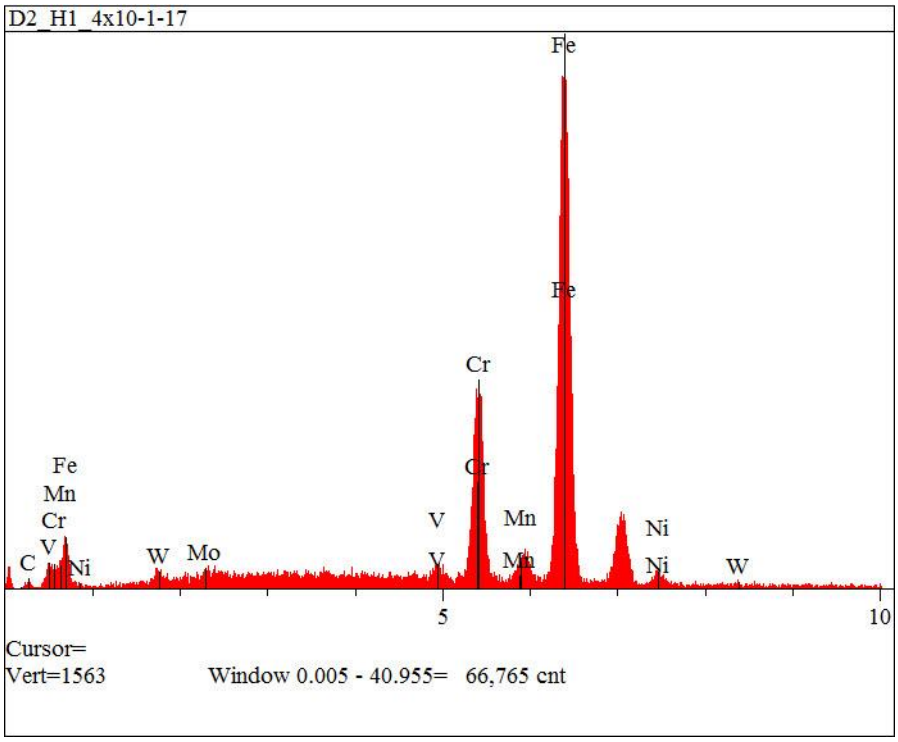
D2_H1_4x10-1-17
Fe
Fe
Cr
Fe
Mn
Cr
V
C
Ni
W
Mo
V
Cr
Mn
Mn
Ni
Ni
W
5
10
Cursor=
Vert=1563
Window 0.005 - 40.955= 66,765 cnt

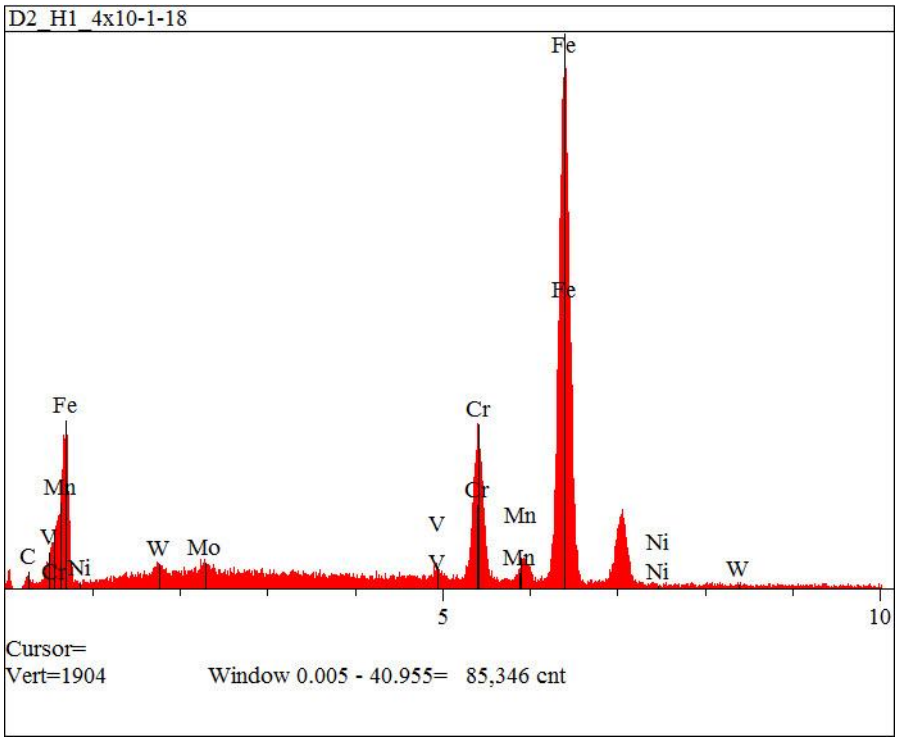
D2_H1_4x10-1-18
Fe
Fe
Fe
Mn
Cr
V
C
Ni
W
Mo
V
Cr
Mn
Mn
Ni
Ni
W
5
10
Cursor=
Vert=1904
Window 0.005 - 40.955= 85,346 cnt

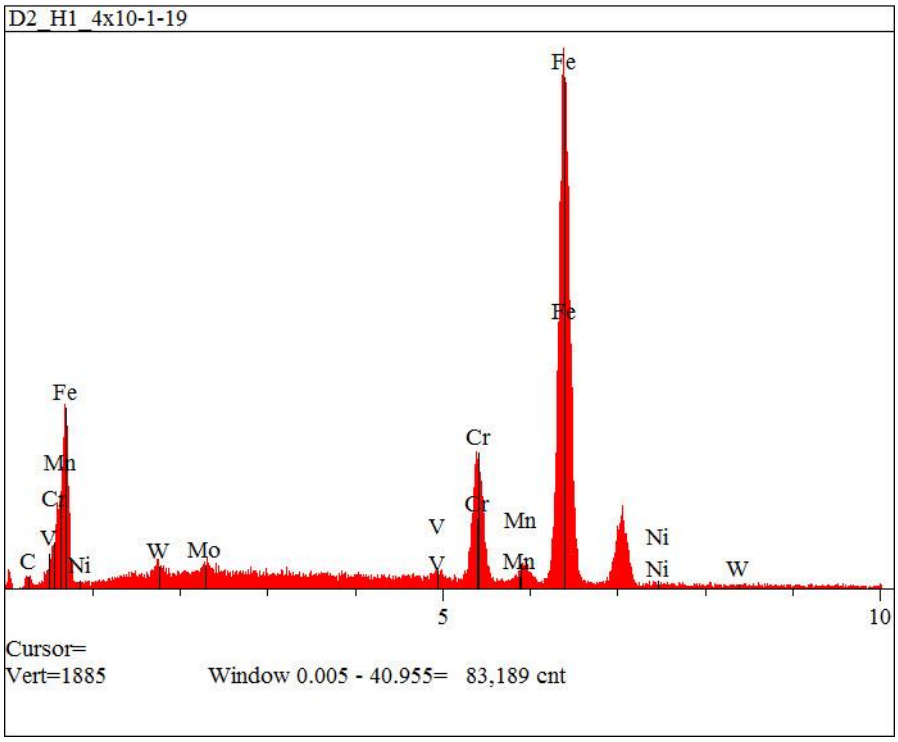
D2_H1_4x10-1-19
Fe
Fe
Fe
Mn
Cr
V
C
Ni
W
Mo
V
Cr
Mn
V
Mn
Ni
Ni
W
5
10
Cursor=
Vert=1885
Window 0.005 - 40.955= 83,189 cnt

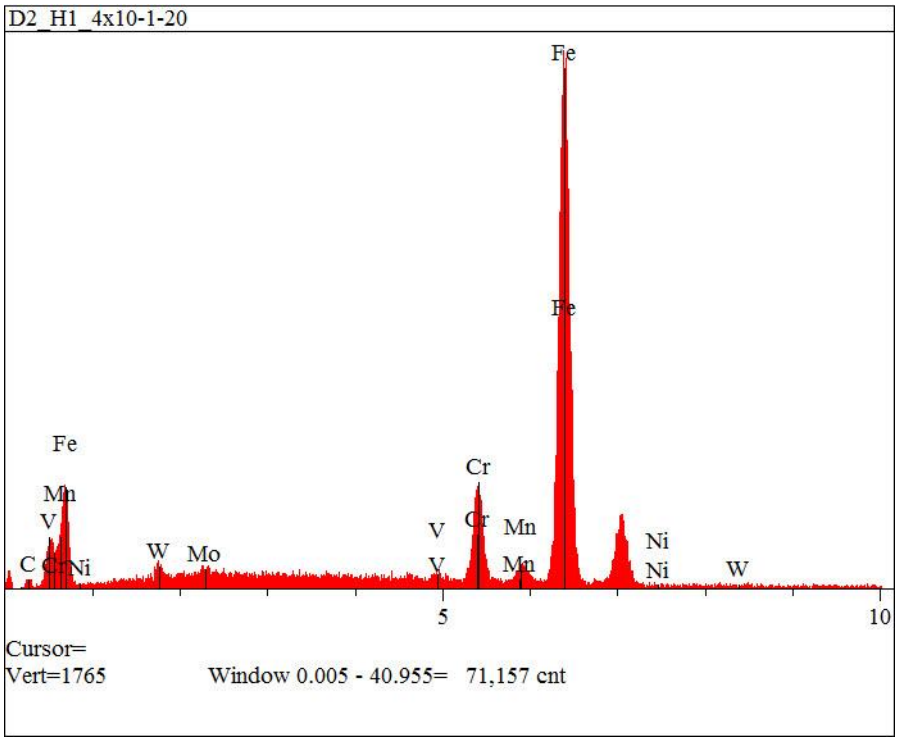
D2_H1_4x10-1-20
Fe
Fe
Fe
Mn
V
C
Ni
W
Mo
Cr
V
Cr
Mn
V
Mn
Ni
Ni
W
5
10
Cursor=
Vert=1765
Window 0.005 - 40.955= 71,157 cnt

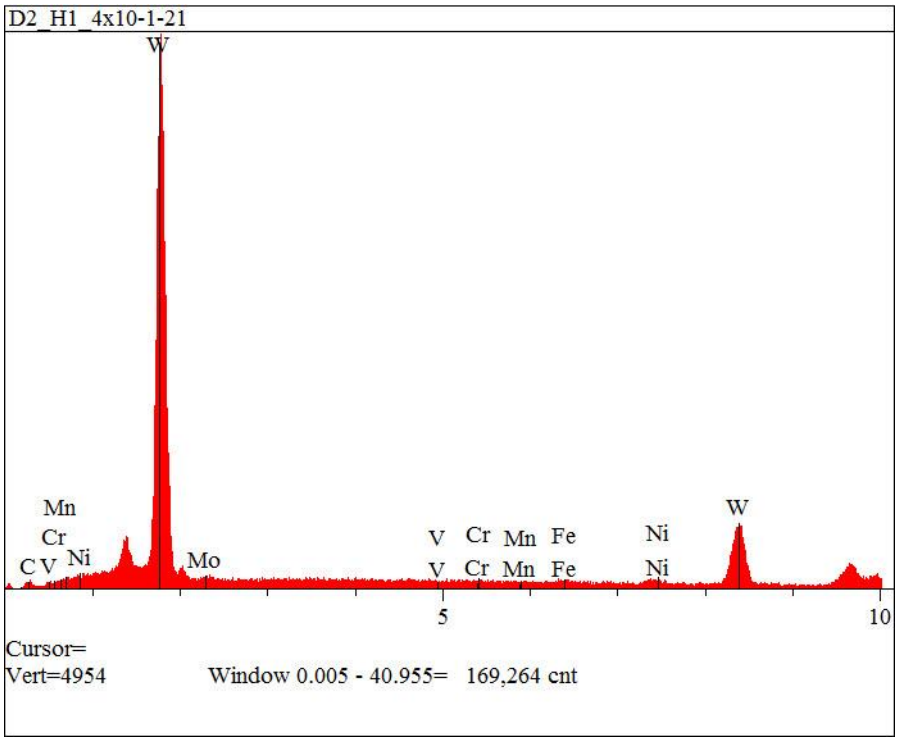
D2_H1_4x10-1-21
W
Mn
Cr
C V Ni
Mo
V Cr Mn Fe Ni
V Cr Mn Fe Ni
W
5
10
Cursor=
Vert=4954
Window 0.005 - 40.955= 169,264 cnt

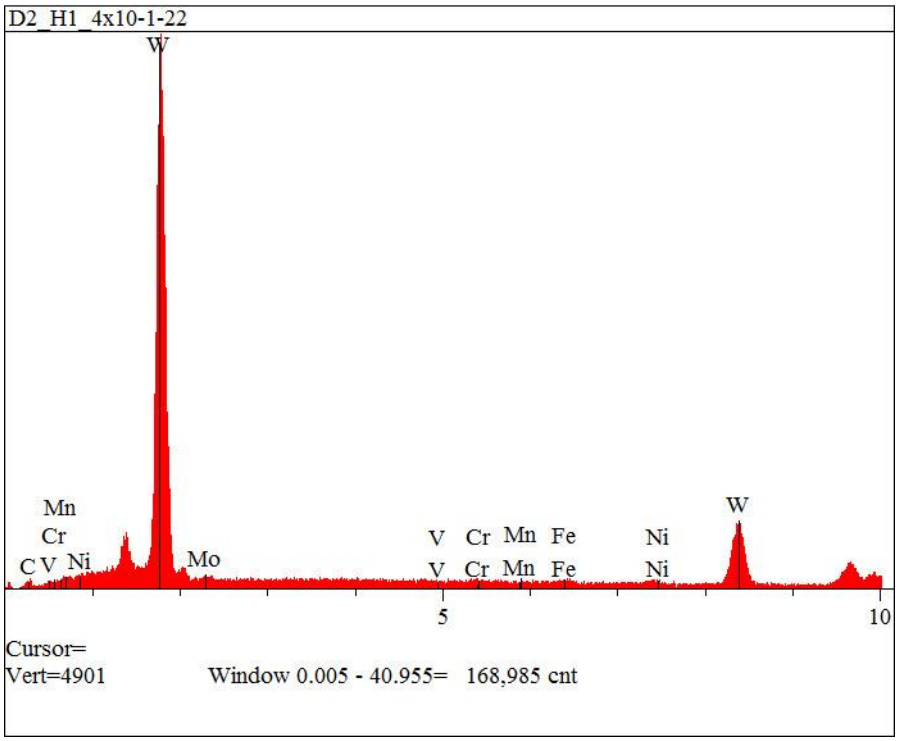
D2_H1_4x10-1-22
W
Mn
Cr
C V Ni
Mo
V Cr Mn Fe Ni
V Cr Mn Fe Ni
W
5
10
Cursor=
Vert=4901
Window 0.005 - 40.955= 168,985 cnt

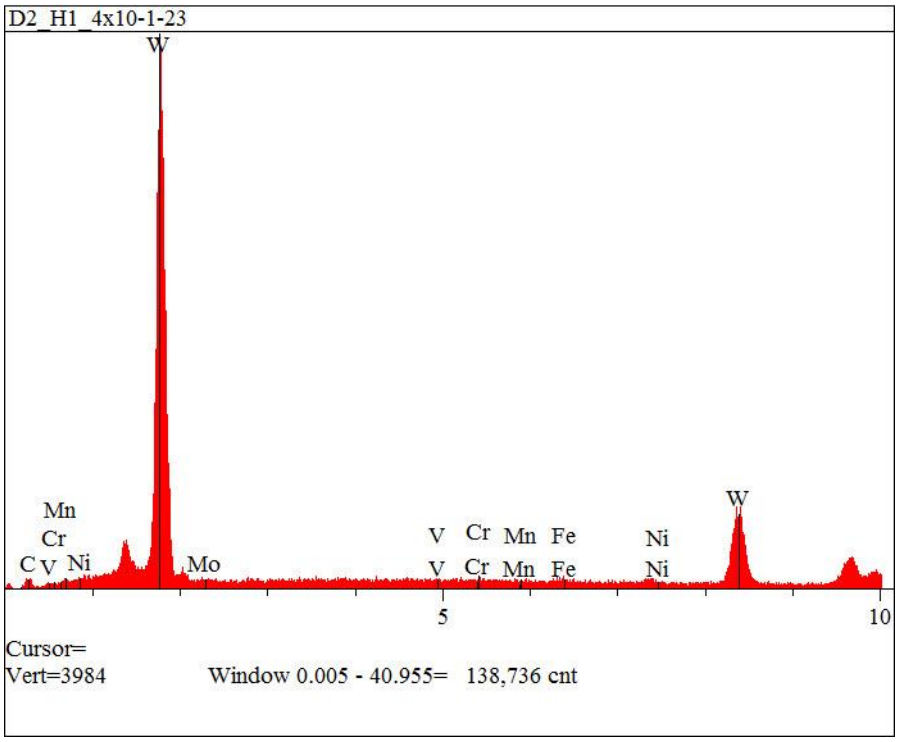
D2_H1_4x10-1-23
W
Mn
Cr
C V Ni
Mo
V Cr Mn Fe
V Cr Mn Fe
Ni
Ni
W
5
10
Cursor=
Vert=3984
Window 0.005 - 40.955= 138,736 cnt

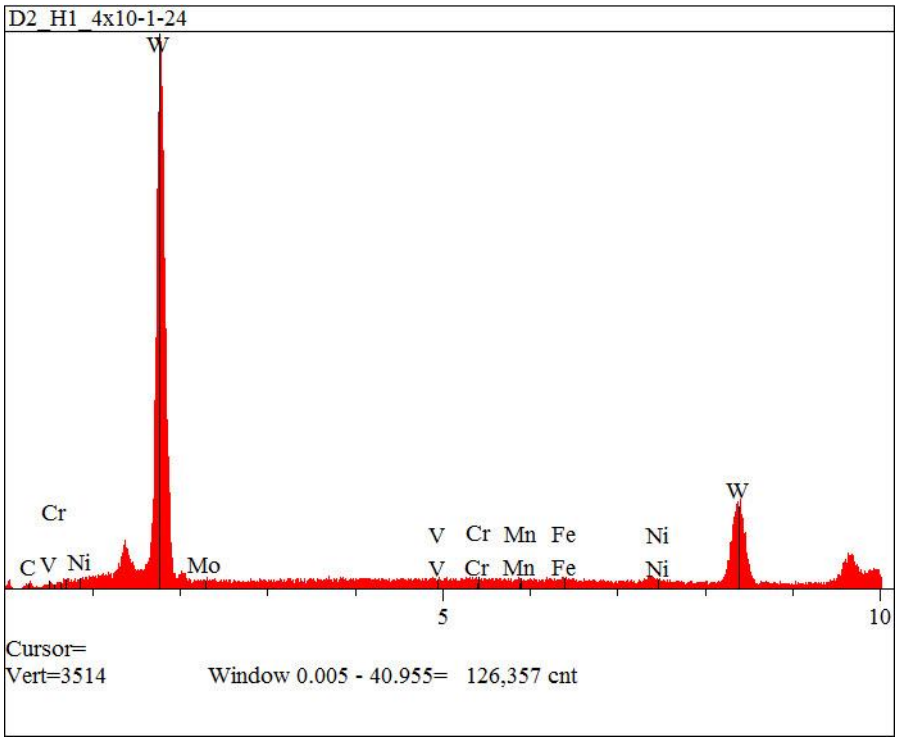
D2_H1_4x10-1-24
W
Cr
C V Ni
Mo
V Cr Mn Fe
V Cr Mn Fe
Ni
Ni
W
5
10
Cursor=
Vert=3514
Window 0.005 - 40.955= 126,357 cnt

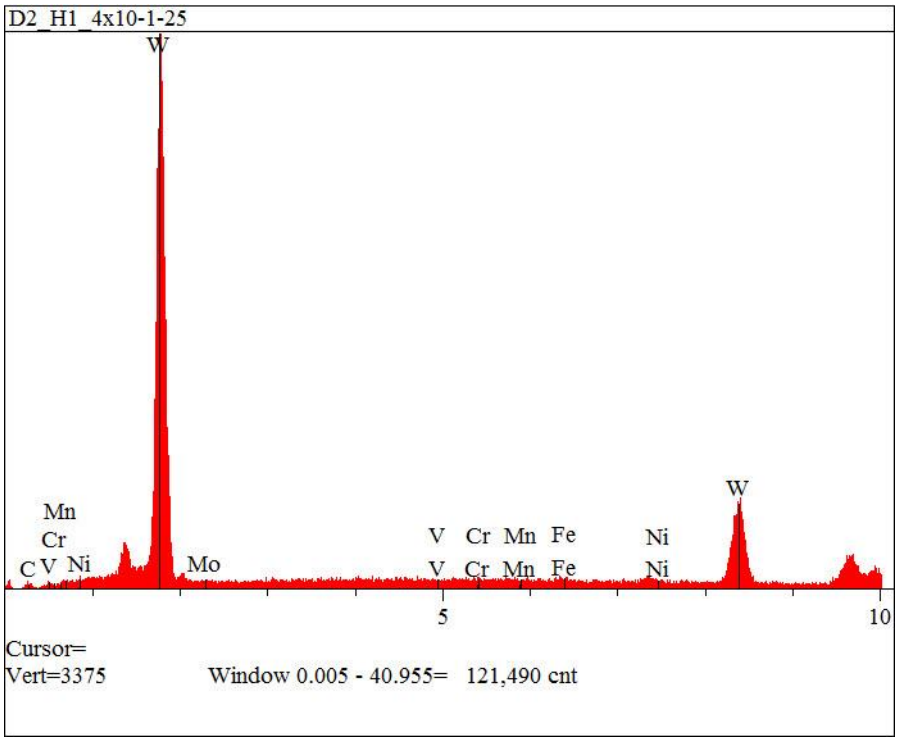
D2_H1_4x10-1-25
W
Mn
Cr
C V Ni
Mo
V Cr Mn Fe
V Cr Mn Fe
Ni
Ni
W
5
10
Cursor=
Vert=3375
Window 0.005 - 40.955= 121,490 cnt

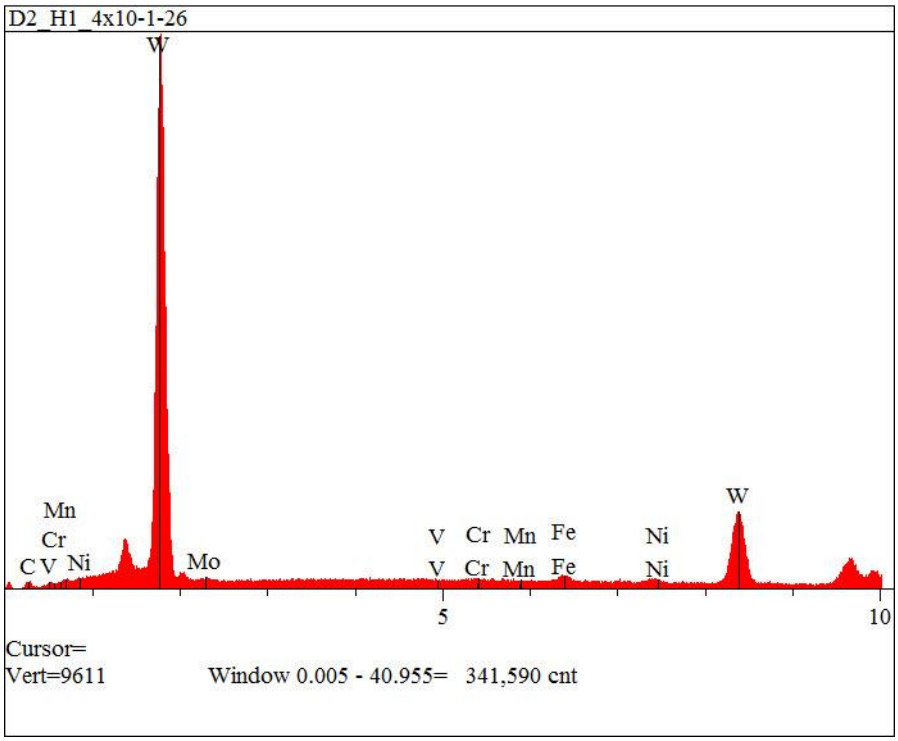
D2_H1_4x10-1-26
W
Mn
Cr
C V Ni
Mo
V Cr Mn Fe
V Cr Mn Fe
Ni
Ni
W
5
10
Cursor=
Vert=9611
Window 0.005 - 40.955= 341,590 cnt

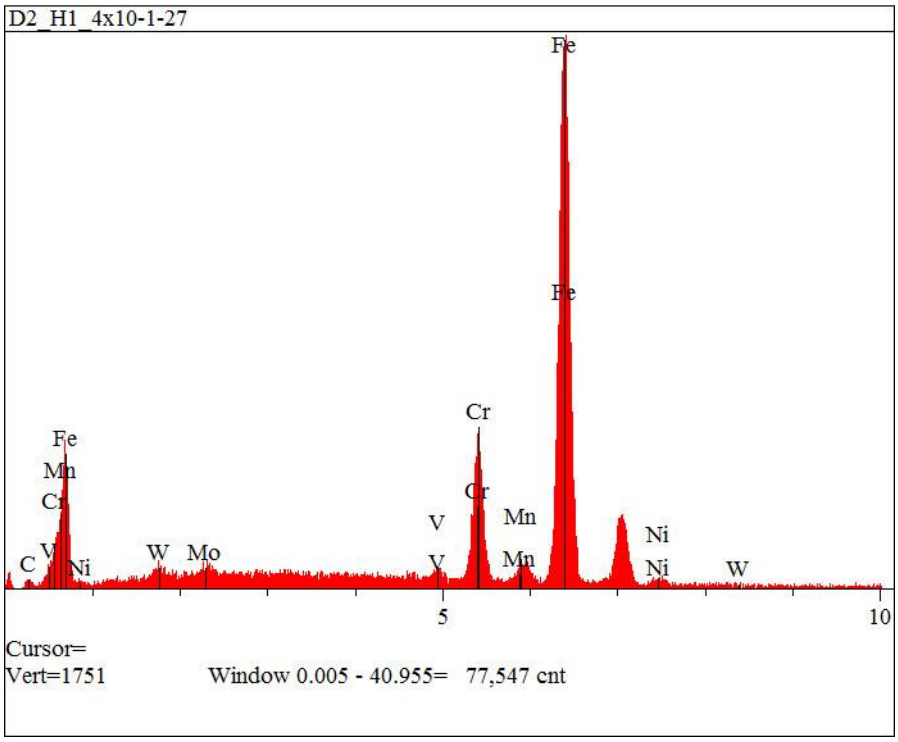
D2_H1_4x10-1-27
Fe
Fe
Cr
Fe
Mn
Cr
Cr
V
Mn
Ni
C
V
Ni
W
Mo
V
Mn
Ni
W
5
10
Cursor=
Vert=1751
Window 0.005 - 40.955= 77,547 cnt

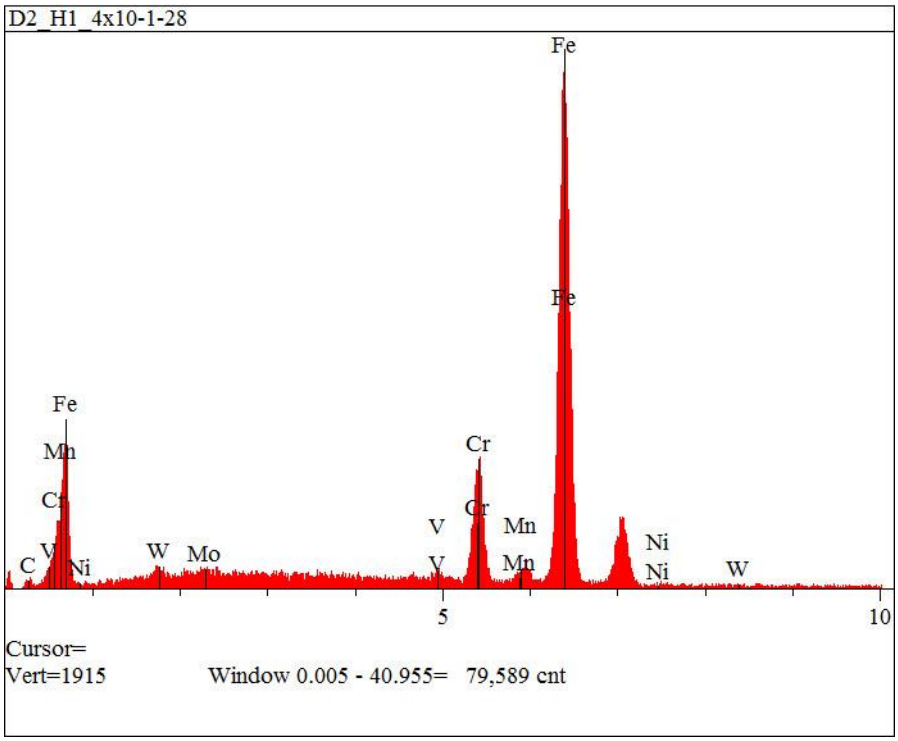
D2_H1_4x10-1-28
Fe
Fe
Fe
Mn
Cr
Cr
V
Mn
Ni
C
V
Ni
W
Mo
V
Mn
Ni
W
5
10
Cursor=
Vert=1915
Window 0.005 - 40.955= 79,589 cnt

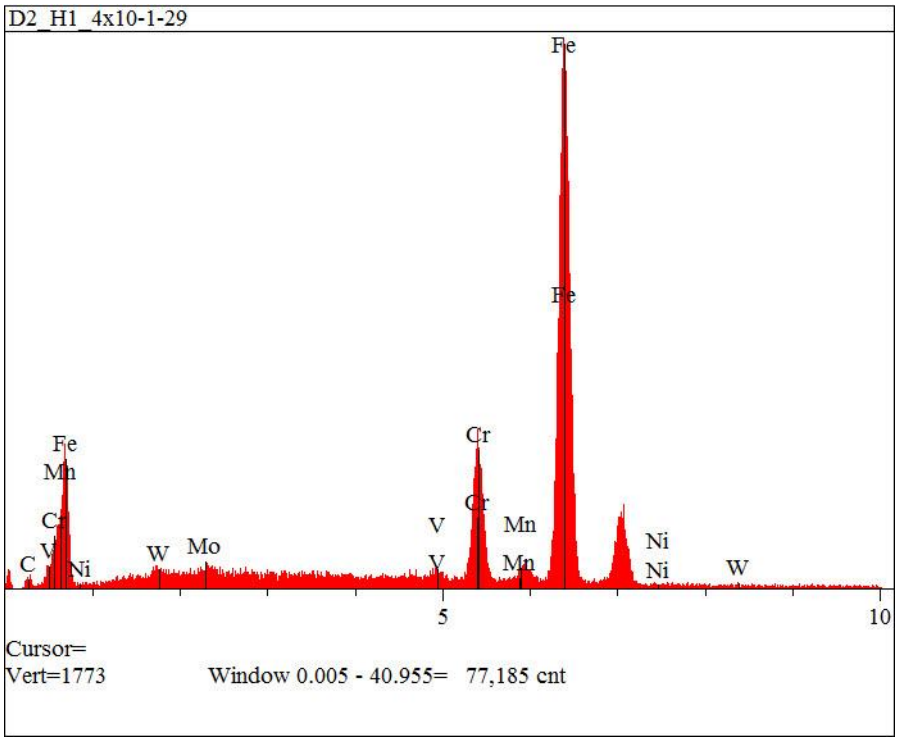
D2_H1_4x10-1-29
Fe
Fe
Fe
Mn
Cr
Cr
C
V
Ni
W
Mo
V
V
Cr
Mn
Mn
Ni
Ni
W
5
10
Cursor=
Vert=1773
Window 0.005 - 40.955= 77,185 cnt

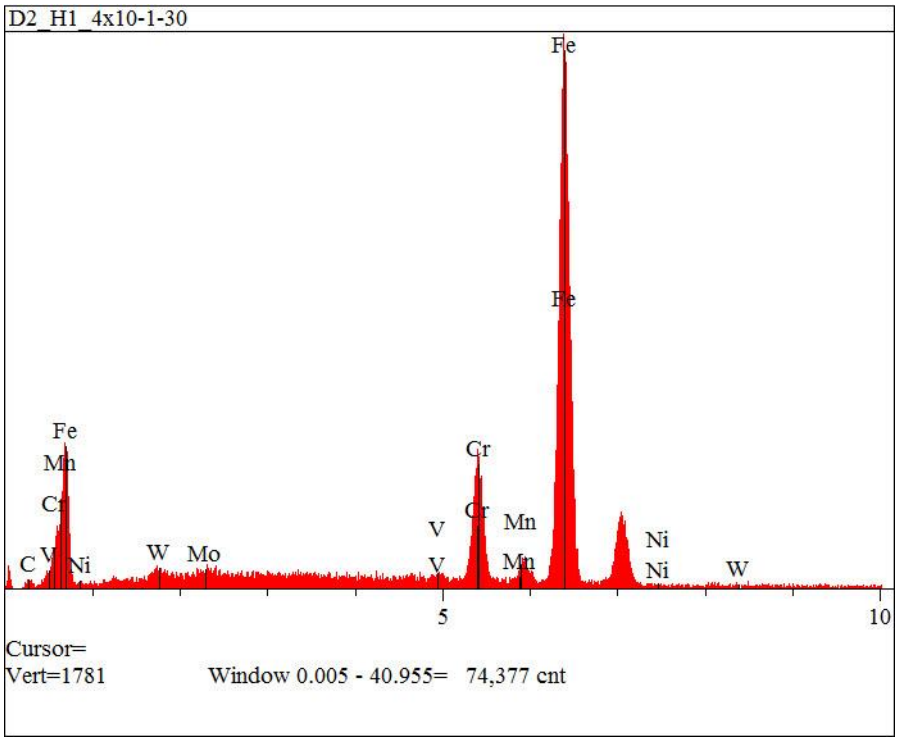
D2_H1_4x10-1-30
Fe
Fe
Fe
Mn
Cr
Cr
C
V
Ni
W
Mo
V
V
Cr
Mn
Mn
Ni
Ni
W
5
10
Cursor=
Vert=1781
Window 0.005 - 40.955= 74,377 cnt

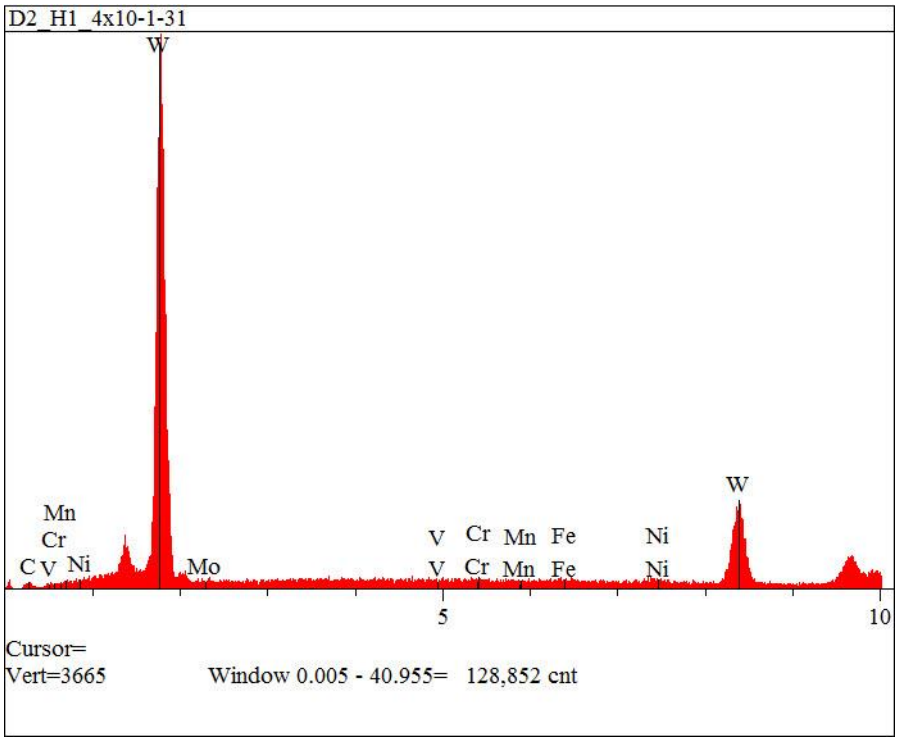
D2_H1_4x10-1-31
W
Mn
Cr
C V Ni
Mo
V Cr Mn Fe Ni
V Cr Mn Fe Ni
W
5
10
Cursor=
Vert=3665
Window 0.005 - 40.955= 128,852 cnt

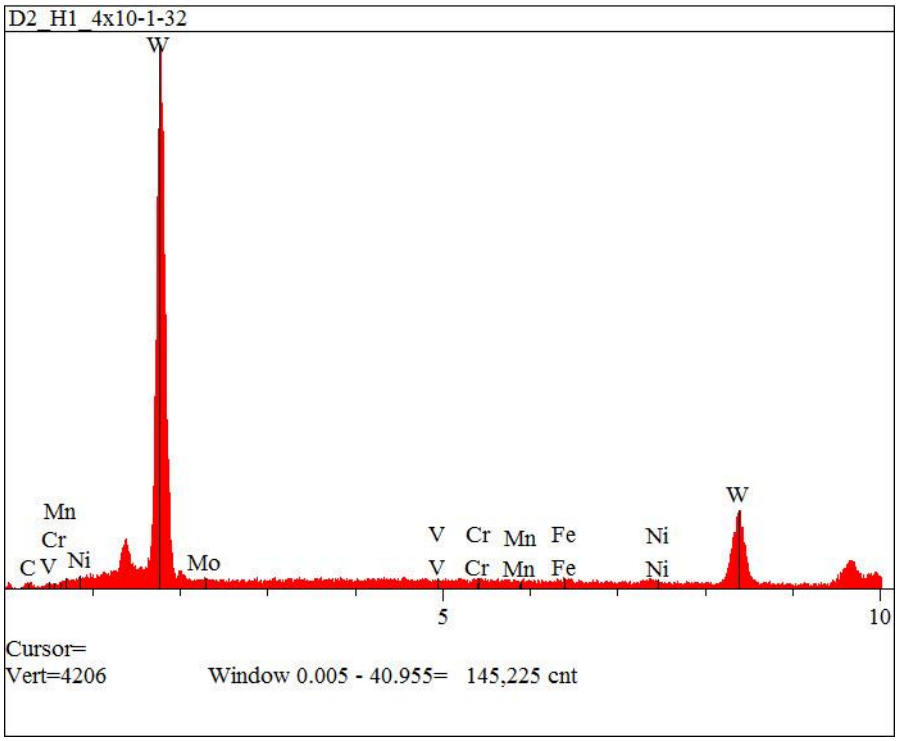
D2_H1_4x10-1-32
W
Mn
Cr
C V Ni
Mo
V Cr Mn Fe Ni
V Cr Mn Fe Ni
W
5
10
Cursor=
Vert=4206
Window 0.005 - 40.955= 145,225 cnt

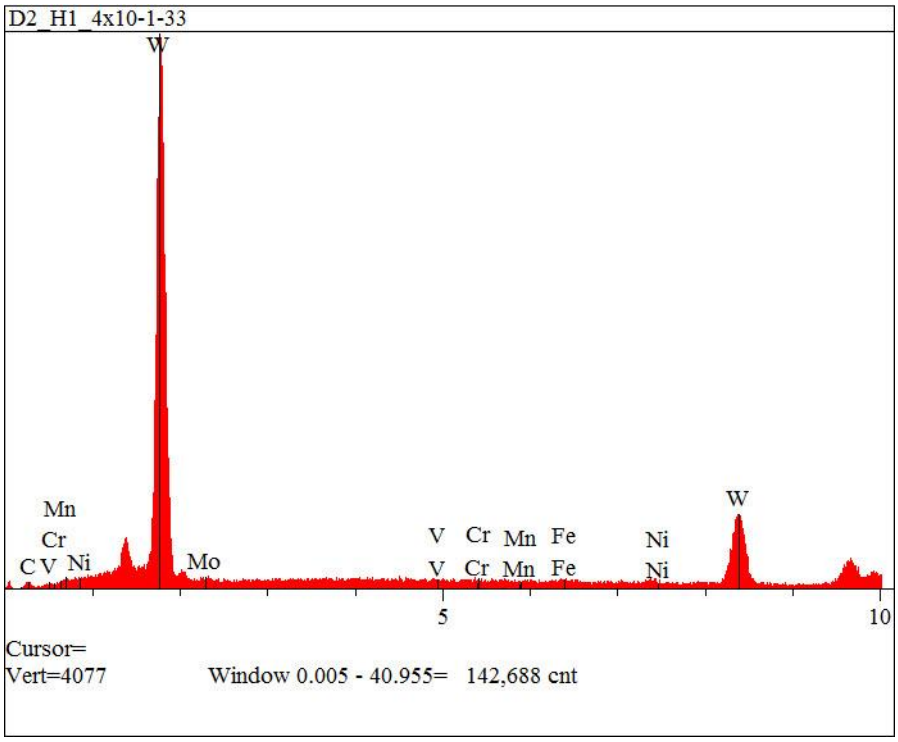
D2_H1_4x10-1-33
W
Mn
Cr
C V Ni
Mo
V Cr Mn Fe
V Cr Mn Fe
Ni
Ni
W
5
10
Cursor=
Vert=4077
Window 0.005 - 40.955= 142,688 cnt

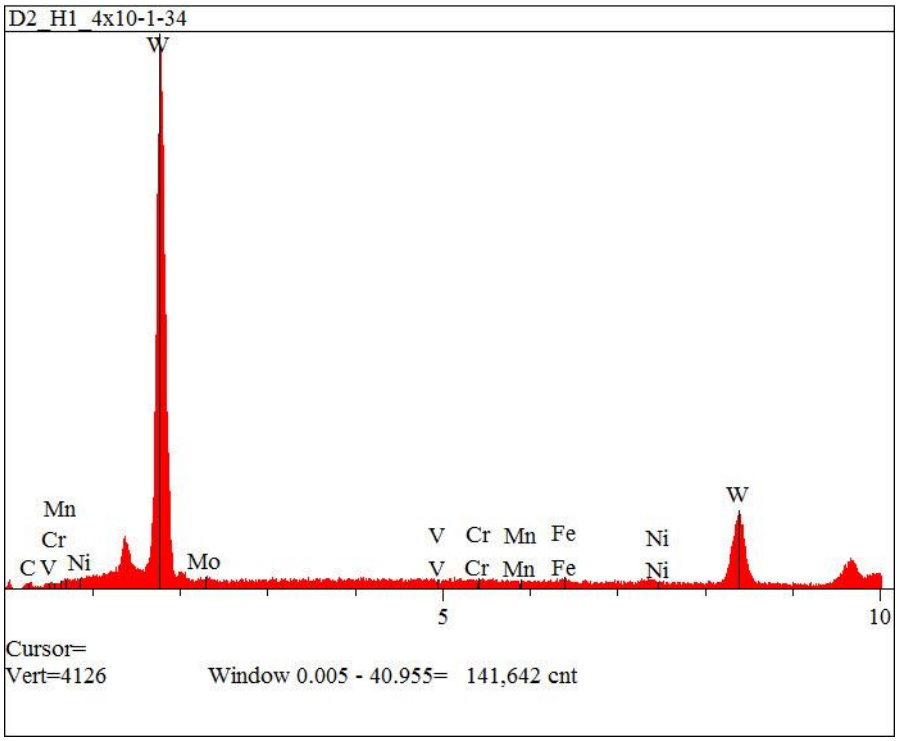
D2_H1_4x10-1-34
W
Mn
Cr
C V Ni
Mo
V Cr Mn Fe
V Cr Mn Fe
Ni
Ni
W
5
10
Cursor=
Vert=4126
Window 0.005 - 40.955= 141,642 cnt

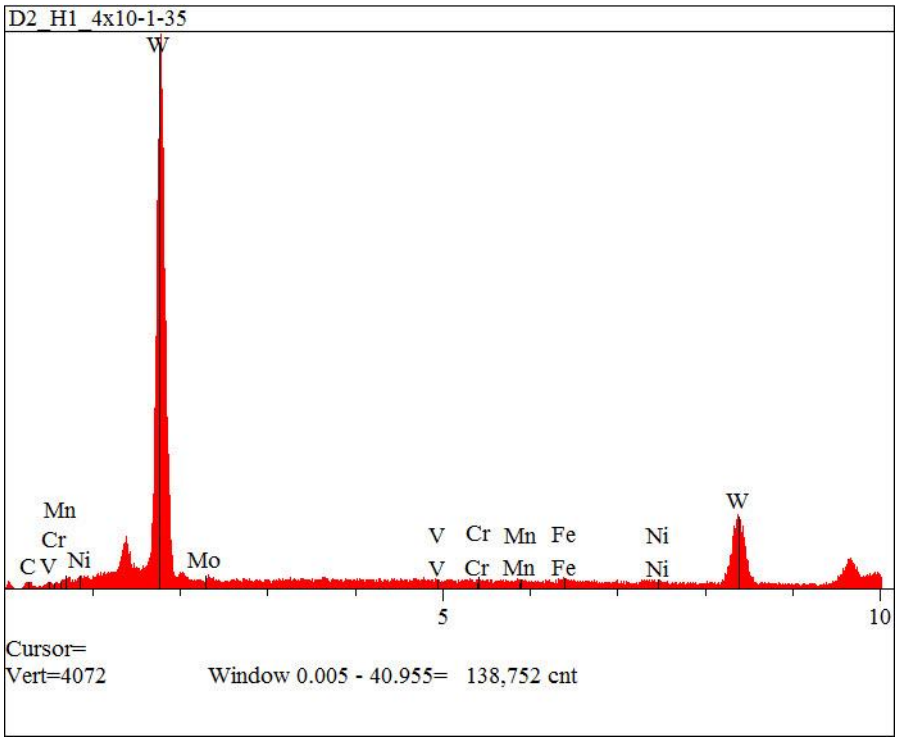
D2_H1_4x10-1-35
W
Mn
Cr
C V Ni
Mo
V Cr Mn Fe Ni
V Cr Mn Fe Ni
W
5
10
Cursor=
Vert=4072
Window 0.005 - 40.955= 138,752 cnt

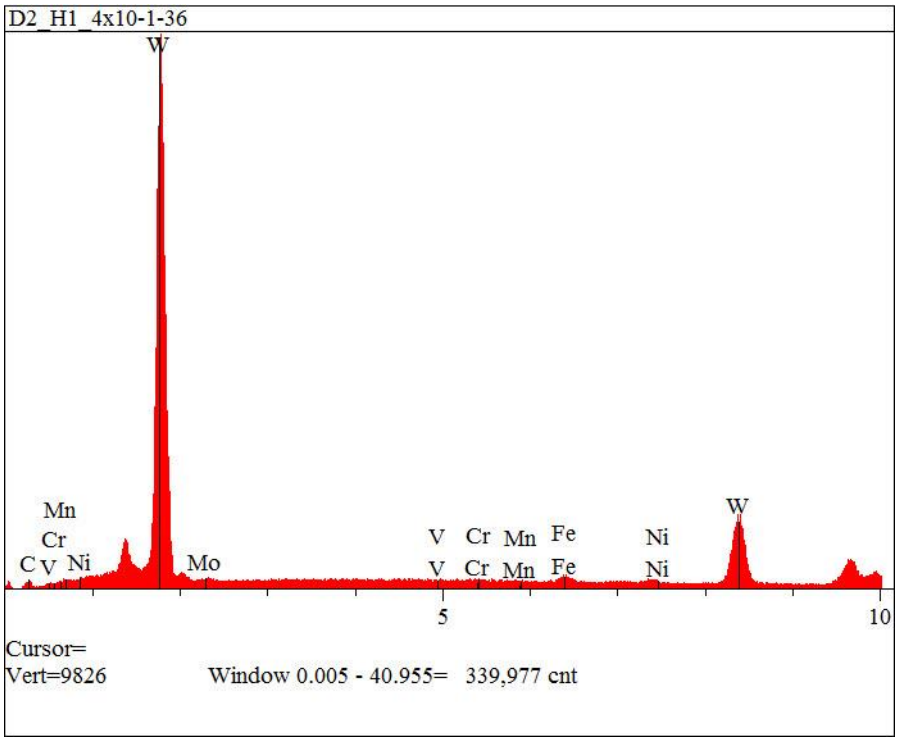
D2_H1_4x10-1-36
W
Mn
Cr
C V Ni
Mo
V Cr Mn Fe Ni
V Cr Mn Fe Ni
W
5
10
Cursor=
Vert=9826
Window 0.005 - 40.955= 339,977 cnt

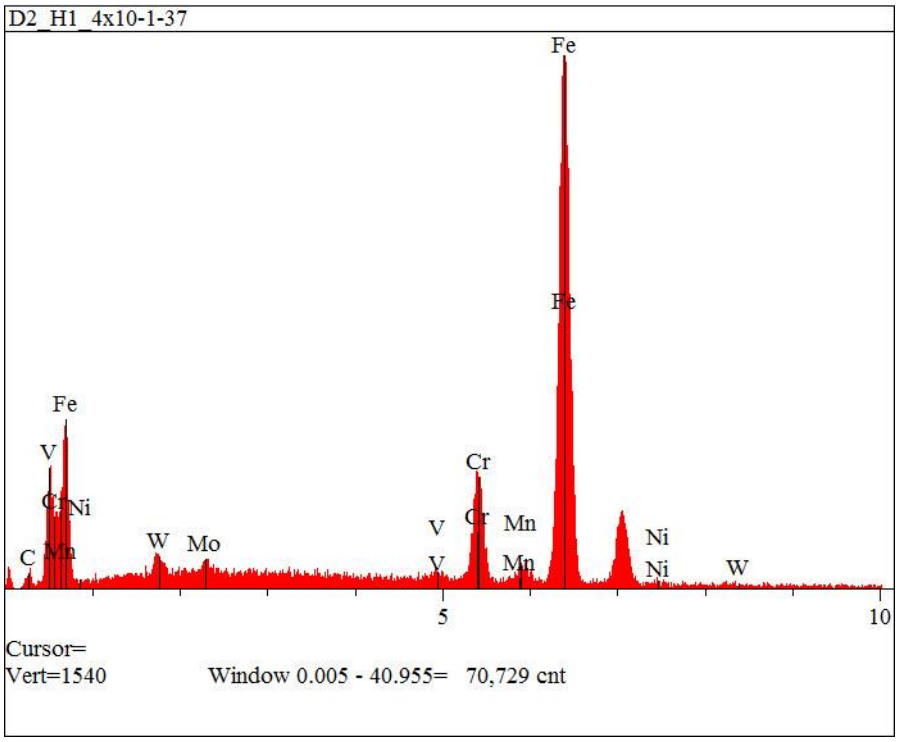
D2_H1_4x10-1-37
Fe
Fe
Fe
V
Cr
Ni
C
Mn
W
Mo
V
Cr
Mn
V
Mn
Ni
Ni
W
5
10
Cursor=
Vert=1540
Window 0.005 - 40.955= 70,729 cnt

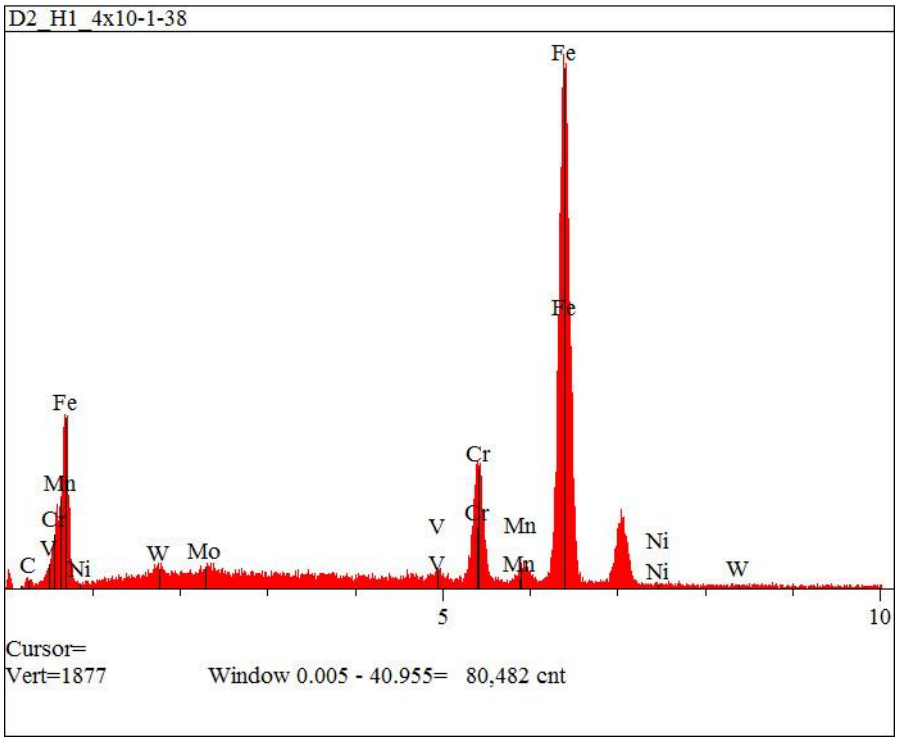
D2_H1_4x10-1-38
Fe
Fe
Fe
Mn
Cr
V
Ni
C
W
Mo
V
Cr
Mn
V
Mn
Ni
Ni
W
5
10
Cursor=
Vert=1877
Window 0.005 - 40.955= 80,482 cnt

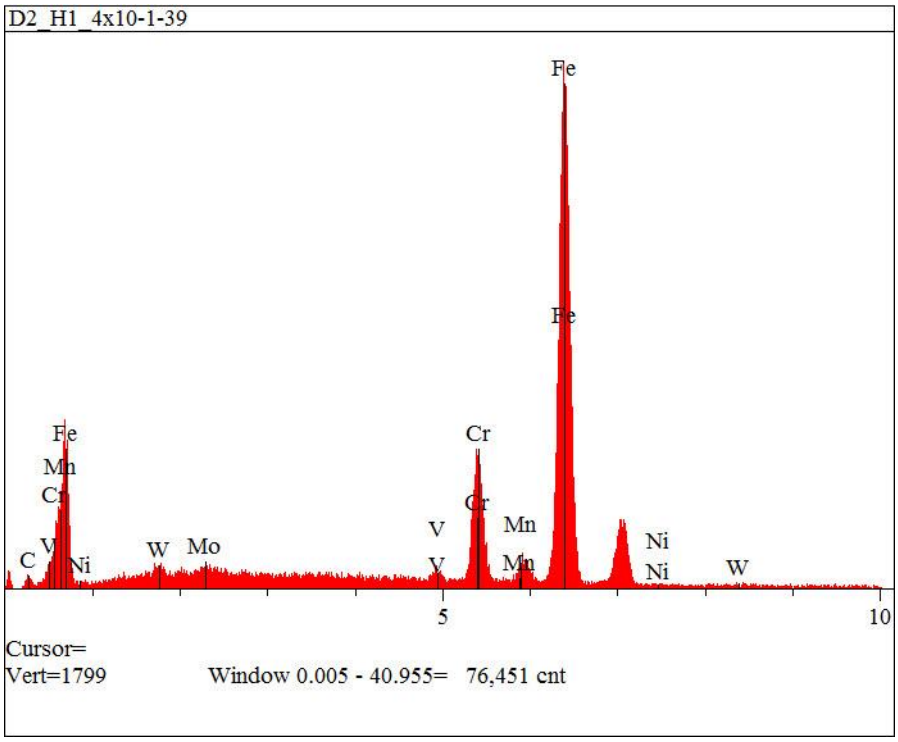
D2_H1_4x10-1-39
Fe
Fe
Fe
Mn
Cr
C
V
Ni
W
Mo
Cr
Cr
V
V
Mn
Mn
Ni
Ni
W
5
10
Cursor=
Vert=1799
Window 0.005 - 40.955= 76,451 cnt

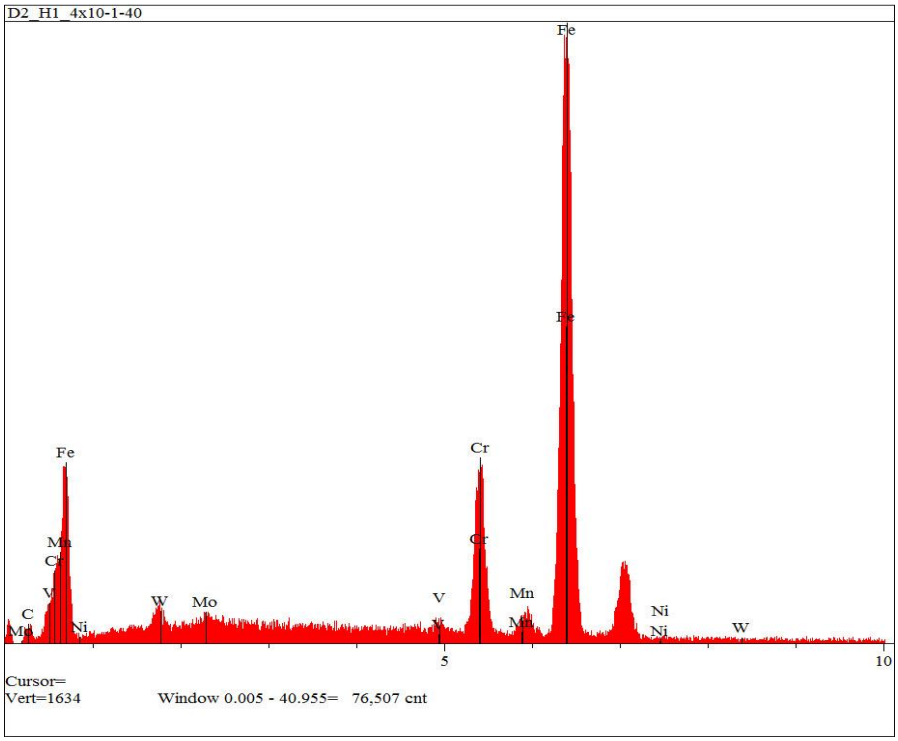
D2_H1_4x10-1-40
Fe
Fe
Fe
Mn
Cr
C
V
Ni
W
Mo
Cr
Cr
V
V
Mn
Mn
Ni
Ni
W
5
10
Cursor=
Vert=1634
Window 0.005 - 40.955= 76,507 cnt

D2_P1_0 Degree 1-10 EDS Plots

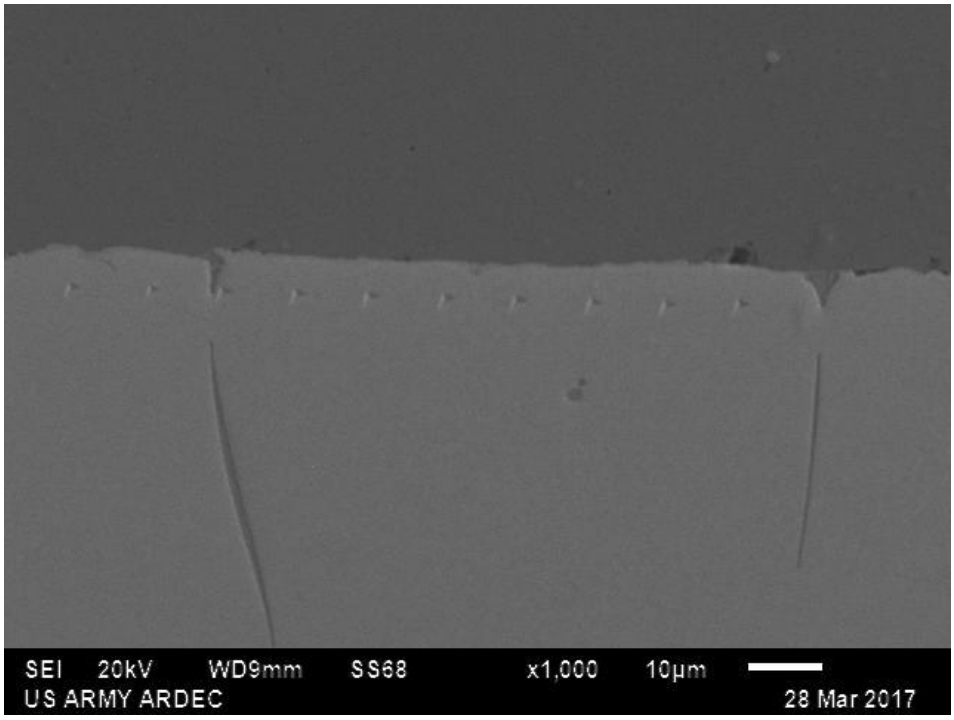

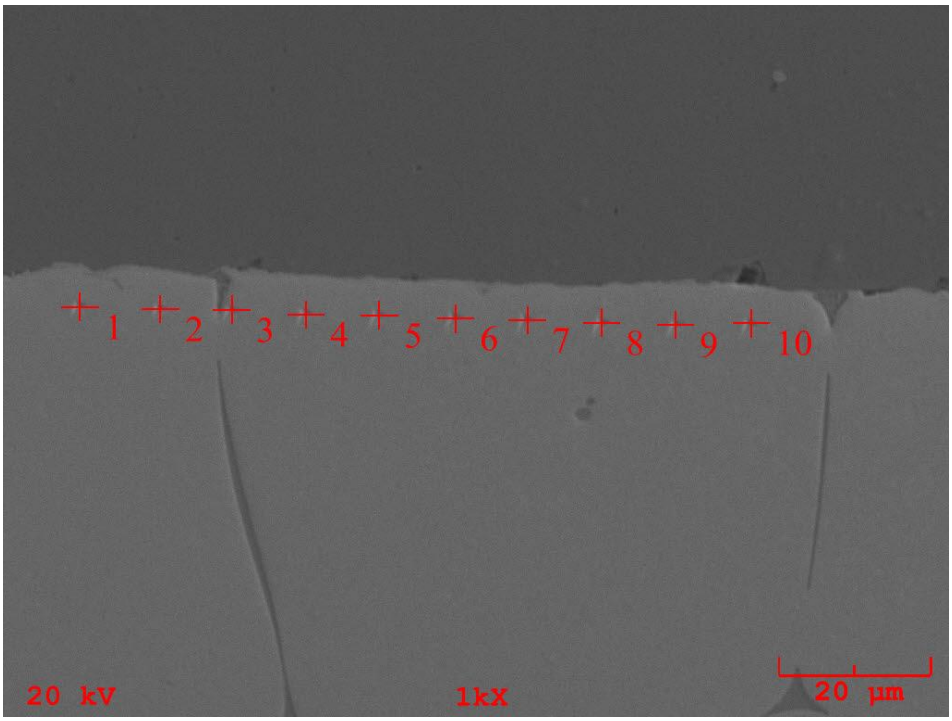

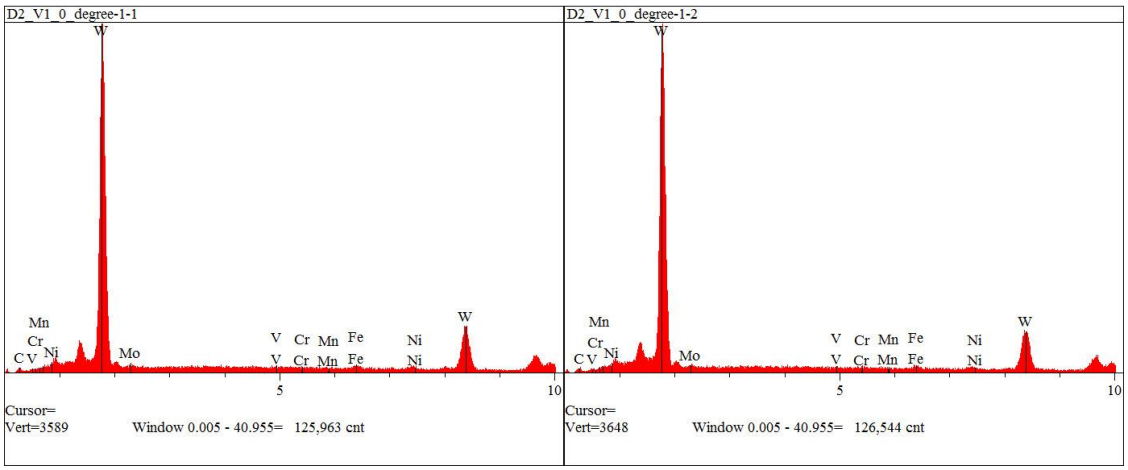
D2_V1_0_degree-1-1
W
Mn
Cr
C V Ni
Mo
V Cr Mn Fe
V Cr Mn Fe
Ni
Ni
W
5
10
Cursor=
Vert=3589
Window 0.005 - 40.955= 125,963 cnt
D2_V1_0_degree-1-2
W
Mn
Cr
C V Ni
Mo
V Cr Mn Fe
V Cr Mn Fe
Ni
Ni
W
5
10
Cursor=
Vert=3648
Window 0.005 - 40.955= 126,544 cnt

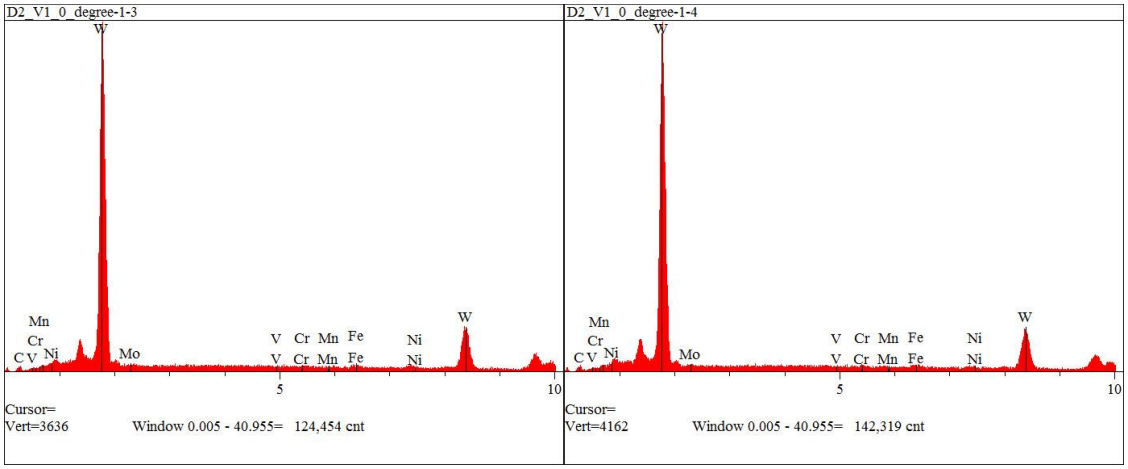
D2_V1_0_degree-1-3
W
Mn
Cr
C V Ni
Mo
V Cr Mn Fe
V Cr Mn Fe
Ni
Ni
W
5
10
Cursor=
Vert=3636
Window 0.005 - 40.955= 124,454 cnt
D2_V1_0_degree-1-4
W
Mn
Cr
C V Ni
Mo
V Cr Mn Fe
V Cr Mn Fe
Ni
Ni
W
5
10
Cursor=
Vert=4162
Window 0.005 - 40.955= 142,319 cnt

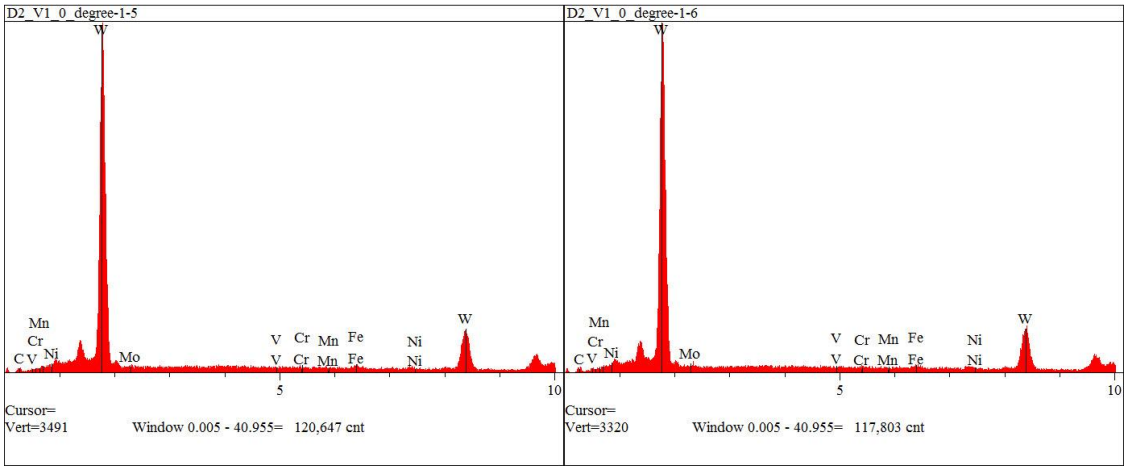
D2_V1_0_degree-1-5
W
Mn
Cr
C V Ni
Mo
V Cr Mn Fe
V Cr Mn Fe
Ni
Ni
W
5
10
Cursor=
Vert=3491
Window 0.005 - 40.955= 120,647 cnt
D2_V1_0_degree-1-6
W
Mn
Cr
C V Ni
Mo
V Cr Mn Fe
V Cr Mn Fe
Ni
Ni
W
5
10
Cursor=
Vert=3320
Window 0.005 - 40.955= 117,803 cnt

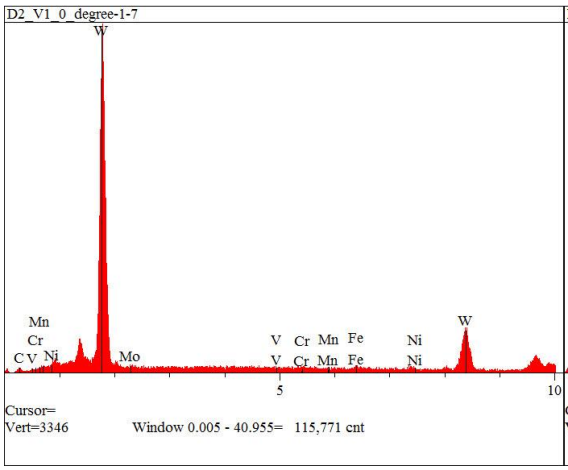
D2_V1_0_degree-1-7
W
Mn
Cr
C V Ni
Mo
V Cr Mn Fe
V Cr Mn Fe
Ni
Ni
W
5
10
Cursor=
Vert=3346
Window 0.005 - 40.955= 115,771 cnt

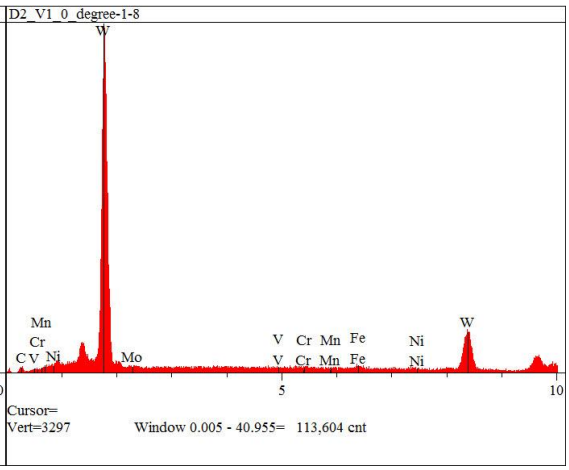
D2_V1_0_degree-1-8
W
Mn
Cr
C V Ni
Mo
V Cr Mn Fe
V Cr Mn Fe
Ni
Ni
W
5
10
Cursor=
Vert=3297
Window 0.005 - 40.955= 113,604 cnt

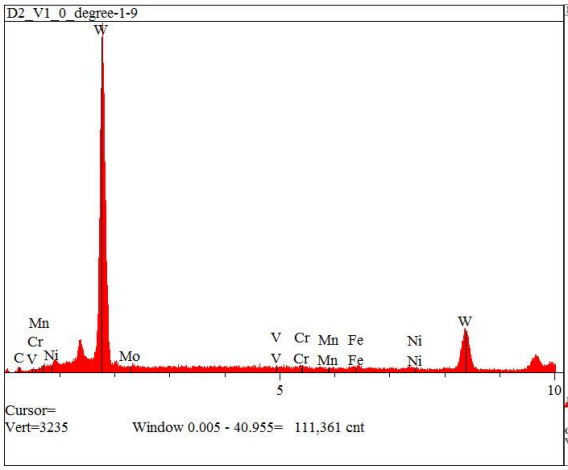
D2_V1_0_degree-1-9
W
Mn
Cr
C V Ni
Mo
V Cr Mn Fe
V Cr Mn Fe
Ni
Ni
W
5
10
Cursor=
Vert=3235
Window 0.005 - 40.955= 111,361 cnt

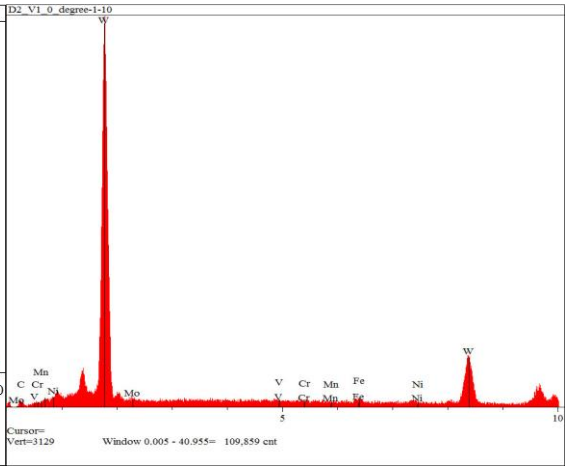
D2_V1_0_degree-1-10
W
Mn
C Cr
V Ni
Mo
V Cr Mn Fe
V Cr Mn Fe
Ni
Ni
W
5
10
Cursor=
Vert=3129
Window 0.005 - 40.955= 109,859 cnt

D2_P1_5 Degree 1-10 EDS Plots

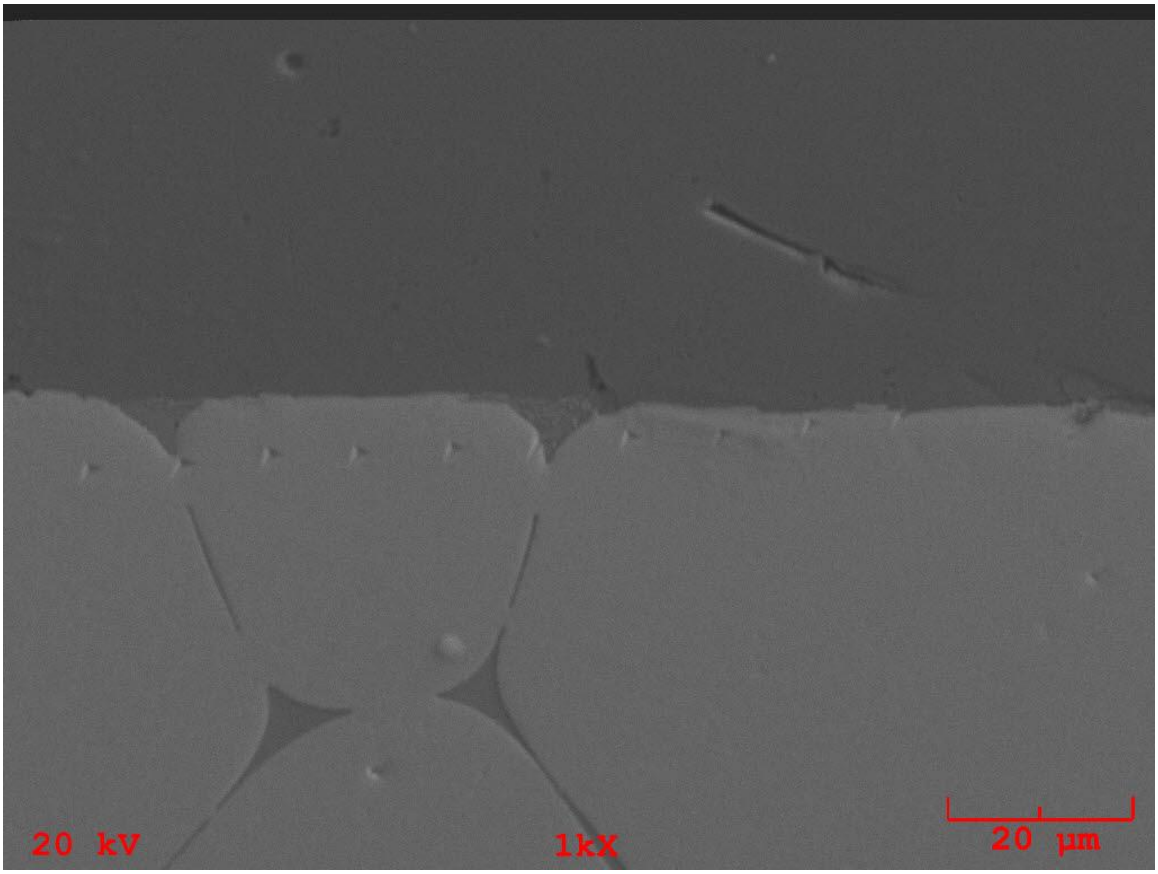

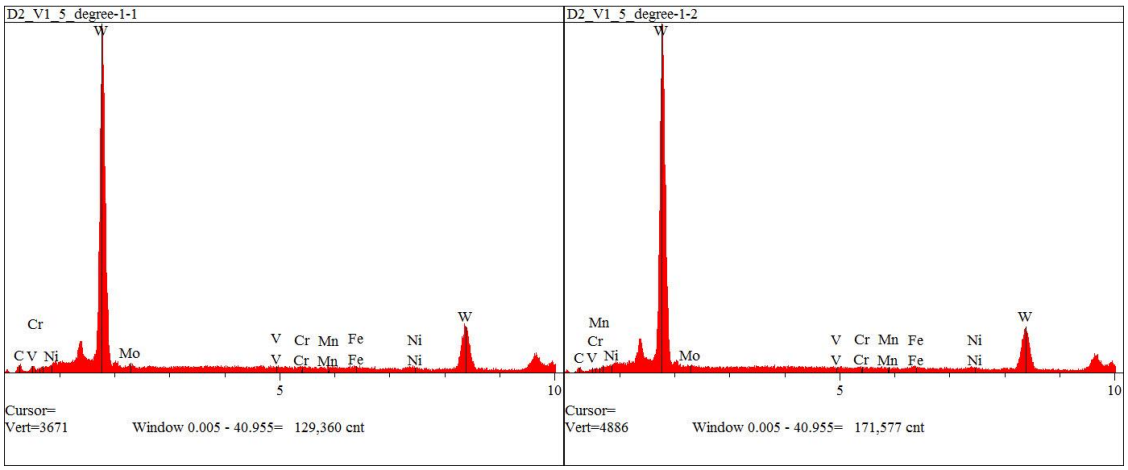
D2_V1_5_degree-1-1
W
Cr
C V Ni
Mo
V Cr Mn Fe Ni
V Cr Mn Fe Ni
W
5
10
Cursor=
Vert=3671
Window 0.005 - 40.955= 129,360 cnt
D2_V1_5_degree-1-2
W
Mn
Cr
C V Ni
Mo
V Cr Mn Fe Ni
V Cr Mn Fe Ni
W
5
10
Cursor=
Vert=4886
Window 0.005 - 40.955= 171,577 cnt

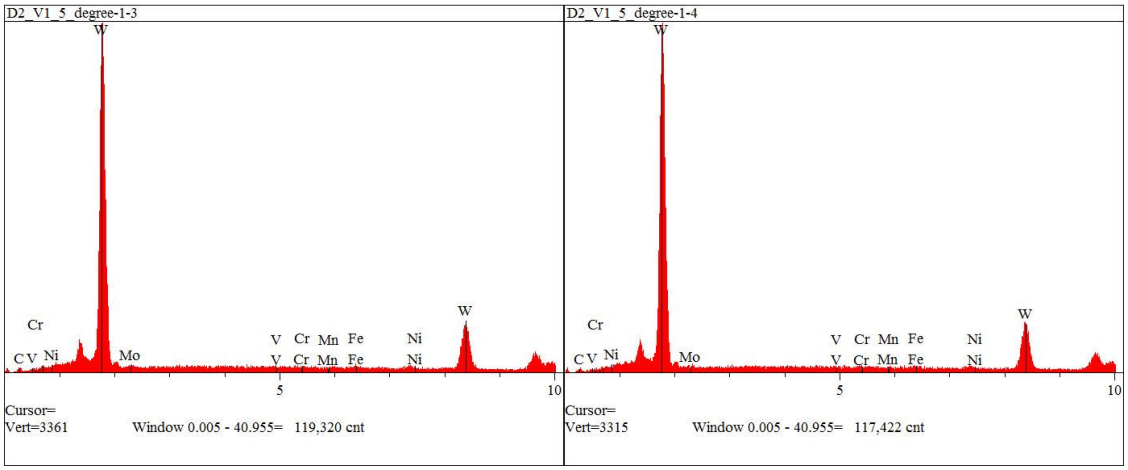
D2_V1_5_degree-1-3
W
Cr
C V Ni
Mo
V Cr Mn Fe Ni
V Cr Mn Fe Ni
W
5
10
Cursor=
Vert=3361
Window 0.005 - 40.955= 119,320 cnt
D2_V1_5_degree-1-4
W
Cr
C V Ni
Mo
V Cr Mn Fe Ni
V Cr Mn Fe Ni
W
5
10
Cursor=
Vert=3315
Window 0.005 - 40.955= 117,422 cnt

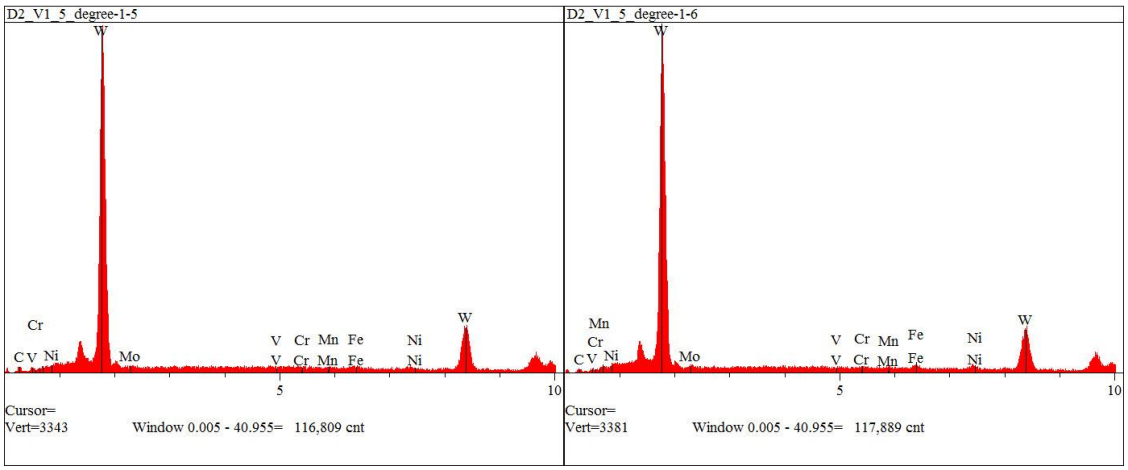
D2_V1_5_degree-1-5
W
Cr
C V Ni
Mo
V Cr Mn Fe
V Cr Mn Fe
Ni
Ni
W
5
10
Cursor=
Vert=3343
Window 0.005 - 40.955= 116,809 cnt
D2_V1_5_degree-1-6
W
Mn
Cr
C V Ni
Mo
V Cr Mn Fe
V Cr Mn Fe
Ni
Ni
W
5
10
Cursor=
Vert=3381
Window 0.005 - 40.955= 117,889 cnt

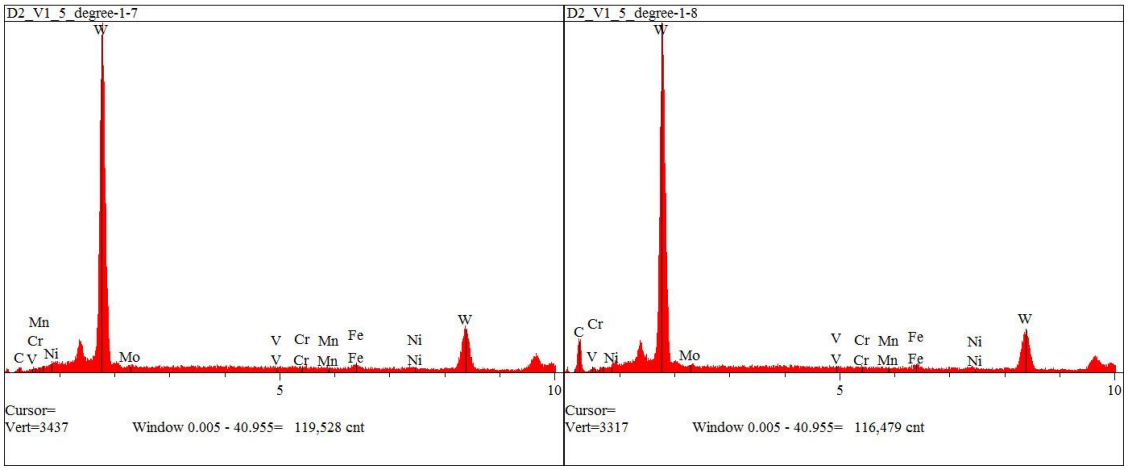
D2_V1_5_degree-1-7
W
Mn
Cr
C V Ni
Mo
V Cr Mn Fe
V Cr Mn Fe
Ni
Ni
W
5
10
Cursor=
Vert=3437
Window 0.005 - 40.955= 119,528 cnt
D2_V1_5_degree-1-8
W
C Cr
V Ni
Mo
V Cr Mn Fe
V Cr Mn Fe
Ni
Ni
W
5
10
Cursor=
Vert=3317
Window 0.005 - 40.955= 116,479 cnt

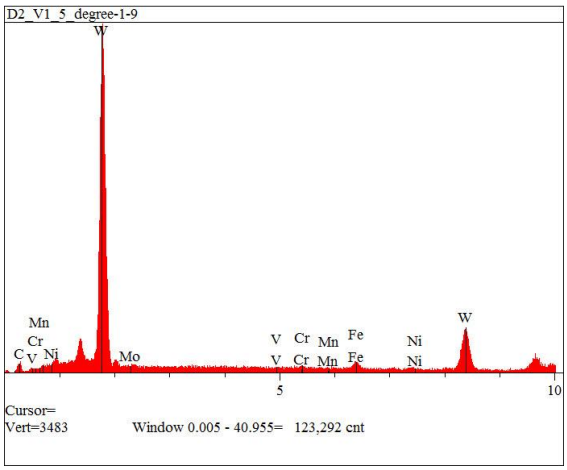
D2_V1_5_degree-1-9
W
Mn
Cr
C V Ni
Mo
V Cr Mn Fe
V Cr Mn Fe
Ni
Ni
W
5
10
Cursor=
Vert=3483
Window 0.005 - 40.955= 123,292 cnt

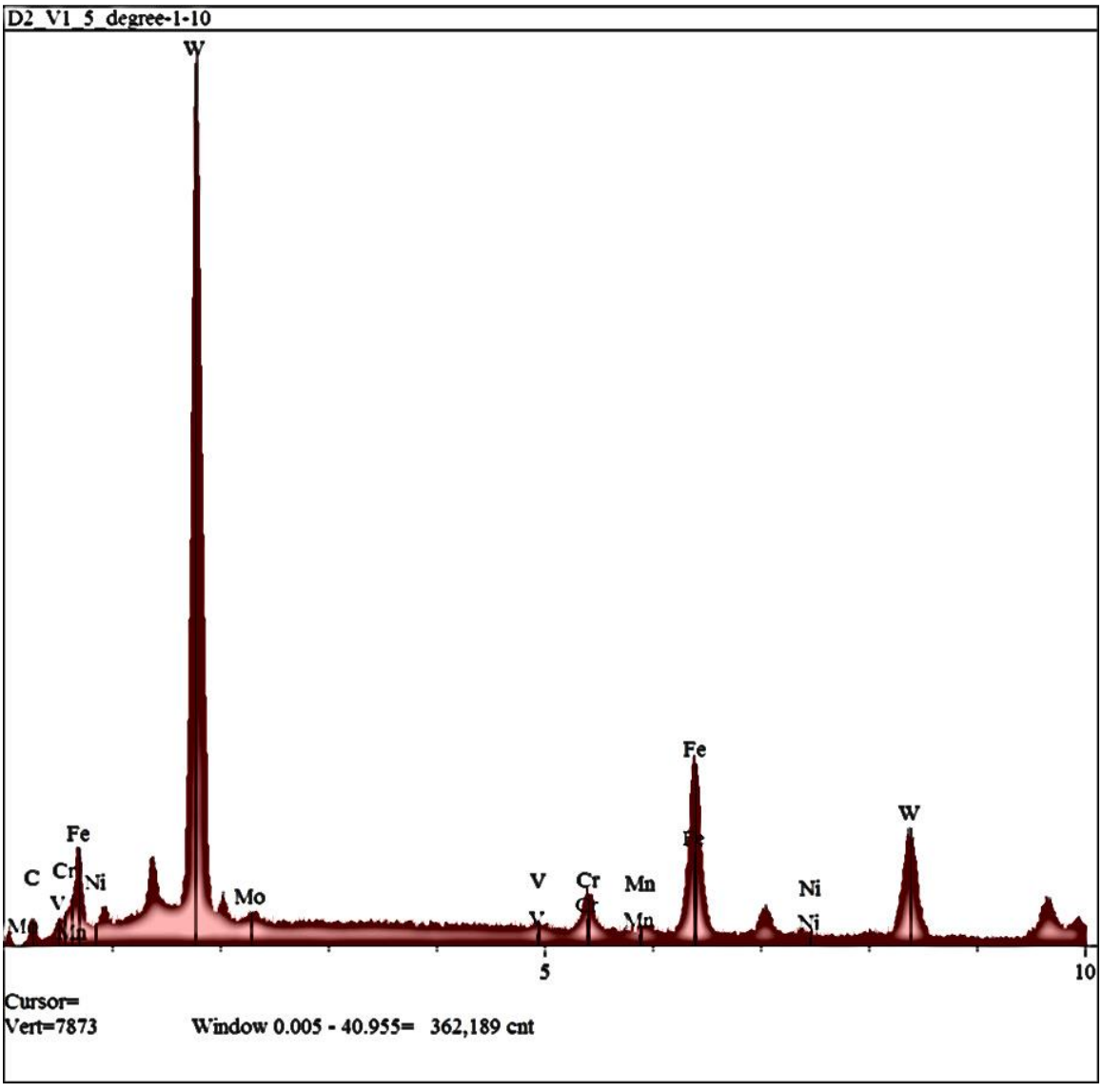
D2_V1_5_degree-1-10
W
Fe
C Cr Ni
V
Mo
V Cr Mn
Fe
Ni
W
5
10
Cursor=
Vert=7873
Window 0.005 - 40.955= 362,189 cnt

D2_P1_10 Degree 1-10 EDS Plots

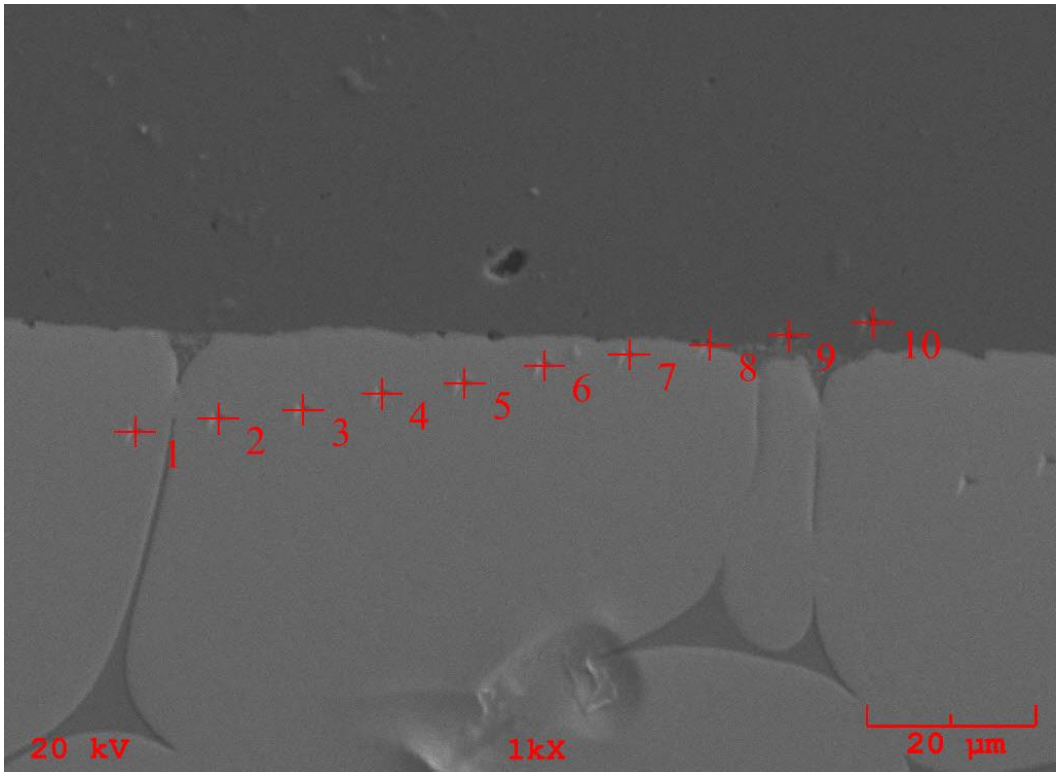

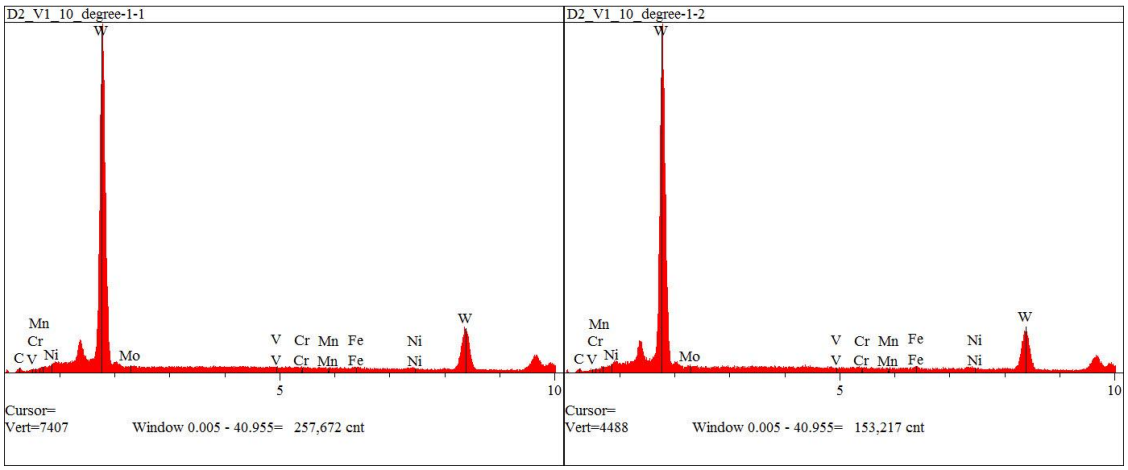
D2_V1_10_degree-1-1
W
Mn
Cr
C V Ni
Mo
V Cr Mn Fe
V Cr Mn Fe
Ni
Ni
W
5
10
Cursor=
Vert=7407
Window 0.005 - 40.955= 257,672 cnt

D2_V1_10_degree-1-2
W
Mn
Cr
C V Ni
Mo
V Cr Mn Fe
V Cr Mn Fe
Ni
Ni
W
5
10
Cursor=
Vert=4488
Window 0.005 - 40.955= 153,217 cnt

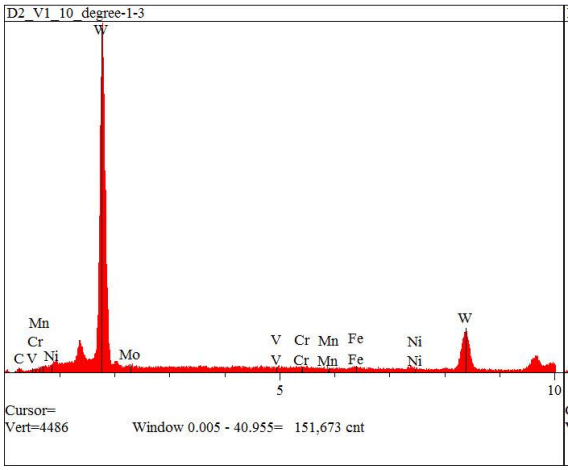
D2_V1_10_degree-1-3
W
Mn
Cr
C V Ni
Mo
V Cr Mn Fe
V Cr Mn Fe
Ni
Ni
W
5
10
Cursor=
Vert=4486
Window 0.005 - 40.955= 151,673 cnt

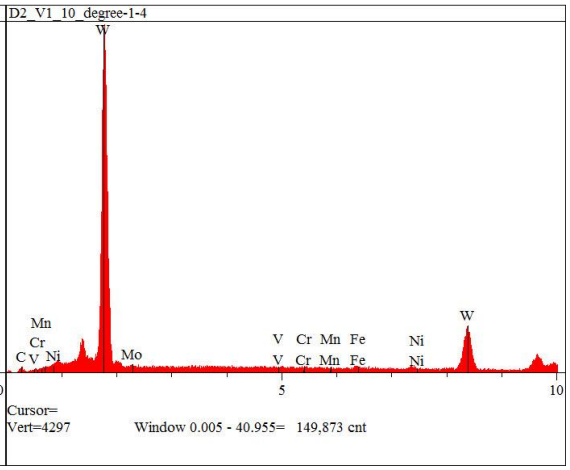
D2_V1_10_degree-1-4
W
Mn
Cr
C V Ni
Mo
V Cr Mn Fe
V Cr Mn Fe
Ni
Ni
W
5
10
Cursor=
Vert=4297
Window 0.005 - 40.955= 149,873 cnt

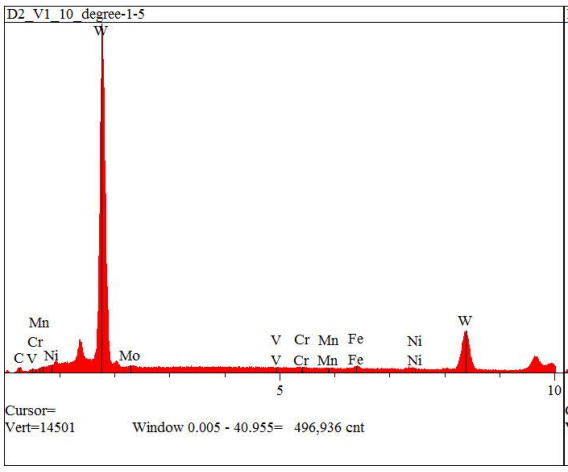
D2_V1_10_degree-1-5
W
Mn
Cr
C V Ni
Mo
V Cr Mn Fe
V Cr Mn Fe
Ni
Ni
W
5
10
Cursor=
Vert=14501
Window 0.005 - 40.955= 496,936 cnt

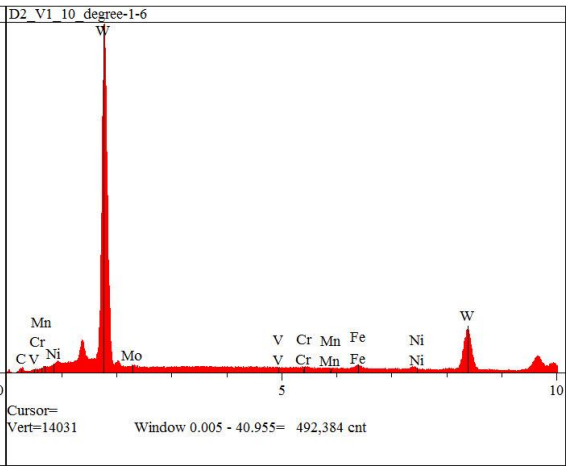
D2_V1_10_degree-1-6
W
Mn
Cr
C V Ni
Mo
V Cr Mn Fe
V Cr Mn Fe
Ni
Ni
W
5
10
Cursor=
Vert=14031
Window 0.005 - 40.955= 492,384 cnt

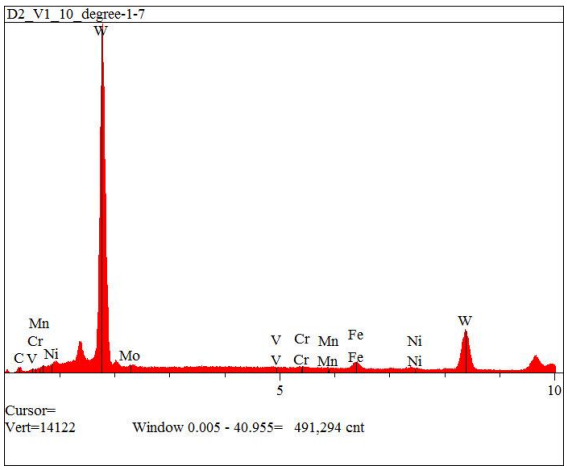
D2_V1_10_degree-1-7
W
Mn
Cr
Ni
C V
Mo
V Cr Mn Fe
V Cr Mn Fe
Ni
Ni
W
5
10
Cursor=
Vert=14122
Window 0.005 - 40.955= 491,294 cnt

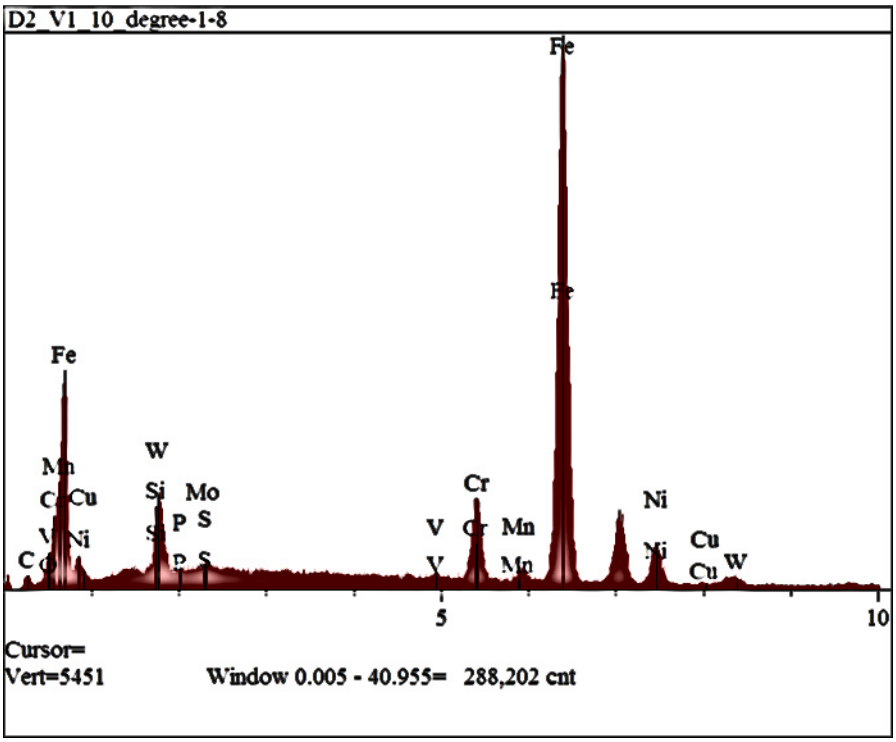
D2_V1_10_degree-1-8
Fe
Fe
Fe
W
Si
Mo
P
S
Mn
Cu
Ni
C
V
Cr
Mn
Ni
Cu
W
5
10
Cursor=
Vert=5451
Window 0.005 - 40.955= 288,202 cnt

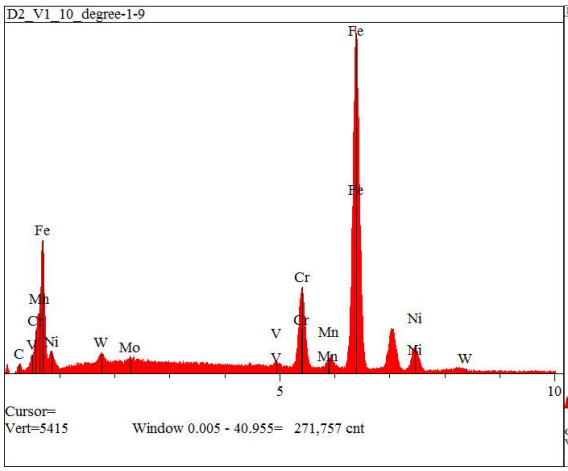
D2_V1_10_degree-1-9
Fe
Fe
Fe
Mn
Cr
Ni
C
W
Mo
V
Cr
Mn
Ni
W
5
10
Cursor=
Vert=5415
Window 0.005 - 40.955= 271,757 cnt

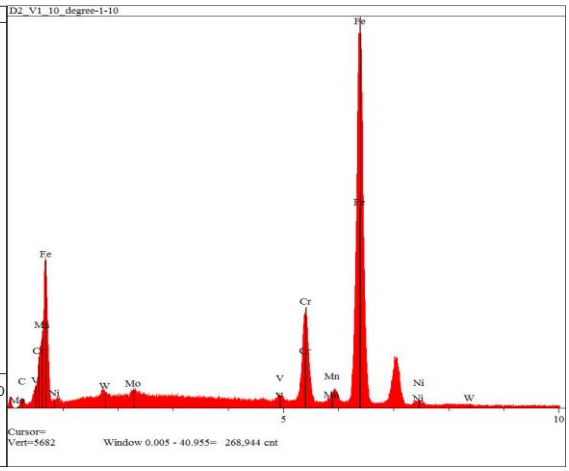
D2_V1_10_degree-1-10
Fe
Fe
Fe
Cr
Mn
Ni
W
Mo
V
Ni
W
5
10
Cursor=
Vert=5682
Window 0.005 - 40.955= 268,944 cnt

D2_P1_15 Degree 1-10 EDS Plots

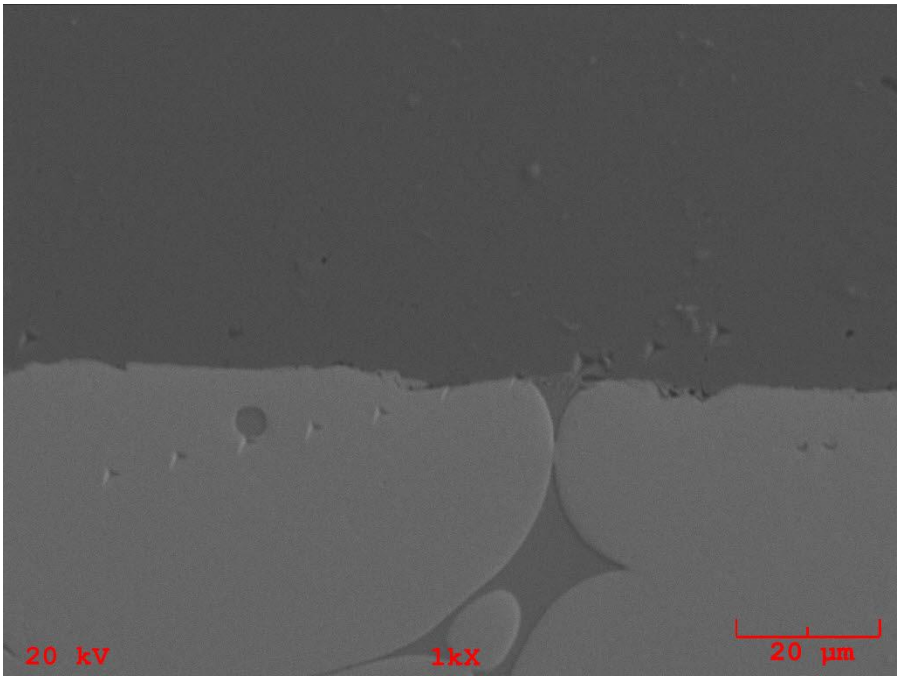

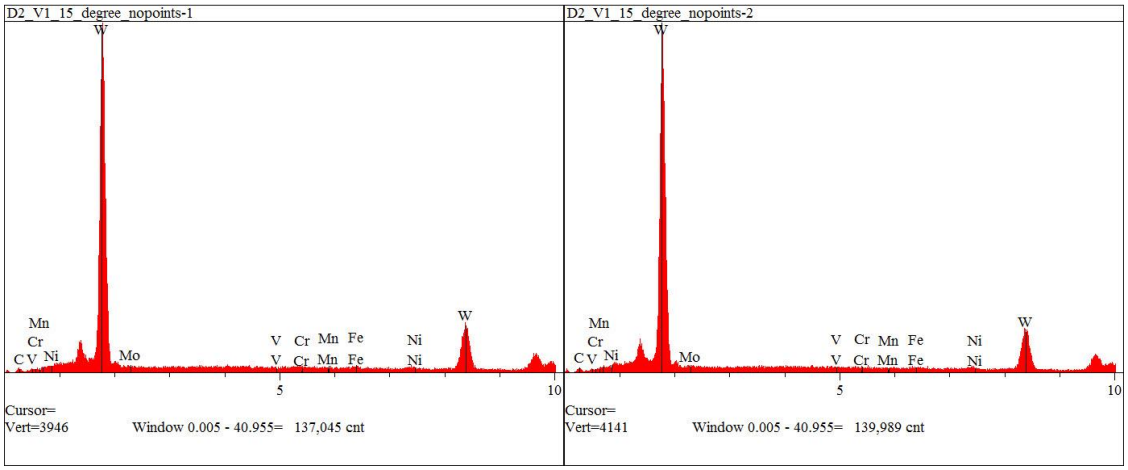
D2_V1_15_degree_nopoints-1
W
Mn
Cr
C V Ni
Mo
V Cr Mn Fe
V Cr Mn Fe
Ni
Ni
W
5
10
Cursor=
Vert=3946
Window 0.005 - 40.955= 137,045 cnt
D2_V1_15_degree_nopoints-2
W
Mn
Cr
C V Ni
Mo
V Cr Mn Fe
V Cr Mn Fe
Ni
Ni
W
5
10
Cursor=
Vert=4141
Window 0.005 - 40.955= 139,989 cnt

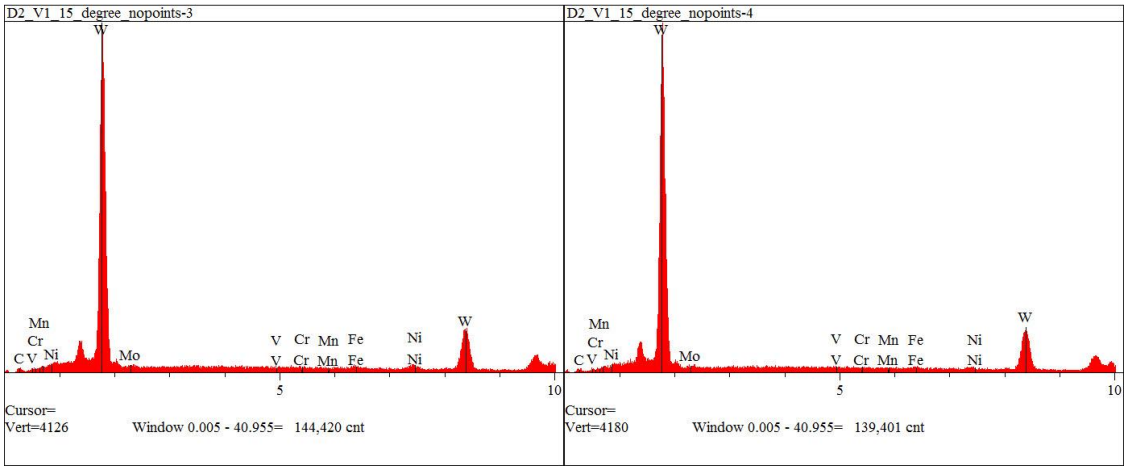
D2_V1_15_degree_nopoints-3
W
Mn
Cr
C V Ni
Mo
V Cr Mn Fe
V Cr Mn Fe
Ni
Ni
W
5
10
Cursor=
Vert=4126
Window 0.005 - 40.955= 144,420 cnt
D2_V1_15_degree_nopoints-4
W
Mn
Cr
C V Ni
Mo
V Cr Mn Fe
V Cr Mn Fe
Ni
Ni
W
5
10
Cursor=
Vert=4180
Window 0.005 - 40.955= 139,401 cnt

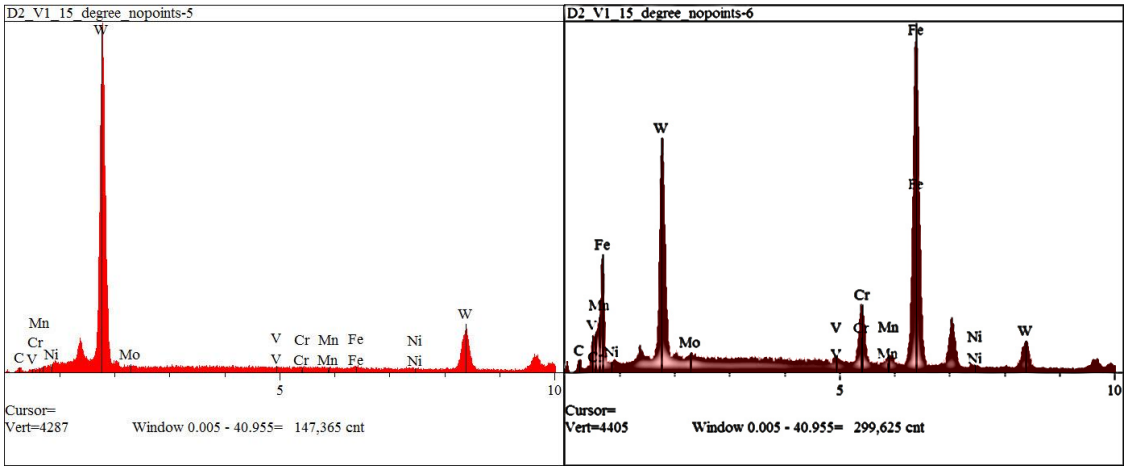
D2_V1_15_degree_nopoints-5
Cursor=
Vert=4287
Window 0.005 - 40.955= 147,365 cnt
D2_V1_15_degree_nopoints-6
Cursor=
Vert=4405
Window 0.005 - 40.955= 299,625 cnt

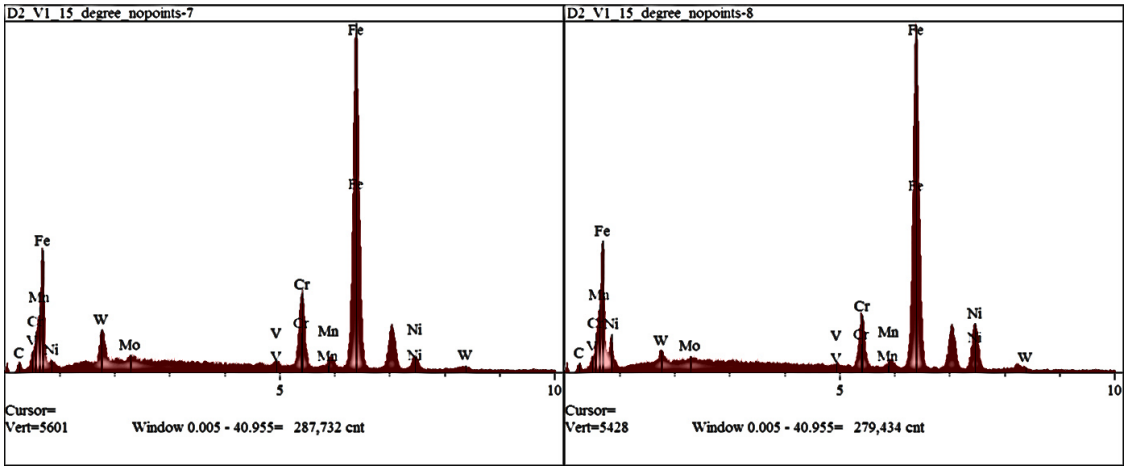
D2_V1_15_degree_nopoints-7
Cursor=
Vert=5601
Window 0.005 - 40.955= 287,732 cnt
D2_V1_15_degree_nopoints-8
Cursor=
Vert=5428
Window 0.005 - 40.955= 279,434 cnt

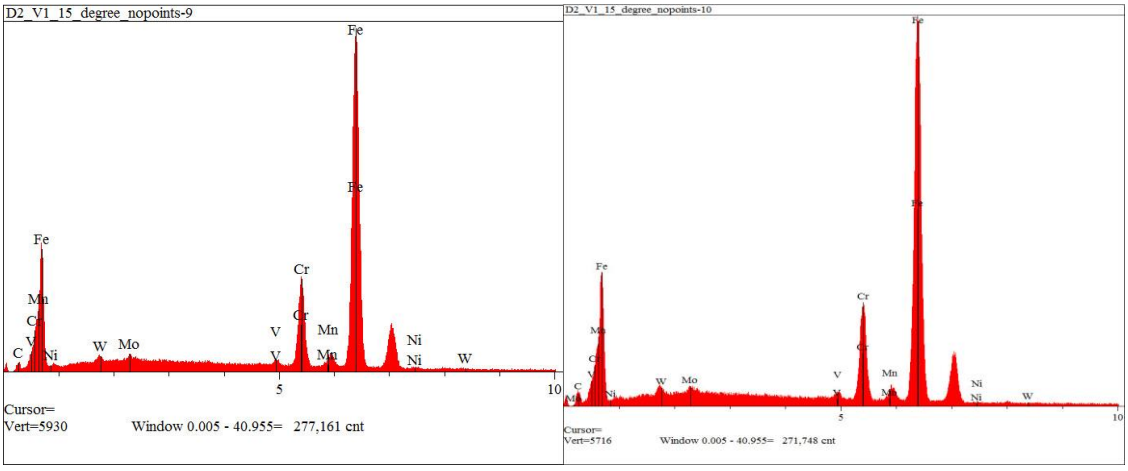
D2_V1_15_degree_nopoints-9
Cursor=
Vert=5930
Window 0.005 - 40.955= 277,161 cnt
D2_V1_15_degree_nopoints-10
Cursor=
Vert=5716
Window 0.005 - 40.955= 271,748 cnt

V2 4x10 1-40 EDS Taken Horizontally

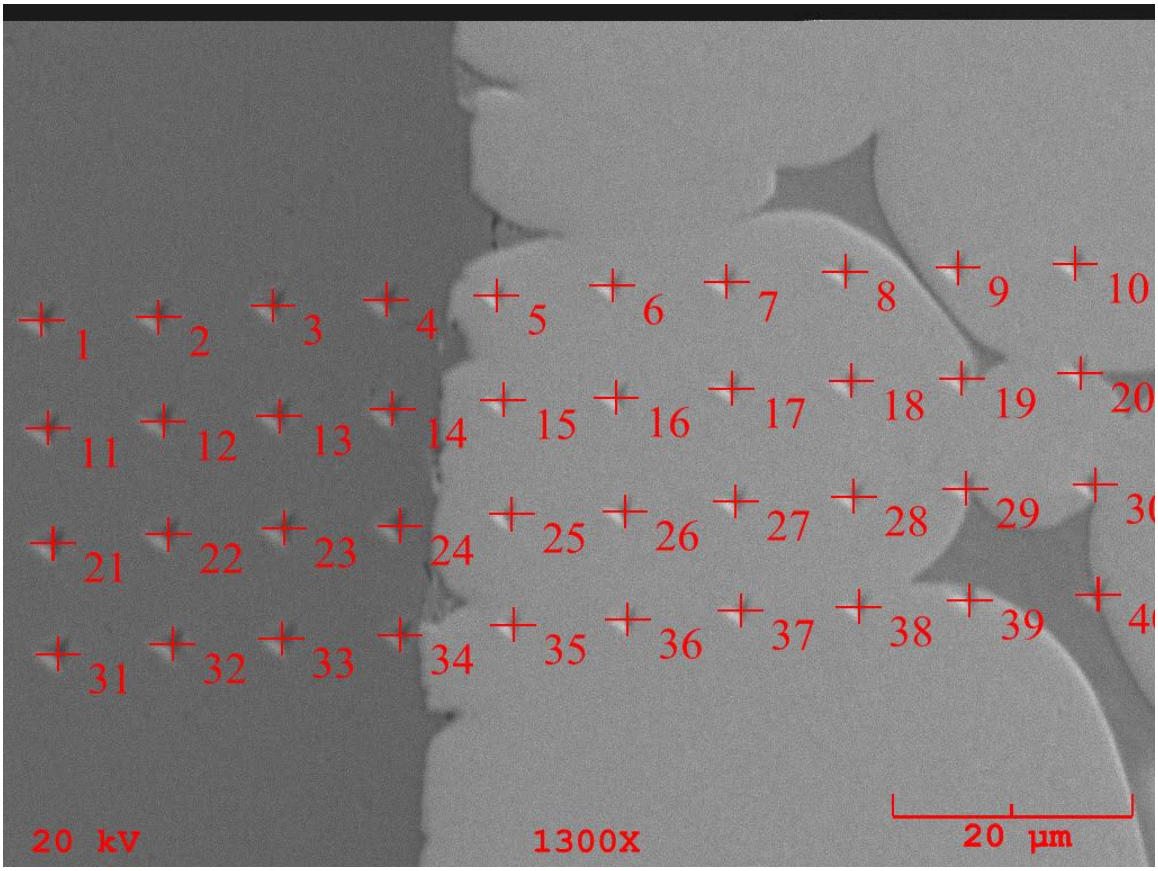

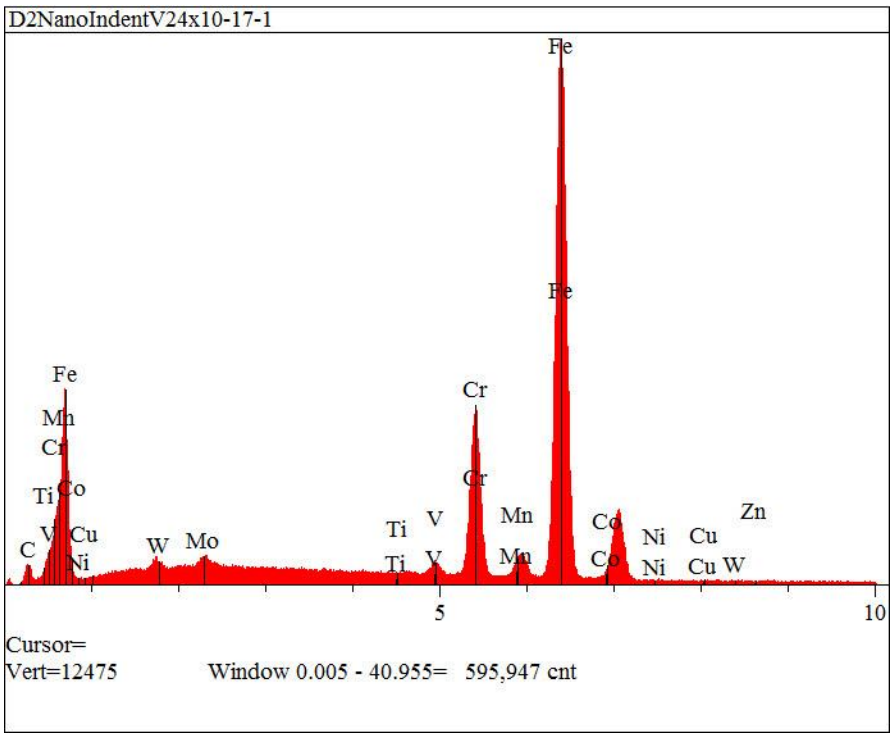
D2NanoIndentV24x10-17-1
Fe
Fe
Fe
Mn
Cr
Ti
Co
V
Cu
Ni
C
W
Mo
Ti
V
Cr
Cr
Mn
Mn
Co
Co
Ni
Ni
Cu
Cu
W
Zn
5
10
Cursor=
Vert=12475
Window 0.005 - 40.955= 595,947 cnt

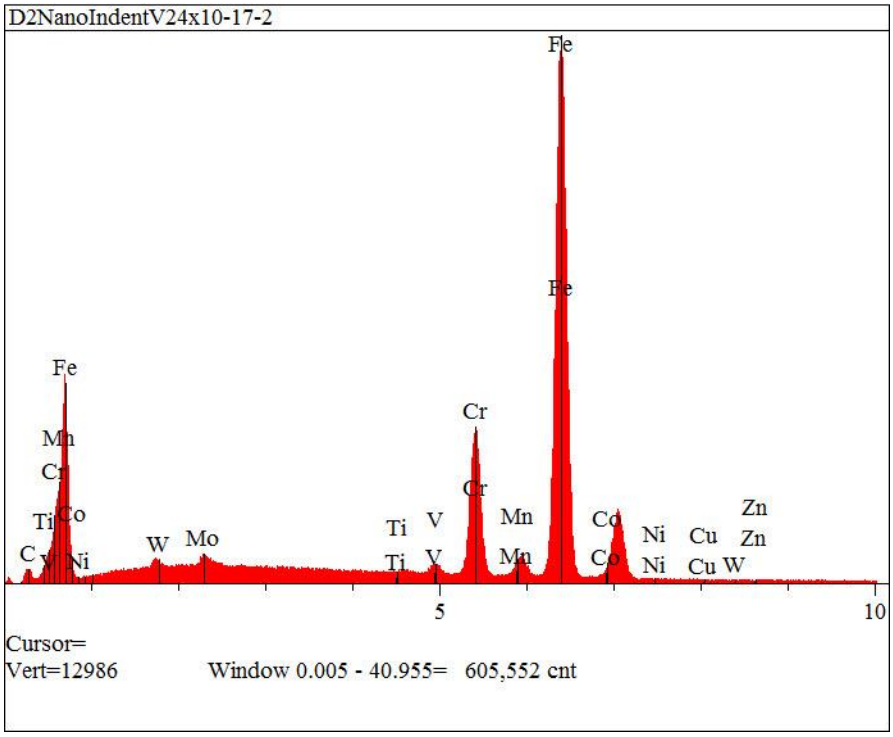
D2NanoIndentV24x10-17-2
Fe
Fe
Fe
Mn
Cr
Ti
Co
V
Ni
C
W
Mo
Ti
V
Cr
Cr
Mn
Mn
Co
Co
Ni
Ni
Cu
Cu
W
Zn
Zn
5
10
Cursor=
Vert=12986
Window 0.005 - 40.955= 605,552 cnt

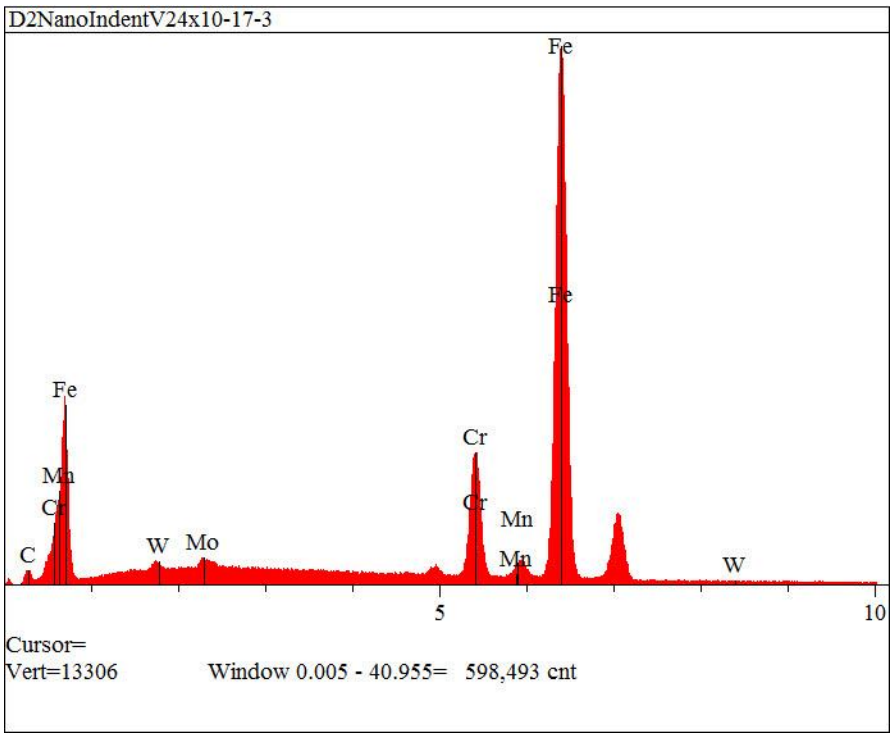
D2NanoIndentV24x10-17-3
Fe
Fe
Fe
Mn
Cr
Cr
Cr
Mn
C
W
Mo
Mn
W
5
10
Cursor=
Vert=13306
Window 0.005 - 40.955= 598,493 cnt

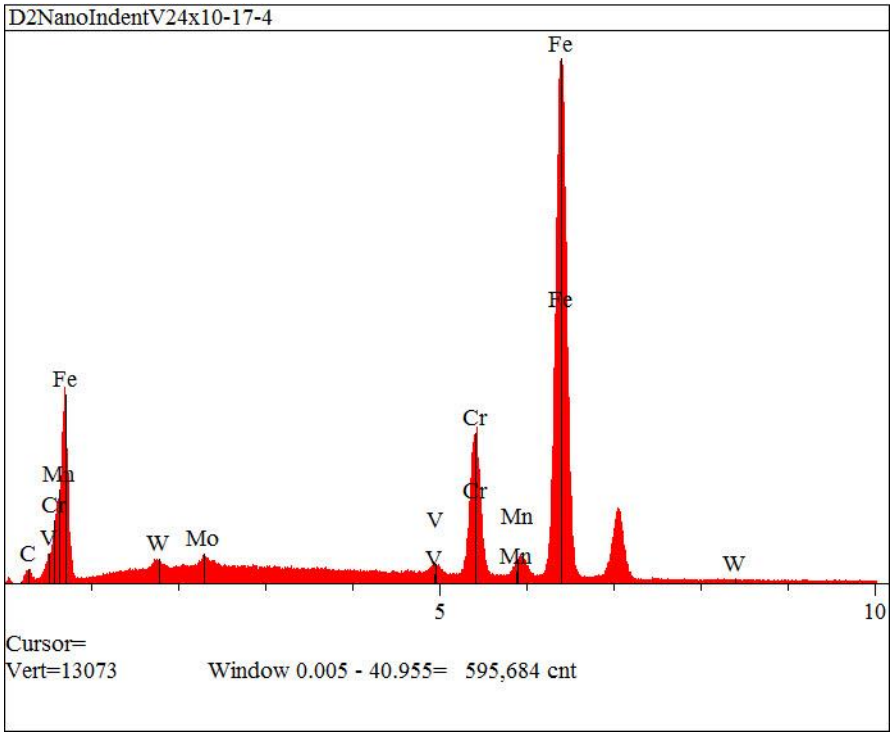
D2NanoIndentV24x10-17-4
Fe
Fe
Fe
Cr
Mn
Cr
Cr
V
Mn
C
V
W
Mo
V
Mn
W
5
10
Cursor=
Vert=13073
Window 0.005 - 40.955= 595,684 cnt

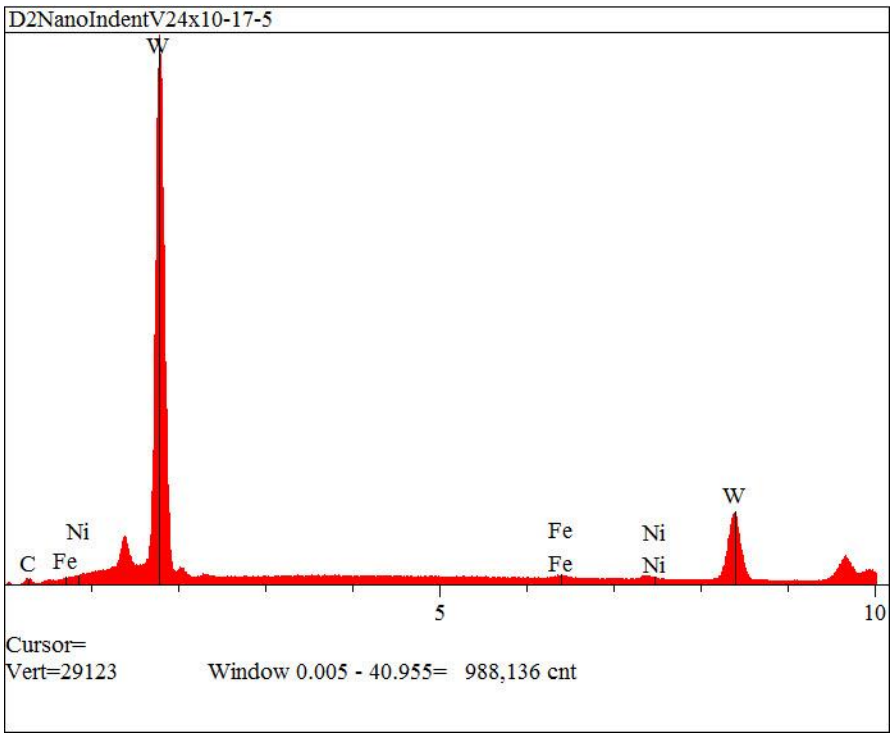
D2NanoIndentV24x10-17-5
W
Ni
C Fe
Fe
Fe
Ni
Ni
W
5
10
Cursor=
Vert=29123
Window 0.005 - 40.955= 988,136 cnt

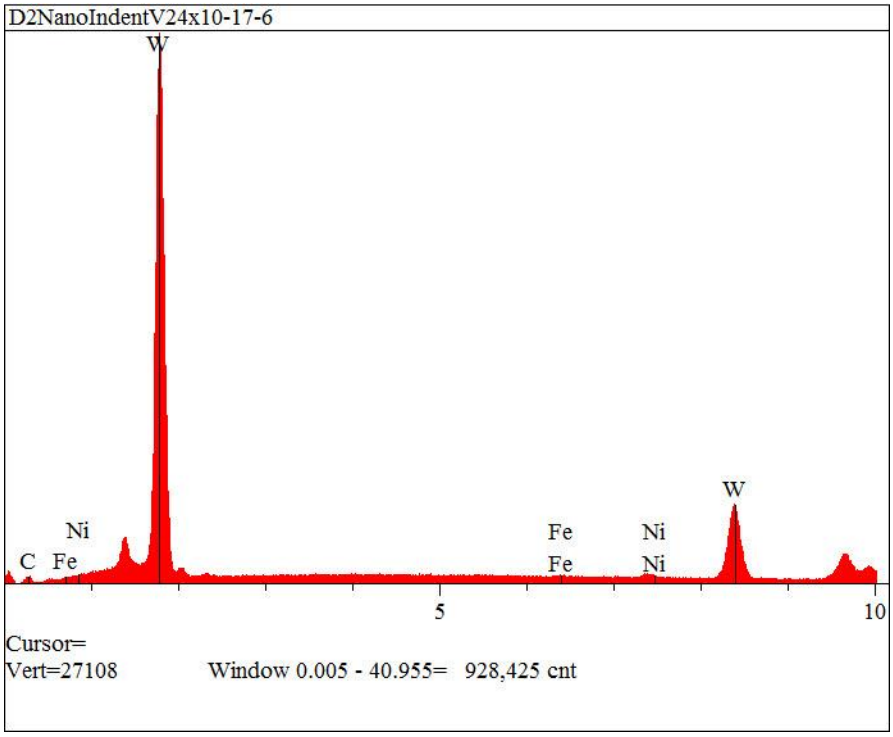
D2NanoIndentV24x10-17-6
W
Ni
C Fe
Fe
Fe
Ni
Ni
W
5
10
Cursor=
Vert=27108
Window 0.005 - 40.955= 928,425 cnt

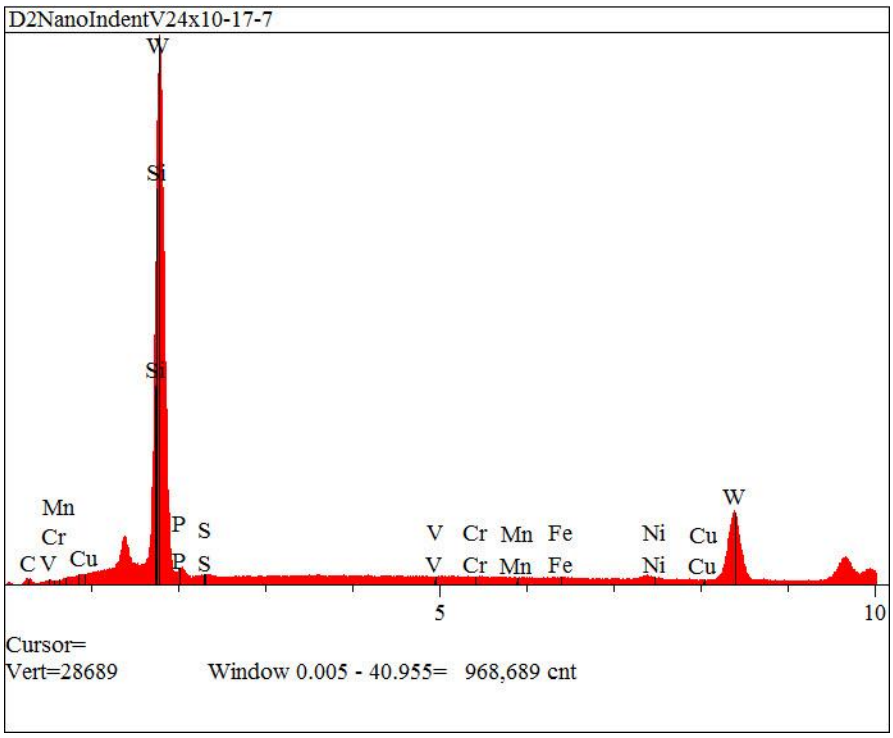
D2NanoIndentV24x10-17-7
W
Si
Si
Mn
Cr
C V Cu
P S
P S
V Cr Mn Fe
V Cr Mn Fe
Ni Cu
Ni Cu
W
5
10
Cursor=
Vert=28689
Window 0.005 - 40.955= 968,689 cnt

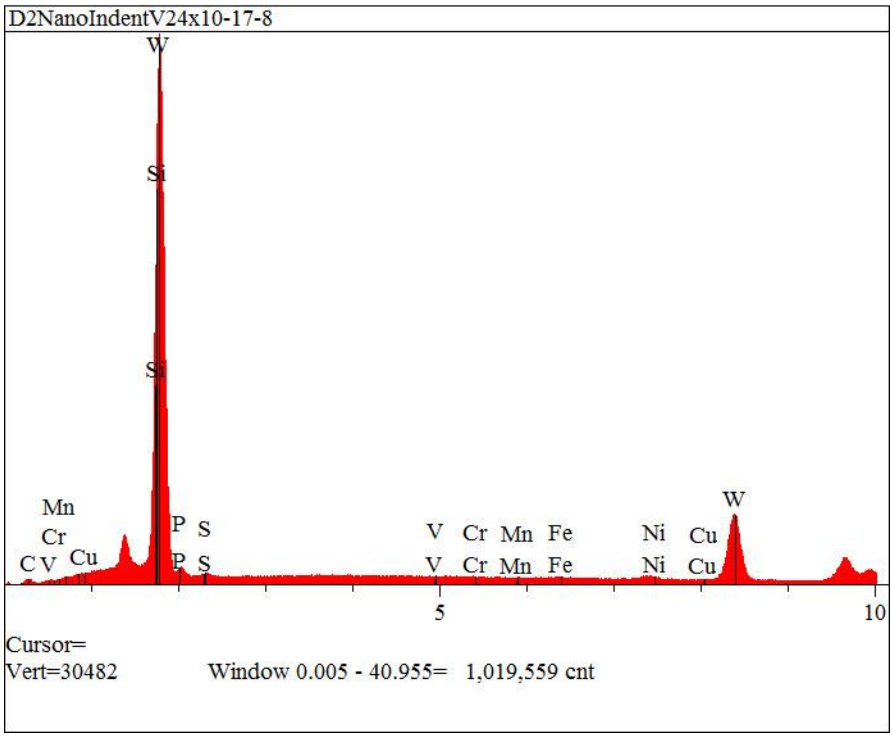
D2NanoIndentV24x10-17-8
W
Si
Si
Mn
Cr
C V Cu
P S
P S
V Cr Mn Fe
V Cr Mn Fe
Ni Cu
Ni Cu
W
5
10
Cursor=
Vert=30482
Window 0.005 - 40.955= 1,019,559 cnt

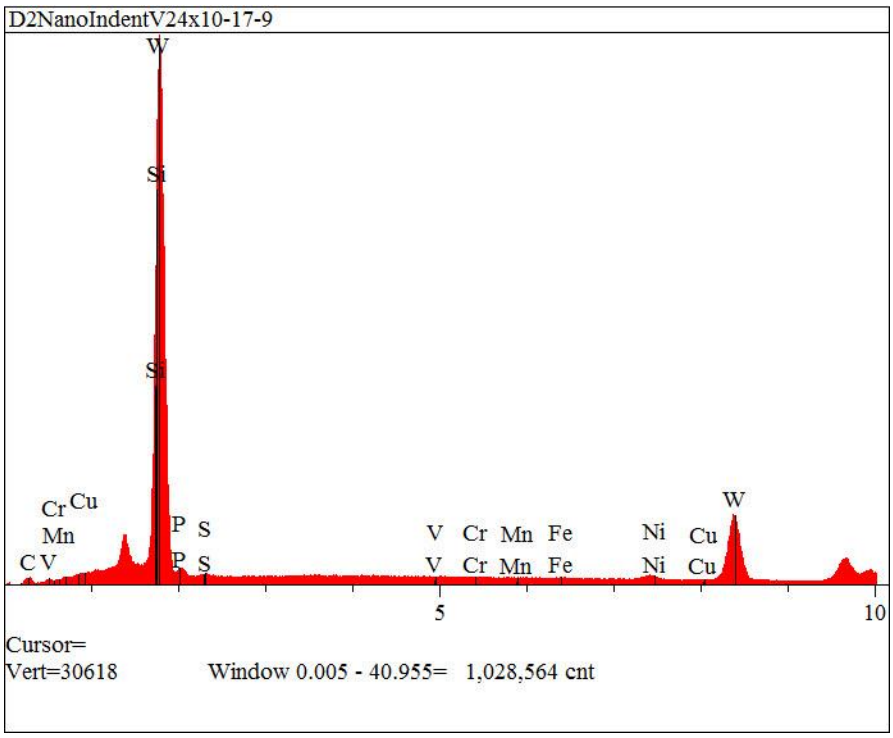
D2NanoIndentV24x10-17-9
W
Si
Si
Cr Cu
Mn
C V
P S
P S
V Cr Mn Fe
V Cr Mn Fe
Ni Cu
Ni Cu
W
5
10
Cursor=
Vert=30618
Window 0.005 - 40.955= 1,028,564 cnt

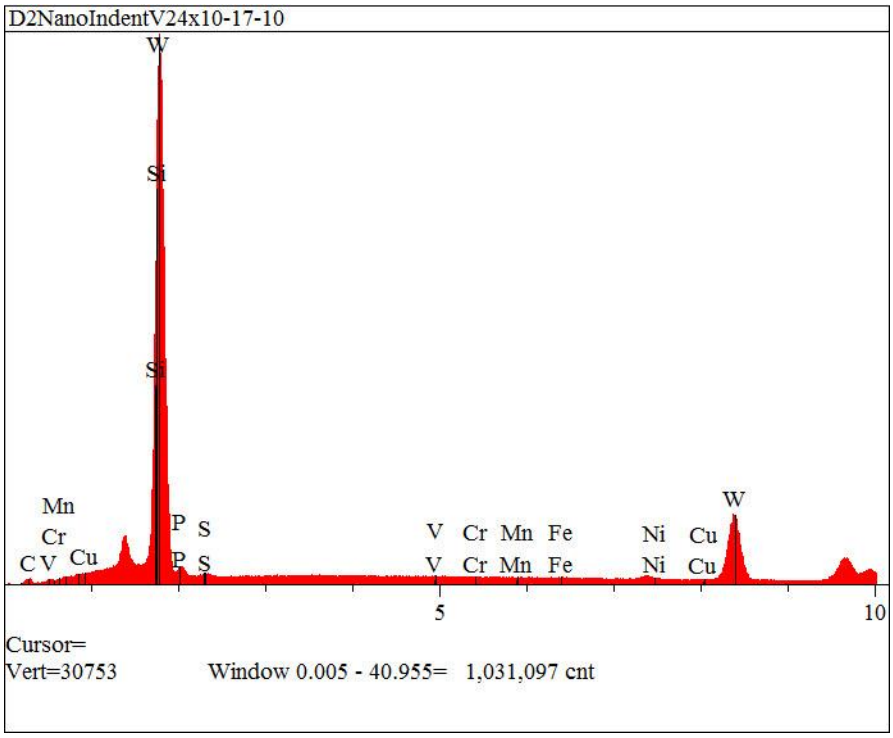
D2NanoIndentV24x10-17-10
W
Si
Si
Mn
Cr
C V Cu
P S
P S
V Cr Mn Fe
V Cr Mn Fe
Ni Cu
Ni Cu
W
5
10
Cursor=
Vert=30753
Window 0.005 - 40.955= 1,031,097 cnt

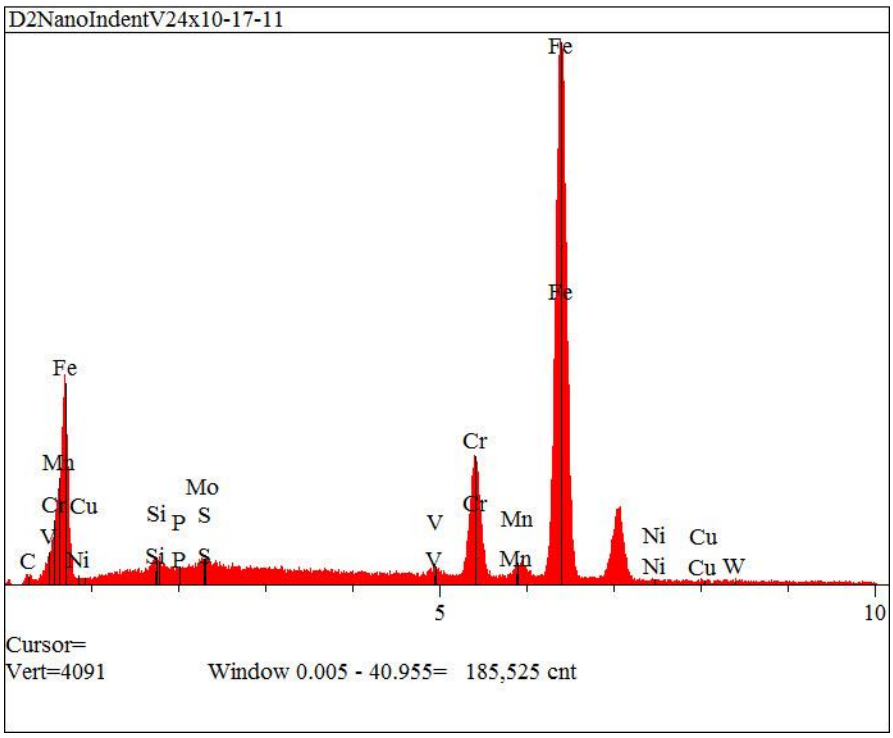
D2NanoIndentV24x10-17-11
Fe
Fe
Fe
Mn
Cr Cu
Si P S
Mo
Cr
V
Mn
Ni Cu
C
Ni
Si P S
V
Mn
Ni Cu W
5
10
Cursor=
Vert=4091
Window 0.005 - 40.955= 185,525 cnt

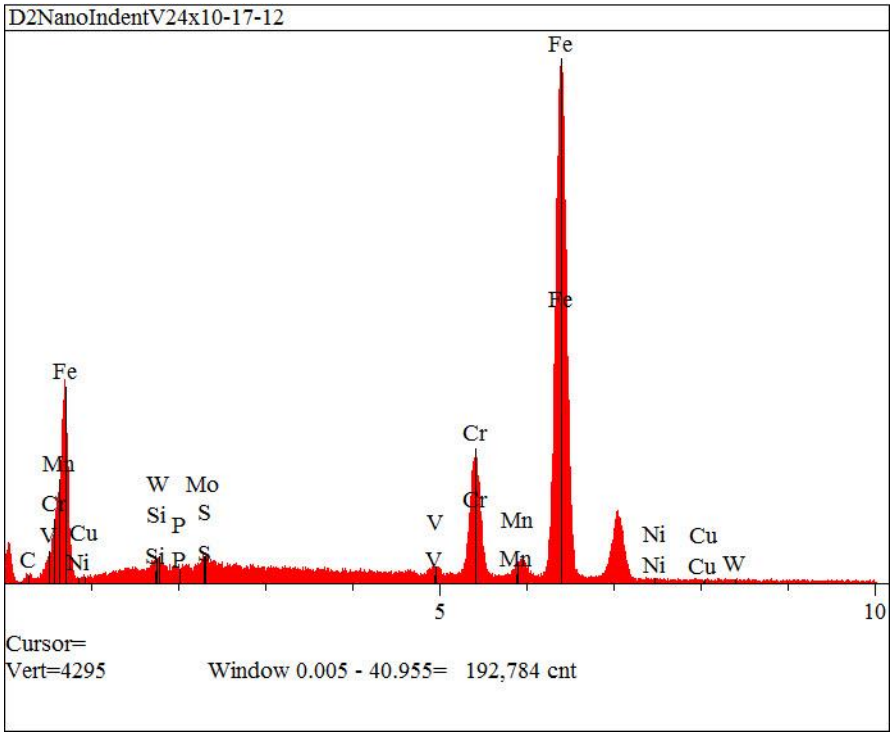
D2NanoIndentV24x10-17-12
Fe
Fe
Fe
Mn
Cr
W Mo
Si P S
Cr
V Cu
Mn
Ni Cu
C
Ni
Si P S
V
Mn
Ni Cu W
5
10
Cursor=
Vert=4295
Window 0.005 - 40.955= 192,784 cnt

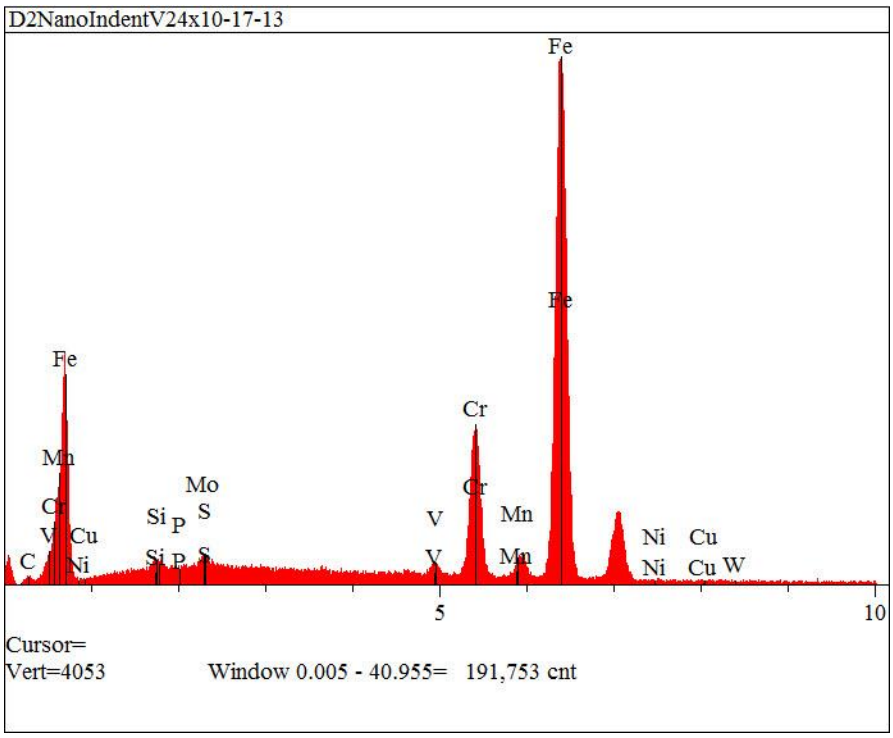
D2NanoIndentV24x10-17-13
Fe
Fe
Fe
Mn
Cr
Mo
Cr
Si P S
V
Mn
Cu
Ni Cu
C
Ni
Ni Cu W
5
10
Cursor=
Vert=4053
Window 0.005 - 40.955= 191,753 cnt

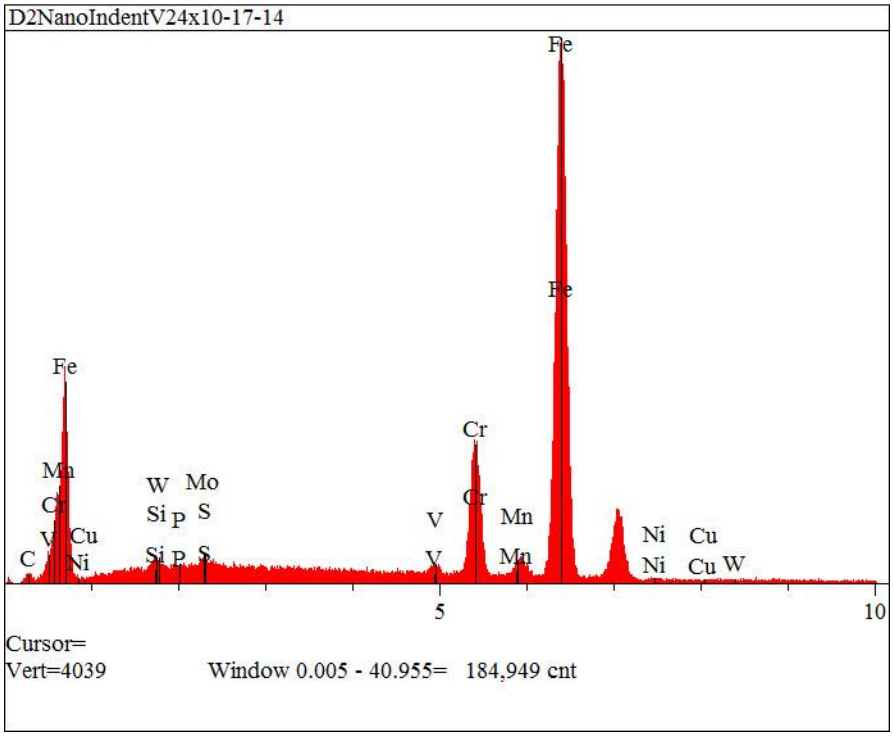
D2NanoIndentV24x10-17-14
Fe
Fe
Fe
Mn
Cr
W Mo
Cr
Si P S
V
Mn
Cu
Ni Cu
C
Ni
Ni Cu W
5
10
Cursor=
Vert=4039
Window 0.005 - 40.955= 184,949 cnt

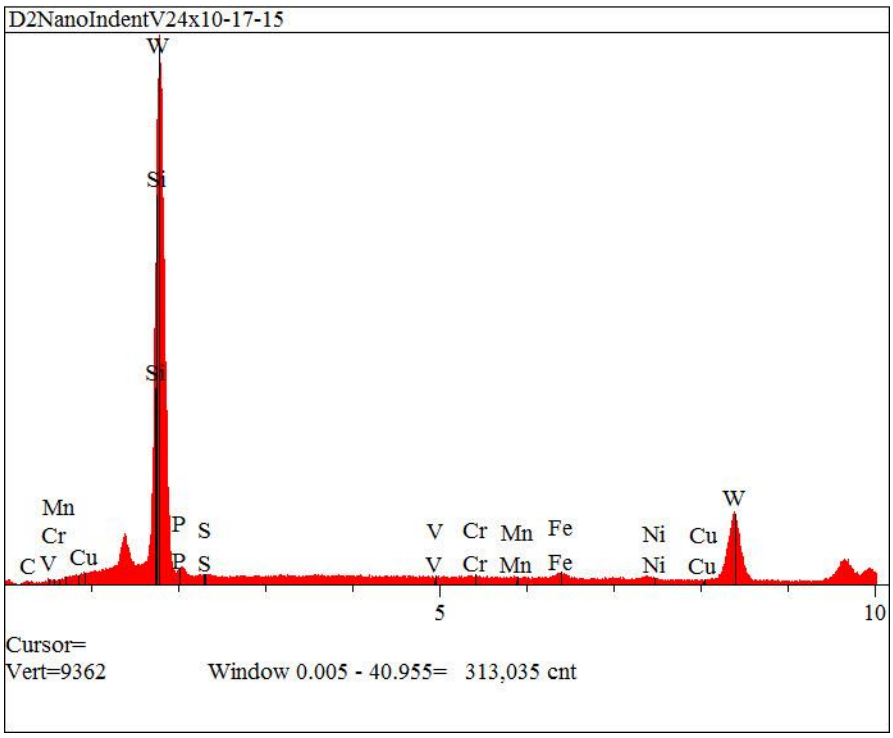
D2NanoIndentV24x10-17-15
W
Si
Si
Mn
Cr
C V Cu
P S
P S
V Cr Mn Fe
V Cr Mn Fe
Ni Cu
Ni Cu
W
5
10
Cursor=
Vert=9362
Window 0.005 - 40.955= 313,035 cnt

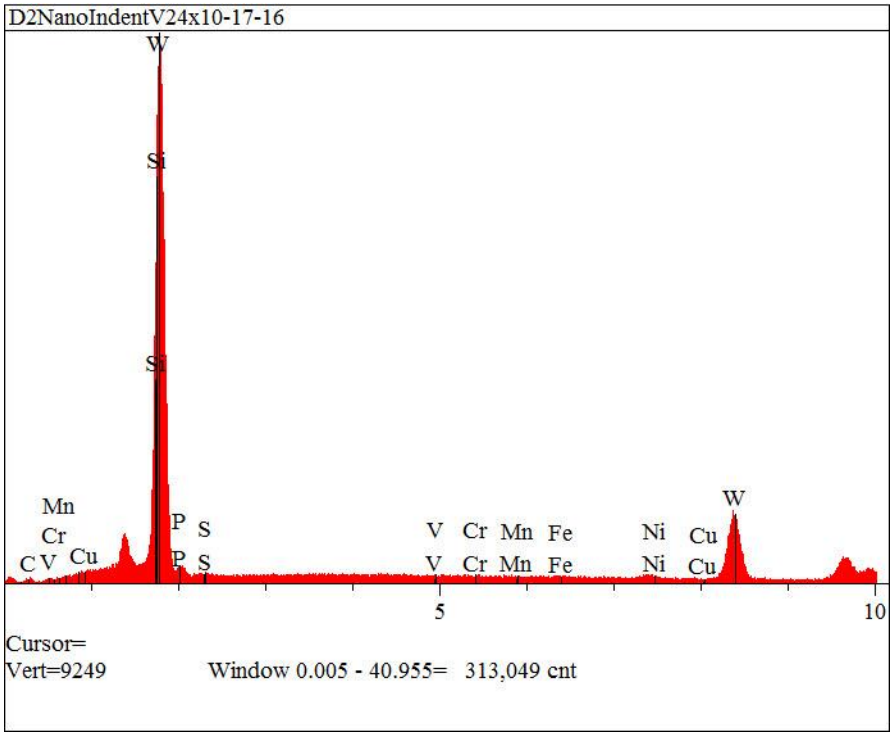
D2NanoIndentV24x10-17-16
W
Si
Si
Mn
Cr
C V Cu
P S
P S
V Cr Mn Fe
V Cr Mn Fe
Ni Cu
Ni Cu
W
5
10
Cursor=
Vert=9249
Window 0.005 - 40.955= 313,049 cnt

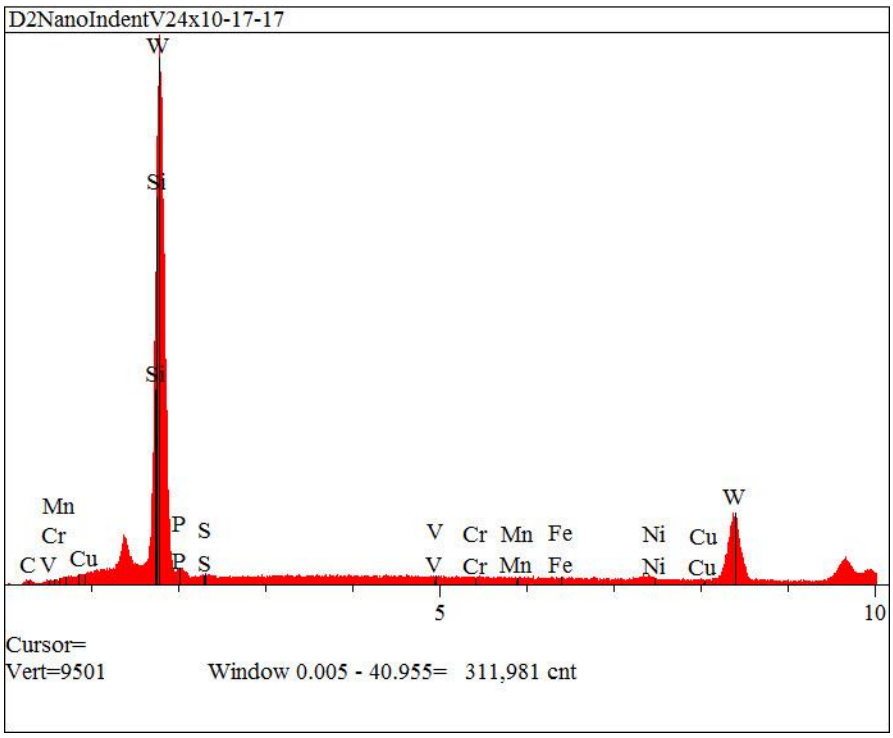
D2NanoIndentV24x10-17-17
W
Si
Si
Mn
Cr
C V Cu
P S
P S
V Cr Mn Fe
V Cr Mn Fe
Ni Cu
Ni Cu
W
5
10
Cursor=
Vert=9501
Window 0.005 - 40.955= 311,981 cnt

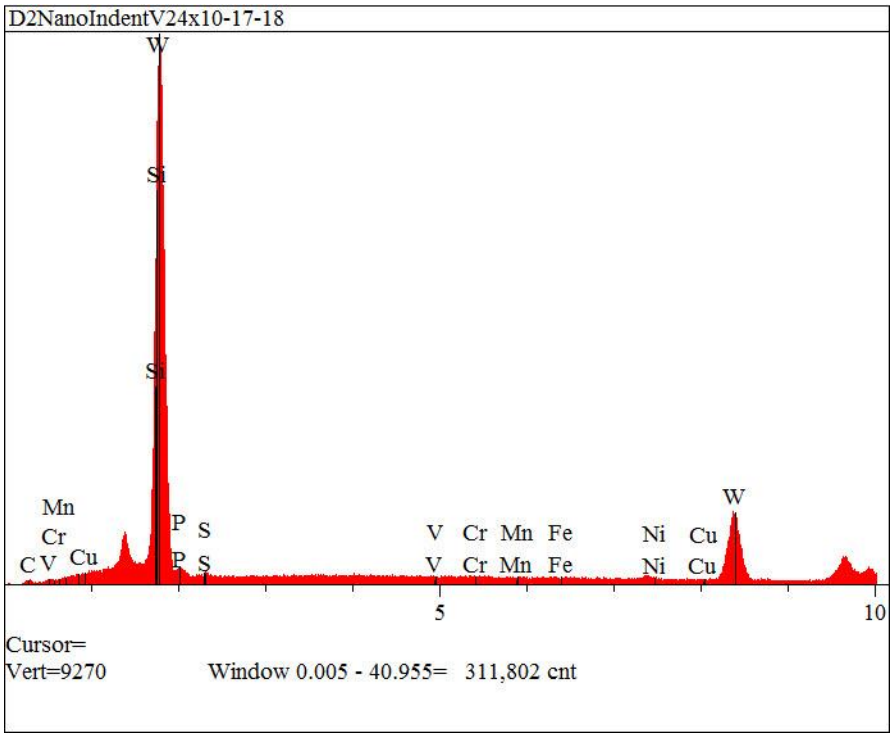
D2NanoIndentV24x10-17-18
W
Si
Si
Mn
Cr
C V Cu
P S
P S
V Cr Mn Fe
V Cr Mn Fe
Ni Cu
Ni Cu
W
5
10
Cursor=
Vert=9270
Window 0.005 - 40.955= 311,802 cnt

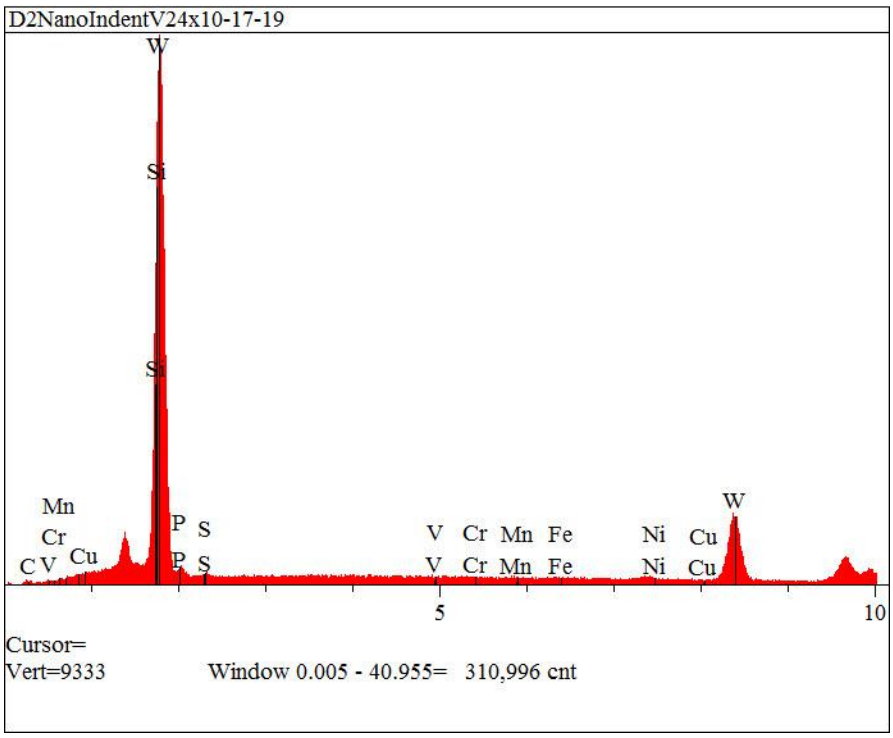
D2NanoIndentV24x10-17-19
W
Si
Si
Mn
Cr
C V Cu
P S
P S
V Cr Mn Fe
V Cr Mn Fe
Ni Cu
Ni Cu
W
5
10
Cursor=
Vert=9333
Window 0.005 - 40.955= 310,996 cnt

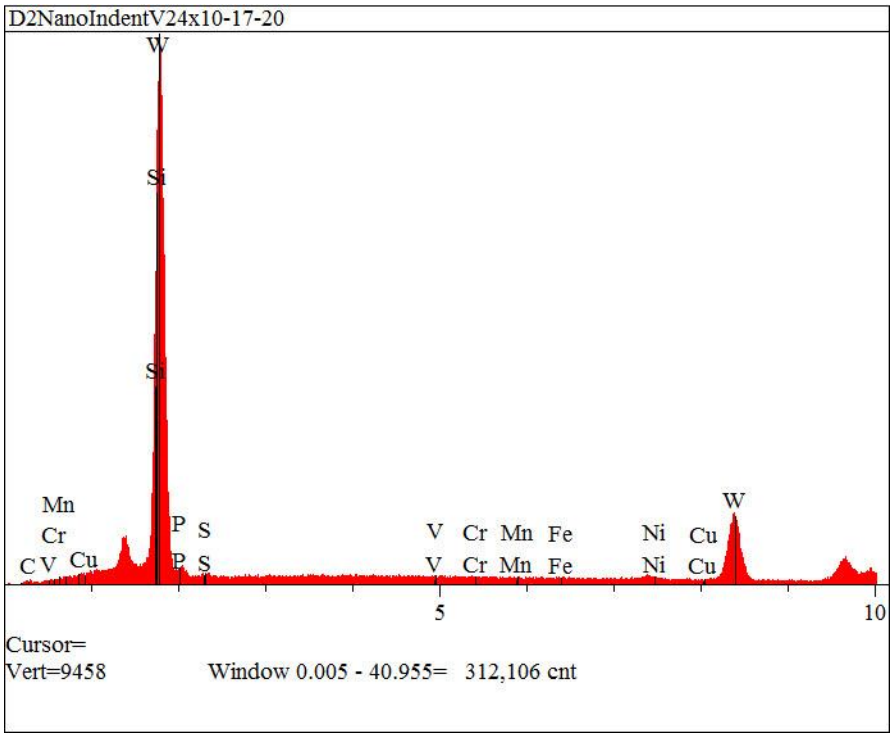
D2NanoIndentV24x10-17-20
W
Si
Si
Mn
Cr
C V Cu
P S
P S
V Cr Mn Fe
V Cr Mn Fe
Ni Cu
Ni Cu
W
5
10
Cursor=
Vert=9458
Window 0.005 - 40.955= 312,106 cnt

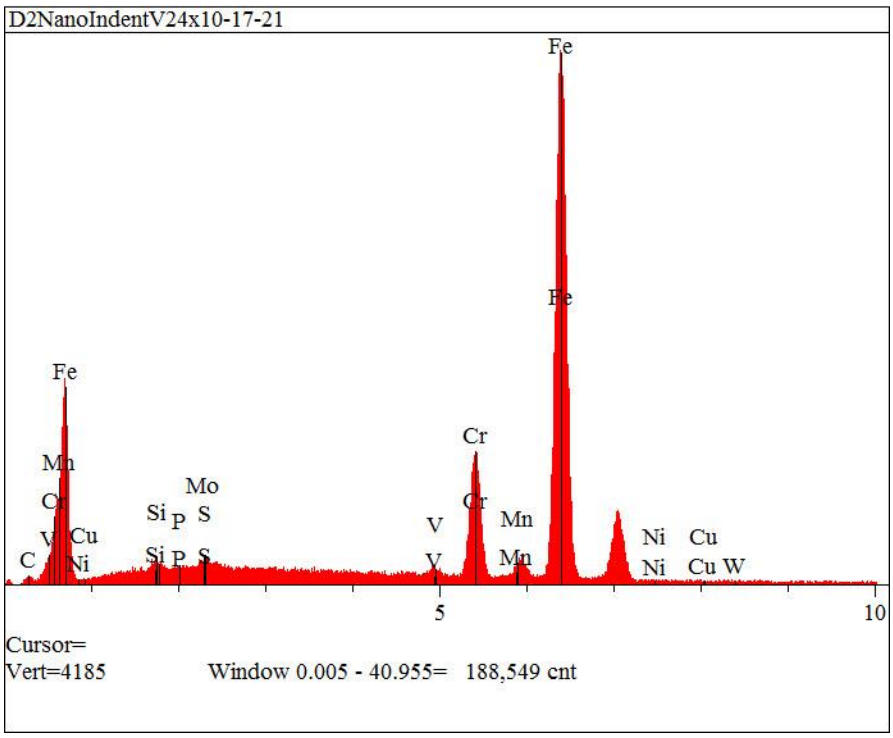
D2NanoIndentV24x10-17-21
Fe
Fe
Fe
Mn
Cr
Mo
Si P S
Cu
Ni
C
Si P S
V
V
Cr
Cr
Mn
Mn
Ni Cu
Ni Cu W
5
10
Cursor=
Vert=4185
Window 0.005 - 40.955= 188,549 cnt

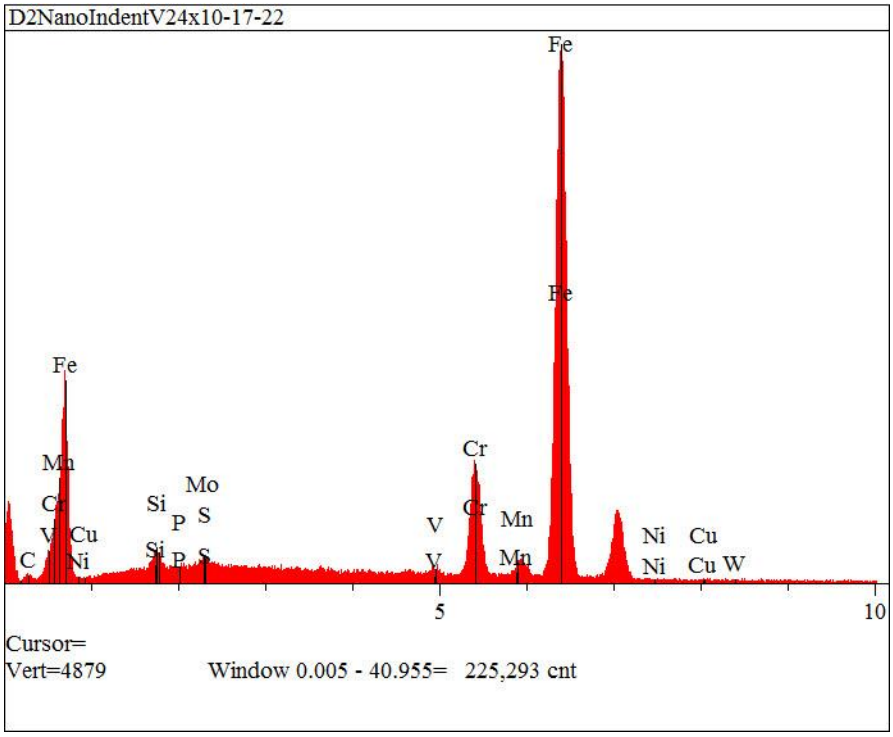
D2NanoIndentV24x10-17-22
Fe
Fe
Fe
Mn
Cr
Mo
Si P S
Cu
Ni
C
Si P S
V
V
Cr
Cr
Mn
Mn
Ni Cu
Ni Cu W
5
10
Cursor=
Vert=4879
Window 0.005 - 40.955= 225,293 cnt

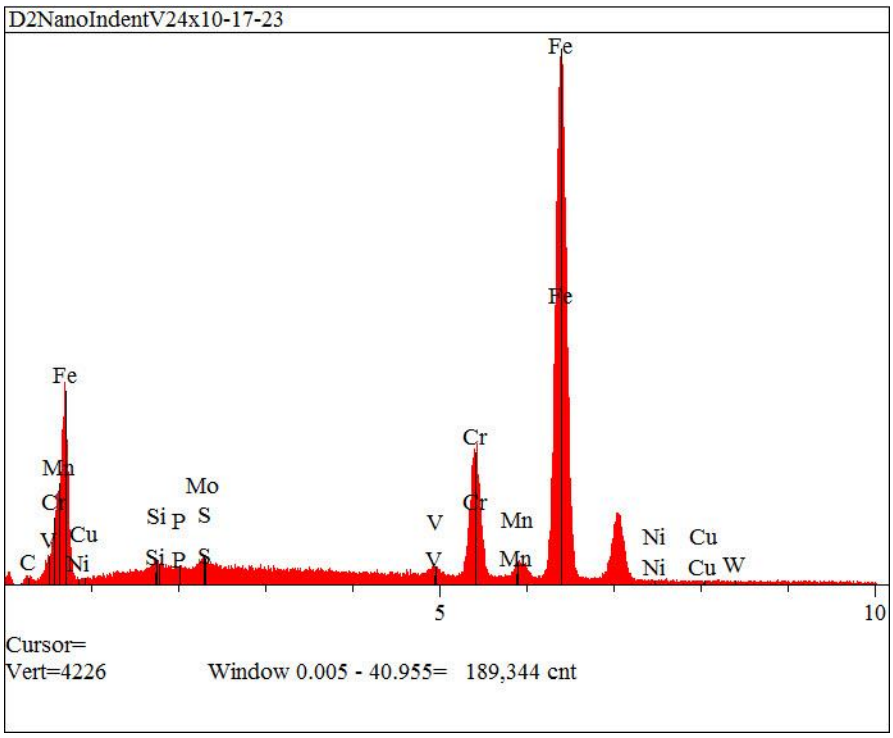
D2NanoIndentV24x10-17-23
Fe
Fe
Fe
Mn
Cr
Mo
Si P S
Cu
Ni
C
Si P S
V
V
Cr
Cr
Mn
Mn
Ni Cu
Ni Cu W
5
10
Cursor=
Vert=4226
Window 0.005 - 40.955= 189,344 cnt

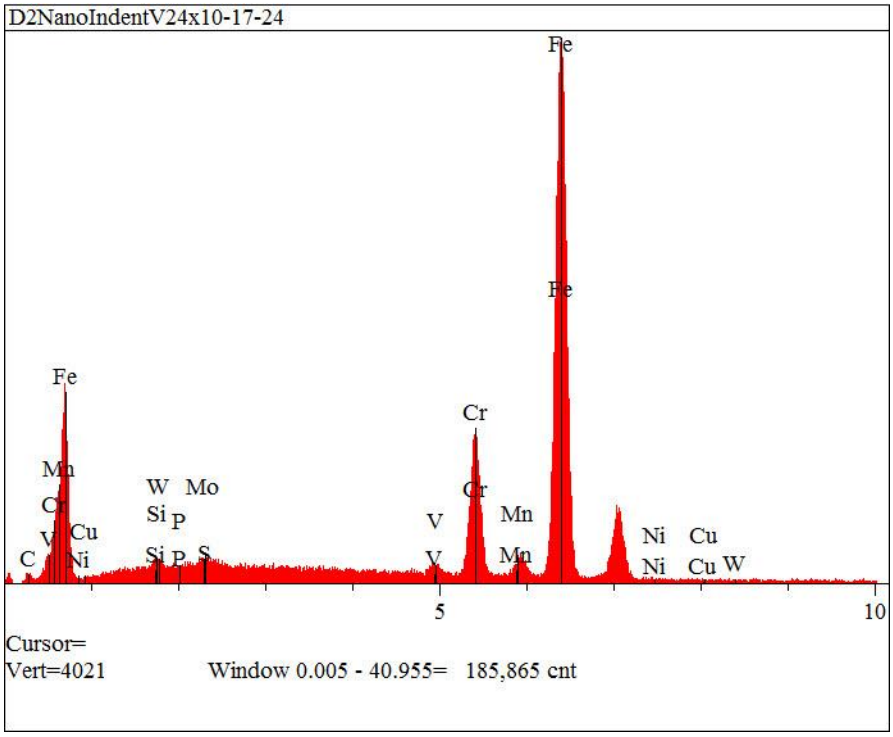
D2NanoIndentV24x10-17-24
Fe
Fe
Fe
Mn
Cr
W Mo
Si P
Cu
Ni
C
Si P S
V
V
Cr
Cr
Mn
Mn
Ni Cu
Ni Cu W
5
10
Cursor=
Vert=4021
Window 0.005 - 40.955= 185,865 cnt

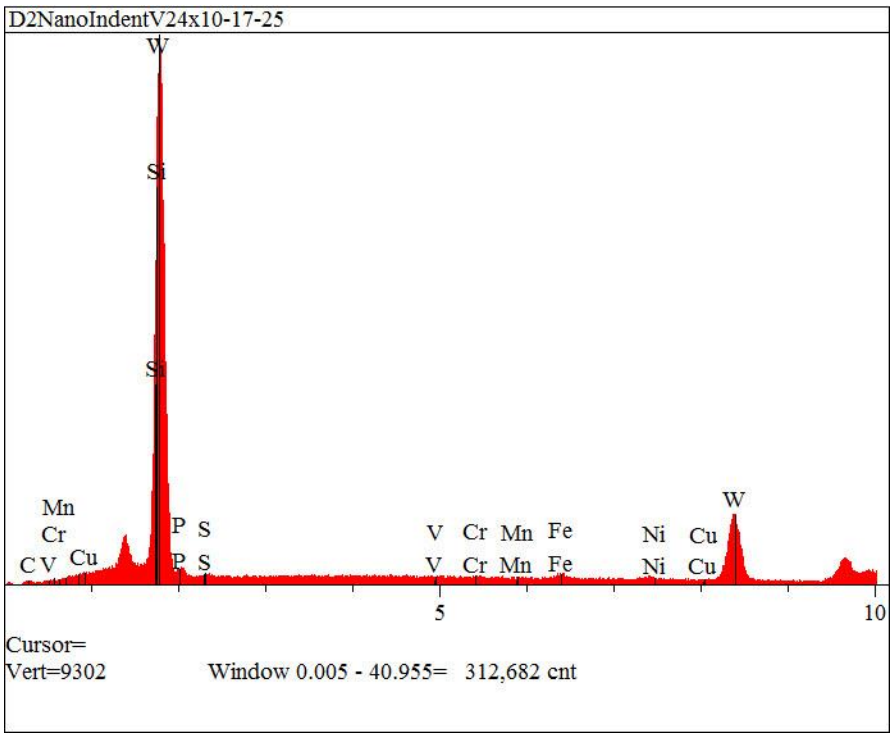
D2NanoIndentV24x10-17-25
W
Si
Si
Mn
Cr
C V Cu
P S
P S
V Cr Mn Fe
V Cr Mn Fe
Ni Cu
Ni Cu
W
5
10
Cursor=
Vert=9302
Window 0.005 - 40.955= 312,682 cnt

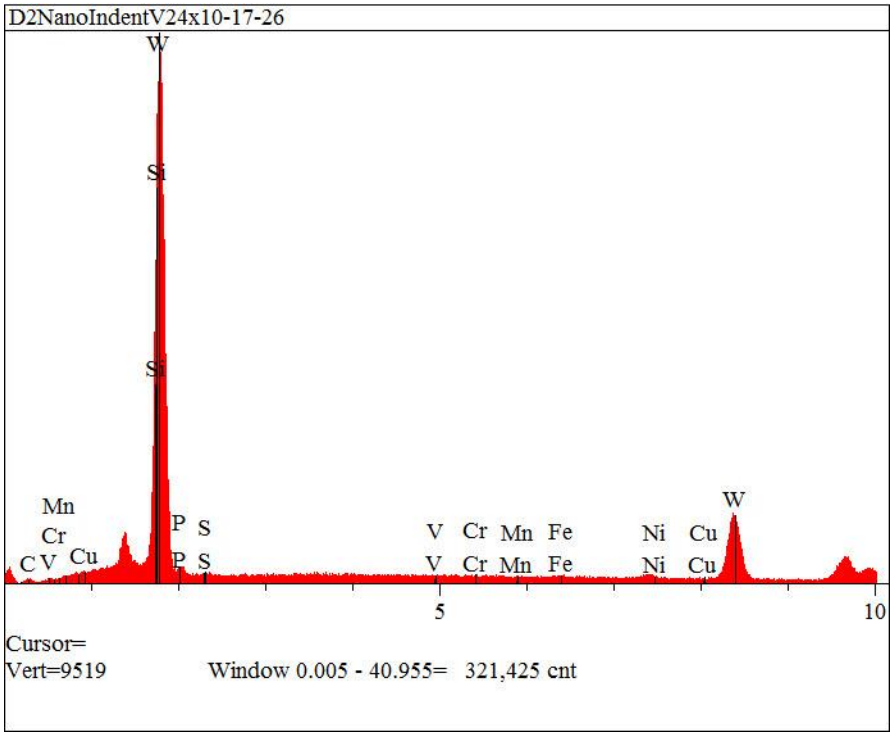
D2NanoIndentV24x10-17-26
W
Si
Si
Mn
Cr
C V Cu
P S
P S
V Cr Mn Fe
V Cr Mn Fe
Ni Cu
Ni Cu
W
5
10
Cursor=
Vert=9519
Window 0.005 - 40.955= 321,425 cnt

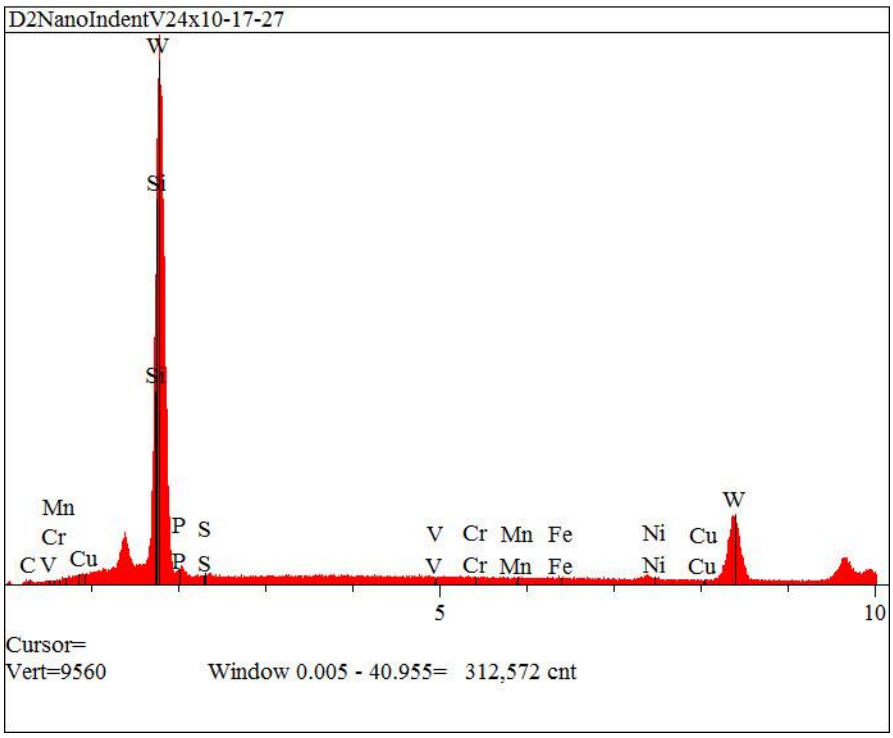
D2NanoIndentV24x10-17-27
W
Si
Si
Mn
Cr
C V Cu
P S
P S
V Cr Mn Fe
V Cr Mn Fe
Ni Cu
Ni Cu
W
5
10
Cursor=
Vert=9560
Window 0.005 - 40.955= 312,572 cnt

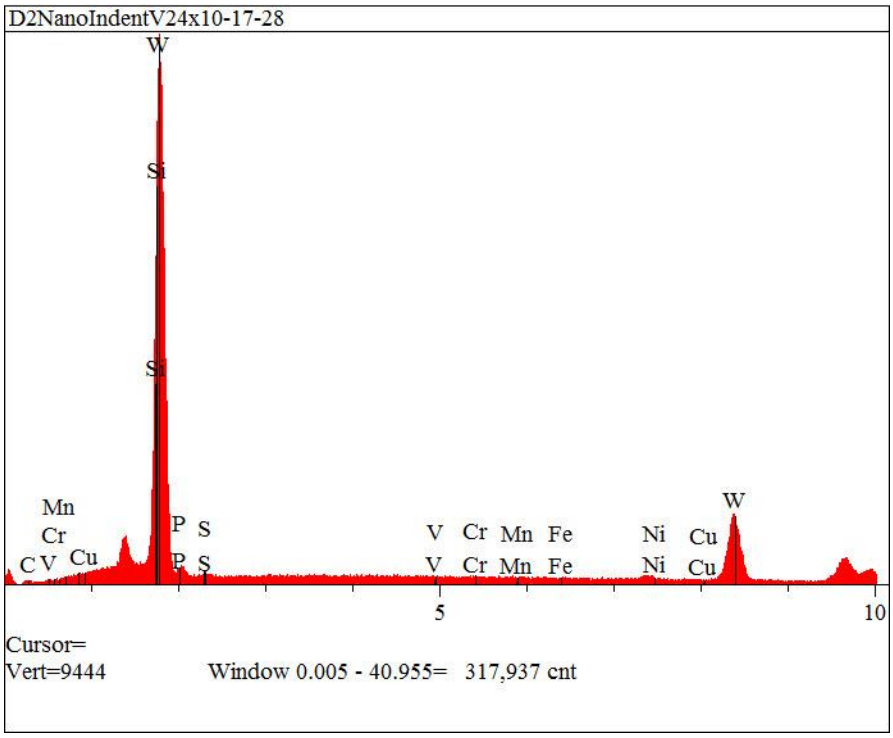
D2NanoIndentV24x10-17-28
W
Si
Si
Mn
Cr
C V Cu
P S
P S
V Cr Mn Fe
V Cr Mn Fe
Ni Cu
Ni Cu
W
5
10
Cursor=
Vert=9444
Window 0.005 - 40.955= 317,937 cnt

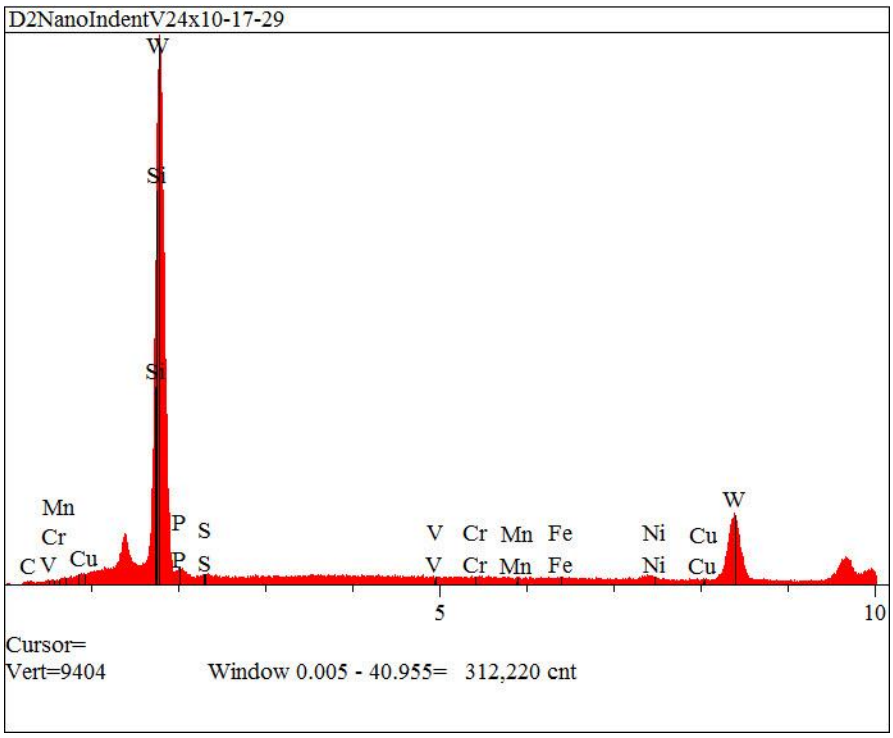
D2NanoIndentV24x10-17-29
W
Si
Si
Mn
Cr
C V Cu
P S
P S
V Cr Mn Fe
V Cr Mn Fe
Ni Cu
Ni Cu
W
5
10
Cursor=
Vert=9404
Window 0.005 - 40.955= 312,220 cnt

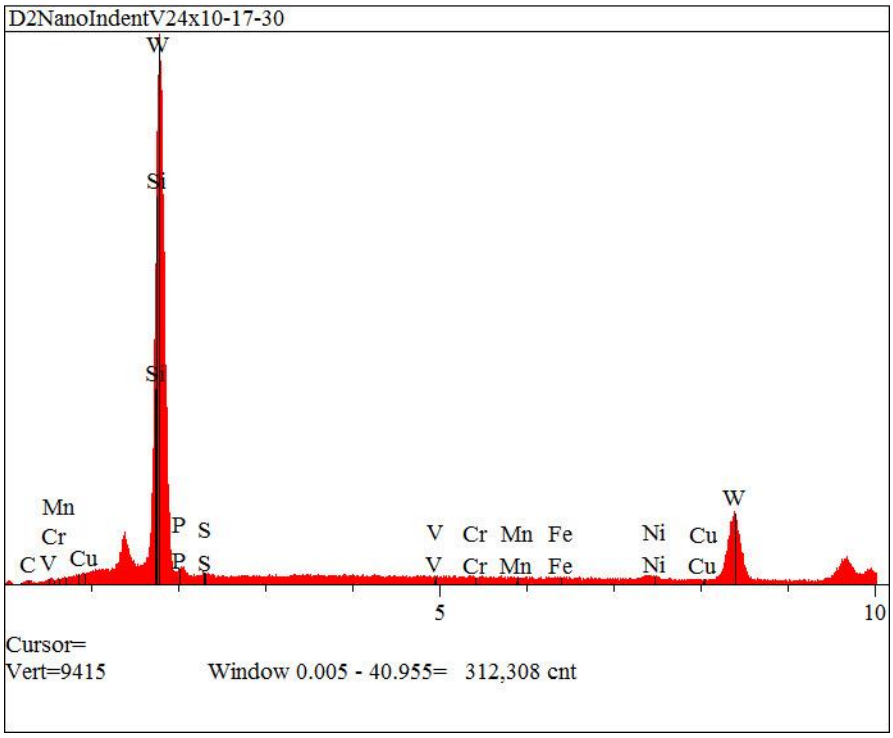
D2NanoIndentV24x10-17-30
W
Si
Si
Mn
Cr
C V Cu
P S
P S
V Cr Mn Fe
V Cr Mn Fe
Ni Cu
Ni Cu
W
5
10
Cursor=
Vert=9415
Window 0.005 - 40.955= 312,308 cnt

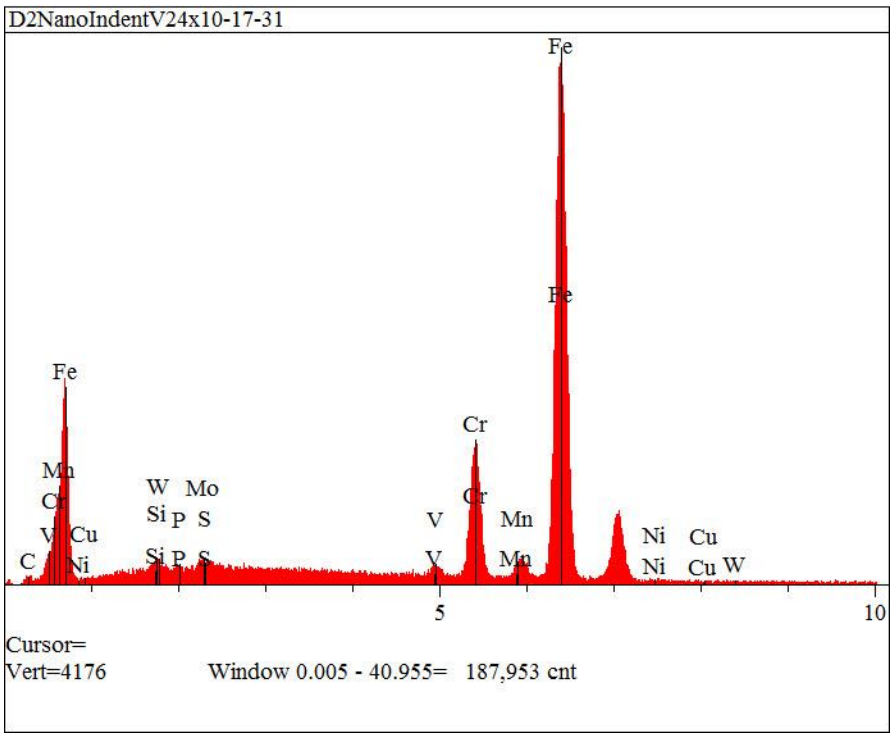
D2NanoIndentV24x10-17-31
Fe
Fe
Fe
Mn
Cr
V
Cu
Ni
C
W
Mo
Si
P
S
Cr
V
Mn
Ni
Cu
W
5
10
Cursor=
Vert=4176
Window 0.005 - 40.955= 187,953 cnt

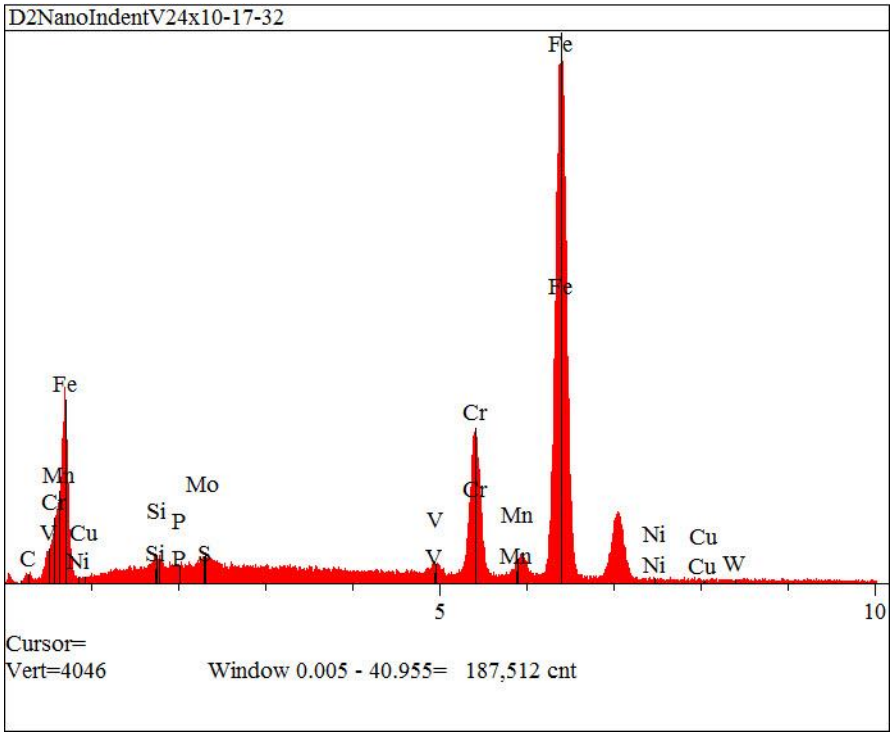
D2NanoIndentV24x10-17-32
Fe
Fe
Fe
Mn
Cr
V
Cu
Ni
C
Mo
Si
P
S
Cr
V
Mn
Ni
Cu
W
5
10
Cursor=
Vert=4046
Window 0.005 - 40.955= 187,512 cnt

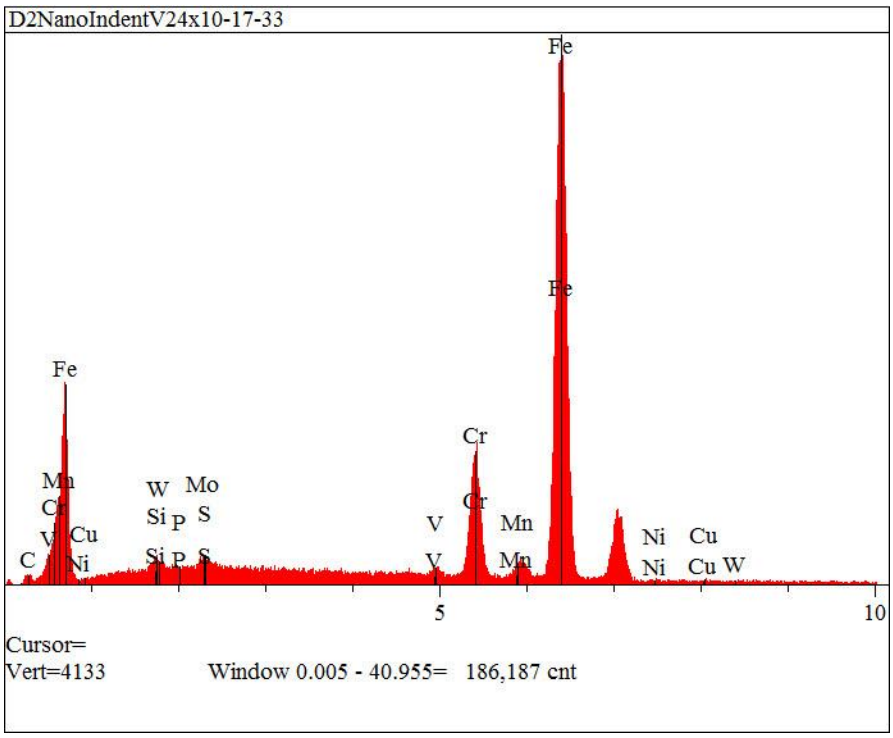
D2NanoIndentV24x10-17-33
Fe
Fe
Fe
Mn
Cr
Cu
Ni
C
W
Mo
Si
P
S
Cr
V
Mn
Ni
Cu
W
5
10
Cursor=
Vert=4133
Window 0.005 - 40.955= 186,187 cnt

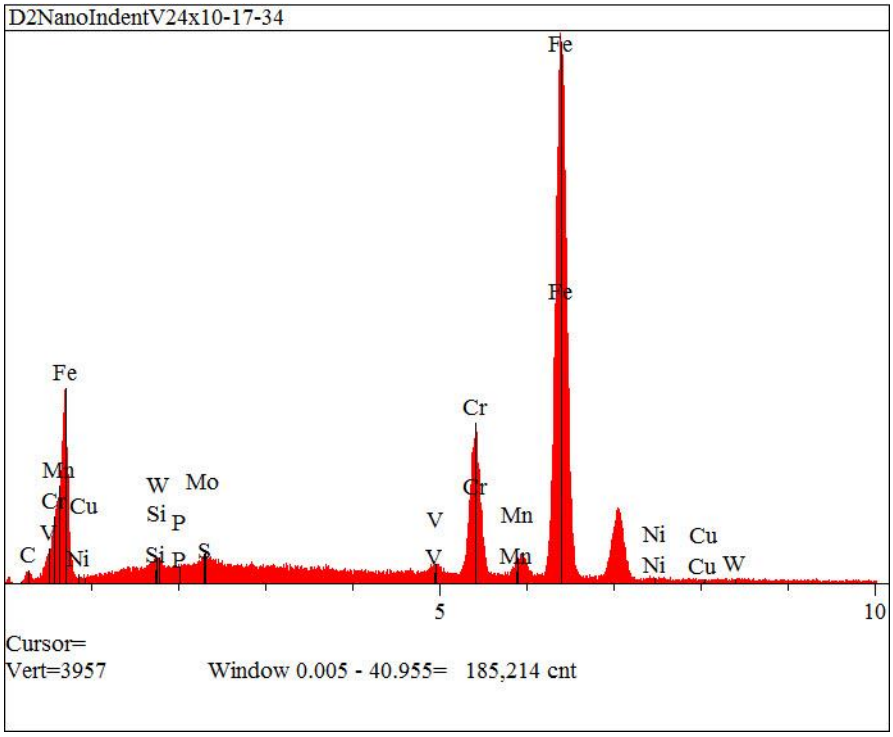
D2NanoIndentV24x10-17-34
Fe
Fe
Fe
Mn
Cr
Cu
Ni
C
W
Mo
Si
P
S
Cr
V
Mn
Ni
Cu
W
5
10
Cursor=
Vert=3957
Window 0.005 - 40.955= 185,214 cnt

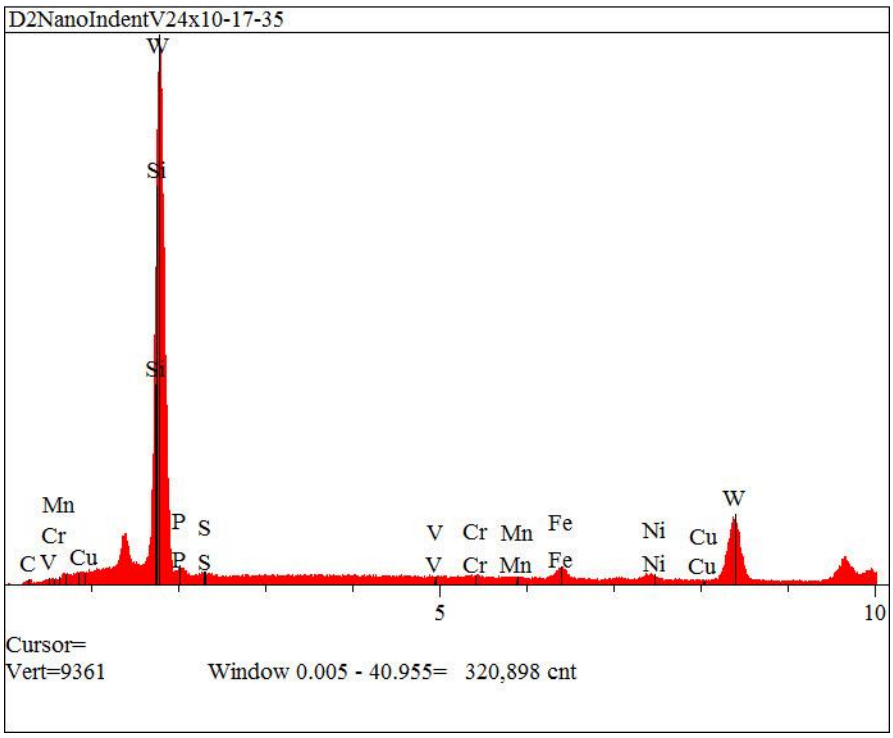
D2NanoIndentV24x10-17-35
W
Si
Si
Mn
Cr
C V Cu
P S
P S
V Cr Mn Fe
V Cr Mn Fe
Ni Cu
Ni Cu
W
5
10
Cursor=
Vert=9361
Window 0.005 - 40.955= 320,898 cnt

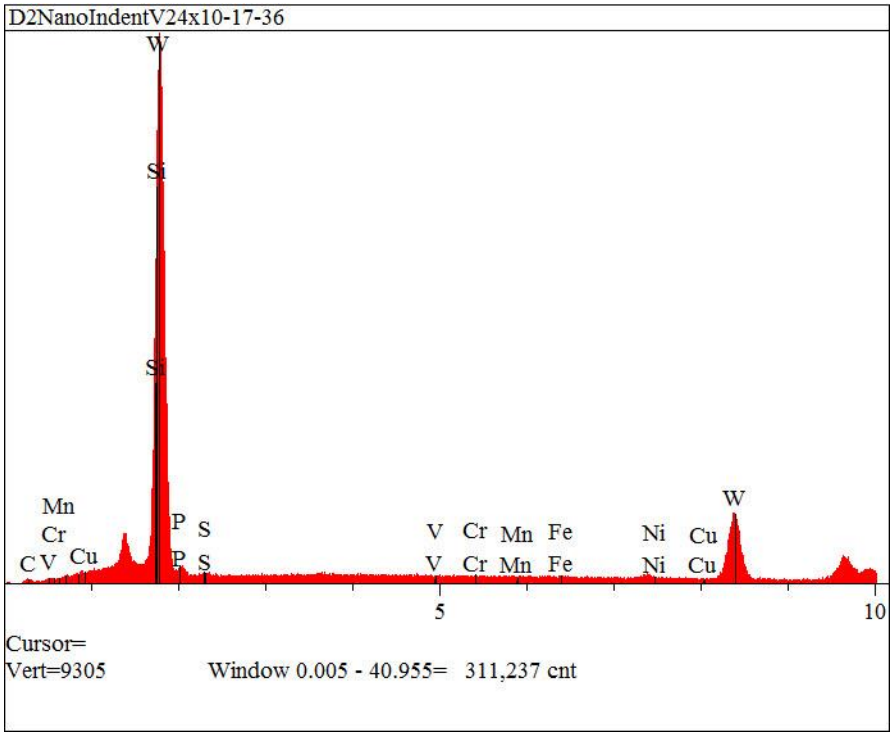
D2NanoIndentV24x10-17-36
W
Si
Si
Mn
Cr
C V Cu
P S
P S
V Cr Mn Fe
V Cr Mn Fe
Ni Cu
Ni Cu
W
5
10
Cursor=
Vert=9305
Window 0.005 - 40.955= 311,237 cnt

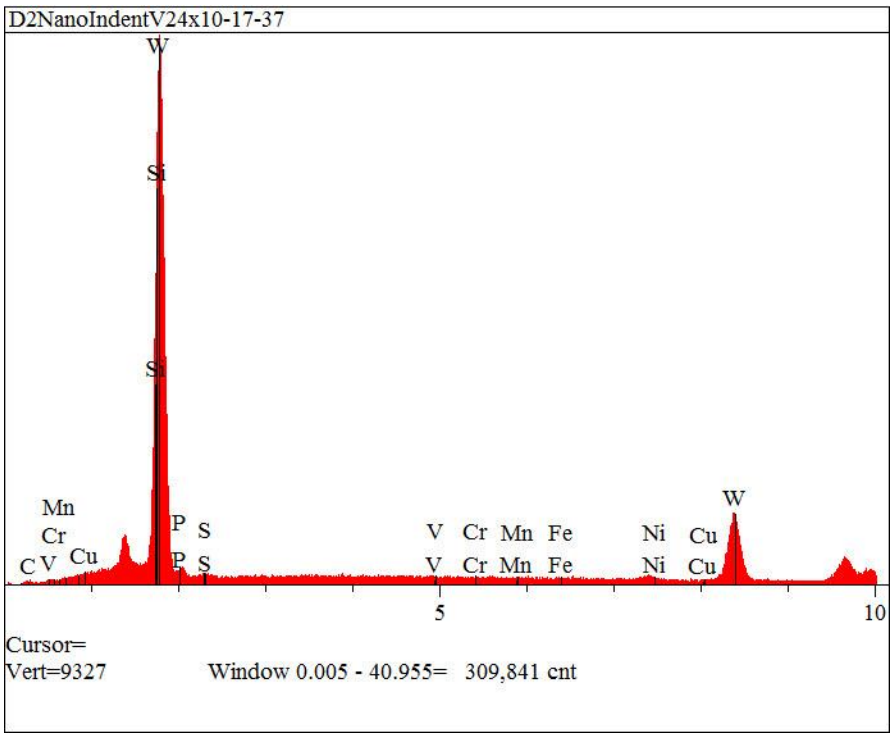
D2NanoIndentV24x10-17-37
W
Si
Si
Mn
Cr
C V Cu
P S
P S
V Cr Mn Fe
V Cr Mn Fe
Ni Cu
Ni Cu
W
5
10
Cursor=
Vert=9327
Window 0.005 - 40.955= 309,841 cnt

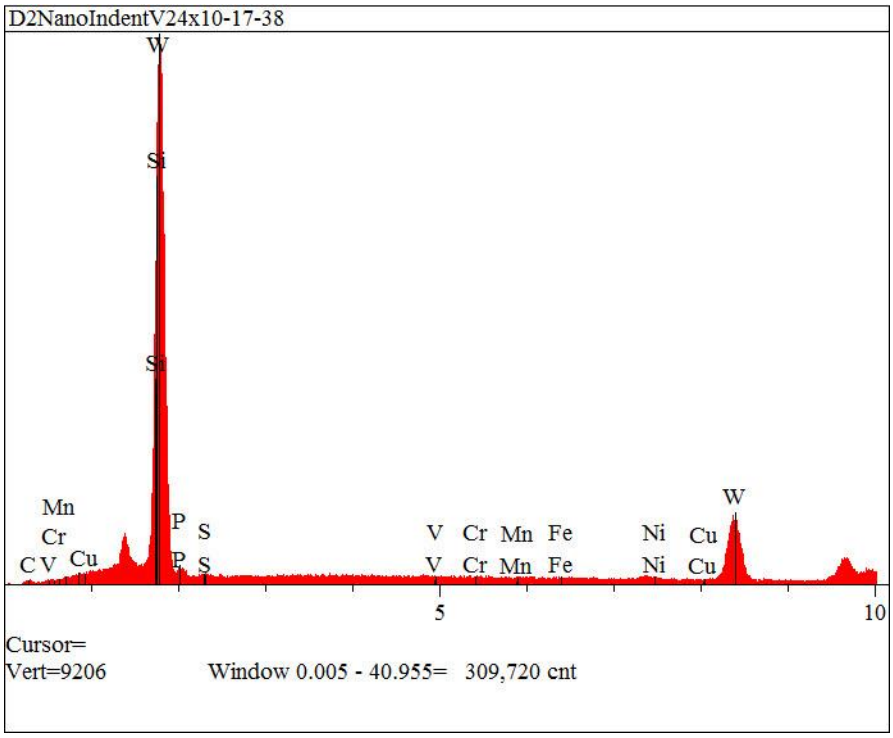
D2NanoIndentV24x10-17-38
W
Si
Si
Mn
Cr
C V Cu
P S
P S
V Cr Mn Fe
V Cr Mn Fe
Ni Cu
Ni Cu
W
5
10
Cursor=
Vert=9206
Window 0.005 - 40.955= 309,720 cnt

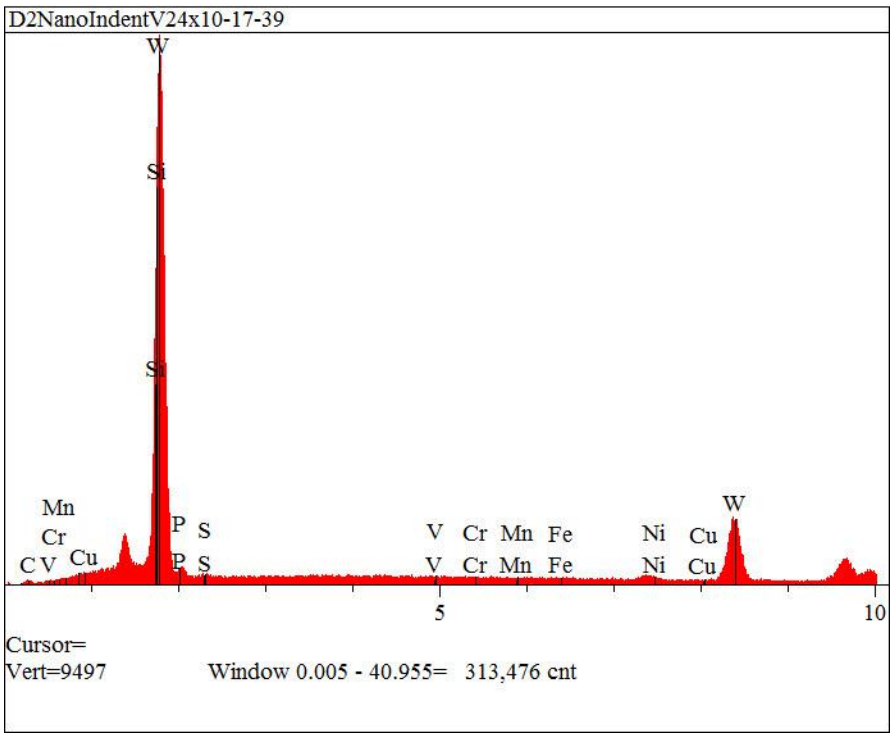
D2NanoIndentV24x10-17-39
W
Si
Si
Mn
Cr
C V Cu
P S
P S
V Cr Mn Fe
V Cr Mn Fe
Ni Cu
Ni Cu
W
5
10
Cursor=
Vert=9497
Window 0.005 - 40.955= 313,476 cnt

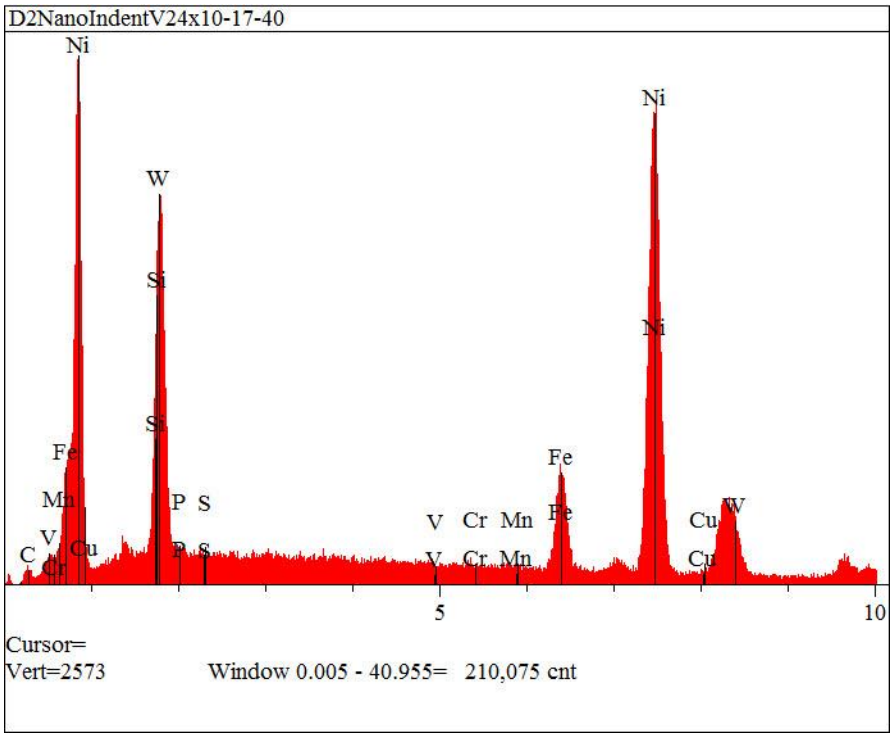
D2NanoIndentV24x10-17-40
Ni
W
Si
Si
Ni
Ni
Fe
Fe
Mn
V
C
Cu
P S
P S
V Cr Mn
V Cr Mn
Cu
Cu
W
5
10
Cursor=
Vert=2573
Window 0.005 - 40.955= 210,075 cnt

V2 10x4 1-40 EDS Taken Vertically

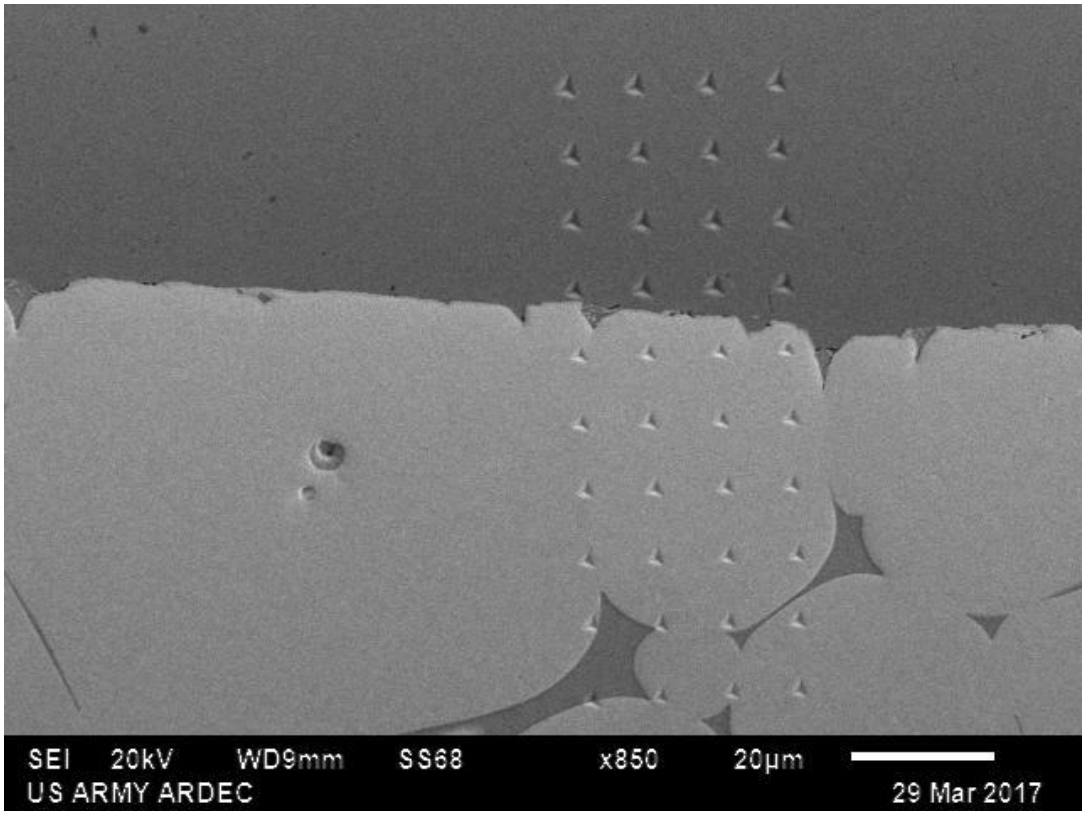

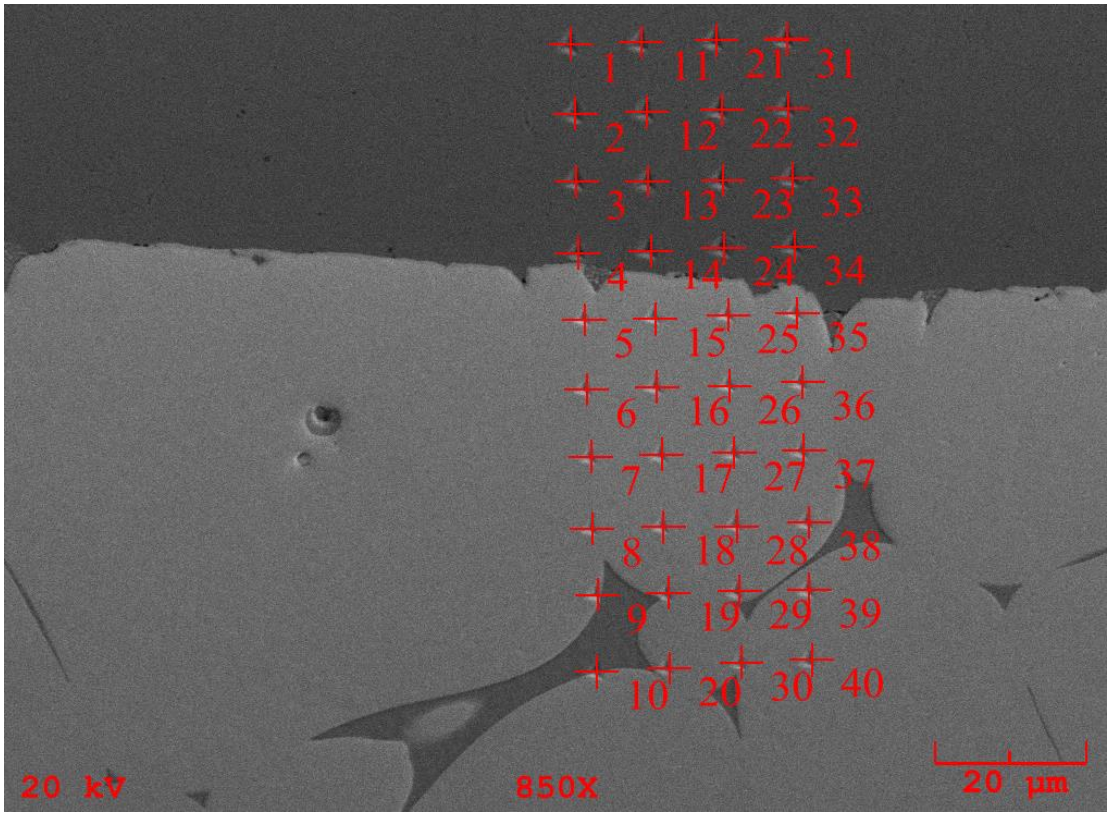
1 11 21 31
2 12 22 32
3 13 23 33
4 14 24 34
5 15 25 35
6 16 26 36
7 17 27 37
8 18 28 38
9 19 29 39
10 20 30 40
20 kV
850X
20 µm

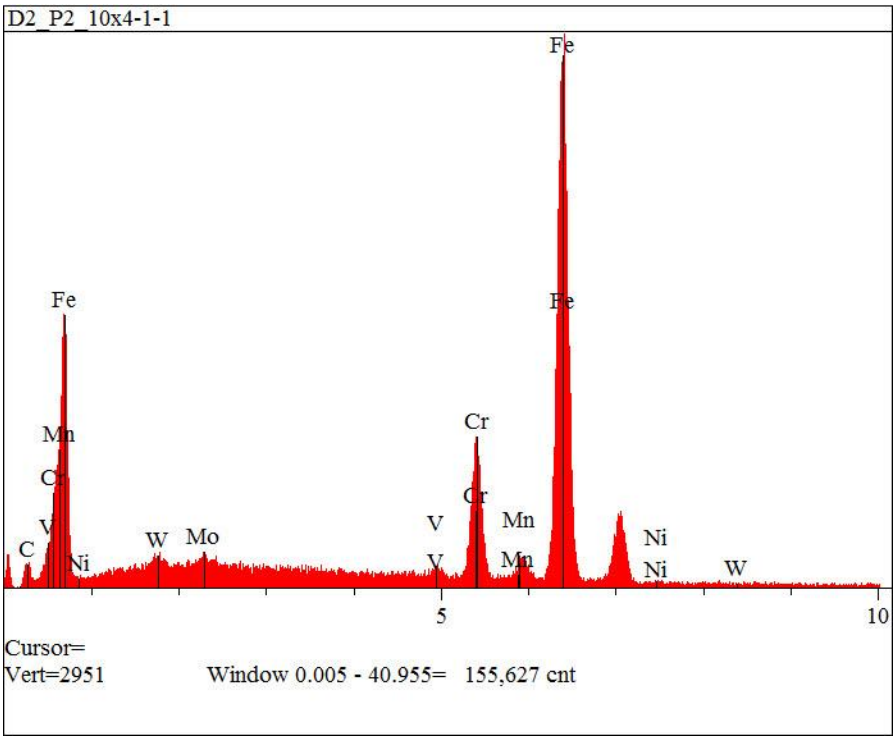
D2_P2_10x4-1-1
Fe
Fe
Mn
Cr
V
C
Ni
W
Mo
Cr
V
Mn
V
Mn
Ni
Ni
W
5
10
Cursor=
Vert=2951
Window 0.005 - 40.955= 155,627 cnt

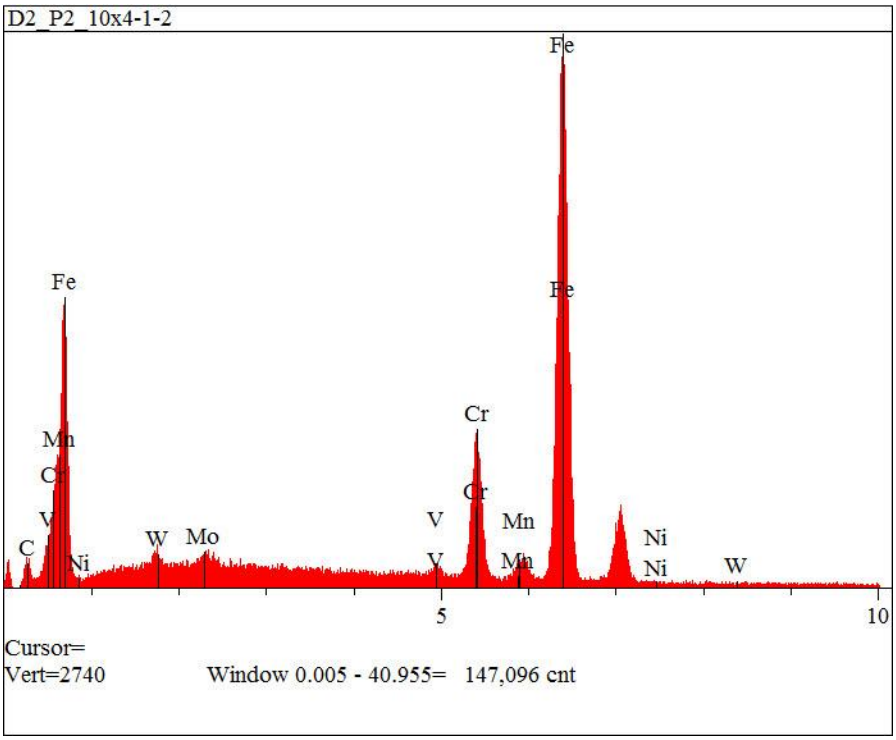
D2_P2_10x4-1-2
Fe
Fe
Mn
Cr
V
C
Ni
W
Mo
Cr
V
Mn
V
Mn
Ni
Ni
W
5
10
Cursor=
Vert=2740
Window 0.005 - 40.955= 147,096 cnt

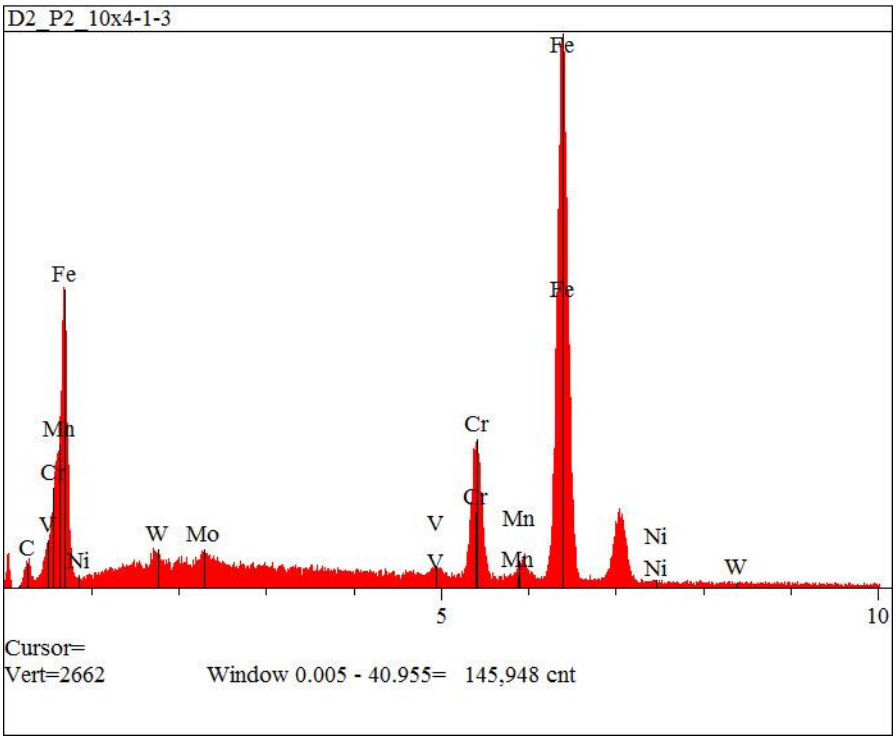
D2_P2_10x4-1-3
Fe
Fe
Mn
Cr
Cr
V
C
Ni
W
Mo
V
Mn
Ni
Ni
W
V
Mn
5
10
Cursor=
Vert=2662
Window 0.005 - 40.955= 145,948 cnt

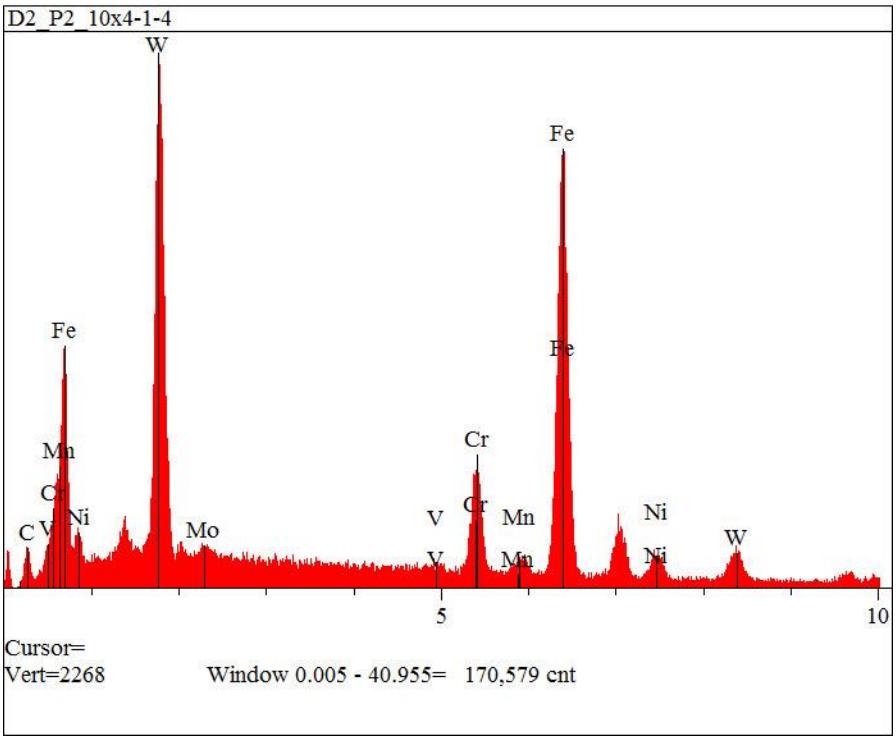
D2_P2_10x4-1-4
W
Fe
Fe
Fe
Mn
Cr
C
V
Ni
Mo
V
Cr
Mn
Ni
W
Ni
V
Mn
5
10
Cursor=
Vert=2268
Window 0.005 - 40.955= 170,579 cnt

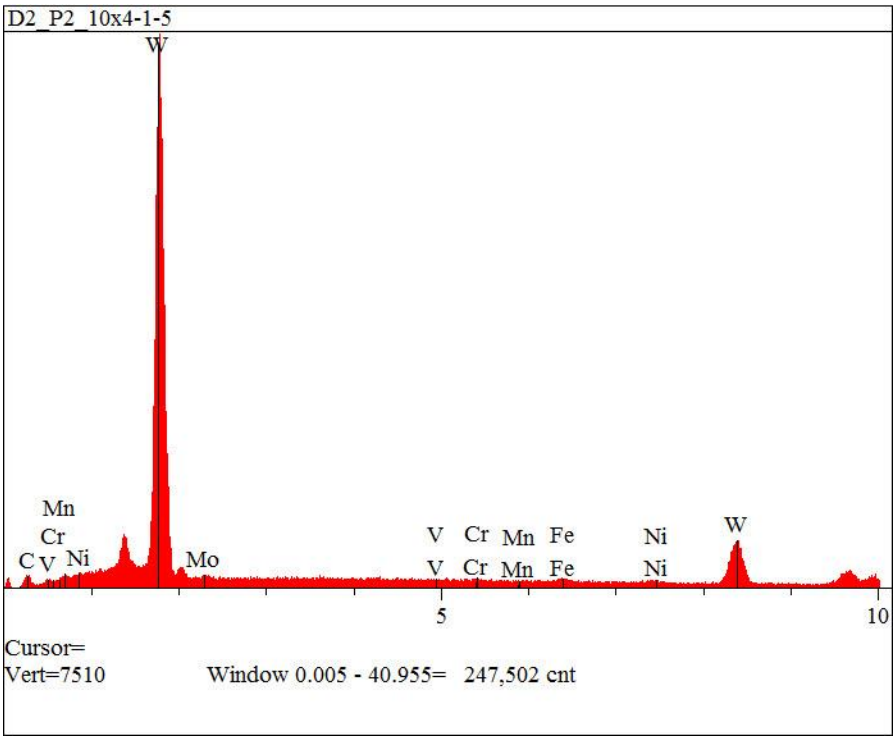
D2_P2_10x4-1-5
W
Mn
Cr
C V Ni
Mo
V Cr Mn Fe Ni
V Cr Mn Fe Ni
W
5
10
Cursor=
Vert=7510
Window 0.005 - 40.955= 247,502 cnt

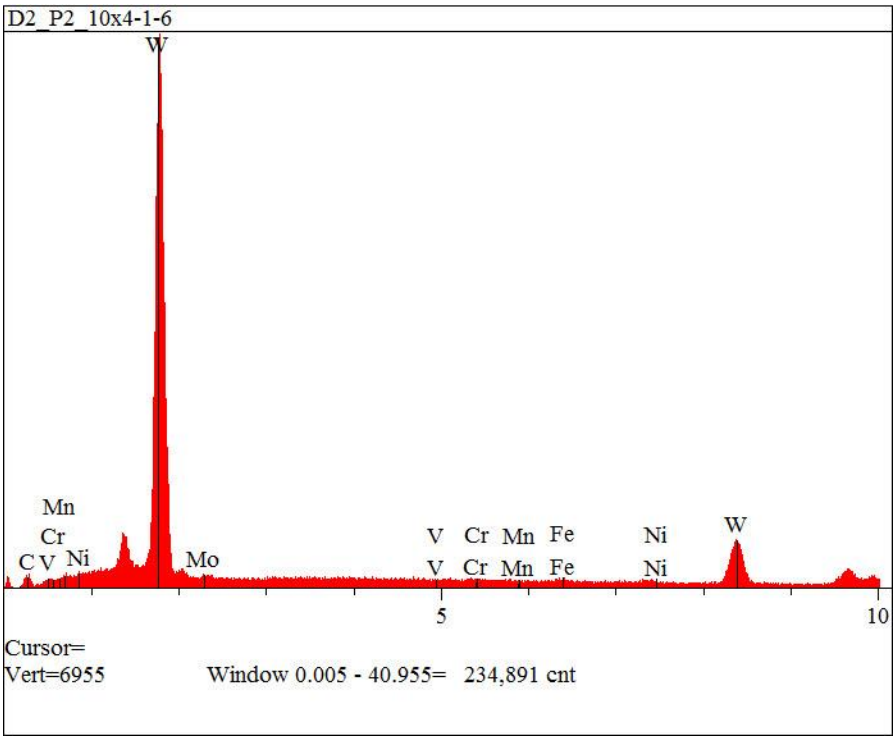
D2_P2_10x4-1-6
W
Mn
Cr
C V Ni
Mo
V Cr Mn Fe Ni
V Cr Mn Fe Ni
W
5
10
Cursor=
Vert=6955
Window 0.005 - 40.955= 234,891 cnt

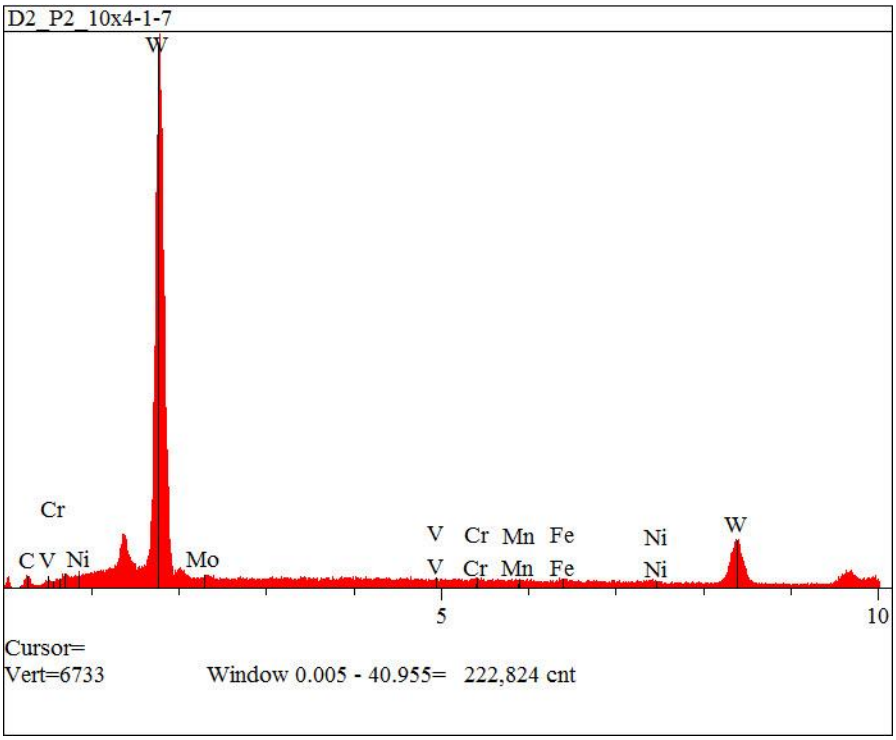
D2_P2_10x4-1-7
W
Cr
C V Ni
Mo
V Cr Mn Fe Ni W
V Cr Mn Fe Ni
5
10
Cursor=
Vert=6733
Window 0.005 - 40.955= 222,824 cnt

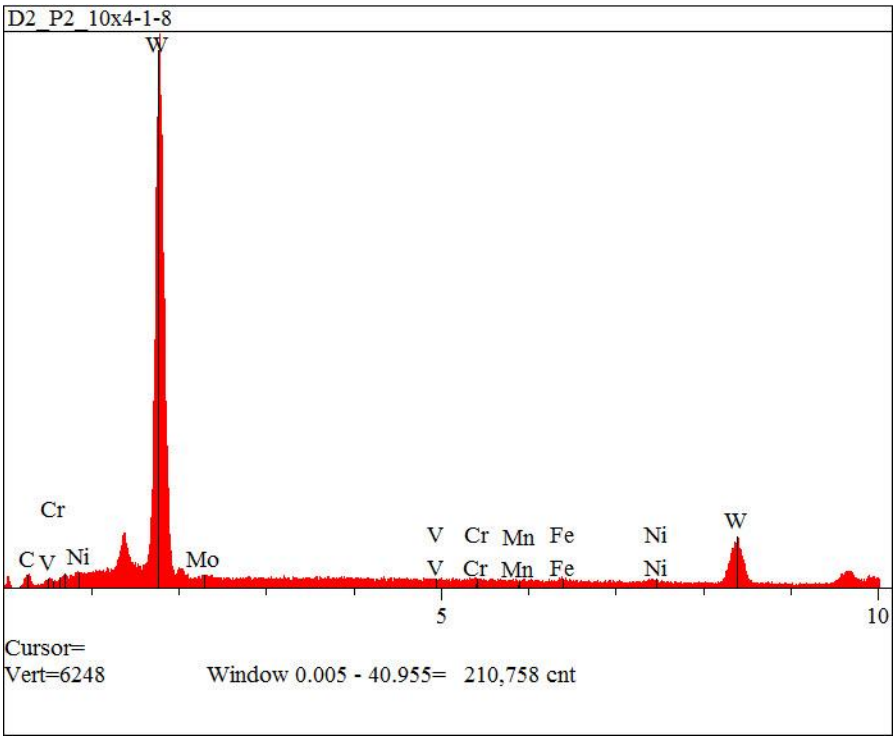
D2_P2_10x4-1-8
W
Cr
C V Ni
Mo
V Cr Mn Fe Ni W
V Cr Mn Fe Ni
5
10
Cursor=
Vert=6248
Window 0.005 - 40.955= 210,758 cnt

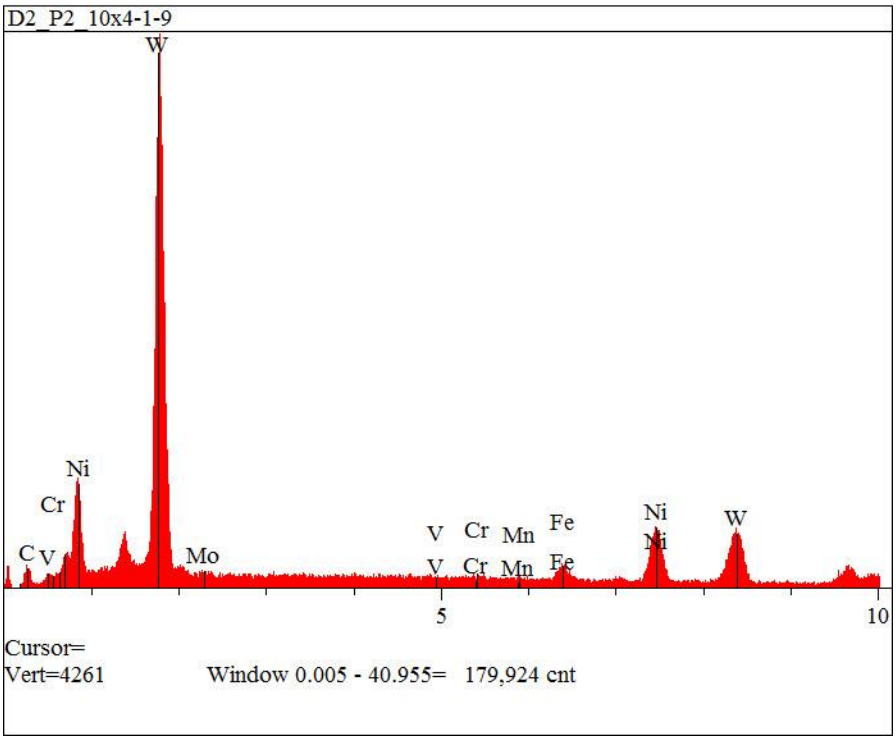
D2_P2_10x4-1-9
W
Ni
Cr
C V
Mo
V Cr Mn Fe
V Cr Mn Fe
Ni
Ni
W
5
10
Cursor=
Vert=4261
Window 0.005 - 40.955= 179,924 cnt

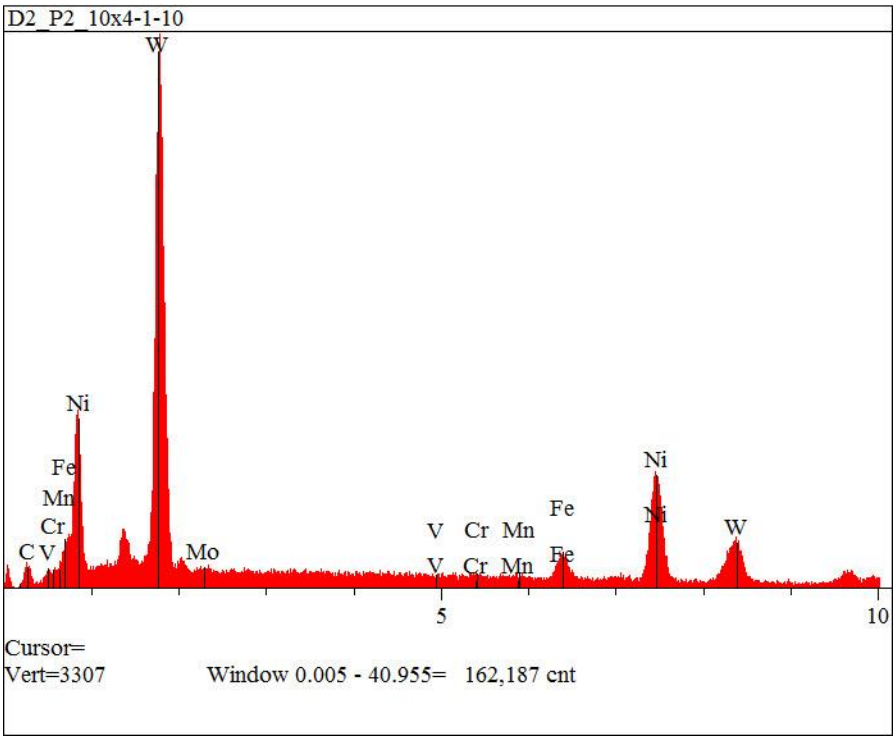
D2_P2_10x4-1-10
W
Ni
Fe
Mn
Cr
C V
Mo
V Cr Mn Fe
V Cr Mn Fe
Ni
Ni
W
5
10
Cursor=
Vert=3307
Window 0.005 - 40.955= 162,187 cnt

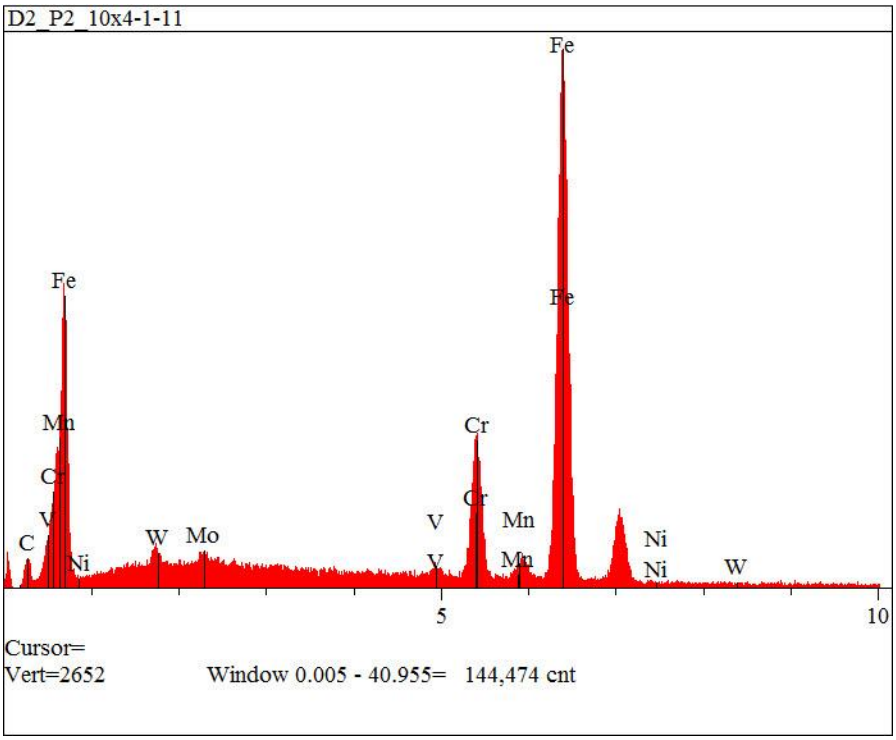
D2_P2_10x4-1-11
Fe
Fe
Mn
Cr
Cr
V
C
W
Mo
V
Mn
Ni
Ni
Ni
V
Mn
W
5
10
Cursor=
Vert=2652
Window 0.005 - 40.955= 144,474 cnt

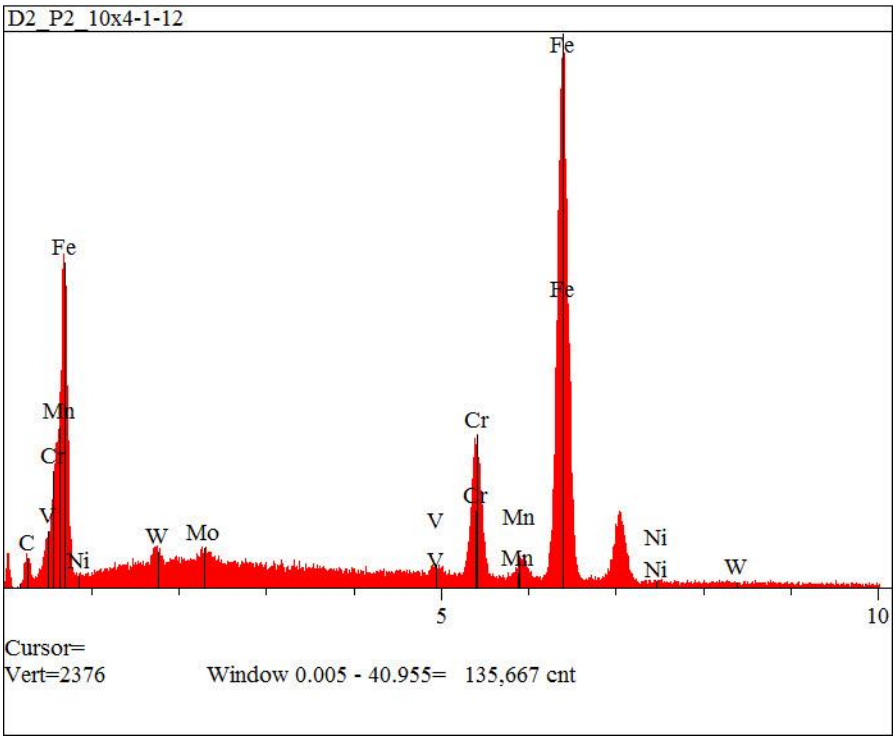
D2_P2_10x4-1-12
Fe
Fe
Mn
Cr
Cr
V
C
W
Mo
V
Mn
Ni
Ni
Ni
V
Mn
W
5
10
Cursor=
Vert=2376
Window 0.005 - 40.955= 135,667 cnt

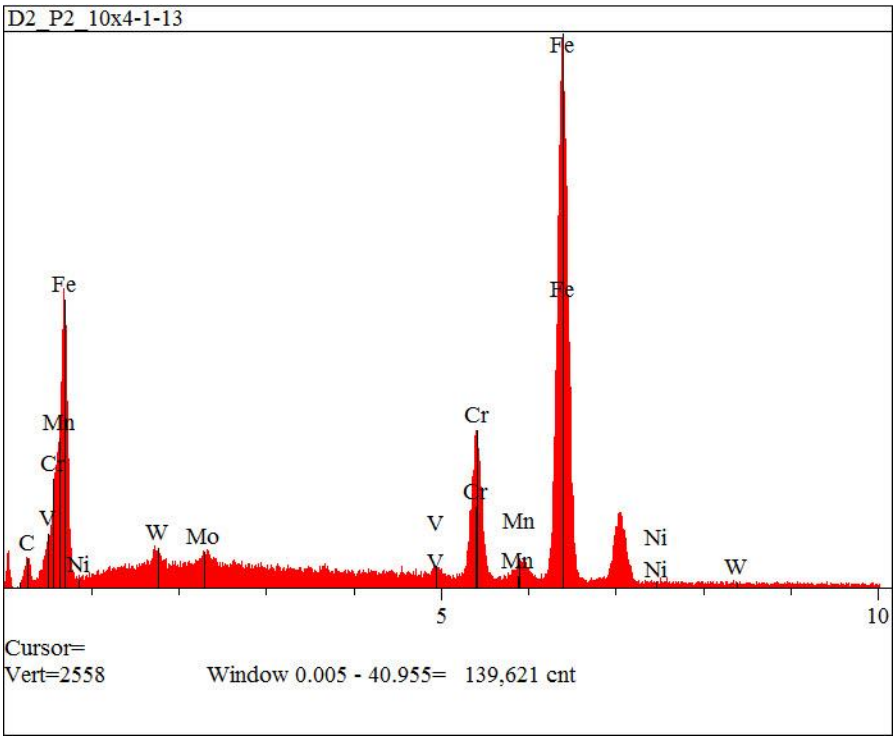
D2_P2_10x4-1-13
Fe
Fe
Mn
Cr
Cr
V
C
W
Mo
V
Mn
Ni
Ni
W
Ni
V
Mn
5
10
Cursor=
Vert=2558
Window 0.005 - 40.955= 139,621 cnt

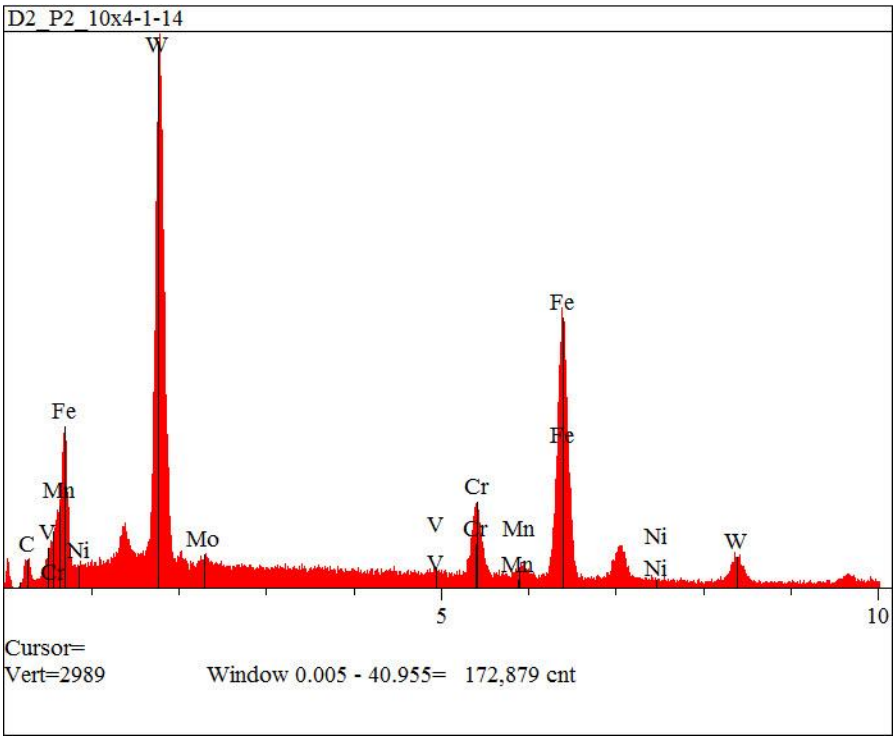
D2_P2_10x4-1-14
W
Fe
Fe
Mn
Cr
V
C
Ni
Mo
V
Cr
Mn
Ni
W
Ni
V
Mn
5
10
Cursor=
Vert=2989
Window 0.005 - 40.955= 172,879 cnt

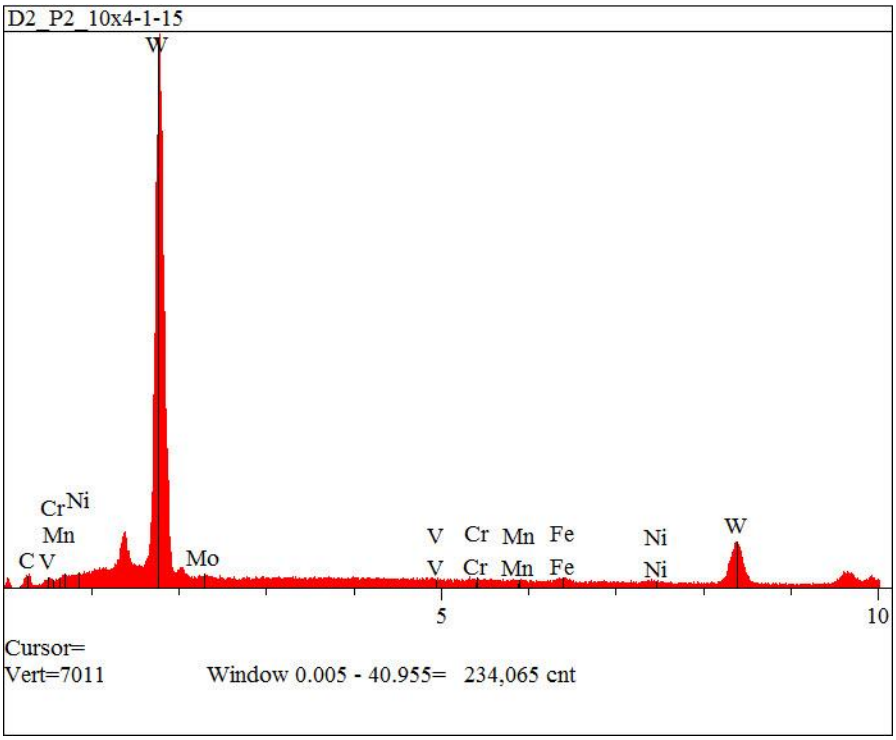
D2_P2_10x4-1-15
W
Cr
Ni
Mn
C V
Mo
V Cr Mn Fe Ni W
V Cr Mn Fe Ni
5
10
Cursor=
Vert=7011
Window 0.005 - 40.955= 234,065 cnt

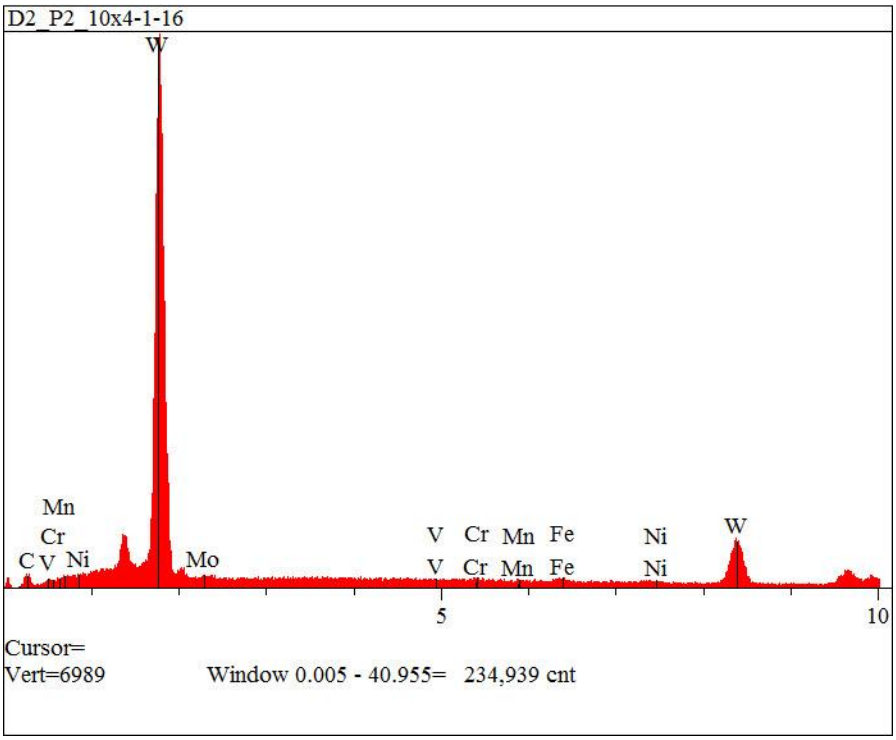
D2_P2_10x4-1-16
W
Mn
Cr
C V Ni
Mo
V Cr Mn Fe Ni W
V Cr Mn Fe Ni
5
10
Cursor=
Vert=6989
Window 0.005 - 40.955= 234,939 cnt

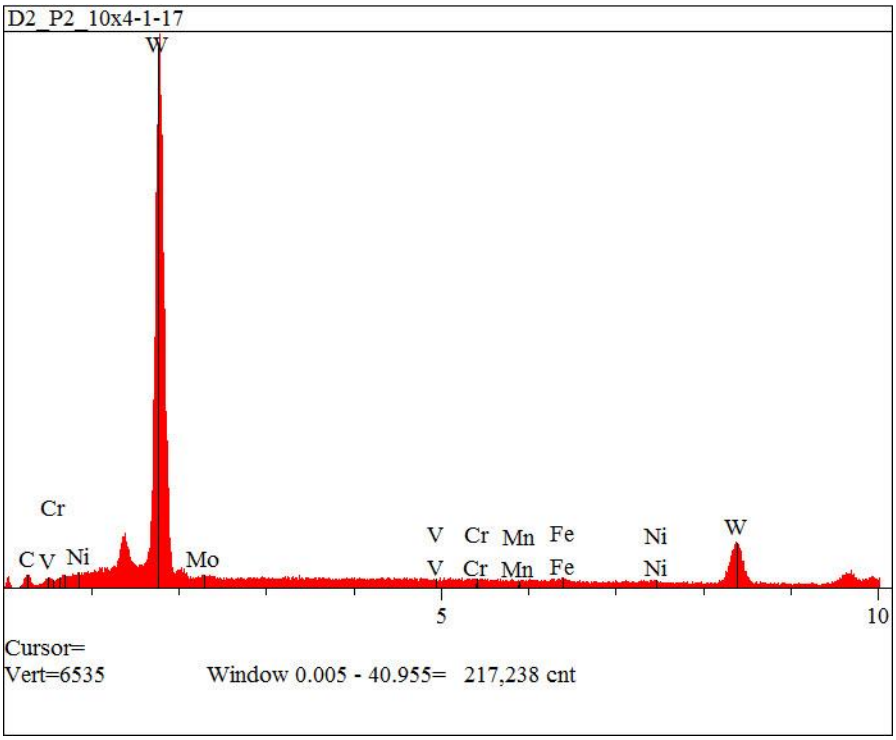
D2_P2_10x4-1-17
W
Cr
C V Ni
Mo
V Cr Mn Fe Ni W
V Cr Mn Fe Ni
5
10
Cursor=
Vert=6535
Window 0.005 - 40.955= 217,238 cnt

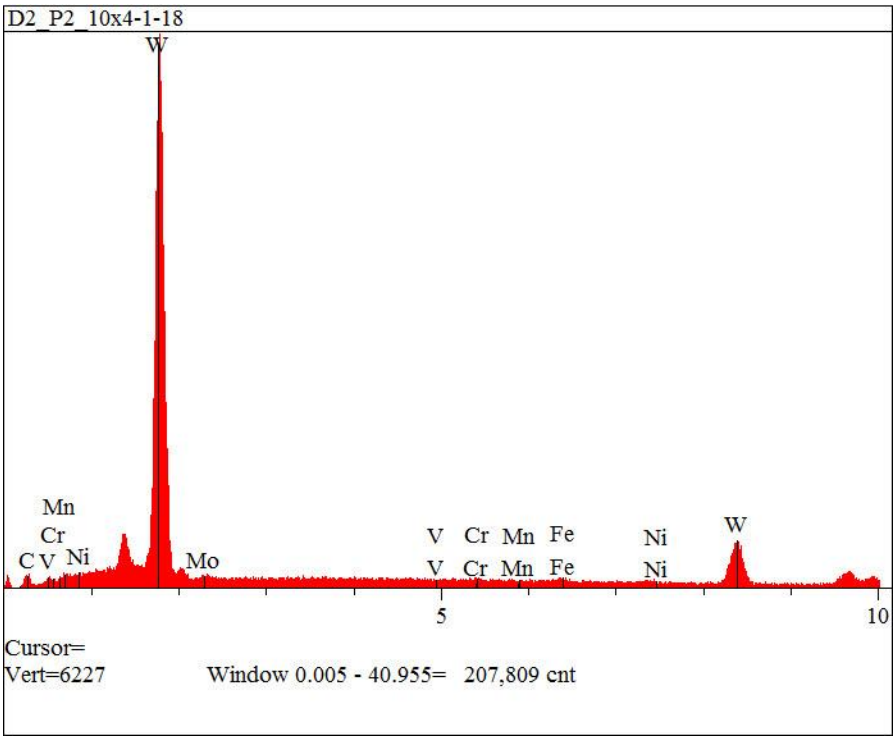
D2_P2_10x4-1-18
W
Mn
Cr
C V Ni
Mo
V Cr Mn Fe Ni W
V Cr Mn Fe Ni
5
10
Cursor=
Vert=6227
Window 0.005 - 40.955= 207,809 cnt

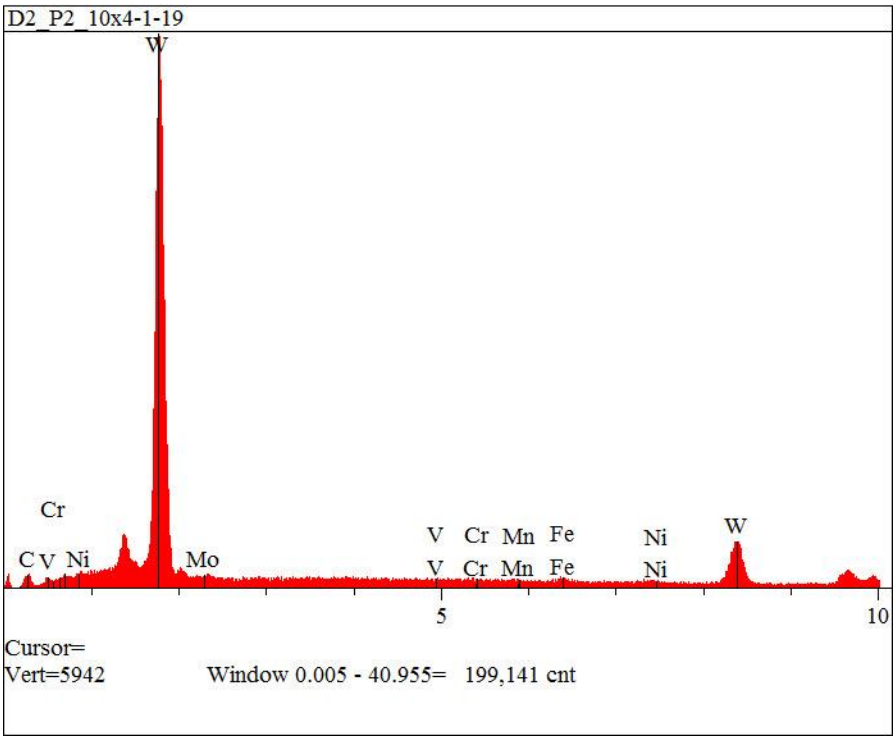
D2_P2_10x4-1-19
W
Cr
C V Ni
Mo
V Cr Mn Fe Ni W
V Cr Mn Fe Ni
5
10
Cursor=
Vert=5942
Window 0.005 - 40.955= 199,141 cnt

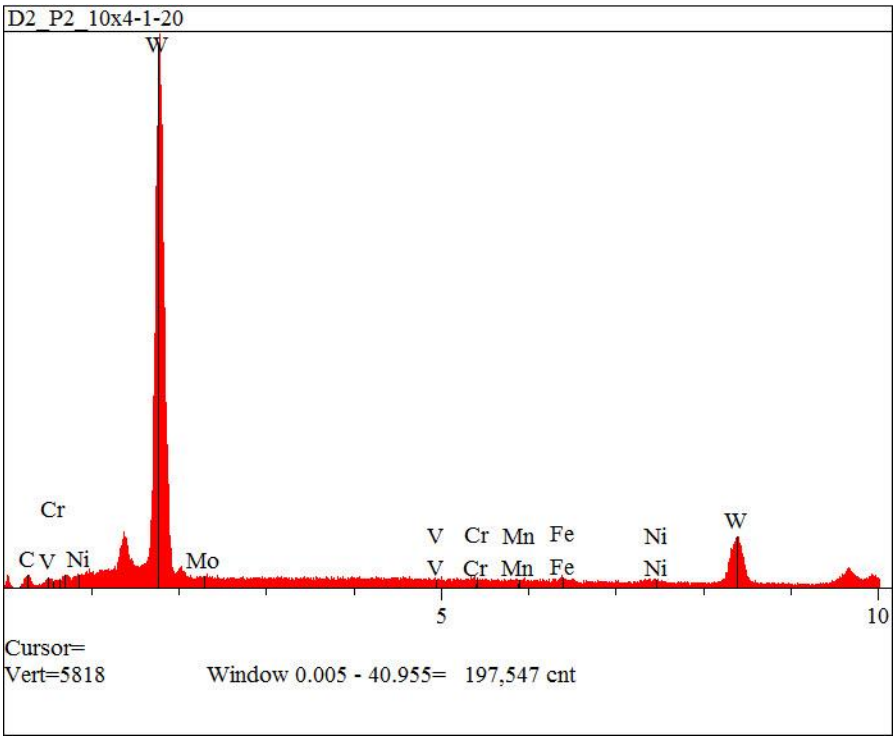
D2_P2_10x4-1-20
W
Cr
C V Ni
Mo
V Cr Mn Fe Ni W
V Cr Mn Fe Ni
5
10
Cursor=
Vert=5818
Window 0.005 - 40.955= 197,547 cnt

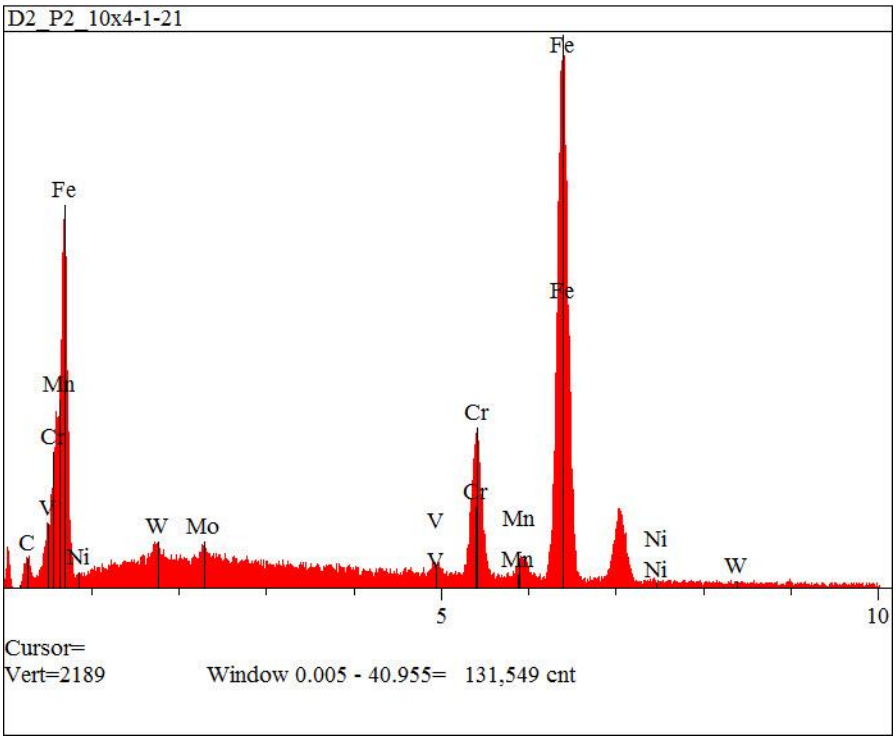
D2_P2_10x4-1-21
Fe
Fe
Mn
Cr
Cr
V
C
W
Mo
V
Mn
Ni
Ni
W
Ni
V
Mn
5
10
Cursor=
Vert=2189
Window 0.005 - 40.955= 131,549 cnt

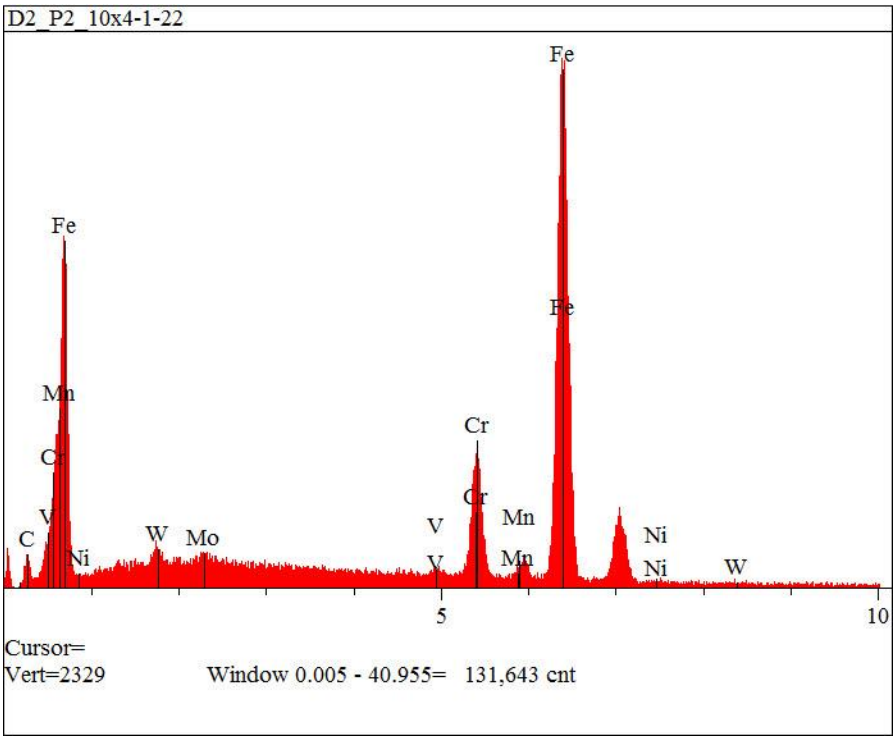
D2_P2_10x4-1-22
Fe
Fe
Mn
Cr
Cr
V
C
W
Mo
V
Mn
Ni
Ni
W
Ni
V
Mn
5
10
Cursor=
Vert=2329
Window 0.005 - 40.955= 131,643 cnt

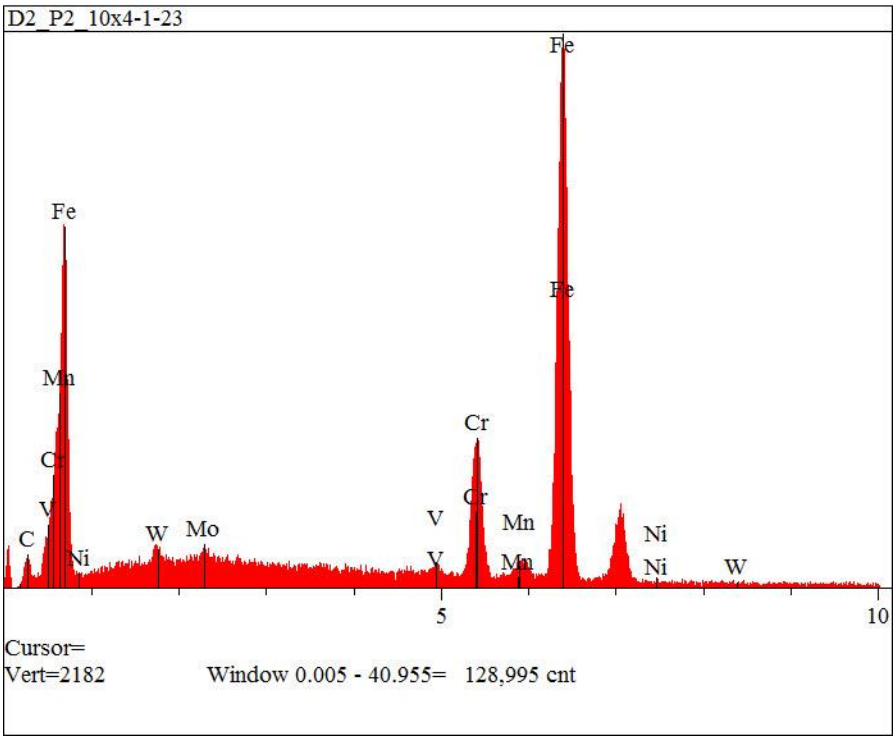
D2_P2_10x4-1-23
Fe
Fe
Mn
Cr
V
C
Ni
W
Mo
V
Cr
Mn
V
Mn
Fe
Ni
Ni
W
5
10
Cursor=
Vert=2182
Window 0.005 - 40.955= 128,995 cnt

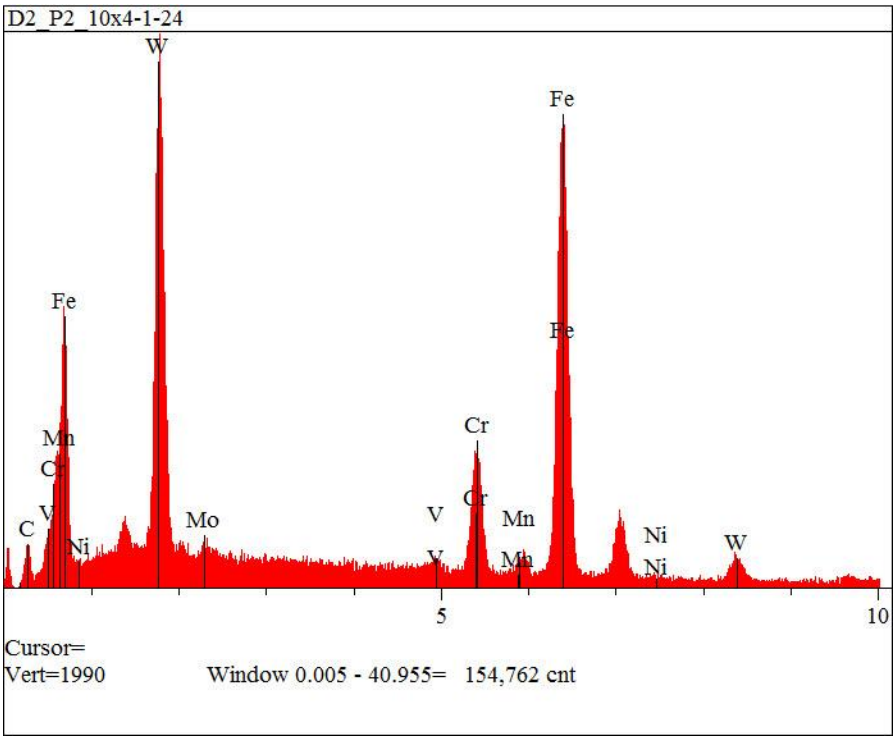
D2_P2_10x4-1-24
W
Fe
Fe
Mn
Cr
V
C
Ni
Mo
V
Cr
Mn
V
Mn
Fe
Ni
Ni
W
5
10
Cursor=
Vert=1990
Window 0.005 - 40.955= 154,762 cnt

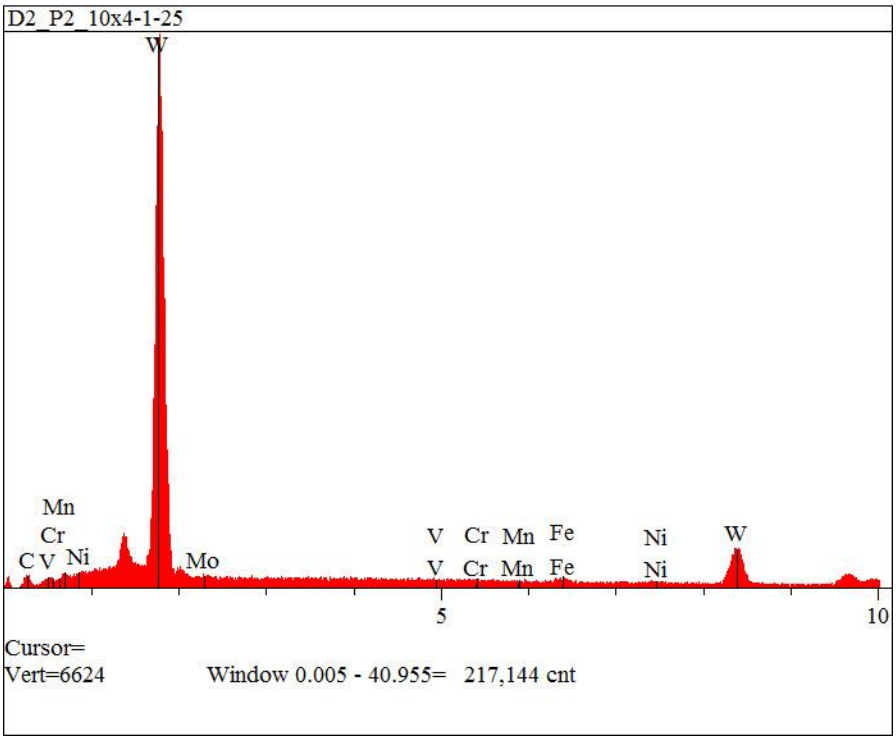
D2_P2_10x4-1-25
W
Mn
Cr
C V Ni
Mo
V Cr Mn Fe
V Cr Mn Fe
Ni
Ni
W
5
10
Cursor=
Vert=6624
Window 0.005 - 40.955= 217,144 cnt

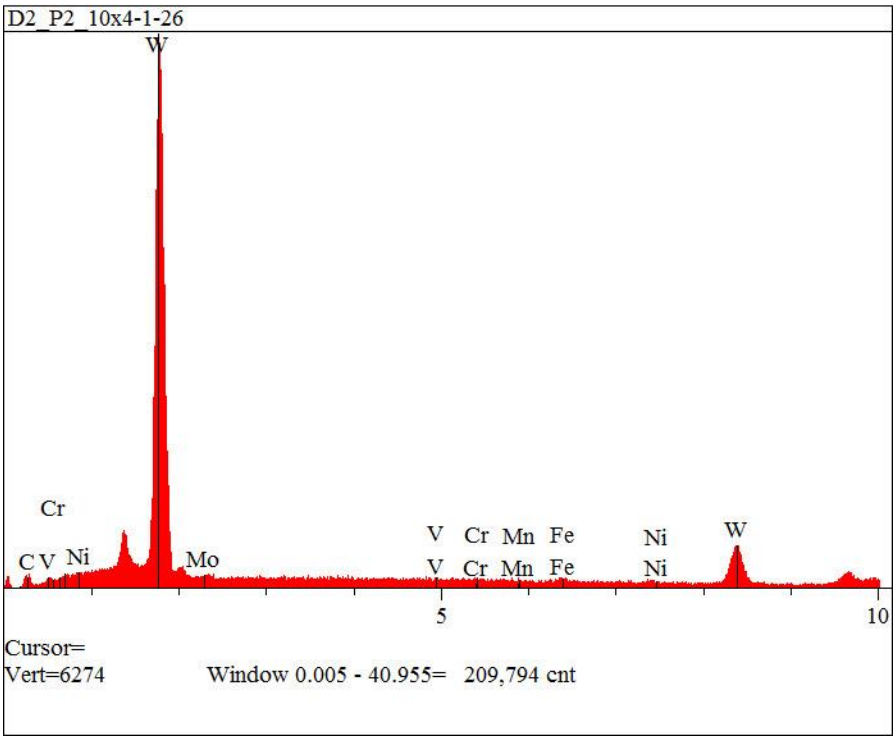
D2_P2_10x4-1-26
W
Cr
C V Ni
Mo
V Cr Mn Fe
V Cr Mn Fe
Ni
Ni
W
5
10
Cursor=
Vert=6274
Window 0.005 - 40.955= 209,794 cnt

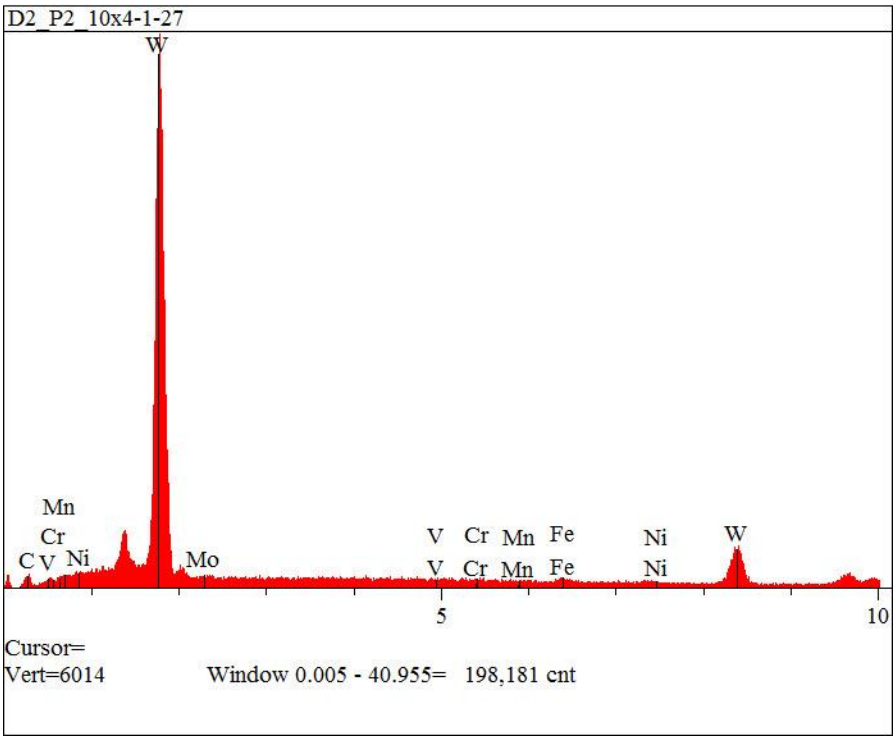
D2_P2_10x4-1-27
W
Mn
Cr
C V Ni
Mo
V Cr Mn Fe Ni W
V Cr Mn Fe Ni
5
10
Cursor=
Vert=6014
Window 0.005 - 40.955= 198,181 cnt

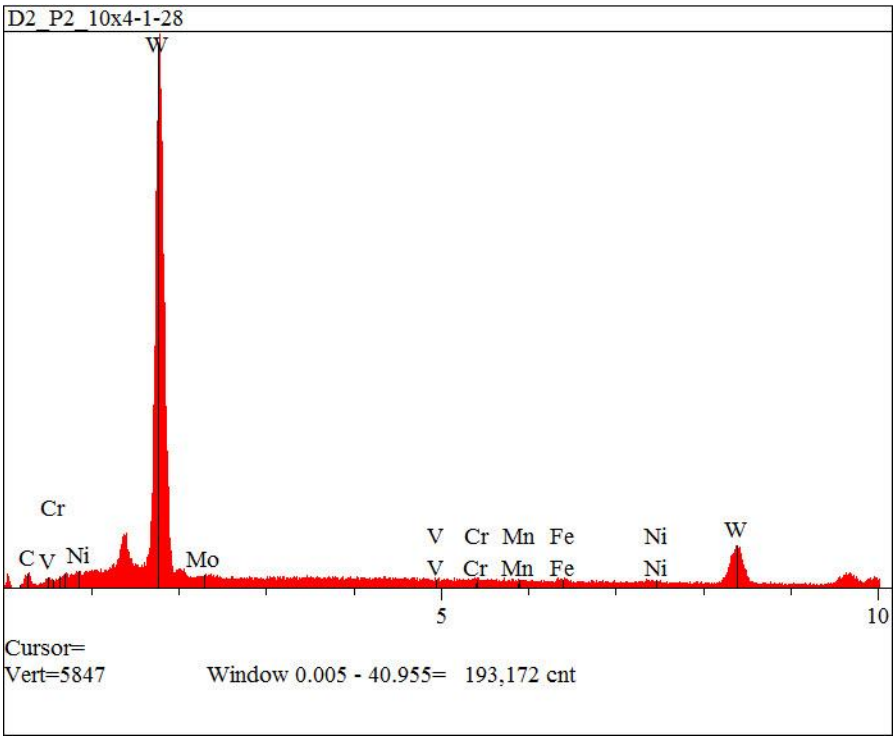
D2_P2_10x4-1-28
W
Cr
C V Ni
Mo
V Cr Mn Fe Ni W
V Cr Mn Fe Ni
5
10
Cursor=
Vert=5847
Window 0.005 - 40.955= 193,172 cnt

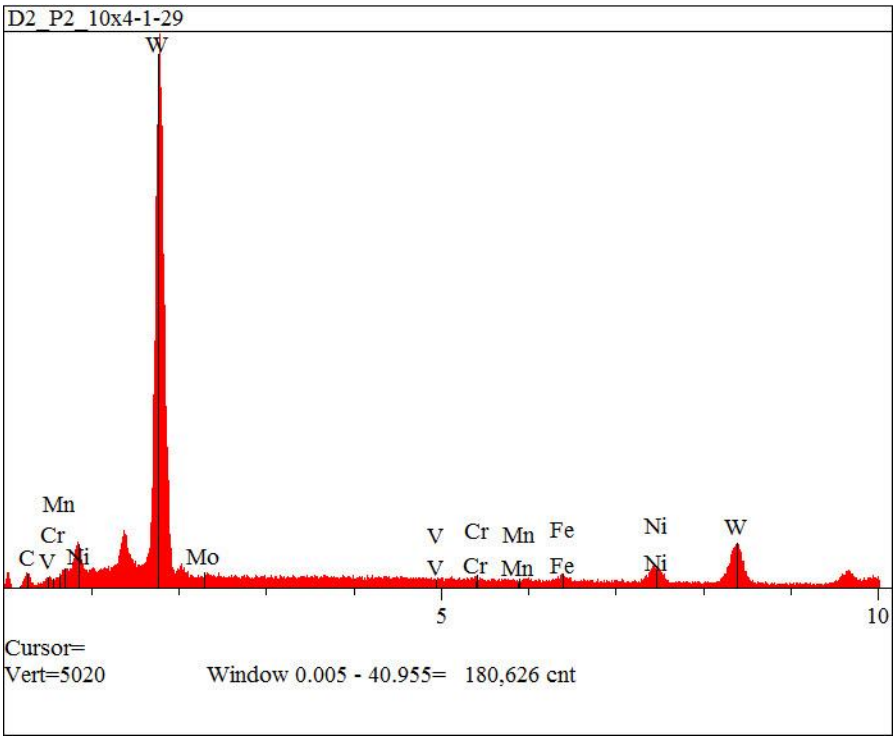
D2_P2_10x4-1-29
W
Mn
Cr
C V Ni
Mo
V Cr Mn Fe
V Cr Mn Fe
Ni
Ni
W
5
10
Cursor=
Vert=5020
Window 0.005 - 40.955= 180,626 cnt

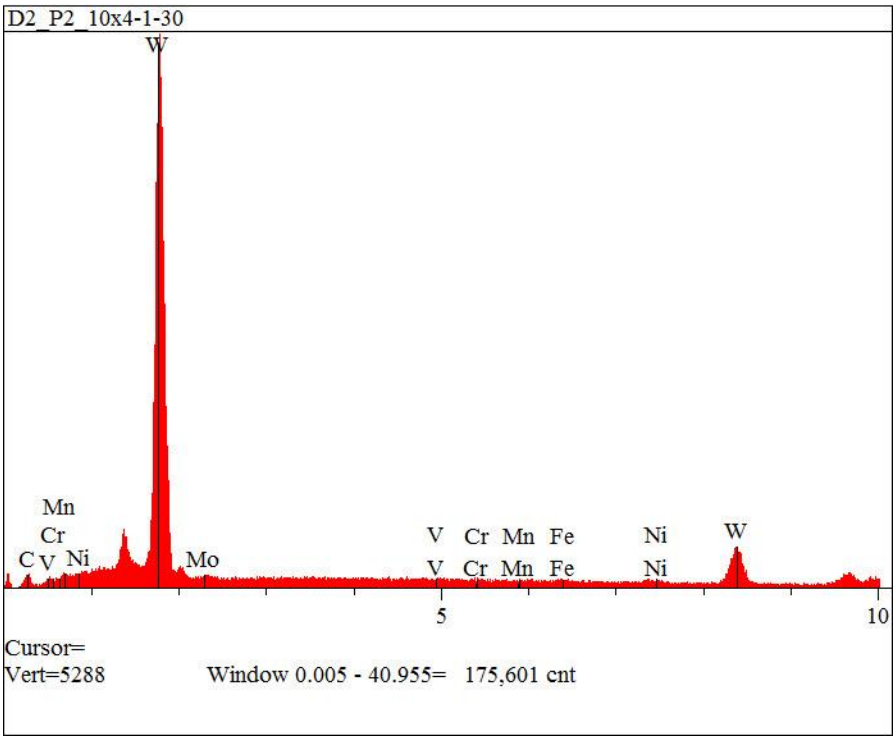
D2_P2_10x4-1-30
W
Mn
Cr
C V Ni
Mo
V Cr Mn Fe
V Cr Mn Fe
Ni
Ni
W
5
10
Cursor=
Vert=5288
Window 0.005 - 40.955= 175,601 cnt

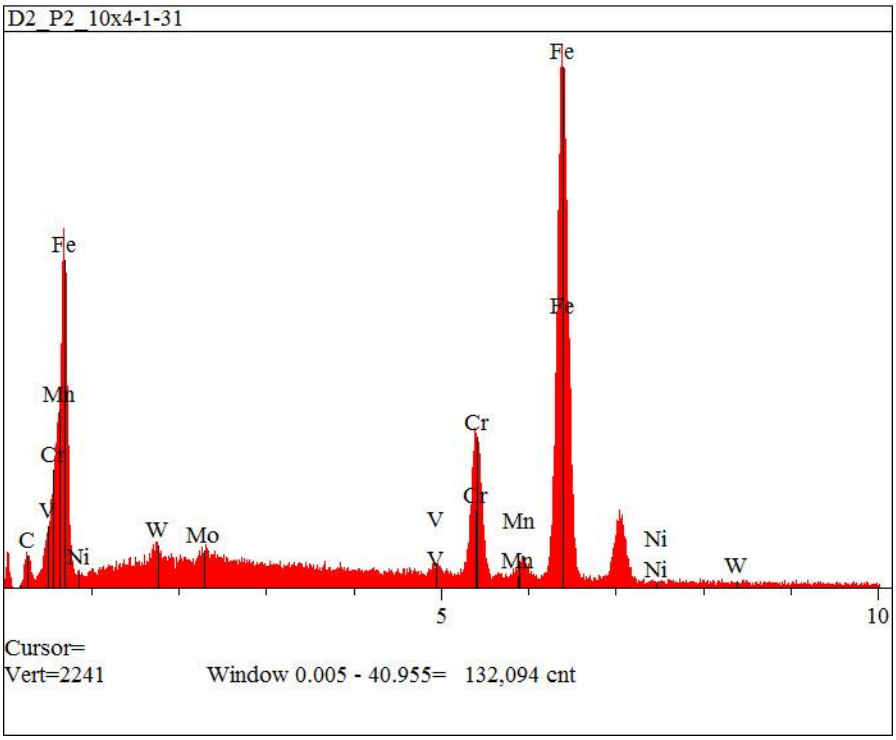
D2_P2_10x4-1-31
Fe
Fe
Fe
Mn
Cr
Cr
V
C
Ni
W
Mo
V
Cr
Mn
V
Mn
Ni
Ni
W
5
10
Cursor=
Vert=2241
Window 0.005 - 40.955= 132,094 cnt

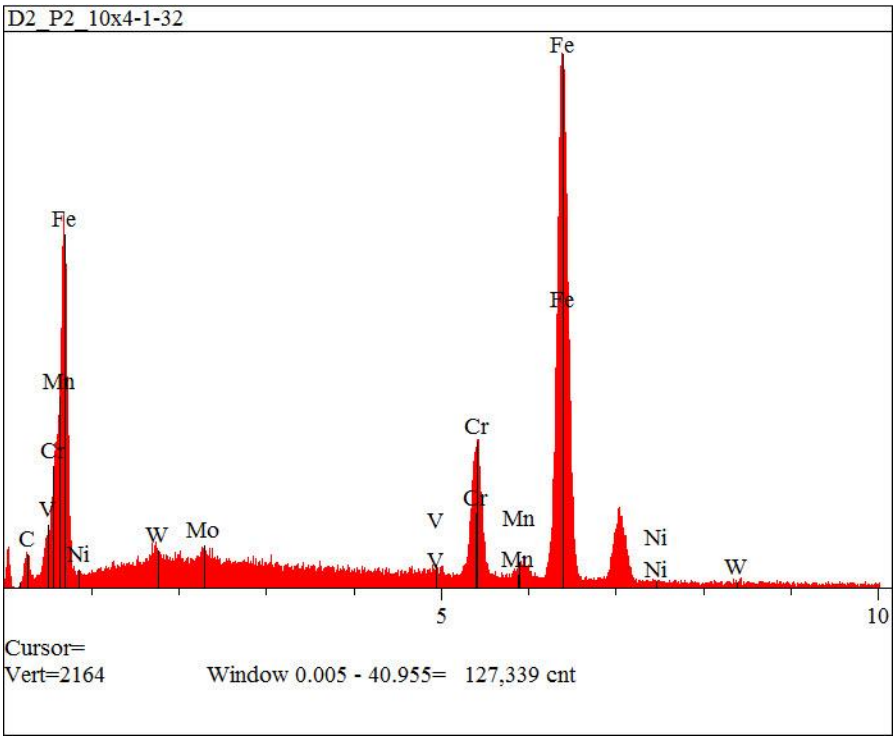
D2_P2_10x4-1-32
Fe
Fe
Fe
Mn
Cr
Cr
V
C
Ni
W
Mo
V
Cr
Mn
V
Mn
Ni
Ni
W
5
10
Cursor=
Vert=2164
Window 0.005 - 40.955= 127,339 cnt

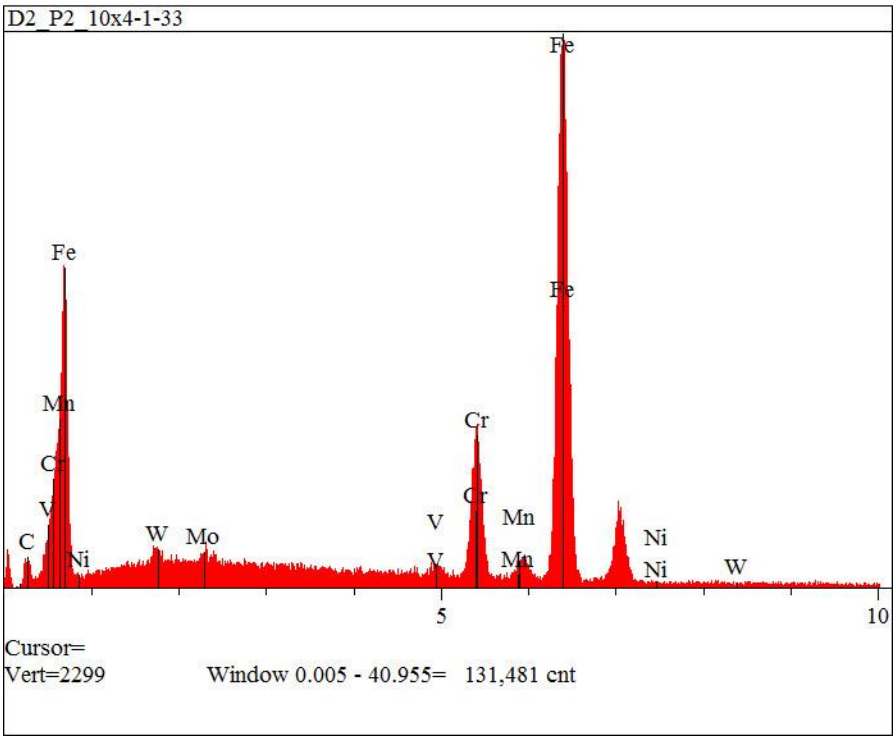
D2_P2_10x4-1-33
Fe
Fe
Mn
Cr
V
C
Ni
W
Mo
Cr
V
Mn
V
Mn
Ni
Ni
W
5
10
Cursor=
Vert=2299
Window 0.005 - 40.955= 131,481 cnt

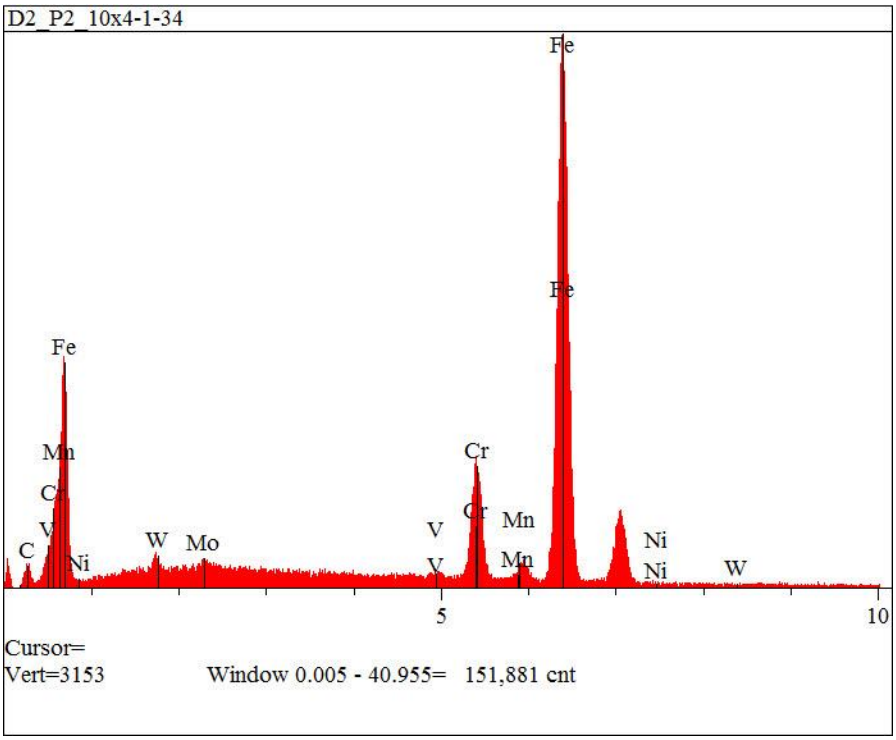
D2_P2_10x4-1-34
Fe
Fe
Mn
Cr
V
C
Ni
W
Mo
Cr
V
Mn
V
Mn
Ni
Ni
W
5
10
Cursor=
Vert=3153
Window 0.005 - 40.955= 151,881 cnt

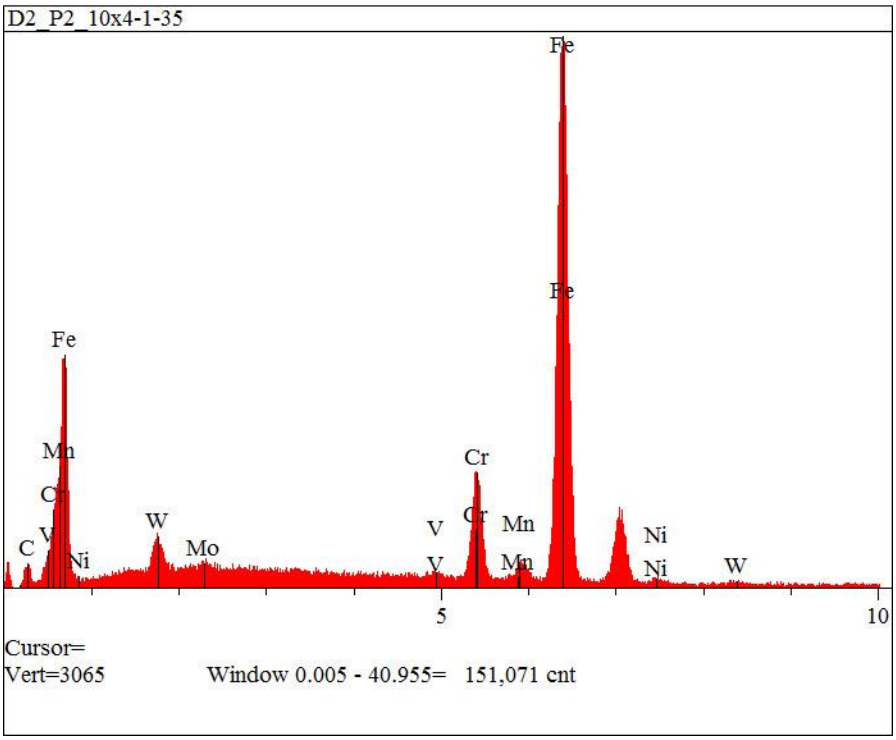
D2_P2_10x4-1-35
Fe
Fe
Fe
Mn
Cr
Cr
W
V
C
Ni
Mo
V
Cr
Mn
Ni
Ni
W
5
10
Cursor=
Vert=3065
Window 0.005 - 40.955= 151,071 cnt

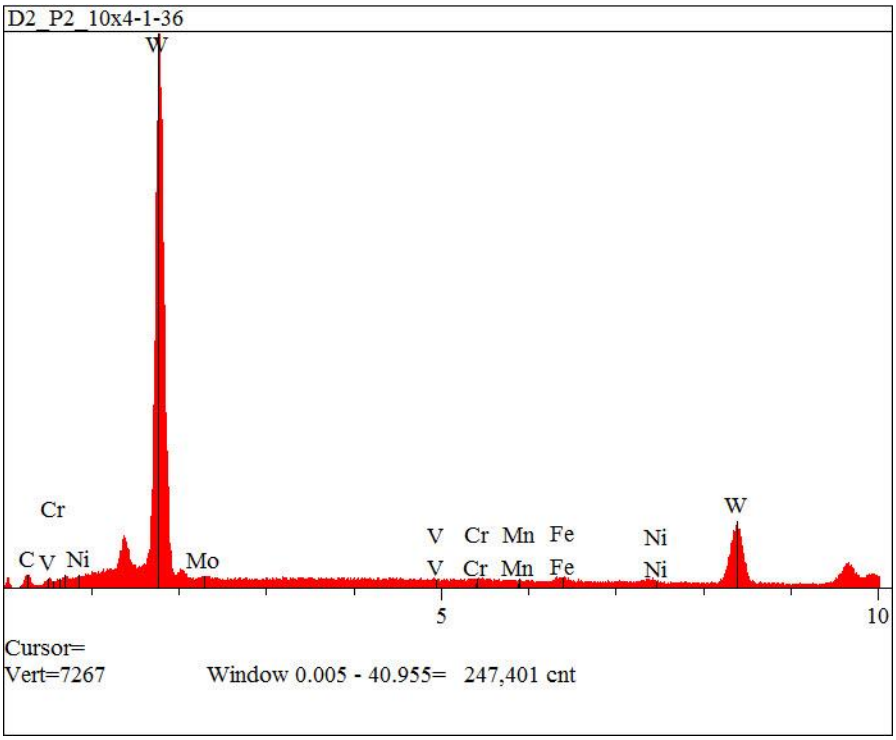
D2_P2_10x4-1-36
W
Cr
C V Ni
Mo
V Cr Mn Fe
V Cr Mn Fe
Ni
Ni
W
5
10
Cursor=
Vert=7267
Window 0.005 - 40.955= 247,401 cnt

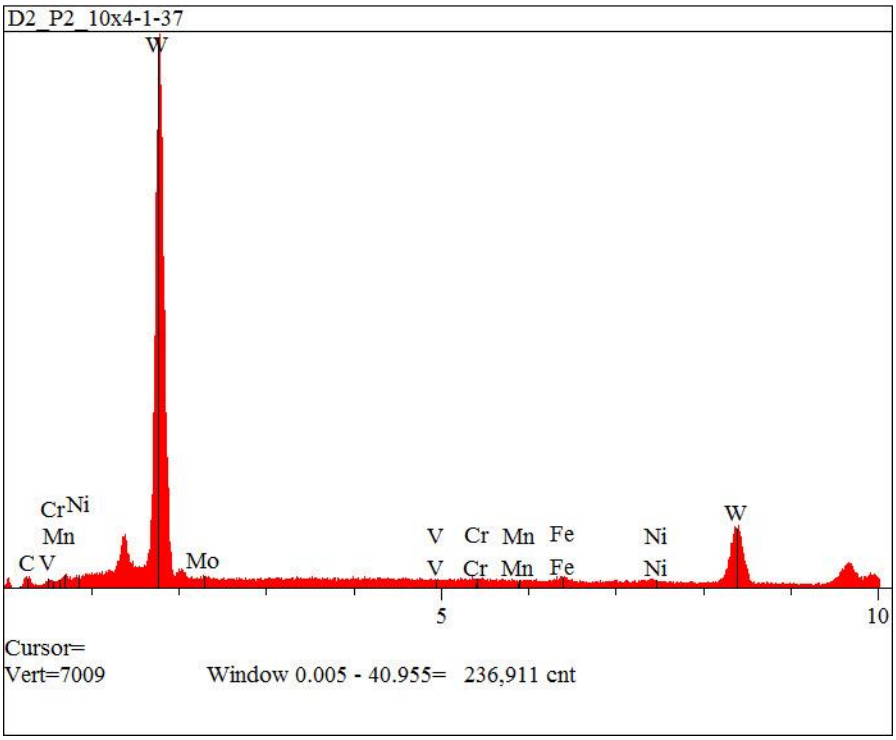
D2_P2_10x4-1-37
W
Cr Ni
Mn
C V
Mo
V Cr Mn Fe Ni
V Cr Mn Fe Ni
W
5
10
Cursor=
Vert=7009
Window 0.005 - 40.955= 236,911 cnt

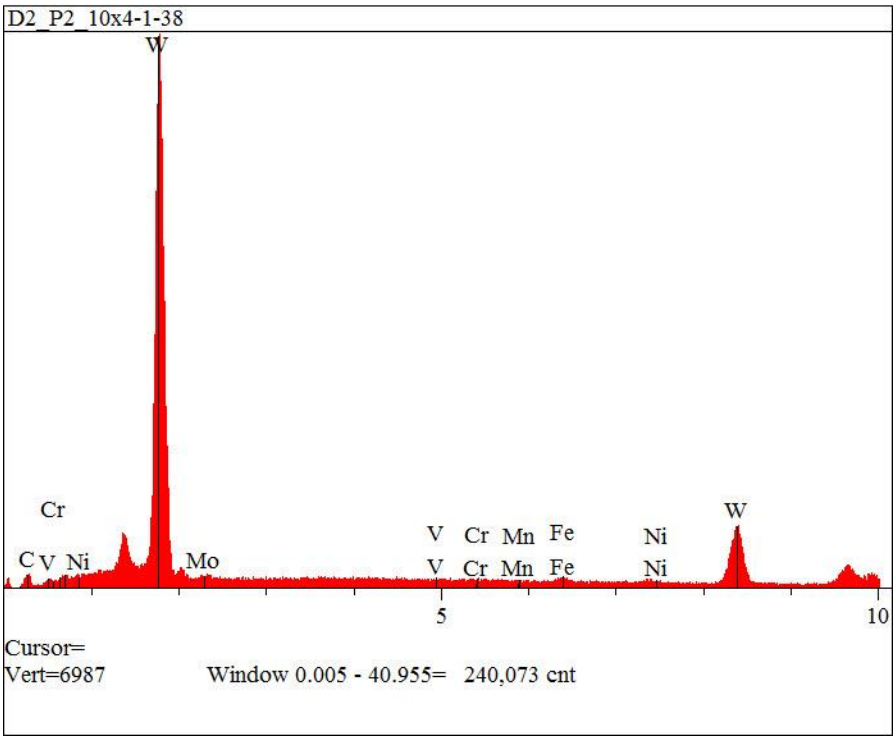
D2_P2_10x4-1-38
W
Cr
C V Ni
Mo
V Cr Mn Fe Ni
V Cr Mn Fe Ni
W
5
10
Cursor=
Vert=6987
Window 0.005 - 40.955= 240,073 cnt

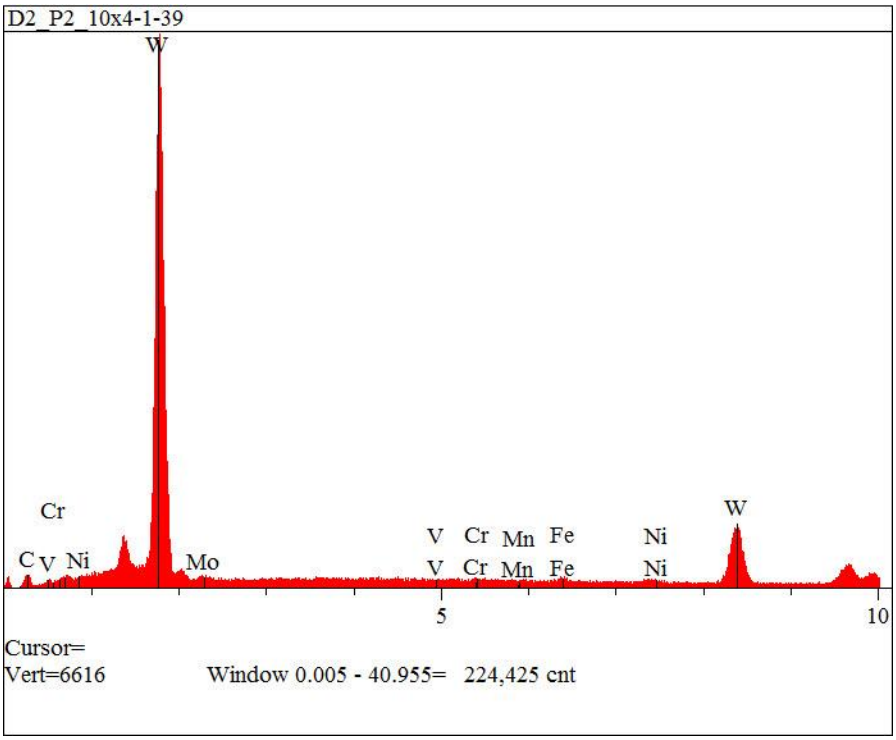
D2_P2_10x4-1-39
W
Cr
C V Ni
Mo
V Cr Mn Fe Ni
V Cr Mn Fe Ni
W
5
10
Cursor=
Vert=6616
Window 0.005 - 40.955= 224,425 cnt

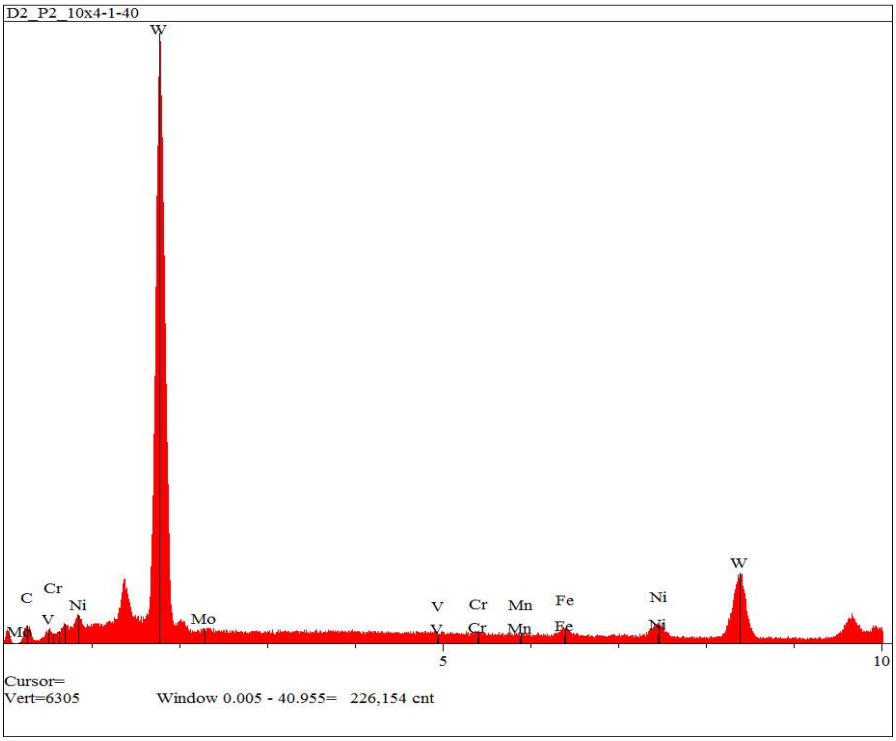
D2_P2_10x4-1-40
W
C
Cr
V
Ni
Mo
V Cr Mn Fe Ni
W
5
10
Cursor=
Vert=6305
Window 0.005 - 40.955= 226,154 cnt

H2 4x10 1-40 EDS Taken Horizontally

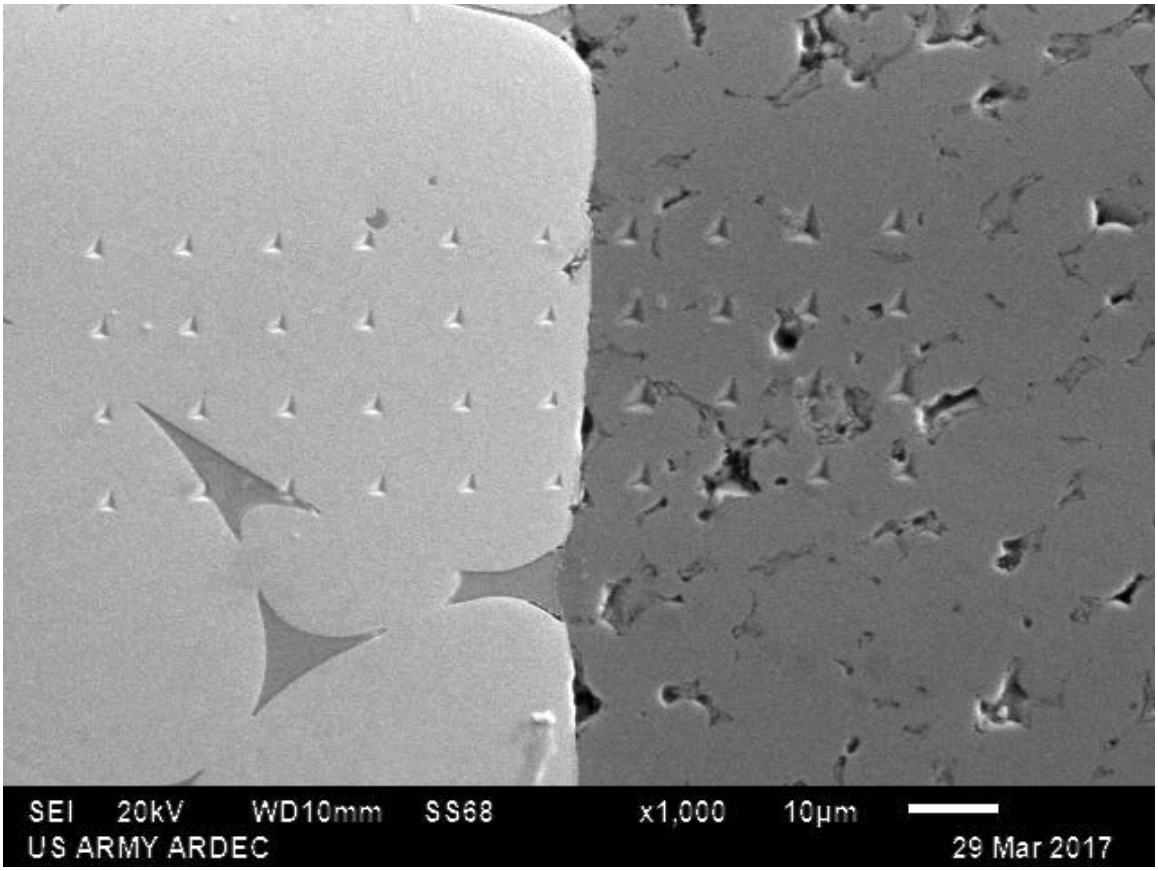

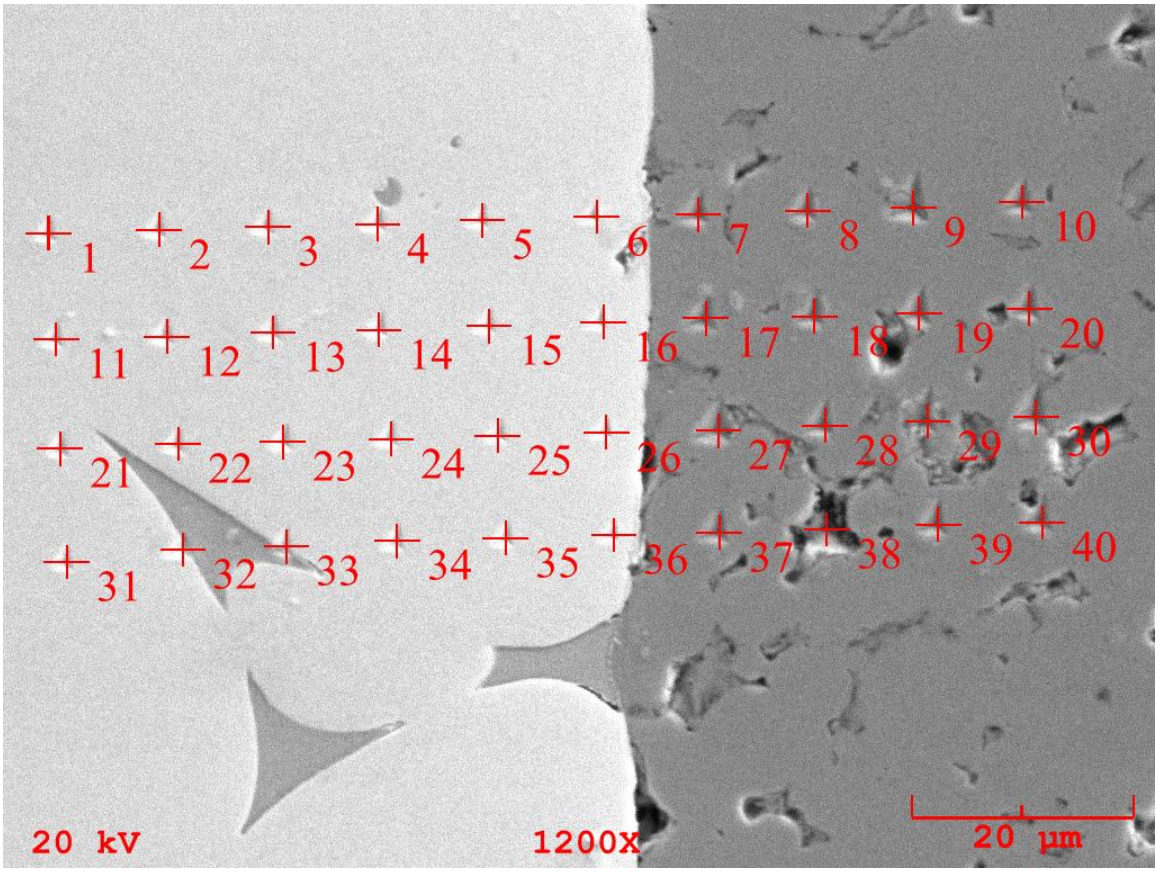
1
2
3
4
5
6
7
8
9
10
11
12
13
14
15
16
17
18
19
20
21
22
23
24
25
26
27
28
29
30
31
32
33
34
35
36
37
38
39
40
20 kV
1200X
20 µm

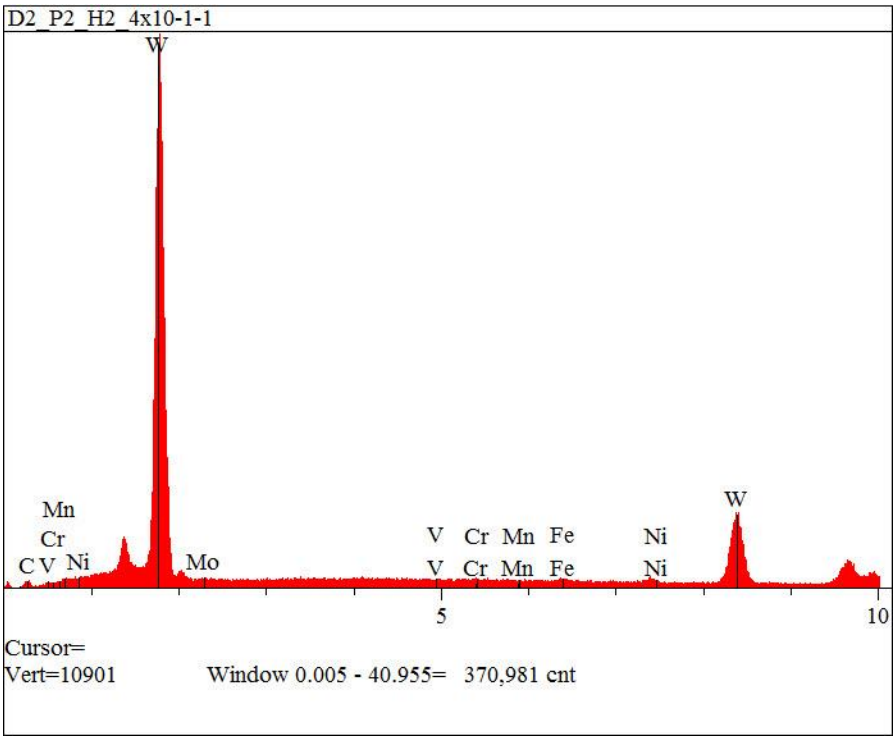
D2_P2_H2_4x10-1-1
W
Mn
Cr
C V Ni
Mo
V Cr Mn Fe
V Cr Mn Fe
Ni
Ni
W
5
10
Cursor=
Vert=10901
Window 0.005 - 40.955= 370,981 cnt

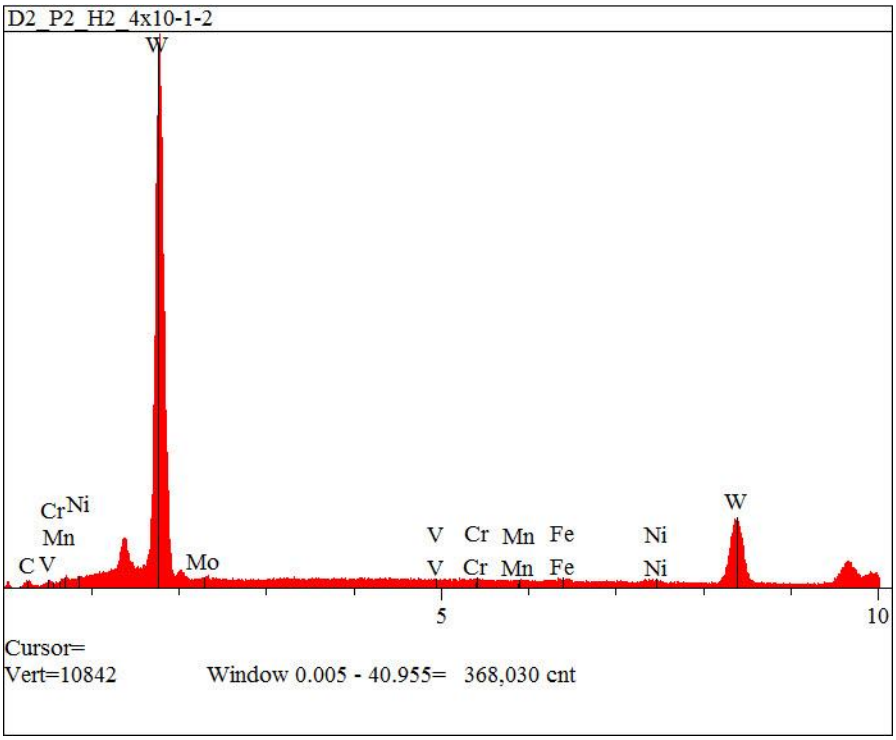
D2_P2_H2_4x10-1-2
W
Cr Ni
Mn
C V
Mo
V Cr Mn Fe
V Cr Mn Fe
Ni
Ni
W
5
10
Cursor=
Vert=10842
Window 0.005 - 40.955= 368,030 cnt

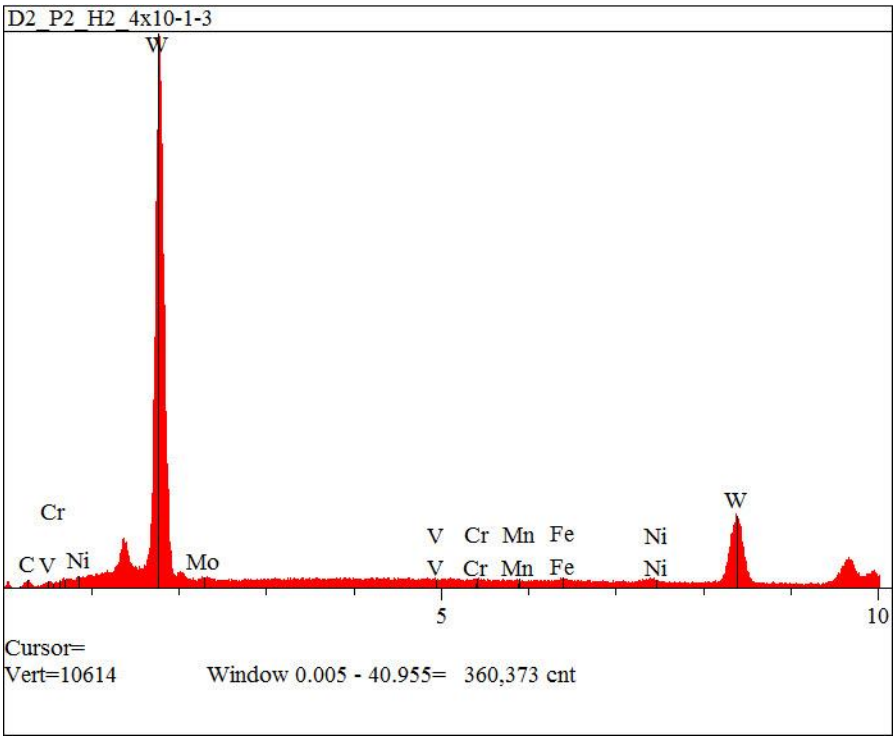
D2_P2_H2_4x10-1-3
W
Cr
C V Ni
Mo
V Cr Mn Fe
V Cr Mn Fe
Ni
Ni
W
5
10
Cursor=
Vert=10614
Window 0.005 - 40.955= 360,373 cnt

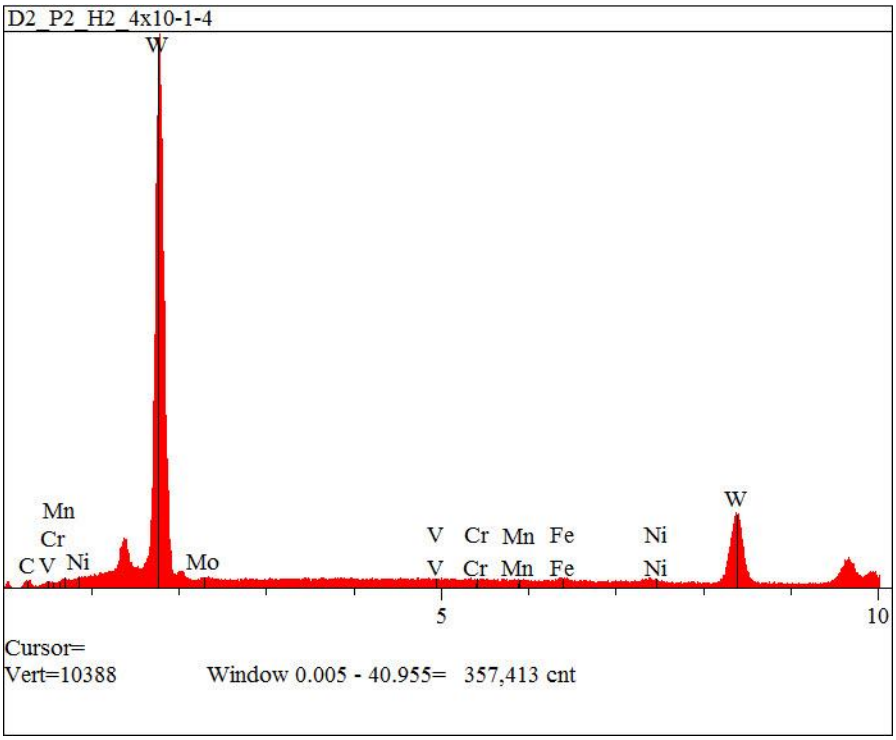
D2_P2_H2_4x10-1-4
W
Mn
Cr
C V Ni
Mo
V Cr Mn Fe
V Cr Mn Fe
Ni
Ni
W
5
10
Cursor=
Vert=10388
Window 0.005 - 40.955= 357,413 cnt

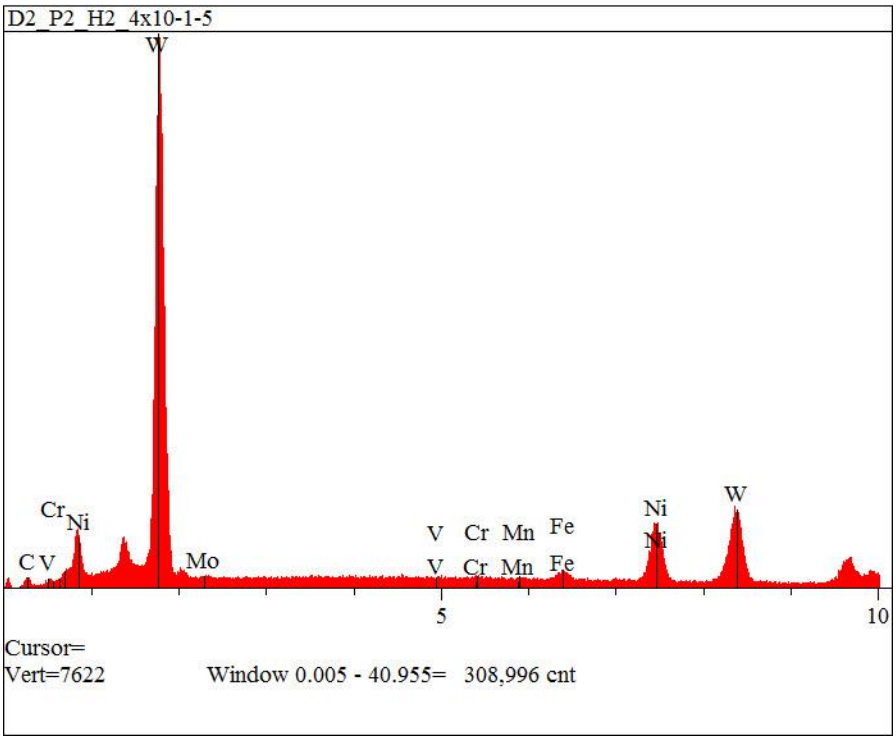
D2_P2_H2_4x10-1-5
W
Cr
Ni
C V
Mo
V Cr Mn Fe
V Cr Mn Fe
Ni
Ni
W
5
10
Cursor=
Vert=7622
Window 0.005 - 40.955= 308,996 cnt

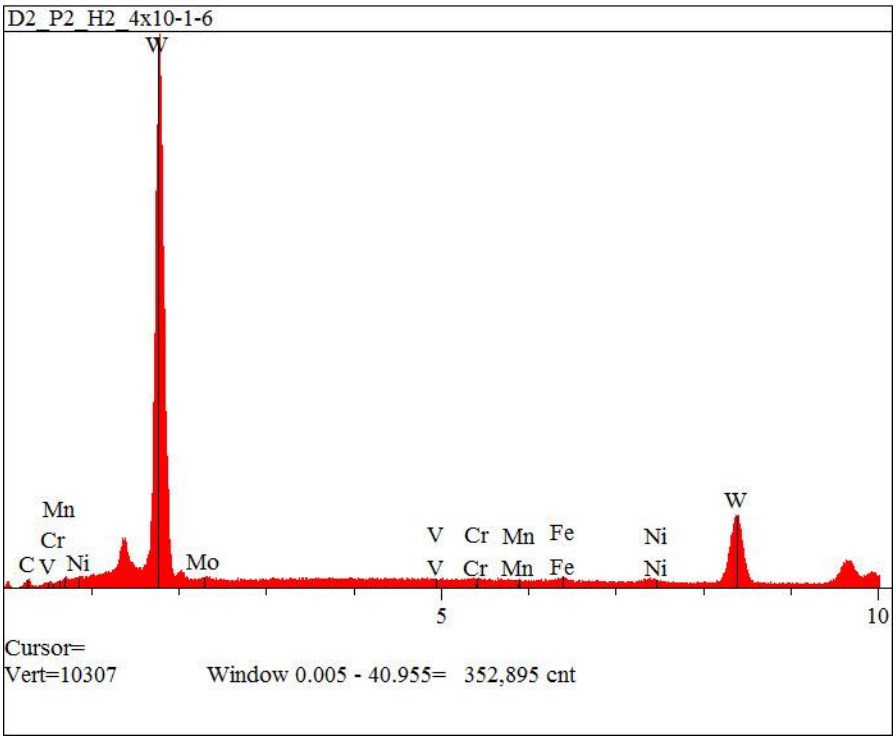
D2_P2_H2_4x10-1-6
W
Mn
Cr
C V Ni
Mo
V Cr Mn Fe
V Cr Mn Fe
Ni
Ni
W
5
10
Cursor=
Vert=10307
Window 0.005 - 40.955= 352,895 cnt

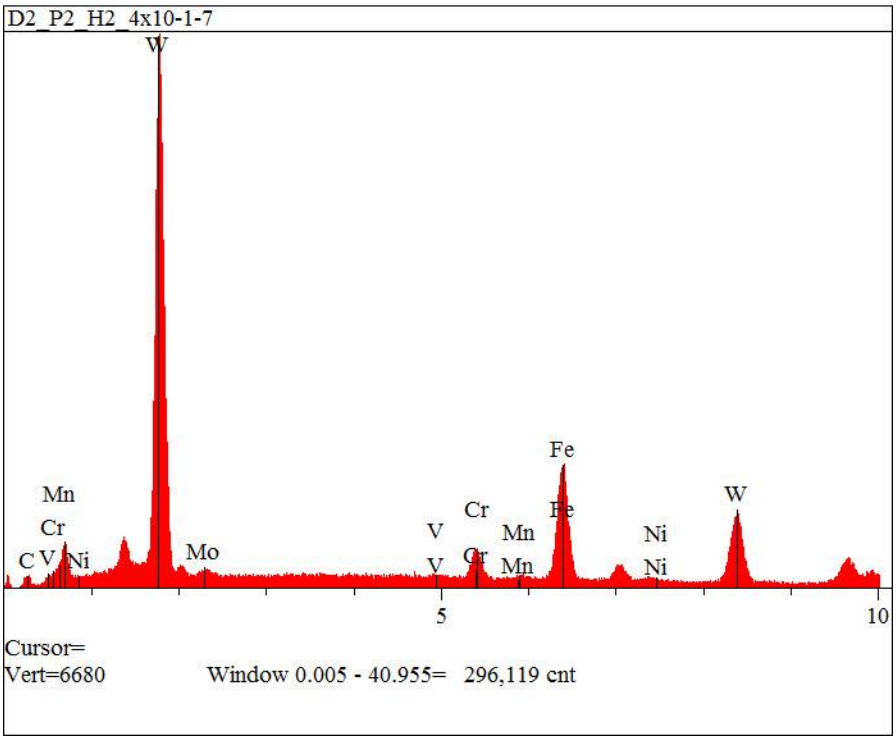
D2_P2_H2_4x10-1-7
W
Mn
Cr
C V Ni
Mo
V
V
Cr
Cr
Mn
Mn
Fe
Fe
Ni
Ni
W
5
10
Cursor=
Vert=6680
Window 0.005 - 40.955= 296,119 cnt

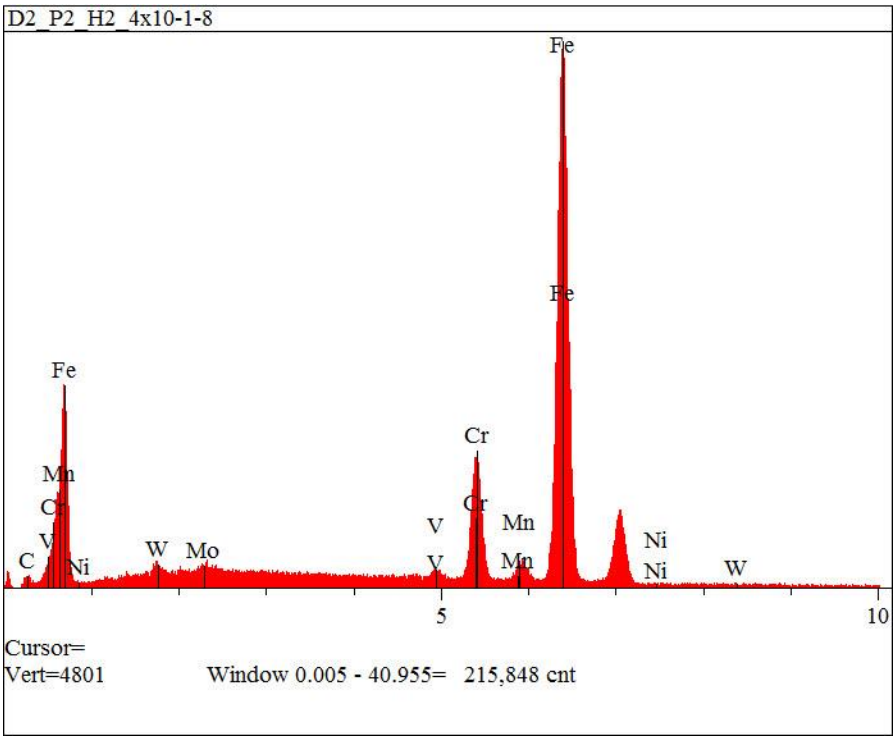
D2_P2_H2_4x10-1-8
Fe
Fe
Fe
Mn
Cr
C V Ni
W Mo
V
V
Cr
Cr
Mn
Mn
Ni
Ni
W
5
10
Cursor=
Vert=4801
Window 0.005 - 40.955= 215,848 cnt

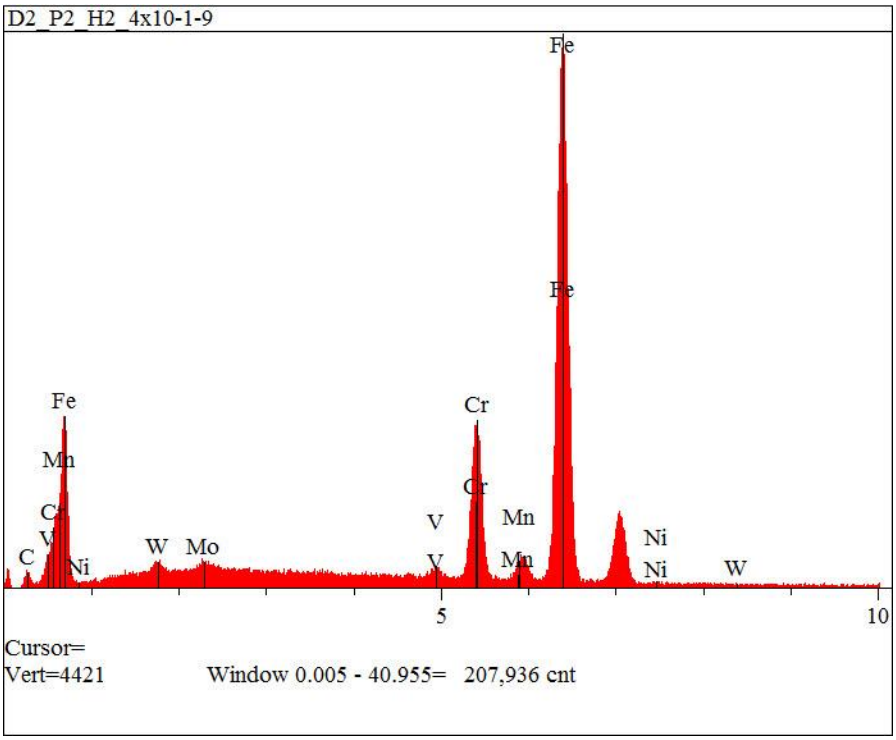
D2_P2_H2_4x10-1-9
Fe
Fe
Fe
Mn
Cr
Cr
C
V
V
W
Mo
Ni
V
Mn
Mn
Ni
Ni
W
5
10
Cursor=
Vert=4421
Window 0.005 - 40.955= 207,936 cnt

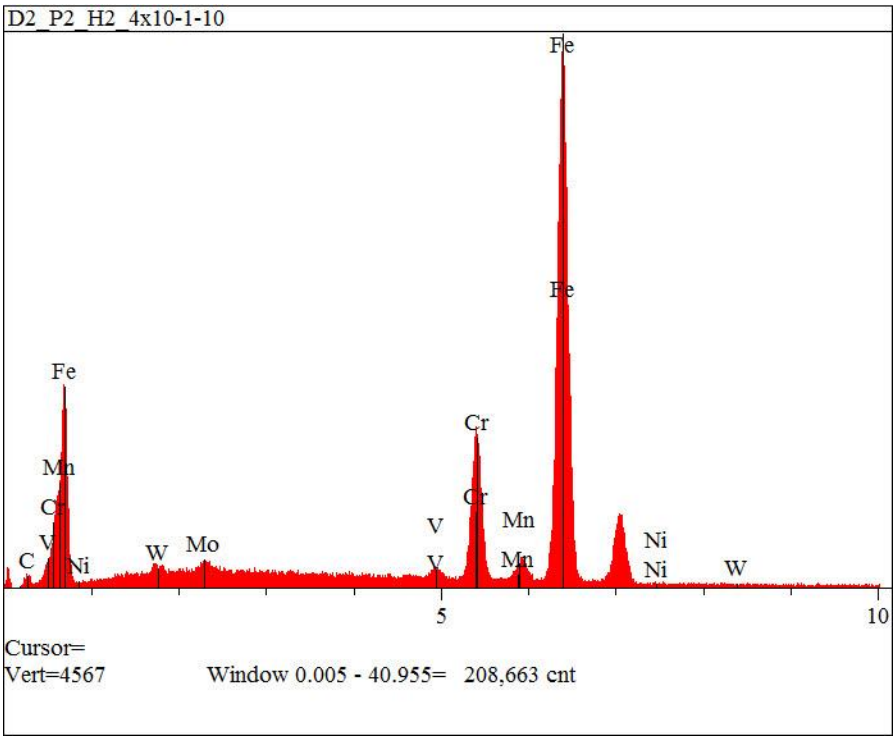
D2_P2_H2_4x10-1-10
Fe
Fe
Fe
Mn
Cr
Cr
C
V
V
W
Mo
Ni
V
Mn
Mn
Ni
Ni
W
5
10
Cursor=
Vert=4567
Window 0.005 - 40.955= 208,663 cnt

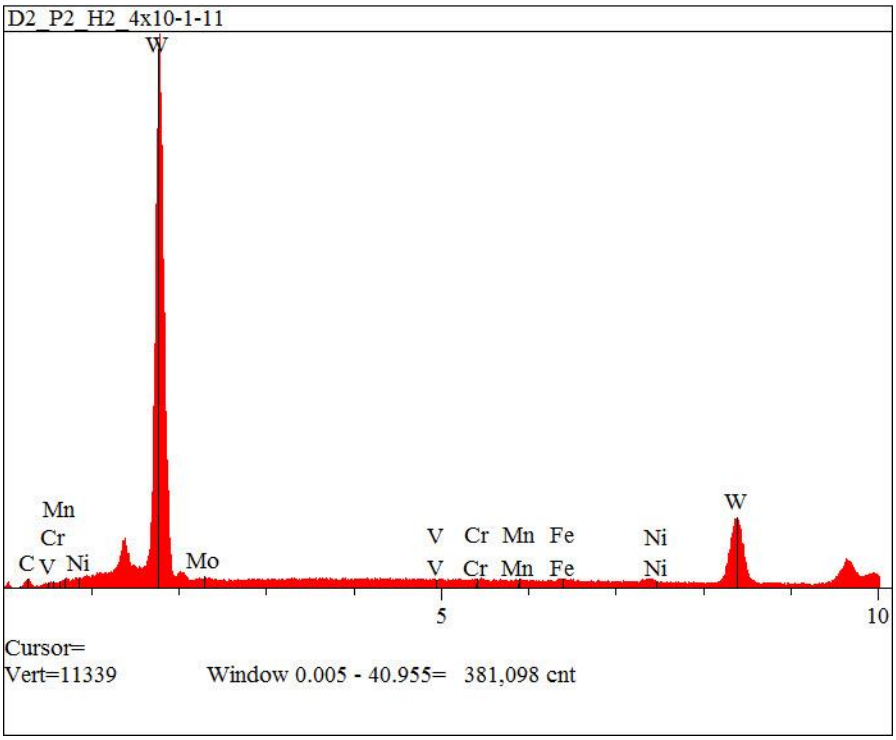
D2_P2_H2_4x10-1-11
W
Mn
Cr
C V Ni
Mo
V Cr Mn Fe
V Cr Mn Fe
Ni
Ni
W
5
10
Cursor=
Vert=11339
Window 0.005 - 40.955= 381,098 cnt

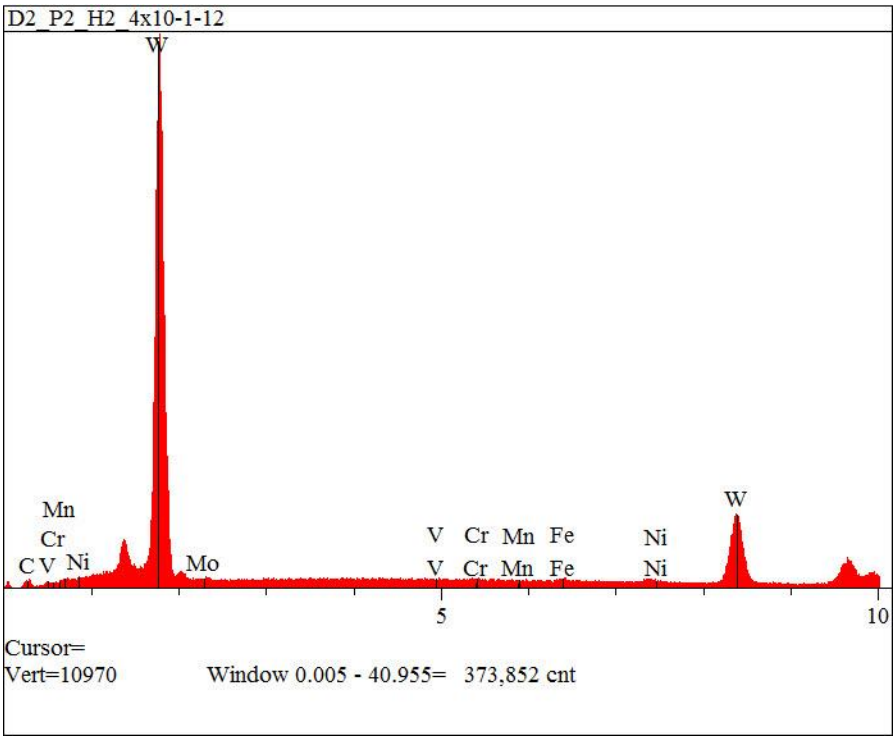
D2_P2_H2_4x10-1-12
W
Mn
Cr
C V Ni
Mo
V Cr Mn Fe
V Cr Mn Fe
Ni
Ni
W
5
10
Cursor=
Vert=10970
Window 0.005 - 40.955= 373,852 cnt

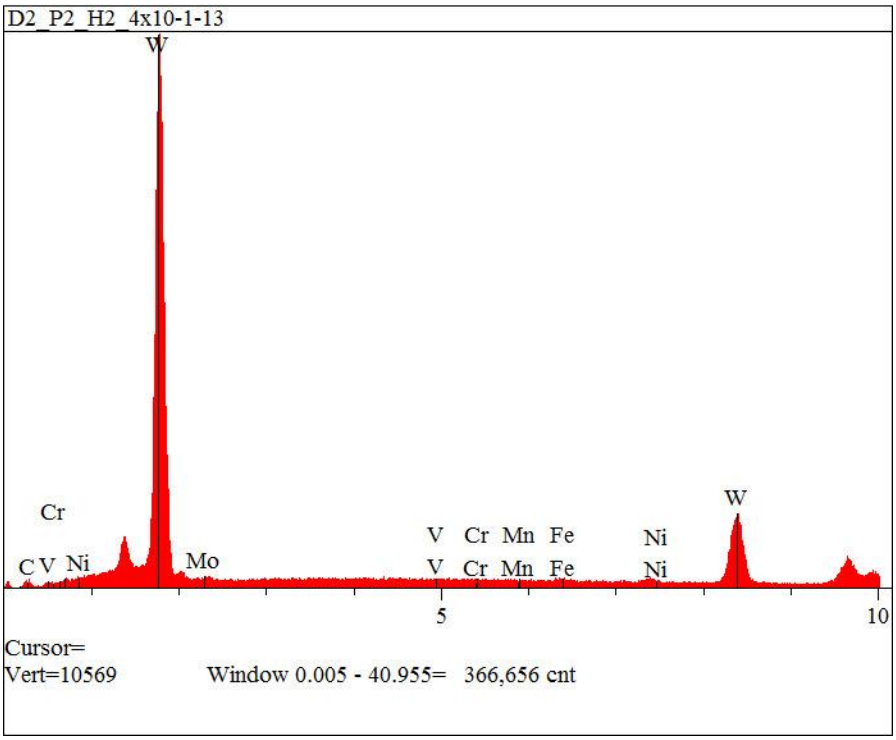
D2_P2_H2_4x10-1-13
W
Cr
C V Ni
Mo
V Cr Mn Fe
V Cr Mn Fe
Ni
Ni
W
5
10
Cursor=
Vert=10569
Window 0.005 - 40.955= 366,656 cnt

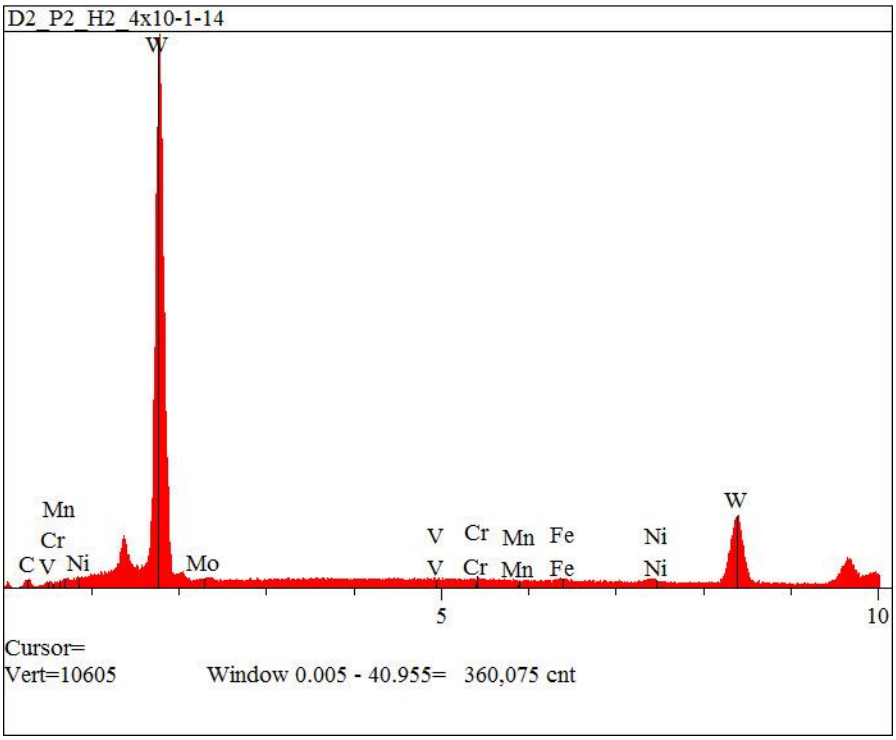
D2_P2_H2_4x10-1-14
W
Mn
Cr
C V Ni
Mo
V Cr Mn Fe
V Cr Mn Fe
Ni
Ni
W
5
10
Cursor=
Vert=10605
Window 0.005 - 40.955= 360,075 cnt

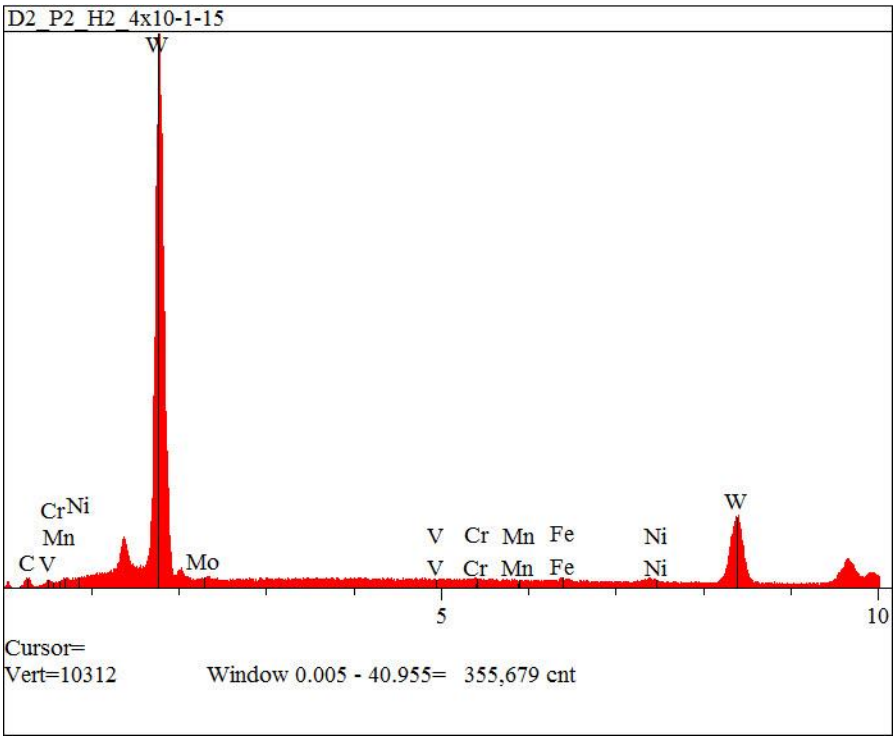
D2_P2_H2_4x10-1-15
W
Cr Ni
Mn
C V
Mo
V Cr Mn Fe Ni
V Cr Mn Fe Ni
W
5
10
Cursor=
Vert=10312
Window 0.005 - 40.955= 355,679 cnt

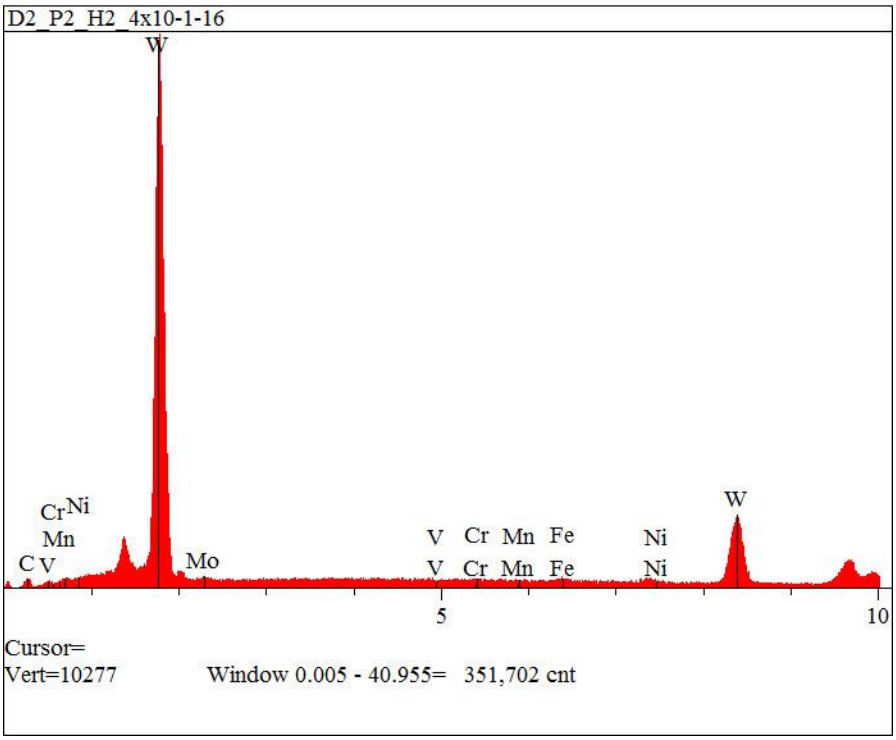
D2_P2_H2_4x10-1-16
W
Cr Ni
Mn
C V
Mo
V Cr Mn Fe Ni
V Cr Mn Fe Ni
W
5
10
Cursor=
Vert=10277
Window 0.005 - 40.955= 351,702 cnt

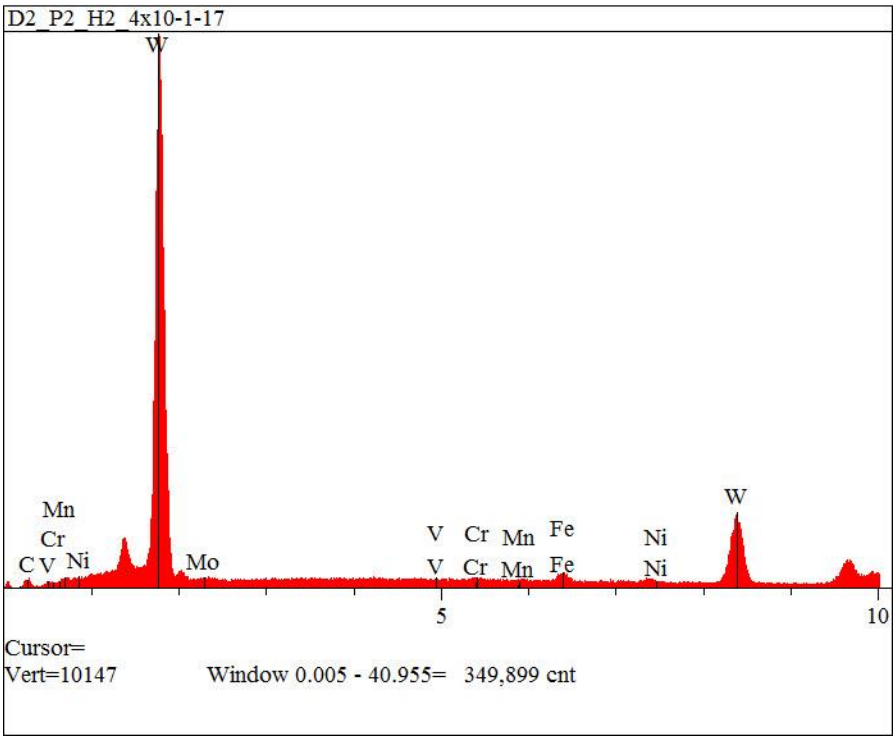
D2_P2_H2_4x10-1-17
W
Mn
Cr
C V Ni
Mo
V Cr Mn Fe
V Cr Mn Fe
Ni
Ni
W
5
10
Cursor=
Vert=10147
Window 0.005 - 40.955= 349,899 cnt

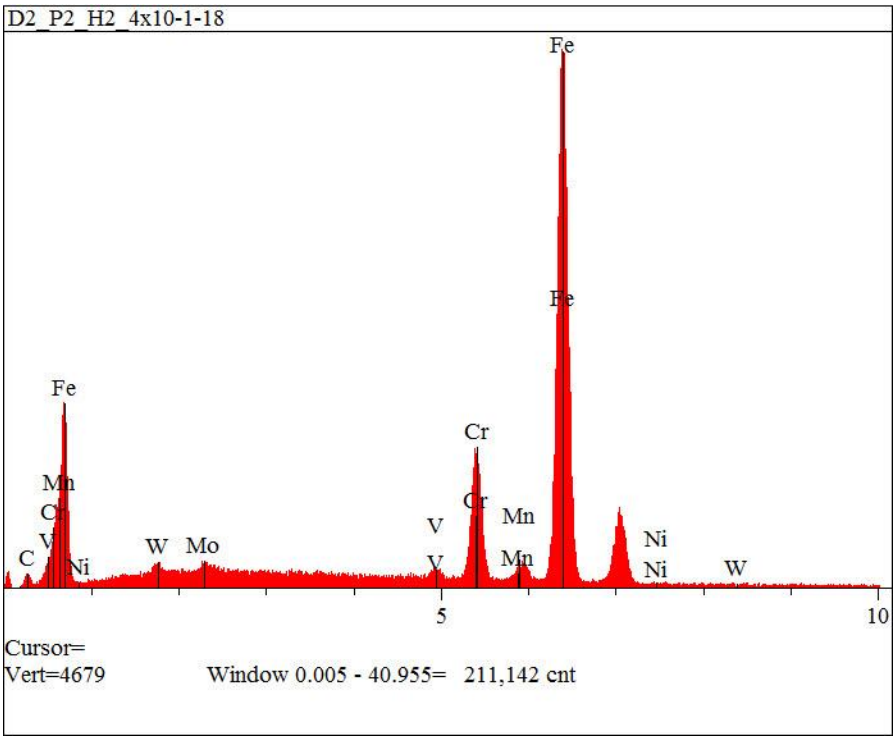
D2_P2_H2_4x10-1-18
Fe
Fe
Fe
Cr
Mn
C
Ni
W Mo
V
Cr
Mn
Mn
Ni
Ni
W
5
10
Cursor=
Vert=4679
Window 0.005 - 40.955= 211,142 cnt

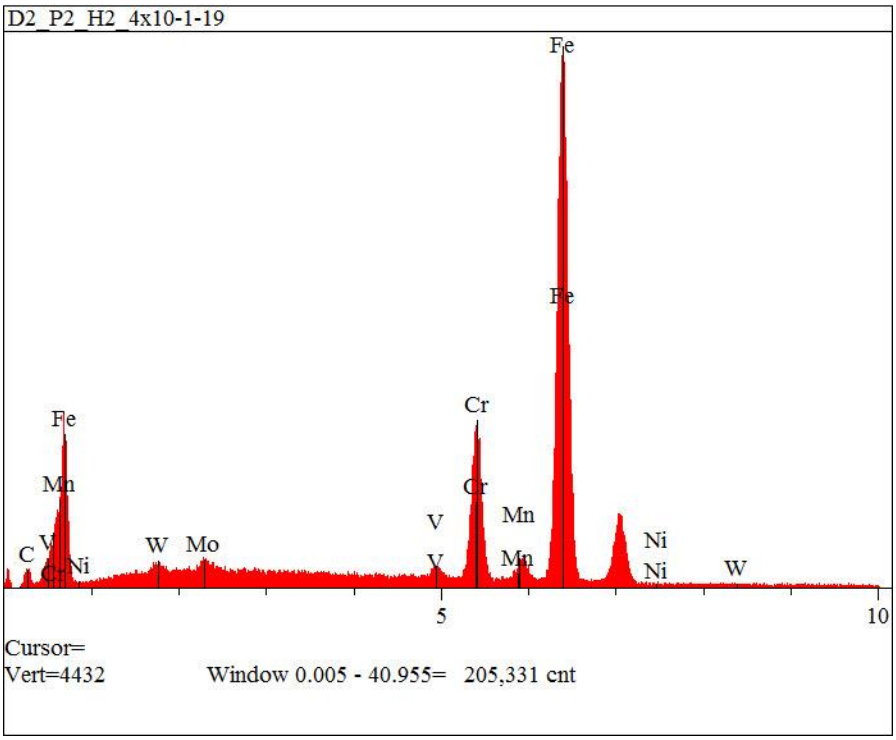
D2_P2_H2_4x10-1-19
Fe
Fe
Fe
Mn
Cr
Cr
V
Mn
C
V
W
Mo
Ni
V
Mn
Ni
Ni
W
5
10
Cursor=
Vert=4432
Window 0.005 - 40.955= 205,331 cnt

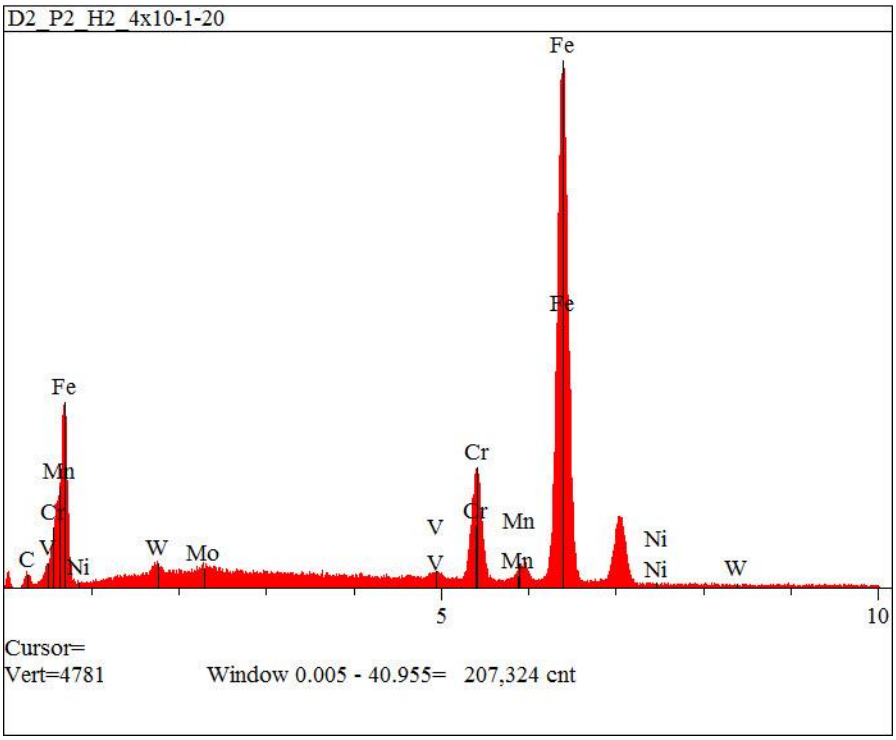
D2_P2_H2_4x10-1-20
Fe
Fe
Fe
Mn
Cr
Cr
V
Mn
C
V
W
Mo
Ni
V
Mn
Ni
Ni
W
5
10
Cursor=
Vert=4781
Window 0.005 - 40.955= 207,324 cnt

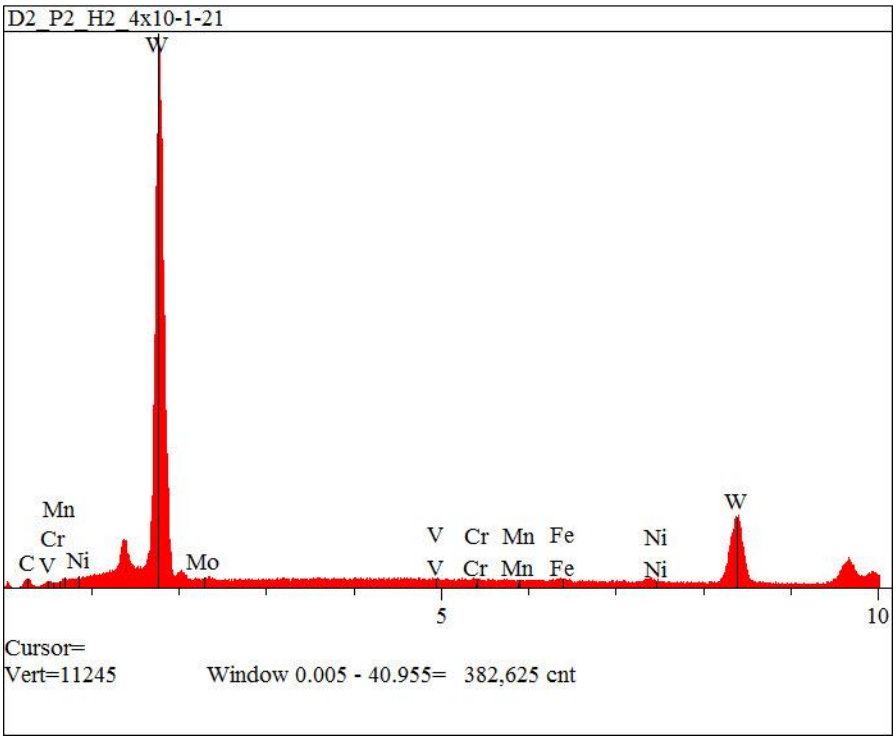
D2_P2_H2_4x10-1-21
W
Mn
Cr
C V Ni
Mo
V Cr Mn Fe
V Cr Mn Fe
Ni
Ni
W
5
10
Cursor=
Vert=11245
Window 0.005 - 40.955= 382,625 cnt

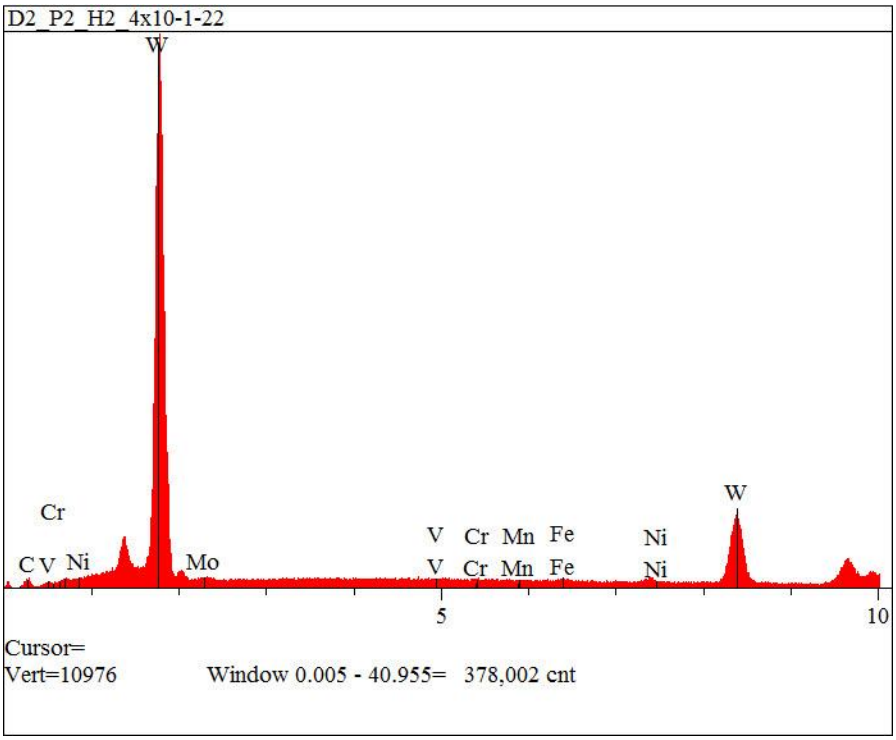
D2_P2_H2_4x10-1-22
W
Cr
C V Ni
Mo
V Cr Mn Fe
V Cr Mn Fe
Ni
Ni
W
5
10
Cursor=
Vert=10976
Window 0.005 - 40.955= 378,002 cnt

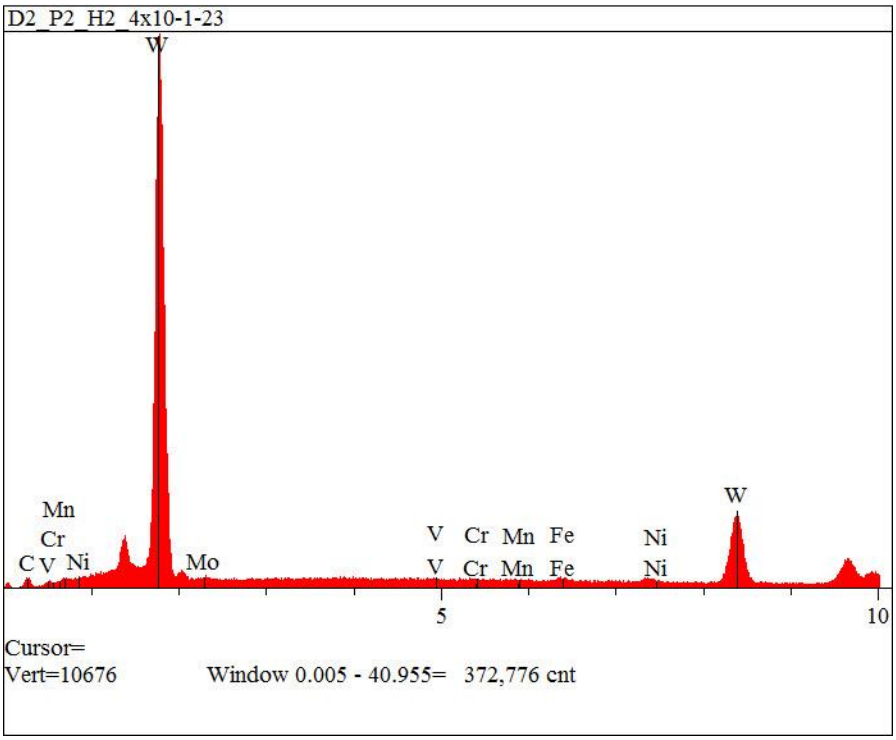
D2_P2_H2_4x10-1-23
W
Mn
Cr
C V Ni
Mo
V Cr Mn Fe
V Cr Mn Fe
Ni
Ni
W
5
10
Cursor=
Vert=10676
Window 0.005 - 40.955= 372,776 cnt

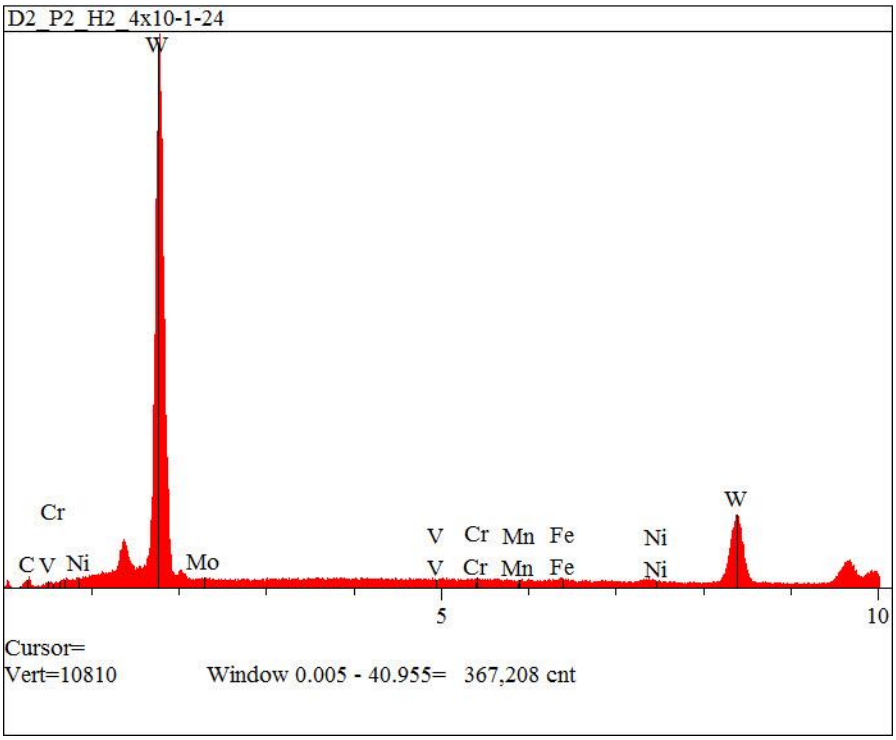
D2_P2_H2_4x10-1-24
W
Cr
C V Ni
Mo
V Cr Mn Fe
V Cr Mn Fe
Ni
Ni
W
5
10
Cursor=
Vert=10810
Window 0.005 - 40.955= 367,208 cnt

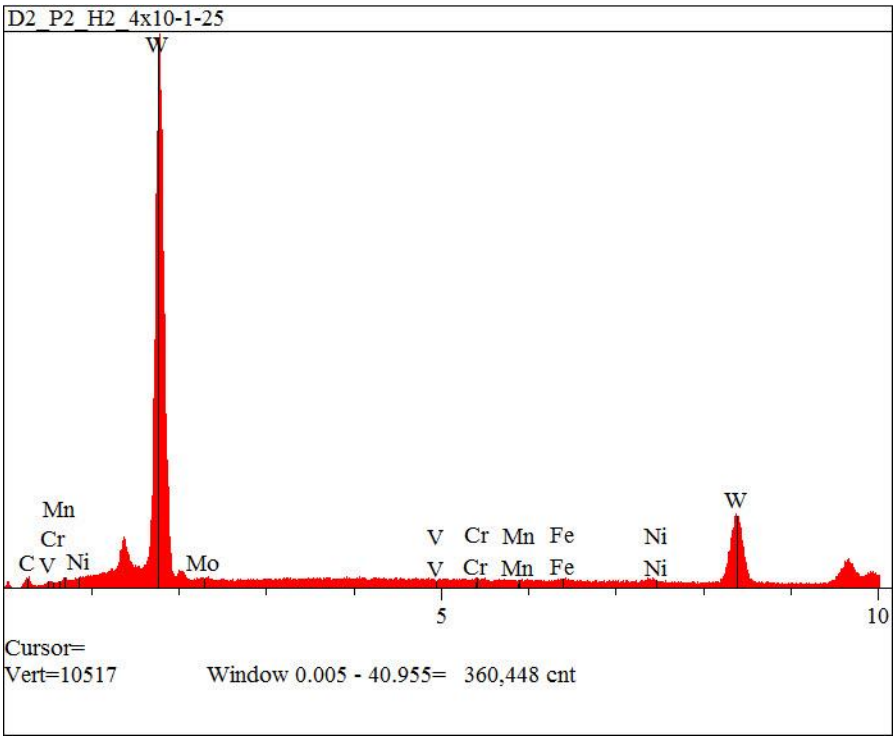
D2_P2_H2_4x10-1-25
W
Mn
Cr
C V Ni
Mo
V Cr Mn Fe Ni
V Cr Mn Fe Ni
W
5
10
Cursor=
Vert=10517
Window 0.005 - 40.955= 360,448 cnt

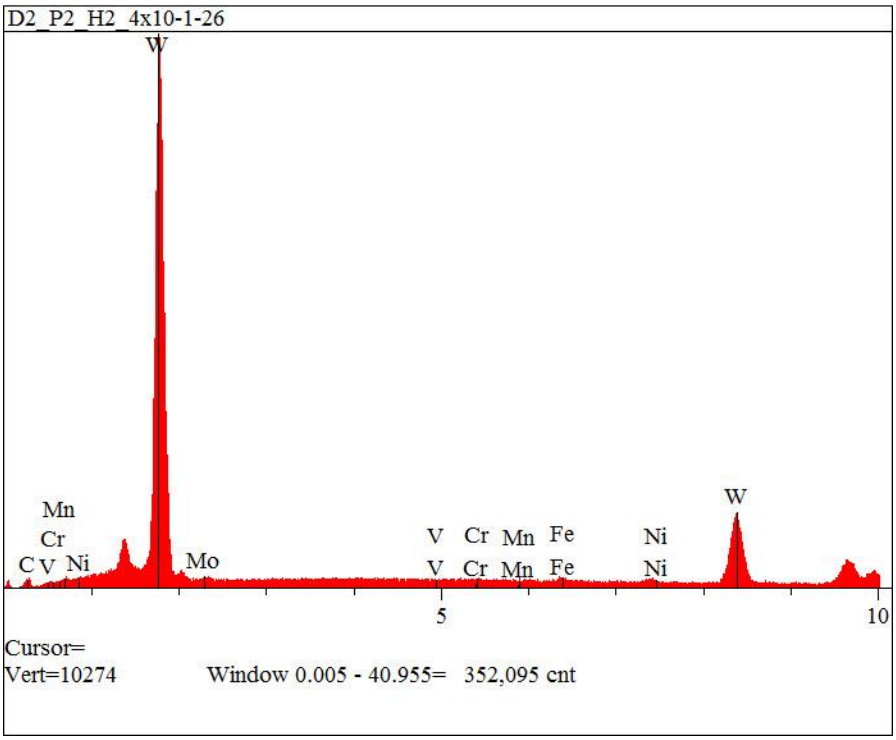
D2_P2_H2_4x10-1-26
W
Mn
Cr
C V Ni
Mo
V Cr Mn Fe Ni
V Cr Mn Fe Ni
W
5
10
Cursor=
Vert=10274
Window 0.005 - 40.955= 352,095 cnt

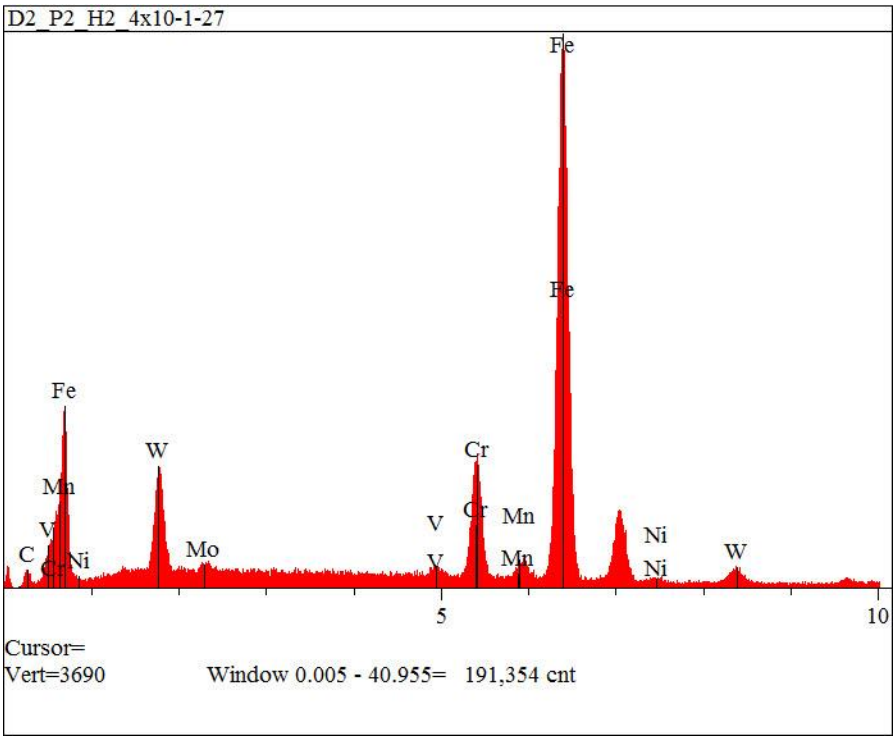
D2_P2_H2_4x10-1-27
Fe
Fe
Fe
W
Cr
Mn
Cr
V
Mn
Ni
C
Ni
Mo
V
Mn
Ni
W
5
10
Cursor=
Vert=3690
Window 0.005 - 40.955= 191,354 cnt

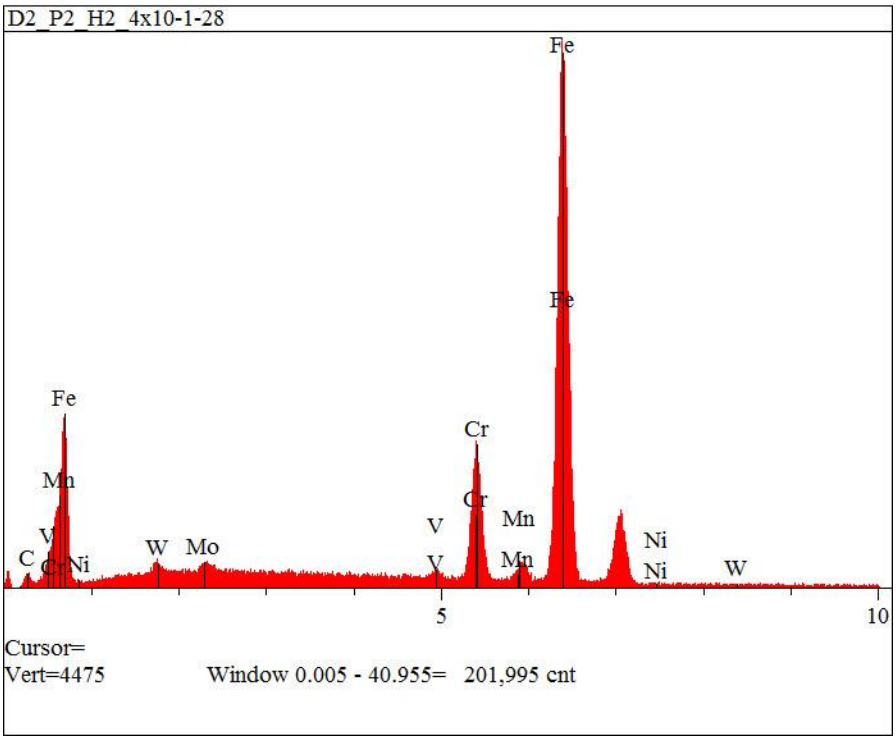
D2_P2_H2_4x10-1-28
Fe
Fe
Fe
Cr
Mn
Cr
V
Mn
Ni
C
Ni
W
Mo
V
Mn
Ni
W
5
10
Cursor=
Vert=4475
Window 0.005 - 40.955= 201,995 cnt

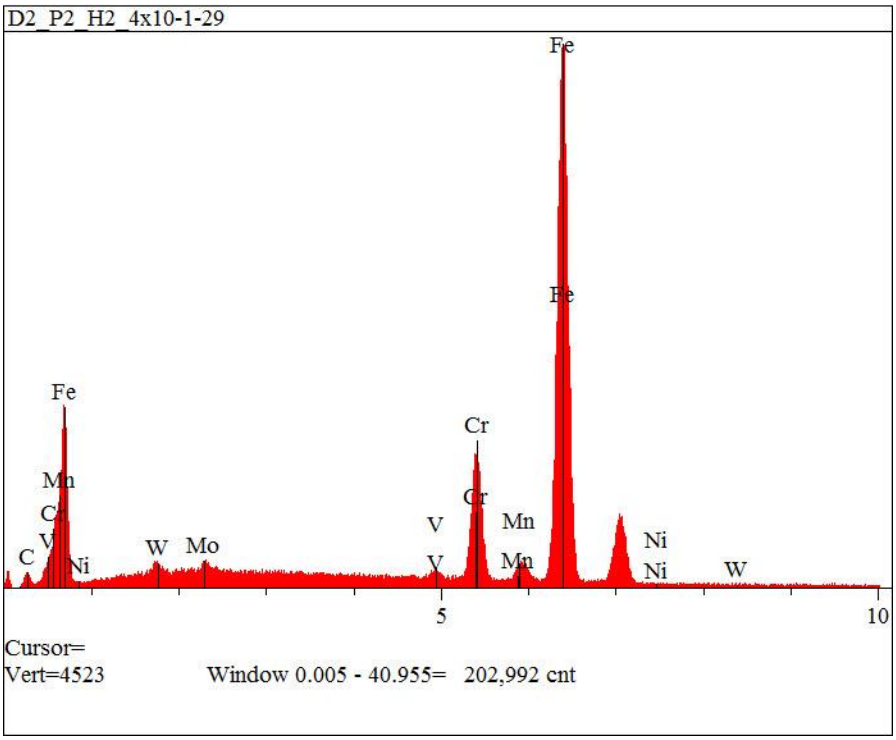
D2_P2_H2_4x10-1-29
Fe
Fe
Fe
Cr
Mn
Cr
C
V
W
Mo
V
Mn
Ni
Ni
W
Ni
5
10
Cursor=
Vert=4523
Window 0.005 - 40.955= 202,992 cnt

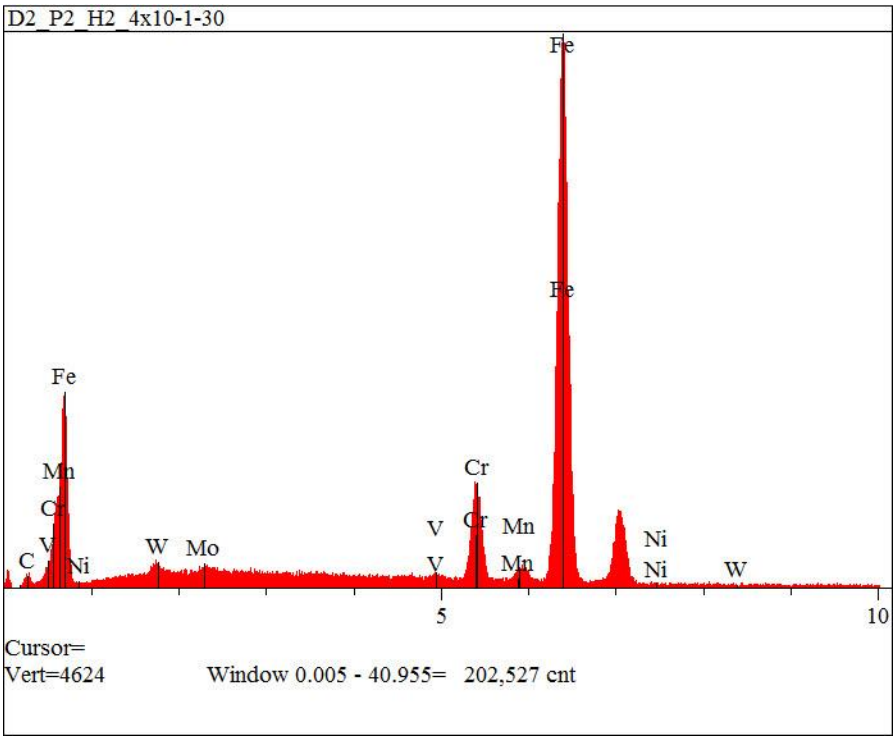
D2_P2_H2_4x10-1-30
Fe
Fe
Fe
Cr
Mn
Cr
C
V
W
Mo
V
Mn
Ni
Ni
W
Ni
5
10
Cursor=
Vert=4624
Window 0.005 - 40.955= 202,527 cnt

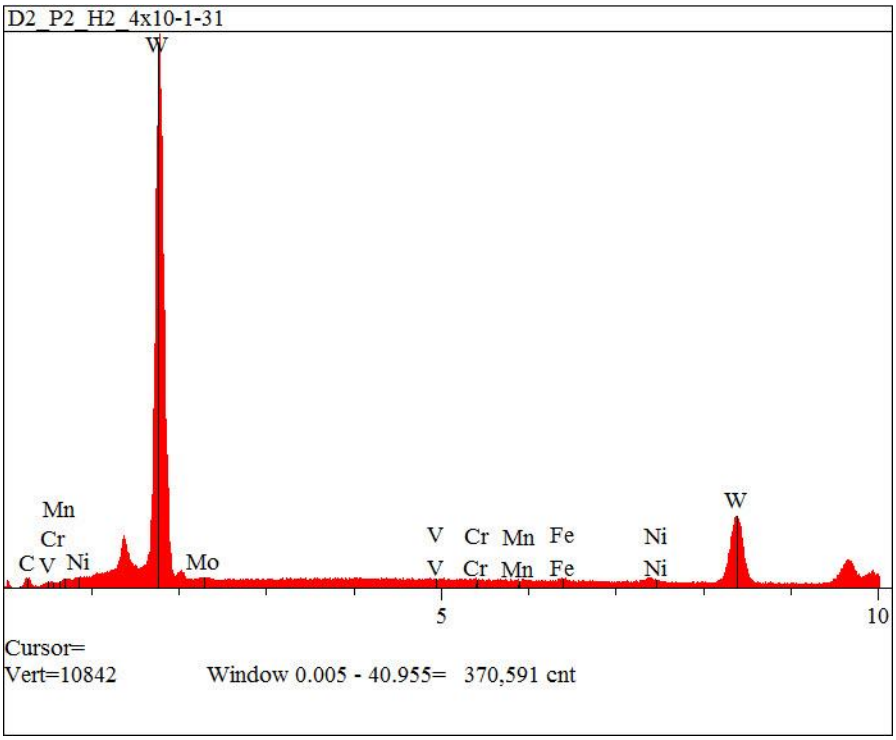
D2_P2_H2_4x10-1-31
W
Mn
Cr
C V Ni
Mo
V Cr Mn Fe
V Cr Mn Fe
Ni
Ni
W
5
10
Cursor=
Vert=10842
Window 0.005 - 40.955= 370,591 cnt

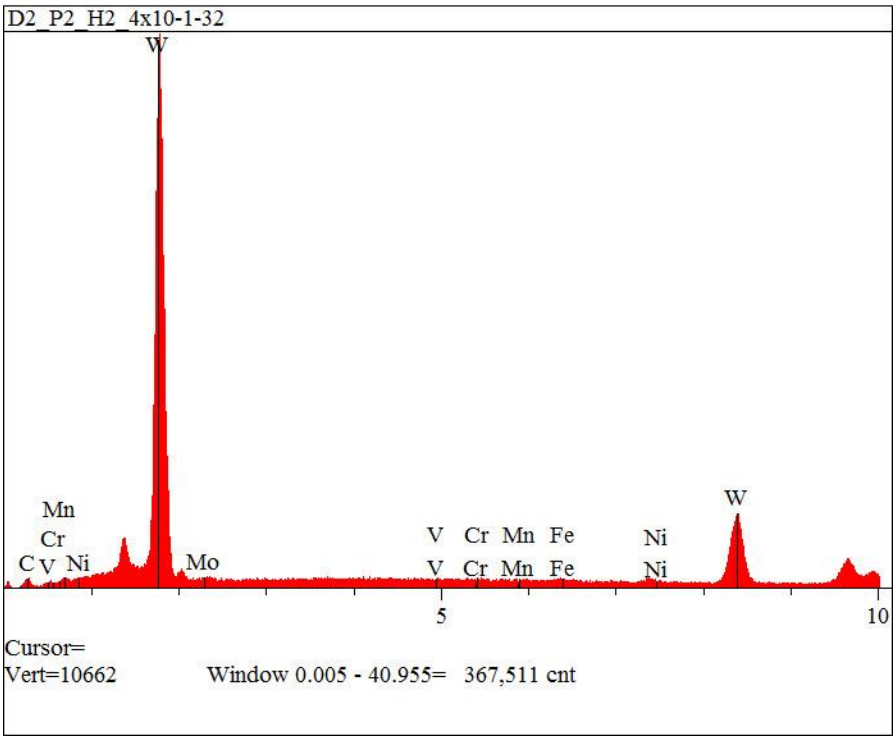
D2_P2_H2_4x10-1-32
W
Mn
Cr
C V Ni
Mo
V Cr Mn Fe
V Cr Mn Fe
Ni
Ni
W
5
10
Cursor=
Vert=10662
Window 0.005 - 40.955= 367,511 cnt

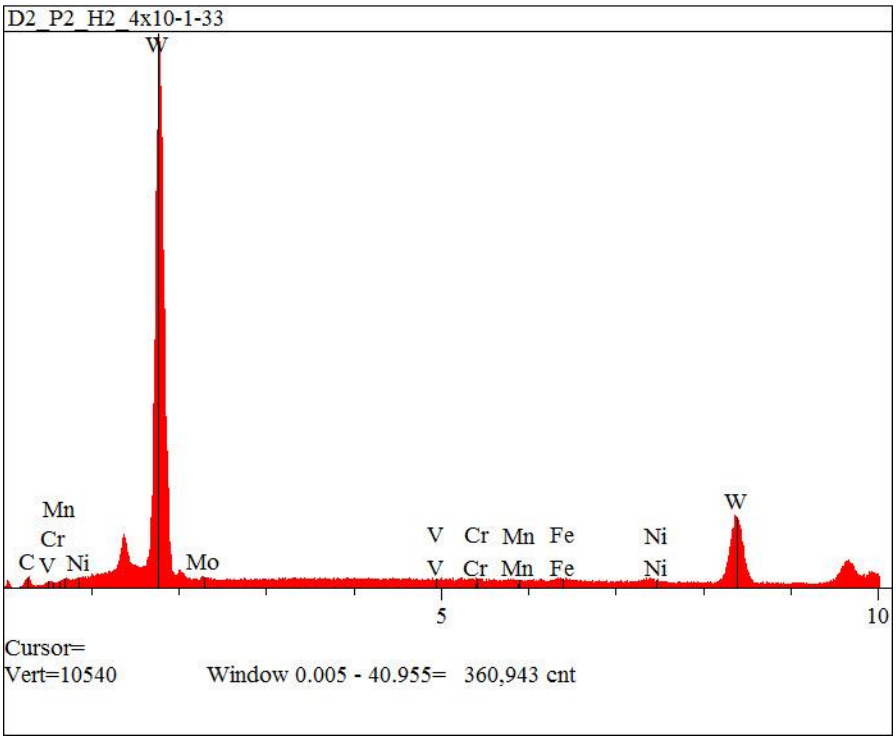
D2_P2_H2_4x10-1-33
W
Mn
Cr
C V Ni
Mo
V Cr Mn Fe Ni
V Cr Mn Fe Ni
W
5
10
Cursor=
Vert=10540
Window 0.005 - 40.955= 360,943 cnt

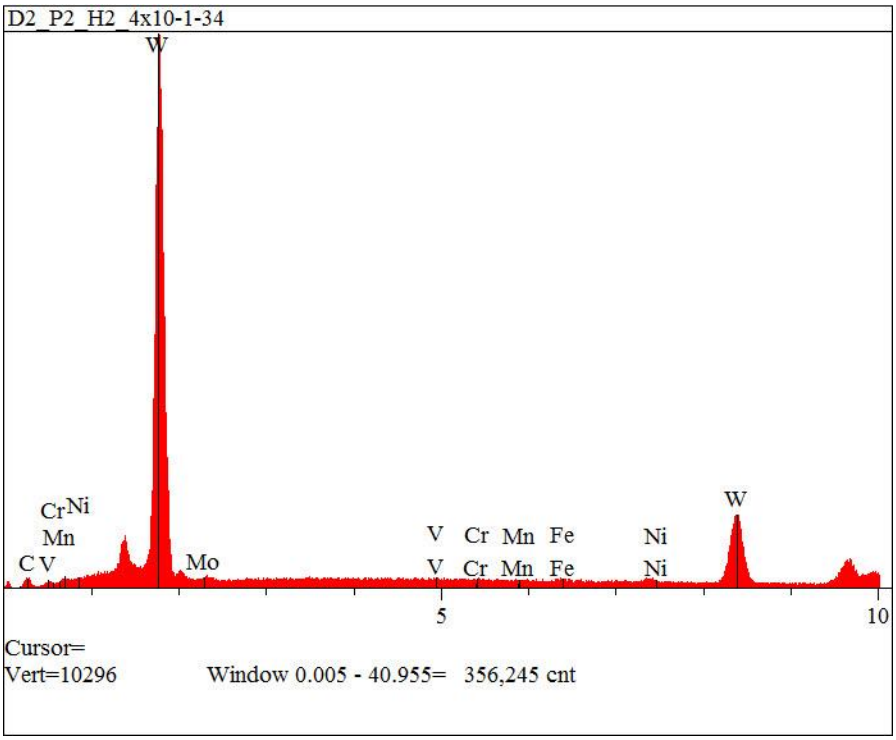
D2_P2_H2_4x10-1-34
W
Cr Ni
Mn
C V
Mo
V Cr Mn Fe Ni
V Cr Mn Fe Ni
W
5
10
Cursor=
Vert=10296
Window 0.005 - 40.955= 356,245 cnt

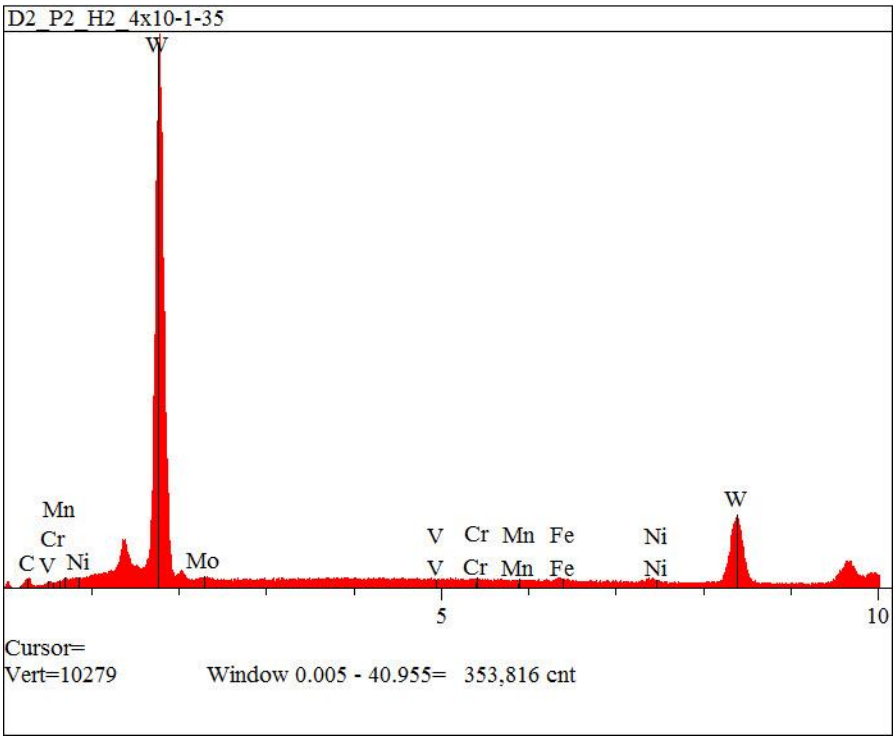
D2_P2_H2_4x10-1-35
W
Mn
Cr
C V Ni
Mo
V Cr Mn Fe
V Cr Mn Fe
Ni
Ni
W
5
10
Cursor=
Vert=10279
Window 0.005 - 40.955= 353,816 cnt

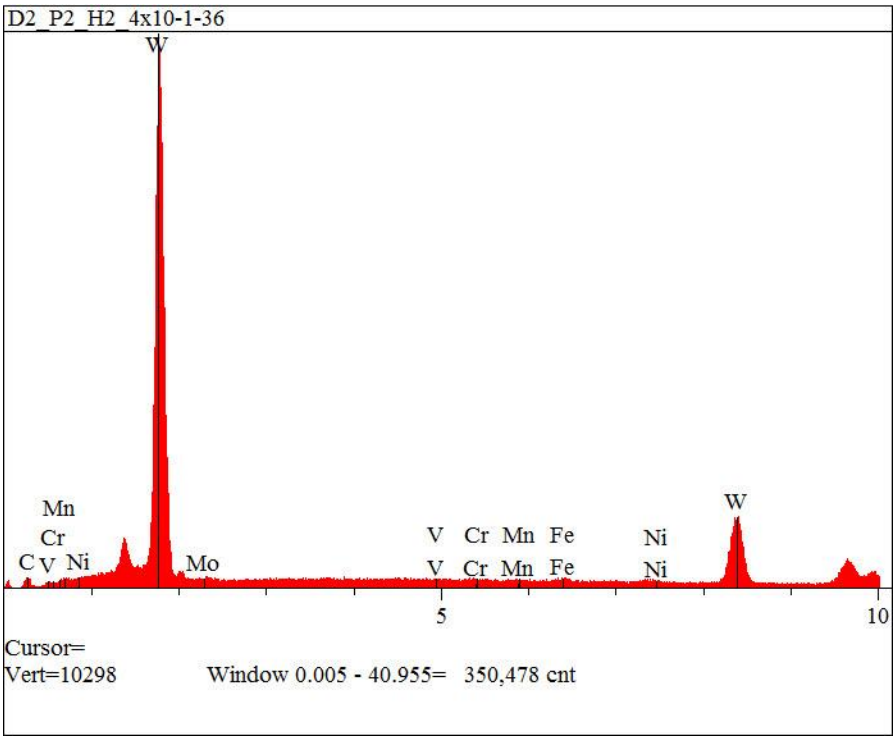
D2_P2_H2_4x10-1-36
W
Mn
Cr
C V Ni
Mo
V Cr Mn Fe
V Cr Mn Fe
Ni
Ni
W
5
10
Cursor=
Vert=10298
Window 0.005 - 40.955= 350,478 cnt

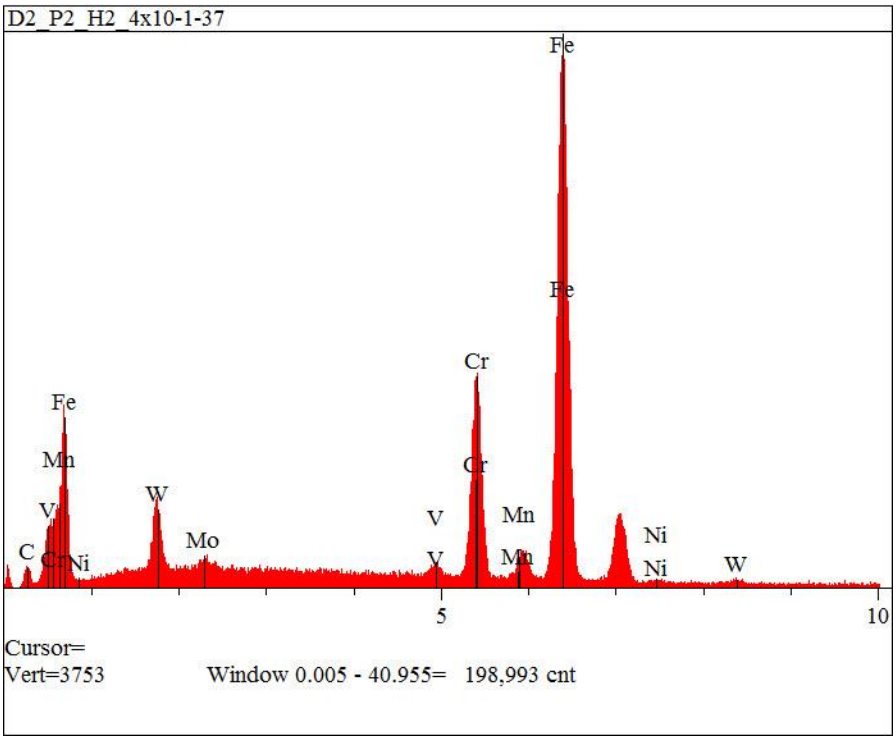
D2_P2_H2_4x10-1-37
Fe
Fe
Cr
Fe
Mn
Cr
W
V
V
Mn
Ni
C
Cr
Ni
Mo
V
Mn
Ni
W
5
10
Cursor=
Vert=3753
Window 0.005 - 40.955= 198,993 cnt

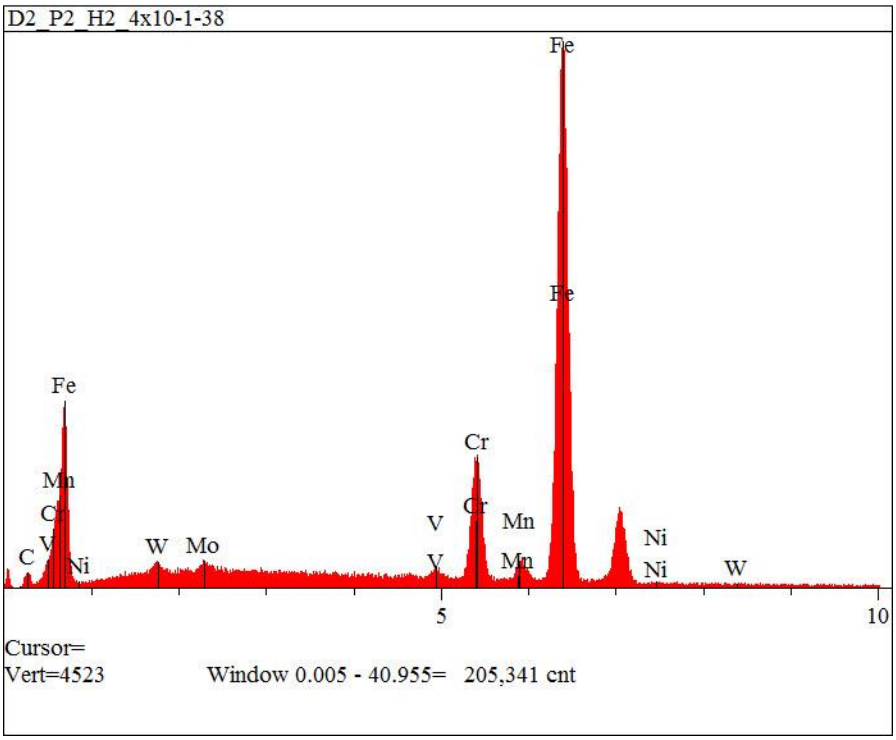
D2_P2_H2_4x10-1-38
Fe
Fe
Fe
Cr
Mn
Cr
V
Cr
V
Mn
Ni
C
V
Ni
W
Mo
V
Mn
Ni
W
5
10
Cursor=
Vert=4523
Window 0.005 - 40.955= 205,341 cnt

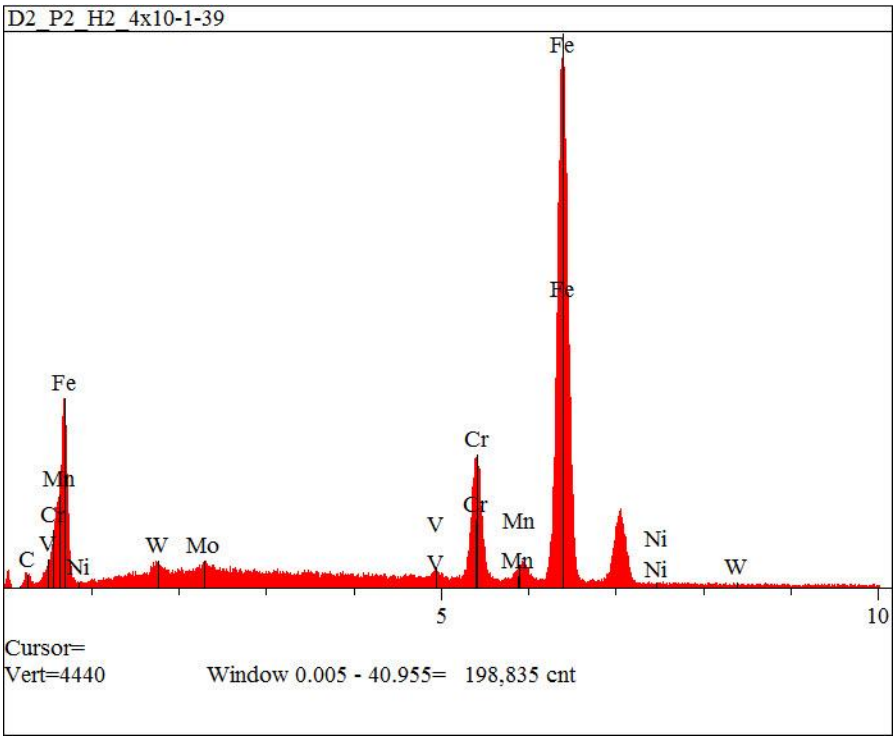
D2_P2_H2_4x10-1-39
Fe
Fe
Fe
Mn
Cr
V
C
Ni
W
Mo
V
Cr
Mn
V
Mn
Ni
Ni
W
5
10
Cursor=
Vert=4440
Window 0.005 - 40.955= 198,835 cnt

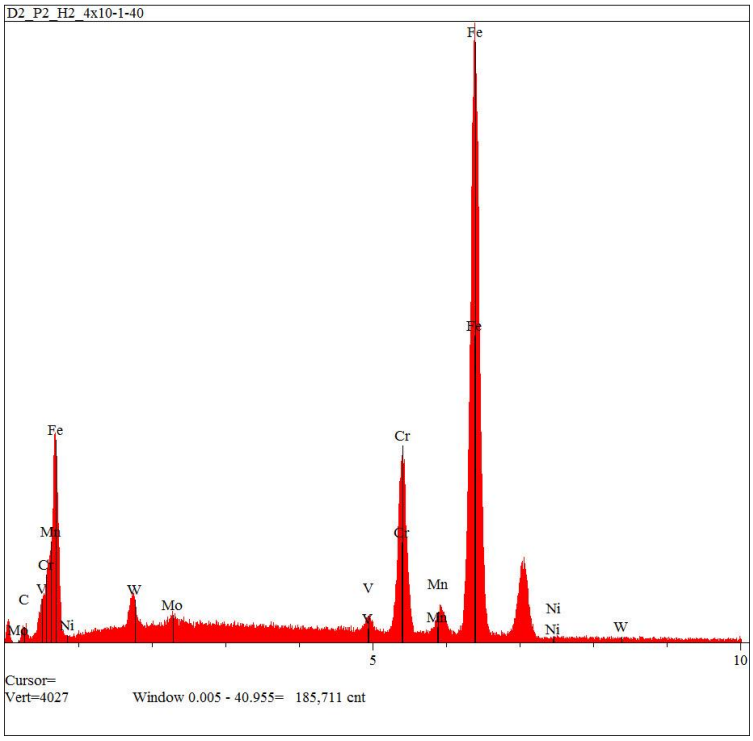
D2_P2_H2_4x10-1-40
Fe
Fe
Fe
Cr
Mn
Cr
C
V
W
Mo
Ni
V
Mn
Ni
W
5
10
Cursor=
Vert=4027
Window 0.005 - 40.955= 185,711 cnt

D2_P2_Marker EDS PLOTS

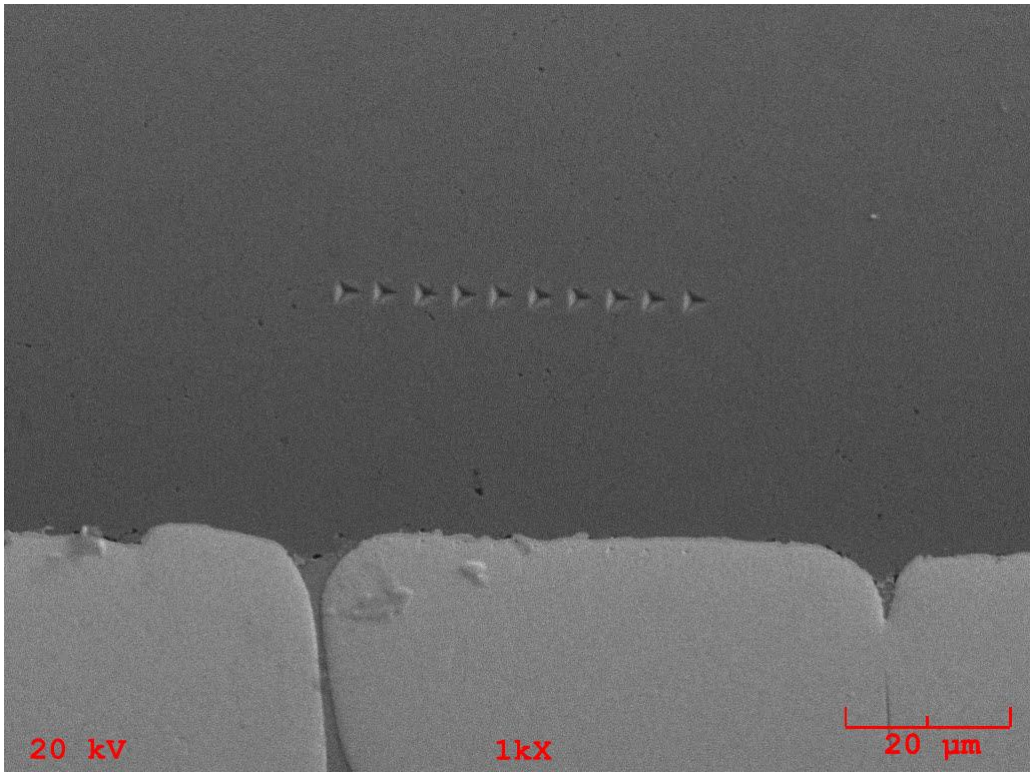

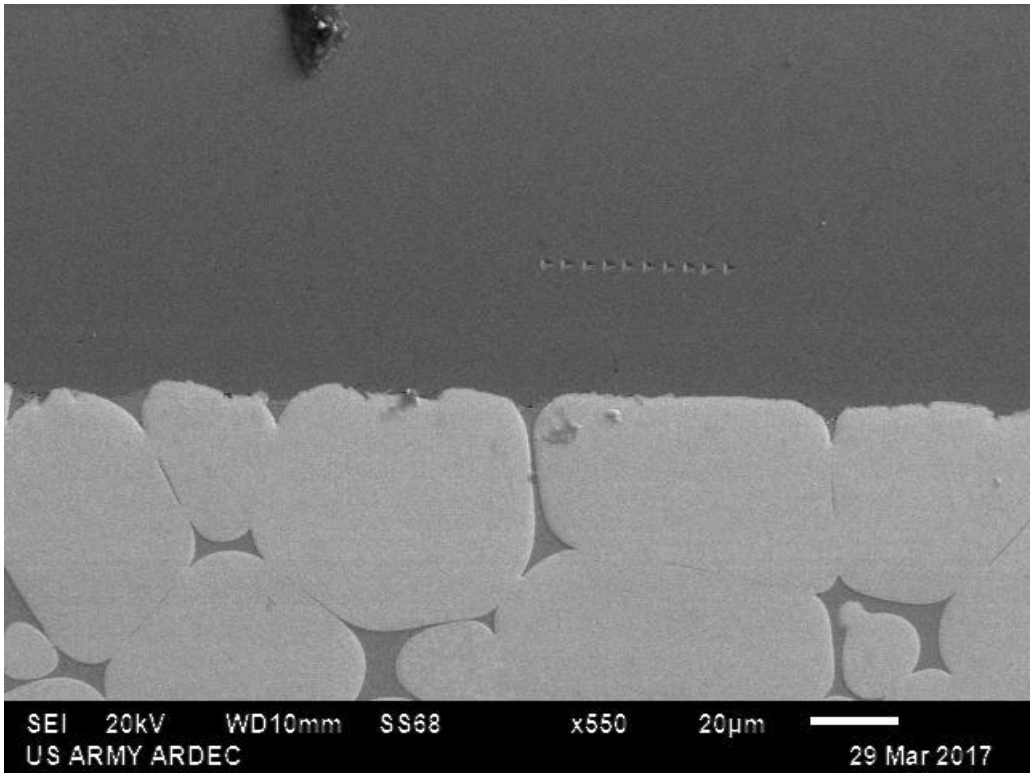

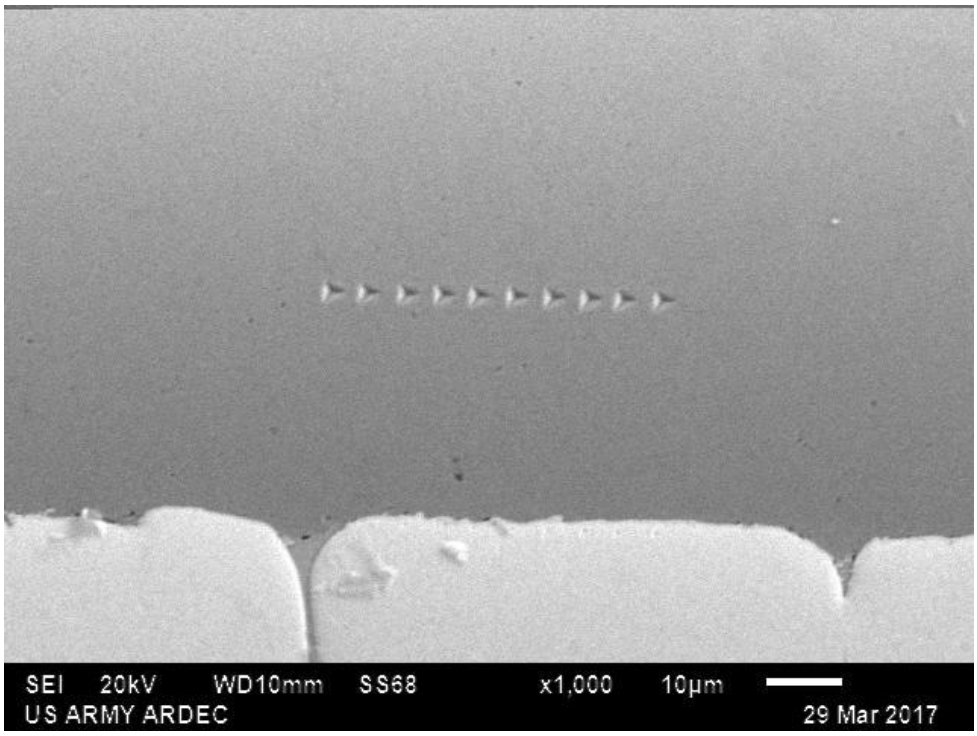
SEI 20kV WD10mm SS68 x1,000 10µm
US ARMY ARDEC
29 Mar 2017

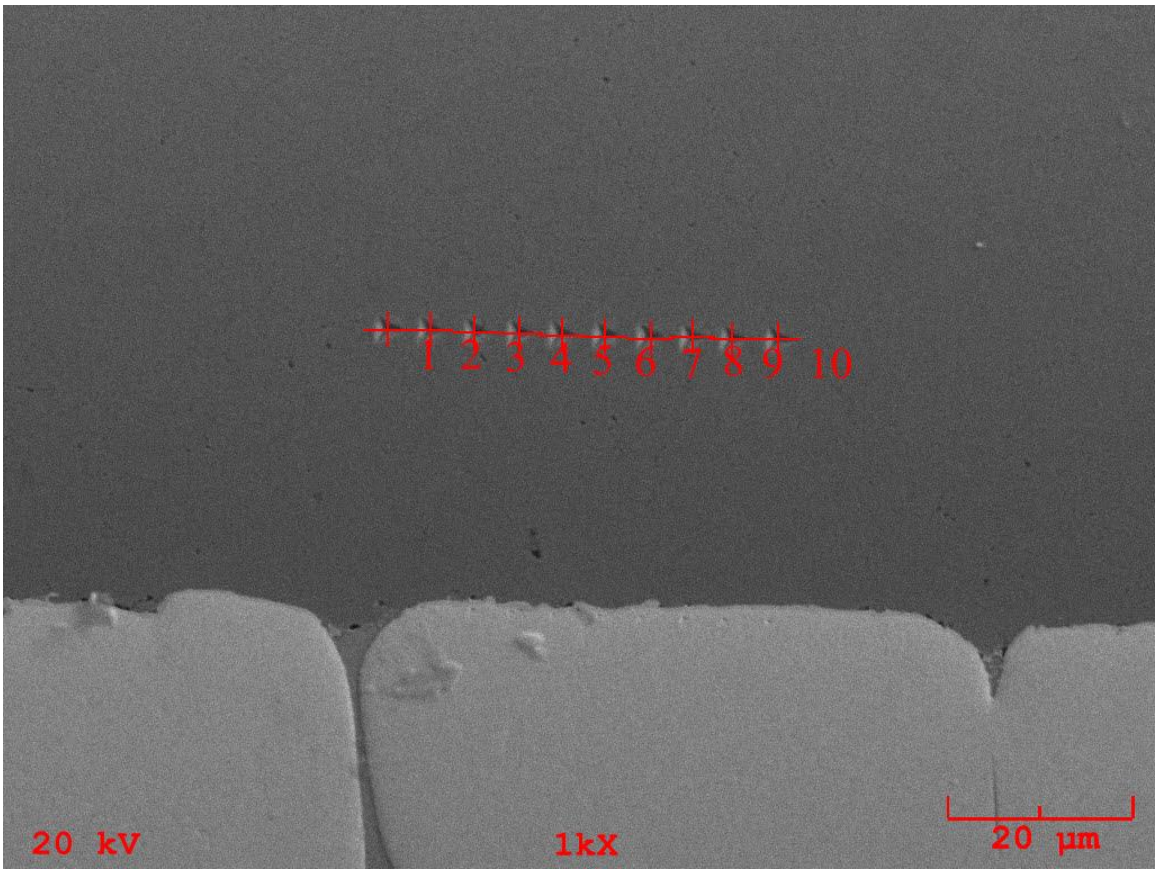
1 2 3 4 5 6 7 8 9 10
20 kV
1kX
20 µm

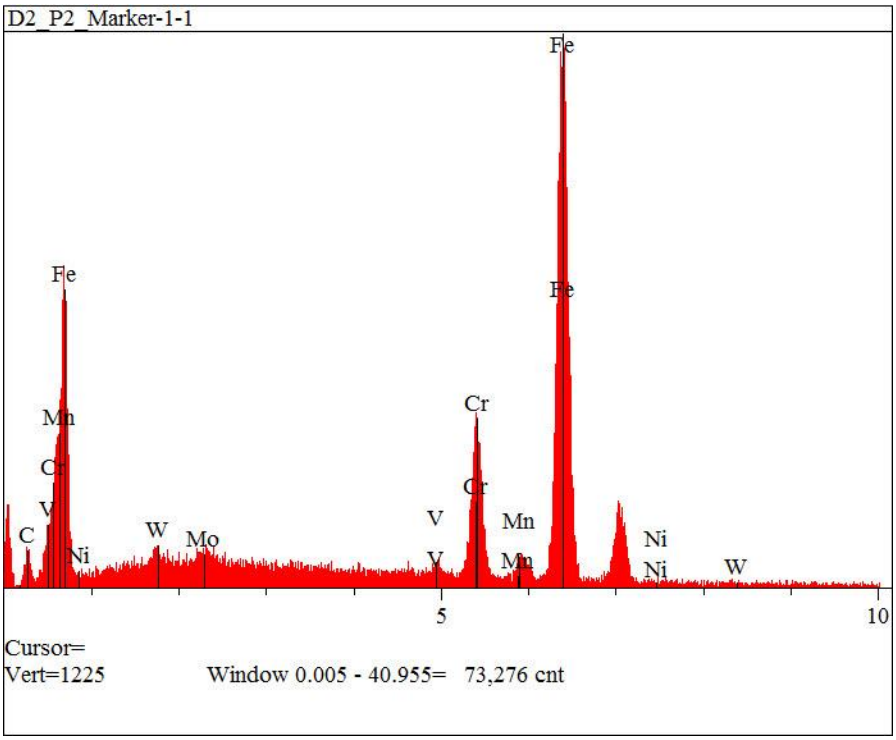
D2_P2_Marker-1-1
Fe
Fe
Mn
Cr
V
C
Ni
W
Mo
Cr
V
Mn
Ni
W
5
10
Cursor=
Vert=1225
Window 0.005 - 40.955= 73,276 cnt

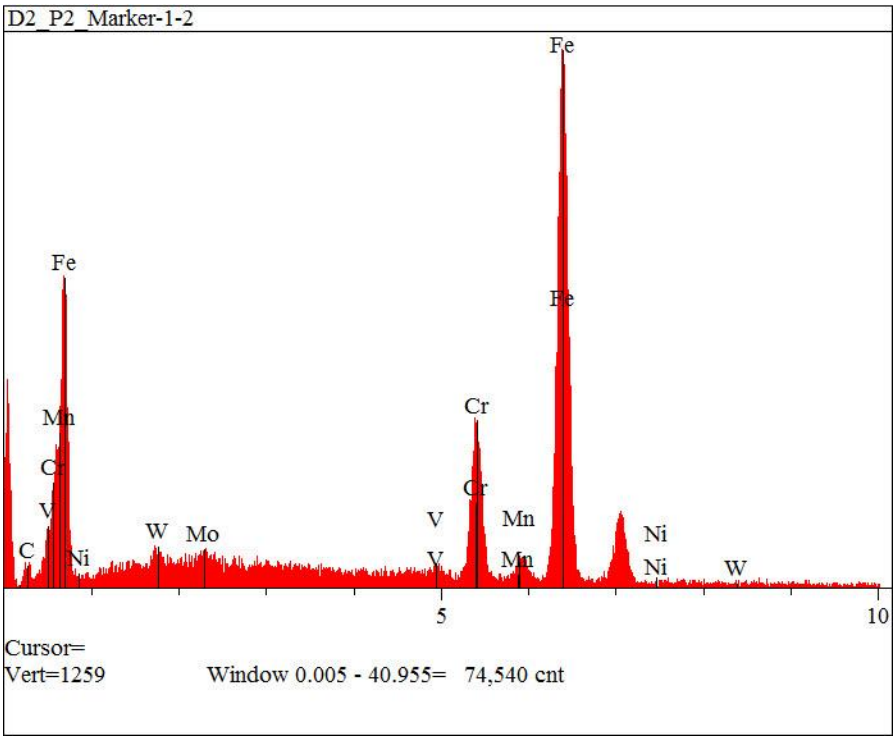
D2_P2_Marker-1-2
Fe
Fe
Mn
Cr
V
C
Ni
W
Mo
Cr
V
Mn
Ni
W
5
10
Cursor=
Vert=1259
Window 0.005 - 40.955= 74,540 cnt

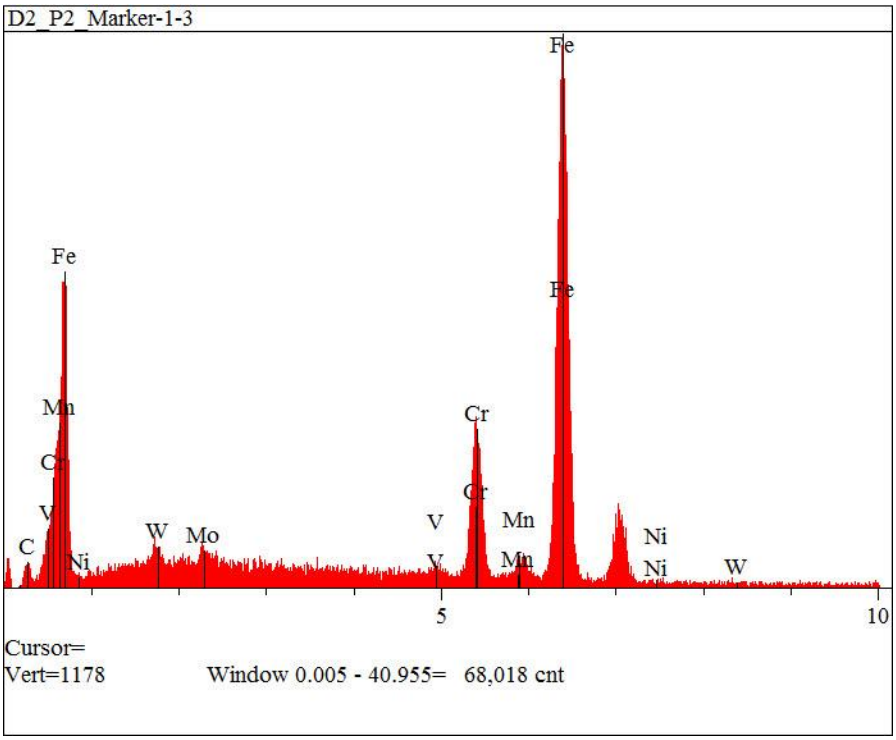
D2_P2_Marker-1-3
Fe
Fe
Mn
Cr
Cr
V
C
W
Mo
Ni
V
Cr
Mn
V
Mn
Ni
Ni
W
5
10
Cursor=
Vert=1178
Window 0.005 - 40.955= 68,018 cnt

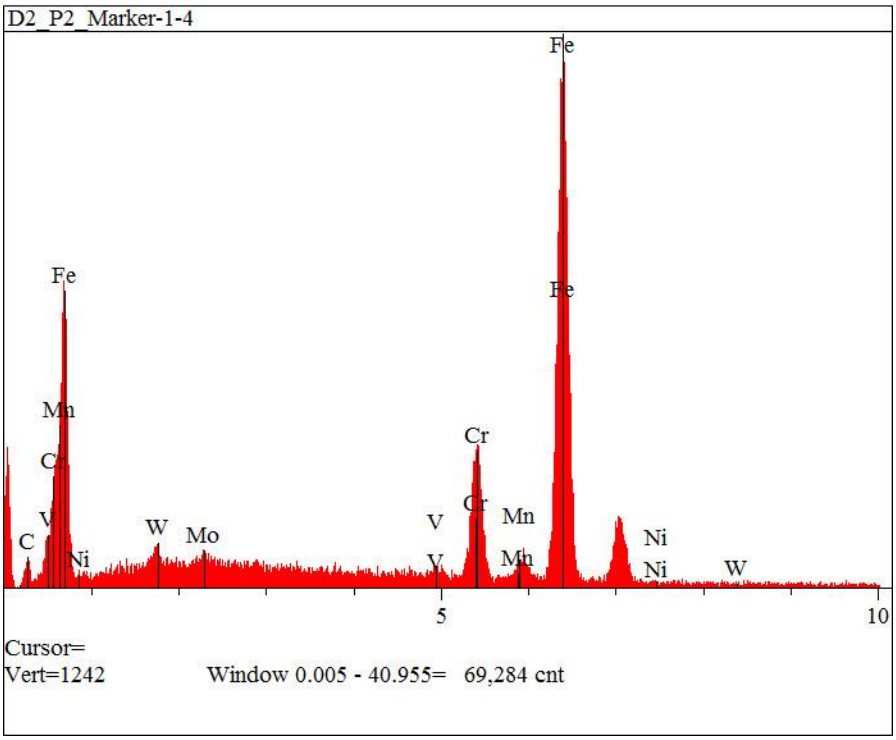
D2_P2_Marker-1-4
Fe
Fe
Mn
Cr
Cr
V
C
W
Mo
Ni
V
Cr
Mn
V
Mn
Ni
Ni
W
5
10
Cursor=
Vert=1242
Window 0.005 - 40.955= 69,284 cnt

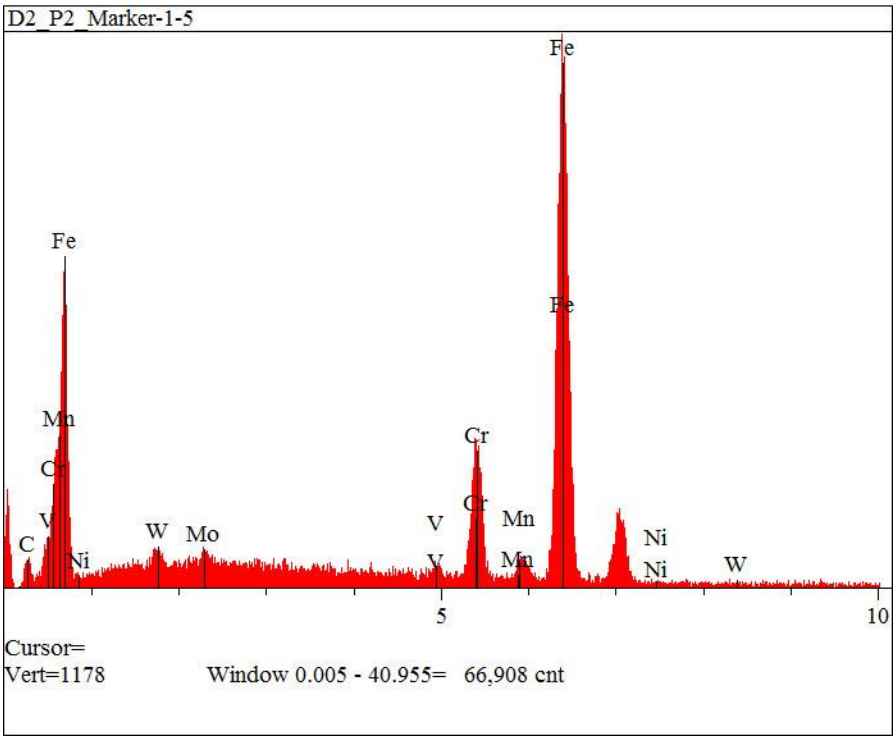
D2_P2_Marker-1-5
Fe
Fe
Mn
Cr
V
C
Ni
W
Mo
V
Cr
Mn
V
Mn
Ni
Ni
W
5
10
Cursor=
Vert=1178
Window 0.005 - 40.955= 66,908 cnt

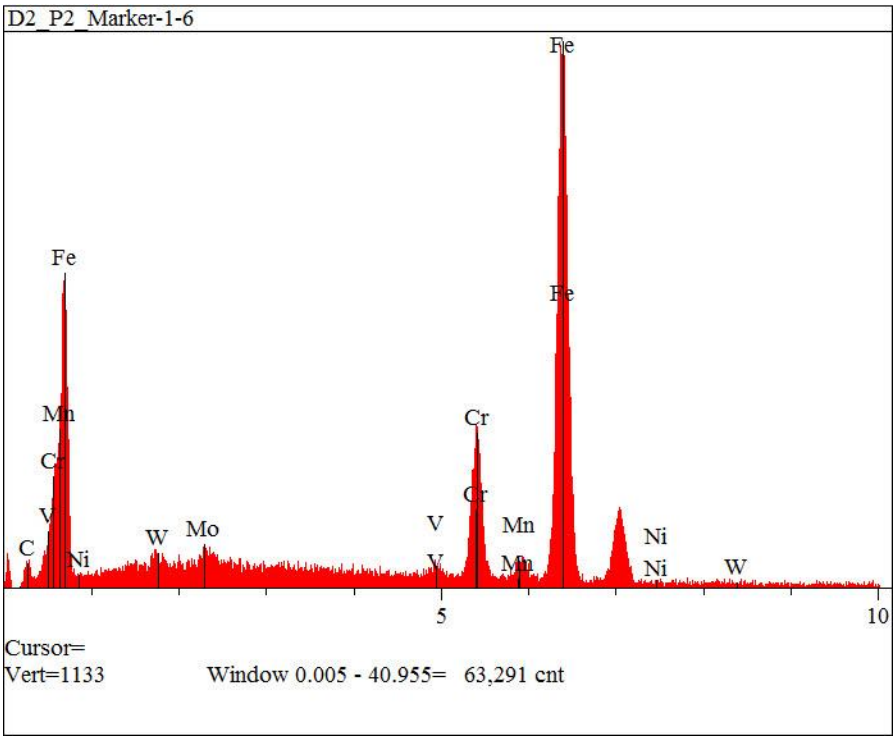
D2_P2_Marker-1-6
Fe
Fe
Mn
Cr
V
C
Ni
W
Mo
V
Cr
Mn
V
Mn
Ni
Ni
W
5
10
Cursor=
Vert=1133
Window 0.005 - 40.955= 63,291 cnt

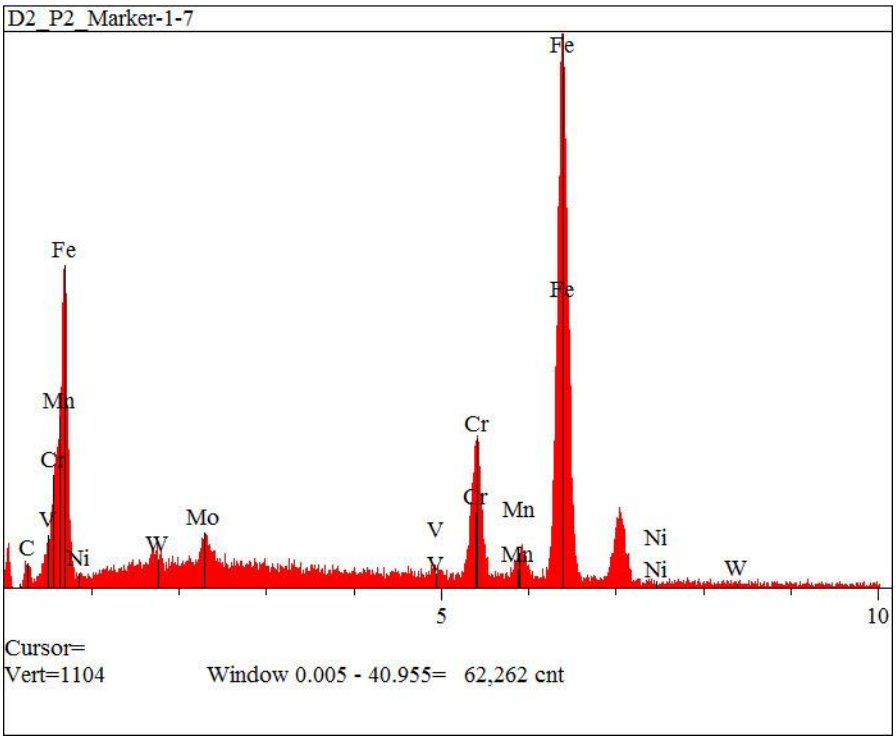
D2_P2_Marker-1-7
Fe
Fe
Mn
Cr
Cr
V
Mo
C
Ni
W
V
V
Cr
Mn
Mn
Ni
Ni
W
5
10
Cursor=
Vert=1104
Window 0.005 - 40.955= 62,262 cnt

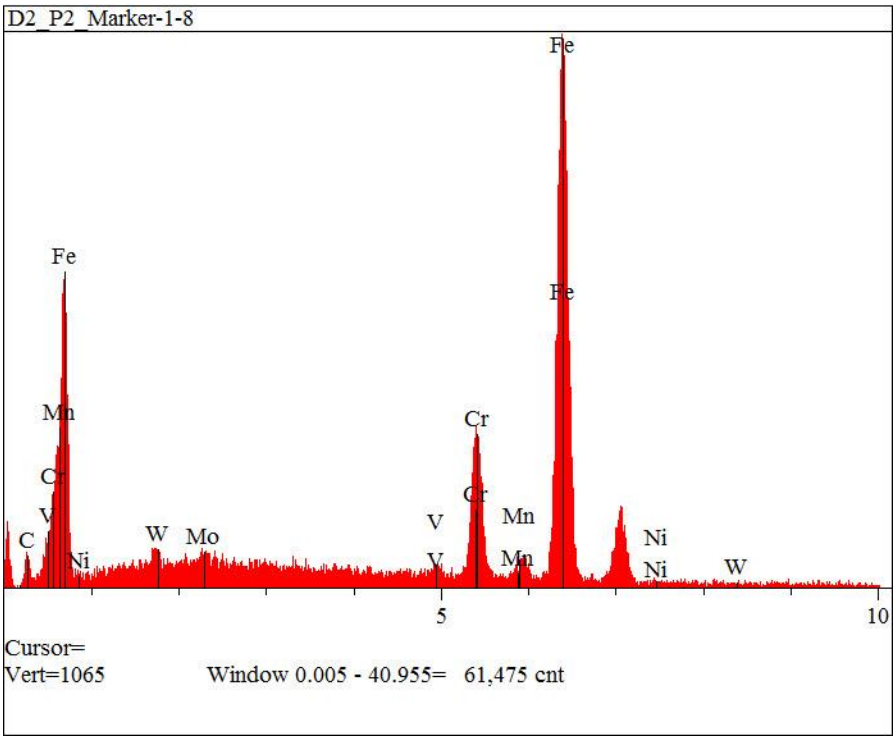
D2_P2_Marker-1-8
Fe
Fe
Mn
Cr
Cr
V
W
Mo
C
Ni
V
V
Cr
Mn
Mn
Ni
Ni
W
5
10
Cursor=
Vert=1065
Window 0.005 - 40.955= 61,475 cnt

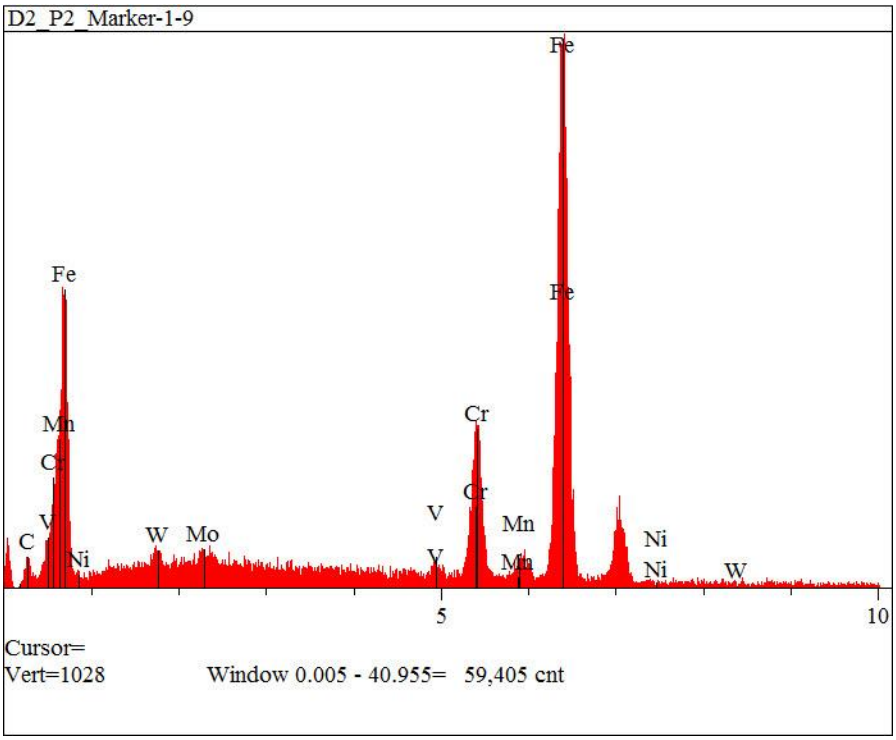
D2_P2_Marker-1-9
Fe
Fe
Mn
Cr
V
C
Ni
W
Mo
Cr
V
Mn
Ni
Ni
W
5
10
Cursor=
Vert=1028
Window 0.005 - 40.955= 59,405 cnt

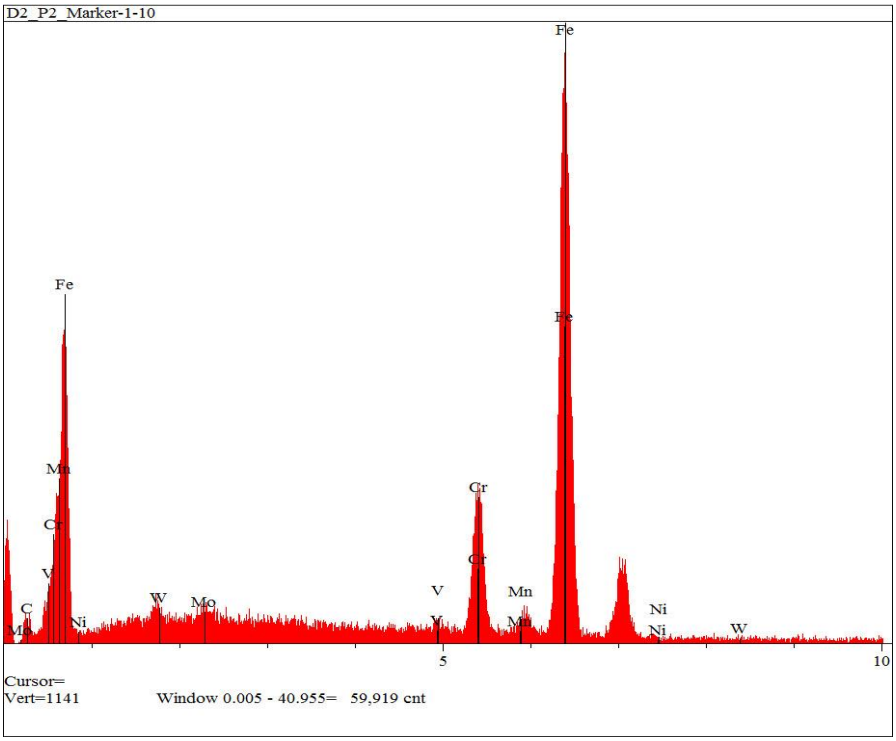
D2_P2_Marker-1-10
Fe
Fe
Mn
Cr
V
C
Ni
W
Mo
Cr
V
Mn
Ni
Ni
W
5
10
Cursor=
Vert=1141
Window 0.005 - 40.955= 59,919 cnt

D2_P2_0degree1-10 EDS Plots

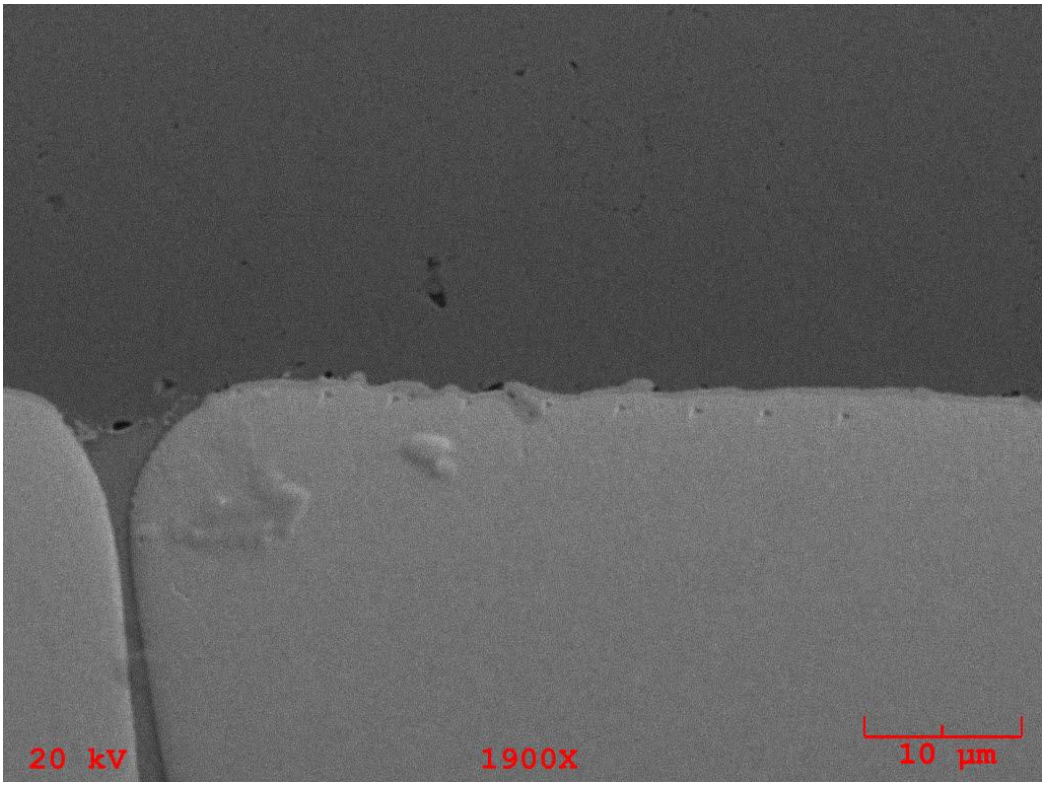

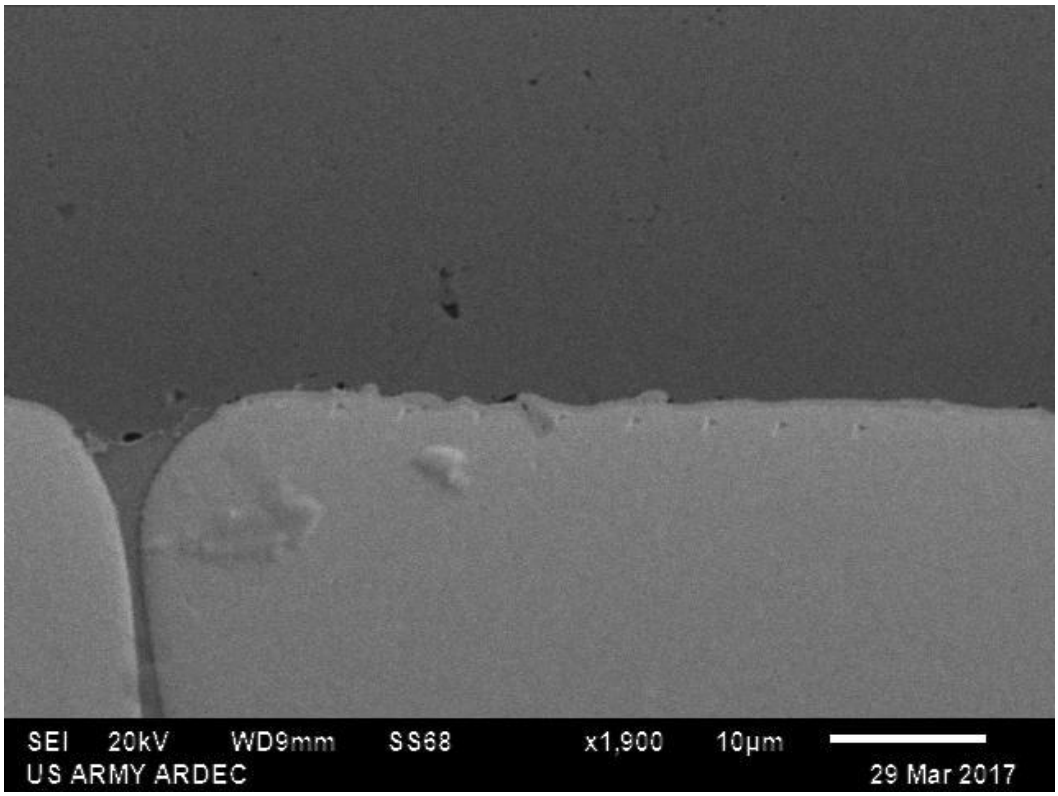

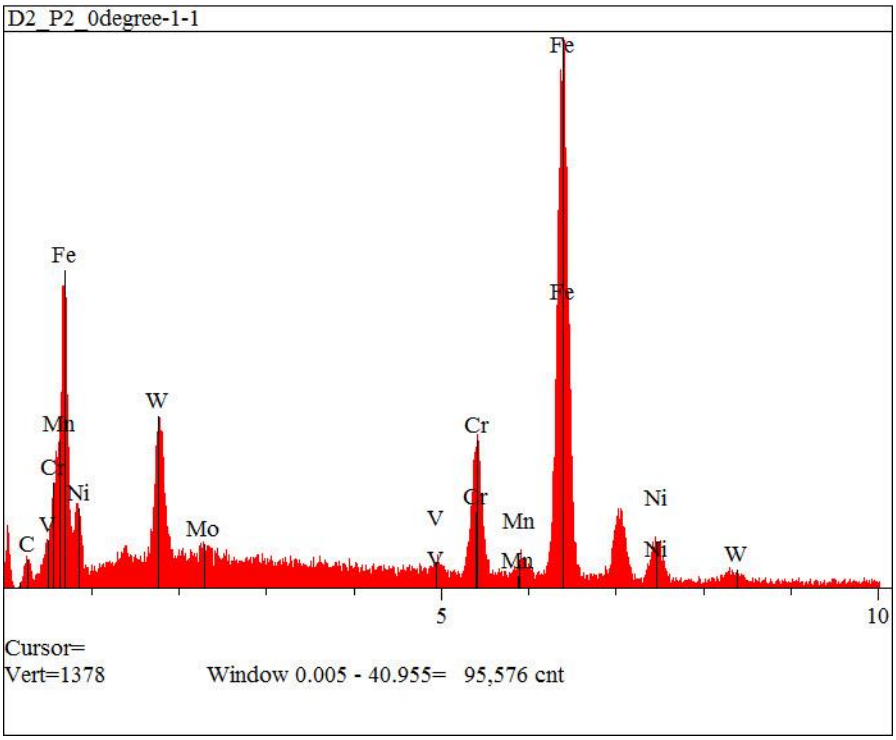
D2_P2_0degree-1-1
Fe
Fe
W
Mn
Cr
Cr
Ni
Ni
V
C
Mo
V
Mn
Mn
W
5
10
Cursor=
Vert=1378
Window 0.005 - 40.955= 95,576 cnt

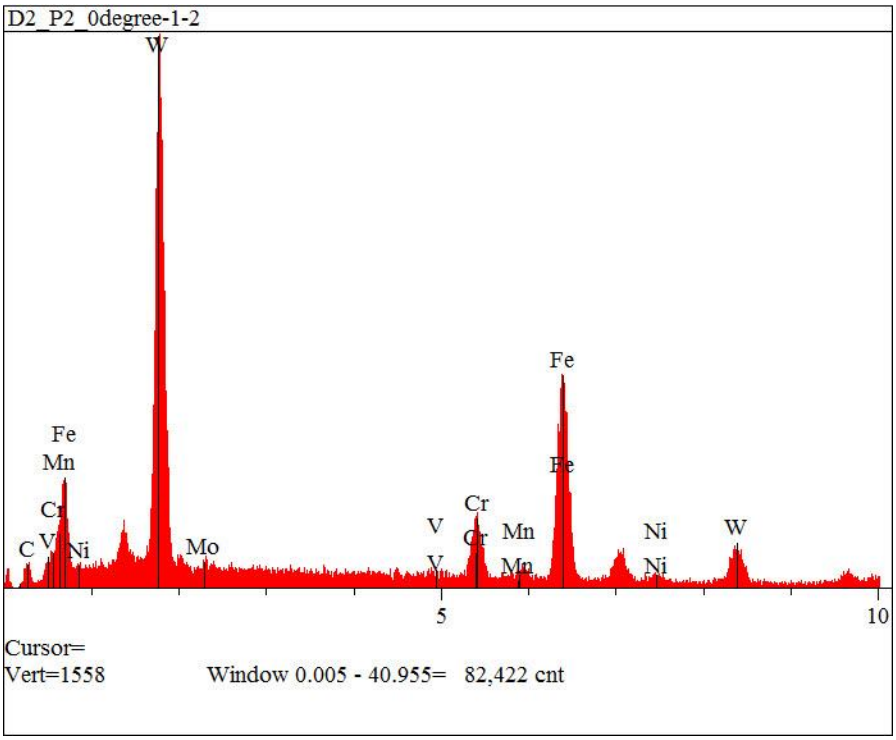
D2_P2_0degree-1-2
W
Fe
Fe
Mn
Fe
Cr
Cr
V
Mn
Ni
W
C
V
Ni
Mo
V
Mn
Ni
5
10
Cursor=
Vert=1558
Window 0.005 - 40.955= 82,422 cnt

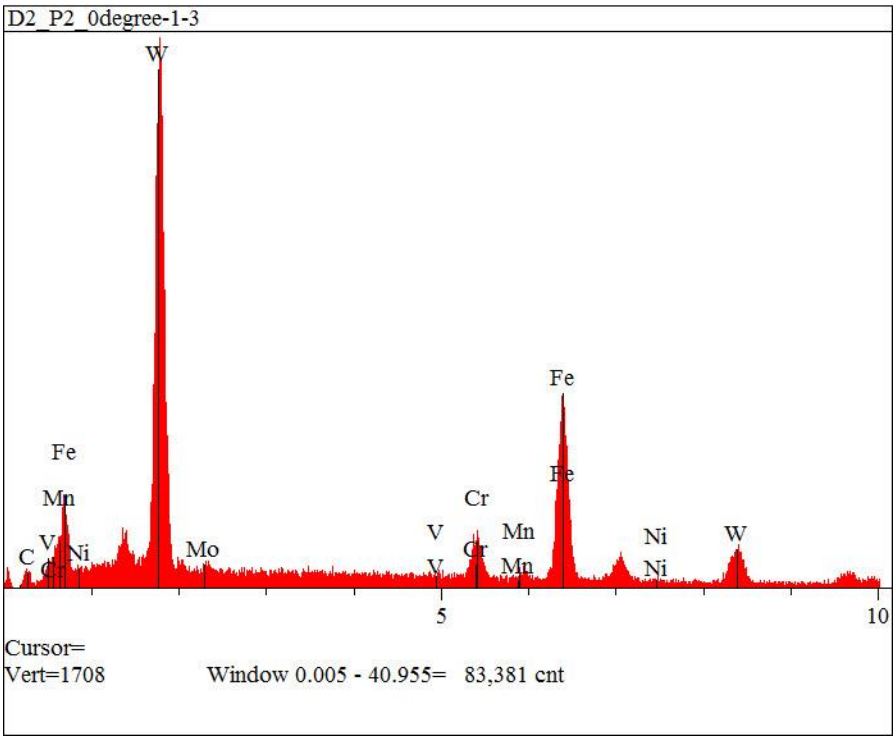
D2_P2_0degree-1-3
W
Fe
Mn
Cr
V
Ni
Mo
C
Fe
Mn
V
Cr
Mn
Ni
W
Ni
5
10
Cursor=
Vert=1708
Window 0.005 - 40.955= 83,381 cnt

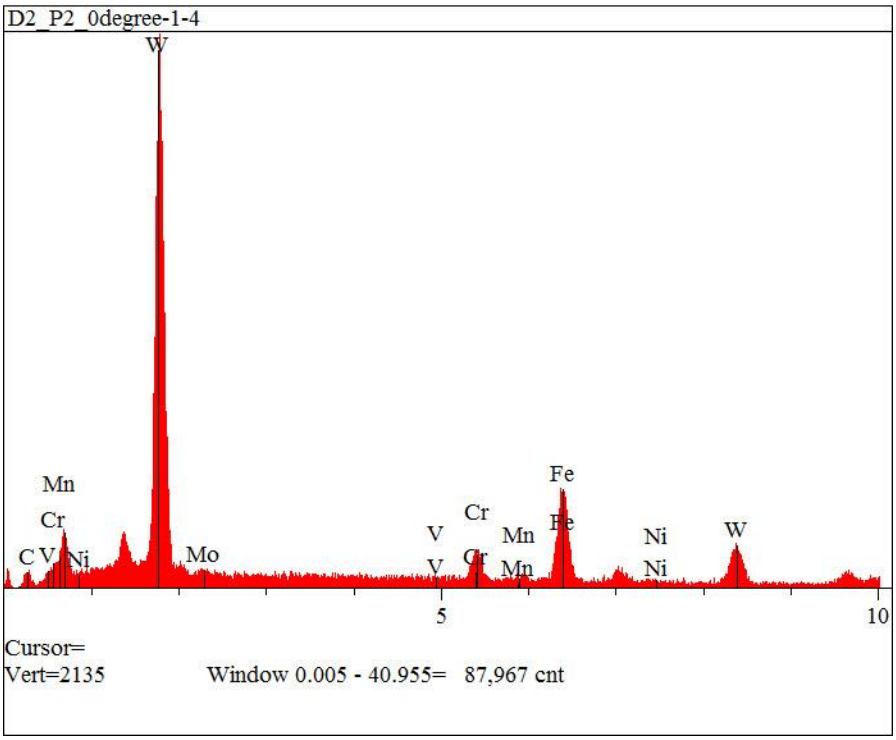
D2_P2_0degree-1-4
W
Mn
Cr
C
V
Ni
Mo
Fe
Cr
Fe
V
Mn
Ni
W
Mn
Ni
5
10
Cursor=
Vert=2135
Window 0.005 - 40.955= 87,967 cnt

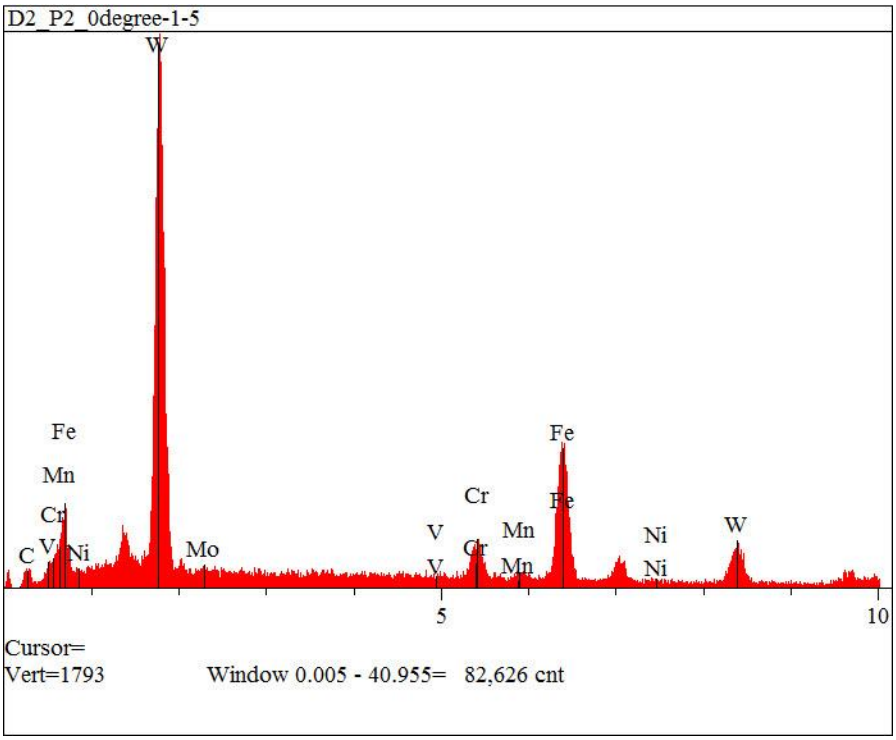
D2_P2_0degree-1-5
W
Fe
Mn
Cr
V
C
Ni
Mo
V
Cr
Mn
Fe
Cr
Fe
Mn
Ni
Ni
W
5
10
Cursor=
Vert=1793
Window 0.005 - 40.955= 82,626 cnt

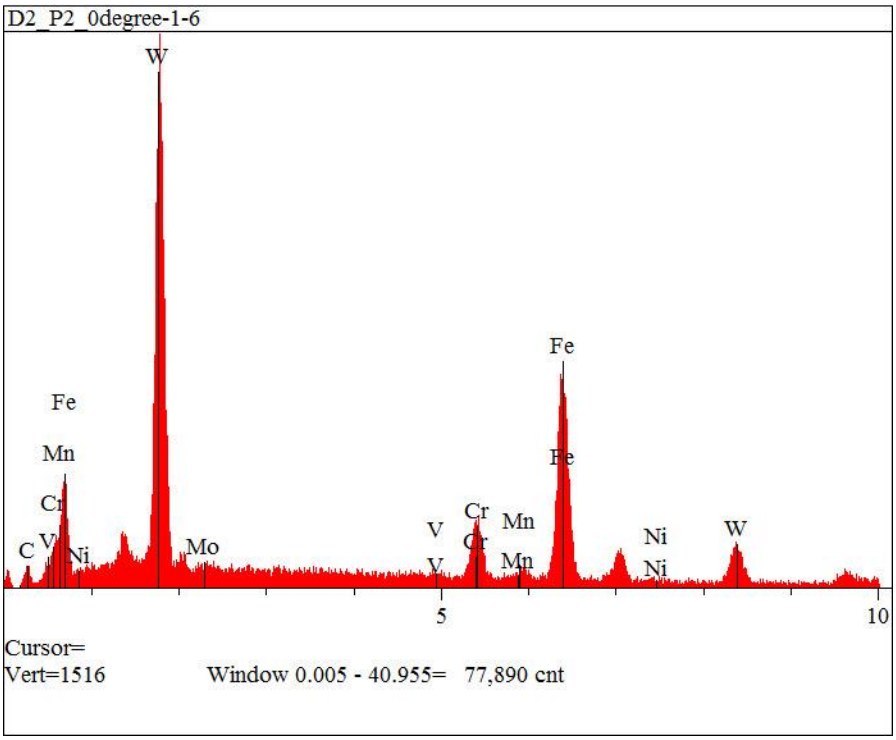
D2_P2_0degree-1-6
W
Fe
Mn
Cr
V
C
Ni
Mo
V
Cr
Mn
Fe
Cr
Fe
Mn
Ni
Ni
W
5
10
Cursor=
Vert=1516
Window 0.005 - 40.955= 77,890 cnt

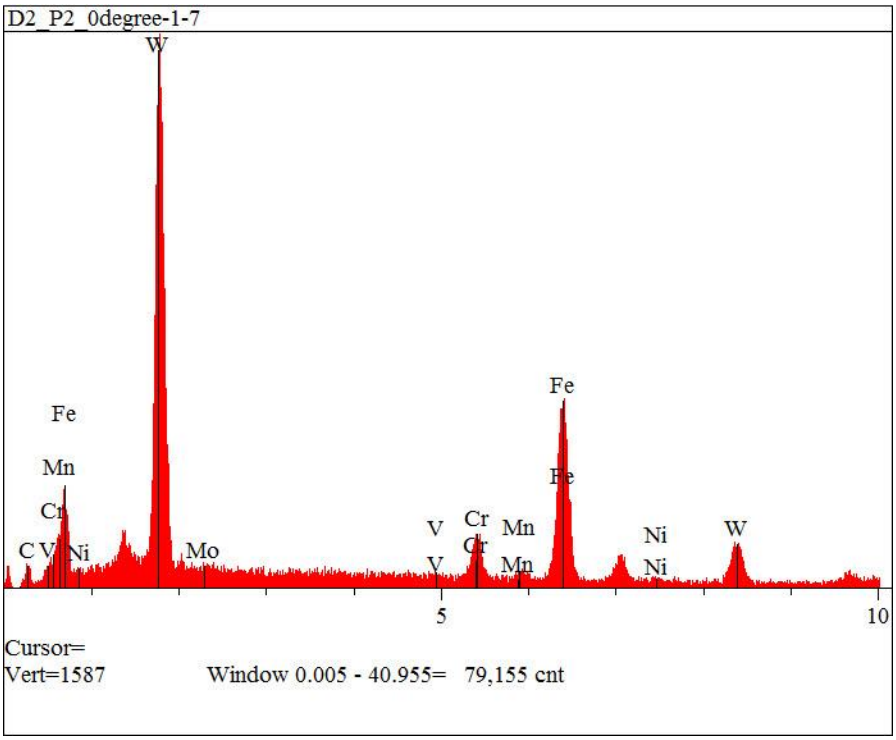
D2_P2_0degree-1-7
W
Fe
Mn
Cr
C V Ni
Mo
V
V
Cr
Cr
Mn
Mn
Fe
Fe
Ni
Ni
W
5
10
Cursor=
Vert=1587
Window 0.005 - 40.955= 79,155 cnt

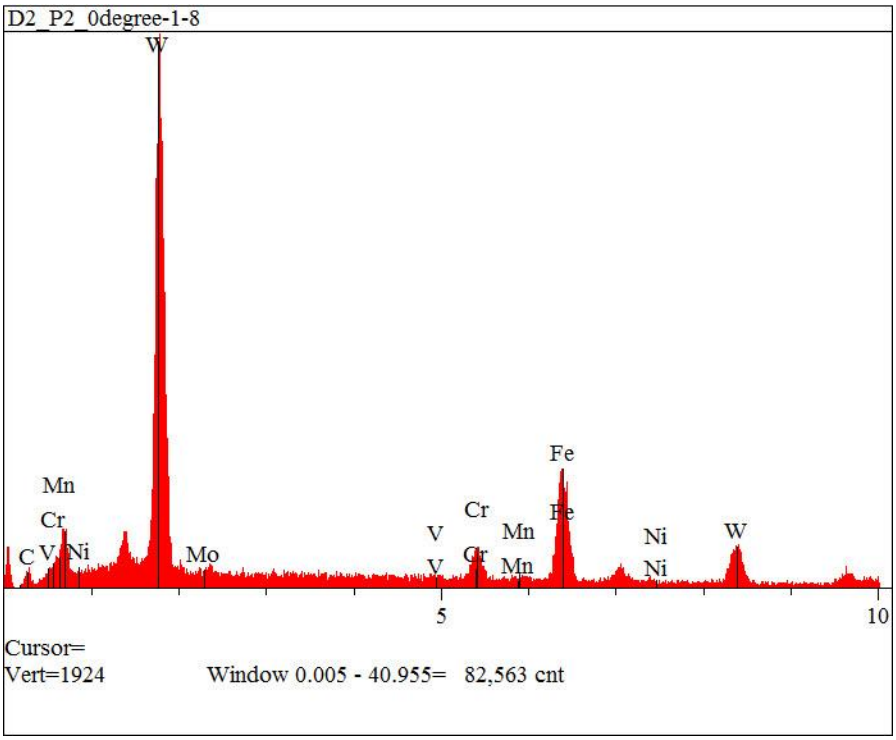
D2_P2_0degree-1-8
W
Mn
Cr
C V Ni
Mo
V
V
Cr
Cr
Mn
Mn
Fe
Fe
Ni
Ni
W
5
10
Cursor=
Vert=1924
Window 0.005 - 40.955= 82,563 cnt

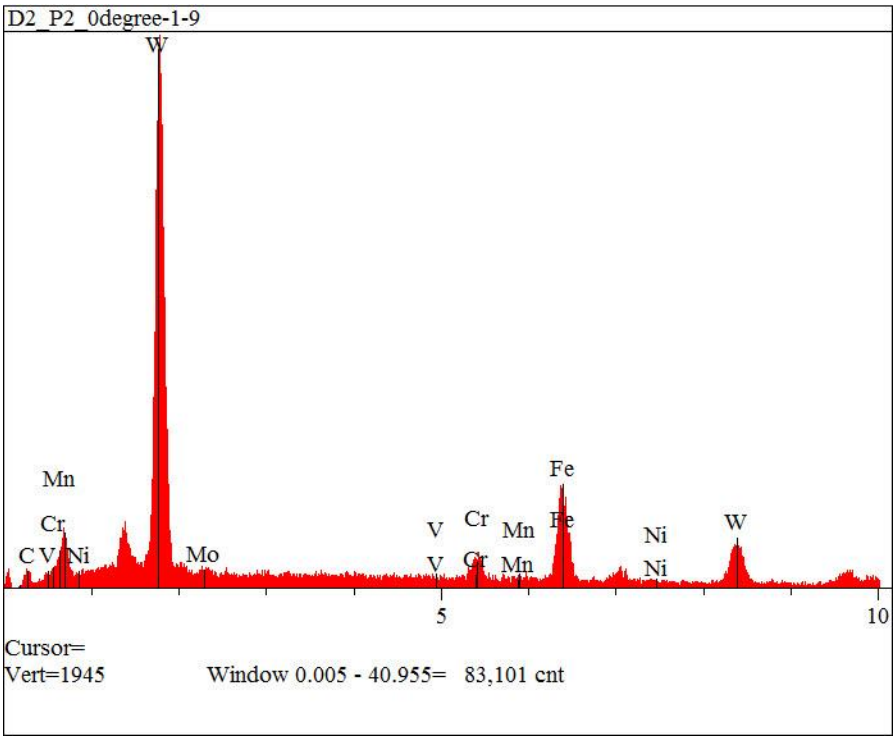
D2_P2_0degree-1-9
W
Mn
Cr
C V Ni
Mo
V
V
Cr
Cr
Mn
Mn
Fe
Fe
Ni
Ni
W
5
10
Cursor=
Vert=1945
Window 0.005 - 40.955= 83,101 cnt

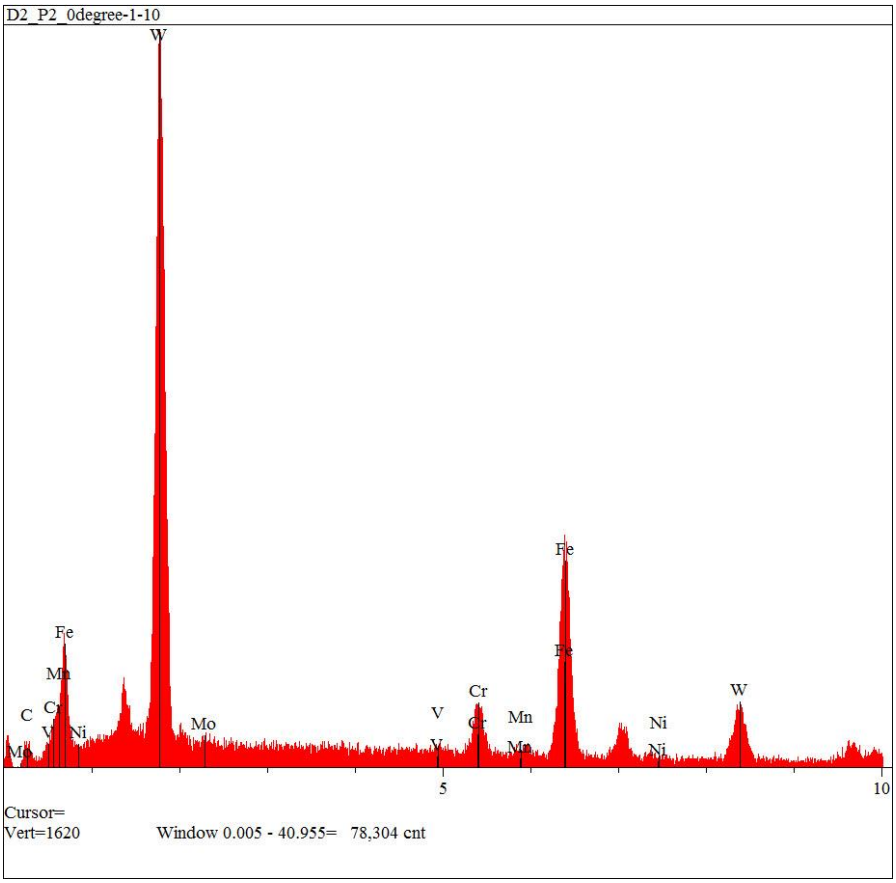
D2_P2_0degree-1-10
W
Fe
Mn
Cr
C
V
Ni
Mo
V
Cr
Cr
Mn
Mn
Fe
Fe
Ni
Ni
W
5
10
Cursor=
Vert=1620
Window 0.005 - 40.955= 78,304 cnt

D2_P2_5degree 1-10 EDS Plots

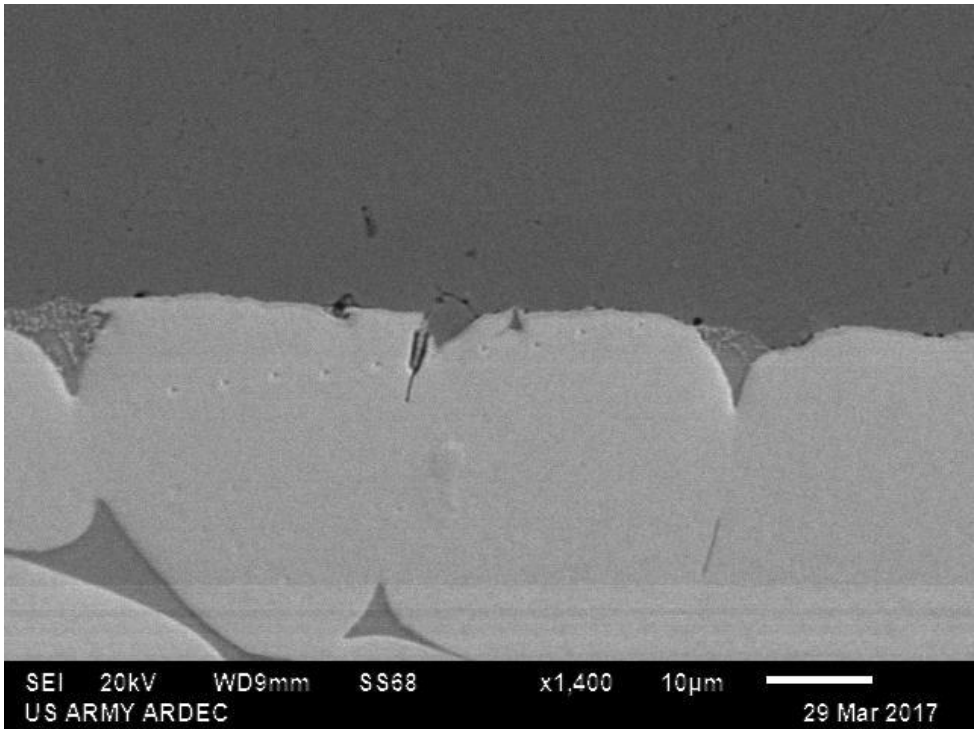

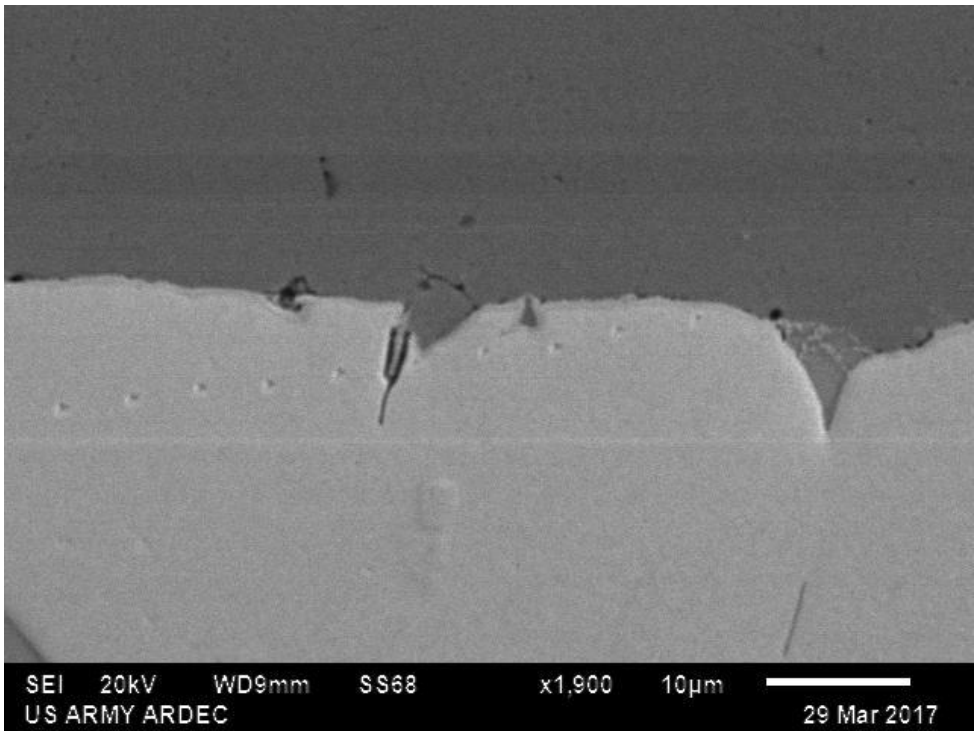

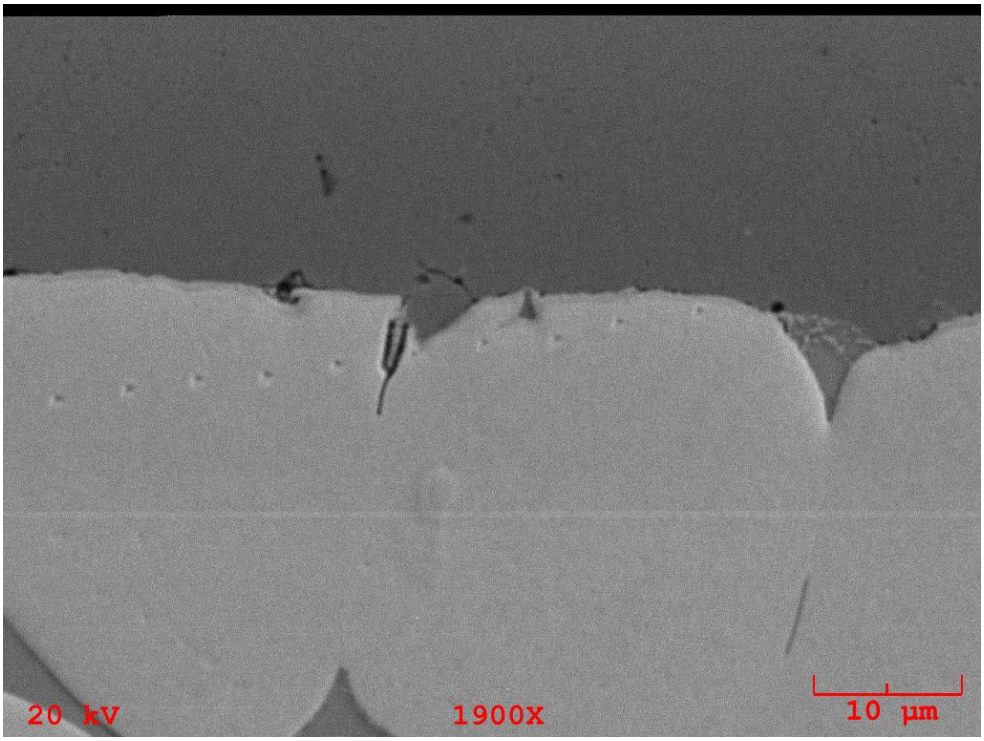
20 kV
1900X
10 µm

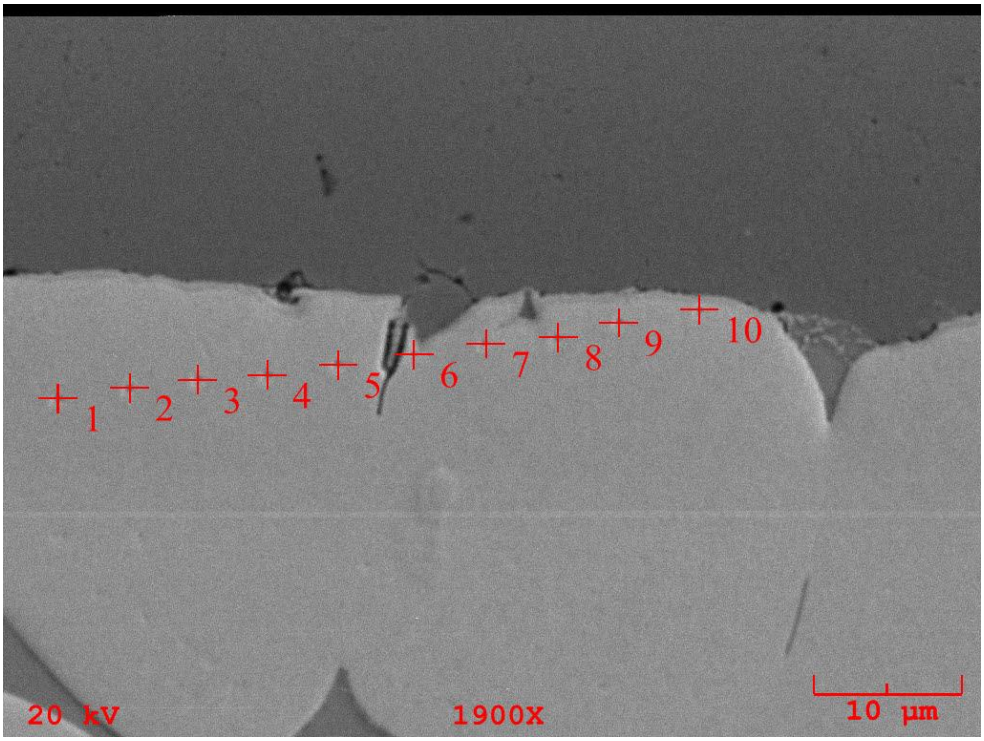
1
2
3
4
5
6
7
8
9
10
20 kV
1900X
10 µm

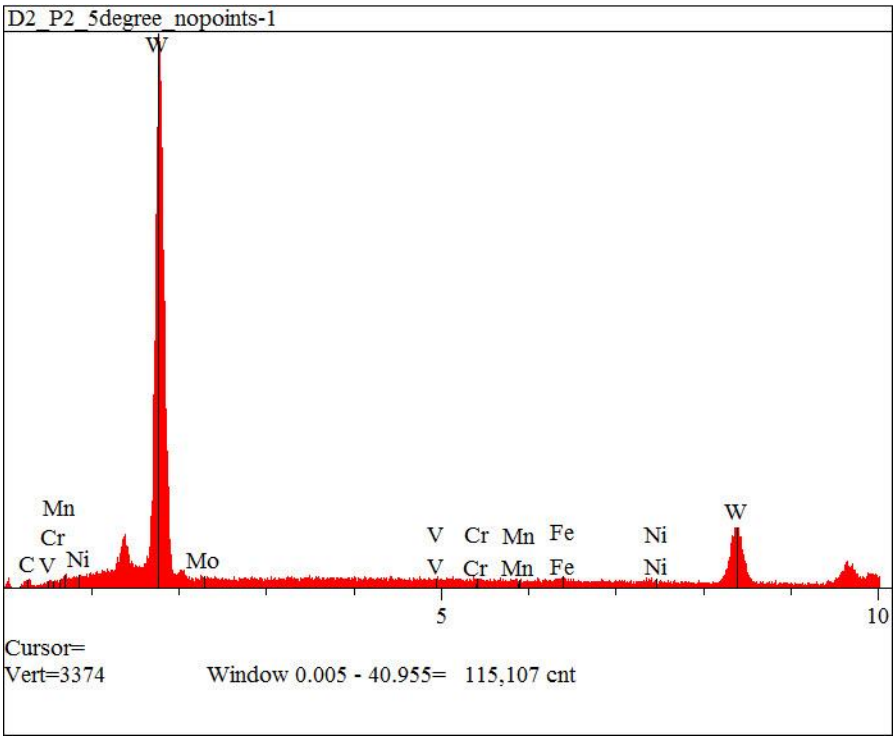
D2_P2_5degree_nopoints-1
W
Mn
Cr
C V Ni
Mo
V Cr Mn Fe
V Cr Mn Fe
Ni
Ni
W
5
10
Cursor=
Vert=3374
Window 0.005 - 40.955= 115,107 cnt

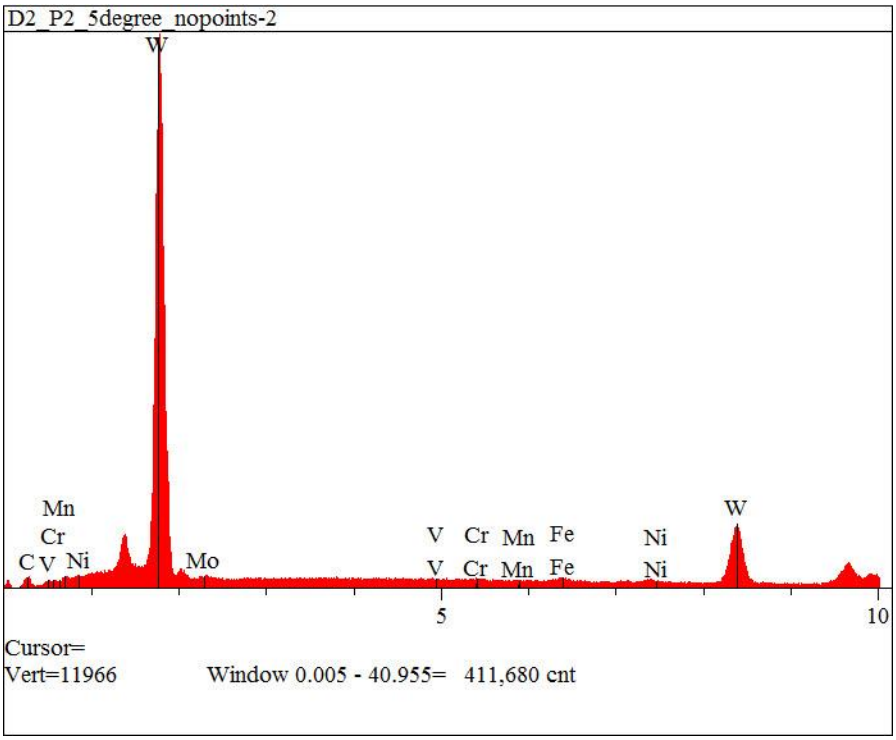
D2_P2_5degree_nopoints-2
W
Mn
Cr
C V Ni
Mo
V Cr Mn Fe
V Cr Mn Fe
Ni
Ni
W
5
10
Cursor=
Vert=11966
Window 0.005 - 40.955= 411,680 cnt

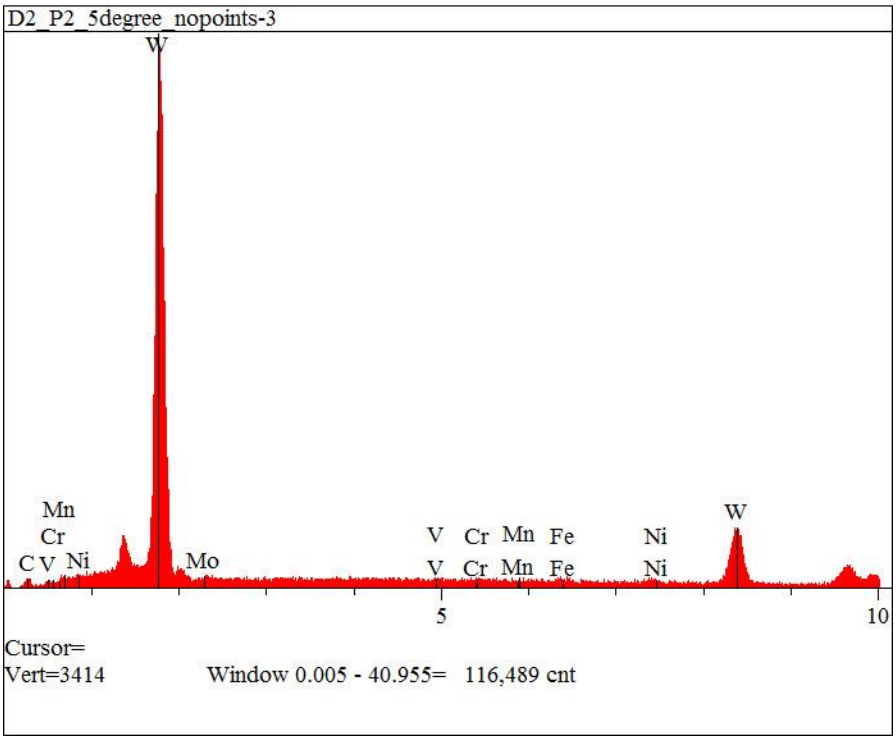
D2_P2_5degree_nopoints-3
W
Mn
Cr
C V Ni
Mo
V Cr Mn Fe Ni
V Cr Mn Fe Ni
W
5
10
Cursor=
Vert=3414
Window 0.005 - 40.955= 116,489 cnt

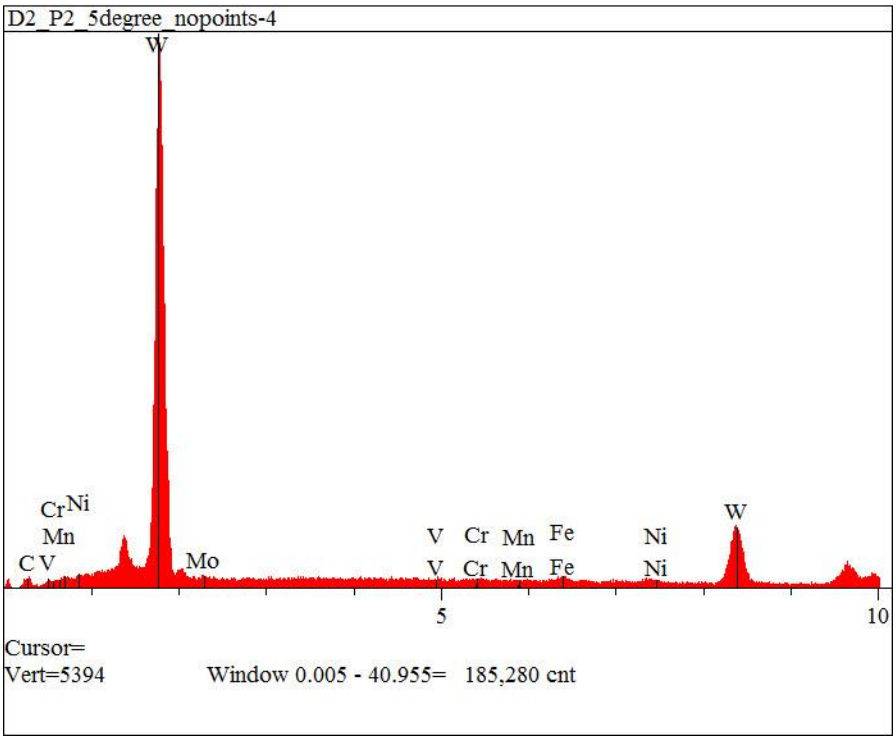
D2_P2_5degree_nopoints-4
W
Cr Ni
Mn
C V
Mo
V Cr Mn Fe Ni
V Cr Mn Fe Ni
W
5
10
Cursor=
Vert=5394
Window 0.005 - 40.955= 185,280 cnt

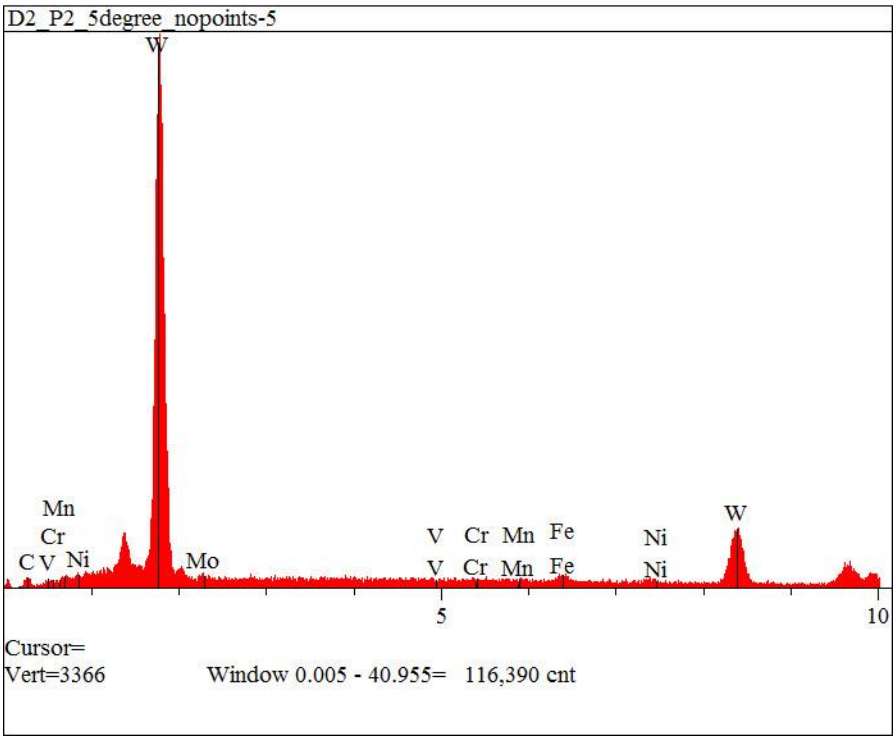
D2_P2_5degree_nopoints-5
W
Mn
Cr
C V Ni
Mo
V Cr Mn Fe
V Cr Mn Fe
Ni
Ni
W
5
10
Cursor=
Vert=3366
Window 0.005 - 40.955= 116,390 cnt

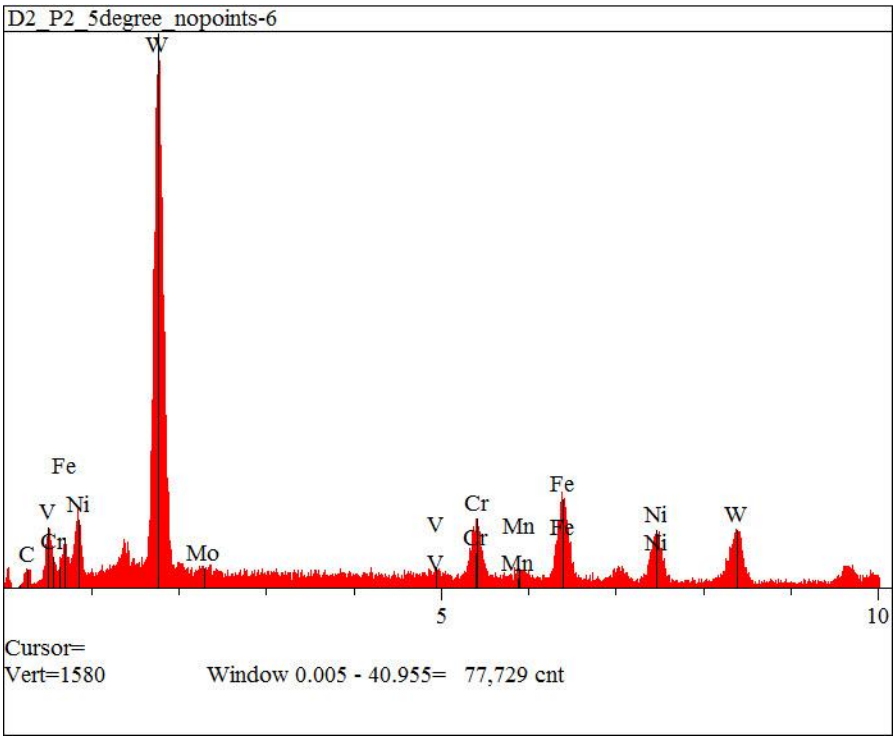
D2_P2_5degree_nopoints-6
W
Fe
V Ni
Cr
C
Mo
V
Cr
Mn
Fe
V
Cr
Mn
Fe
Ni
Ni
W
5
10
Cursor=
Vert=1580
Window 0.005 - 40.955= 77,729 cnt

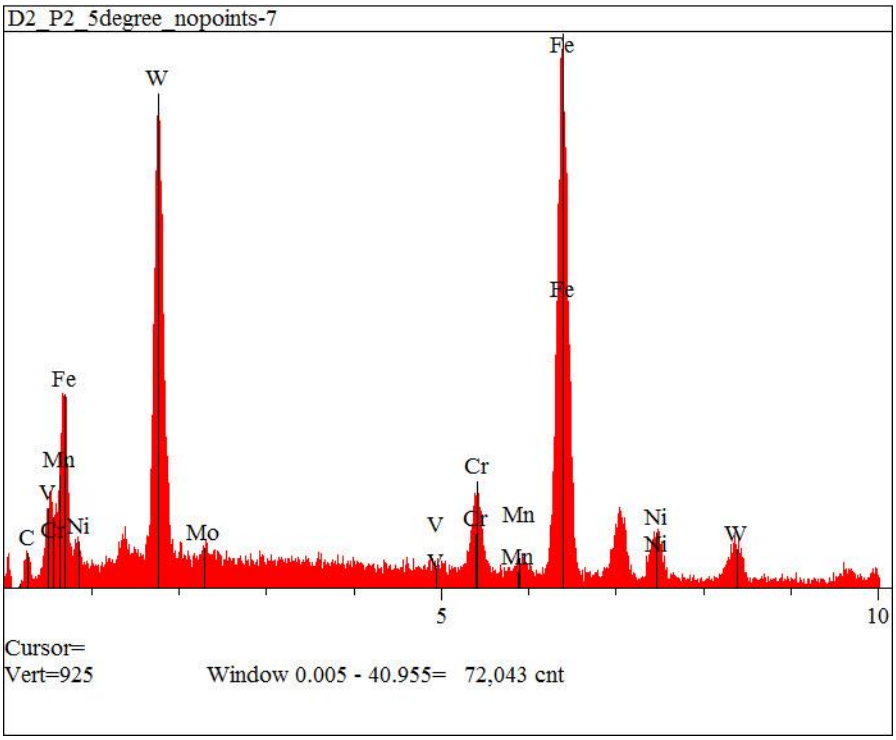
D2_P2_5degree_nopoints-7
Fe
W
Fe
Fe
Mn
V
C
Cr
Ni
Mo
V
Cr
Mn
Cr
Mn
Ni
Ni
W
5
10
Cursor=
Vert=925
Window 0.005 - 40.955= 72,043 cnt

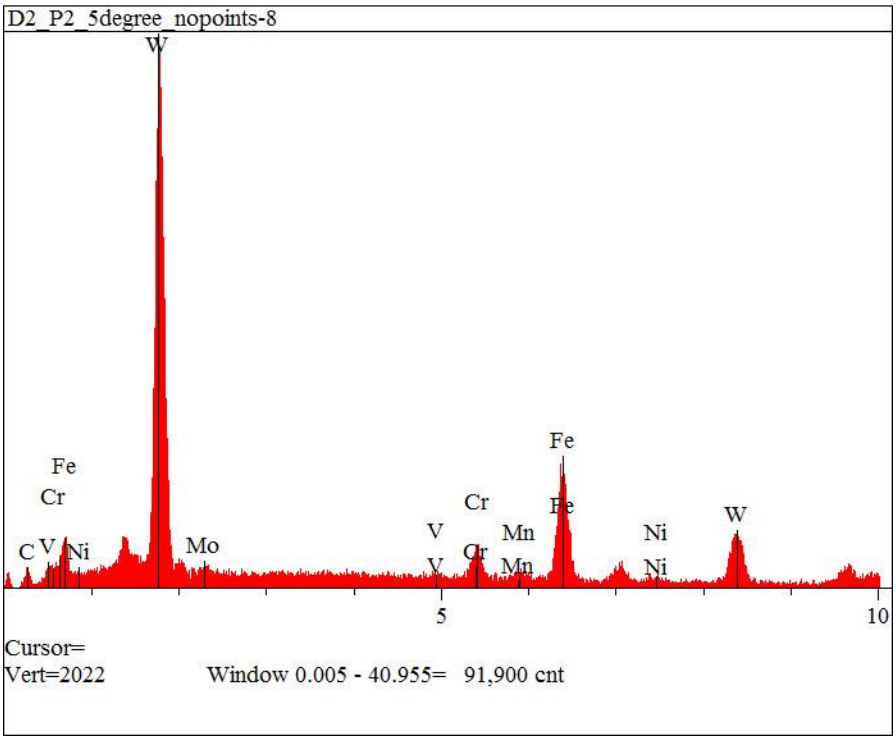
D2_P2_5degree_nopoints-8
W
Fe
Cr
C
V
Ni
Mo
V
Cr
Mn
Fe
Ni
W
5
10
Cursor=
Vert=2022
Window 0.005 - 40.955= 91,900 cnt

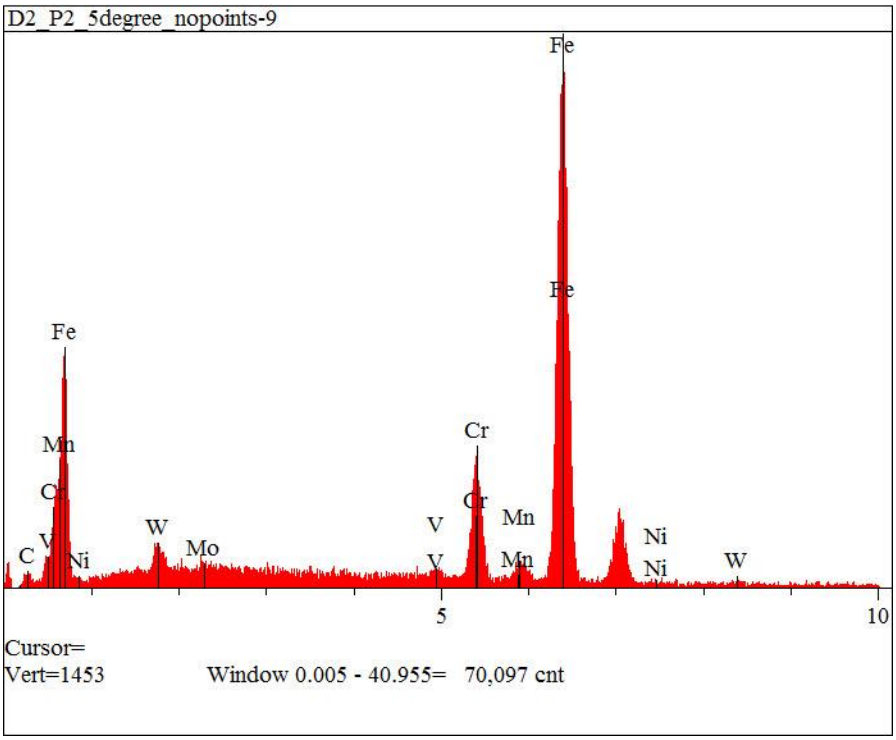
D2_P2_5degree_nopoints-9
Fe
Fe
Mn
Cr
C
V
Ni
W
Mo
V
Cr
Mn
Ni
W
5
10
Cursor=
Vert=1453
Window 0.005 - 40.955= 70,097 cnt

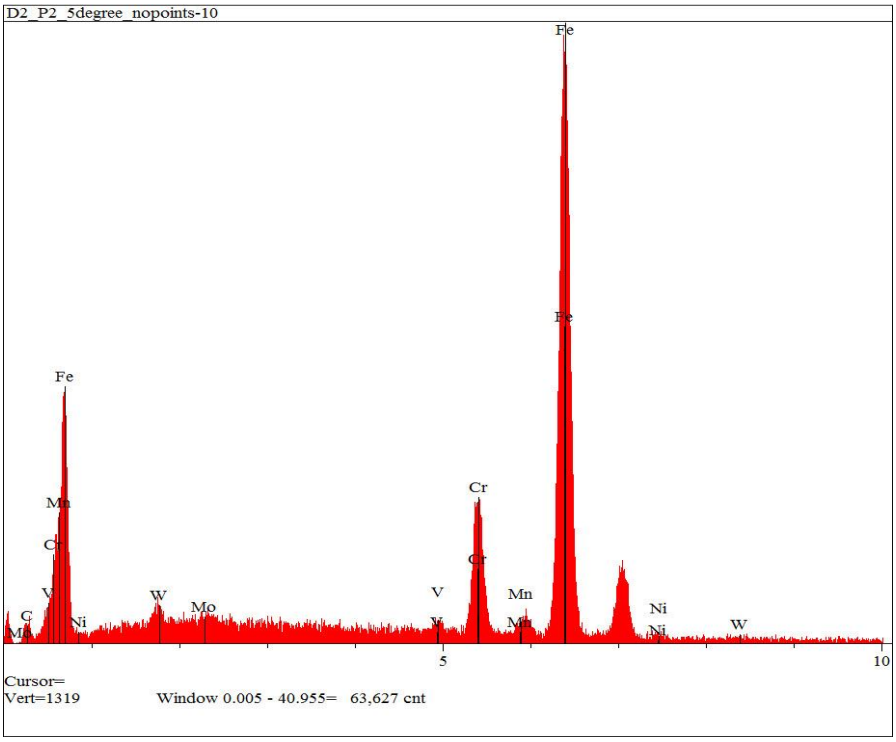
D2_P2_5degree_nopoints-10
Fe
Fe
Fe
Mn
Cr
Cr
V
W
Mo
V
Mn
Ni
Ni
W
5
10
Cursor=
Vert=1319
Window 0.005 - 40.955= 63,627 cnt

D2_P2_10degree 1-10 EDS Plots

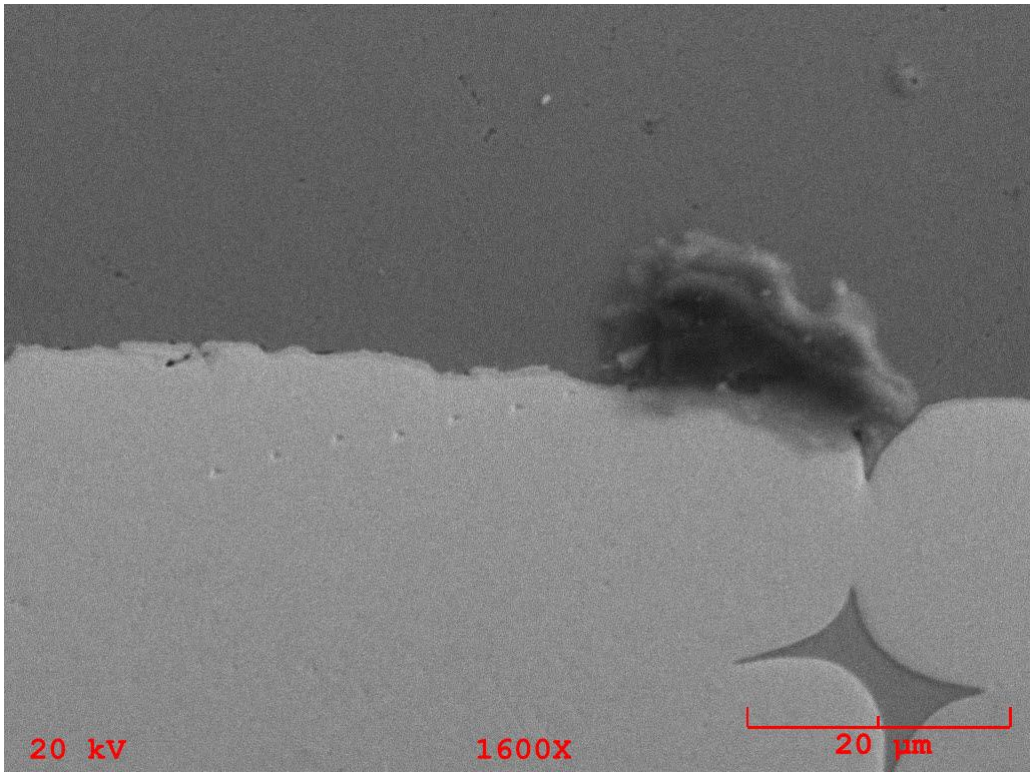

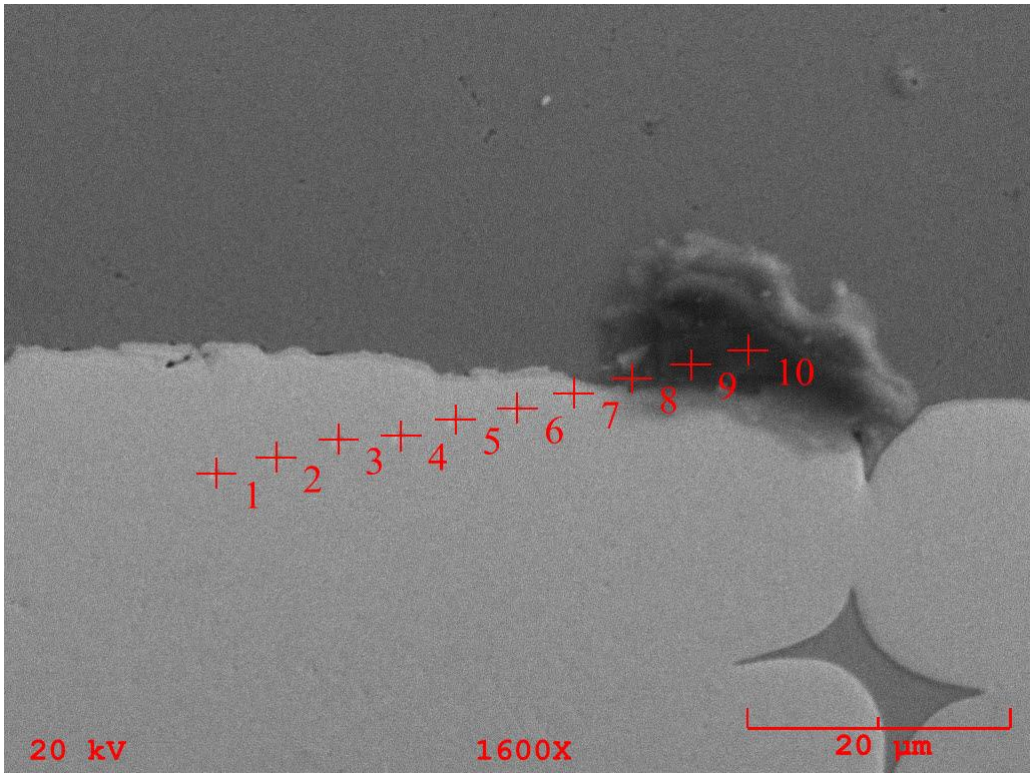

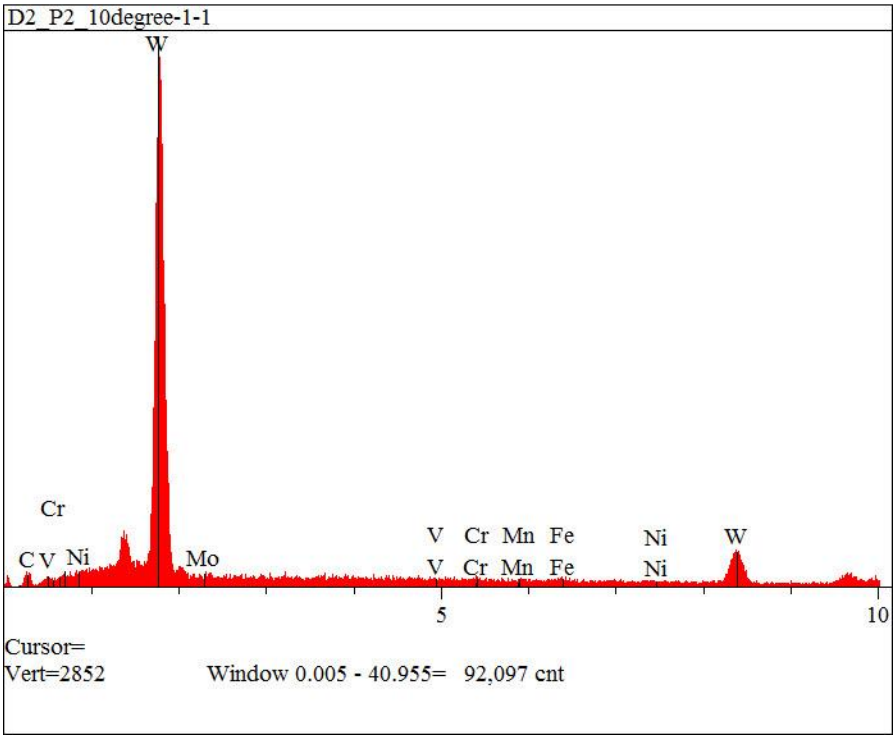
D2_P2_10degree-1-1
W
Cr
C V Ni
Mo
V Cr Mn Fe Ni W
V Cr Mn Fe Ni
5
10
Cursor=
Vert=2852
Window 0.005 - 40.955= 92,097 cnt

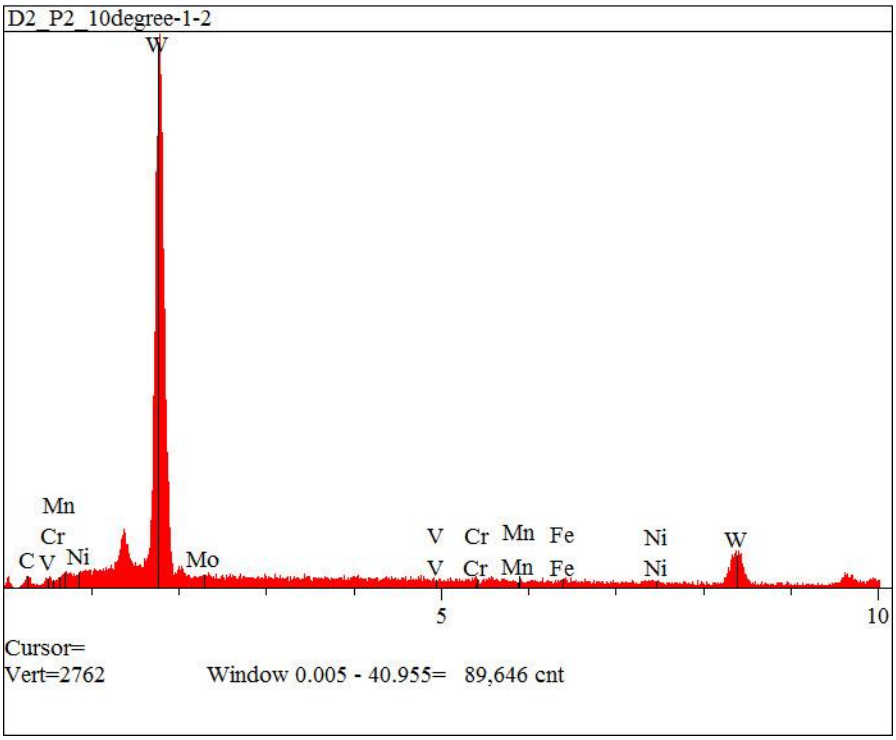
D2_P2_10degree-1-2
W
Mn
Cr
C V Ni
Mo
V Cr Mn Fe Ni W
V Cr Mn Fe Ni
5
10
Cursor=
Vert=2762
Window 0.005 - 40.955= 89,646 cnt

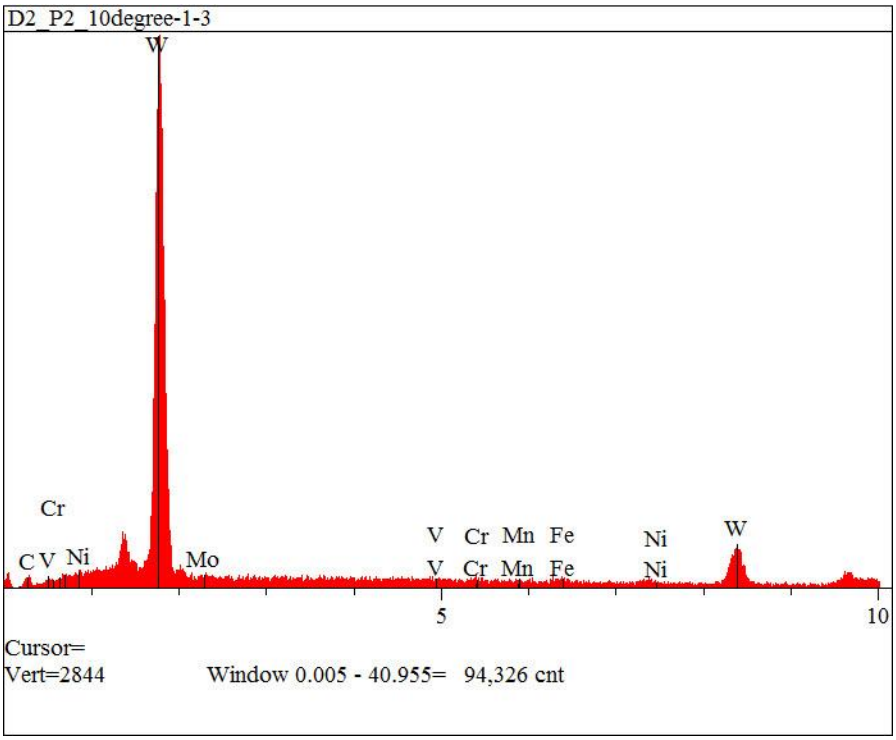
D2_P2_10degree-1-3
W
Cr
C V Ni
Mo
V Cr Mn Fe
V Cr Mn Fe
Ni
Ni
W
5
10
Cursor=
Vert=2844
Window 0.005 - 40.955= 94,326 cnt

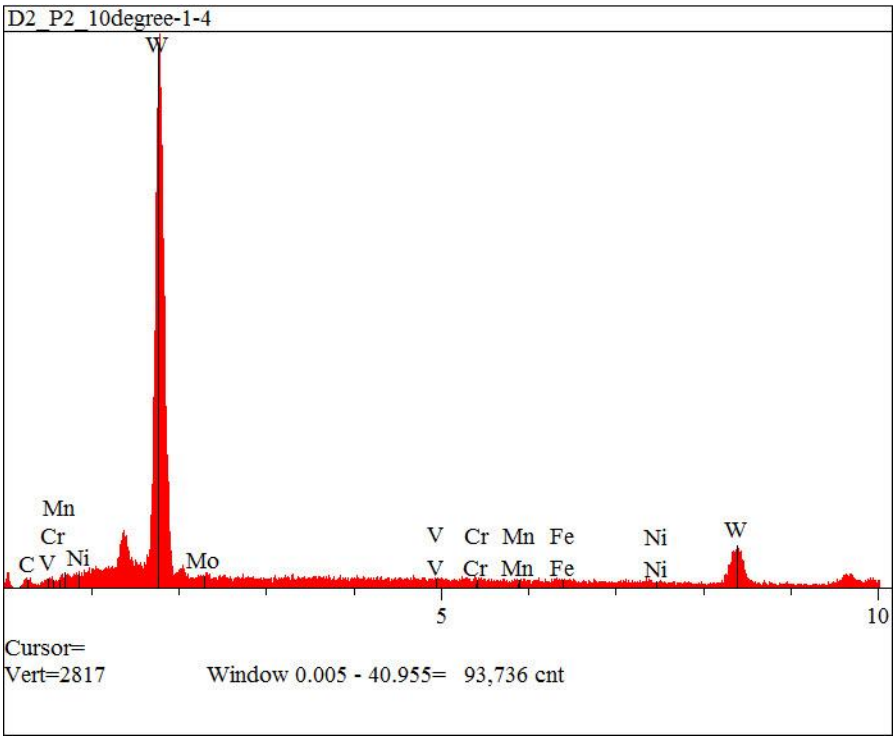
D2_P2_10degree-1-4
W
Mn
Cr
C V Ni
Mo
V Cr Mn Fe
V Cr Mn Fe
Ni
Ni
W
5
10
Cursor=
Vert=2817
Window 0.005 - 40.955= 93,736 cnt

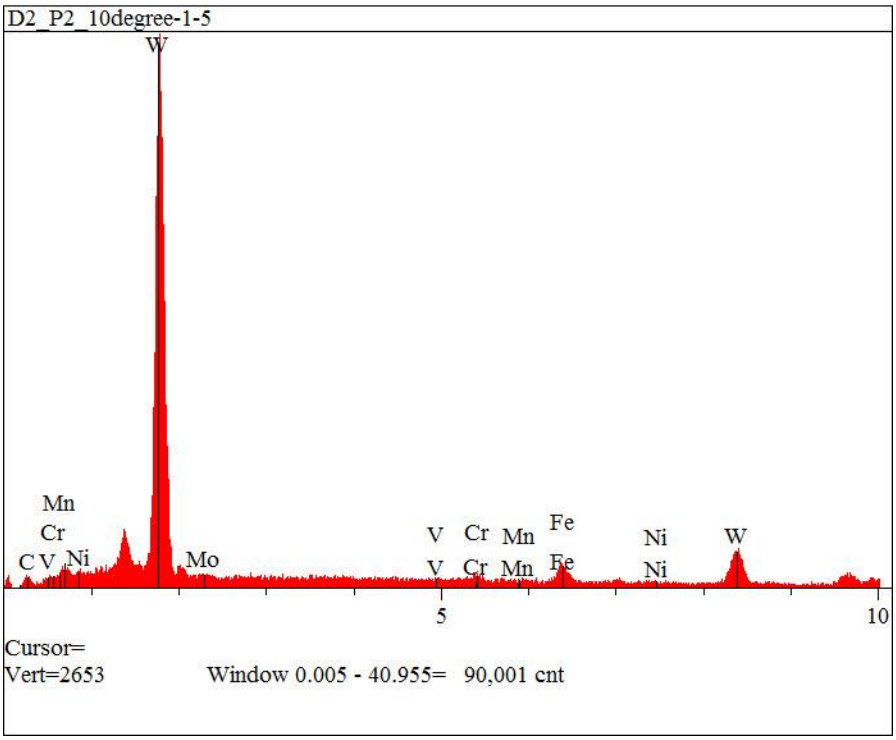
D2_P2_10degree-1-5
W
Mn
Cr
C V Ni
Mo
V Cr Mn Fe
V Cr Mn Fe
Ni W
Ni
5
10
Cursor=
Vert=2653
Window 0.005 - 40.955= 90,001 cnt

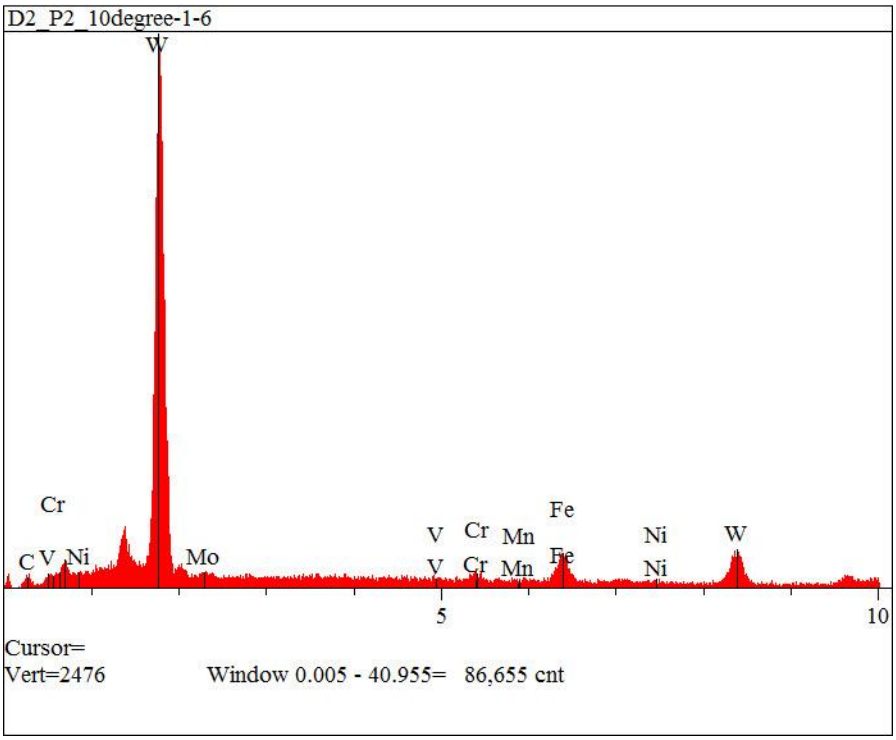
D2_P2_10degree-1-6
W
Cr
C V Ni
Mo
V Cr Mn Fe
V Cr Mn Fe
Ni W
Ni
5
10
Cursor=
Vert=2476
Window 0.005 - 40.955= 86,655 cnt

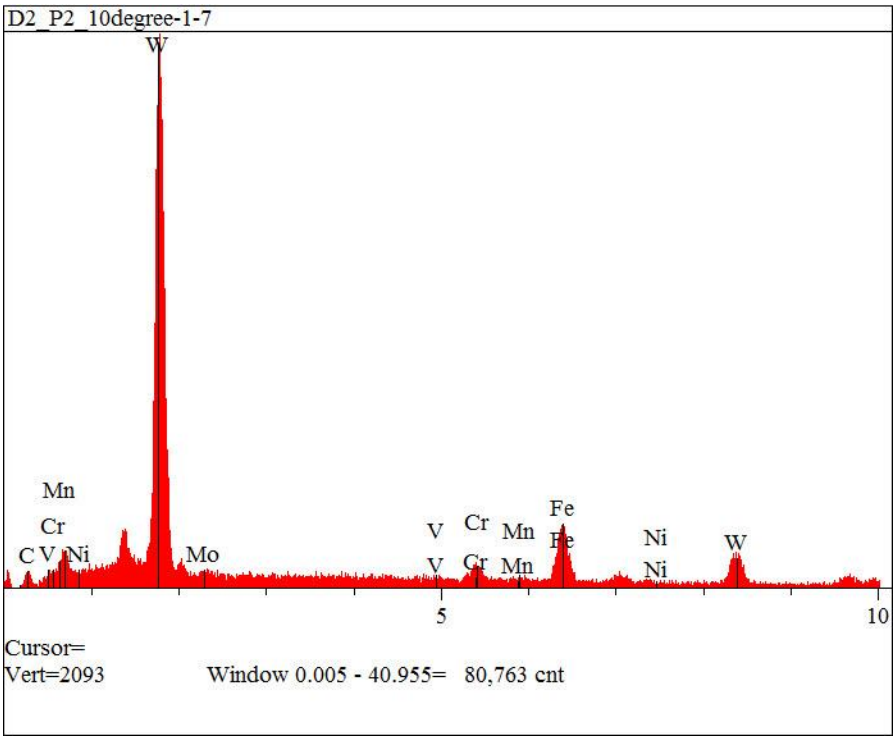
D2_P2_10degree-1-7
W
Mn
Cr
C V Ni
Mo
V
V
Cr
Cr
Mn
Mn
Fe
Fe
Ni
Ni
W
5
10
Cursor=
Vert=2093
Window 0.005 - 40.955= 80,763 cnt

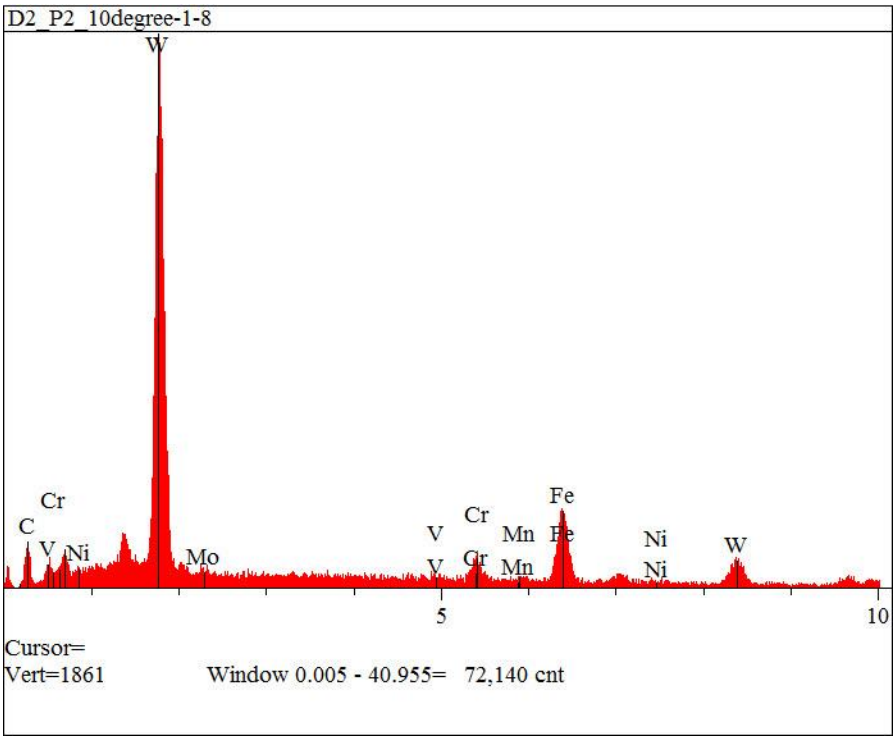
D2_P2_10degree-1-8
W
Cr
C
V Ni
Mo
V
V
Cr
Cr
Mn
Mn
Fe
Fe
Ni
Ni
W
5
10
Cursor=
Vert=1861
Window 0.005 - 40.955= 72,140 cnt

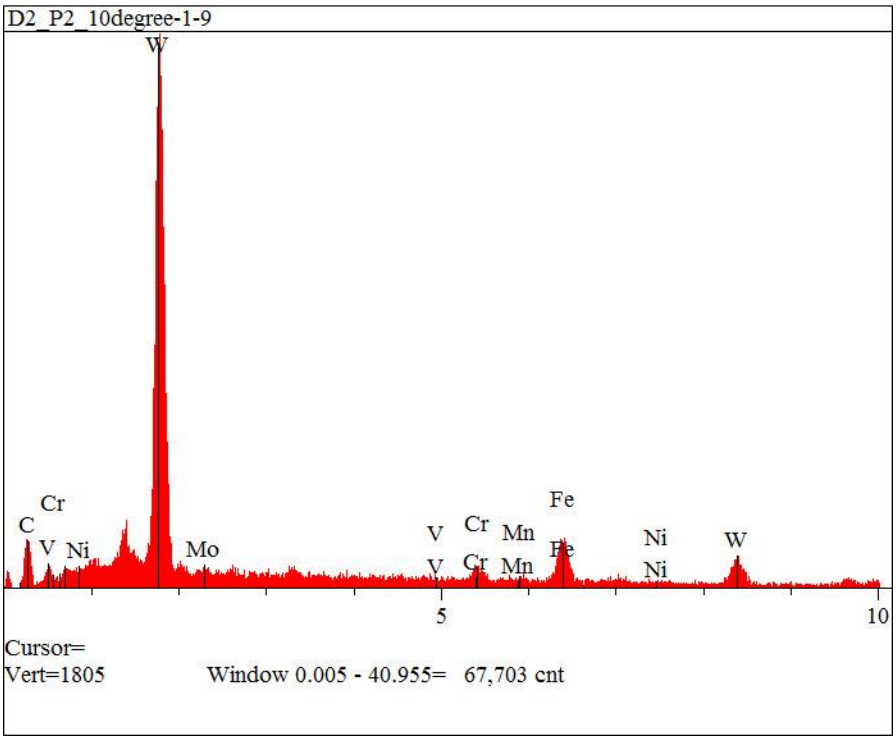
D2_P2_10degree-1-9
W
C
Cr
V
Ni
Mo
V
Cr
Mn
Fe
Ni
W
5
10
Cursor=
Vert=1805
Window 0.005 - 40.955= 67,703 cnt

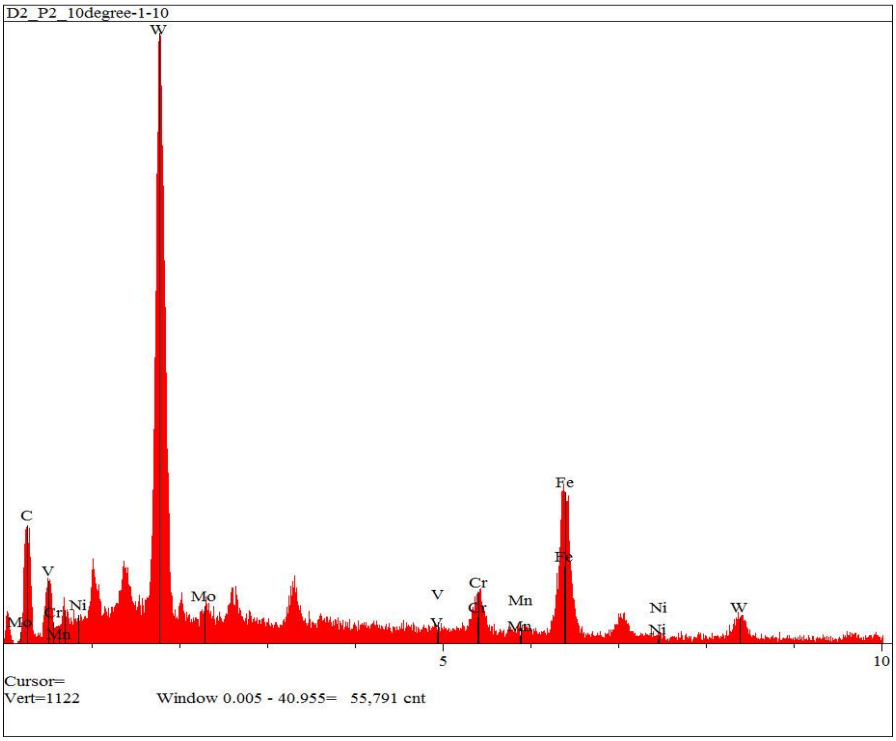
D2_P2_10degree-1-10
W
C
V
Mo
Ni
Fe
Cr
Mn
Ni
W
5
10
Cursor=
Vert=1122
Window 0.005 - 40.955= 55,791 cnt

D2_P1_10x4_Interpulate 1-26 1.5-1.6 µm spacing with pt 12 on interface 1-10 EDS Plots

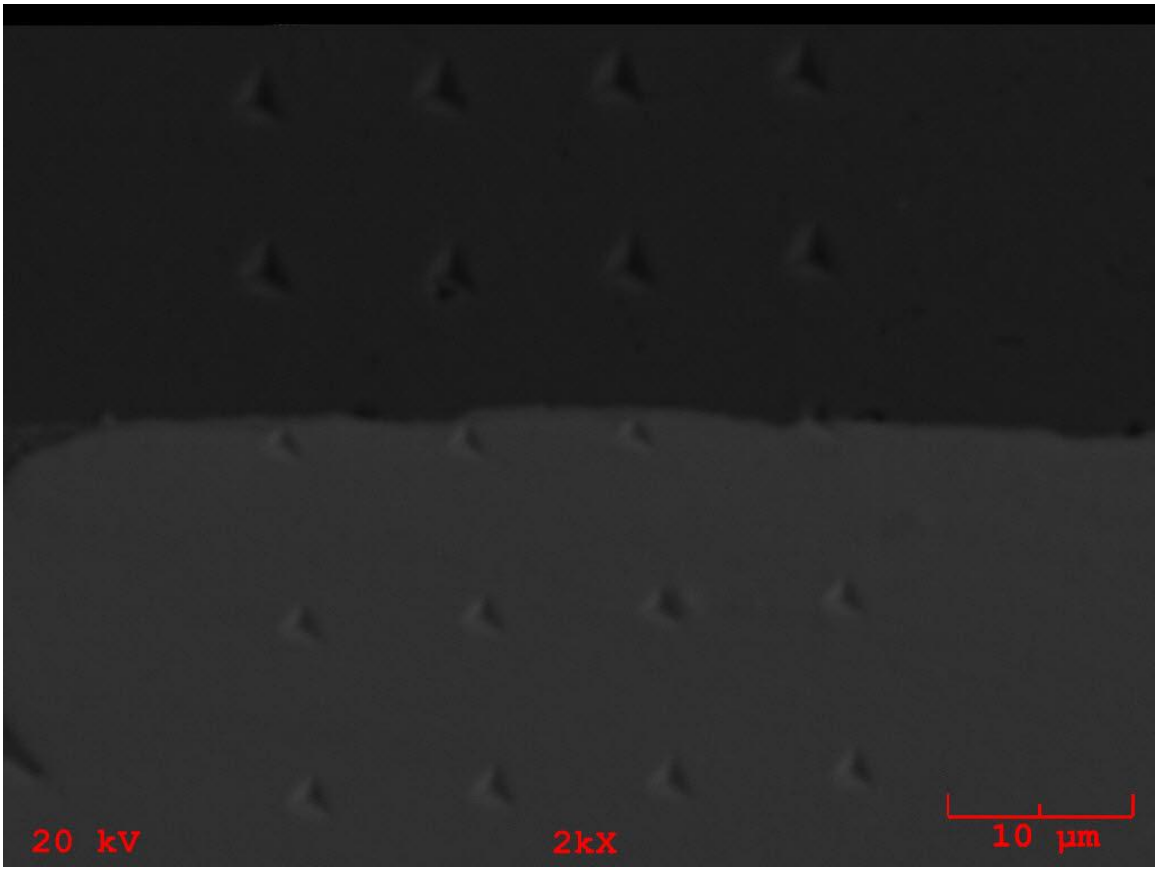

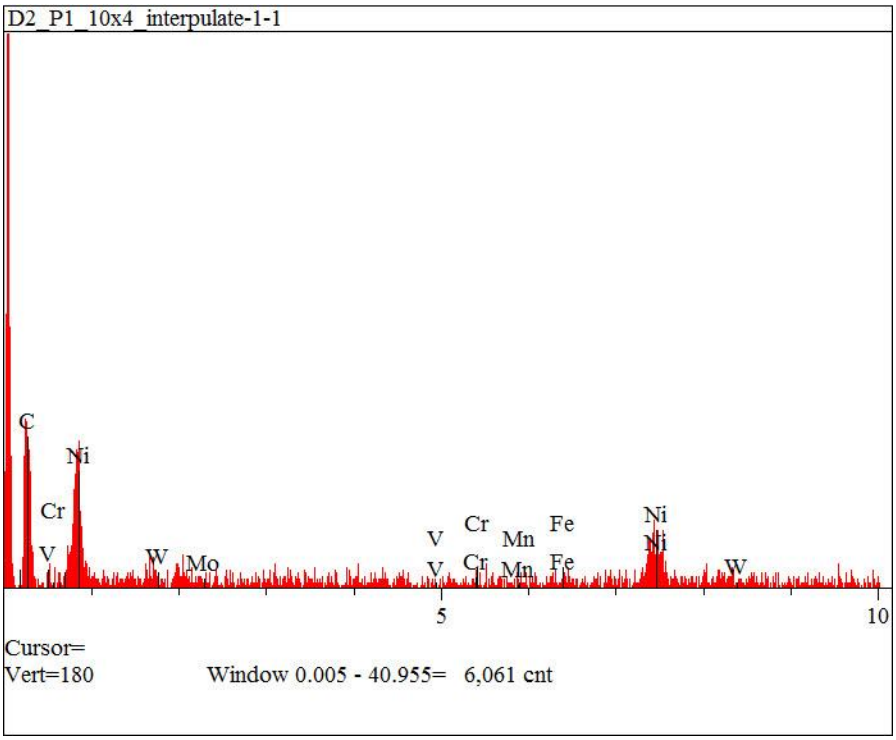
D2_P1_10x4_interpulate-1-1
C
Ni
Cr
V
W
Mo
V
Cr
Mn
Fe
Ni
W
5
10
Cursor=
Vert=180
Window 0.005 - 40.955= 6,061 cnt

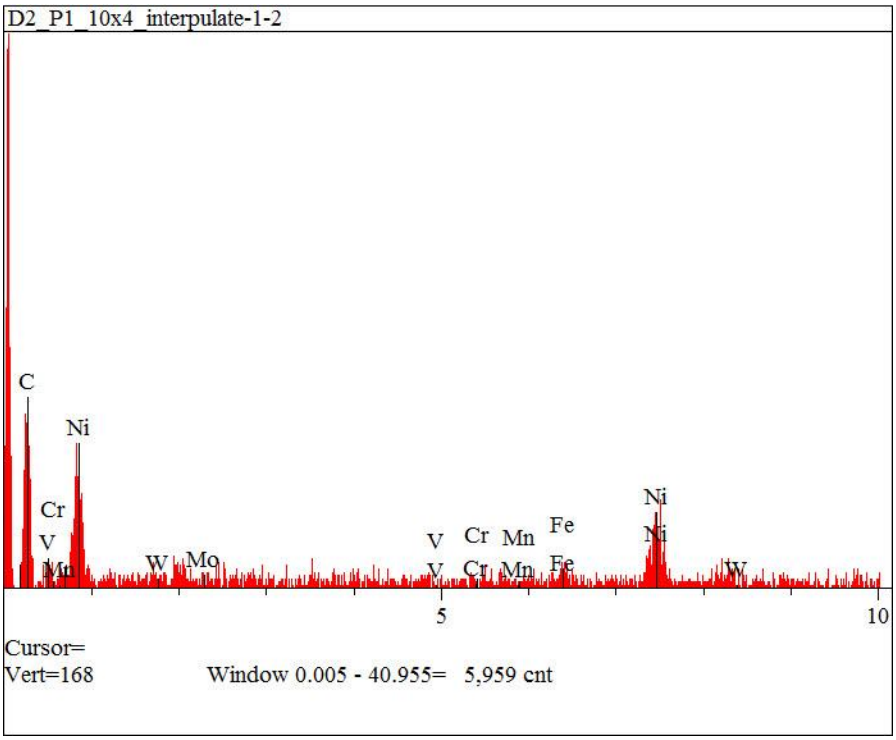
D2_P1_10x4_interpulate-1-2
C
Ni
Cr
V
W
Mo
V
Cr
Mn
Fe
Ni
W
5
10
Cursor=
Vert=168
Window 0.005 - 40.955= 5,959 cnt

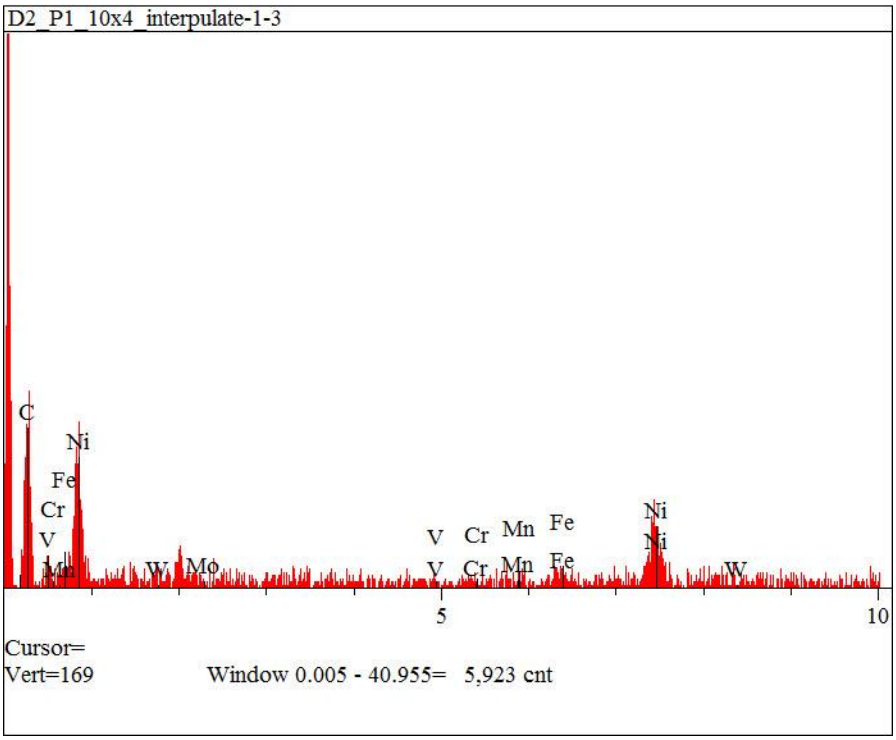
D2_P1_10x4_interpulate-1-3
C
Ni
Fe
Cr
V
W
Mo
V Cr Mn Fe
Ni
W
5
10
Cursor=
Vert=169
Window 0.005 - 40.955= 5,923 cnt

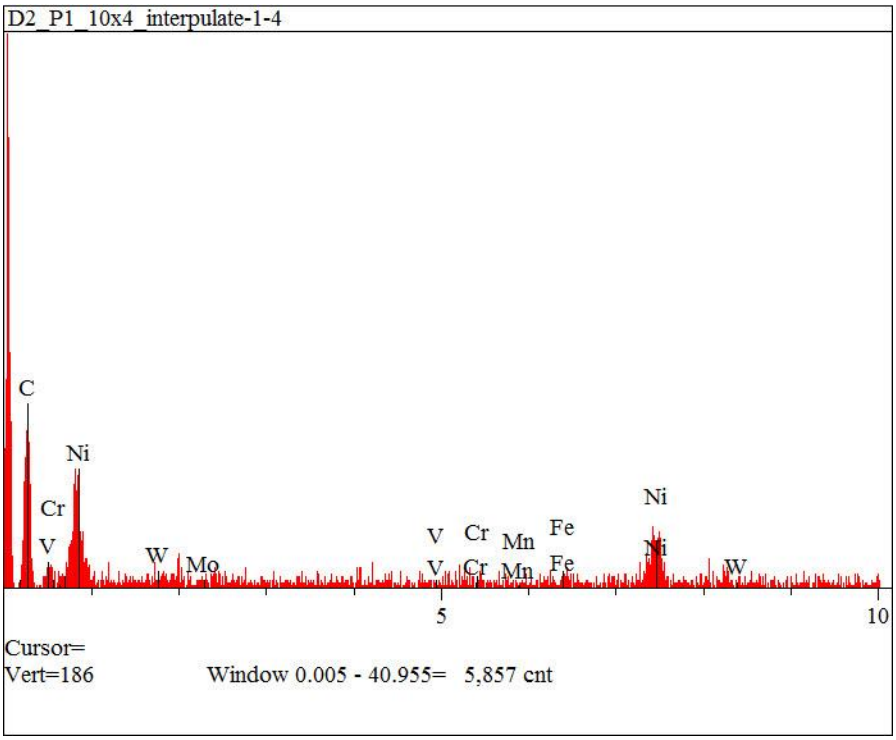
D2_P1_10x4_interpulate-1-4
C
Ni
Cr
V
W
Mo
V Cr Mn Fe
Ni
W
5
10
Cursor=
Vert=186
Window 0.005 - 40.955= 5,857 cnt

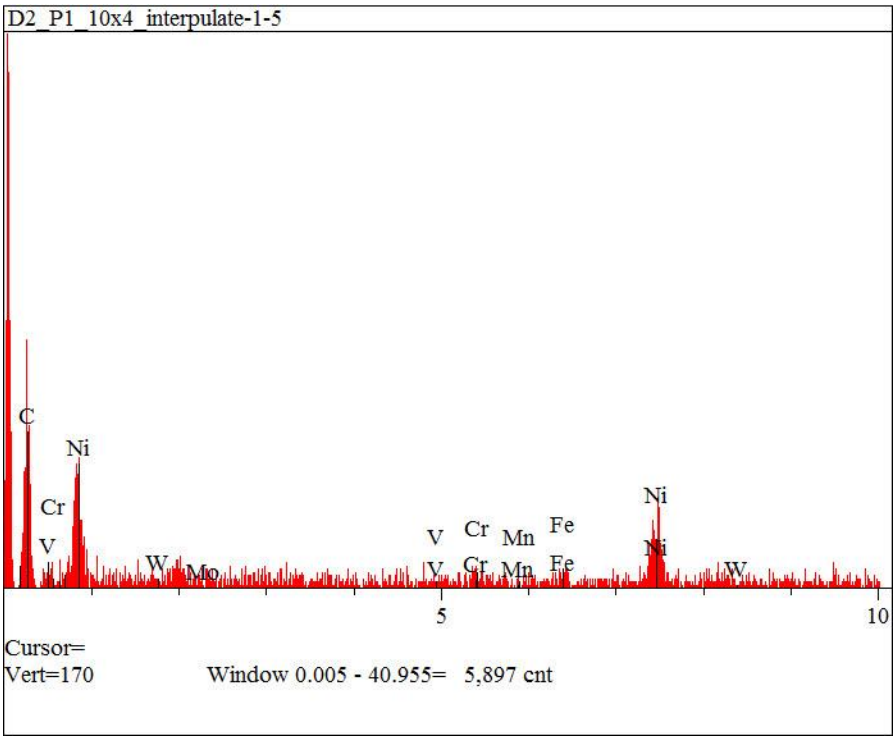
D2_P1_10x4_interpulate-1-5
C
Ni
Cr
V
W
Mo
V
Cr
Mn
Fe
V
Cr
Mn
Fe
Ni
Ni
W
5
10
Cursor=
Vert=170
Window 0.005 - 40.955= 5,897 cnt

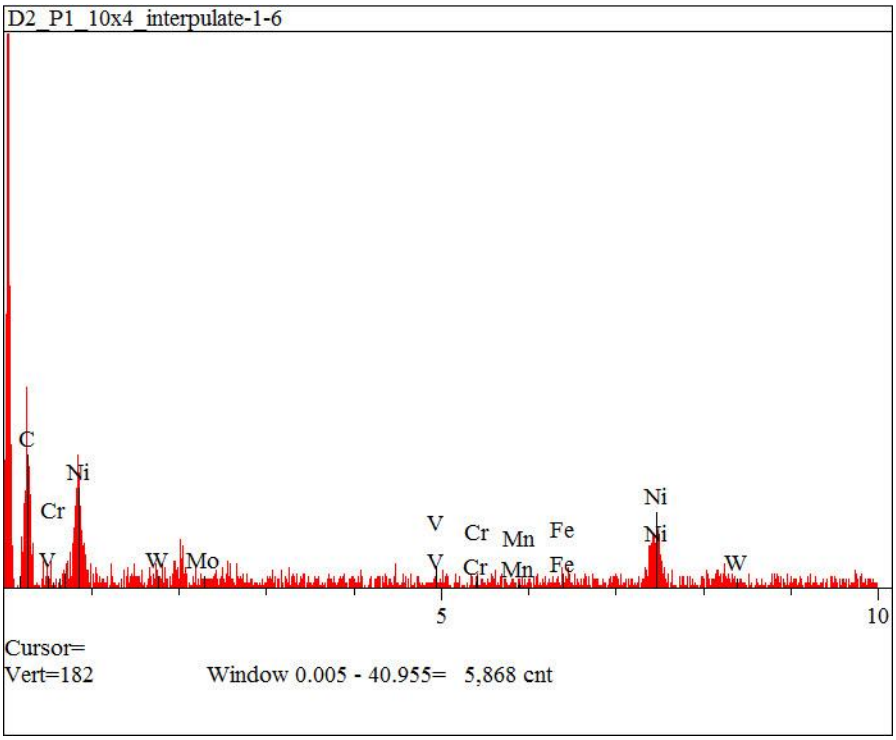
D2_P1_10x4_interpulate-1-6
C
Ni
Cr
V
W
Mo
V
Cr
Mn
Fe
V
Cr
Mn
Fe
Ni
Ni
W
5
10
Cursor=
Vert=182
Window 0.005 - 40.955= 5,868 cnt

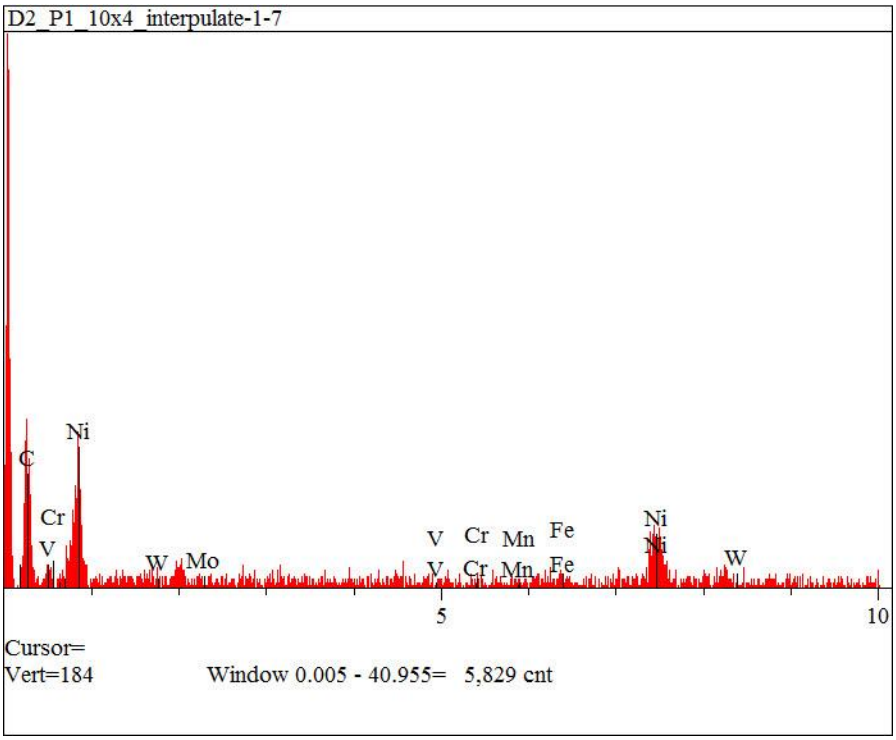
D2_P1_10x4_interpulate-1-7
C
Ni
Cr
V
W
Mo
V
Cr
Mn
Fe
Ni
W
5
10
Cursor=
Vert=184
Window 0.005 - 40.955= 5,829 cnt

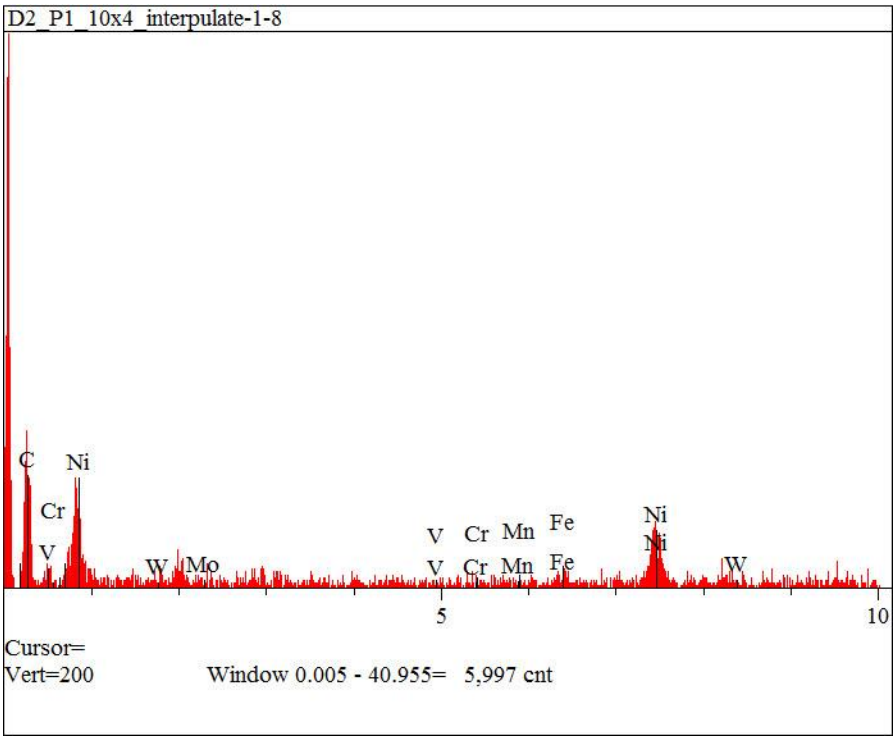
D2_P1_10x4_interpulate-1-8
C
Ni
Cr
V
W
Mo
V
Cr
Mn
Fe
Ni
W
5
10
Cursor=
Vert=200
Window 0.005 - 40.955= 5,997 cnt

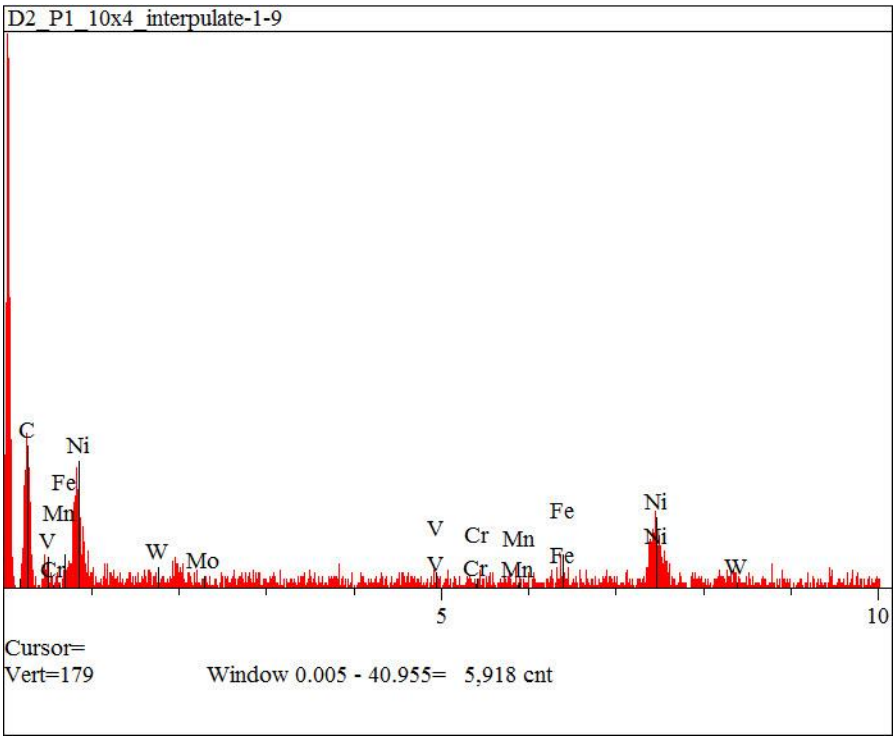
D2_P1_10x4_interpulate-1-9
C
Ni
Fe
Mn
V
Cr
W
Mo
V
Cr
Mn
Fe
Ni
W
5
10
Cursor=
Vert=179
Window 0.005 - 40.955= 5,918 cnt

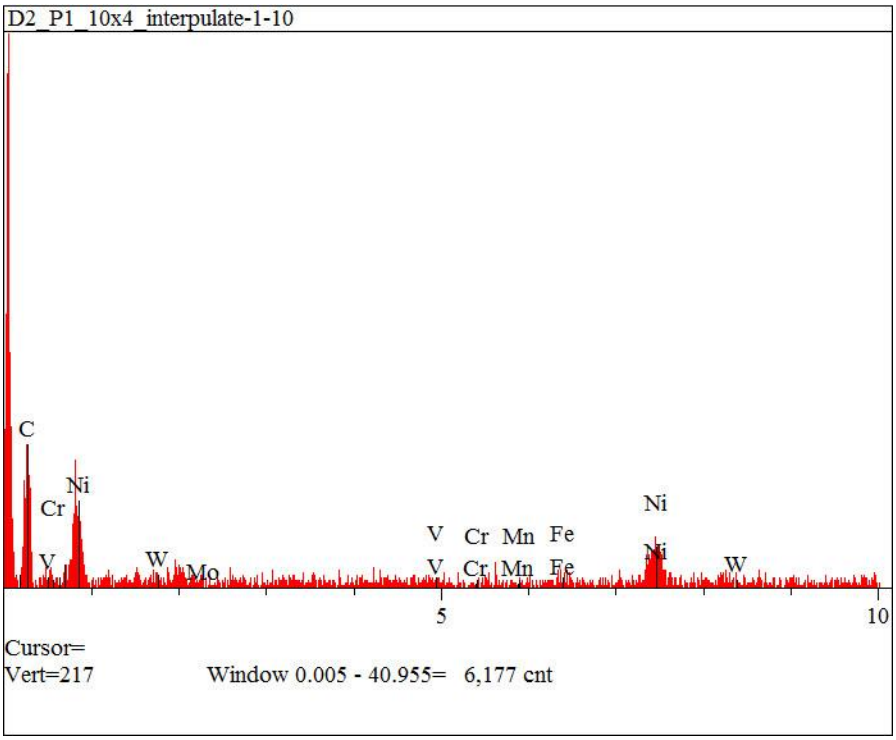
D2_P1_10x4_interpulate-1-10
C
Ni
Cr
V
W
Mo
V
Cr
Mn
Fe
Ni
W
5
10
Cursor=
Vert=217
Window 0.005 - 40.955= 6,177 cnt

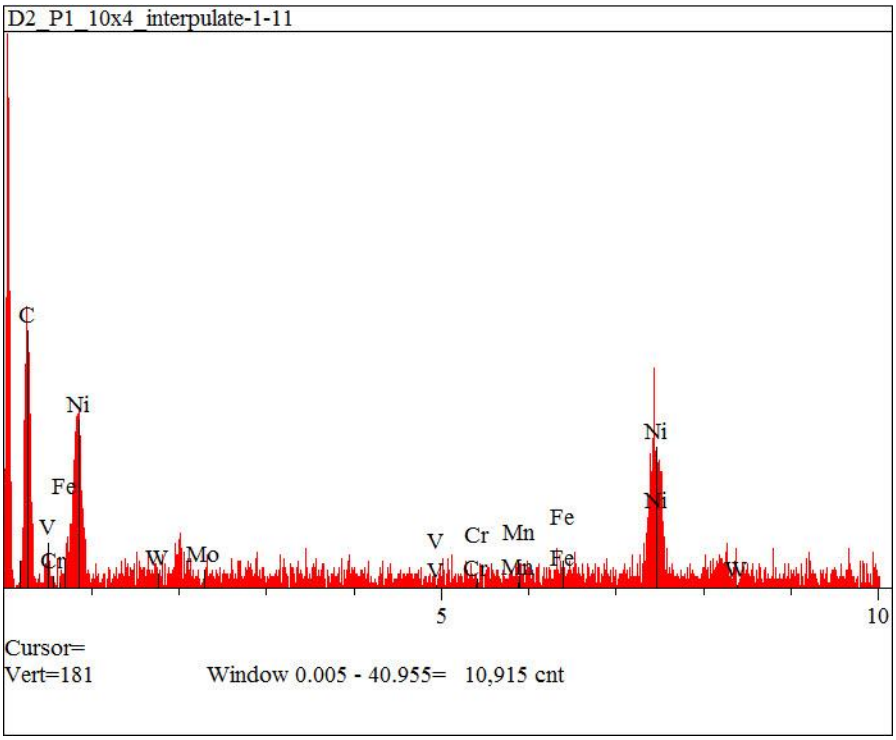
D2_P1_10x4_interpulate-1-11
C
Ni
Fe
V
Cr
W
Mo
V
Cr
Mn
Fe
Ni
Ni
Fe
Mn
Cr
V
W
5
10
Cursor=
Vert=181
Window 0.005 - 40.955= 10,915 cnt

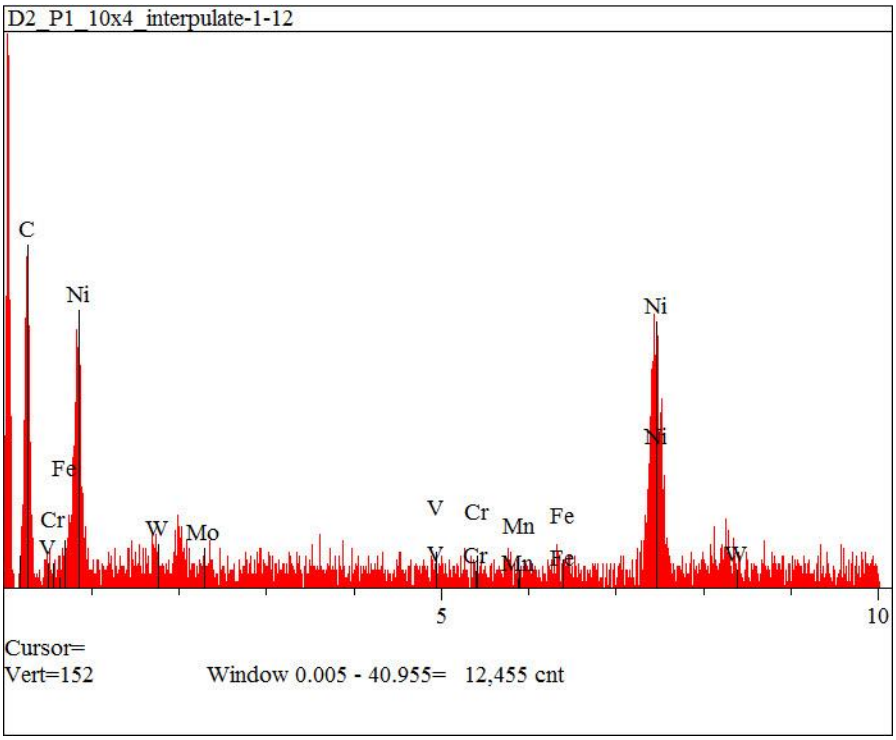
D2_P1_10x4_interpulate-1-12
C
Ni
Fe
Cr
V
W
Mo
V
Cr
Mn
Fe
Ni
Ni
Fe
Mn
Cr
V
W
5
10
Cursor=
Vert=152
Window 0.005 - 40.955= 12,455 cnt

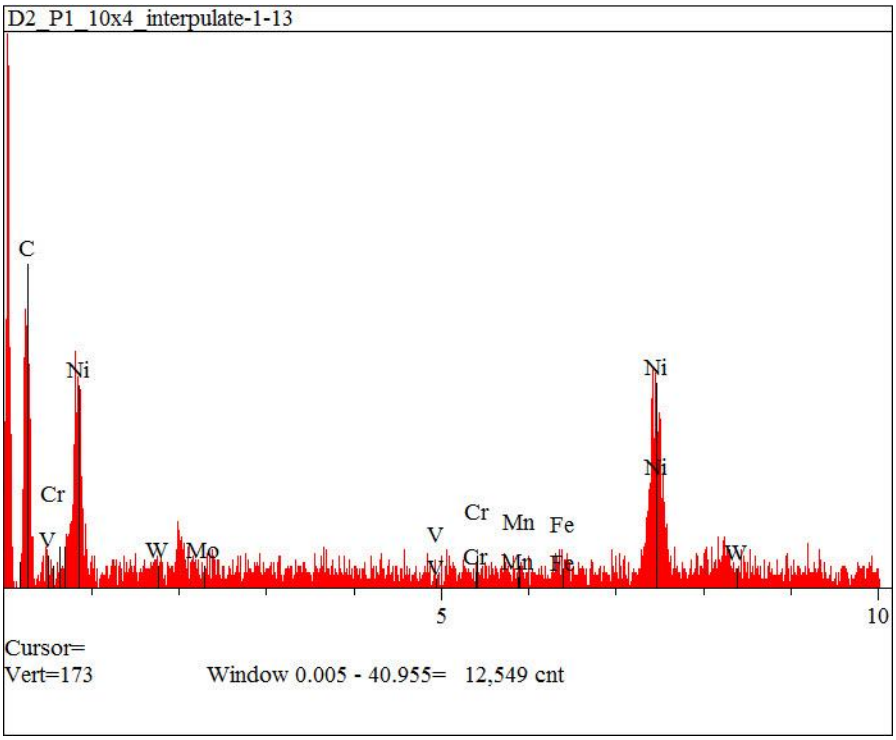
D2_P1_10x4_interpulate-1-13
C
Ni
Cr
V
W
Mo
V
Cr
Mn
Fe
Ni
Ni
W
5
10
Cursor=
Vert=173
Window 0.005 - 40.955= 12,549 cnt

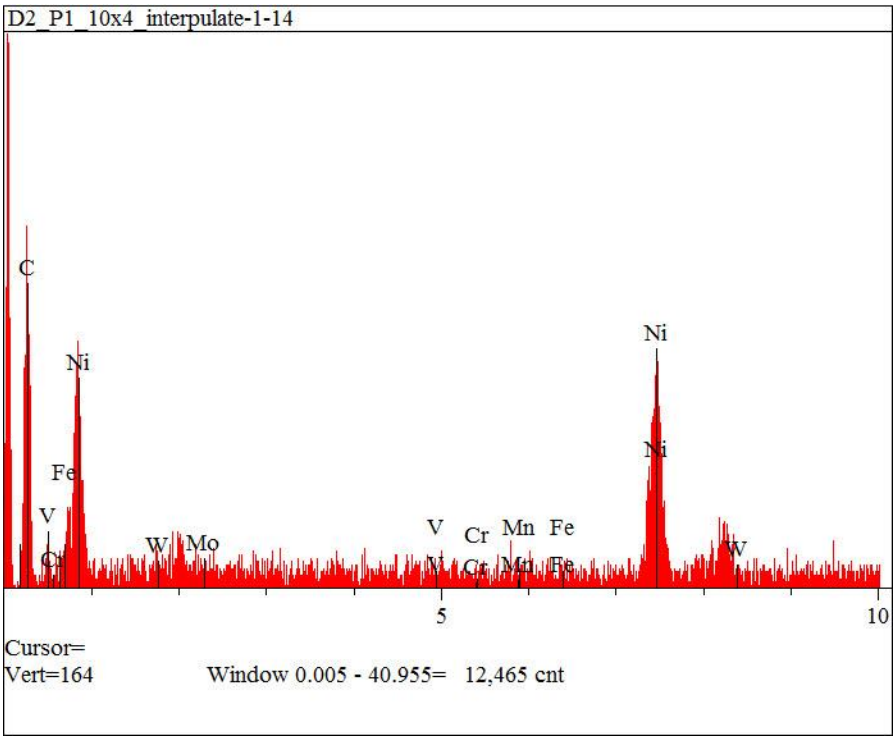
D2_P1_10x4_interpulate-1-14
C
Ni
Fe
V
Cr
W
Mo
V
Cr
Mn
Fe
Ni
Ni
W
5
10
Cursor=
Vert=164
Window 0.005 - 40.955= 12,465 cnt

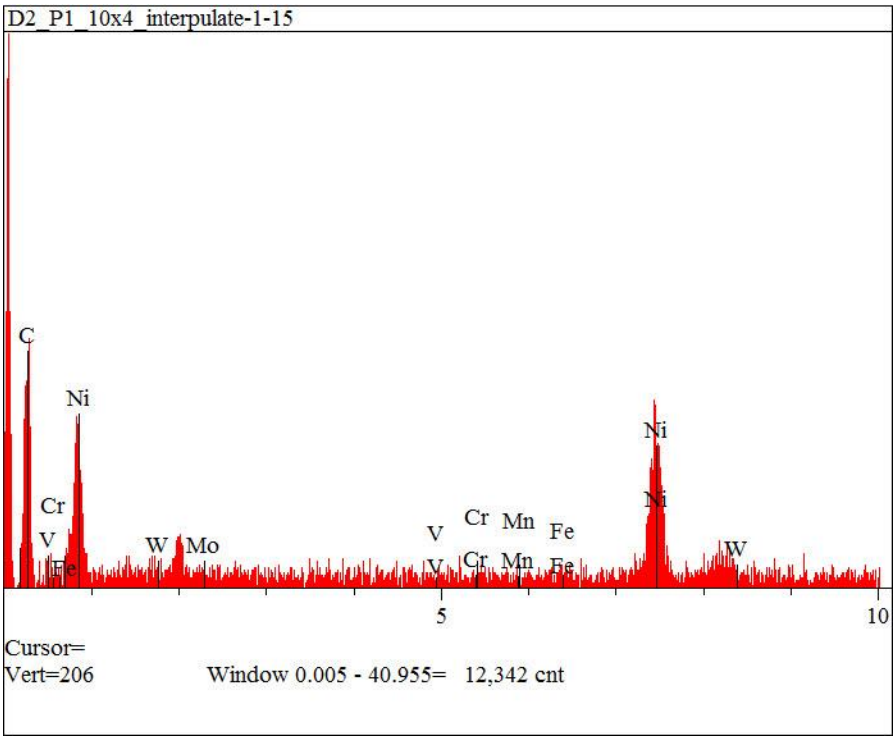
D2_P1_10x4_interpulate-1-15
C
Ni
Cr
V
Fe
W
Mo
V
Cr
Mn
Fe
Ni
Ni
W
5
10
Cursor=
Vert=206
Window 0.005 - 40.955= 12,342 cnt

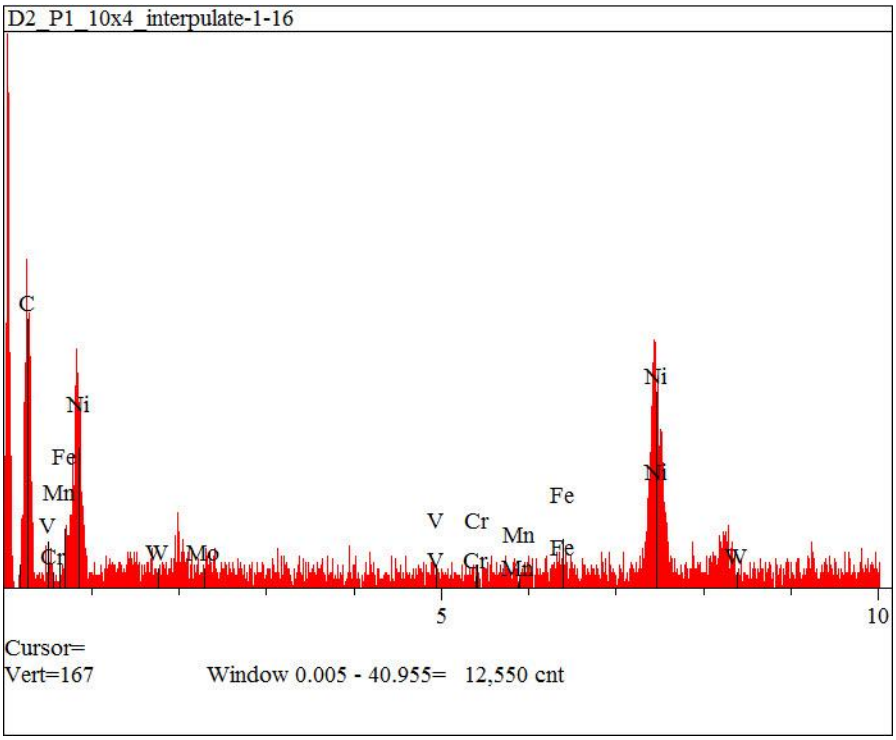
D2_P1_10x4_interpulate-1-16
C
Ni
Fe
Mn
V
Cr
W
Mo
V
Cr
Mn
Fe
Ni
Ni
W
5
10
Cursor=
Vert=167
Window 0.005 - 40.955= 12,550 cnt

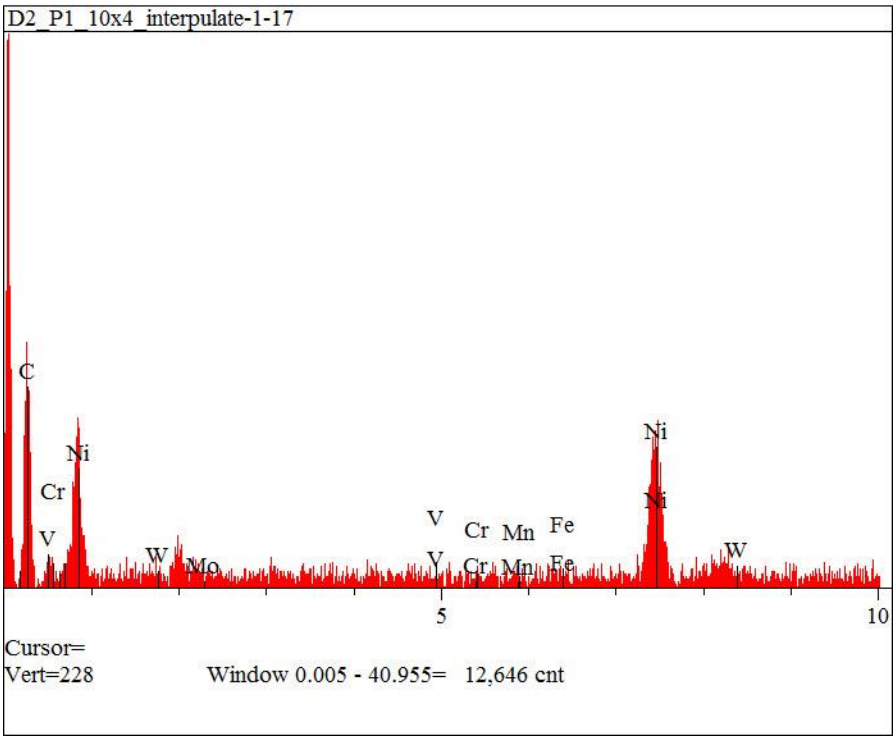
D2_P1_10x4_interpulate-1-17
C
Ni
Cr
V
W
Mo
V
Cr
Mn
Fe
Ni
W
5
10
Cursor=
Vert=228
Window 0.005 - 40.955= 12,646 cnt

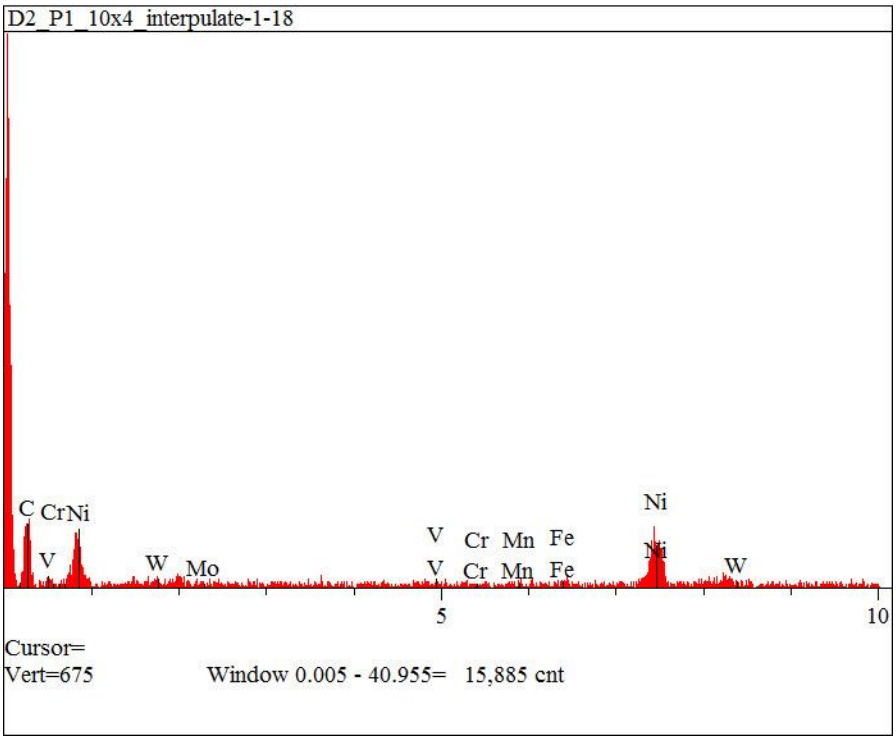
D2_P1_10x4_interpulate-1-18
C
Cr
Ni
V
W
Mo
V
Cr
Mn
Fe
Ni
W
5
10
Cursor=
Vert=675
Window 0.005 - 40.955= 15,885 cnt

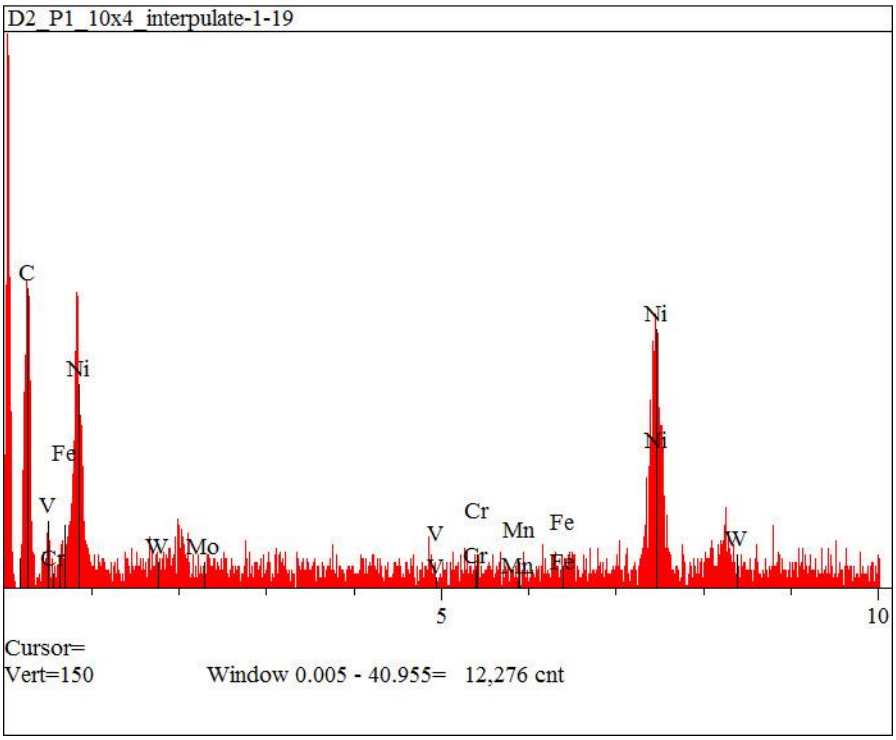
D2_P1_10x4_interpulate-1-19
C
Ni
Fe
V
Cr
W
Mo
V
Cr
Mn
Fe
Ni
Ni
W
5
10
Cursor=
Vert=150
Window 0.005 - 40.955= 12,276 cnt

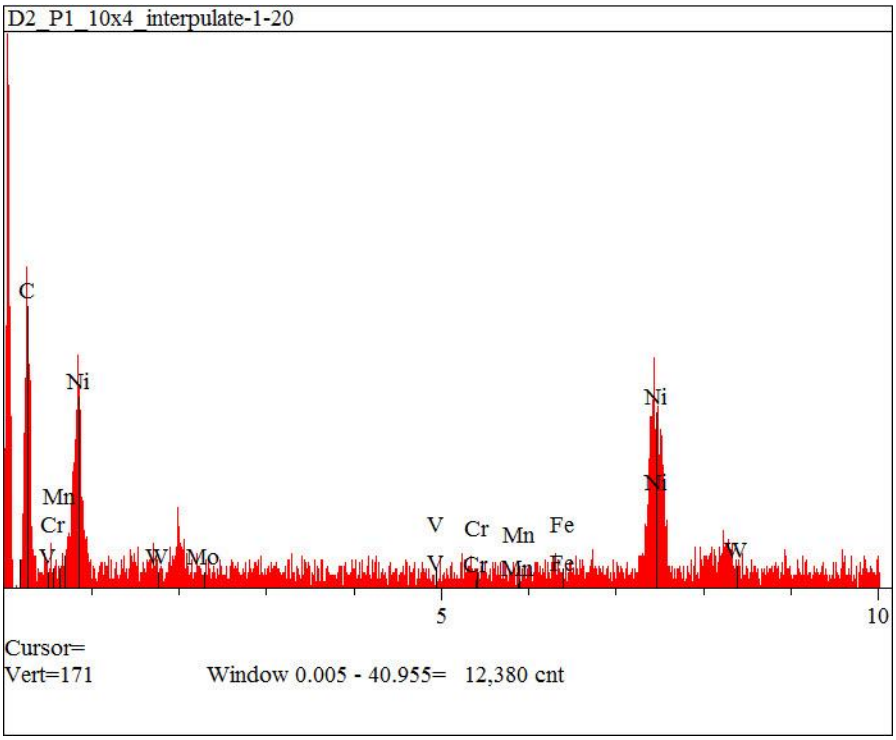
D2_P1_10x4_interpulate-1-20
C
Ni
Mn
Cr
V
W
Mo
V
Cr
Mn
Fe
Ni
Ni
W
5
10
Cursor=
Vert=171
Window 0.005 - 40.955= 12,380 cnt

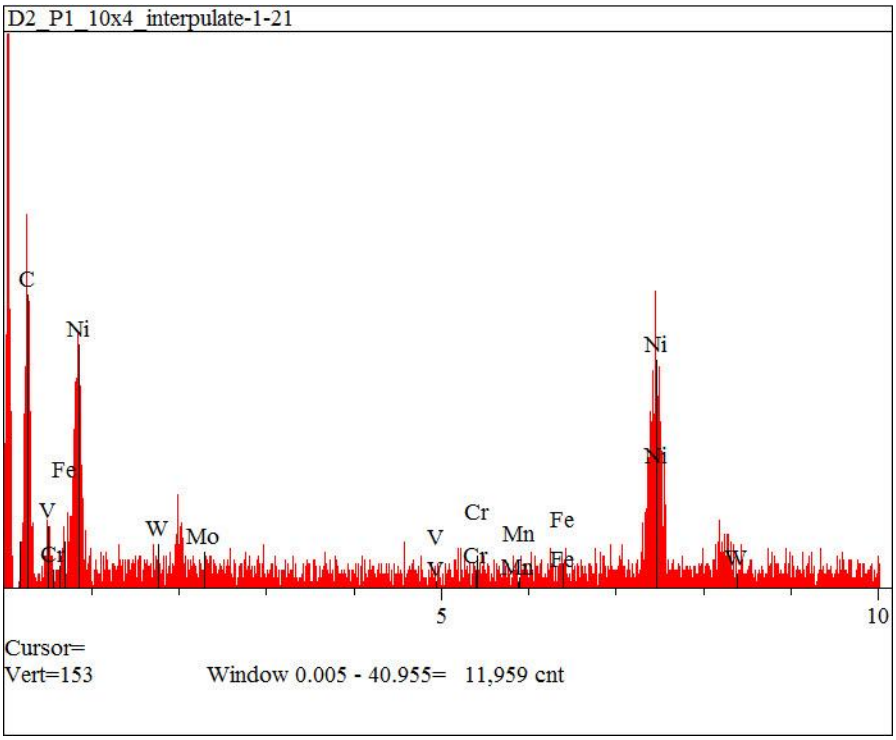
D2_P1_10x4_interpulate-1-21
C
Ni
Fe
V
Cr
W
Mo
V
Cr
Mn
Fe
Ni
Ni
W
5
10
Cursor=
Vert=153
Window 0.005 - 40.955= 11,959 cnt

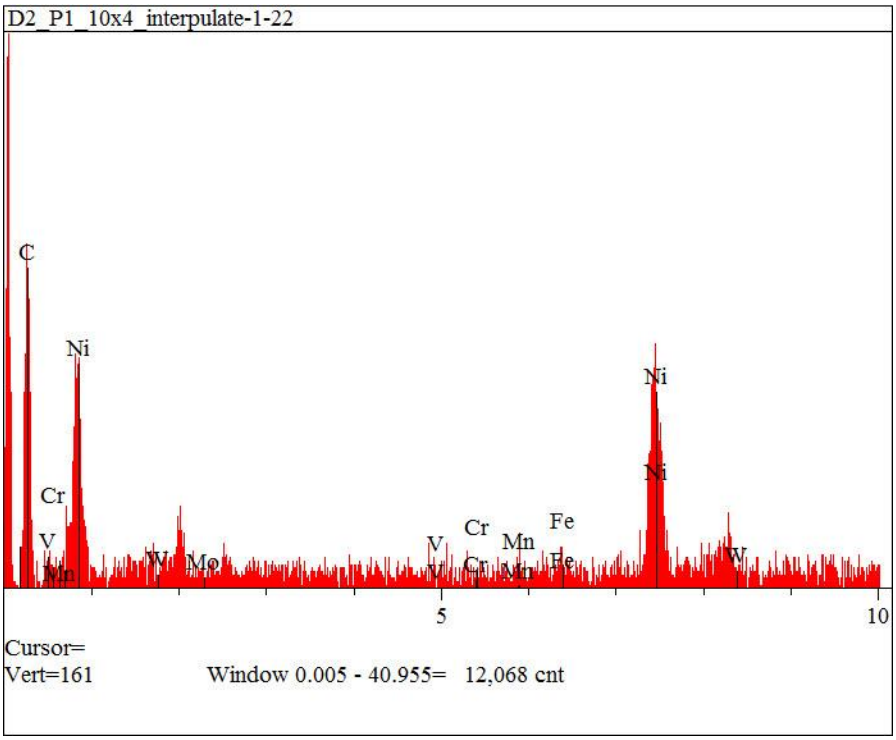
D2_P1_10x4_interpulate-1-22
C
Ni
Cr
V
Mn
W
Mo
V
Cr
Mn
Fe
Ni
Ni
W
5
10
Cursor=
Vert=161
Window 0.005 - 40.955= 12,068 cnt

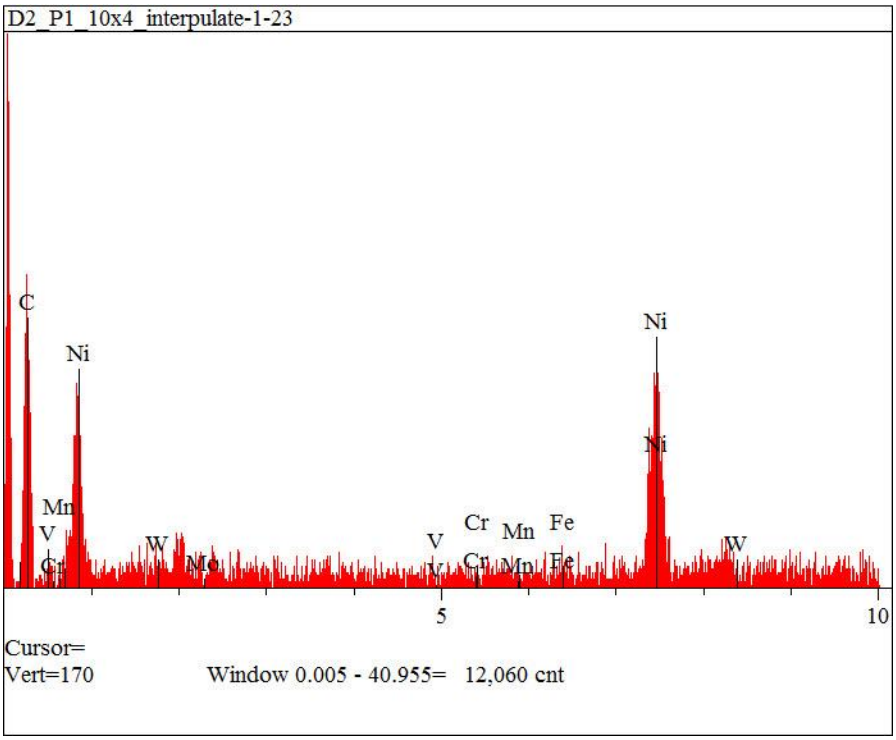
D2_P1_10x4_interpulate-1-23
C
Ni
Mn
V
Cr
W
Mo
V
Cr
Mn
Fe
Ni
Ni
W
5
10
Cursor=
Vert=170
Window 0.005 - 40.955= 12,060 cnt

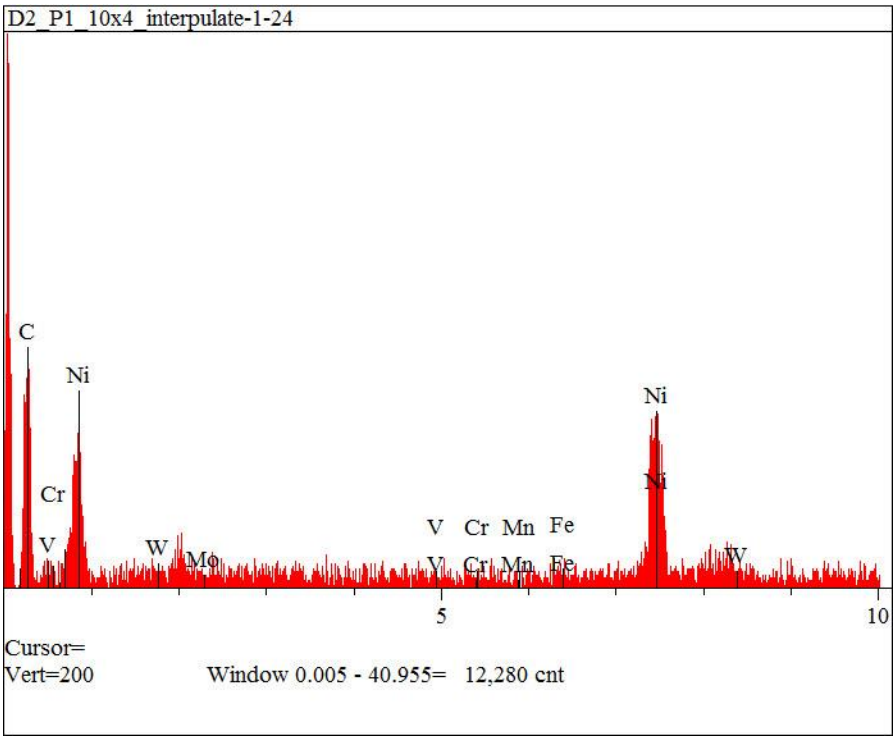
D2_P1_10x4_interpulate-1-24
C
Ni
Cr
V
W
Mo
V
Cr
Mn
Fe
Ni
Ni
W
5
10
Cursor=
Vert=200
Window 0.005 - 40.955= 12,280 cnt

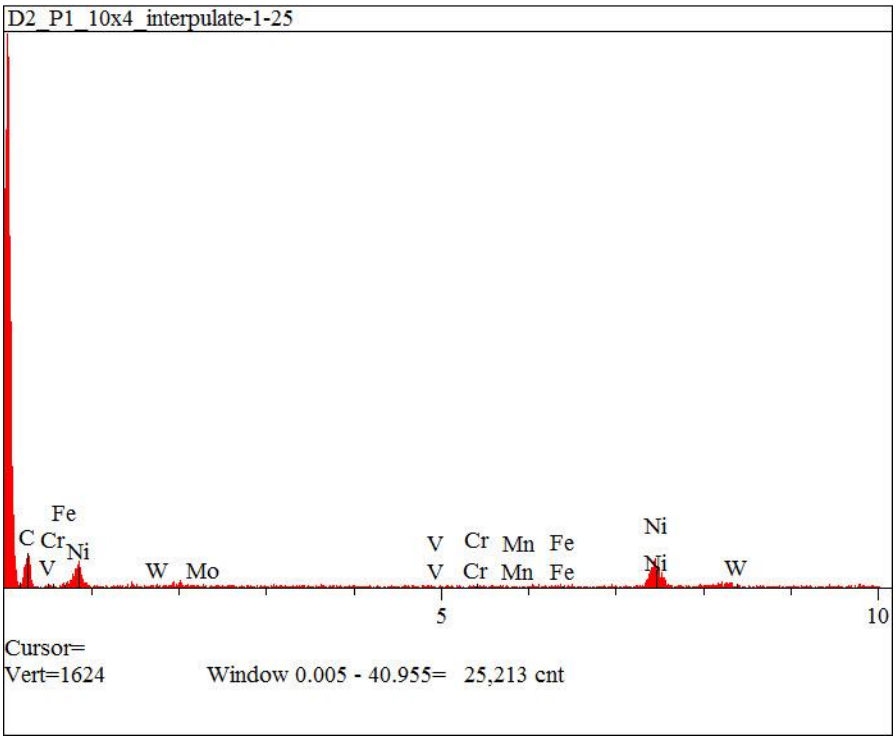
D2_P1_10x4_interpulate-1-25
C
Cr
V
Fe
Ni
W
Mo
V
Cr
Mn
Fe
Ni
5
10
Cursor=
Vert=1624
Window 0.005 - 40.955= 25,213 cnt

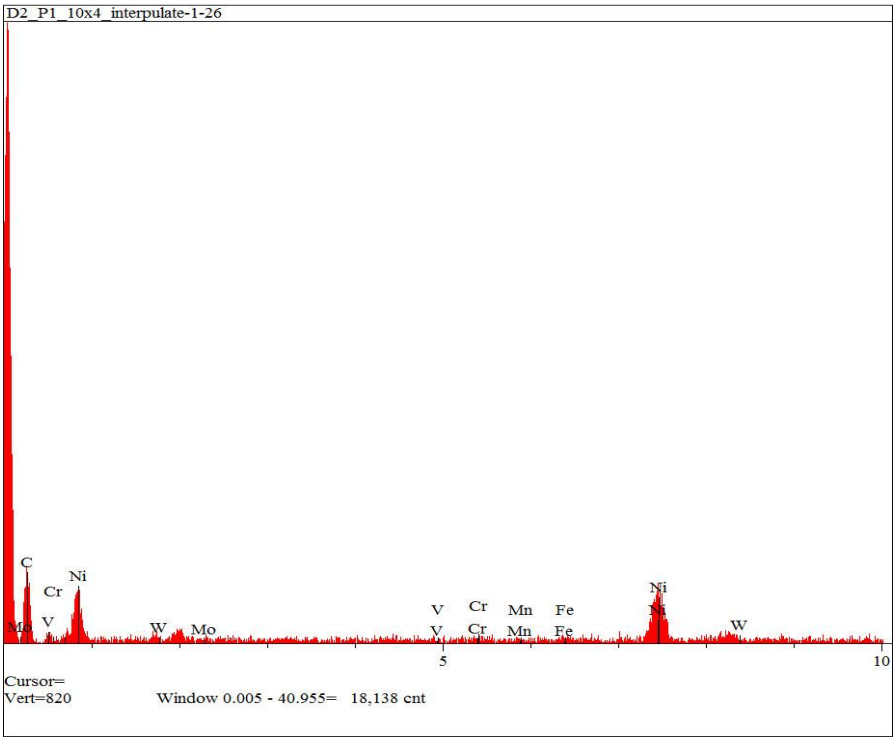
D2_P1_10x4_interpulate-1-26
C
Cr
V
Ni
Mo
W
Mo
V
Cr
Mn
Fe
Ni
W
5
10
Cursor=
Vert=820
Window 0.005 - 40.955= 18,138 cnt

Unconsolidated Powder P1 at 1700x

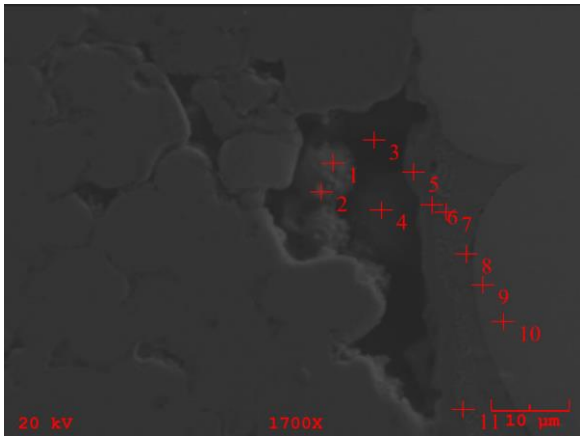

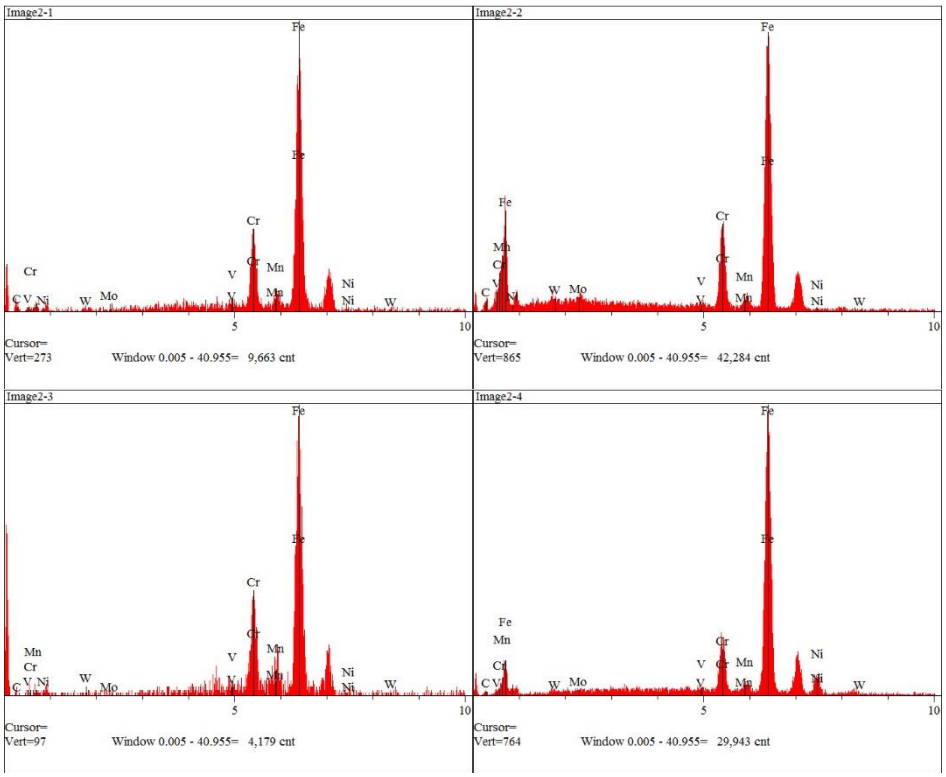

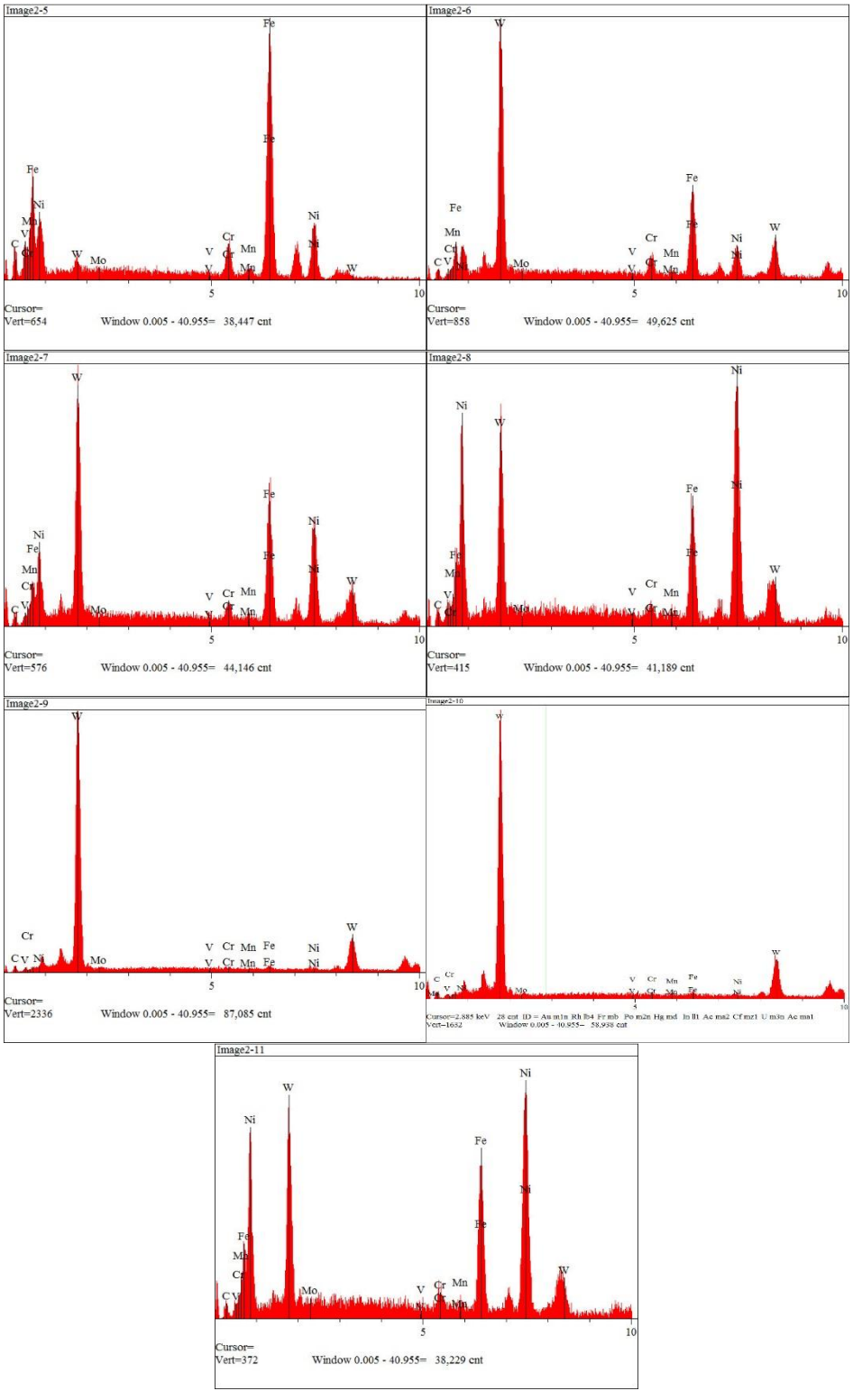
Image2-5
Cursor=
Vert=654
Window 0.005 - 40.955= 38,447 cnt
Image2-6
Cursor=
Vert=858
Window 0.005 - 40.955= 49,625 cnt
Image2-7
Cursor=
Vert=576
Window 0.005 - 40.955= 44,146 cnt
Image2-8
Cursor=
Vert=415
Window 0.005 - 40.955= 41,189 cnt
Image2-9
Cursor=
Vert=2336
Window 0.005 - 40.955= 87,085 cnt
Image2-10
Image2-11
Cursor=
Vert=372
Window 0.005 - 40.955= 38,229 cnt

APPENDIX E: D2 P1 10x4 EDS-IXRF Map at x450